DESIGN OF UNBAFFLED STIRRED TANK WITH CONCAVE BLADE IMPELLER

A thesis submitted

in partial fulfillment of the requirement for the degree of

Doctor of Philosophy

By

THIYAM TAMPHASANA DEVI

DEPARTMENT OF CIVIL ENGINEERING
INDIAN INSTITUTE OF TECHNOLOGY,
GUWAHATI – 781039 (INDIA)

JANUARY-2014

DESIGN OF UNBAFFLED STIRRED TANK WITH CONCAVE BLADE IMPELLER

A thesis submitted

in partial fulfillment of the requirement for degree of

Doctor of Philosophy

By

THIYAM TAMPHASANA DEVI

DEPARTMENT OF CIVIL ENGINEERING
INDIAN INSTITUTE OF TECHNOLOGY,
GUWAHATI – 781039 (INDIA)

JANUARY-2014

DECLARATION

I, hereby declare that the thesis titled **"Design of unbaffled stirred tank with Concave blade impeller"** submitted herein has been carried out by me in the Department of Civil Engineering of Indian Institute of Technology, Guwahati. The work is original and has not been submitted earlier as a whole or in part for the award of any degree/ diploma at this or any other Institute/ University.

Date:

Thiyam Tamphasana Devi
Registration No.: 10610410
Research Scholar
Department of Civil Engineering
Indian Institute of Technology Guwahati

CERTIFICATE

This is hereby certify that thesis entitled **"Design of unbaffled stirred tank with Concave blade impeller"** submitted by **Thiyam Tamphasana Devi** (Registration No.: 10610410) to the Indian Institute of Technology Guwahati for the award of the degree of Doctor of Philosophy is a record bonafide research work carried out by her under my supervision and guidance. The thesis work, in my opinion has reached the requisite standard fulfilling the requirements for award of the degree of Doctor of Philosophy.

This work has not been submitted earlier for the award of any degree or diploma to the best of my knowledge.

Date:

(**Dr. Bimlesh Kumar**)
Supervisor
Assistant Professor
Department of Civil Engineering
Indian Institute of Technology Guwahati

ACKNOWLEDGEMENTS

It would not have been possible to write this doctoral thesis without the help and support of the kind people around me, to only some of whom it is possible to give particular mention here.

Foremost, I would like to express my sincere gratitude and respect to my thesis supervisor Dr. Bimlesh Kumar, Assistant Professor, Department of Civil Engineering for the continuous support of my PhD study and research, for his patience, motivation, enthusiasm, and immense knowledge. His constant and excellent guidance helped me in all the time of research and writing of this thesis. I could not have imagined having a better advisor and mentor for my PhD study. I have been extremely lucky to have a supervisor who cared and inspired so much about my work, who made himself available all the time despite of his busy academic activities, and who responded to my questions and queries so promptly.

Besides my supervisor, I would like to express my sincere thanks to my Doctoral Committee members Prof. Subashisa Dutt, Dr. Ajay Kalamdhad and Dr. Debasish Das for their valuable suggestions, motivation, insightful comments and encouragement at various stages of my research work.

I am extremely honored to express my thankfulness to Dr. Praveen Kumar (Department of EEE, IITG) and Dr. Ajay Kalamdhad (Department of Civil Engineering, IITG) for their kind assistance to complete my laboratory work.

I wish to take this opportunity to put on record my respects to the Head of the Department, Professor S.K Deb (former) and Professor A.K. Sarma (present) for providing me various facilities during course of my research work. I also thank to all the office staffs of the department for extending their all possible help during my research work. My special thanks go to office staff Mr. Rajib Gogoi, who help me without hesitation to prepare official documents for applying financial assistance to attend conferences.

I also would like to acknowledge the financial support in terms of scholarship awarded by Ministry of Human Research and Development (MHRD) to pursue my doctoral studies and

financial assistance from Department of Biotechnology, MHRD, Government of India for attending international conference. I could not forget to acknowledge the academic and technical support of the Indian Institute of Technology Guwahati provided throughout my research work.

I thank the Editors and Reviewers of all my manuscript published in the respective Journals and Conferences proceedings for their valuable comments provided to improve my research study.

My sincere and grateful thanks are also to my friends Mr. Mahesh Patel, Ms. Thokchom Bebina Devi, Mr. Vishal Despande, Mr. Subadeep Chakraboty, Mr. Somesoran, Ms. Swati Bhave and Ms. Swapnali Barman for their kind support and help. I also would like to thank Bajal dada for his brotherly help during my thesis work.

I am extremely happy to thank Mr. Sanasam Robert Singh who extended all possible help, understanding, moral support and encouragement during my adverse situations of research work.

Last but not the least, I would like to thank my parents, my two brothers that I could not have realized this dream without the understanding and support given by them. I deeply appreciate the encouragement and moral support extended by them during my research work.

Thiyam Tamphasana Devi

ABSTRACT

The wide applicability of mechanically stirred tanks in industry demands a comprehensive understanding of hydrodynamics controlling the performance of these fundamental units. Standard Rushton impellers in baffled tanks are widely used in mechanically agitated reactors because of the high dispersion efficiency and its flexibility of operation. However, unbaffled tanks are used in many industrial stirred tank systems where the presence of baffles is undesirable. Both experimental investigations and computational studies to analyze the fluid flow hydrodynamics which often shows good potential for industrial use of unbaffled of stirred tanks. Unbaffled tanks are also advisable in crystallizers, where the presence of baffles may promote the particle attrition phenomenon. Unbaffled tanks give rise to higher fluid particle mass transfer rates for a given power consumption, which may be desirable in a number of processes. Regarding Rushton impeller, several researchers argue its inferior efficiency as compared with other types of impeller. Compared to the Rushton impeller, Concave blade impellers were reported to provide at least the same gas handling capacity, equivalent fluid homogenization performance, similar gas holdup characteristics and less power fluctuations. Impeller position (impeller clearance depth, C, when single impeller is used and bottom impeller clearance depth, C_1 and impeller spacing, C_2 when dual impeller is used) should be the major concern as an influencing parameter in impeller driven stirred system apart from other affecting parameters as the flow pattern generated inside the vessel is dependent on it. Not only the flow pattern but also the purpose of stirred tank is also dependent on it. Compared with single impeller, dual combination has more advantages, such as efficient gas distribution, longer gas phase residence time, increased gas hold-up, superior liquid flow characteristics and lower power consumption per impeller.

The aim of this research is to establish the design criteria for Concave blade impeller stirred unbaffled tank. This was accomplished through experimentation on unbaffled stirred tank in single and dual impeller with and without sparging system. The influence of impeller diameter (ratio of d/D is taken as 0.2, 0.3 & 0.4), impeller clearance depth (ratio of C/D is taken from 0.3 to 0.9 with 0.1 interval for single impeller and C_1/D of 0.15 to 0.85 with 0.05 interval for dual impeller) and spacing between two impeller (C_2/D of 0.2 to 0.8) are studied for the governing process dynamics at various impeller rotational speed (N=100 to 1200rpm).

Computational fluid dynamics (CFD) has been also used to assess the impact of different cases. Modified drag law considering turbulence nature of flow and degassing boundary condition was applied on the top surface of the tank (by developing user defined function). In numerical modeling, turbulence model was extended by using more advanced turbulence model (Large Eddy Simulation) in order to capture more realistic turbulent flow nature inside the stirred tank.

Dimensionless correlations were created from experimental data to act as a guide for future production scale stirred tank design. Furthermore, the correlations found from the experimental data in this study are of great benefit in the design of production scale stirred tank of Concave blade.

Another key aspect of the present work is to establish the stable flow pattern regime in unbaffled stirred tank with dual Concave blade impeller. The stable flow regime is generally found in available literature for Rushton impeller driven stirred tank. The stable flow regime has a profound effect on process dynamic governing the system. Experiments and numerical simulations done in the present work have shown that the optimal systems can be referred to the stable flow regime.

The comparative experiments of the unbaffled Concave blade system with baffled and Rushton impeller system has shown that higher mass transfer is produced by baffled system but consumes significant power than the unbaffled system. So, overall performance is found better by unbaffled system based on mass transfer rate and power consumption when the reduction of power consumption is a priority. Better mass transfer rate and lower power consumption is produced by Concave blade system as compared with Rushton type impeller system.

Keywords: design criteria, Concave blade, unbaffled stirred tank, dual impeller, impeller clearance depth, mass transfer rate, gassed power input, vortex depth

CONTENTS

LIST OF FIGURES

LISTS OF TABLES

Title **Captions** **Page No.**

NOTATIONS

Abbreviations

CFD=Computational Fluid Dynamics
DO=dissolved oxygen
LES=Large Eddy Simulation
MRF=Multiple Reference Frame
RANS=Reynolds Averaged Navier-Stokes
RNG=Renormalization Group
rpm=revolution per minute
rps=revolution per second
RSM=Reynolds Stress Model
SM=sliding model
TKE=turbulent Kinetic Energy
UDF=user defined functions

Symbols

$C_v = 0.5$

ϕ=diameter of holes in ring sparger [L^2]

η=efficiency [%]

ϕ_s=tube diameter of ring sparger [L^2]

U_i [LT^{-1}] mean velocity of i^{th} phase [LT^{-1}]

G_K = generation term [$ML^{-1}T^{-2}$]

$P_v = \dfrac{P_g}{V\gamma(g\upsilon)^{1/3}}$ = non-dimensional form of effective power per unit volume [-]

c_μ =0.09

σ_{lg} =0.75

σ_k =1

$c_{3\varepsilon}$ =1.2

$c_{3\varepsilon}$ =1.2

σ_ε =1.3

$c_{1\varepsilon}$ =1.44

$c_{2\varepsilon}$ =1.92

N_i =angular velocity of i^{th} phase [T^{-1}]

$\overline{u_i' u_j'}$ =average Reynolds stresses [$ML^{-1}T^{-2}$]

F_i =Coriolis and centrifugal forces [MLT^{-2}]

C_D =drag coefficient [-]

$\bar{\bar{\tau}}_{eff}$ =effective stresses [$ML^{-1}T^{-2}$]

u_i' =fluctuating velocity of i^{th} phase

$U_{g,\text{inlet}}$ =gas inlet velocity at ring sparger [LT^{-1}]

$\langle K_L a_{20} \rangle$ =global mass transfer coefficient at 20^0C [T^{-1}]

R_i =inter-phase forces [MLT^{-2}]

$\bar{\bar{\tau}}_{lam}$ =laminar stress [$ML^{-1}T^{-2}$]

U_i=mean velocity of i^{th} phase [LT^{-1}]

$k_c = K_L a_{20} \left(\upsilon / g^2 \right)^{1/3}$ =non-dimensional mass transfer parameter [-]

G_{kl} =rate of production of turbulent kinetic energy [$ML^{-1}T^{-2}$]

$X = Fr^{4/3} Re^{1/3} = N^3 d^2 / g^{4/3} \upsilon^{1/3}$ =theoretical power per unit volume [-]

$\bar{\bar{\tau}}_t$ =turbulent stress [$ML^{-1}T^{-2}$]

$\bar{\bar{I}}$ =unit tensor [-]

α =volume fraction [-]

A=constant in Equation 3.8

A=cross sectional area of vessel [L^2]

a=interfacial area [L^{-1}]

$A_{reactor}$=cross sectional area of tank [L^2]

$A_{sparger}$=cross sectional area of ring sparger [L^2]

b=width of blade [L]

C=impeller clearance depth [L]

C_0=initial concentration of dissolved oxygen at any time [ppm]

c_1=1.44

C_1=lower impeller clearance depth [L]

c_2=1.92

C_2=spacing between two impellers [L]

C_3=height of upper impeller measured from top of tank [L]

$C_{kL}a$, a, b=constants in Equation 2.46 [-]

C_s=saturation of dissolved oxygen at test conditions [ppm]

C_t = concentration of dissolved oxygen at any time t [ppm]

c_μ=0.09

d=diameter of impeller [L]

D=diameter of tank [L]

d_b=bubble diameter [L]

D_g= coefficient of gas diffusivity [L^2T^{-1}]

D_l = coefficient of gas diffusivity [L^2T^{-1}]

ds=diameter of ring sparger [L^2]

$Fl=Q_g/Nd^3$=flow number [-]

$Fr= Nd^2/g$=Froude number [-]

g=9.81= acceleration due to gravity [LT^{-2}]

$Ga=Re^2/Fr$=Galineo number [-]

h=height of sparger from tank bottom [L]

H=height of water [L]

H_G=height of water after aeration [L]

I=current [$ML^2T^{-2}Q$]

k =turbulent kinetic energy [L^2T^{-2}]

K=constant in Equation 3.33 [-]

K=exchange coefficient of Equation 2.39 [$ML^{-3}T^{-1}$]
K_L=liquid film mass transfer coefficient [T^{-1}]
$K_La_{20=}$mass transfer coefficient at 20^0C temperature [T^{-1}]
$K_La_{T=}$mass transfer coefficient at any temperature [T^{-1}]
l=length of blade [L]
L=length-scale characteristic [L]
N=impeller speed [T^{-1}]
n=number of rotor blades=6
N_c=critical speed [s^{-1}]
$N_p=\frac{P_{eff}}{\rho N^3 d^5}$ =power number [-]
p =pressure [$ML^{-1}T^{-2}$]
P=power input [ML^{-1}]
P_{eff}=effective power [ML^{-1}]
P_f=power factor [-]
P_g/P_u= relative power draw [-]
P_g=gassed power input [ML^{-1}]
$P_{operating}$=operating pressure=101235 [$ML^{-1}T^{-2}$]
$P_{sparger}$=pressure at sparger [$ML^{-1}T^{-2}$]
P_u=ungassed power input [ML^{-1}]
Q_g=volumetric gas flow rate [L^3T^{-1}]
r=radial distance [L]
r_0=critical radius [L]
$Re=Nd^2/v$=Reynolds number [-]
Re_p=relative Reynolds number [-]
S=height of upper impeller from tank bottom [L]
s=surface renewal rate [T^{-1}]
T=temperature [^{0}C]
t=time [T]
t_0=initial time [T]
t_e =contact time [-]
u'=turbulent velocity characteristic [LT^{-1}]
u=axial velocity [LT-1]
$u_{slip}=u_g-u_l$=slip velocity [LT^{-1}]
$u_{tip}=\pi Nd$ [-]
v=radial velocity [LT^{-1}]
V=volume of tank [L^3]
V_d=vortex depth [L]
$v_g=Q_g/A$=superficial gas velocity [LT^{-1}]
V_t=voltage [QT^{-1}] used in Equation 2.19
We=Weber number [-]
z=axial height [L]
γ=unit weight of fluid [$ML^{-2}T^{-2}$]
Δp=pressure difference [$ML^{-1}T^{-2}$]
ε =dissipation rate [L^2T^{-3}]

ε_G=gas hold up [-]
θ=1.024 [-] used in Equation 2.8
θ=angular co-ordinate [degree]
μ =dynamic viscosity of fluid [$ML^{-1}T^{-1}$]
μ_t= turbulent viscosity [$ML^{-1}T^{-1}$]
ν= kinematic viscosity [L^2T^{-1}]
π=3.14
ρ=998.2=density of fluid [ML^{-3}]
ρ_a =density of air [ML^{-3}]
ρ_w=density of water [ML^{-3}]
σ_k=1
σ_ε=1.314.
τ=torque [ML^2T^{-2}]

Subscript
i,*j*,*k*=phase number & co-ordinate system
eff =effective
g =gas
l =liquid
lam =laminar
t =turbulent

CHAPTER 1

INTRODUCTION

The performance of stirred vessels has been the subject of research by a great number of investigators as these have been extensively used for mixing in the chemical, food, petroleum and pharmaceutical industries (Charpentier, 1981; Kawase and Moo-Young, 1988; Gracia-Ocha and Gomez, 1998; Fujasova et al., 2007). Popular applications are fermentation (Gracia-Ochoa and Gomez, 1998; Vaconcelos et al., 2000; Fujasova et al., 2007; Scargiali et al., 2007; Cabaret et al., 2008; Hoffmann et al., 2008), carbonation, oxidation (Oldshue, 1983; Scargiali et al., 2007), chlorination (Oldshue, 1983; Fujasova et al., 2007; Scargiali et al., 2007), hydrogenation (Shewale and Pandit, 2006; Fujasova et al., 2007; Murthy et al., 2007; Scargiali et al., 2007), dissolution, polymerization (Shewale and Pandit, 2006), chemical synthesis, and wastewater treatment (Ogut and Hatch, 1988; Shewale and Pandit, 2006; Cabaret et al., 2008).

About 50% of all chemical productions, by value, take place in stirred vessels representing an annual turnover value of €1370 billion worldwide indicating the importance of stirred tank reactors (Butcher and Eagles, 2002). The correct design and operation of these reactors can be crucial to the profitability of a process by virtue of its influence on the reaction yield or productivity. It has been documented that the cost of poor mixing in a large chemical company could be as high as $100 million per year (Paul et al., 2004). The significant impact of mixing problems on the operating costs of any process and the economical benefits derived from any improved mixing technology are a clear motivation to perform research on this main unit operation. The modification of existing stirred reactors for better efficiency, as well as the design of new mixing systems or new type of impellers, requires an accurate knowledge of the flows induced by the impellers in the vessel. Over the years a great deal of effort has been devoted to the optimization of mixing processes in stirred tanks with respect to power consumption, mass transfer and other process variables (Benkreira, 1990). For a particular mixing system, vessels with different geometries employing a variety of impeller types have been used. However, there is no universal design of impeller or mixing tank

which can be employed for all mixing applications. This necessity has urged investigators to undertake many experimental investigations.

1.1. Stirred tank

Figure 1.1 shows single impeller system with unbaffled single phase (left) and dual impeller system of sparged condition with ring sparger (right). In literature, generally height of water (H) is made equal to tank diameter (D) (Smith, 1991) with impeller position (C) at 0.3D and impeller diameter (d) of 0.3D (Scargiali et al, 2013). Blade height (b) is made 0.2d with blade length of 0.25d. Number of blade is maintained at 6. This is for single impeller system. For dual impeller system, the changes will be at lower impeller clearance depth (C_1) and their spacing (C_2). A stirred tank can be operated with or without sparger. A condition of stirred tank operated with sparger is termed as gassed or sparged system where additional gas is supplied through sparger (may be ring sparger or internal draft tube). Stirred tank of ungassed condition is termed as single phase and gassed condition is as multiphase (such as two phase system or gas-liquid phase system when gas and liquid is used as operating fluid). Stirred tank can also be employed one or more impeller on the same shaft with or without baffles. Stirred tank operated without baffle is termed as unbaffled stirred tank system.

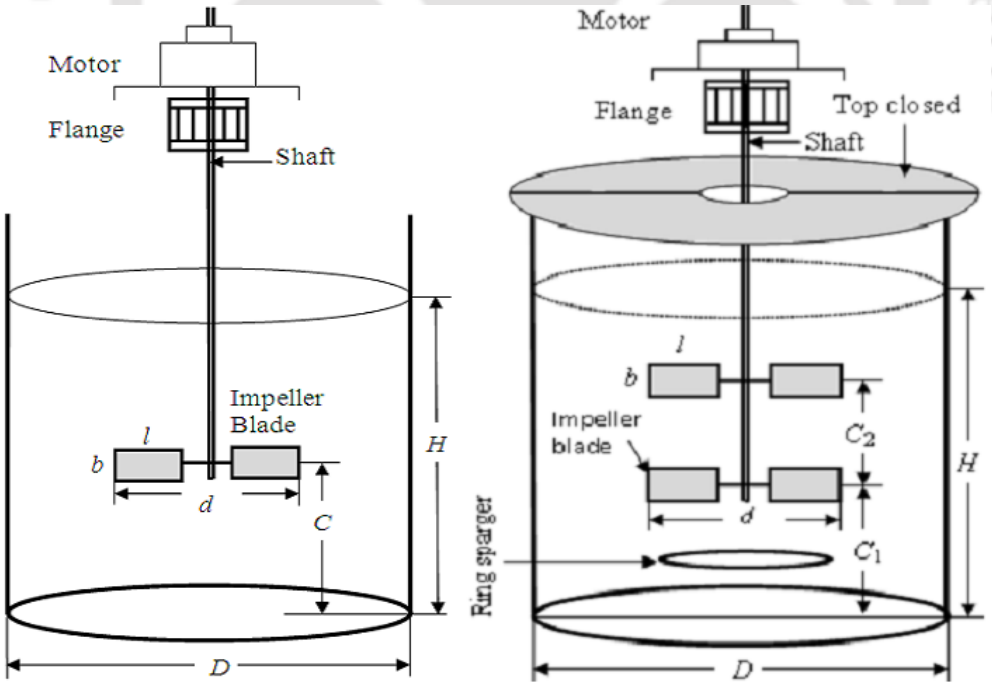

Figure 1.1: Schematic diagram of unbaffled stirred tank of single impeller in un-sparged (left) and dual impeller in sparged condition with ring sparger (right)

1.2. Types of impeller

Impeller is an important integral part of a stirred tank. According to Paul et al. (2004), impellers are broadly classified as following (Table 1.1):

Table 1.1: Types of impeller with their specific types (Paul et al., 2004)

Impeller types	Specific types
Axial flow	Propeller, pitched blade turbine, hydrofoils
Radial flow	Flat-blade impeller, disk turbine (Rushton), hollow-blade turbine(Smith)
High shear	Cowles, disk, bar, pointed blade impeller
Specialty	Retreat curve impeller, sweptback impeller, spring impeller, glass-lined turbines
Up/down	Disks, plate, circles

As far as chemical/bio-chemical operations are concerned, impellers belonging to distinct hydrodynamic behaviors can be represented in Figure 1.2a (radial flow impeller) and 1.2b (axial flow impeller).

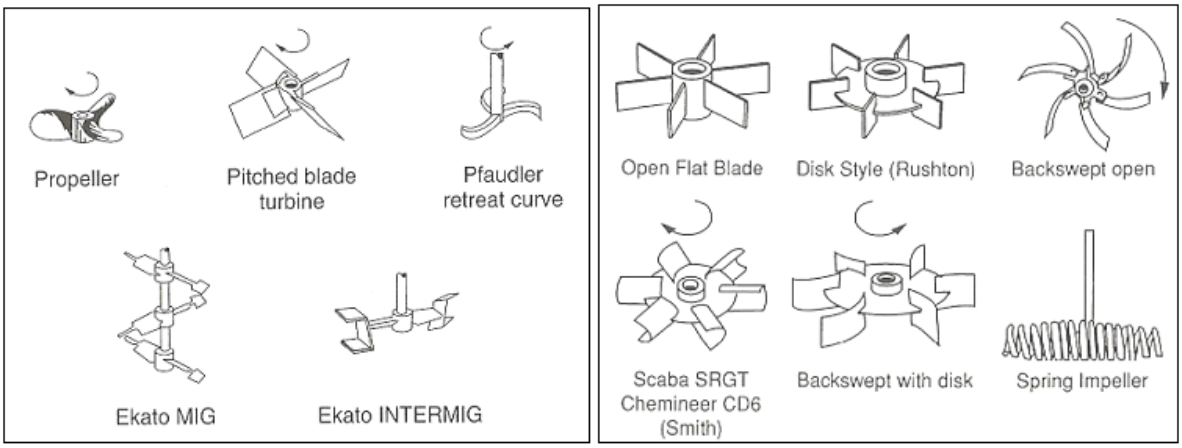

(a) Axial flow impeller (b) Radial flow impeller

Figure 1.2: Types of impeller with their specific types (Paul et al., 2004)

Several types of impellers are available and they are usually derived from standard impellers by changing in shape, size, number of blade and its angular orientation, etc. The ongoing demand for the improved impeller designs usually comes from the users of industrial mixing equipment when the vessels are to be designed for new plants or improvement in the existing design is desired for enhancing quality, capacity, process efficiency and energy efficiency (Kumaresan and Joshi, 2006). Flow patterns are associated with impeller types and forms

different flow patterns i.e., radial flow impeller forms radial flow pattern and axial flow impeller forms axial flow pattern which is shown in Figure 1.3. The blades of a radial flow impeller are parallel to the stirrer shaft and tank walls. When fluid comes in contact with the motion of these impellers, the fluid is dispersed toward the tank walls, or in a radial direction.

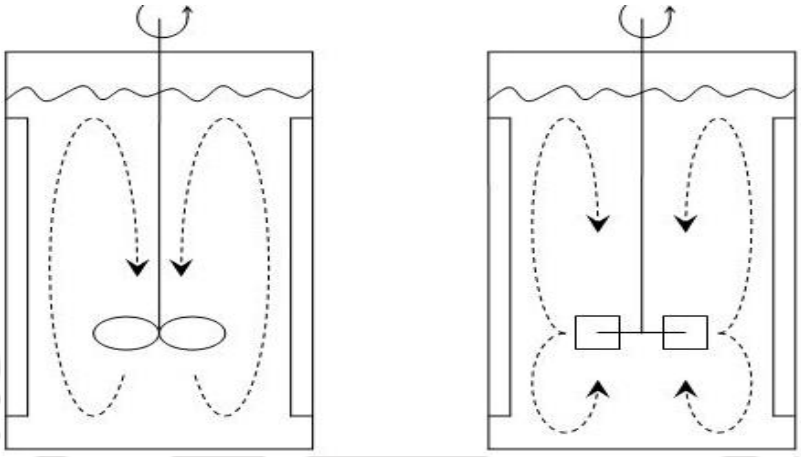

Axial flow pattern Radial flow pattern

Figure 1.3: Typical diagram showing flow pattern generated by axial impellers (left) and radial impellers (right)

Using of standard impeller (Rushton) in stirred tank reactor is very common but several researchers argue its inferior efficiency (Nienow, 1996; Yoshida et al., 1996; Myers et al., 1999; Bakker, 2000; Sardeing et al., 2004; Albaek et al., 2008; Gimbun et al., 2009; Ahmed et al., 2010; Suhaili et al., 2010 & 2011) as compared with other types of impeller. The concept of modifying the flat blade into concave blade was originally introduced by Van't Reit (1976). In practice, the drive motor of a Rushton impeller needs to be sized to cope with the full-speed ungassed situation. Consequently, less than about 50% of the installed power of the motor is put to effective use during normal operations. Since the gas-liquid mass transfer coefficient is directly related to the power input from the impeller (Westerterp et al., 1963, Van't Riet, 1979), there is a considerable potential for mass transfer which is not fully utilized. The fall in the gassed power is due to the gas-filled cavity structure formed behind the blades of the Rushton impeller (Van't Riet and Smith, 1973, Bruijn et al., 1974, Myers et al., 1999; Gimbun et al., 2009, Suhailli et al., 2011). Van't Riet et al. (1976) first showed that the power decrease on gassing can be significantly reduced by replacing the six flat plates of the Rushton turbine with pipe segments concave in the direction of rotation. This reduction

of the power drop was because of the fact that the concave geometry of the blades did not allow large cavities to form easily at low gas flow rate; while at higher gas flow rates, the cavities behind the concave blades have smaller dimensions compared to those behind standard flat blades (Van't Riet et al., 1976). Since then, impellers with different kinds of concave blades have been reported, including impellers with blade shape close to (Van't Riet et al., 1976, Smith and Katsanevakis, 1993, Mishra and Joshi, 1993) or equal to a semicircle (Warmoeskerken and Smith, 1989; Linek et al., 1991; Rielly et al., 1992; Karcz and Kaminska-Brzoska, 1994; Myers et al., 1994; Mhetras et al., 1994; Bakker et al., 1994) and approximately parabolic as in the case of a Scaba 6SRGT (Cooke et al., 1988, Nienow, 1990, Saito et al., 1992, Galindo and Nienow, 1993, Hjorth, 1994, Nienow et al, 1995, Nienow, 1996, Bujalski et al, 1996). For low viscosity liquids, the gassed power ratio, i.e., P_g/P_u in the fully turbulent region and at high aeration rates was reported to be about 0.7 and 1 for semi-circular blade impellers (Warmoeskerken and Smith, 1989) and the Scaba 6SRGT (Saito et al., 1992), respectively, while the Rushton turbine gives P_g/P_u of around 0.4 (Warmoeskerken and Smith, 1989, Galindo and Nienow, 1993). Such a relatively high gassed power ratio for concave blade impellers significantly facilitates the design and operation of the agitators. The gassed power ratio for the Scaba 6SRGT in medium and high viscosity liquids was also much higher than that for the Rushton impeller (Galindo and Nienow, 1993). Further, compared to the Rushton impeller, concave blade impellers were reported to provide at least the same gas handling capacity (Saito et al., 1992, Bakker et al., 1994), equivalent fluid homogenization performance (Saito et al., 1992), similar gas holdup characteristics (Saito et al., 1992, Bakker et al., 1994) and less torque fluctuations (Bujalski et al, 1996). Better performance in agitated boiling systems and gas-inducing impeller agitated reactors by replacing the Rushton turbine with the concave blade impellers have also been reported (Rielly et al., 1992; Smith and Katsanevakis, 1993; Suhaili et al., 2011; Verma and Tyagi, 2012) and have shown that heat transfer coefficients in a jacketed tank using concave and convex semicircular blade impellers were about 15% and 10% lower, respectively, than those using the Rushton impeller. Warmoeskerken and Smith (1989) reported that the gas-liquid mass transfer in an agitated tank due to a semi-circular blade impeller is at least 20% higher than that of a Rushton impeller at the high power dissipation levels. The reason of improved performance by concave blade impeller over the flat impeller was explained by

Warmoeskerken and Smith (1989) and Gimbun et al. (2009) saying that concave blade reduces cavity formation behind the blades. By using geometrically similar vessel and impeller as those used by Warmoeskerken and Smith (1989), Linek et al. (1991) found that a simple exchange of the Rushton turbine for the semi-circular blade impeller resulted in an insignificant decrease in the mass transfer coefficient under the same gassed power level and gas flow rate in water.

1.3. Impeller position

Impeller position (impeller clearance depth, C, when single impeller is employed or lower impeller clearance depth, C_1, and impeller spacing, C_2, when dual impeller is employed) should be the major concern geometric parameter (Zundelevich, 1979; Joshi, 1980; Saravanan et al., 1994; Mohammed et al., 2008; Cheng et al., 2012) in impeller driven stirred system apart from other affecting parameters as the flow pattern generated inside the vessel is majorly dependent on it. Unfortunately, the influences of impeller clearance and their spacing are seldom reported in literature (Chudacek, 1985). There are few studies (Chudacek, 1985; Rutherford et al, 1996; Yoshida et al., 2002; Garcia-Cortes et al., 2004) which are devoted on impeller position. Most studies have been carried out at the standard impeller clearance (one-third of the tank diameter). However, literature (Bates et al., 1963; Saravanan et al., 1998; Montante et al., 2001; Yoshida et al., 2002; Ameur et al., 2011) suggests that the impeller clearance does affect the fluid flow pattern. The impeller clearance (often expressed in relative terms as the impeller off-bottom clearance to tank diameter ratio, C/D) significantly influences hydrodynamics. Literature suggests the two hydrodynamic regimes depending on the impeller clearance. At high values of these variable, large vortices above and below the impeller are present. At low values, the lower vortices are absent. Also, the decrease of the power consumption in this region can be noticeable, since a considerable amount of power dissipated is caused by the vortices below the impeller. Conti et al. (1981) noted that by lowering C, the hydrodynamic regime changed from one with large vortices above and below the impeller (the so-called dual-eight figure) to that where the lower vortices were absent (single-eight) with Rushton turbine. The value of C at which the change occurred was always equal to about $0.22D$ in the various systems examined. The power decrease at $C/D = 0.22$ was very considerable. The results showed that the dissipated power were strongly dependent on the hydrodynamic regime. Gray (1987) also found that the dependence of the power on

the type of impeller was highly dependent upon the pattern observed. For the same flow pattern, the dependence was found to be similar for each type of impeller (radial or axial). For disk impellers, the pattern change was found to occur at C/D = 0.22 as found by Conti et al (1981) for eight-blade flat-blade disk turbine agitating in flat bottom tanks. For six-blade flat-blade impellers, the flow pattern changed at C/D = 0.17, similarly to that observed by Nienow (1968), for six-blade flat-disk impellers. Axial-flow impellers maintained the "single-eight" flow pattern for propellers up to C/D = 0.35 in a flat bottom tank. Armenante and Li (1993) noted that for the case of one radial-flow impeller the flow pattern below the impeller was a function of the impeller clearance of the tank bottom. For low C/D values (corresponding to C/D< 0.21), the flow pattern was observed to be swirling outwards of the tank. For high values of C/D (corresponding to C/D>0.26), the swirling action turned inward. For intermediate values of C/D, a transition region consisting of an unstable flow pattern was noticed. The value of the impeller clearance, at which this hydrodynamic change occurs, depends on the impeller type. The dual impeller configuration is often used in stirred tanks to enhance the overall performance of the system. Compared with single impellers, dual combination has more advantages, such as efficient gas distribution, longer gas phase residence time, increased gas hold-up, superior liquid flow (plug flow) characteristics, and lower power consumption per impeller (Gogate et al., 2000). Mohammed et al (2008) also explained why dual impeller is more efficient than single impeller system in terms of gas induction. They explained that the rate of gas induction decreases with increase in the impeller submergence from the top. Therefore, the impeller needs to be close to the surface as possible but in contrast to this the dispersion ability of the impeller decreases as the impeller is brought closer to the liquid surface. Such kind of limitation of the single impeller system can be overcome by using a dual impeller system. The top impeller acts as a gas-inducing impeller, and the second impeller distributes the gas bubbles throughout the vessel. Thus the functions of gas introduction and gas dispersion are assigned to two impellers. Another advantage of second impeller is that when the bottom impeller is closer to tank bottom, it is more effective for the purpose of solid suspension (Mohammed et al., 2008). Thus, the induction, the dispersion, and suspension ability of the two impeller system are far superior to those of the single impeller system which motivates the research work on two impeller systems. As each impeller produces its own flow pattern, the coupling becomes

more intricate and the regularities in single systems are no longer valid for dual impeller combinations. Consequently the research on dual impeller systems is with great significance. The flow pattern created by impeller is the major concern in dual impeller system as the other governing process parameters (mass transfer rate, power consumption, gas hold up, etc) are eventually affected by the pattern of flow generated. The flow patterns are very important to the mixing efficiency in stirred reactors; especially with impeller more than one is employed (Taghavi et al., 2011). These flow patterns are majorly dependent on the impeller clearances (C_1 or C_3) and their spacing (C_2). The spacing between two impellers, C_2, determines the degree of interaction between the impeller discharge streams (Chunmei et al., 2008). According to the specific C_1 and C_2 value, the flow pattern may be classified as parallel, merging and diverging flow pattern (Rutherford et al, 1996). These three flow patterns are known as stable flow pattern because it produces stabilized liquid flow circulation which is very important in order to sustain the vessel from rupture or damage caused from unstable flow generation. Saravanan et al. (1994) studied on impeller bottom clearance (C_1) and spacing (C_2); and found that the rate of gas induction decreases with increase in impeller bottom clearance from bottom but it increases when impeller spacing is decreased. They explained the reason for the first cause as that decreasing the bottom clearance will cut the bubbles profile in the region between the tank bottom and the lower impeller that led to increase the momentum of eddies near the surface impeller and hence increasing the vacuum near the impeller tip so higher gas rate induction is occurred.

1.4. Baffled and unbaffled

Most industrial stirred vessels are equipped with baffles aimed at breaking undesired tangential velocity components, so avoiding the formation of a pronounced central vortex at high angular speeds. Moreover the presence of baffles increases axial and radial velocities so guaranteeing a better circulation and faster mixing than in their absence (Nagata, 1975). Although baffled tanks are widely used in industrial applications, there are cases in which the use of unbaffled tanks may be desirable. For example removing the baffles will change the flow characteristics and therefore the mixing rate, thus altering the effectiveness of the tank design for reaction and phase contacting processes (Glover and Fitzpatrick, 2007). Unbaffled systems are, infact, employed for specific applications (Pacek et al., 2001; Assirelli et al., 2008) where the presence of baffles results into drawbacks. Baffled tanks give rise to dead

zones, actually worsening the mixing performance of an aeration system (Nagata, 1975). For example, in the food and pharmaceutical industries it is a matter of primary importance to keep the reactor as clean as possible; in crystallization processes (Hekmat et al., 2007) and biological applications (Aloi and Cherry, 1996) shear and impact are to be minimized; in precipitation processes baffles may suffer from incrustation problems (Rousseaux et al., 2001). Scientific literature shows an increasing interest towards unbaffled stirred vessels: both experimental investigations (Pinelli et al., 2001; Abatan et al., 2006; Kagoshima and Mann, 2006; Montante et al., 2006; Rao and Kumar, 2007; Tezura et al., 2007; Galletti and Brunazzi, 2008; Shan et al., 2008a; Yoshida et al., 2008; Hirata et al., 2009; Brucato et al., 2010; Tamburini et al., 2011b, 2012b; Wang et al., 2012) and computational studies (to analyze the fluid flow hydrodynamics) (Armenante et al., 1997; Shekhar and Jayanti, 2002; Alcamo et al., 2005; Sbrizzai et al., 2006; Glover and Fitzpatrick, 2007; Assirelli et al., 2008; Mahmud et al., 2009; Ciofalo et al., 1996; Lamberto et al., 1999, 2001; Shekhar and Jayanti, 2002; Derksen, 2004, 2006; Alcamo et al., 2005; Cokljat et al., 2006; Sbrizzai et al., 2006; Shan et al., 2008b) were carried out, often showing good potential for some industrial use of such type of stirred tanks. For example, Brucato et al. (2010) found that the minimum power requirements for complete suspension in top-covered unbaffled vessels are lower than those in corresponding baffled tanks. Literature also suggests higher values of the mass transfer coefficient obtained in unbaffled vessels, at the same value of mechanical power dissipation than baffled tanks (Grisafi et al., 1994; Yoshida et al., 2008; Rao and Kumar, 2009).

1.5. Scale up

Designing stirred tanks for industrial use, one may require scale-up criteria for different process parameters, which include mass transfer, power consumption, vortex, gas holdup etc… The objective of doing studies on stirred tank is to interpret laboratory results into information necessary for the field installation. This means scaling up of laboratory geometric, dynamic and physical parameters for the field installation. It requires a geometrical similarity condition that is to say that the field installation should be built on a definite geometric ratio of the laboratory setup. "Scale-up" is an inherent part of process development. Using the definition by Bisio and Kabel (1985) scale-up can be defined as: 'the successful startup and operation of a commercial unit whose design and operation procedures

are in part based upon experimentation and demonstration at a smaller scale of operation." Scale-up has been successfully achieved when yields and productivities, previously demonstrated on a small scale, have been produced in larger capacity units. "Scale-up" is an inherent part of process development; in fact the terms are virtually synonymous for many people. Generally, two basic approaches to scale-up are available; first, extrapolation of model experiments based on the principles of similitude and, second, mathematical analysis of the complete (or controlling) mechanism (Johnstone and Thring, 1957; Metzner and Pigford, 1958). While the second of these has unlimited potential value, it also has serious limitations in practice. Often the relationships are too involved to permit rigorous definition or the resultant mathematical expressions are too complex for economical solution, even with computing equipment. This leaves us with scale-up from model experiments by the principles of similitude as the main technique in practice. To scale-up by similitude, one must first establish some functional relationship between the various dimensionless parameters, which can be used to characterize the system. Process characteristics that have been suggested to be maintained constant during scale-up include:

1. Reactor geometry
2. Mass transfer rate (mass transfer coefficient, $K_L a_T$)
3. Power input (Power number, N_p and gassed power (P_g) per unit volume of liquid)
4. Gas flow rate (Volumetric gas flow rate per unit volume of liquid, Q_g/V, Superficial gas velocity, v_g)
5. Viscosity of fluid, v, and gravitational force, g (Reynolds number, Re and Froude number, Fr)

Criterion 1 was based on known empirical correlations for scale-up that have been developed experimentally for reactors with similar geometries. Reactor geometry consists of different geometrical parameters such as impeller diameter, tank diameter, dimensions of blade, the height of liquid and the tank. Knowledge of gas-liquid mass transfer and therefore volumetric gas-liquid mass transfer coefficient ($K_L a_T$) is very important in designing or in the scale-up of stirred tank reactors. Constant $K_L a_T$ ensures equal mass transfer rates at the various scales of operation. In the literature, $K_L a_T$ is correlated either by using dimensionless groups (Smith and Warmoeskerken, 1985; Smith, 1991) or energy input criterion (Smith et al., 1977; Van't

Riet, 1979; Hickman, 1988; Whiton and Nienow, 1993) based on Kolmogoroff's theory. Applying the approach of dimensional analysis, thus mass transfer can be correlated to as follows (Yawalkar et al., 2002):

$$\left.\begin{array}{l} \text{for single phase } K_L a_T = f\left(Re, Fr, \text{geometrical parameters}\right) \\ \text{for gas-liquid phase } K_L a_T = f\left(Re, Fr, FI, \text{geometrical parameters}\right) \end{array}\right\} \quad (1.1)$$

Another approach, which is based on energy input criterion are of the form (Calderbank, 1958; Van't Riet, 1979; Smith et al., 1977; Smith and Warmoeskerken, 1985; Linek et al., 1987; Hickman, 1988; Smith, 1991; Whitton and Nienow, 1993; Zhu et al., 2001; Yawalkar et al., 2002) as:

$$\left.\begin{array}{l} \text{for single phase } K_L a_T = f\left(P/V\right) \\ \text{for gas-liquid phase } K_L a_T = f\left(P/V, V_g\right) \end{array}\right\} \quad (1.2)$$

One of the significant design parameters for a stirred tank reactor is the power draw by the agitator which is affected by the physical properties, operating parameters, and geometrical parameters. It is defined as the amount of energy necessary in a period of time, in order to generate the movement of the fluid within a vessel by means of mechanical or pneumatic agitation (Taghavi et al., 2011). Economic selection criteria for an impeller are greatly influenced by the power input for stirred tank application. Equal N_p and P_g/V has been used in several fermentation studies as a scale-up parameter in shear-sensitive operations. The mechanical agitation power requirements of an ungassed (single phase using water as operating fluid) Newtonian liquid can be predicted fairly well from semi-theoretical correlations of the Power Number, N_p ($= \dfrac{P_{eff}}{\rho N^3 d^5}$, where P_{eff} is the effective power input in single phase, N is impeller speed, ρ is density of liquid) with the Reynolds Number and Froude number (Rushton et al.,1950; Holland and Chapman, 1966; Houcine and David, 2000; Deshmukh and Joshi, 2006; Tahgavi et al., 2011) as:

$$Np = f(Re, Fr, \text{geometrical parameters}) \quad (1.3)$$

Turbulence and viscous effects can be described by Reynolds number (*Re*) and the surface wave action can be described by Froude number (*Fr*). Hence, both *Re* and *Fr* are important to

stirred tank. As the effects of gravitational force are negligible in baffled tank (Nagata, 1975; Novak et al., 1982); so *Fr* can be eliminated. In the case of unbaffled stirred tanks, inclusion of *Fr* in any scale-up criteria is necessary to characterize the fluid motion in the absence of baffles. The influence of *Fr* becomes important in unbaffled system because of the vortex formation which increases *Re*, therefore, inclusion of *Fr* for understanding of N_p in unbaffled system is needed (Bates et al., 1963; Houcine and David, 2000). Contrary to single phase system, it is difficult to predict power demand in gas-liquid systems. It is well known that in similar conditions, i.e., at equal impeller speeds, the gassed power consumption is lower than that in the ungassed system. Researchers (Bouaif and Roustan, 2001; Lane et al., 2005; Martin et al., 2008 & 2010; Taghavi et al., 2011) have proposed different correlations to quantify the gassed power input (gas-liquid phase). The power draw in gas-liquid systems is estimated in terms of relative power draw (ratio of gassed to ungassed power input) for understanding the power characteristics of gassed condition with ungassed condition. Gassed to ungassed power (P_g/P_u) in dimensionless form can be correlated with *Re*, *Fr*, *Fl* with other geometrical parameters (Taghavi et al., 2011) and is given as:

$$\frac{P_g}{P_u} = f\left(Re, Fr, Fl, \text{ geometrical parameters}\right) \tag{1.4}$$

Vortex is produced due to centrifugal force acting on the rotating liquid. Vortex depth (V_d) is the depth of vortex measured from free water surface to the maximum depression depth at the centre of the tank (Figure 1.4) and is a function of *Re* and *Fr* (Wong and Hayduk, 1987) with other geometrical parameters (Reiger et al., 1979; Markopoulos and Kontogeorgaki, 1995) and can be written as:

$$V_d = f\left(Re, Fr, \text{geometrical parameters}\right) \tag{1.5}$$

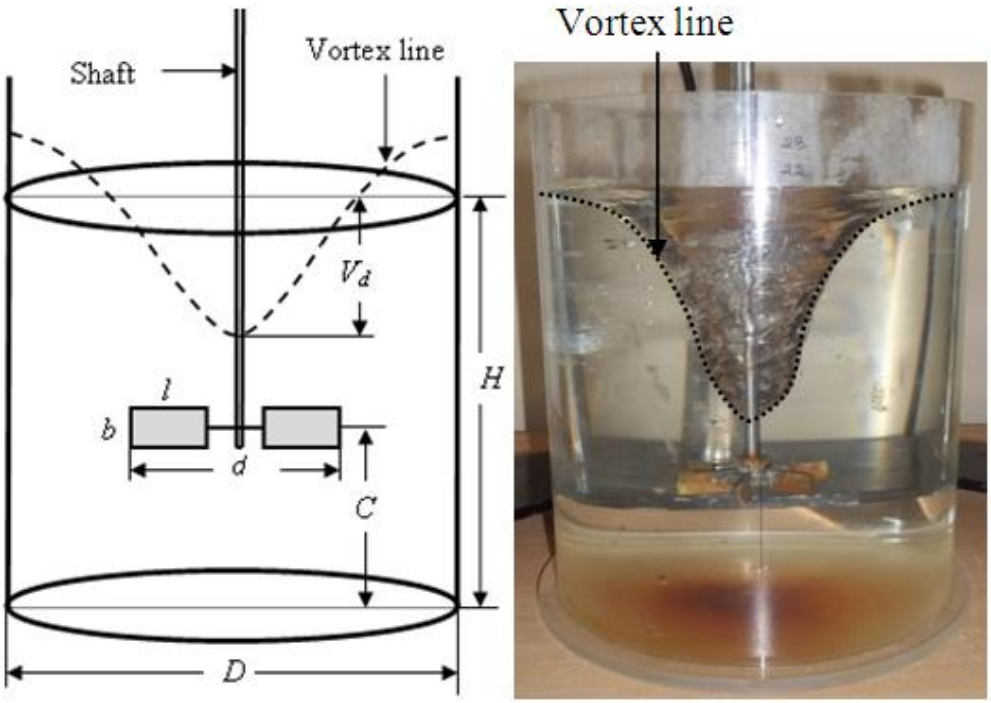

Figure 1.4: Typical diagram showing vortex depth

Gas hold up (ε_G) is other key parameters that describe the quality of gas dispersion and the effectiveness of gas-liquid mass transfer (Gogate et al., 2000). Gas hold up is a function of the impeller power consumption and superficial gas velocity; and geometric parameters such as impeller to diameter ratio (*d/D*) and impeller clearance (Moucha et al., 2003) and is expressed as (Smith, 1991; Patwardhan and Joshi, 1997):

$$\varepsilon_G = f\left(P_g/V, v_g, \text{geometrical parameters}\right) \quad (1.6)$$

Table 1.2 enlist of the some of the representative available correlations of mass transfer rate, power input, vortex depth and gas hold up.

Table 1.2: Representative correlations for process parameters in stirred tank

Parameters	Operating condition	Researchers	Correlation	Geometrical parameters
Mass transfer	Single phase	Kozinski and King (1966)	$K_L a_{20} = (P_{eff}/V)^a$; a=0.2-0.4	
		Hwang (1983)	$K_L a_{20} = 0.332(P_{eff}/V)^{0.97}$	
		Hsieh (1991)	$K_L a_{20} = 0.167(P_{eff}/V)^{0.483}$	
		Forrester et al. (1998)	$K_L a_{20} = (76 \pm 21)10^{-6}(P_{eff}/V)^{0.80\pm0.06}$	
	Gas-liquid phase (air-water)	Calderbank (1958), Van't Riet (1979)	$K_L a_T = 0.026\left(P_g/V\right)^{0.4}\left(v_g\right)^{0.5}$	V=2-2600L, $500<P_g/V<10000$ W/m^3
		Linek et al. (1987)	$K_L a_T = 4.95\times10^{-3}\left(P_g/V\right)^{0.593}\left(v_g\right)^{0.4}$	Single Disc turbine, D=0.29m, N=4.17-14.17rps, v_g=2.12-4.24mm/s
		Nocenti et al. (1993)	$K_L a_T = 0.015\left(P_g/V\right)^{0.59}\left(v_g\right)^{0.55}$	Single Rushton, D=0.232m, Q_g=0.1-0.7vvm, d/D=1/3, Re>1000
		Moucha et al. (1995)	$K_L a_T = 0.0177\left(P_g/V\right)^{0.58}\left(v_g\right)^{0.588}$	Four Rushton, D=0.19m, $d=D/3$, V_g=2.12-8.48mm/s, N=5.5-18.8rps
		Arjunwadkar et al. (1998)	$K_L a_T = 0.00204\left(P_g/V\right)^{0.68}\left(v_g\right)^{0.58}$	One Disk turbine and one Pitched-blade down flow, D=0.18m, V_g=0.98-3.3mm/s, N=6.6-12.5rps
		Vrabel et al (1999)	$K_L a_T = 0.0083\left(P_g/V\right)^{0.62}\left(v_g\right)^{0.49}$	Douuble Rushton, D=0.392m, P_g/V=0.125-4kW/m^3
		Smith (1991)	$K_L a_T = 1.25\times10^{-4}\left(d/D\right)^{2.8}\left(Fr\right)^{0.6}\left(Re\right)^{0.7}\left(Fl\right)^{0.45}\left(d/g\right)^{-0.5}$	Single Rushton, D=0.6m
Power input	Single phase	Nagata et al. (1956)	$Np = 23\left(d/D\right)^{-1}\left(b/D\right)^{1.27}$	D=0.15-1.17m, d/D=0.3-0.8, b/T=0.05-0.2
		Gray et al. 1982)	$Np = 5.17\left(C/D\right)^{0.29}$	Baffled, single Disc turbine, D=0.762m, H=0.5m, C/D<1.1

		Wu (1995)	$Np = 1.73(Fr)^{-0.37}$	Single Rushton, D=0.2-0.3m, d/D=0.5, S/D=0-0.62, H/D=1, N=0-14rps
		Deshmukh and Joshi (2006)	$Np = 0.34\times10^{-3}(Re)^{-0.23}(Fr)^{-0.23}(C/S)^{-4.09}(D^2H/d^2S)^{4.5}$	Single Disk turbine, D=0.5, 1 and 1.5, C/d=1-1.76, S/d=0.23-0.3 S=impeller submergence depth
		Rao and Kumar (2009)	$Np = 1.023/(Fr^{4/3}Re^{1/3})^{0.4}$	Unbaffled circular tank, A=1, 0.512 and 0.168m^2, l/d=0.3, b/d=1.25, H/d=1, C/H=0.94
		Taghavi et al. (2011)	$P_{eff}/V = 6\times10^{-12}(Re)^{2.921}$	Baffled, dual Rushton, Re>10^4, D=0.3m, d=D/3, b=1/5d, C_1=0.55D, C_2=0.7D, H=0.54m
		Scargiali et al. (2013)	For, 200<Re<30000 $Np = 19.5(Re)^{-0.3}$ and $Np = 21.36(Re)^{-0.32}(Fr)^{-0.37}$	Unbaffled, single Rushton, D=0.19m, H=D, d=D/3,
	Gas-liquid phase (Air-water)	Taghavi et al. (2011)	$\frac{P_g}{P_u} = 0.19(Fl)^{-0.28}(Fr)^{-0.127}(b/d)^{0.18}(d/D)^{-0.65}$	Baffled, dual Rushton, Re>10^4, D=0.3m, d=D/3, b=1/5d, C_1=0.55D, C_2=0.7D, H=0.54m
		Wang et al. (2010)	For N=10rps $\frac{P_g}{P_u} = 1+123.9Fr$ For N=11.67rps $\frac{P_g}{P_u} = 1+232.8Fr$	Baffled, dual impeller, D=0.38m, d=0.127m, H/D=1.3,C_1=C_2=D/3
		Petrov (2005)	$\frac{P_g}{P_u} = 0.53(Fl)^{-0.014}$	Baffled, single impeller, D=0.12m, d=0.058m, H=D, l=0.014m, b=0.012m, N=100-2000/min, Q_q=16.67x10^{-6}
		Reiger et al. (1979)	$\frac{V_d}{d} = 1.52\pm0.02(Ga)^{0.069}(D/d)^{-0.38}(Fr)^{1.14Ga^{-0.008}(D/d)^{0.008}}$	Single flat blade turbine, D/d=3-6, C-b/2=d, b/d=0.2, Ga=8x10^6-10^{10}
Vortex depth	Single phase	Markopoulos and Kontogeorgaki (1993)	$\frac{V_d}{d} = 1.67\pm3.4\%(Ga)^{0.05}Fr(D/d)^{-0.1}(C_2/d)^{-0.054}$	Dual disc turbine, D/d=1.9-2.37, C_1/d=0.2-1.25, C_2/d=0.4-1.25, H/D=1.42, Ga=6.2x10^7-9.8x10^9, Fr=0.168-0.44

		Markopoulos and Kontogeorgaki (1993)	$\frac{V_d}{d}=1.6\pm5.6\%\left(Ga\right)^{0.05}Fr\left(D/d\right)^{-0.1}$	Single disc turbine, D/d=1.0-2.37, b/d=0.2, l/d=0.25, C/D=0.2-1.25, Ga=6.2x10^{7}-9.8x10^{9}, Fr=0.168-0.362
		Zlokarnik (1971)	$\frac{V_d}{d}=62Fr\left(0.1-Ga^{-0.18}\right)\left(\frac{H-C}{d}\right)^{-0.16}$	Single disc turbine, D/d=3.33, C/d=1, H/D=1-1.75, Ga=2.7x10^{6}-1.7x10^{10}
		Le Lan and Angelino (1972)	$\frac{V_d}{d}=\pi^2\left(\frac{Re}{3.27Re+4400}-0.05D/d\right)Fr\left(D/d\right)$	Single disc blade turbine, D/d=1.39-4.55, C-b/2=d/2-2d/3, Re=5000-7x10^{4}
		Smith (1991)	$\varepsilon_G=0.85\left(ReFrFl\right)^{0.35}\left(d/D\right)^{1.25}$	Single Rushton, D=1m, d=0.25, 0.33 and 0.5m, C=0.25D, H=D
		Zhengming et al. (1996)	$\varepsilon_G=0.195\left(P_g/V\right)^{0.28}\left(v_g\right)^{0.56}\left(D\right)^{0.45}$	Baffled, single Rushton, D=0.287, 0.495 and 1.1m, H=D, d=D/3, v_g=0.003-0.0344m/s, P_g/V=0.15-5.2x10^{3}W/m^{3}
		Moucha et al. (2003)	For single impeller: $\varepsilon_G=0.01686\left(P_g/V\right)^{0.6241}\left(v_g\right)^{0.5669}$ For dual impeller: $\varepsilon_G=0.05051\left(P_g/V\right)^{0.4903}\left(v_g\right)^{0.5788}$	Baffled, Rushton, D=0.29m, d=D/3, C=C_1=d, C_2=D, v_g=2.12, 4.24 and 8.48mm/s, N=4.17-14.17rps
		Fadavi and Chisti (2007)	$\varepsilon_G=2.47\left(v_g\right)^{0.97}$	D=0.1484m,V=0.01625m^{3}, $v_g\le0.04$m/s

1.6. Objectives

Understanding the necessity of having comprehensive design criteria for Concave blade impeller, the following objectives have been devised in this study:

1. Development of design criteria for single stirred unbaffled tank with Concave blade impeller: The scope of the objectives is as follows:

1.1. Single phase

- To monitor the influence of impeller diameter (d) and its position (C) in terms of mass transfer coefficient, power input and vortex formation.
- To predict the flow pattern, velocity profile and turbulent kinetic energy and dissipation rate numerically at different impeller clearance depth and to present a qualitative modeling of vortex formation.
- To compare the unbaffled system with baffled system and Concave blade type impeller with Rushton impeller
- To develop a design criteria inclusive of geometric parameters for each process variables (mass transfer coefficient, power input and vortex depth).

1.2. Gas-liquid phase/sparged condition

- To monitor the influence of impeller diameter and its position in terms of mass transfer coefficient, power input and gas hold up experimentally.
- To predict the flow pattern, velocity profile, gas volume fraction and mass transfer coefficient numerically at different impeller clearance depth.
- To compare the unbaffled system with baffled system and Concave blade type impeller with Rushton impeller.
- To develop a design criteria inclusive of geometric parameters for each process variables (mass transfer coefficient, power input and gas hold up).

2. Development of design criteria for dual stirred unbaffled tank with Concave blade impeller: The scope of the objectives is as follows:

2.1. Single phase

- To find the optimum impeller clearance depth (C_1) and their spacing and (C_2) and optimum impeller diameter using univariant approach.

- To predict flow pattern, velocity profile, turbulent kinetic energy and dissipation rate at the optimal configuration of impeller clearance depth and spacing and to present a qualitative modeling of vortex formation.
- To compare the unbaffled system with baffled system and Concave blade type impeller with Rushton impeller in terms with their respective same combination and with mix combination.
- To develop a design criteria for optimal geometric similar systems.

2.2. Gas-liquid phase/sparged condition

- To find the optimum impeller clearance depth and their spacing using univariant approach.
- To predict flow pattern, gas volume fraction and mass transfer coefficient at the optimal configuration of impeller clearance depth and spacing.
- To compare the unbaffled system with baffled system and Concave blade type impeller with Rushton impeller in terms with their respective same combination and with mix combination.
- To develop a design criteria for optimal geometric similar systems.

3. Application of Computational Fluid Dynamics in stirred tank modeling: The scope of the objectives is as follows:

- Comparison of Concave blade with Rushton impeller in single phase system of single and dual impeller system.
- Comparison of Concave blade with Rushton impeller in gas-liquid phase system of single and dual impeller system.
- Comparison of Concave blade with Rushton impeller by using advanced turbulence model (Large Eddy Simulation) of turbulent flow in single stirred tank.

A schematic view of objectives adopted in the present work can be summarized as depicted in the Figure 1.5.

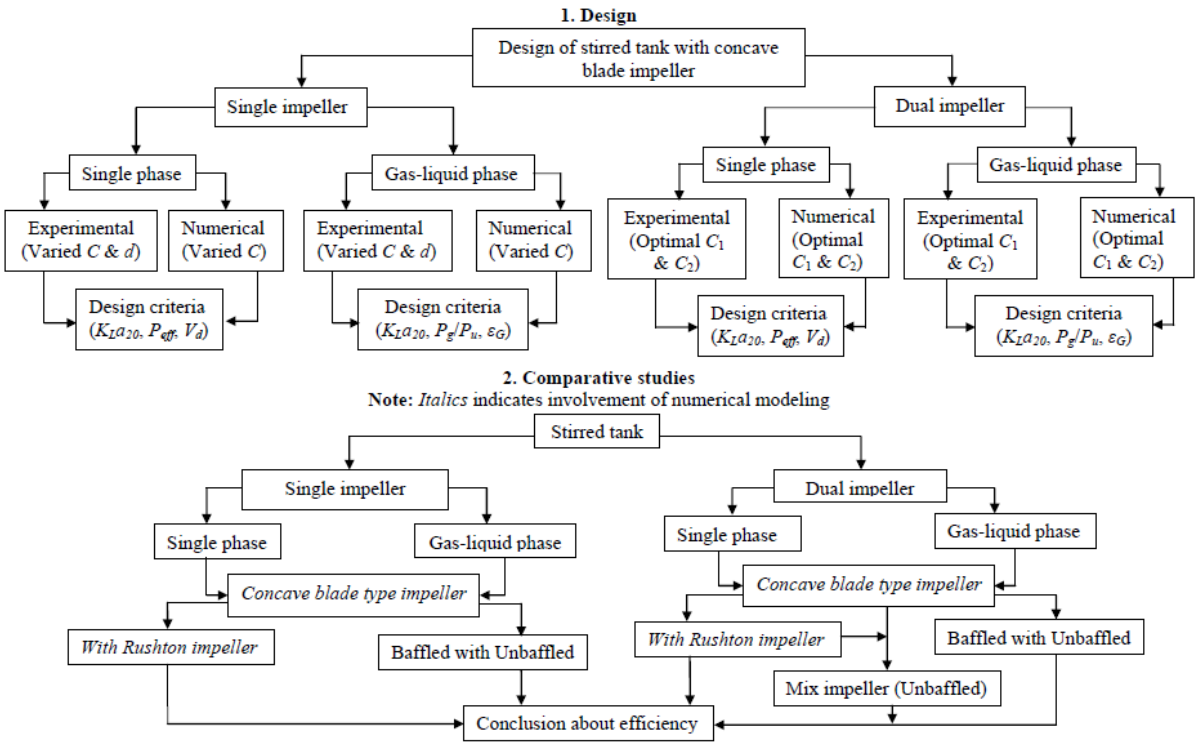

Figure 1.5: Flow chart of objectives

1.7. Thesis organization

The thesis is divided into six Chapters. Chapter 1 highlights the introductory part of stirred tank, its uses and a brief discussion on types of impeller & its position and on baffled & unbaffled system. The scale up of various process dynamic characteristics of stirred tank in single phase and sparged condition were also discussed. Some of the existing correlation based on mass transfer coefficient, power input, vortex depth and gas hold up are also listed in this chapter.

Chapter 2 describes the process and methods involved in experimental and numerical studies of designing of Concave blade unbaffled stirred tank.

Chapter 3 details the design of unbaffled stirred tank with Concave blade for single impeller. Study of singular impeller operated with single phase and sparged condition will be discussed in this chapter. The experimental measurement of mass transfer coefficient and power consumption was performed to monitor the influence of impeller position. Vortex behavior is studied for unbaffled stirred tank of single phase system and gas hold up is studied for sparged system. Numerical modeling of flow pattern and mass transfer coefficient

were also presented. Scale up criteria for mass transfer co-efficient, power consumption, gas hold up and vortex depth were developed for single impeller system.

Chapter 4 is study on dual impeller system. System is studied on single phase and sparged condition in terms of mass transfer, power consumption, gas hold up and vortex formation to monitor the influence of impeller position and their spacing. Numerical modeling of flow pattern and mass transfer coefficient were also presented. Scale up criteria for mass transfer co-efficient, power consumption, gas hold up and vortex depth were developed for dual impeller system.

Chapter 5 represents the studies based on numerical modeling of stirred tank. It includes single phase as well as gas-liquid phase condition of single impeller and dual impeller stirred tank system. The basic objective of this chapter is to compare the impeller types between Concave blade impeller with Rushton impeller. Numerical modeling of the single phase system in single impeller of Concave blade type with Rushton impeller is compared with experimental results found in literature. So, this chapter aims in representing the successful application of numerical modeling of stirred tank reactor.

Chapter 6 is all about advanced modeling of turbulent flow. This chapter is extension of numerical modeling considering advanced turbulent modeling in stirred tank reactor. Large Eddy Simulation (LES) turbulent model is used to model the flow pattern, velocity profile, turbulent kinetic energy and turbulent dissipation rate in baffled system of single impeller in single phase system.

Chapter 7 gives the overall conclusions drawn from this study and also outlined the proposed future work aimed by the authors.

CHAPTER 2

METHODOLOGY

This chapter describes the experimental and numerical techniques used in this study. The process and methods used in the experimental measurement of mass transfer coefficient, power consumption, vortex formation and gas hold up will be discussed in this chapter. The basic equations and theoretical part involved in numerical simulation will also be explained in detail in this chapter.

2.1. Experimental Setup

The stirred tank operated in this study is in single phase as well as in gas-liquid phase in order to understand the underlying hydrodynamics when the system is operated in different conditions. The system is employed with single and dual impeller. Two types of impeller is studied (Rushton and Concave blade type impeller). Baffled system is also employed to compare with unbaffled system. Detail of schematic diagram of these systems is shown in Figure 2.1.

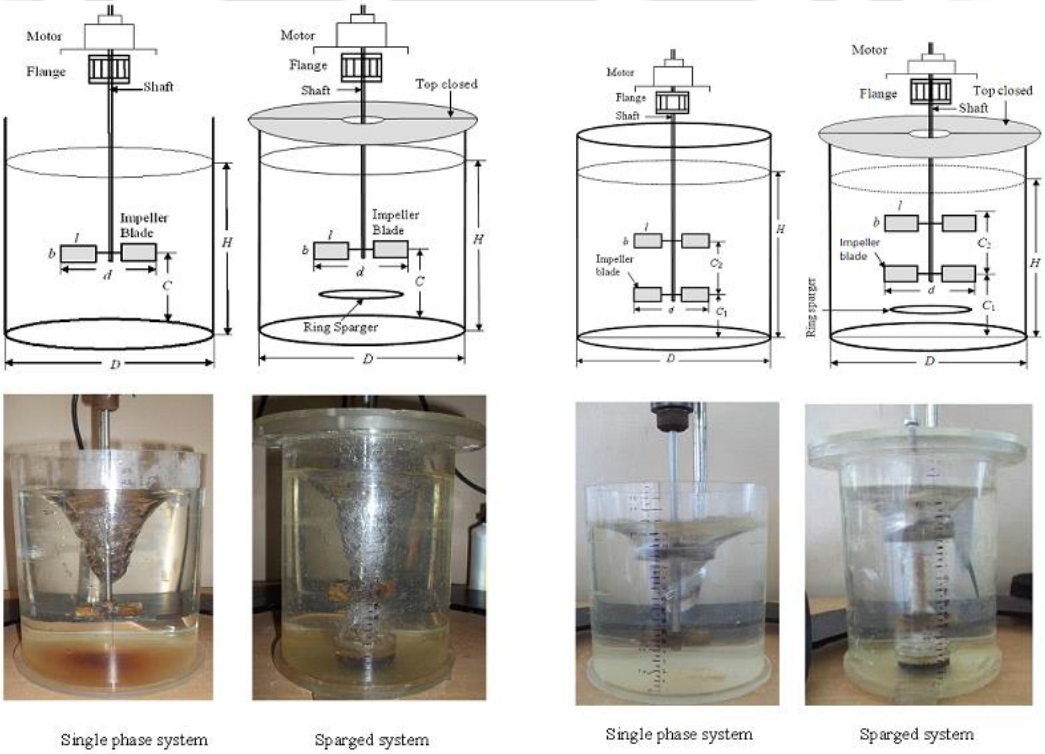

(a) Single impeller system (b) Dual impeller system

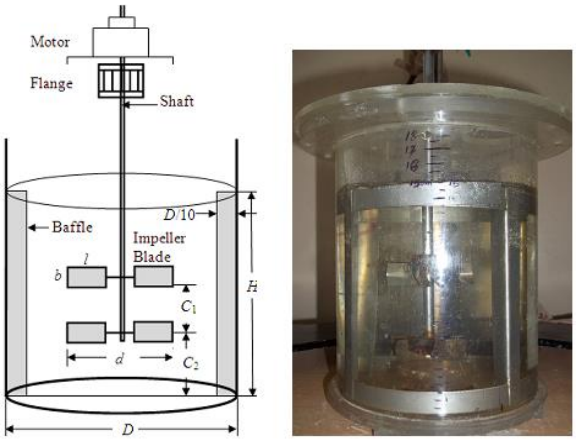

(c) Baffled system

Figure 2.1: Schematic diagram and experimental set up of different conditions of stirred tank system

Two sizes of circular unbaffled tank of diameter (*D*) 200 mm and 150 mm have been tested under laboratory conditions. In order to compare baffled with unbaffled tank, 150mm tank diameter has been used. Height of water is equal to tank diameter (*H*=*D*). Water at standard temperature (20^0C) has been used in this study having density, ρ_l=998.2 kg/m^3 and dynamic viscosity, μ_l=0.001003 Pa.s. Concave blade type impellers (total curve angle of 140^0) with different diameters (30 to 80 mm) have been used in the experiments and conventional Rushton impeller (30 to 80 mm) has been also used to analyze and compare the mass transfer rate efficiency of concave blade type impeller (Figure 2.2).

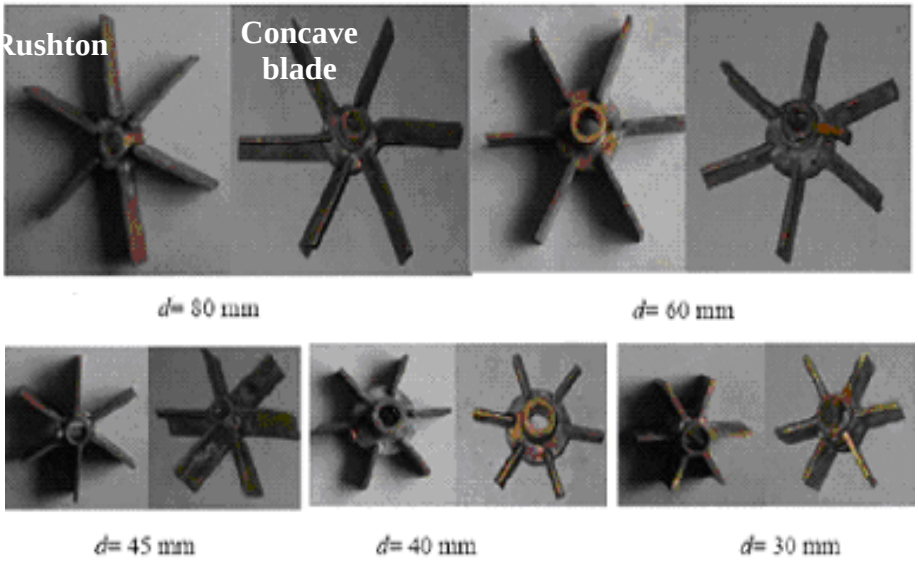

Figure 2.2: Different size of impeller used in this study

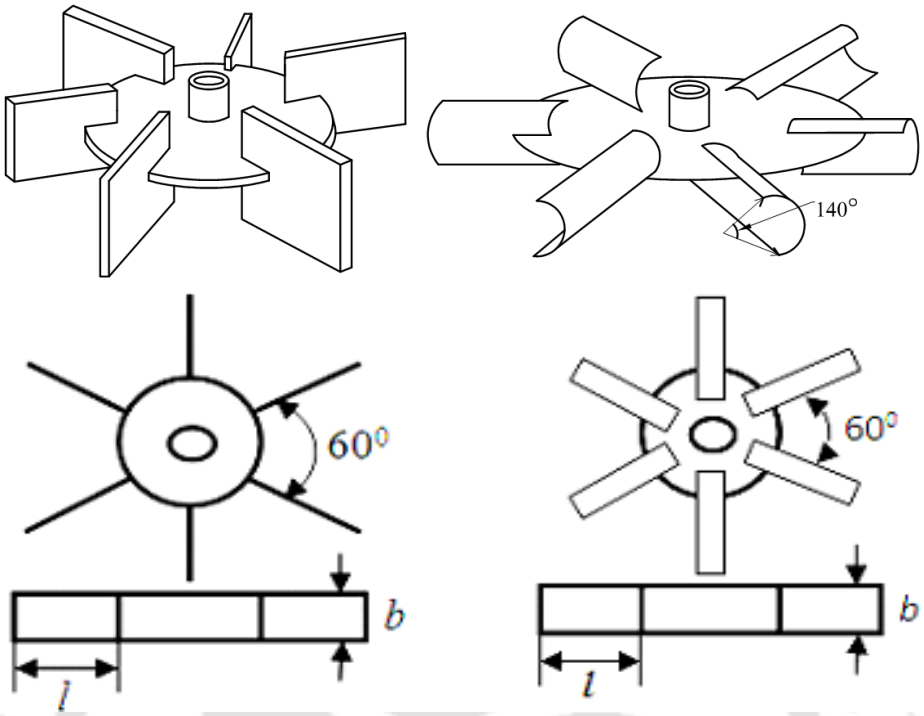

Rushton impeller Concave blade impeller

Figure 2.3: Impeller types and its detail

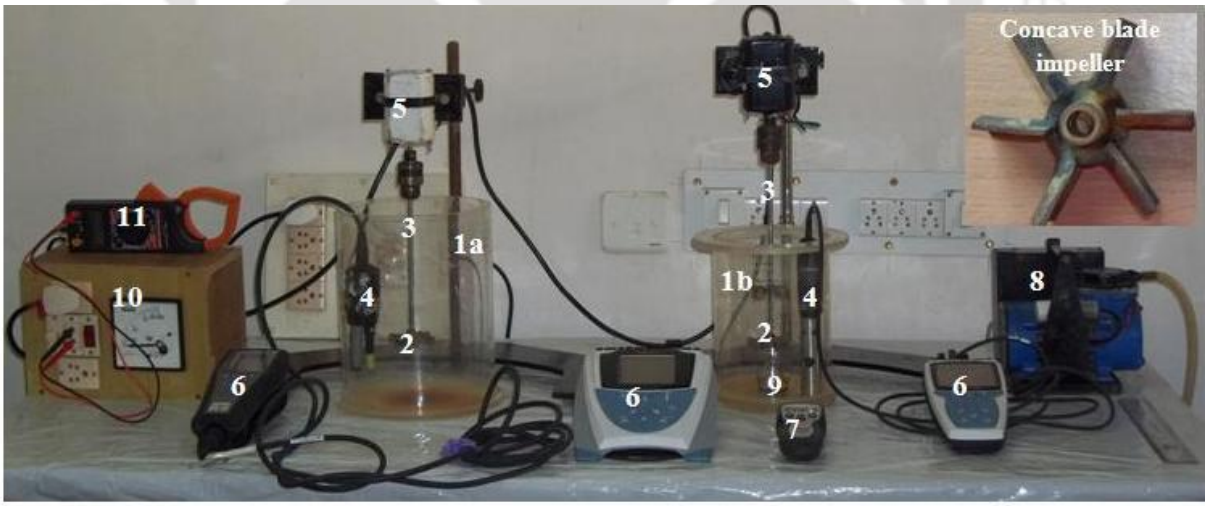

Notations: **1a**-stirred tank of single impeller without sparger, **1b**-stirred tank of dual impeller with sparger, **2**-impeller, **3**-shaft, **4**-DO probe, **5**- motor, **6**-DO meter, **7**- tachometer used to measure impeller speed, **8**-air supplier, **9**-ring sparger, **10**-wattmeter (to measure power), **11**-multimeter (for measurement of current and voltage)

Figure 2.4: Experimental set up

The geometric parameters of the impeller used in the present study have been given in the Table 2.1.

Table 2.1: Rotor properties

Rotor diameter, *d* (mm)	**Blade length, *l* (mm)**	**Blade width, *b* (mm)**
80	20	16
60	15	12
45	11.25	9
40	10	8
30	7.5	6

2.1.1. Mass transfer measurements

Present work deals with single phase (liquid mixing) and multiphase (gas in liquid) system. In the first system, air is entrained from the free surface of the liquid and gas is being sparged into the later systems. Hence different methods have been used for mass transfer measurement in the present work. The chemical methods namely Sulfite method has been used for single phase stirred tank and standard dynamic method for multiphase stirred tank.

2.1.1.1. Sodium sulfite oxidation method

This method is based on the reaction of sodium sulfite, a reducing agent, with the dissolved oxygen to produce sulfate, in the presence of a catalyst (usually a divalent cation of Cu++ or Co++) (Cooper et al., 1944); the reaction can be expressed as:

$$2SO_4^{-2} - O_2 - 2SO_3^{-2} = 0 \qquad (2.1)$$

Initially the experimental setup is made ready with all the desired geometric dimensions of the tank. After measuring initial concentration of dissolved oxygen (DO) of water in the tank, water is deoxygenated by adding appropriate quantities of cobaltous chloride and sodium sulphite (Metcalf and Eddy, 1991). About 8 mg/l of sodium sulphite and 0.1 to 0.5 mg/l of cobaltous chloride are to be added per each mg/l of DO present in the water. The chemicals are mixed thoroughly to complete the deoxygenation. When the deoxygenation takes place, i.e., when the DO concentrations has come down to almost 0 mg/l, the experiment is started by setting the required speed of the rotation of the rotor. Once the rotor starts rotating, DO meter reading is noted at regular interval up to the point of saturation. A Thermo Orion® DO meter which is used to measure the concentration and has 0.1 mg/l accuracy in measurement.

The said DO meter is being calibrated by the modified Winkler's method. The sodium sulfite oxidation method (Dussap et al., 1985; Ogut and Hatch, 1988; Thibault et al., 1990; Yasukawa et al., 1991; Yang and Wang, 1992; Benadda et al., 1997; Garcia-Ochoa and Gomez, 1998; Liu et al., 2006) is relatively easy to carry out.

2.1.1.2. Standard dynamic method

For implementing the standard dynamic method (Garcia-Ochoa and Gomez, 1998; Sanchez et al., 2000; Puthli et al., 2005; Djelal et al., 2006), the liquid phase was deoxygenated by flushing with nitrogen. Then, after replacing nitrogen by air, the variation in dissolved oxygen concentrations with time was measured until reaching the saturation. It is necessary to take into account that the response time of the electrode is a critical parameter for the determination of accuracy values of oxygen concentration. This response can affect the correct determination of the mass transfer coefficient if the time characteristic for the oxygen transport, $1/ K_L a_T$, is of the same order than the response time of the electrode, defined as the time necessary to reach 63% of the final value measured when exposed to a step change of concentration (Van't Riet, 1979). The response time of the electrode can be determined by transferring the oxygen electrode from a solution with sodium sulfite (whose oxygen concentration is zero) to another dissolution saturated with air (100% of saturation). In order to account the probe response with the presence of air bubble during sparging, mass transfer values have been calculated by using the dynamic method.

2.1.1.3. Mass transfer rate calculation

The basic theory used in the Standard is the well-known "Two-film Theory" from Lewis and Whitman (1924), which states that transfer rate can be expressed in terms of an overall transfer coefficient and resistances on either side of the interface. Among the theories describing gas transfer through the gas-liquid interface, the "two-film theory" is best known and most widely used theory.

The basic concept of this theory is the existence of a thin gas film on the gas side of the interface and a thin liquid film on the liquid side of the inter face between the gas and liquid. Two-film theory as devised by Lewis and Whitman (1924) is basically an extension of Nernst's theory of solubility of solids developed in 1893. According to Nernst (1893), when

solids dissolve in liquids, a saturated solution of the given substance in the liquids exists at the interface between the bulk of the liquid and the solid. The rate of solid dissolution is determined by the rate of diffusion of the substance from the saturated solution in to the bulk of the liquid. Lewis and Whitman (1924) used Nernst's basic concept when analyzing the process developing at the interfacial area. Figure 2.5 gives the schematic representation of the Two-film theory.

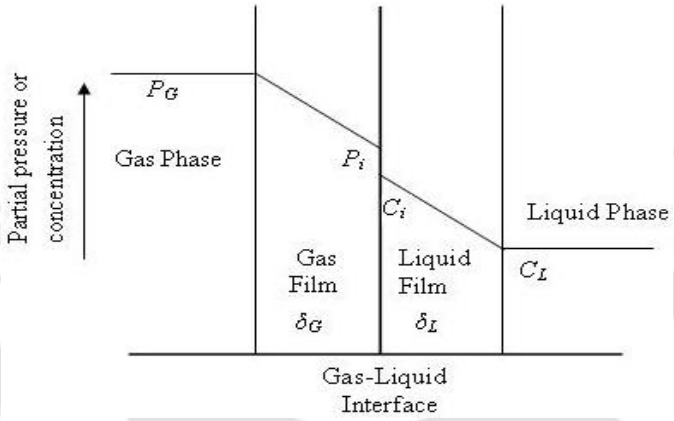

Figure 2.5: Schematic representation of Two-Film theory

The basic concepts and assumptions of the Two-Film theory are:

1. On the side of each phase boundary films (gas film, liquid film etc.) appear at the interface (gas-liquid, vapour-liquid, liquid-liquid), offering the main resistance to the transport of mass from one phase into the other.
2. Created at the interface, between the two films, are conditions of dynamic equilibrium, i.e., steady-state mass transfer sets in.
3. Within the limits of each phase, the diffusion flux of a component is linearly proportional to the difference in concentrations.

The two films or boundary layers, one gas and one liquid; provide the bulk of the resistance for the passage of gas molecules between the bulk liquid and the bulk gaseous phases. It is important to note that the bulk liquid and bulk gas phases are assumed completely mixed. Under steady state, the rate of mass transfer of a gas through the gas film must be equal to the rate of mass transfer through the liquid film. From Fick's first law, the mass flux for each phase is as follows:

$$r = k_G\left(P_G - P_i\right) = k_L\left(C_i - C_L\right) \qquad (2.2)$$

where r = rate of mass transferred per unit area per unit time, k_G = gas film mass transfer coefficient, P_G = partial pressure in the bulk of the gas phase, P_i = partial pressure at the interface in equilibrium with concentration C_i of liquid, k_L = liquid film mass transfer coefficient, C_i = concentration at the interface in equilibrium with P_i of in the gas phase and C_L = concentration in the bulk liquid phase. The concentration differences in the above Equation 2.2 represent the driving forces causing mass transfer in the gas phase or liquid phase. If each difference is divided by its respective film thickness the driving force can be expressed in terms of unit thickness. Therefore if the thickness of the film is reduced the degree of mass transfer can be enhanced. In practice it is difficult to measure the values of k_G and k_L at the interface so the overall coefficients K_G and K_L are used instead. It is said that (McWhirter et al., 1995) all the resistance to mass transfer is in the liquid side so the equation becomes:

$$r = K_L (C_s - C_L) \tag{2.3}$$

Where r = rate of mass transfer per unit are per unit time, K_L = overall liquid mass transfer coefficient and C_s=concentration at the interface in equilibrium with the concentration in the bulk gas phase and C_L=concentration in the bulk liquid phase. To estimate the flux of a slightly soluble gas from the gas phase to the liquid phase the above equation can be changed by swapping C_L with C_t.

The new equation is: $r = K_L (C_s - C_t)$ (2.4)

Where, C_t = concentration of constituent A in the bulk liquid phase at time t.

The rate of mass transfer can be found by multiplying by the area and dividing by the volume, giving

$$\frac{dC}{dt} = K_L \left(\frac{A}{V}\right)(C_s - C_t) = K_L a_T (C_s - C_t) \tag{2.5}$$

Where, dC/dt = change in concentration per unit time, $K_L a_T$ = volumetric mass transfer coefficient, A = area through which mass is transferred, V = volume in which constituent concentration is increasing and a_T = area for mass transfer per unit volume. The term $K_L a_T$

depends on the liquid characteristics and type of equipment being used for mass transfer and is unique for each situation.

Integrating Equation 2.5 and establishing the dissolved oxygen concentration at the initial time, t_0, as C_0, yields two additional forms of the basic model: the logarithmic form, illustrated in Equation 2.6 and the exponential form, illustrated in Equation 2.7 as:

$$\ln \frac{(C_s - C_t)}{(C_s - C_0)} = -K_L a_T (t - t_0) \tag{2.6}$$

$$C_t = C_s - (C_s - C_0) e^{-K_L a_T (t - t_0)} \tag{2.7}$$

While each of the above equations will produce a resultant oxygen transfer rate for a given set of data, the resultant oxygen transfer rates generated using a particular form of the model may differ significantly from that generated using another form of the same model. Further, no specific form of the model has yielded consistently reliable results for all data sets analyzed. As such, it is important to carefully consider the model form used when analyzing a specific data set as well as the behaviour of the data set itself. The ASCE Method, which has also been called the Nonlinear Regression Method, is based on nonlinear regression of Equation 2.6. A variety of non-linear regression methods can be used and produce identical results when the methods converge (Stenstrom et al., 1981). Indeed, this form is linear in $K_L a_T$ and does not require the specification of a value for C_s in order to perform the least squares analysis (Brown and Baillod, 1982).The value of C_s used in the Equation 2.5 may be based on field measurement, published value, or simple assumption (Brown and Baillod, 1982). However, selection of the "correct" value for C_s is, perhaps, not as straightforward as simply referencing published tables of such values (Boyle et al., 1974). Common practice has typically been to select an appropriate value from a published table and apply adjustments for temperature, pressure and salinity. Care must be used when employing this technique as deviations between published tables have been observed, particularly within the acceptable temperature range for aeration equipment performance evaluations, 10°C to 30°C (Boyle et al., 1974). The use of Equation 2.4-2.6 to characterize the oxygen mass transfer performance of surface aeration systems implies a number of simplifying assumptions which require critical examination relative to the actual mass transfer process involved. The primary assumptions inherently embodied in Equations 2.4-2.6 are as follows:

(a) The bulk test liquid under aeration is completely mixed (of a uniform DO concentration throughout) at all times

(b) A single and constant value of C_s is adequately representative of the equilibrium DO concentration for liquid phase oxygen mass transfer for the entire aeration system

(c) A single value of $K_L a_T$ is a meaningful representation of the total oxygen transfer process

(d) Other test condition environmental factors such as the temperature and humidity of the atmospheric air do not affect the oxygen mass transfer process and can be ignored (McWhirter et. al., 1995)

2.1.1.4. Theory and mechanism of operation of the dissolved oxygen sensor

Digital DO meter (Thermo Orion®) has been used to measure the DO content during experiments. The Dissolved Oxygen Sensor has a polarographic probe composed of a platinum cathode and a silver anode surrounded by a potassium chloride electrolyte solution. The sensor functions by measuring the electric current produced in a chemical reaction in the probe. The chemical reaction involves the reduction of oxygen molecules (O_2) and the oxidation of the silver atoms of the cathode electrode. Figure 2.6 shows the Orion probe with digital display meter.

Figure 2.6: Oxygen molecules pass through the semi permeable silicon membrane into the electrolyte solution surrounding the electrodes

When the dissolved O_2 probe is placed in an aqueous medium, such as de-ionized water that contains dissolved O_2, the dissolved O_2 molecules diffuse across a thin silicon membrane into the electrolyte that surrounds the electrodes of the probe. The membrane is semi permeable, allowing the dissolved O_2 to pass through it, but preventing passage by most other molecules that might interfere with the chemical reactions at the electrodes. The chemical reactions produce electrons that cause electric current to flow through the sensor's electric circuit. Since the rate of diffusion is dependent on the concentration of the dissolved O_2, the number of diffused O_2 molecules will vary approximately in direct proportion to the concentration of dissolved O_2 in the test solution. Accordingly, the number of electrons produced by the redox chemical reactions of the dissolved O_2 will be almost directly proportional to the concentration of dissolved O_2 in the test solution. The current due to the chemical reactions of the O_2 molecules must be corrected for temperature variations, since the rate of reaction varies directly with the temperature. The correction is accomplished through the use of a temperature-sensing thermistor that is built into the probe. With the temperature sensing thermistor, the temperature of the probe is monitored, and the gain of the amplifier is automatically adjusted to compensate for the temperature dependence of the chemical reactions in the probe. The dynamics of the oxygen probe can be described using a first order differential equation (Eckenfelder and O'Connor, 1961). The time constant of the oxygen probe was equal to 10s. This latter value remained small when compared to mass transfer characteristic times, $1/ K_L a_T$. A voltage representing the temperature–compensated dissolved O_2 concentration of the solution is displayed in the meter. Calibration of this type of probe can be done in water-saturated air and is frequently done in a special calibration chamber with a water reservoir. Under equilibrium conditions, the partial pressure of oxygen in air-saturated water is equal to that of partial pressure of oxygen in water-saturated air, i.e., air at 100% relative humidity. This means that a probe calibrated in water-saturated air will correctly read the partial pressure of oxygen in a water sample.

2.1.1.5. Mass Transfer Coefficient ($K_L a_T$)

The known values of DO measurements in terms of C_t at regular intervals of time t (including the known value of C_0 at $t = 0$) a line is fitted, by linear regression analysis of Equation 2.6, between the logarithm of (C_s-C_t) and t, by assuming different but appropriate values of C_s such that the regression that gives the minimum "standard error of estimate" is

taken and thus the values of $K_L a_T$ and C_s were obtained simultaneously. Oxygen transfer modeling by Two-film theory assumes that a single and constant value of C_s is adequately representative of the equilibrium DO for the liquid phase oxygen mass transfer for the entire aeration systems and the transfer process is predominately liquid phase mass transfer controlled and the gas phase resistance to transfer can be ignored. Now by fixing the value of C_s, the value of $K_L a_T$ has been determined by the best fit straight line, semi-logarithmic plot of (C_s-C_t) and t. It may be noted that the value of C_s used in the log-deficit approach can be based on field measurement, published value, or simple assumption (Brown and Bailod, 1982). It is a common practice to fix the value of C_s around the maximum DO value with some increment in it, as long as it gives the best fit. The slope of such a straight line, semi-logarithmic is equal to-$K_L a_T$. It is worth noting that selection of a particular value for C_s will influence the resultant value for $K_L a_T$ determined by this approach. This is illustrated in the Figure 2.7. The mass transfer coefficient calculated using this method may have errors, because the method used requires a straight line to fit the data, the error could be reduced if the linear regression coefficient of the chosen line is high. In that case the slope of the line would accurately represent the oxygen transferred to the water. Generally, for computing the results of such experiments, the overall oxygen transfer coefficient $K_L a_T$ determined at any temperature T^0 C is converted to the overall oxygen transfer coefficient at a standard temperature of 20^0 C, by the following Equation (Eckenfelder and O'Connor, 1961; Bewtra et al., 1970; Hassan et al., 2012) as:

$$K_L a_{20} = K_L a_T \big/ \theta^{T-20} \qquad (2.8)$$

Where, θ is a constant (=1.024) (Bouaifi, and Roustan, 1998, Sardeing et al., 2004; Estradal et al., 2013) and depends on temperature, t (Eckenfelder and O'Connor, 1961).

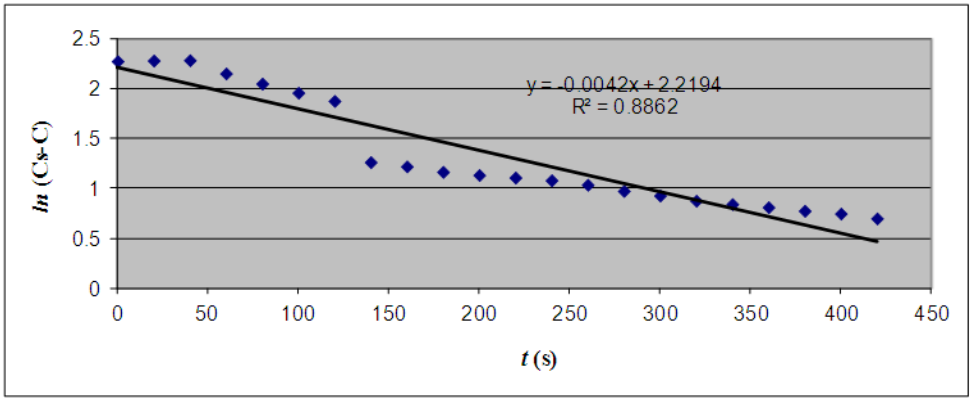

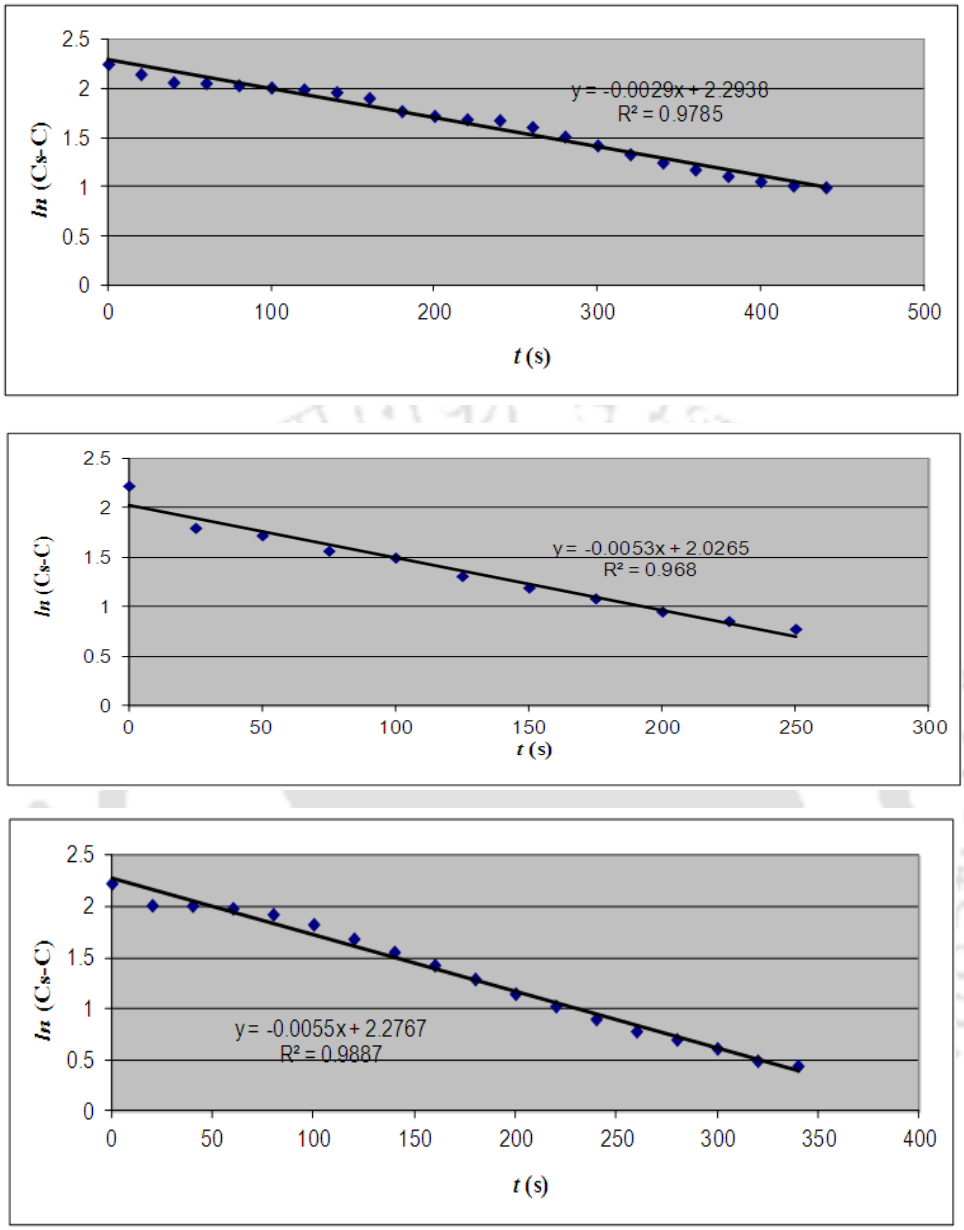

Figure 2.7: Determination of $K_L a_T$

2.1.2. Gas hold up

Gas hold up was measured by visual method (Krishna et al., 1999; Venneker et al., 2002; Deshmukh and Joshi, 2006; Shewale and Pandit, 2006; Ahmed et al., 2010). A graduated graph paper was pasted on the outside of the vessel. By noting the difference between level with and without aeration the hold up was found out. It has been cross-checked with by analyzing digital images taken during the experimentation. The following equation was used.

$$\varepsilon_G = \left(H_G - H\right) / H_G \qquad (2.9)$$

Where H_G=Height of liquid after aeration (m), H=Height of clear liquid without aeration (m) and ε_G= (fractional) gas hold up.

2.1.3. Vortex analysis

The main feature of unbaffled stirred tanks is the highly swirling liquid motion, which leads to the formation of a central vortex on the liquid free surface, when the vessel is operated without top-cover. The shape of the vortex such as height is important for design purposes, as the liquid side wall rise under stirring clearly depends on vortex shape. In the present work, edge detection technique with measure tool (http://www.mathworks.nl/matlabcentral/fileexchange/25964-image-measurement-utility) has been employed to investigate the shape of free surface vortexes and height formed in stirred tank. Digital images were taken during each and every experiments and being processed through edge detection techniques. Edge detection is a type of image segmentation techniques which determines the presence of an edge or line in an image and outlines them in an appropriate way (Frei and Chen, 1977). The main purpose of edge detection is to simplify the image data in order to minimize the amount of data to be processed (Canny, 1986). Generally, an edge is defined as the boundary pixels that connect two separate regions with changing image amplitude attributes such as different constant luminance and tristimulus values in an image (Frei and Chen, 1977; Gonzalez and Woods, 2001; Pratt, 1991). The detection operation begins with the examination of the local discontinuity at each pixel element in an image. Amplitude, orientation, and location of a particular sub area in the image that is of interest are essentially important characteristics of possible edges (Frei and Chen, 1977). Based on these characteristics, the detector has to decide whether each of the examined pixels is an edge or not. Frei and Chen (1977) suggest that edge detection is best carried out by simple edge detector, followed by a morphological thinning and linking process to optimize the boundaries. Two different techniques namely; Canny edge detection and fuzzy detection have been used to interpret the vortex height from the digital images.

2.1.3.1. Canny Edge detector

The Canny edge detector is widely used in computer vision to locate sharp intensity changes and to find object boundaries in an image. The Canny edge detector classifies a pixel as an

edge if the gradient magnitude of the pixel is larger than those of pixels at both its sides in the direction of maximum intensity change. The algorithm runs in 5 separate steps:

A. Smoothing: It is inevitable that all images taken from a camera will contain some amount of noise. To prevent that noise is mistaken for edges, noise must be reduced. Therefore the image is first smoothed by applying a Gaussian filter.

B. Finding gradients: The Canny algorithm basically finds edges where the grayscale intensity of the image changes the most. These areas are found by determining gradients of the image. Gradients at each pixel in the smoothed image are determined by applying the Sobel-operator. First step is to approximate the gradient in the x- and y-direction respectively by applying the kernels as shown in Figure 2.8.

$$K_{GX} = \begin{bmatrix} -1 & 0 & 1 \\ -2 & 0 & 2 \\ -1 & 0 & 1 \end{bmatrix} \quad K_{GY} = \begin{bmatrix} 1 & 2 & 1 \\ 0 & 0 & 0 \\ -1 & -2 & -1 \end{bmatrix}$$

Figure 2.8: Sobel operator

The Sobel operator consists of a pair of 3×3 convolution kernels as shown in Figure 2.9. One kernel is simply the other rotated by 90°. These kernels are designed to respond maximally to edges running vertically and horizontally relative to the pixel grid, one kernel for each of the two perpendicular orientations. The kernels can be applied separately to the input image, to produce separate measurements of the gradient component in each orientation (call these *Gx* and *Gy*).

$$\begin{bmatrix} -1 & 0 & +1 \\ -2 & 0 & +2 \\ 1 & 0 & 1 \end{bmatrix} \qquad \begin{bmatrix} +1 & +2 & +1 \\ 0 & 0 & 0 \\ -1 & -2 & -1 \end{bmatrix}$$

G_x G_y

Figure 2.9: Convolution kernels in Sobel Filter

These can then be combined together to find the absolute magnitude of the gradient at each point and the orientation of that gradient. The gradient magnitude is given as $|G| = \sqrt{G_x^2 + G_y^2}$.

Typically, an approximate magnitude is computed using: $|G|=|G_x|+|G_y|$ which is much faster to compute.

The angle of orientation of the edge (relative to the pixel grid) giving rise to the spatial gradient is given by: $\theta = \arctan\left(\frac{G_x}{G_y}\right)$

C. Non-maximum suppression: The purpose of this step is to convert the "blurred" edges in the image of the gradient magnitudes to "sharp" edges. Basically this is done by preserving all local maxima in the gradient image, and deleting everything else. The algorithm is for each pixel in the gradient image:

(i) Round the gradient direction θ to nearest 45^0, corresponding to the use of an 8-connected neighbourhood.

(ii) Compare the edge strength of the current pixel with the edge strength of the pixel in the positive and negative gradient direction. That is if the gradient direction is north (θ=90°), compare with the pixels to the north and south.

(iii) If the edge strength of the current pixel is largest; preserve the value of the edge strength. If not, suppress (i.e. remove) the value.

D. Double thresholding: The edge-pixels remaining after the non-maximum suppression step are (still) marked with their strength pixel-by-pixel. Many of these will probably be true edges in the image, but some may be caused by noise or colour variations for instance due to rough surfaces. The simplest way to discern between these would be to use a threshold, so that only edges stronger that a certain value would be preserved. The Canny edge detection algorithm uses double thresholding. Edge pixels stronger than the high threshold are marked as strong; edge pixels weaker than the low threshold are suppressed and edge pixels between the two thresholds are marked as weak.

E. Edge tracking by hysteresis: Strong edges are interpreted as "certain edges", and can immediately be included in the final edge image. Weak edges are included if and only if they are connected to strong edges. The logic is of course that noise and other small variations are unlikely to result in a strong edge (with proper adjustment of the threshold levels). Thus

strong edges will (almost) only be due to true edges in the original image. The weak edges can either be due to true edges or noise/colour variations. The latter type will probably be distributed independently of edges on the entire image, and thus only a small amount will be located adjacent to strong edges. Weak edges due to true edges are much more likely to be connected directly to strong edges.

The results are shown below (Figure 2.10):

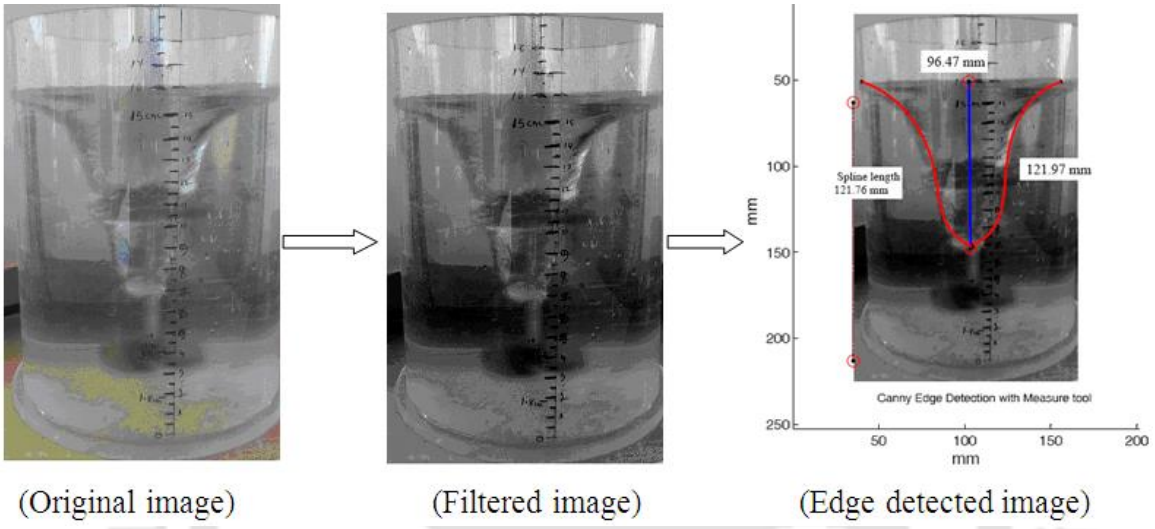

Figure 2.10: Result from Canny edge detection method

2.1.3.2. Fuzzy Edge detector

After applying Canny edge detector, the resulting vortex depth obtained is 96.47 mm. The value obtained seems comparable with naked eye vision analysis of digital images. However, it has been tried to apply more advanced methodology for edge detection to obtain the more refined and probable correct estimate of vortex depth as it governs the basic hydrodynamics as discussed above. Thus, fuzzy edge detection algorithm has been applied to ensure the correct determination of the vortex depth. The procedure is as follows: Continuing from the gradient G_x and G_y defined earlier, an edge can be found by the following formula as:

$$\nabla f = \begin{bmatrix} G_x \\ G_y \end{bmatrix} = \begin{bmatrix} \frac{\partial f}{\partial x} \\ \frac{\partial f}{\partial y} \end{bmatrix} \tag{2.10}$$

Solution of Equation 2.10 is given as:

$$\nabla f = mag(\nabla f) = \left[G_x^2 + G_y^2\right]^{\frac{1}{2}} = \left[\left(\frac{\partial f}{\partial x}\right)^2 + \left(\frac{\partial f}{\partial x}\right)^2\right]^{\frac{1}{2}} \quad (2.11)$$

∇f in Equation 2.11 can be an edge, a line or a point at x and/or y direction. The first order numerical derivative calculated by the following formulas:

$$\frac{\partial f}{\partial x} = f(x+1) - f(x) = f(x) - f(x-1), \frac{\partial f}{\partial y} = f(y+1) - f(y) = f(y) - f(y-1) \quad (2.12)$$

By assigning center and its neighbor pixels in a sample matrix to *z* coefficients the following equations are possible.

$$\begin{aligned} z_1 &= f(x-1, y-1) \quad z_2 = f(x, y-1) \quad z_3 = f(x+1, y-1) \\ z_4 &= f(x-1, y) \quad z_5 = f(x, y) \quad z_6 = f(x+1, y) \\ z_7 &= f(x-1, y+1) \quad z_8 = f(x, y+1) \quad z_9 = f(x+1, y+1) \end{aligned} \quad (2.13)$$

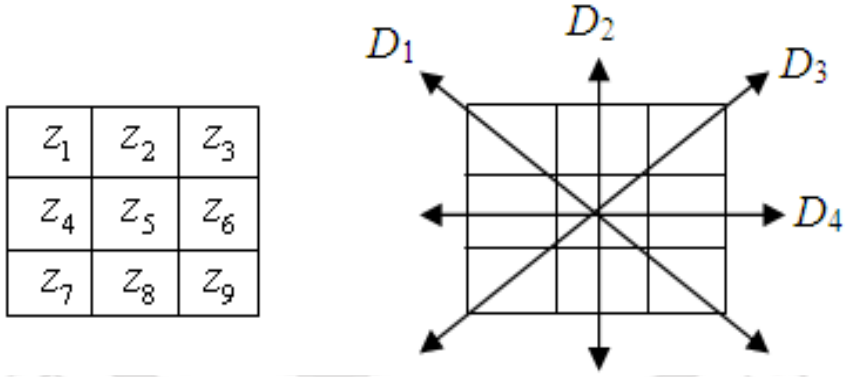

Figure 2.11: Coefficient and possible edge directions for 3x3 sample matrix

The first order derivative values can be calculated using Equation 2.12 for all directions shown in Figure 2.11.

$$\begin{aligned} \nabla D_1 &= (z_5 - z_1)^2 + (z_9 - z_5)^2, \nabla D_2 = (z_5 - z_2)^2 + (z_8 - z_5)^2 \\ \nabla D_3 &= (z_5 - z_3)^2 + (z_7 - z_5)^2, \nabla D_4 = (z_5 - z_4)^2 + (z_6 - z_5)^2 \end{aligned} \quad (2.14)$$

And by applying Equation 2.11, possible edge values are calculated by the following formula:

$$\nabla D = \left[\nabla D_1 + \nabla D_2 + \nabla D_3 + \nabla D_4\right]^{\frac{1}{2}} \tag{2.15}$$

The computational burden of implementation Equations 2.14 & 2.15, it is common practice to approximate the magnitude of the gradient by using absolute values instead of squares and square roots. So, the Equations 2.14 & 2.15 is converted as:

$$\begin{aligned} &\nabla D_1 = |z_5 - z_1| + |z_9 - z_5|,\ \nabla D_2 = |z_5 - z_2| + |z_8 - z_5| \\ &\nabla D_3 = |z_5 - z_3| + |z_7 - z_5|,\ \nabla D_4 = |z_5 - z_4| + |z_6 - z_5| \end{aligned} \tag{2.16}$$

$$\nabla D = \nabla D_1 + \nabla D_2 + \nabla D_3 + \nabla D_4 \tag{2.17}$$

In order to implement a new fuzzy edge detection system $\nabla D_1, \nabla D_2, \nabla D_3$ and ∇D_4 are calculated and put into place of the fuzzy system that uses membership functions like Figure 2.12. The fuzzy system uses singleton fuzzifier and zero-order Sugeno Inference System. Membership functions type is triangle and shown in Figure 2.12.

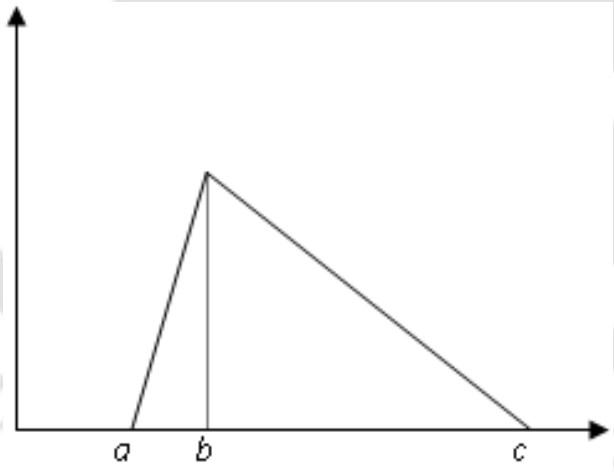

Figure 2.12: Triangle membership function

Results are shown below in Figure 2.13 as:

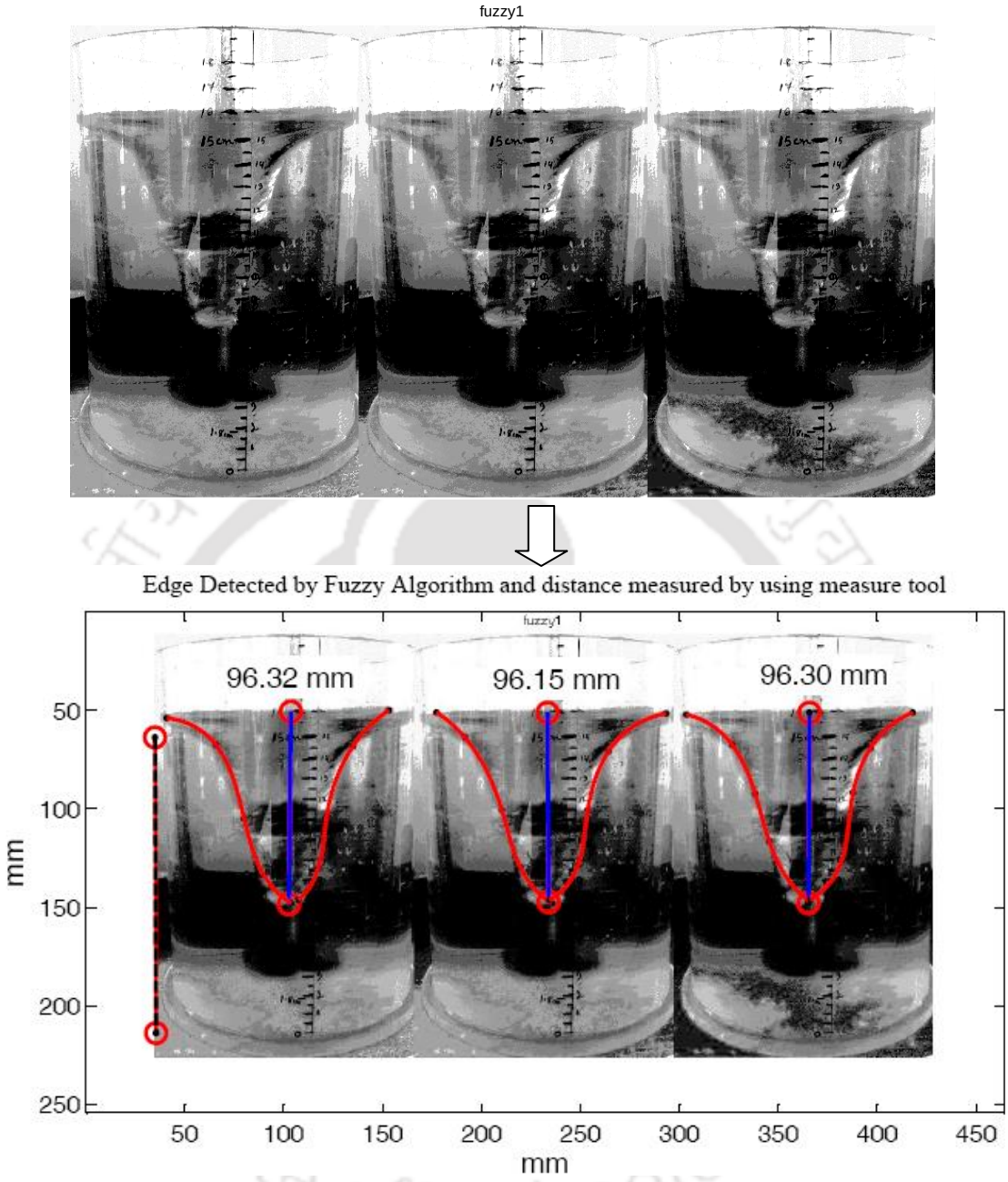

Figure 2.13: Result from Fuzzy Algorithm

Here, the vortex depth obtained from edge detection and fuzzy algorithm is comparable. The vortex depth obtained by canny edge detection method earlier is 96.47mm and by fuzzy algorithm, it gives three values viz, 96.32mm, 96.15mm and 96.30mm. By taking average of these three values, it is 96.26mm; which is adopted for further analysis against the 96.47mm obtained by edge detection method. Same procedure has been followed for each and every experimental runs. (Codes of the above used edge detection method is given in Appendix 1).

2.1.4. Measurement of power consumption

Electrical measurement is a well known technique to measure the power in a stirred tank (Asai and Kono, 1982; Brown, 1997; Nienow et al., 1994; Oosterhuis and Kossen, 1981; Ahmed et al., 2010; Taghavi et al., 2011; Karimi et al., 2011 & 2013). As pointed out by King et al. (1988), electrical measurements can be a suitable methodology, provided the power losses occurring in the motor and in the agitation system are known and subtracted from the total power draw. Depending on the motor used, electrical measurements can be of two different types: direct or alternating current. Power draw in these systems could be properly measured by means of an ammeter, as well as directly by a wattmeter. Universal motor has been used in the present work. Electrical analysis of the motor has been done to ascertain the different characteristics of motor courtesy Electrical Engineering Department, Indian Institute of Technology Guwahati. As we have generally supplied AC current to the motor (except some electricity outage condition), it is essential to know the different parameters which will affect the output power. With the help of ANSOFT Maxwell (Courtesy: Dr. Praveen Kumar, Electrical Engineering Department, IIT Guwahati), the characteristics curve with different rotational speed has been estimated. The output power (mechanical) can be calculated as follows:

$$P_{output} = P_{input}\eta \tag{2.18}$$

Assuming steady state operation and for single phase motor, Equation 2.18 can be written as:

$$P_{output} = VI\cos\varphi\eta \tag{2.19}$$

Where, V_t=voltage, I=current. Power factor and efficiency curve with speed has been developed as shown in the Figure 2.14.

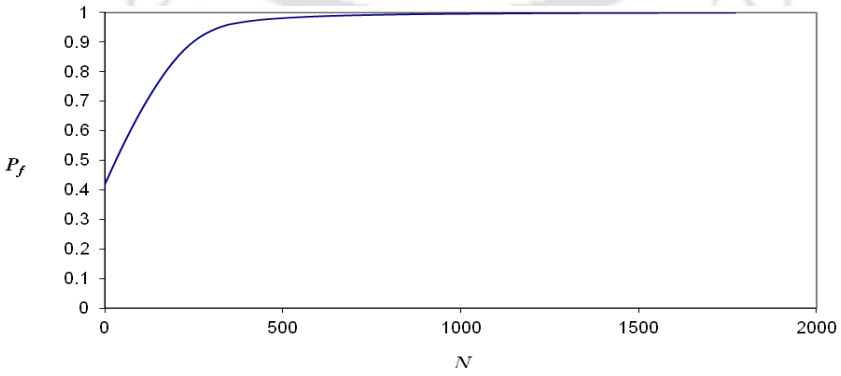

(a) Power factor

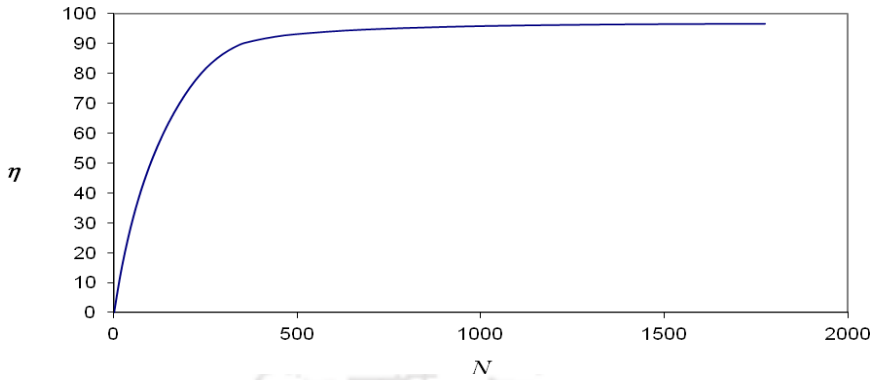

(b) Efficiency

Figure 2.14: Graph showing (a) power factor and (b) efficiency for the measured speed

Power factor is the ratio of the active power to the apparent power expressed as a percentage. It is numerically equal to the cosine of the angle of lag of the input current with respect to its voltage, multiplied by 100. Active power is the power that does work; apparent power has a reactive component. A power factor close to unity (100 percent) is most desirable. The rotational speed of the rotor was measured by using a digital speed indicator or tachometer. The efficiency and power factor for the measured speed has been determined by using Figure 2.14. Thus, the mechanical power has been calculated.

2.2. Ring sparger

Rewatkar et al. (1993) have studied the gas hold-up in gas-liquid reactors using a down-pumping pitched blade turbine with several types and configurations of spargers. Of all the spargers tested, the ring sparger gives the highest gas hold-up: 18 to 25% higher than that obtained when using a single point sparger. The sparger position, on the other hand, has an important effect on mass transfer. It is most advantageous to position the sparger in a location which favours the gas to be entrained into the circulation loop present in the lower part of the tank. The gas then has a longer residence time in the vessel, which promotes mass transfer able to break up the bubbles and to disperse the gas throughout the vessel more compared with the other conditions. Rewatkar et al. (1993) found that a sparger located above the impeller always gives a lower gas hold-up than a sparger located below the impeller. Rewatkar et al. (1993) observed that a ring sparger of diameter equal to 0.8d and 2d gives the maximum gas hold-up. In the case of the ring sparger, a smaller number of holes and holes of

a smaller size give a larger gas hold-up. A ring sparger of 0.8*d* with 6 holes of 3mm diameter has been used to supply air. The air supply from the compressor to the ring sparger was controlled by valve. A rotameter has been fixed before valve to measure the volumetric flow rate (1 L/min to 5 L/min). The location of the sparger is fixed in each experiment at 0.09*D* from the bottom of the tank. There are six holes having diameter (φ) of 3mm and its tube diameter (φ_s) is 5mm. Figure 2.15 shows the details of ring sparger.

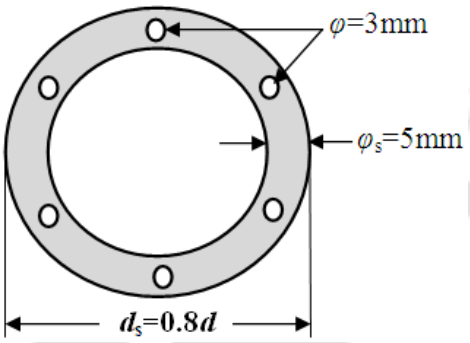

Figure 2.15: Details of ring sparger

2.3. Numerical modeling

The potentiality of Computational fluid dynamics (CFD) as a powerful tool for the design of and scale-up of mechanically stirred reactors has been reported by many researchers e.g. Lane et at. (2005); Deglon and Meyer (2006); Gaubert et at. (2006); Zadghaffari et al. (2010). In recent years, CFD techniques are being increasingly used as a substitute for experiments to obtain the detailed flow field for a given set of fluid, impeller and tank geometries (Ranade et al., 1991). Computational fluid dynamics (CFD) is an accepted and well-used means of assessing and optimizing process designs without necessarily incurring the expense of prototype development (Bridgeman, 2011). One advantage with CFD based prediction methods is that they do not have scaling up or scaling down problems as they solve the fundamental equations governing fluid flow (Zadghaffari et al., 2010). CFD provides a powerful tool for investigating flows at a lower expense than the one required by a high-quality experimental facility (Gentric et al., 2005). Deglon and Meyer 2006) suggested from their study that 'computationally light' conditions may be used if only the mean fluid flow is required but that 'computationally intensive' conditions are required for accurate prediction of turbulence.

2.3.1. Theory of CFD simulation

Computational fluid dynamics is the prediction of fluid flow with the complications of simultaneous flow of heat, mass transfer, phase change, chemical reaction, etc using computers. The numerical modeling part in this study defines about the governing equations and governing parameters involved in Computational fluid dynamics (CFD) simulation. In this study CFD code FLUENT® is used to solve the flow patterns inside the stirred tank. In CFD simulation two main equations are involved as continuity and momentum equation. These equations describe the motion of fluid substances and are solved by iteration process in CFD simulation. In the main momentum equation, one more term called Reynolds stresses (velocity component) by averaging the mean and fluctuating velocity is added, and the new equation is known as RANS (Reynolds Averaged Navier-Stokes) equations. To solve this Reynolds stresses, several turbulence models (*k-ε*; *k-ω*; Large eddy simulation, LES; Reynolds stress model, RSM; etc.) are available based on certain assumptions.

2.3.1.2. Single phase

The governing equations involved in solving the single phase system will be discussed in this section.

2.3.1.2.1. Governing equations

Computational fluid dynamics is the numerical simulation of laminar and turbulent fluid flow regimes. Theoretical predictions were obtained by solving the two equations e.g. conservation of mass and conservation of momentum (Reynolds-averaged Navier-Stokes) simultaneously.

Continuity equation:

The continuity equation is a statement of conservation of mass.

$$\frac{\partial \rho}{\partial t} + \frac{\partial}{\partial x_i}(\rho U_i) = 0 \qquad (2.20)$$

U_i is the i^{th} component of the fluid velocity, and partial derivatives with respect to x_i are assumed to correspond to one of the three coordinate directions. The density can vary in time and in space.

Momentum equation:

The momentum equation is a statement of conservation of momentum in each of the three component directions. The three momentum equations are collectively called the Navier-Stokes equations. Apart from momentum transport by convection and diffusion, several momentum sources are also involved.

$$\frac{\partial(\rho U_i)}{\partial t}+\frac{\partial}{\partial x_i}(\rho U_i U_j)=-\frac{\partial p}{\partial x_i}+\frac{\partial}{\partial x_j}[\mu(\frac{\partial U_i}{\partial x_j}+\frac{\partial U_j}{\partial x_i}-\frac{2\partial U_k}{3\partial x_k}\delta_{ij})]+\rho g_i+F_i \qquad (2.21)$$

In Equation 2.21, the convection terms are on the left. The terms on the right hand side are the pressure gradient, a source term; the divergence of the stress tensor, which is responsible for the diffusion of momentum; the gravitational force, another source term; and other generalized forces (source terms), respectively.

2.3.1.2.2. Governing parameters

A CFD model of a stirred tank requires one to select, amongst others, an appropriate turbulence model (Jaworski and Dudczak, 1998; Aubin et al., 2004; Gentric et al., 2005; Rahimi and Parvareh, 2005; Khopkar et al., 2006; Singh et al., 2007; Kasat et al., 2008; Gimbun et al., 2009; Jahoda et al., 2009), impeller model (Luo et al., 1994; Murthy and Mathur, 1994; Lane et al., 2005; Kasat et al., 2008; Zadghaffari et al., 2010), discretization schemes (Aubin et al., 2004; Deglon and Meyer, 2006), grid resolution (Deglon and Meyer, 2006), convergence criteria, etc. The selection of these, largely numerical considerations, can have a dramatic influence on both the accuracy of the CFD simulation and the associated computational expense (Deglon and Meyer, 2006). The important governing parameters involved in CFD simulation are turbulence model, impeller model, discretization schemes, grid resolution and convergence criteria. These parameters will be discussed in the following subsequent sections.

1. Turbulence model:

In turbulent flow modeling, the most important aspect to be considered for accurate analysis is turbulence modeling. In literature there are several approaches of turbulence models (k-ε; k-ω; Reynolds stress model, RSM; Large eddy simulation, LES; etc.) and most of the studies were performed based on k-ε and RSM models. The under-prediction of dissipative scales is quite often mentioned in many studies when k-ε and RSM models are used especially near the impeller region where the flow is extremely anisotropic (Mostek et al., 2005; Yeaoh et

al., 2004). To overcome such under-prediction of dissipative scale; more delicate in terms of accounting to lower scales of turbulence, LES model is introduced and first applied by Eggels (1996) (application on LES model will be discussed in chapter 6). The three families of *k*-*ε* turbulence model are standard, renormalization group (RNG) and realizable. Several turbulence models such as *k*-*ε*, RSM, LES, *e*tc. are available for carrying out simulation. Among these models *k*-*ε* model is widely used because of its reasonable accuracy for a wide range of turbulent condition in an agitated vessel (Rao and Sivashanmugam, 2010). So, standard *k*-*ε* is used in this study. Reynolds number is one of the parameters to be considered in turbulence model for classifying the flow regimes and is expressed as:

$$Re = \frac{Nd^2\rho}{\mu} \tag{2.22}$$

In the turbulent regime, fluctuations in the mean velocity and other variables occur, and their effect needs to be incorporated into the CFD model in order for the model to be able to provide meaningful results. This is done through the use of a turbulence model. A process of time averaging the conservation equations for turbulence is included in Navier-Stokes equations. When the turbulence is included the transported quantity (velocity), is assumed to be the sum of an equilibrium and a fluctuating component, $U_i + u_i^{'}$. After time-averaging over many cycles of the fluctuation, terms containing factors of the fluctuating component average to zero. Hence Equation (2.21) becomes

$$\frac{\partial(\rho U_i)}{\partial t} + \frac{\partial}{\partial x_i}(\rho U_i U_j) = -\frac{\partial p}{\partial x_i} + \frac{\partial}{\partial x_j}[\mu(\frac{\partial U_i}{\partial x_j} + \frac{\partial U_j}{\partial x_i} - \frac{2\partial U_k}{3\partial x_k}\delta_{ij})] + \frac{\partial}{\partial x_j}(-\rho\overline{u_i^{'}u_j^{'}}) + \rho g_i + F_i \tag{2.23}$$

Equation 2.23 is called Reynolds-Averaged Navier-Stokes, RANS equation for momentum. The new term, $\overline{u_i^{'}u_j^{'}}$ (bar indicates average) is called the Reynolds stresses.

In standard *k*-*ε* turbulence model, two additional transport equations must be solved in order to compute the Reynolds stresses. It is applicable to a wide variety of turbulent flows and serving from many years in the fluid community modeling (Marshall and Bakker, 2002). It is a semi-empirical and the two transport equations that need to be solved for this model are for the kinetic energy of turbulence, *k*, and the rate of dissipation of turbulence, *ε*:

$$\frac{\partial(\rho k)}{\partial t}+\frac{\partial}{\partial x_i}(\rho U_i k)=\frac{\partial}{\partial x_i}(\mu+\frac{\mu_t}{\sigma_k})\frac{\partial k}{\partial x_i}+G_k-\rho\varepsilon \quad (2.24)$$

$$\frac{\partial(\rho\varepsilon)}{\partial t}+\frac{\partial}{\partial x_i}(\rho U_i \varepsilon)=\frac{\partial}{\partial x_i}(\mu+\frac{\mu_t}{\sigma_\varepsilon})\frac{\partial \varepsilon}{\partial x_i}+c_1\frac{\varepsilon}{k}G_k+c_2\rho\frac{\varepsilon^2}{k} \quad (2.25)$$

c_1, c_2, σ_k and σ_ε are empirical constants. G_k is the generation term; the product of velocity gradients and depends on turbulent viscosity:

$$G_k=\mu_t(\frac{\partial U_i}{\partial U_j}+\frac{\partial U_j}{\partial x_i})\frac{\partial U_j}{\partial x_i} \quad (2.26)$$

$$\mu_t=\rho c_\mu\frac{k^2}{\varepsilon} \quad (2.27)$$

The solutions for k and ε are used for solving the turbulent viscosity, μ_t. Using the values of μ_t and k, the Reynolds stresses can be calculated in Equation 2.23 and the new velocity components are used to update the turbulence term, G_k, and the iteration is repeated until the desired convergence criteria is achieved. The values of constants are c_μ=0.09, c_1=1.44, c_2=1.92, σ_k=1 and σ_ε=1.314.

2. Impeller rotation model:

Stirred tanks typically contain one or more impellers mounted on a shaft. There are many types of impeller model exist for example; multiple reference model (MRF), rotating frame model, snapshot model, sliding model (SM) etc. The difficulties face while CFD simulation of mechanically stirred baffled tanks due to the interaction between static baffles and rotating impeller has been reported by Singh et al. (2007).They reviewed various techniques to overcome this problem. They mentioned about the three main generalized impeller model as MRF (Gentric et al., 2005; Deglon and Meyer, 2006; Singh et al., 2007), SM (Zadgaffari et al., 2010; Shekhar and Jayanti, 2002) and snapshot (Ranade and Dometti, 1996; Ranade et al., 2001) model. While the first two approaches is a steady state approach allowing for the modeling of baffled stirred tanks and tanks with other complex (rotating or stationary) internals (Marshall and Bakker, 2002) and produce time averaged flow field, the third approach involve transient computations to produce time accurate flow (Singh et al., 2007). A modification of the rotating frame model is the MRF model (Luo et al., 1994). The modification is that more than one rotating or non rotating reference frames can be in a

simulation (Saito et al., 1992). MRF impeller model was selected in this study to design the impeller in 3D simulation of unbaffled stirred tank. Its successful application in unbaffled stirred tank modeling was also shown by Hormann et al. (2011). In MRF approach, a rotating frame is used for the region of the rotating components while a stationary frame is used for stationary regions. Impeller is at rest in the rotating frame and the tank walls are at rest in the stationary frame. Deglon and Meyer (2006) studied on different impeller models and found MRF model gives adequate results for the steady-state simulation of stirred tanks. The momentum equations inside the rotating frame are solved in the frame of the enclosed impeller while those outside the rotating frame are solved in the stationary frame.

3. Discretization scheme:

For solving the differential governing equations numerically, it is required to be discretized i.e. change from continuous to discontinuous movement of fluid in space and time. In simple word, the region where the fluid flows needs to be described by a series of connected control volumes or computational cells (Marshall and Bakker, 2002). The order of discretization refers to the convective terms in the governing equations. The discretization schemes are upwind differencing scheme, central differencing scheme, power law differencing schemes, QUICK differencing Scheme, etc.

Rahimi and Parvareh (2005) demonstrated that the grid resolution and discretization scheme influence the accuracy of the predicted power number and by using very fine grids and higher-order discretization schemes, power number can be predicted accurately. Aubin et al. (2004) also investigated on three discretization methods (first order-upwind, upwind-central hybrid, QUICK) and found that the choice of the discretization scheme had no effect on the mean velocities, except that the upwind scheme was observed under-predict the swirling region below the impeller. The order of discretization refers to the convective terms in the governing equations. The CFD available discretization schemes are central differencing scheme, first order and second order differencing scheme, Quick differencing scheme. Central differencing scheme is suitable for when the LES (large eddy simulation) turbulence model is used. First order upwind differencing scheme is suitable when the convection dominates and the flow is aligned with the grid. Second order is modified version of first order and QUICK is also similar with second order upwind differencing scheme (Marshall

and Bakker, 2002). In this study, initially first order discretization scheme is used until the solution starts converging and once the solution is converged, it switches to second order scheme in order to enhance the results.

2.3.1.3. Gas-liquid phase

The governing equation in gas-liquid phase modeling is different from single phase condition where one more term for gas phase has to be included in the respective governing equations. The impeller model, discretization scheme, grid size and convergence criteria are same with single phase condition. The changes in phase interaction equations and turbulence model will be discussed in this section.

2.3.1.3.1. Governing equations

The hydrodynamics of transport characteristic and power consumptions in gas-liquid stirred tank are successfully predicted using Computational Fluid Dynamics (CFD). It is an effective tool in modeling of fluid related systems. In this technique, various multiphase models are available, however, Eulerian-Eulerian model is the most successfully and commonly used model without incorporating the distributions of bubbles (Deen et al., 2002; Lane et al., 2004; Khopkar et al., 2006; Montante et al., 2007; Scargiali et al., 2007).

Eulerian-Eulerian multiphase model is used to simulate the hydrodynamics of flow in this study. The phases (continuous and disperse) are treated as interpenetrating media identified by their local volume fractions. The volume fractions sum to unity and are calculated by using continuity equation. The Reynolds averaged mass and momentum balance equations are solved for each of the phases and are given as follows:

Continuity equation:

$$\frac{\partial}{\partial t}\left(\alpha_i \rho_i\right) + \nabla.\left(\alpha_i \rho_i U_i\right) = 0 \tag{2.28}$$

$$\alpha_l + \alpha_g = 1 \tag{2.29}$$

Where, ρ_i, α_i and U_i are density, volume fraction and mean velocity, respectively, of phase i (l or g).

Momentum equation:

$$\frac{\partial}{\partial t}\left(\alpha_i \rho_i U_i\right)+\nabla.\left(\alpha_i \rho_i U_i U_i\right)=-\alpha_i \nabla p+\nabla.\bar{\bar{\tau}}_{eff\,i}+R_i+F_i+\alpha_i \rho_i g \tag{2.30}$$

Where, p is the pressure shared by the two phases and R_i is the inter-phase momentum exchange terms. F_i, represents the Coriolis and centrifugal forces applies in MRF (multiple reference frame) impeller model which is used in this study as impeller model.

$$F_i=-2\alpha_i \rho_i N_i \times U_i-\alpha_i \rho_i N_i \times\left(N_i \times \vec{r}\right) \tag{2.31}$$

Where, N_i is angular velocity (rad s^{-1}) and $\vec{r}$ is position vector (m).

The Reynolds stress tensor $\bar{\bar{\tau}}_{eff\,i}$ is the laminar and turbulent stresses and by Boussinesq hypothesis, it is given as

$$\bar{\bar{\tau}}_{\text{eff}i}=\alpha_i\left(\mu_{\text{lam},i}+\mu_{t,i}\right)\left(\nabla U_i+\nabla U_i\right)-\frac{2}{3}\alpha_i\left(\rho_i k_i+\left(\mu_{\text{lam},i}+\mu_{t,i}\right)\nabla.U_i\right)\bar{\bar{I}} \tag{2.32}$$

$\mu_{\text{lam},i}$ and $\mu_{t,i}$ are laminar and turbulent viscosity for phase i. k_i is turbulent kinetic energy for phase i and $\bar{\bar{I}}$ is unit tensor.

2.3.1.3.2. Turbulence model

Standard k-ε turbulence model is adequate for many engineering applications (Ranade, 2002) and is used in this study with dispersed k-ε multiphase turbulence model to simulate the gas-liquid phase flow as gas (secondary phase) is dispersed in continuous liquid (primary phase). The governing equations of turbulent kinetic energy, k and turbulent dissipation rate, ε, are solved only for liquid phase as

$$\frac{\partial}{\partial t}\left(\rho_l \alpha_l k_l\right)+\nabla.\left(\rho_l \alpha_l U_l k_l\right)=\nabla.\left(\alpha_l \frac{\mu_{t.l}}{\sigma_k}\nabla k_l\right)+\alpha_l G_{kl}-\rho_l \alpha_l \varepsilon_l+\rho_l \alpha_l \prod_{kl} \tag{2.33}$$

$$\frac{\partial}{\partial t}\left(\rho_l \alpha_l \varepsilon_l\right)+\nabla.\left(\rho_l \alpha_l U_l \varepsilon_l\right)=\nabla.\left(\alpha_l \frac{\mu_{t.l}}{\sigma_\varepsilon}\nabla \varepsilon_l\right)+\alpha_l \frac{\varepsilon_l}{k_l}\left(c_{1\varepsilon} G_{kl}-c_{2\varepsilon}\rho_l \varepsilon_l\right)+\rho_l \alpha_l \prod_{\varepsilon l} \tag{2.34}$$

Turbulent liquid viscosity is given as:

$$\mu_{t.l}=\rho_l c_\mu \frac{k_l^2}{\varepsilon_l} \tag{2.35}$$

G_{kl} is the rate of production of turbulent kinetic energy. $\prod_{kl}$ and $\prod_{\varepsilon l}$ represents the influence of the dispersed phase on the continuous phase (Elgobashi and Rizk, 1989). $c_\mu, c_{1\varepsilon}, c_{2\varepsilon}, c_{3\varepsilon}$,

σ_k and σ_ε are constants of standard *k*-ε model. Their values are 0.09, 1.44, 1.92, 1.2, 1.0 and 1.3 respectively.

$\prod_{kl}$ and $\prod_{\varepsilon l}$ takes into account the turbulence interaction between the water and air phases and modeled as:

$$\prod_{kl} = \frac{C_D}{\alpha_l \rho_l}\left(C_{lg} - 2k_l + U_{lg}.U_{dr}\right) \tag{2.36}$$

Where, C_{lg} is the covariance of the velocities of air and water; $U_{lg}\,(=U_g - U_l)$ is the relative velocity of air and water; and U_{dr} is the drift velocity.

$$C_{lg} = 2k_l\left(\frac{b+\eta_{lg}}{1+\eta_{lg}}\right)$$
$$U_{dr} = -\left(\frac{D_g}{\sigma_{lg}\alpha_g}\nabla\alpha_g - \frac{D_l}{\sigma_{lg}\alpha_l}\nabla\alpha_l\right) \tag{3.37}$$

Here, $b = (1+C_v)\left(\frac{\rho_l}{\rho_g}+C_v\right)^{-1}$; $C_v = 0.5$; D_g and D_l are diffusivities; and σ_{lg}=0.75 (default) is a dispersion Prandtl number. Details of D_g, D_l and η_{lg} can be obtained from the work of Simonin and Violett (1990). According to Elgobashi and Rizk (1989):

$$\prod_{\varepsilon l} = c_{3\varepsilon}\frac{\varepsilon_l}{k_l}\prod_{kl} \tag{3.38}$$

Where, $c_{3\varepsilon}$=1.2.

2.3.1.3.3. Inter-phase momentum exchange

Interphase momentum term comprises of Basset force, the virtual mass force, the lift force and the drag force. Basset force arises due to the development of a boundary layer around bubbles and is relevant only for unsteady flows. The magnitude of the Basset force is much smaller than that of the interphase drag force and inclusion of this force consumes longer time to evaluate (Khopkar et al., 2003). Lift force is significant if the velocity gradients are large but in stirred vessel, it is very small in bulk region and it significance is only near the impeller region. Near the impeller, the pressure gradients and the drag forces mainly dominate the bubble motion. An order of magnitude analysis indicates that the magnitude of

the lift force is much smaller than the drag force (Lane et al., 2000). They showed that the effect of the virtual mass force is significant near the impeller blades and that in the bulk volume the effect diminishes. Similar result was also obtained by Khopkar et al (Khopkar et al., 2003). Even after neglecting the lift forces one can still lead to good comparison with experimental data (Pan et al., 1999, 2000; Pan and Dudokovic, 2001). Scargiali et al., (2007) and Sanyal et al. (1999) studied about the effects of all inter-phase forces (Basset, lift, virtual mass and drag) and they found that effects of the other forces are too small as compared to drag force. Because of this reason, several authors (Aubin et al., 2004; Kerdouss et al., 2006; Ranganathan and Sivaraman, 2011; Buffo and Marchisio, 2012) preferred to consider only drag force particularly for the modeling of gas-liquid stirred tank in order to save the computational cost which is very essential in the field of commercial modeling. Drag force is the only controlling force in stirred tanks and for other equipments (i.e., bubble column), the other forces are also relevant (Buffo and Marchisio, 2012). Drag force is the most important inter-phase force acting on the bubbles resulting from the mean relative velocity between the two phases and an additional contribution resulting from turbulent fluctuations in the volume fraction due to averaging of momentum equations (Fluent, 2006). By keeping all these in view, we also preferred to use only drag force in our study intentionally to save the modeling expenses understanding that the results are not going to affect much.

Considering only the drag force, R_i from Equation 2.30 reduced only to drag force as:

$$R_l = -R_g = K\left(U_g - U_l\right) \tag{2.39}$$

K is the liquid-gas exchange co-efficient given as:

$$K = \frac{3}{4}\rho_l \alpha_l \alpha_g \frac{C_D}{d_b}\left|U_g - U_l\right| \tag{2.40}$$

d_b is the bubble diameter and C_D is the drag co-efficient defined as function of relative Reynolds number, Re_p. The standard formulation of Re_p does not account the effect of turbulence on bubble movement. Hence, Re_p has been modified (code of modified drag law is given in Appendix 1) to include the effect of turbulence (Bakker and Akker, 1994):

$$Re_p = \frac{\rho_l \left|U_g - U_l\right| d_b}{\mu_l + C\mu_{t,l}} \tag{2.41}$$

C is the model parameter introduced to account for the effect of the turbulence in reducing slip velocity. This parameter is set to 0.3 (Kerdouss et al., 2008). Drag co-efficient is then calculated using standard correlation of Schiller and Naumann (Ishii and Zuber, 1979) which is written as:

$$C_D = \begin{cases} \dfrac{24\left(1+0.15Re_p^{0.687}\right)}{Re_p}, & Re_p \le 1000 \\ 0.44, & Re_p > 1000 \end{cases} \quad (2.42)$$

Originally this drag model was developed based on Stokes law for single rigid sphere in gas-solid systems for very low Reynolds number (Re_p>1) and later for higher range of Re, this model exists as Schiller and Naumann (Ishii and Zuber, 1979) drag model. Stokes law is applicable in gas-liquid systems also as the small solid particles can be assumed as bubbles. And bubbles adopt a smaller range of shape and are spherical under certain circumstances (Clift et al., 1978). So, by considering the bubbles are spherical in shape adopting very small size of bubble (d_b=2mm), Schiller and Naumann drag model is used in gas-liquid flows of this study.

2.3.1.3.4. Mass transfer model

There are several model available in literature for calculating local mass transfer co-efficient (K_L) but commonly used model are based on penetration theory (Higbie, 1935) and surface renewal model (Danckwerts, 1951) when the bubble diameter is known. Higbie (1935) penetration theory expressed that the liquid phase mass transfer coefficient of a bubble with a mobile surface as:

$$K_L = \frac{2}{\sqrt{\pi}}\sqrt{\frac{D_l}{t_e}} \quad (2.43)$$

Where t_e is the contact time and is calculated based on Kolmogorov's Length scale of isotropic turbulence as $t_e = \sqrt{\nu_l / \varepsilon_l}$; ε_l is turbulent dissipation rate and ν_l is the kinematic viscosity of liquid (Kolmogorov's, 1941). So, Equation 2.43 becomes as:

$$K_L^{\,penetration} = \frac{2}{\sqrt{\pi}} D_l^{0.5}\left(\frac{\varepsilon_l}{\nu_l}\right)^{0.25} \quad (2.44)$$

And this model is denoted as $K_L^{penetration}$. D_l is the diffusion co-efficient.

Volumetric mass transfer co-efficient (K_La_{20}) is the combination of K_L and a, where a is the interfacial specific area and is a function of local volume fraction, α_g and bubble diameter, d_b. Therefore, a is expressed as

$$a = \frac{6\alpha_g}{d_b} \tag{2.45}$$

The global mass transfer co-efficient $\langle K_L a_{20} \rangle$ for an air-water stirred tank is given as:

$$\langle K_L a_{20} \rangle = C_{k_L a} \left(\frac{P_g}{V} \right)^a v_g{}^b \tag{2.46}$$

According to Van't Riet (1979), the values of constant $C_{kL}a$, a and b are 0.026, 0.4 and 0.5 respectively obtained from a fit to experimental measurements.

2.3.2. Prediction of power input

Power consumption/ input is a crucial characteristic of stirred tank reactors (Zadghaffari et al., 2010). In this study, power input was estimated based on total torque required to rotate the impeller and the relation of torque for each blade can be written as:

$$\tau = \Sigma (\Delta p)_i A_i r_i \tag{2.47}$$

Where, the summation is over the control cells i corresponding to each blade, Δp is the pressure difference between the front and the back side of the blade at the surface element I, and r_i is the radial distance from the axis of the shaft on which the impeller is mounted. The power required for the rotation of the impeller at a steady rotational speed of N revolution per second for an impeller having n number of blades is given by the following relation as:

$$P = 2\pi N n \tau \tag{2.48}$$

This power input may be in single phase or in sparged condition (for single phase P is denoted as P_{eff} and for sparged condition it is as P_g). Power consumption is generally expressed in terms of power number and is given as:

$$N_p = P / (\rho N^3 d^5) \tag{2.49}$$

2.3.3. Boundary condition

In numerical simulation of stirred tank, adoption of suitable boundary condition is required in order to represent the real physical boundary condition of the domain. Boundary condition is different for different operation of system, for example, for single phase system, there is no

much complexity in deciding the boundary condition but for gas-liquid phase where ring sparger is used as gas supplier to the system, there is little care to be taken in deciding the suitable boundary condition. In order to understand the suitable boundary condition in single phase as well as in gas-liquid phase, the existing boundary conditions will be discussed.

The existing boundary conditions in single phase system where the operating fluid is water and tank top is open to atmosphere are at walls (shaft walls, impeller walls, tank side walls, tank bottom wall, and baffle walls; if baffle is provided) and on the top surface of the tank (Figure 2.16). No slip condition is applied at all walls. So, the additional boundary condition exists in gas-liquid phase is at ring sparger.

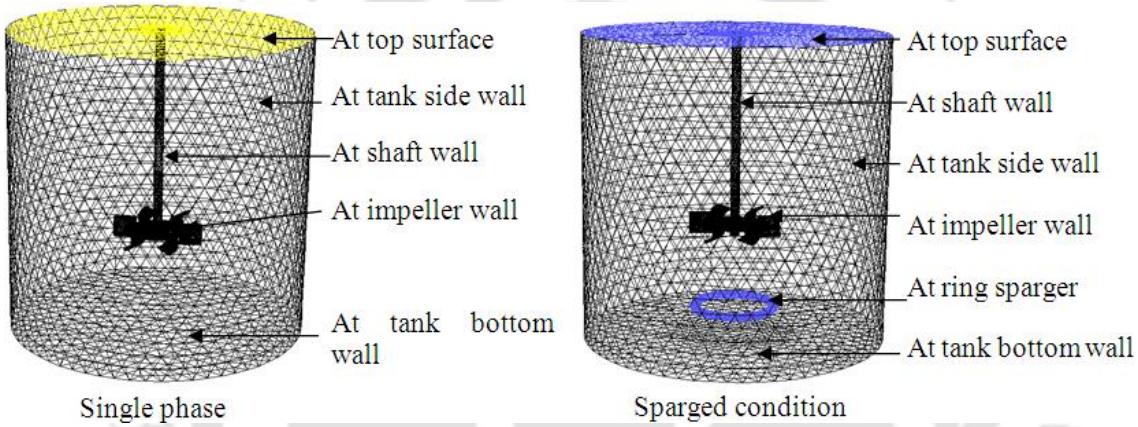

Figure 2.16: Applicable boundary condition exists in stirred tank for single phase (left) and sparged condition (right)

The top surface, which is open to atmosphere, the boundary conditions should satisfy that the gas should escape from the computational domain and liquid is not allowed to escape. So, the researchers have used various boundary conditions such as symmetry (default in FLUENT), walls (Wadnerkar et al., 2012); velocity-inlet and pressure-outlet (Gimbun et al., 2009); pressure-inlet (Montante et al., 2007) and degassing condition (Moullec et al., 2010) which is achieved through user defined functions (UDF). The commonly used boundary conditions at top surface are velocity-inlet (Khopkar and Tanguy, 2008; Taghavi et al., 2011; Elqotbi et al., 2013) and degassing condition (Raouf, 2001; Kshatriya et al., 2007; Scargiali et al., 2007; Ranganathan and Sivaraman, 2011). After several studies on these boundary conditions and comparing with possible outcomes, degassing boundary condition is chosen in this study as it is better inclined to reality. So, top surface is applied as degassing boundary condition

through user-defined functions which satisfies that the gas should escape from the computational domain and liquid (water) will remain inside the domain. Only the axial gas velocity component is considered. Water velocity is taken as zero. Operating pressure is considered as atmospheric pressure (101235pa). Velocity-inlet boundary condition (Panda, 2011) is applied at the ring sparger of volume fraction equal to 1. The inlet gas velocity ($U_{g,\text{inlet}}$) at the sparger is calculated as (Panda, 2011):

$$U_{g,\text{inlet}} = \frac{v_g}{\alpha_g} \frac{A_{reactor}}{A_{sparger}} \frac{P_{operating}}{P_{sparger}} \tag{2.50}$$

$A_{reactor}$ and $A_{sparger}$ are the cross-sectional area of the stirred tank and sparger. $P_{operating}$ is the operating pressure. $P_{sparger}$ is the corresponding pressure at the sparger which is calculated as:

$$P_{sparger} = P_{operating} + \rho_l g h \tag{2.51}$$

Where, ρ_l (998.2kg/m^3) and g (9.81m/s^2) are the density of liquid and acceleration due to gravity. h is the height of sparger from tank bottom.

2.3.4. Grid generation and its size

The starting point for all problems is "geometry." The geometry describes the shape of the problem to be analyzed. It consists of volumes, faces (surfaces), edges (curves) and vertices (points). Notations of generated grids are:

- Cell = control volume into which domain is broken up
- Node = grid point
- Cell center = center of a cell
- Edge = boundary of a face
- Face = boundary of a cell
- Zone = grouping of nodes, faces, and cells
- Domain = group of node, face and cell zones.

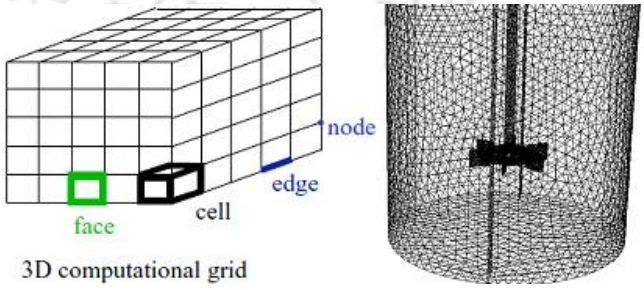

Figure 2.17: Details of 3D mesh (centre) and representation of generated grid (coarse grid) of stirred tank (right)

The grid, also called a mesh, consists of discrete elements located throughout the computational domain and fits the contours of the vessel and its internals. After defining the model, a computational domain is to be generated that is defined by a grid. This grid is used as the basis of the solution procedure. In mixing simulations, the computational domain is the volume occupied by the fluid inside the vessel. Discrete elements are formed by lines (in 2D) or surfaces (in 3D) of different shapes and sizes. Together these elements constitute a grid. In a CFD analysis, conservation equations for flow and heat transfer are solved in each of these elements, or control volumes, throughout the domain. A good quality grid is an essential ingredient for a successful and accurate solution. If the grid is too coarse, the resulting solution may be inaccurate and if the grid is too fine, the computational cost may become prohibitive. So, the cost and accuracy of the solution are directly dependent on the quality of the grid.

Representation of mesh formation and generated grid is shown in Figure 2.17. Size of grid is represented by number of cells with number of faces and nodes, for example, the size of grid for the above shown diagram (Figure 2.17 right side) has cells=236700, nodes=480070 and faces=42856. Grid may be tetrahedral or triangular shape. Generally tetrahedral are generated in literature. Finer grid resolution gives better results than the coarse grid but it is more costly than the coarse grid. Convergence criteria are the preset conditions for the residuals. The solution is no longer changing when the condition is reached and that there is an overall mass balance throughout the domain. For a good accuracy higher convergence is needed. In this study, a 3D grid is generated in Gambit software.

By taking an example of single phase dual impeller system, sensitivity of grid size is done. For this particular computational domain (D=H=150mm), grids are classified based on number of cells generated as (Figure 2.18):

(i) Fine: 564377 cells, 1157203 nodes, 142306 faces

(ii) Intermediate: 506692 cells, 1119072 nodes, 138205 faces

(iii) Coarse: 350549 cells, 750451 nodes, 8810 faces

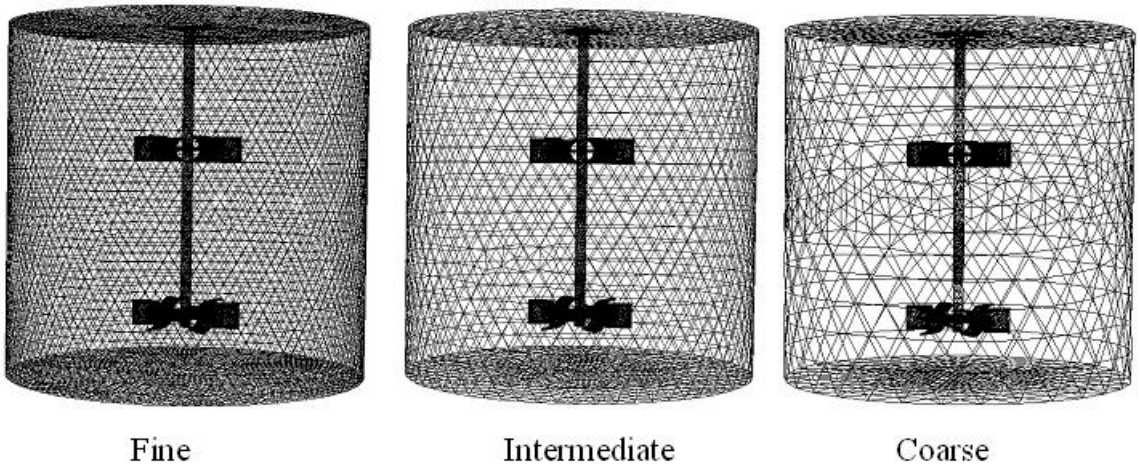

Figure 2.18: Different sizes of grid

Power number (*Np*) has been found experimentally as 63.21 while numerically fine grid predicts 60.47, intermediate grid gives 56.32 and for coarse grid, it is 49.326. By considering the above discussed trade off conditions, intermediate grid size has been adopted which gives reasonable result as well as computational cost. Such type of study was repeated for single phase and for sparged condition in both single and dual impeller system which will be explained in the respective chapters. Detail of cell skewness of the intermediate grid size is given as:

485950 cells below 0.6 (95.997991 %)

12950 cells between 0.6 and 0.65 (2.4403716 %)

5134 cells between 0.65 and 0.7 (1.029174 %)

2040 cells between 0.7 and 0.75 (0.40893799 %)

561 cells between 0.75 and 0.8 (0.11207632 %)

57 cells between 0.8 and 0.85 (0.011448657 %)

0 cells between 0.85 and 0.9 (0 %)

0 cells between 0.9 and 0.95 (0 %)

0 cells between 0.95 and 1 (0 %)

0 cells above 1 (0 %)

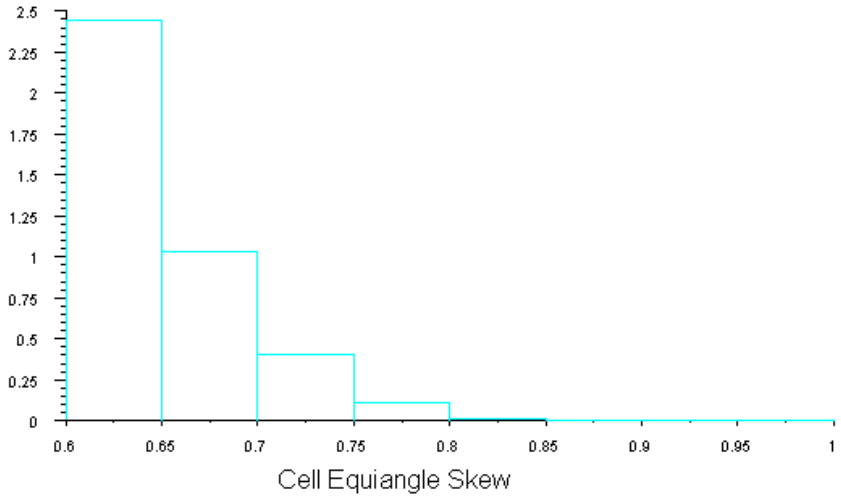

Figure 2.19: Graphical representation of cell skewness of the intermediate grid

Figure 2.19 shows the cell skewness of the generated grid of the stirred tank. Around 96% of cells are below cell skewness of 0.6 which is within fair cell quality (Table 2.2). This is acceptable cell quality in the generation of grid in numerical modeling.

Table 2.2: Range of cell skewness

Value of skewness	**Cell quality**
1	degenerate
0.9- 1	bad (sliver)
0.75-0.9	poor
0.5-0.75	fair
0.25-0.5	good
0-0.25	excellent
0	equilateral

CHAPTER 3

DESIGN OF UNBAFFLED STIRRED TANK WITH SINGLE CONCAVE BLADE IMPELLER

3.1. Introduction

Single impeller stirred tanks are very commonly and frequently used in process industries as bioreactors and chemical reactors for carrying out operations like blending of fluids, dispersing two immiscible fluids, suspension of solids, heat and mass transfer and chemical reactions. An appropriate design model of stirred tank requires the information of various transport, kinetic, and mixing parameters (Pangarkar et al., 2002). The modification of existing stirred tank for better efficiency, as well as the design of new mixing systems or new type of impellers requires an accurate knowledge of the flows induced by the impellers in the vessel (Mahmoudi, 1993). The prediction of performance of stirred tank reactors still remains a challenging problem on account of the complex hydrodynamics generated by the rotating stirrers. The correct design and operation of these reactors can be crucial to the profitability of a process by virtue of its influence on the reaction yield or productivity (Patwardhan and Joshi, 1998). Literature is replete with the simulation and scale up criteria for standard Rushton impeller in baffled condition ((Reed et al., 1997, Ng and Yianneskis, 2000; Assirelli et al., 2008; Chunmei et al., 2008; Zadghaffari et al., 2010; Li et al., 2011; Taghavi et al., 2011) but it is very less based on concave blade impeller except some few studies discussed earlier.

Thus, the objective of the present chapter is to investigate the effect of impeller clearance in unbaffled single impeller stirred system with concave blade impeller in single phase (un-sparged) and gas-liquid phase (sparged) conditions. The idea is to come up with design criteria with impeller clearance and a general scale up criteria inclusive of effect of impeller clearance and impeller size. In order to characterize the hydrodynamics in terms of velocity, turbulent statistics, vortex, mass transfer and power number, numerical simulations will be carried out to ascertain the effect of impeller clearance in unbaffled system stirred with concave blade impeller.

3.2. Experimental tank geometry

This unbaffled single impeller tank will be studied on un-gassing (single phase/un-sparged) and gassing (gas-liquid/sparged) system (Figure 3.1).

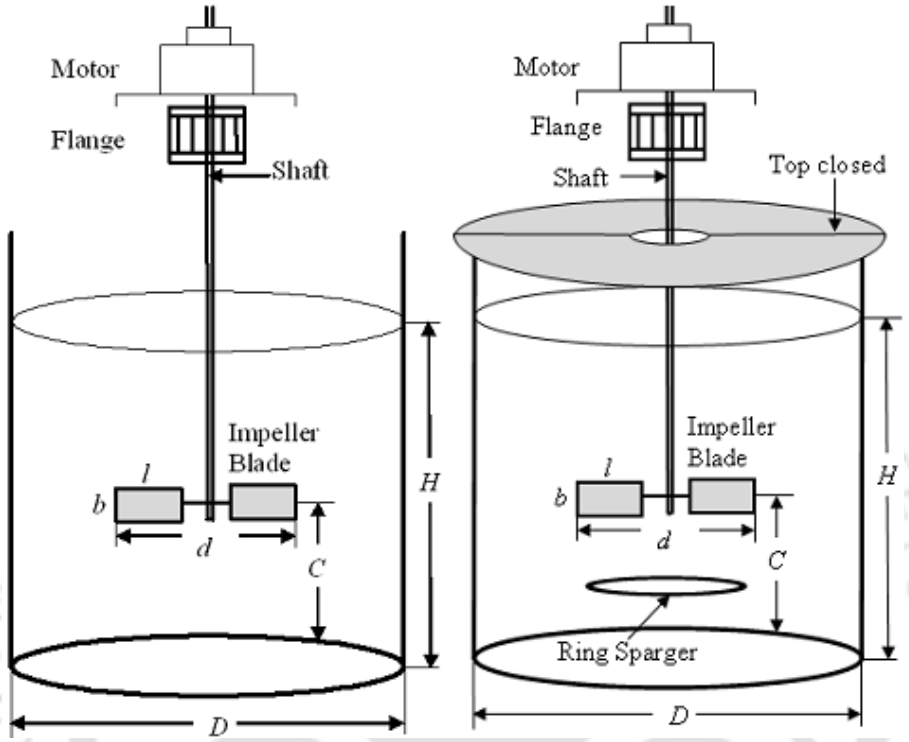

Figure 3.1: Schematic diagram and experimental set up of stirred tank for un-sparged (left) and sparged system (right).

Circular tank of 150 and 200mm diameter (D) were used with different impeller diameter (d). Impeller to tank diameter (d/D) is taken as 0.2, 0.3 & 0.4. The ratio of impeller clearance depth (C) to tank diameter (D) was varied from 0.3 to 0.9. Tank is filled with water of height equal to tank diameter (H/D=1). Table 3.1 gives the details of stirred tank geometry used in this study.

Table 3.1: Details of stirred tank geometry

	Tank dia. (D)	Impeller dia. (d)
Height of water (H)=D=150mm	150mm	30mm,45mm,60mm
Length of blade (l/d)=0.25	200mm	40mm,60mm,80mm
Width of blade (b/d)=0.2		
Number of blade (n)=6		
Thickness of blade (t_b)=1mm		
C=0.3D to 0.9D		

In sparged system, additional source of gas (air) is supplied in order to enhance the mixing mechanisms expecting better mass transfer rate from un-sparged system. Gas is supplied through ring sparger kept below the impeller. A transparent lid was located on the top to eliminate or limit the free surface interaction. Details of sparger design have already been given in Chapter 2 of experimentation part. The result which is to be discussed in this chapter is only for 150 mm tank diameter except for scale up relationship. Results of 200mm tank diameter are listed in Appendix 2.

3.3. Single phase

The system of stirred tank where only one medium (water) is employed as an operating fluid inside the vessel is termed as single phase system. Single phase stirred tank has several applications in various mixing process especially in bioreactors where microbial activities are taken place. In such systems, specific amount dissolved oxygen which can be quantified by mass transfer coefficient need to be maintained in order to increase the cell growth. The interaction between atmospheric gas (oxygen) from surroundings and liquid (water) inside the vessels takes place even without gassing system because of the continuous movement of the impeller in single phase stirred tanks. In recent years, there has been an increased awareness for the treatment of aqueous waste streams. Wastewater treatment operation often involves solid particles (dirt, grit, microorganisms, etc.). If a sparger system were to be used for such operations then there exists a possibility that the sparger holes can get partly blocked causing excessive pressure drop and poor aeration characteristics. Use of a stirred tank without sparging may eliminate all such problems. In such systems, the stirred tanks usually have to perform three functions, namely, transfer of oxygen from air to the liquid phase, mixing of the liquid phase and suspension of the microorganisms. The design and scale-up relationship is extremely important in such applications.

3.3.1. Mass transfer rate

Mass transfer rate expressed by coefficient of mass transfer rate ($K_L a_{20}$) is an important aspect to understand in designing of stirred tank. It is also the major factor affecting parameter of mixing mechanisms in impeller driven stirred tanks.

3.3.1.1. Effect of impeller clearance depth (C)

In order to understand the effects of impeller clearance depth (C) on K_La_{20}, experimental observations were done on various C/D values (0.3 to 0.9) with different impeller rotational speeds (N). Experimental values of K_La_{20} are plotted against N at different C/D for a particular impeller to tank diameter ratio (d/D) in Figure 3.2. K_La_{20} increases with increase in N. Increasing speed increases the turbulence and surface renewal rate at the gas-liquid surface and consequently $K_La_{20.}$ In all the cases of different d/D, there is no significant efficient/optimal impeller clearance depth observed based on K_La_{20} except closer observation reveals slight higher values of K_La_{20} at higher clearance. The reason behind this could be as the impeller clearance increases, at a given impeller speed, the amount of energy reaching the liquid surface increases. Therefore, the intensity of surface aeration increases. This also increases the air-water mass transfer rate and thus increasing the overall mass transfer rate.

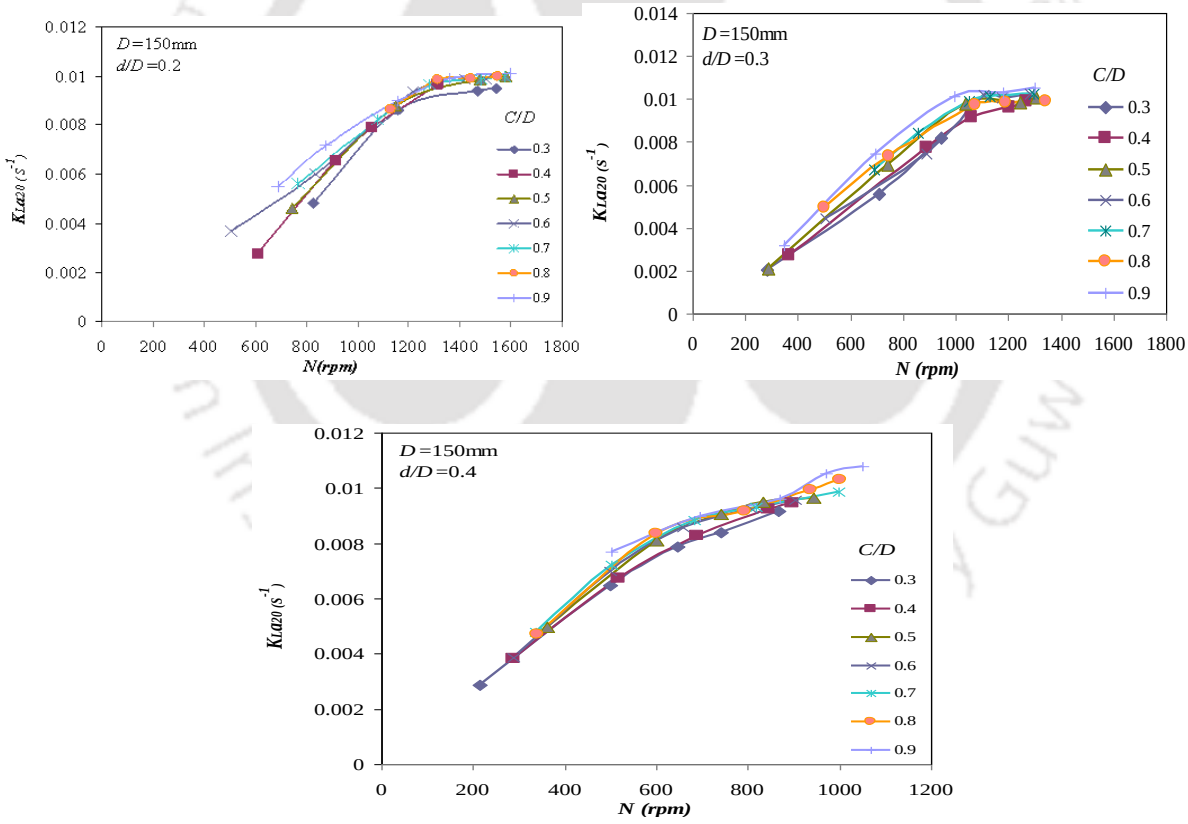

Figure 3.2: K_La_{20} with N for different C/D

3.3.1.2. Effect of impeller diameter (d)

Impeller diameter plays major role in the performance of stirred tank. In order to understand its effect on K_La_{20}, the measured K_La_{20} at different impeller speed at a particular impeller

clearance depth is presented in Figure 3.3. It shows that K_La_{20} increases with increase in impeller to tank diameter (d/D) ratio with different impeller clearance depth. This means that K_La_{20} increases with increase in impeller diameter when the tank diameter is constant. This may be because of the fact that the volume of water swept by the impeller increases with increasing impeller diameter when the tank diameter is constant. It leads to increase the area of strong flow circulation and eventually increases mass transfer rate. When the impeller diameter is increased while the tank diameter is constant, the influence of flow comes out from the continuous movement of impeller strikes on the wall of the tank with stronger intensity and increases the intensity of turbulence inside the vessel. Such kind of strong intensity flow turbulence may create higher mass transfer rate as a whole.

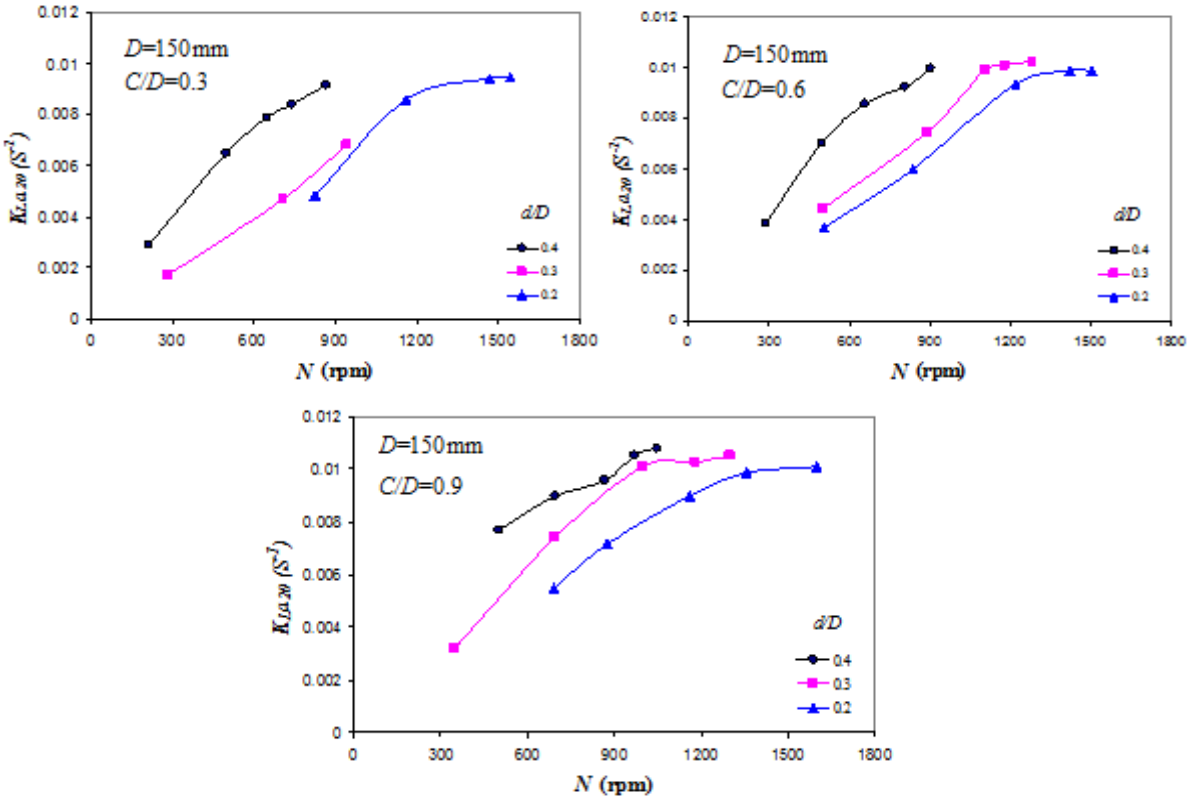

Figure 3.3: K_La_{20} with N for different d/D

3.3.1.3. Design criteria for mass transfer rate

The variables influencing the mass transfer coefficient (K_La_{20}) at standard temperature (20^{o}C) for a given shape of a stirred tank are given (Rao and Kumar, 2007) as:

$$K_La_{20} = f\left(H, D, d, l, b, C, n, N, g, \rho_{a,}\rho_{w,}\upsilon\right) \quad (3.1)$$

Where, l is the blade length, b is blade height, n is the number of the blade (6 in the present work), g is the gravitational acceleration, ρ_a and ρ_w is the density of air and water respectively and υ is the kinematic viscosity of the water. Equation 3.1 may be expressed in terms of non-dimensional parameters as follows:

$$k_c = f\left(H/D, d/D, l/d, b/d, C/D, n, \rho_a/\rho_w, Re, Fr\right) \tag{3.2}$$

Where, $k_c = K_L a_{20}\left(\upsilon/g^2\right)^{1/3}$ is the non-dimensional mass transfer parameter, $Re = Nd^2/\upsilon$ is called Reynolds number and $Fr = N^2 d/g$ is the Froude number. As H/D, n, l/d and b/d are maintained constant at 1, 6, 0.25 and 0.2 respectively and parameter ρ_a/ρ_w is assumed as invariant, hence these parameters can be eliminated from the analysis. Thus, Equation 3.2 reduces to the following form as:

$$k_c = f(d/D, C/D, Re, Fr) \tag{3.3}$$

The intensity of turbulence and wave action on the water are the major factors normally associated with unbaffled stirred tank. Turbulence and viscous effects are generally described by the Reynolds number (Re), whereas the surface wave action is described by the Froude number (Fr). In the case of unbaffled tanks, swirl exists, giving the necessity of correlating Froude number in the analysis (Rushton et al., 1950). Reynolds and Froude number can be further combined into a new number $X\left(=Fr^{4/3}Re^{1/3} = N^3 d^2/\mathrm{g}^{4/3}\upsilon^{1/3}\right)$, called theoretical power per unit volume as proposed by Rao and Kumar (2009). Thus, Equation 3.3 assumes the following form:

$$k_c = f\left(C/D, d/D, X\right) \tag{3.4}$$

Equation 3.4 suggests that for a constant C/D, k_c is the function of d/D and X. The function, which governs the Equation 3.4 for constant C/D, has been developed statistically. The form of the function is kept as follows:

$$10^5 k_c = \alpha(d/D)^{\beta} X^{\gamma} \tag{3.5}$$

Where α, β and γ are the parameters of the function, which is optimized to get the maximum correlation coefficient (R^2) and minimum standard error based on experimental observation. Statistical details of the parameters used in Equation 3.5 are given in the Table 3.2.

Table 3.2: Statistical details of Equation 3.5 for different *C*/*D*

C/D	***α***	***β***	***Γ***	**Overall std. error**
0.3	1.7 (2.25e-2)	0.82 (1.44e-2)	0.28 (3.13 e-2)	1.19e-2
0.4	1.44 (2.76e-2)	0.76 (1.17e-2)	0.28 (4.1e-3)	2.26e-2
0.5	1.42 (2.02e-2)	0.7 (5.6e-2)	0.27 (2.44e-2)	2.47e-2
0.6	1.46 (2.59e-2)	0.75 (1.17e-2)	0.27 (2.01e-2)	2.46e-2
0.7	1.5 (1.18e-2)	0.75 (1.13e-2)	0.27 (3.03e-3)	1.19e-2
0.8	1.4 (1.13e-2)	0.72 (1.15e-2)	0.3 (3.11e-2)	1.23e-2
0.9	1.47 (2.04e-2)	0.77 (1.14e-2)	0.3 (1.04e-3)	1.25e-2

Standard error of the parameter has been given in bracket term.

The observed and predicted mass transfer rate (Equation 3.5) is plotted in Figure 3.4. The regression equations show that at each *C*/*D*, the variations of *d*/*D* and *X* are nearly comparable.

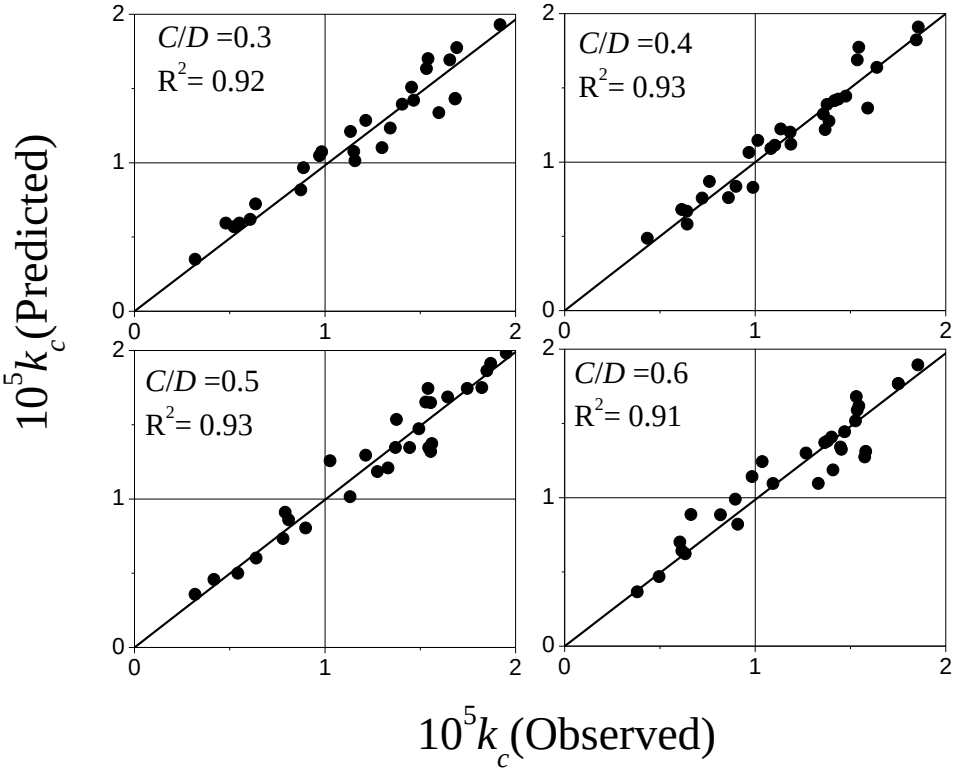

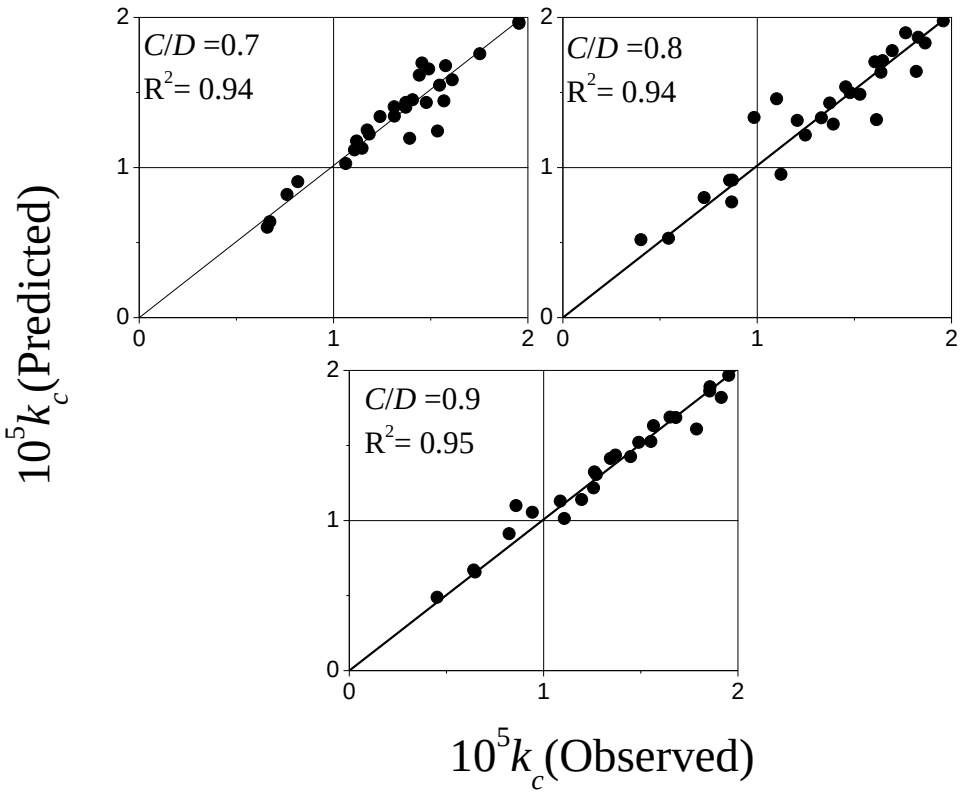

Figure 3.4: Scale up criteria for k_c at different *C/D*

The regression analysis of Equation 3.5 suggests that the functional form can be generalized into a single equation as there are very small variations among parameters, the deviation shown in the Figure 3.4 can be attributed to the variation in *d*/*D*. Given small variation in parameters governing *d*/*D* and *X*, it is tried to develop the scale up criteria for Equation 3.4. The form of the regression equation has been maintained same as Equation 3.5 with one extra term $(C/D)^{\gamma}$. The final form of the regression equation is as follows:

$$10^5 k_c = \alpha (d/D)^{\beta} (C/D)^{\delta} X^{\gamma} \quad (3.6)$$

The value of α is 0.6 with standard error 3.85e-2, β is 0.23 with 3.87e-2, δ is 0.04 with 3.12e-2 and γ is 0.3 with 1.35e-2. The prediction analysis is shown in the Figure 3.5. As shown in the Figure 3.5, the correlation coefficient is 0.92 with standard error 1.19e-2. The performance of the Equation 3.6 can be said satisfactory considering the variance of impeller clearance and *d/D* ratio. Equation 3.6 can utilized to simulate mass transfer rate under different impeller clearance and impeller to tank diameter ratio from 0.2 to 0.4 with constant *H*/*D* (=1) and blade dimensions (*l*/*d*) of 0.25 and (*l*/*d*) of 0.2.

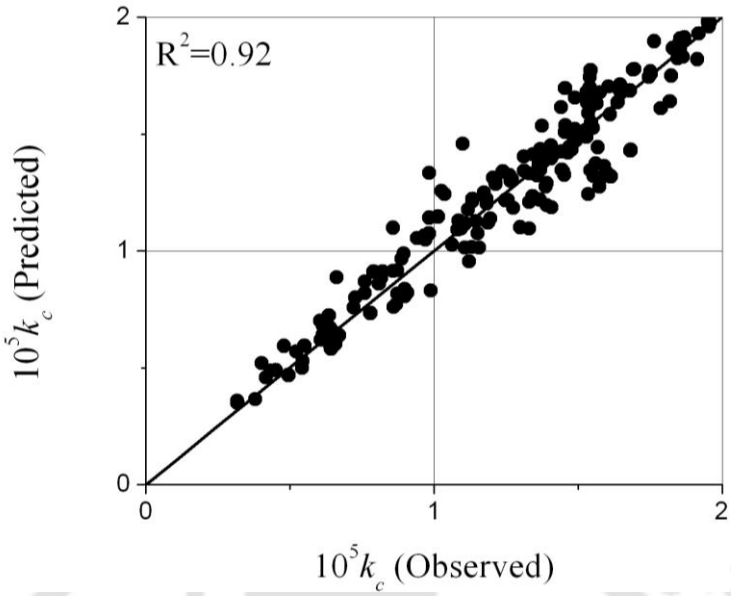

Figure 3.5: Parity plot of mass-transfer correlation for unbaffled stirred tanks:

3.3.2. Singnificance of *X*

Power is required to agitate the water body in the tank by rotating the rotor or impeller blades. According to the basic hydrodynamic principles, the power P is generally expressed as $P \approx Qh_f$, where Q is the discharge of water being pumped by the rotation of the impeller blades of dimensions b and l and the head loss h_f due to rotational movement of water in the tank. The characteristic tangential velocity of water v *may* be considered as proportional to Nd. Because of geometric similarity, $b \approx d$ and $l \approx d$, then the cross-sectional area of the blades $bl \approx d^2$. Therefore the water discharge due to the rotor action can be expressed as $Q \approx Nd^3$. The head loss h_f may be considered to be proportional to the velocity head $\upsilon^2/2g$, where $\upsilon \approx Nd$, and g is the gravitational constant. Therefore, the power $P \approx N^3d^5$. From the geometric similarity as, the volume of water in the tank $V \approx d^3$. Therefore, the power per unit volume, P/V, is proportional to N^3d^2. The dimensional parameter N^3d^2 is converted to a non-dimensional parameter, X, by expressing it in terms of $Fr = N^2d/g$, and $Re = Nd^2/\upsilon$ as:

$$X = N^3d^2/\,(g^{4/3}\upsilon^{1/3}) = Fr^{4/3}Re^{1/3} \qquad (3.7)$$

Here, $X = Fr^{4/3}Re^{1/3}$ is considered as the parameter representing the theoretical power per unit volume.

The mean flow in stirred reactors can be characterized by power consumption in stirred tanks and by the velocity and turbulence properties in the vicinity of the impeller (Yianneskis et al., 1987). Concern with the local rates of energy dissipation is based on the frequently made observation that power per unit volume is a very useful criterion of agitation. Kolmogorov's theory of local isotropy (Hinze, 1959) provides an explanation of this observation in terms of the intensity of the small-scale eddies in the turbulent flow, since the theory predicts that those eddies are isotropic and their intensity in a turbulent flow depends only on the local rate of energy dissipation. Turbulence is said to be homogeneous when its quantities have the same structure in all part of the flow field; and turbulence is called isotropic if its statistical features have no preference for any direction. Although it is difficult to construct homogeneous isotropic turbulence in reality, people generally use it to explore momentum transfer mechanisms in turbulent flows. In fact, many turbulent flows can be considered "locally isotropic" based on the Kolmogorov hypotheses. The viscosity of fluids will result in the conversion of kinetic energy of flow into heat. Thus turbulent flow is dissipative in nature. If there is no continuous external source of energy for the continuous generation of the turbulent motion, the motion will decay. Other effects of viscosity are to make the turbulence more homogeneous and isotropic.

Considering a fully turbulent flow at high Reynolds number, one has observed that the turbulent motion ranges in size from the width of the flow to much smaller scales, which become progressively smaller as the Reynolds number increases. The turbulent kinetic energy enters at the largest scales of motion, and then transfers to smaller and smaller scales until, at the smallest scales; it is dissipated by viscous action. Turbulence can be considered to be composed of eddies of different sizes. The large eddies are unstable and break up, transferring their energy to somewhat smaller eddies. These smaller eddies undergo a similar breakup process, and transfer their energy to yet smaller eddies. This energy cascade --- in which energy is transferred to successively smaller and smaller eddies --- continues until the eddy motion is stable, and molecular viscosity is effective in dissipating the kinetic energy. Kolmogorov's Hypothesis of Local Isotropy concerns the isotropy of the small-scale motions: At sufficiently high Reynolds number, the small-scale turbulent motions are statistically isotropic. Kolmogorov argued that in the chaotic-scale reduction process, the directional biases of the large scales are lost, all information about the geometry of the large

eddies is also lost. This hypothesis means that the statistics of the small-scale motions are in a sense universal --- similar in every high-Reynolds number turbulent flow.

The determination of the local dissipation rate of turbulent kinetic energy (ε) is important. However, the direct measurement of ε is very difficult, since it needs to capture precisely the smallest turbulent structures (Saarentine and Piirto, 2000). In the past, several methods were developed to estimate the dissipation rate of turbulent kinetic energy:

- Kinetic energy balance term averaged over a control volume (Cutter, 1966; Wu and Patterson, 1989; Zhou and Kresta, 1996a).
- Integration of dissipation spectrum (Okamota et al., 1981; Costes and Couderc, 1988).
- Dimensional analysis (Zhou and Kresta, 1996b).

The dimensional argument is based on the fact, that all the kinetic energy, which is transferred from the large-scale, eddies must be dissipated by the small-scale eddies. The dissipation rate is given (Hinze, 1959):

$$\varepsilon \square = A\, u'^{3} / L \qquad (3.8)$$

Where, A is a constant, u' is a turbulent velocity characteristic and L is a length-scale characteristic. The length scale, L, can be taken as proportional to the impeller diameter, d: $L=d$ (Costes and Couderc, 1988), $L= d/2$ (Stoots and Calabrese, 1989) or $L = d/10$ (Kresta and Wood, 1991).

However, this dimensional analysis assumes that the turbulence is fully developed. The larger free eddies formed in the usual turbulence production by an impeller are not isotropic, however, though as the energy is transferred to smaller and smaller eddies, the geometric orientation becomes lost, and the very small eddies produced are of random orientation, i.e., they are isotropic. This range of turbulent eddy spectrum is independent of the details of the agitation and depends only on the power supplied and on viscous dissipation. Now in Equation 3.8, u' can be represented as Nd, where N is the rotation of impeller of diameter, d.

$$\varepsilon \square \approx (Nd)^{3}/d \qquad (3.9)$$

$$\varepsilon \square \approx N^{3}d^{2} = X \quad (\varepsilon \text{ also can be non-dimensionalized as the same way as } X) \qquad (3.10)$$

Based on the Equation 3.10, one can see that the parameter, X is a very powerful parameter dealing with agitation and it can be used in scaling up the stirred tanks.

3.3.3. Power consumption

Power consumed by the rotating impeller is also a very important design aspect to be considered and it is an integral part of impeller driven mechanical stirred tanks. The hydrodynamic conditions of stirred tank can be characterized by interpreting power consumption of rotating impeller as power number (N_p), which is defined as $P/\rho_w N^3 D^5$, where P is the effective input power to the impeller. Extensive works have been published in the literature to correlate the Power number (N_p) with Reynolds number (Re), which represents the resistance or power characteristics of baffled systems (Rao and Kumar, 2009). However, these correlations do not fully represent the phenomena associated with the unbaffled tank. In the case of unbaffled system, there is a necessity of incorporating the Froude number (Fr) in the correlation of power number. The parameter X, which combines the Reynolds and Froude number, may also be considered for simulating the power characteristics of stirred tanks. According to Uhl and Gray (1966), power number (N_p) is analogous to the friction factor (λ) for pipes or coefficient of drag (C_D) of immersed bodies, reflecting the resistance characteristics of unbaffled stirred tanks.

The general dimensionless equation for the impeller power was derived by the earlier investigators using dimensional analysis (Uhl and Gray, 1966, Horvath, 1984). They considered that the impeller power should be a function of the geometry of the impeller and the vessel (D, H, d, l & b), the properties of the fluid (water density, ρ_w and kinematic viscosity, υ), the rotational speed of the impeller (N) and the acceleration due to gravity (g). The function for such a stirred tank system may be expressed as:

$$f(P, D, H, C, d, l, b, n, N, \rho_w, \rho_a, \nu, g) = 0 \tag{3.11}$$

The dimensional analysis of the various variables can be formulated in terms of dimensionless variables as:

$$f\left(\frac{Nd^2}{\nu}, \frac{N^2 d}{g}, \frac{P}{\rho_w N^3 d^5}, n, \frac{l}{d}, \frac{b}{d}, \frac{H}{D}, \frac{C}{D}, \frac{d}{D}\right) = 0 \tag{3.12}$$

The last four terms in Equation 3.12 represents the condition the geometrical similarity that requires that all such dimensionless variables are to be maintained as constant irrespective of the size of the tanks. Hence, the above equations can be reduced to the following equation under geometrically similar conditions as:

$$f\left(\frac{Nd^2}{\nu},\frac{N^2d}{g},\frac{P}{\rho_w N^3 d^5}\right)=0 \tag{3.13}$$

The first term in Equation 3.13 is analogous to Reynolds number and called as impeller Reynolds number (*Re*). And second term is impeller Froude number (*Fr*). The last term is called as power number (N_p). Therefore, Equation 3.13 may be expressed as:

$$N_p = f\left(Re, Fr\right) \tag{3.14}$$

The effects of the Froude number are considered to be unimportant for baffled tanks (Uhl and Gray, 1966; Nagata, 1975). Accordingly by neglecting the effect of Froude number, a curve has been reported (Rushton, 1952; Uhl and Gray, 1966; Nagata, 1975) in literature correlating power number (N_p) to Reynolds number (*Re*) generally named as power curve. In the case of unbaffled tanks, swirl exists, giving the necessity of correlating Froude number in the analysis (Rushton, 1952; Uhl and Gray, 1966). As for vortexing system, it is required to incorporate the Froude number in the any analysis (Rushton, 1952). On the system consists of vortex, the earliest correlation of power number with Reynolds number and Froude number is given by the Rushton (1952). Rushton (1952) suggested that power number divided by the function of Froude number is proportional to Reynolds number. Mathematically he expressed it as $\left[\frac{N_p}{Fr^n}\alpha\, f(Re)\right]$, where exponent *n* has to be solved by a trial and error method using experimental observations. In general any given exponent (*n*) can depend on all other dimensionless variables. Therefore, including one of the variables directly to the power number without a variable exponent requires that its effect be the same on power number regardless of the values of all other variables. Thus it cannot be a criterion for simulation in stirred tanks. It is natural to consider the friction factor of pipe and solve the mixing problem analogous to it. However pipe flow characteristics are very much different from flow characteristics of a stirred tank. Hence concepts developed for pipe flow may not be directly applicable to the stirred tanks. That is why the friction factor of stirred tanks (analogous to pipe friction factor) is not uniquely related to Reynolds number as in the case of pipe flow.

Another approach for scale up of power number can be summarized as follows: Fluid motion in an agitated system must obey the laws of conservation of mass and momentum. For a constant-density, the Navier-stokes equation can be written as follows:

$$\rho_w \frac{dv}{dt} = -g\nabla p + \mu\nabla^2 v + \rho_w g \qquad (3.15)$$

By using dimensional analysis and substituting the dimensionless velocity as $v^*=v/Nd$, dimensionless time $t^* = tN$ and dimensionless pressure as $p^* = p/\rho_w N^2 d^2$, Equation 3.15 can be rewritten as follows:

$$\frac{dv^*}{dt^*} = -\nabla^* p^* + \left[\frac{\mu}{d^2 N \rho_w}\right]\nabla^{*2} v^* + \left[\frac{g}{dN^2}\right] \qquad (3.16)$$

In Equation 3.16, the term $\frac{\mu}{d^2 N \rho_w}$ represents the reciprocal of the Reynolds number (*Re*) for agitation and the term $\frac{g}{dN^2}$ represents the reciprocal of the Froude number (*Fr*). For a given set of initial and boundary conditions that requires geometrical similarity, the pressure distributions can be expressed as a function of the Reynolds and Froude number (Dickey, 1993).

$$p^*(x, y, z, t) = f(Re, Fr) \qquad (3.17)$$

According to Perry et al. (1984), the relationship between the fluid pressures (p) adjacent to the blade and power (P) is such that $p \propto P/Nd^3$. As $p^* = p/\rho_w N^2 d^2$, substituting the vales of p gives as $p^* = P/\rho_w N^3 D^5$. So, p^* can be further simplified as $N_p = P/\rho_w \square VN^3 d^{2,}$ where V is the volume of water ($\approx d^3$) and it is called as power number which relates imposed forces to inertial forces.

If we consider the fundamental forces acting on the stirred tank, we can also reach to above mentioned conclusions as follows; Assuming the forces that may act on a fluid element in a tank during agitation are the viscous force F_V, drag force on impeller F_D, and gravity force F_G, each of which can be expressed with characteristic quantities associated with the agitating system. The viscous force can be represented by the Newton's laws of viscosity as $F_V = \mu\left(\frac{\partial u}{\partial y}\right)A$. It can be assumed (Perry et al., 1984) that the average velocity gradient is

proportional to agitation speed N and the area A is proportional to d^2, which results $F_V \sim \mu N d^2$. The drag force F_D can be characterized in an agitating system as (Lee, 1992), $F_D \sim P/Nd$ and gravity force, $F_G \sim \rho_w g d^3$. The summation of all forces gives the inertial force, $F_I \sim \rho_w d^4 N^2$ in an agitated system, as $F_I = F_D + F_V + F_G$. It can be simplify as $F_D/F_I + F_V/F_I + F_G/F_I = 1$. First term is called as power number (N_p) and relates the drag force to the inertial force and it is equal to $N_p = P/\rho_w N^3 d^5$ or $N_p = P/\rho_w V N^3 d^2$. Second and third terms are well known and are called as Reynolds (Re) and Froude number (Fr) respectively. Above analysis is showing that these three numbers, N_p, Re and Fr, can represent the hydrodynamics characteristics of an agitated system. In general, as given in the literature (Rushton, 1952; Maise, 1970), these numbers can be expressed as follows:

$$N_p = f(Re, Fr) \tag{3.18}$$

Rushton (1951) has shown that when a vortex forms, it is impossible to scale-up the power requirements for agitation in geometrically similar vessels (Weinstein and Treybal, 1973). In unbaffled systems it is not possible to achieve dynamic similarity at different scales even in geometrically similar systems by using Rushton correlation $N_p = K Re^m Fr^n$ unless the fluid is changed (Green, 1953). Also, there is no fundamental fluid mechanical reason why N_p should remain constant at high Reynolds number (Bujalski et al., 1987). It is also appropriate to mention that Clark and Vermeulen (1964) has mentioned that even for baffled tank, the Froude number should be used in correlating dynamic behavior.

3.3.3.1. Effect of impeller clearance depth (C)

Power number depends principally on the tip speed and on the projected area of the blades. The projected area depends on variables such as impeller diameter d, blade width and blade length (Bates et al., 1963). It can be assumed that the size of the tank is largely relative to the flow around the impeller blades. This allows geometric variables involving the tank diameter to be eliminated, however results suggests that power number does get affected by the variation in impeller clearance and with d/D ratio. N_p is plotted against the theoretical power per unit volume (X) which is the function of Reynolds number (Re) and Froude number (Fr). Figure 3.6 shows the variation of measured N_p for different X values at particular impeller clearance depth (C). N_p decreases with increaseing X and C/D at all the cases of d/D.

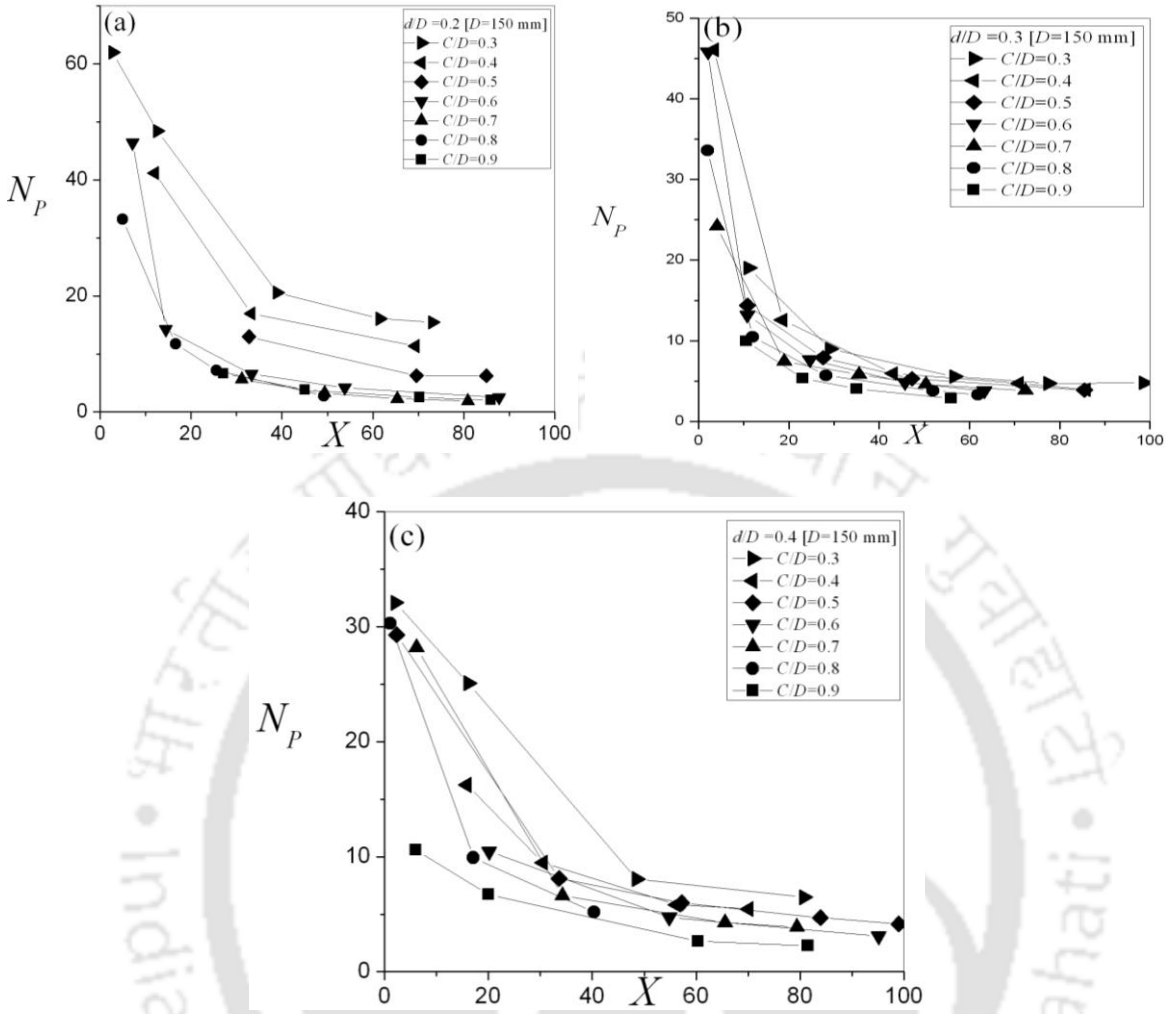

Figure 3.6: N_p with X for different C/D at (a) d/D=0.2 (b) d/D=0.3 and (c) d/D=0.4

It is known that when a liquid is stirred in an unbaffled tank, a vortex is formed around the shaft. The depth of this vortex increases with the impeller speed. Clark and Vermeulen (1964) reported that, for such unbaffled systems, the power number decreases continuously as the impeller Reynolds number or X increases. The continuous decrease in power number can be attributed to the progressively increasing vortex depth. Greaves and Kobbacy (1981) have also investigated the mechanism and observed that as the impeller speed increases the liquid velocity generated increases, and larger and larger bubbles are carried down into the impeller region. This causes a reduction in the average density in the impeller region, and also gas cavities get formed behind the impeller blades. Therefore, a rapid drop in power number occurs. In unbaffled stirred tank, increasing the impeller clearance decreases the power consumption as shown in Figure 3.6. Dispersion of gas in stirred tank and

consequently cavity formation behind the impeller blades is the major factor for power reduction. Due to high impeller clearance, the relative rate of gas entrained from the surface is higher than the lower clearance. If the impeller is located closer to the tank bottom, increased viscous resistance occurs, which limits the flow around the agitator leading to a high power consumption. These could be the reason behind the observations shown in the Figure 3.6.

3.3.3.2. Effects of impeller diameter (*d)*

The increase in impeller diameter increases the impeller blade width which increases the radial component of the liquid velocity and requires more power. Effect of impeller diameter on power number is shown in the Figure 3.7.

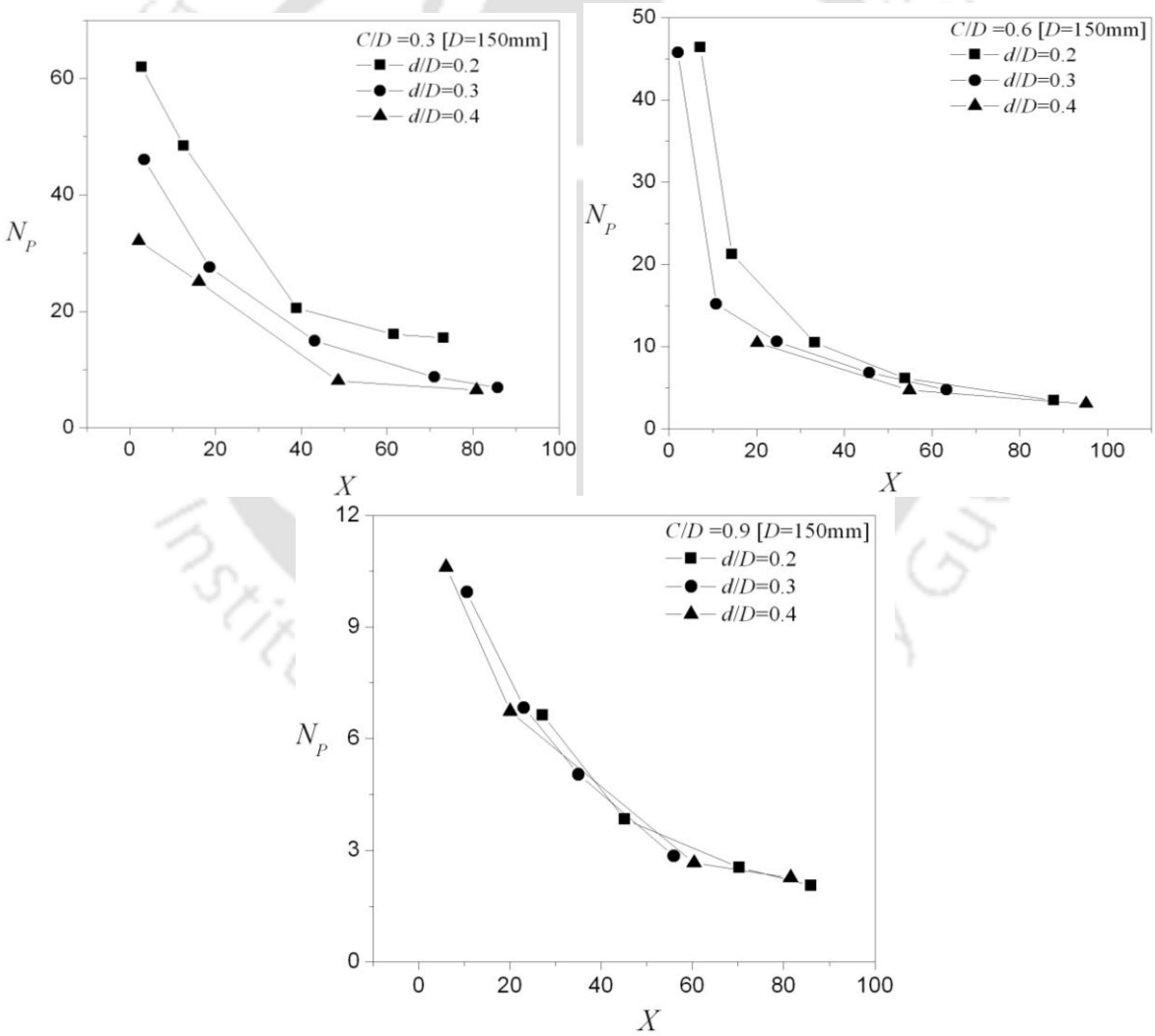

Figure 3.7: N_p with X for different d/D

Results show that power number decreases with an increase in impeller diameter. The reason could be the proportionality factor related to the impeller diameter, as N_p is inversely related to d^5 keeping other parameters at constant. The effect of *d/D* is more pronounced at low impeller clearance and also at low impeller speed. It can be seen from the Figure 3.7, there is no appreciable effect of *d/D*, when impeller clearance is high and running at higher speed.

3.3.3.3. Design criteria for power number

As power number (N_p) is a function of several variables as shown in Equation 3.12 in dimensionless form, it can be written again by keeping some geometrical variables as constant (*H/D*=1,*n*=6, *l/d*=0.25, *b/d*=0.2):

$$N_p = f(C/D, d/D, Re, Fr) \tag{3.19}$$

By incorporating *X*, Equation 3.19 is written as:

$$N_p = f(C/D, d/D, X) \tag{3.20}$$

So, for different *C/D* ratio (0.3 to 0.9), a statistical relationship between *d/D* and *X* is developed as:

$$N_p = \alpha(d/D)^{\beta}(X)^{\gamma} \tag{3.21}$$

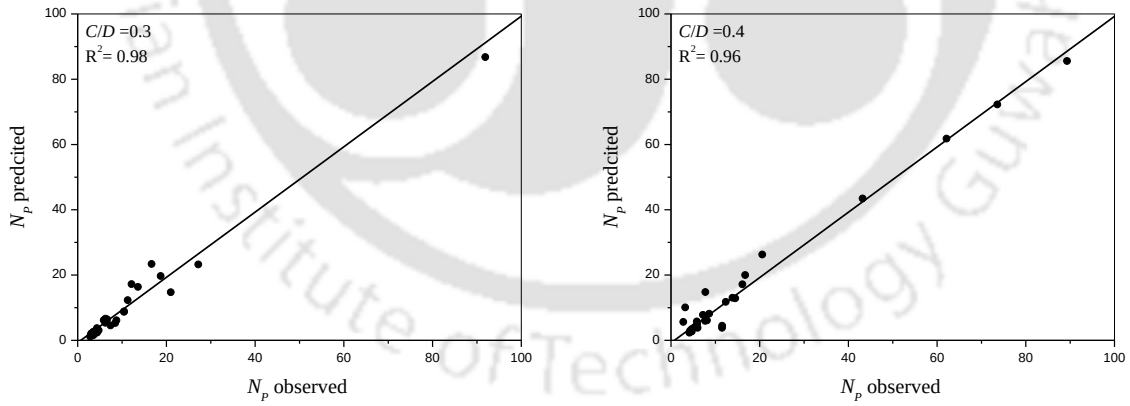

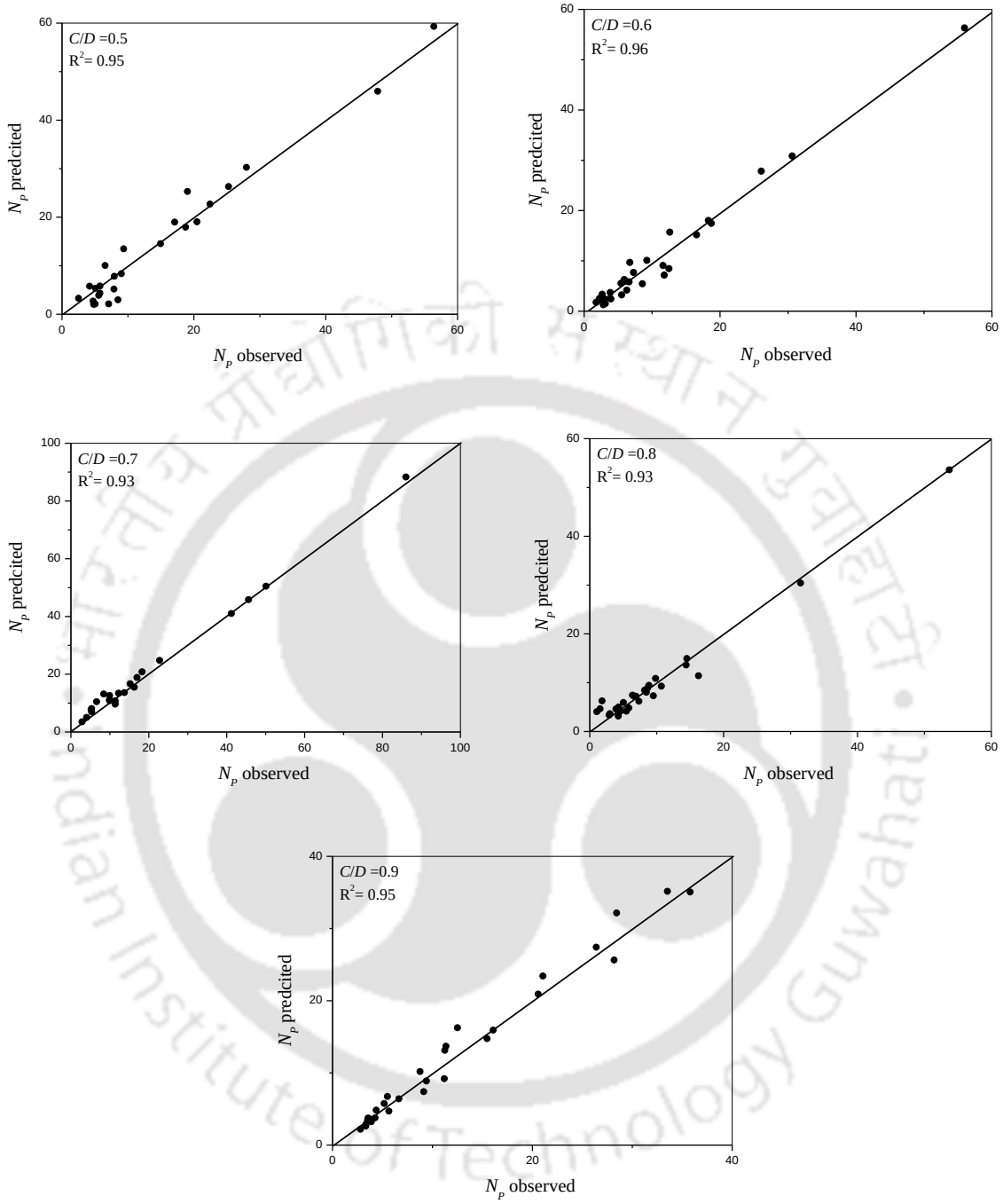

Figure 3.8: Scale up criteria for N_p at different *C/D*

Figure 3.8 shows the predicted observed N_p for different *C/D*. The prediction capability of the Equation 3.21 can be said satisfactory. Table 3.3 gives the parametric details of Equation 3.21. The regression equations show that at each *C*/*D*, the variations of *d*/*D* and *X* are nearly comparable.

Table 3.3: Statistical details of Equation 3.21

C/D	*α*	*β*	*γ*	**Overall std. error**
0.3	10.16 (2.35e-2)	-2.53 (1.94e-2)	-1.05 (2.46e-2)	3.32e-2
0.4	65.51 (1.87e-1)	-0.63 (2.52e-2)	-0.89 (7.51e-2)	7.94e-2
0.5	44.76 (1.13e-2)	-1. 62 (3.74e-2)	-0.87 (8.17e-2)	1.04e-2
0.6	11.59 (2.69e-2)	-2.24 (3.12e-2)	-0.96 (4.04e-2)	4.09e-2
0.7	14.05 (6.34e-2)	-1.85 (4.14e-3)	-0.76 (7.81e-2)	1.21e-2
0.8	53.36 (1.74e-2)	-0.21 (3.93e-2)	-0.68 (6.86e-2)	3.21e-2
0.9	10.20 (1.81e-2)	-1.99 (1.16e-2)	-0.81 (3.78e-2)	7.82e-2

Similar to the case of mass transfer rate, it is tried to develop the design/scale up criteria for Equation 3.20. In order to account the effect of ratio of impeller clearance depth to tank diameter (*C/D*), one extra term, $(C/D)^{\delta}$ is added in Equation 3.21 as:

$$N_p = \alpha (d/D)^{\beta} (C/D)^{\delta} (X)^{\gamma} \tag{3.22}$$

Equation 3.22 gives the generalized scale up criteria of power number for geometrically similar systems and the details of the statistical values are tabulated in Table 3.4.

Table 3.4: Statistical details of Equation 3.22

α	*β*	*δ*	*Γ*	**Overall std. error**
34.69 (5.74e-2)	-0.97 (3.85e-2)	-0.5 (7.77e-2)	-0.98 (1.33e-2)	1.15e-2

The behavior observed during effect of impeller diameter and clearance can also be deduced from Equation 3.22 such as N_p will reduce with *C/D* and *d/D*. Experimental observations have been plotted in the Figure 3.9. As shown in the Figure 3.9, the correlation coefficient is 0.95 with standard error 1.15e-1. The performance of the Equation 3.22 can be said satisfactory considering the different operational conditions.

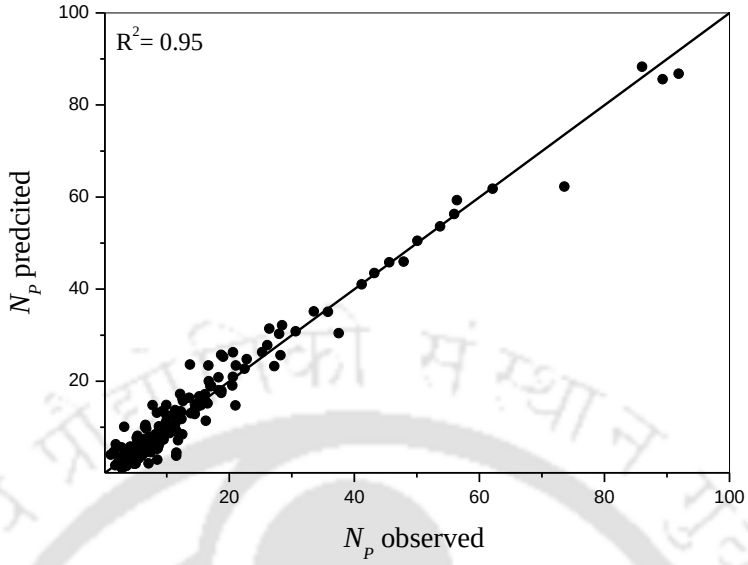

Figure 3.9: Parity plot of power number correlation for unbaffled stirred tanks:

3.3.4. Vortex analysis

Study of vortex formation caused by unbaffled condition of the system is closely associated with power consumption in the system as it is widely known that unbaffled system consumes less power (Assirelli et al., 2008) than the baffled system. Because of the small power consumption in unbaffled vessels, connected with the need to save energy in chemical industry, show the real importance of vortex formation research in agitated vessels (Markopoulos and Kontogoeorgaki, 1995). Vortex depth can be analyzed theoretically as well as experimentally. Experimental determination can be done by visually monitoring during experimentation which the scales are marked on the tank or by processing the photographs of the vortex formation in software (for example edge detection method and measure tool in MATLAB®). Figure 3.10 shows the schematic diagram of an unbaffled stirred tank where the central vortex formation is taken place when the impeller is rotated at a particular speed. Experimental photographs were taken during experimentation at every speed and the same photograph is used to determine the vortex depth.

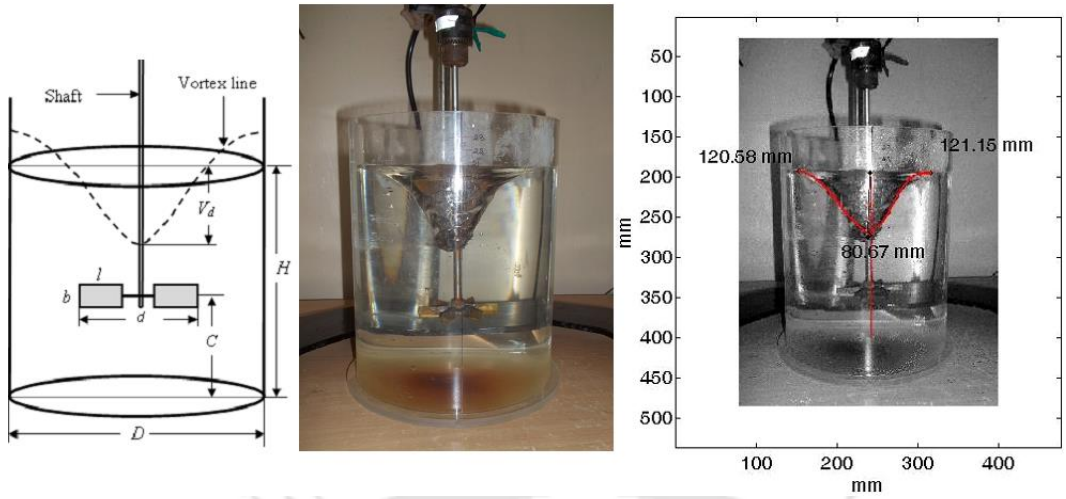

Figure 3.10: Schematic diagram (left) and experimental view (centre) of the formation of vortex in unbaffled stirred tank and vortex detected by edge detection method (right)

A theoretical expression for the vortex depth would require the knowledge of velocity and pressure profiles in an unbaffled stirred tank with agitation. These profiles can be obtained by simultaneously solving the equations of motion and continuity with the corresponding boundary conditions. Continuity equation for an incompressible fluid is written as:

$$\nabla \vec{v} = 0 \tag{3.23}$$

And the equation of motion (Navier-Stokes equation) is given as:

$$\rho_w \frac{d\vec{v}}{d\vec{t}} = -\nabla p + \mu \nabla^2 \vec{v} + \rho_w \vec{g} \tag{3.24}$$

The corresponding boundary conditions are as follows: (l) liquid velocity at the liquid/impeller interface is equal to the tangential component of impeller velocity, (2) liquid velocity at the vessel wall is zero (3) the resulting force influencing the gas- liquid inter-phase tends to get to the surface perpendicularly. The last condition implies as:

$$\vec{n}\,\vec{\sigma} = -\vec{n} p_0 \tag{3.25}$$

The analytical solution of Equations 3.23, 3.24 and 3.25 is not possible due to geometrical complexity of impellers. Therefore, the method of dimensional analysis is used and the following dimensionless variables were introduced as:

$$\vec{v}^* = \vec{v}/Nd,\ t^* = Nt,\ \nabla^* = d\nabla,\ \vec{g}^* = \vec{g}/g,\ \vec{\sigma}^* = \vec{\sigma}/\rho_w N^2 d^2,\ p^* = p/\rho_w N^2 d^2 \tag{3.26a-f}$$

Substituting dimensionless variables of Equation 3.26a-f into the equation of motion (Equation 3.24) and into the third boundary condition obtaining as:

$$\frac{d\vec{v}^*}{dt^*} = -\nabla^* p^* + \frac{1}{Re}\nabla^{*2}\vec{v}^* + \frac{1}{Fr}\vec{g}^* \quad (3.27)$$

$$\vec{n}\,\vec{\sigma}^* = -\vec{n}p_0^* \quad (3.28)$$

Using the dimensionless analysis Equation 3.27 can be written for a steady state operation as:

$$\vec{v}^* = \vec{v}^*(x^*, Re, Fr) \text{ and } p^* = p^*(x^*, Re, Fr) \quad (3.29a,b)$$

Combining Equations 3.29(a,b) and (3.28) obtains the dimensionless equation describing the vortex geometry as:

$$x_L^* = x_L^*(Re, Fr) = x_L^*(Ga, Fr) \quad (3.30)$$

Where, $Ga = Re^2/Fr$ (Galileo number). The vortex depth can be determined from Equation 3.30 as the vertical parameter characterizing depth of the gas/liquid interface in the vortex centre as:

$$\frac{V_d}{d} = f(Re, Fr) = f(Ga, Fr) \quad (3.31)$$

Equation 3.31 indicates that relative vortex depth (V_d/d) is function of impeller speed and impeller diameter, however, vortex depth may also affect by other geometrical dimensions other than impeller diameter. As objective of this study is to analyze the impeller clearance depth on various process dynamics characteristics, it is also required to incorporate impeller clearance depth (C) in the analysis of vortex depth. So, by keeping other geometrical parameters as constant and only varying tank diameter and impeller clearance, the following dimensionless relation of vortex depth can be written as:

$$\frac{V_d}{d} = f\left(\frac{D}{d}, \frac{C}{D}, Ga, Fr\right) \quad (3.32)$$

Markopoulos and Kontogeorgaki (1995) also shown that relative vortex depth is function of impeller diameter (d), tank diameter (D), impeller speed (N), viscosity of fluid (v), gravitational force (g) and impeller clearance depth (C). In the following sections, the influence of d, D, C and N on relative vortex depth will be discussed.

3.3.4.1. Effects of impeller clearance depth *(C)*

As mentioned in Equation 3.32, vortex depth is also a function of impeller clearance depth, relative vortex depth (V_d/d) against Fr at various C/D for a constant impeller diameter is plotted in Figure 3.11. Vortex depth increases with increase in Froude number. There is

variation of vortex depth with changing in impeller clearance in all the cases of different impeller to tank diameter of 0.2, 0.3 and 0.4 and vortex depth is high at lower impeller clearance.

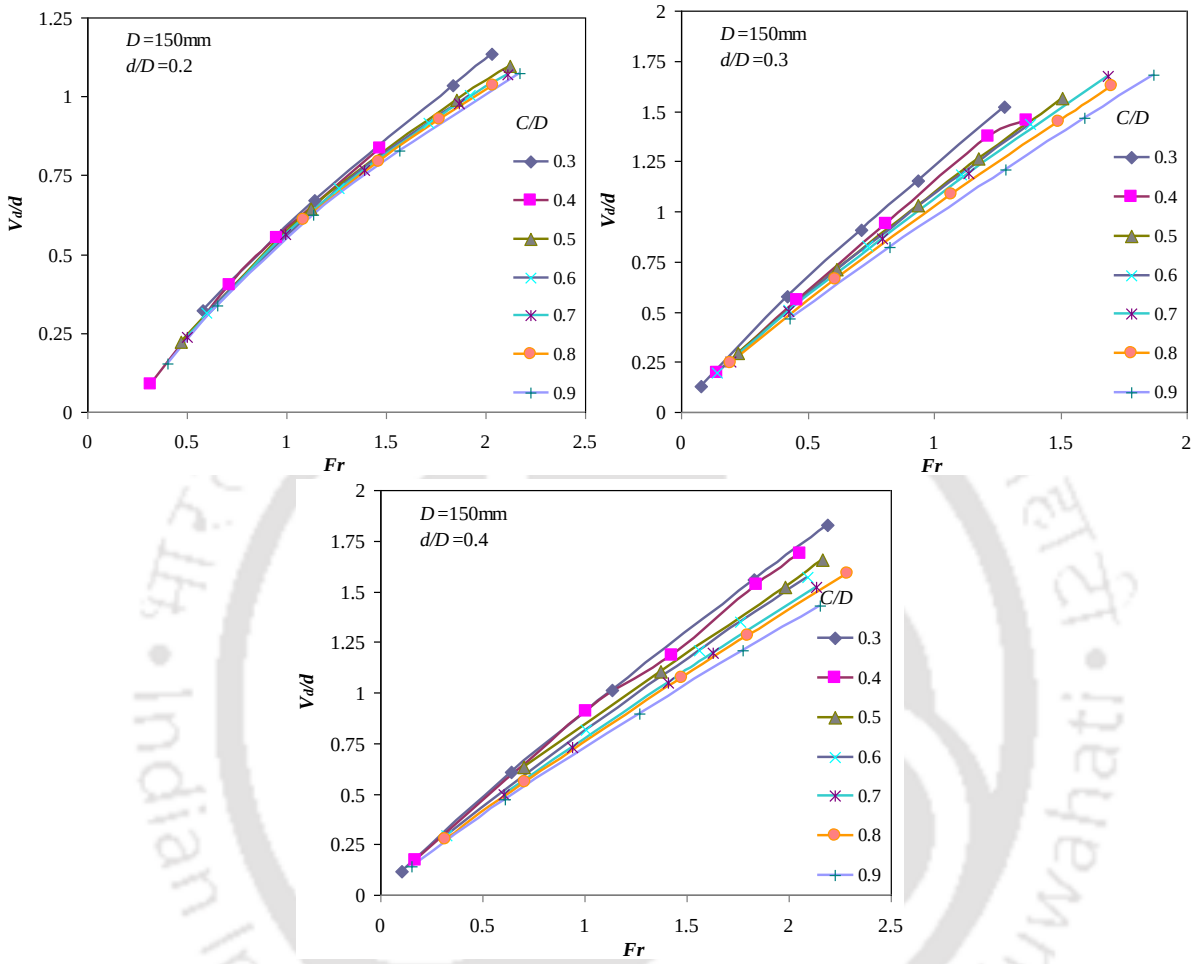

Figure 3.11: Relative vortex depth (V_d/d) with various Fr for different C/D

Markopoulos and Kontogeorgaki (1995) expressed that the significance of C/D on the determination of V_d/d is not very significant in single impeller system and such finding is also witnessed from our study.

3.3.4.2. Effects of impeller diameter (d)

(a) When d is varied: As vortex depth is a function of Reynolds number and Froude number shown in Equation 3.31, diameter of impeller (d) is very important geometrical parameter to understand the vortex depth.

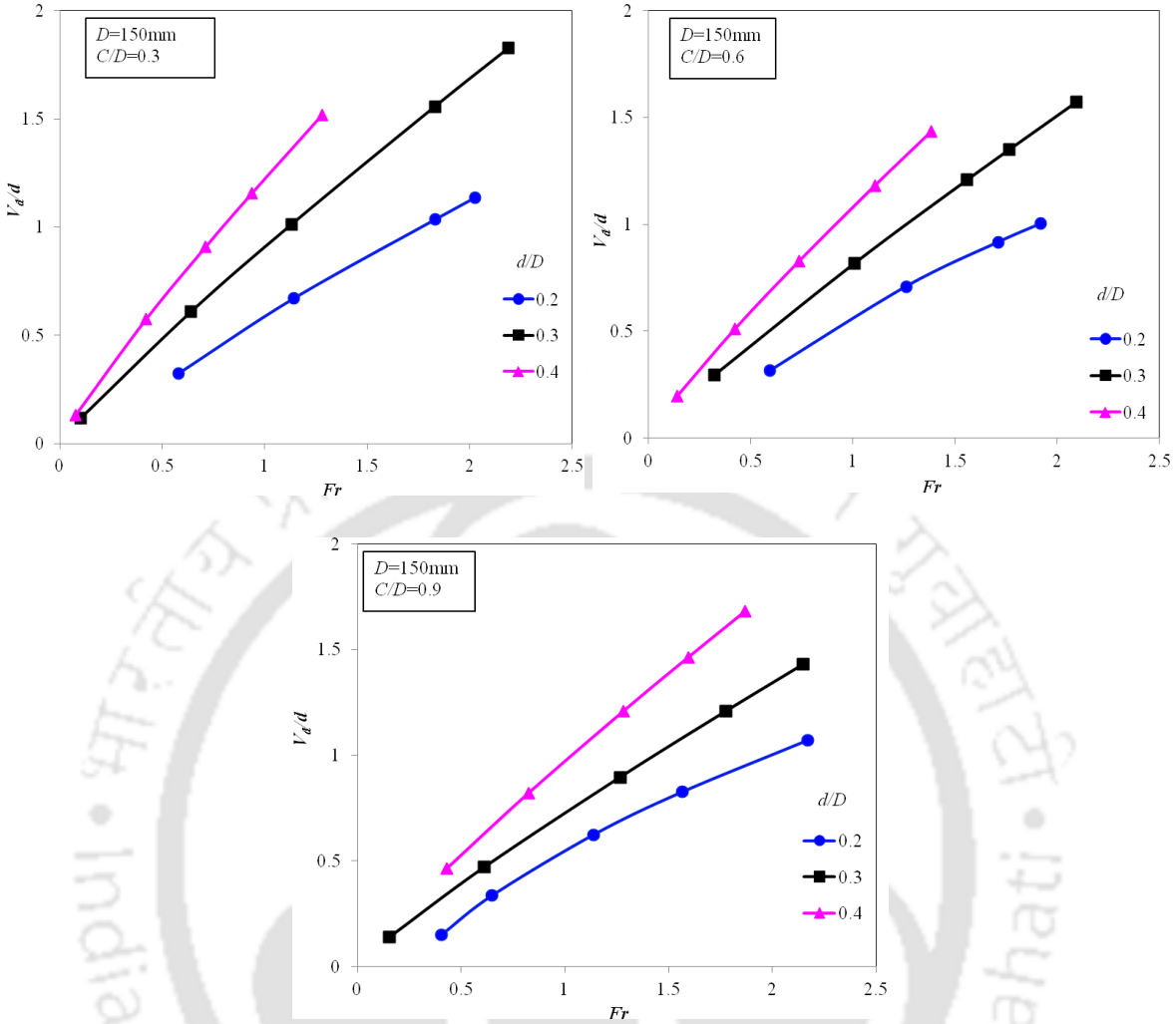

Figure 3.12: Relative vortex depth (V_d/d) with Fr

Figure 3.12 shows relative vortex depth with Froude number for different impeller diameter at a particular impeller clearance. Vortex depth increases with increase in impeller diameter at all the cases of impeller clearance (C/D=0.3, 0.6 and 0.9). So, higher V_d/d is observed at d/D=0.4 (higher d value when D is constant) and lower at d/D=0.2.

(b) When d is constant: As it has been understood from the previous observation that relative vortex depth increases with increase in impeller diameter when the tank diameter is constant, now it is also interesting to understand that how does relative vortex behave when the condition is reversed.

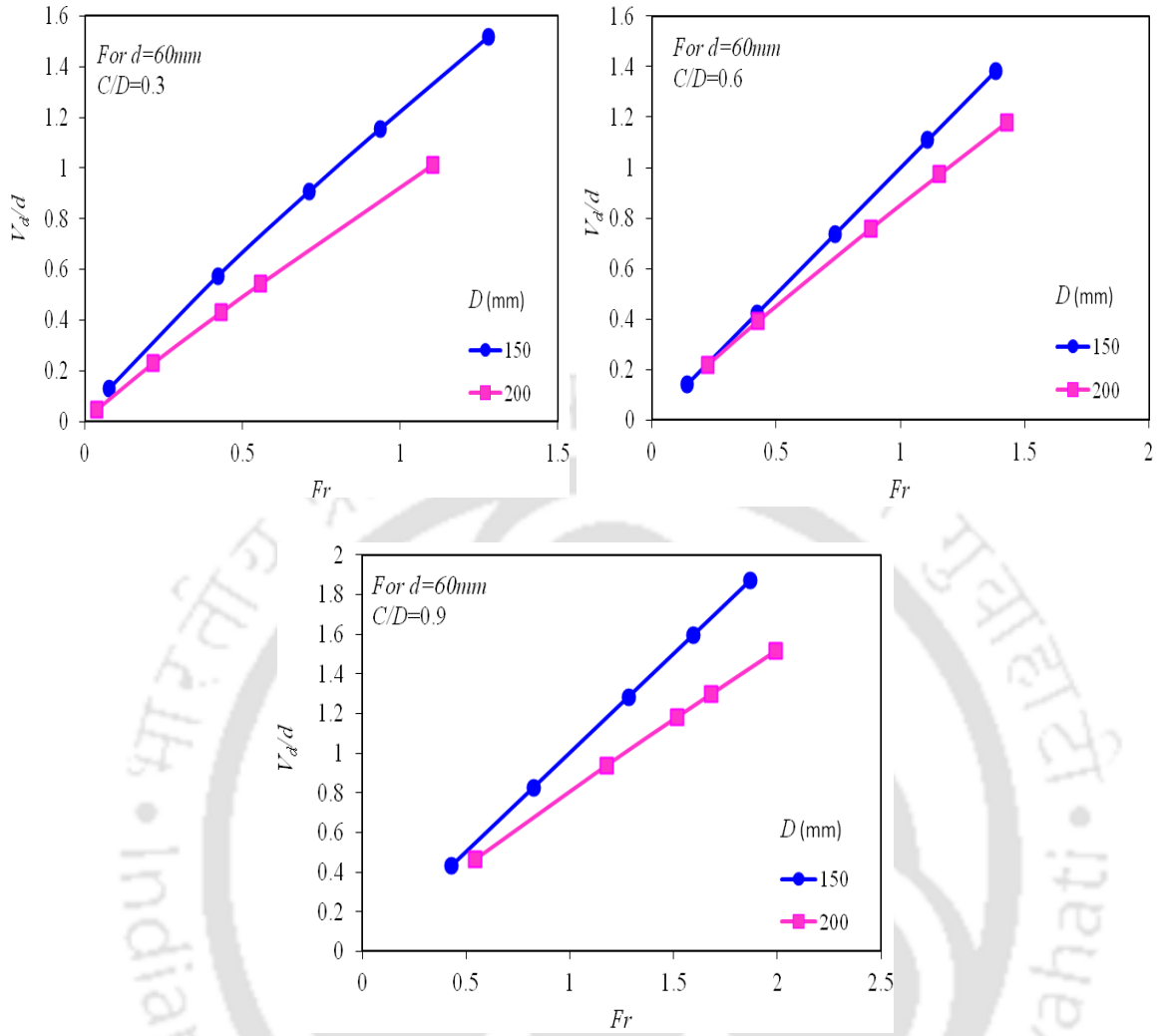

Figure 3.13: Comparison of vortex depth between D=150mm and 200mm when d=60mm (constant)

Figure 3.13 shows the comparison of relative vortex depth for different tank diameter when the impeller diameter is constant at different impeller clearance depth. At all the cases of impeller clearance depth (C/D=0.3, 06 and 0.9), V_d/d is observed higher in the smaller tank diameter.

3.3.4.3. Critical speed

The critical impeller speed (N_c) is the speed of the stirrer at which the impeller blade level is reached by the vortex and air entrainment is occurred. This impeller speed is the most important parameter from the practical point of view because of the entrainment of gas at this speed as a result of the gas/liquid interface reaching the impeller (Reiger et al., 1979). Reason for understanding the critical impeller speed was given by them as: above the critical speed,

the resulting gas/liquid heterogeneous system gives good conditions for mass transfer between the phases involved. On the other hand, mixing below the critical impeller speed is often desired to avoid aeration and strong vibration of the rotating impeller shaft that may lead to mechanical failure. In the scale up process when large scale is used, the swirling and unstable flow conditions found when the central vortex reaches the impeller can also give rise to mechanical damage (Assirelli et al, 2008). The determination of critical speed can be analyzed in terms of energy balance. Referring to Figure 3.10, between the top edge of the vortex and the center of the vortex, there is difference in potential energy. To maintain this potential energy difference between the two points, there should be a continuous conversion of kinetic energy (impart by the impeller rotation) into potential energy. The most convenient term to choose to represent this kinetic energy is the one related to the speed at the tip of the rotating blades (Tsao, 1968). The energy balance is shown in Equation 3.33 as:

$$V_d \rho g = K(\pi^2 d^2 N^2 \rho)/2 \tag{3.33}$$

Or, it can be written as follows:

$$\frac{V_d}{d} = K\frac{N^2 d}{g} = K F_r \tag{3.34}$$

The value of K can be derived by analyzing the observations of vortex depth and Froude number of the stirred tanks shown in the Figure 3.11. Figure 3.14 shows the calculated critical impeller speed at different impeller clearance depth for different *d/D* ratio. This shows that N_c decreases with increase in *C/D* and increasing of *d/D*. That means larger the impeller diameter, lower is the critical speed when tank diameter is constant. Markopoulos and Kontogeorgaki (1995) reviewed various experimental results and correlations of relative vortex depth and concluded that the critical impeller speed increases with increasing of *D/d* value. That means N_c increases with either increasing *D* when *d* is constant or decreasing *d* when *D* is constant. The same pattern is achieved in this study too as can be seen from Figure 3.14. The reason for increasing the N_c with increase in *D* or decreasing *d* when the another variable is kept constant may be because of the fact that N_c is the speed when the vortex reaches the impeller blade as mentioned above, it is obvious thing that higher *d* produces deeper V_d leading to reach the blade level faster than the lower *d* value while maintaining the same speed. In case of higher *D* value when *d* is constant the case is reversed which means

that the vortex of higher D requires higher speed to reach the blade level than the lower D while constant N and d is still maintaining and this leads to increase in N_c.

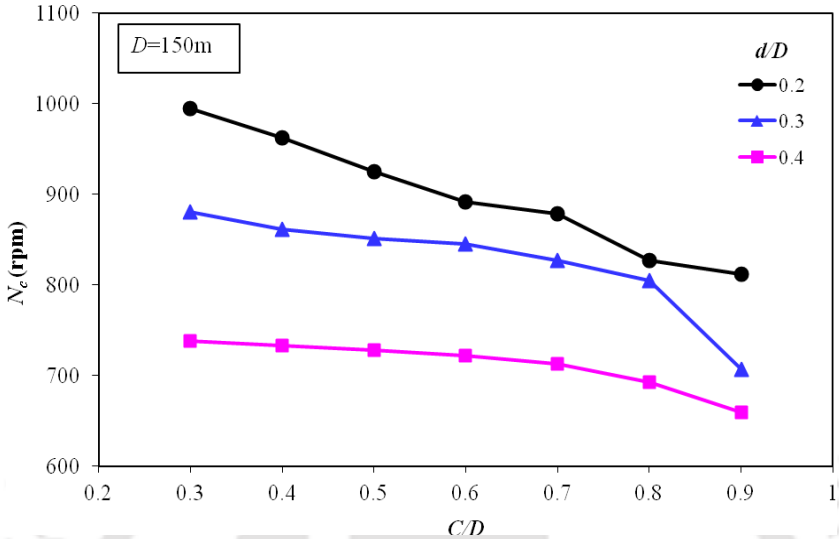

Figure 3.14: Critical speed (N_c) for different d/D at various C/D

3.3.4.4. Design criteria for vortex depth

As shown in Equation 3.32 that vortex depth is function of Reynolds number and Froude number with diameter of impeller and impeller clearance depth. In order to establish a generalized scale criterion for vortex depth considering the parameters which affects to it can be written as:

$$\frac{V_d}{d} = \alpha Ga^{\beta}(D/d)^{\gamma} Fr^{\delta Ga^{\eta}(D/d)^{\lambda}} (C/D)^{\phi} \qquad (3.35)$$

The statistical details of the developed relation are tabulated in Table 3.5. The standard error obtain is found to be satisfactory. The R^2 value is 0.81 and which is acceptable value in engineering applications of predicted parameters. Figure 3.15 shows the overall generalized relationship of predicted V_d/d with observed V_d/d.

Table 3.5: Statistical details of Equation 3.35

A	β	γ	δ	η	λ	φ	**Std. error**
0.63 (1.23e-1)	0.069 (2.11e-2)	-1.39 (7.32e-2)	1.14 (1.02e-2)	-0.008 (4.56e-3)	0.008 (1.16e-3)	-0.79 (1.15e-2)	1.363e-02

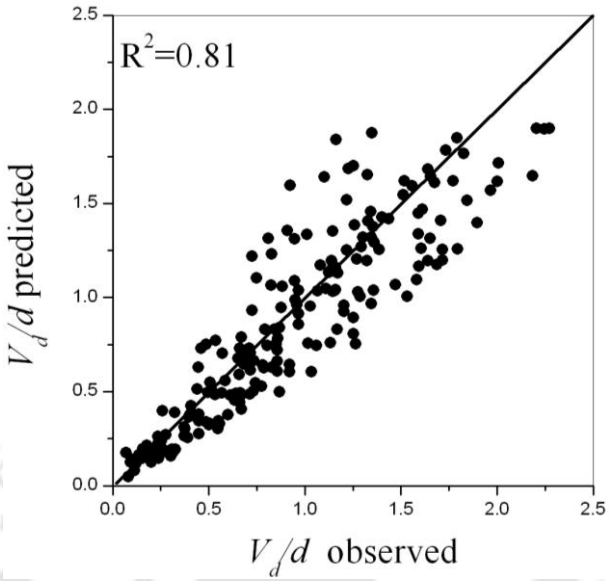

Figure 3.15: Parity plot of relative vortex depth correlation for unbaffled stirred tanks

With *C/D* constant at 1/3, Reiger et al. (1979) have developed vortex depth relationship for different impeller type (disc blade, flat blade, pitched blade). Reiger et al. (1979) found the constants as α=1.51±0.03, β=0.069, γ=-0.38, δ=1.14, η=-0.008, λ=0.008. Present relationship which has given in Equation 3.35 has found similar constant values after the inclusion of *C/D* except the value of α and γ and the extra φ values. Such modification may be due to the different impeller employed in the present work and inclusion of impeller clearance.

3.3.5. Comparative studies

Impeller types and baffled system also plays important role in mass transfer rate and power consumption in impeller driven stirred tank. In order to understand the effects of impeller type, concave blade type impeller is compared with Rushton impeller and baffled with unbaffled system.

(a) With Rushton impeller

Rushton impeller type has flat or straight type blade which is different from concave blade type impeller which has deep concave blade type structure. Such type of impeller is modified from Rushton type impeller which is also known as standard impeller and commonly used impeller in process industries. So, the expectation for modifying such new concave type impeller from standard impeller is to give higher efficiency to the system like in terms of better mass transfer rate with lower power consumption (Myers et al., 1999; Gimbun et al.,

2009). Figure 3.16 shows the comparison between concave blade with Rushton impeller at a particular impeller submergence depth (C/D=0.3, 0.6 & 0.9) in terms of K_La_{20} and P_{eff} for different impeller speed (N=200 to 1500 rpm). At all the cases of C/D values, concave blade type impeller shows higher mass transfer rate and lower power consumption. Better performance shown by the concave type impeller over the Rushton impeller is because of the unique shape of blade in concave blade type impeller which helps in pumping up of higher amount of fluid volume at one complete circulation which leads to strong interaction to the surrounding fluid particles within a confined vessel making higher rate of homogenization. Because of its concave blade type, it makes easy to pass through the layers of fluid particles leading to consume lesser power to circulate the fluid particles. Higher rate of mass transfer is caused by the higher turbulence nature of the fluids and because of its higher turbulence nature, the blade does not require extra effort to move the fluid particles instead it helps to move the fluid particles faster and subsequently leading to consume lesser power. Hence, unbaffled system of concave blade type impeller gives higher mass transfer rate as well as lesser power consumption at a certain impeller speed.

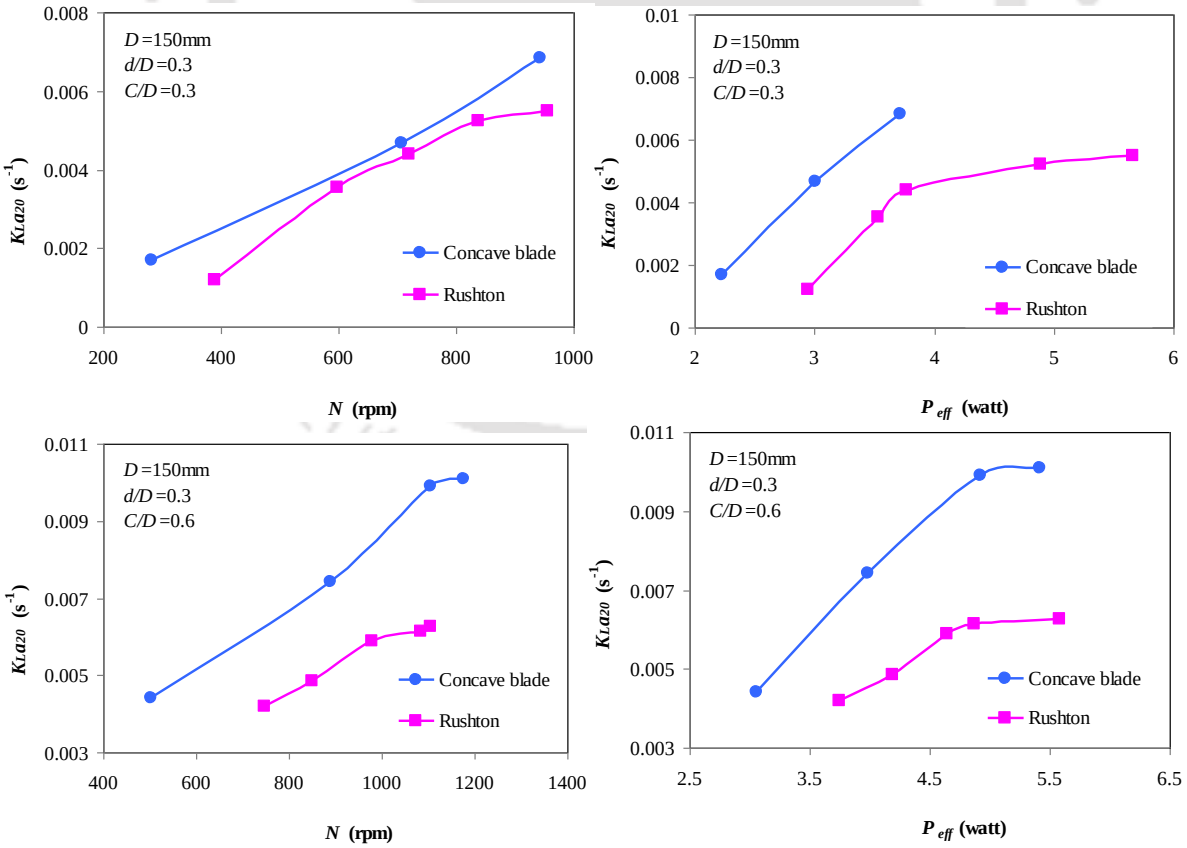

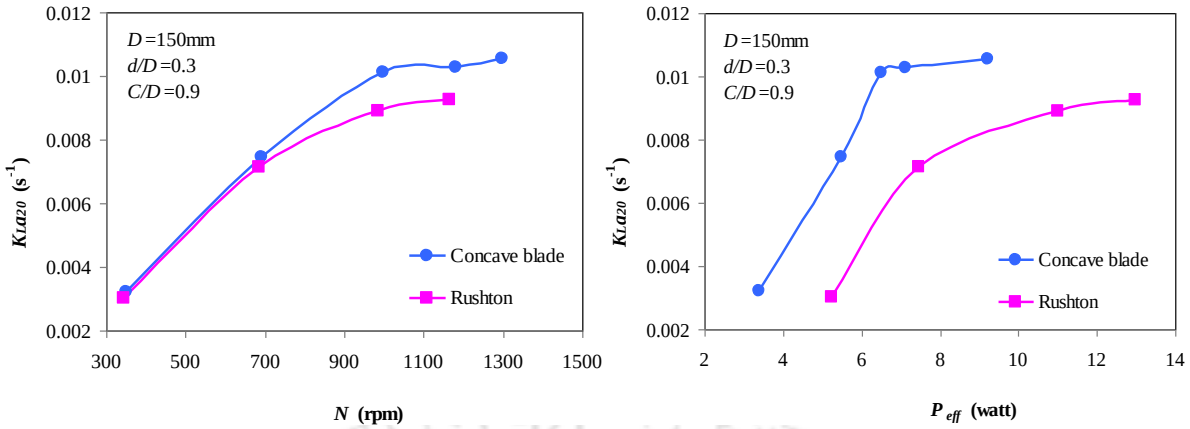

Figure 3.16: Comparison between Concave blade and Rushton impeller at different speed with K_La_{20} (left) and P_{eff} (right) for different C/D

(b) With baffled system (Concave blade)

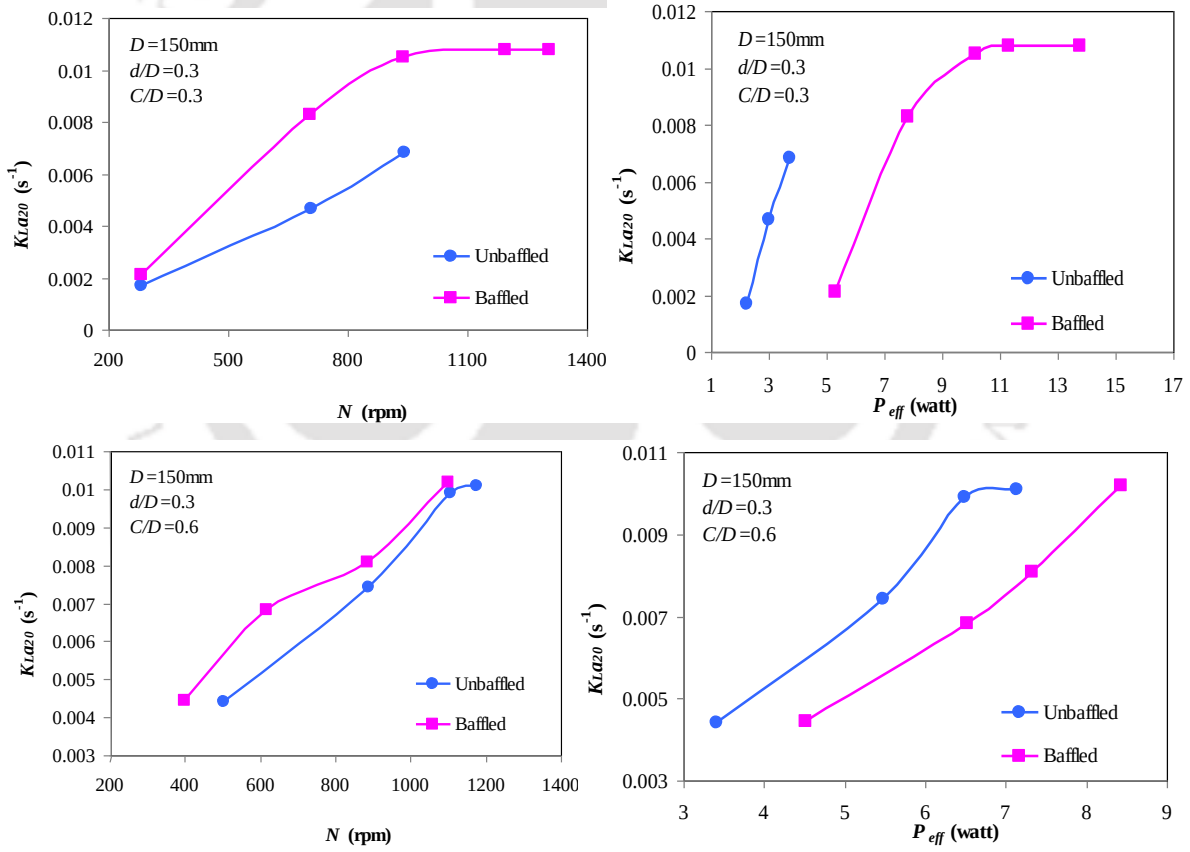

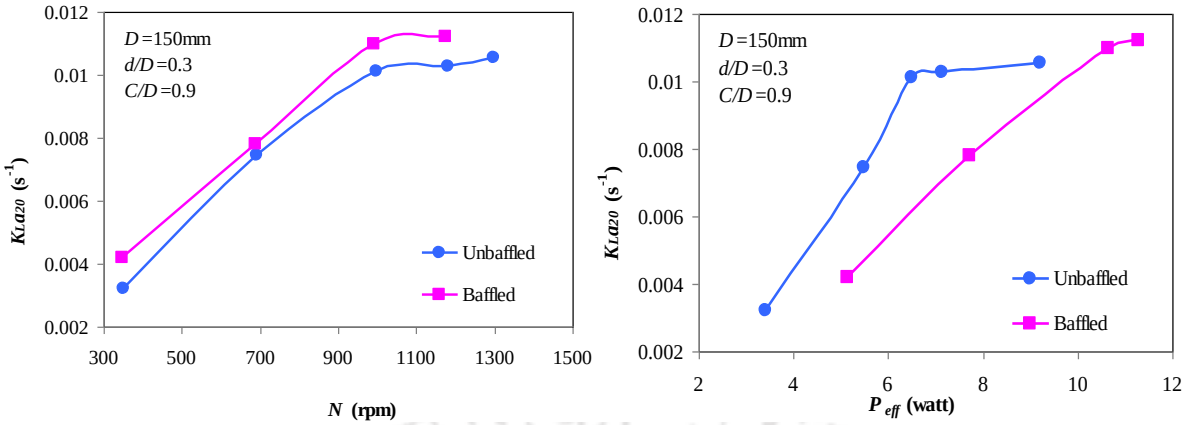

Figure 3.17: Comparison between unbaffled and baffled system at different speed with K_La_{20} (left) and P_{eff} (right) for different C/D

Figure 3.17(a-c) shows the comparison between unbaffaled system with baffled system in terms of mass transfer rate and effective power input at particular impeller clearance depth. Baffled sytem gives higher K_La_{20} as well as P_{eff} than the unbaffled system at all the cases of C/D for a particular impeller and tank diameter. So, in order to achieve the same amount of mass transfer rate between unbaffled and baffled system, it has been shown from the analysis that unbaffled system requires lesser power consumption than the baffled system. The results have been in line with the observations reported by various researchers (Johnson and Huang, 1956; Grisafi et al., 1994; Ciofalo et al., 1996; Assirelli et al., 2008; Yoshida et al., 2008). It is expected to give higher mass transfer rate in baffled system than the unbaffled system and it is because of the fact that the baffling arrangement creates obstruction to the fluid particles leading to enhance in fluid turbulence and subsequently producing higher mass transfer rate.

3.3.6. Numerical modeling

The main objective of performing the numerical modeling is to understand the process dynamics of unbaffled stirred systems. This numerical modeling has been carried out to analyze the flow pattern with turbulence scale characteristics like turbulent kinetic energy rate and dissipation rate at different impeller clearance depth.

3.3.6.1. Generated grid of the tank

The modeling of stirred tank is performed for D=150mm and d=45mm for all the cases of C/D (0.3, 0.4, 0.5, 0.6, 0.7, 0.8, 0.9). The geometry of grid generated (intermediate grid size) is shown in Figure 3.18.

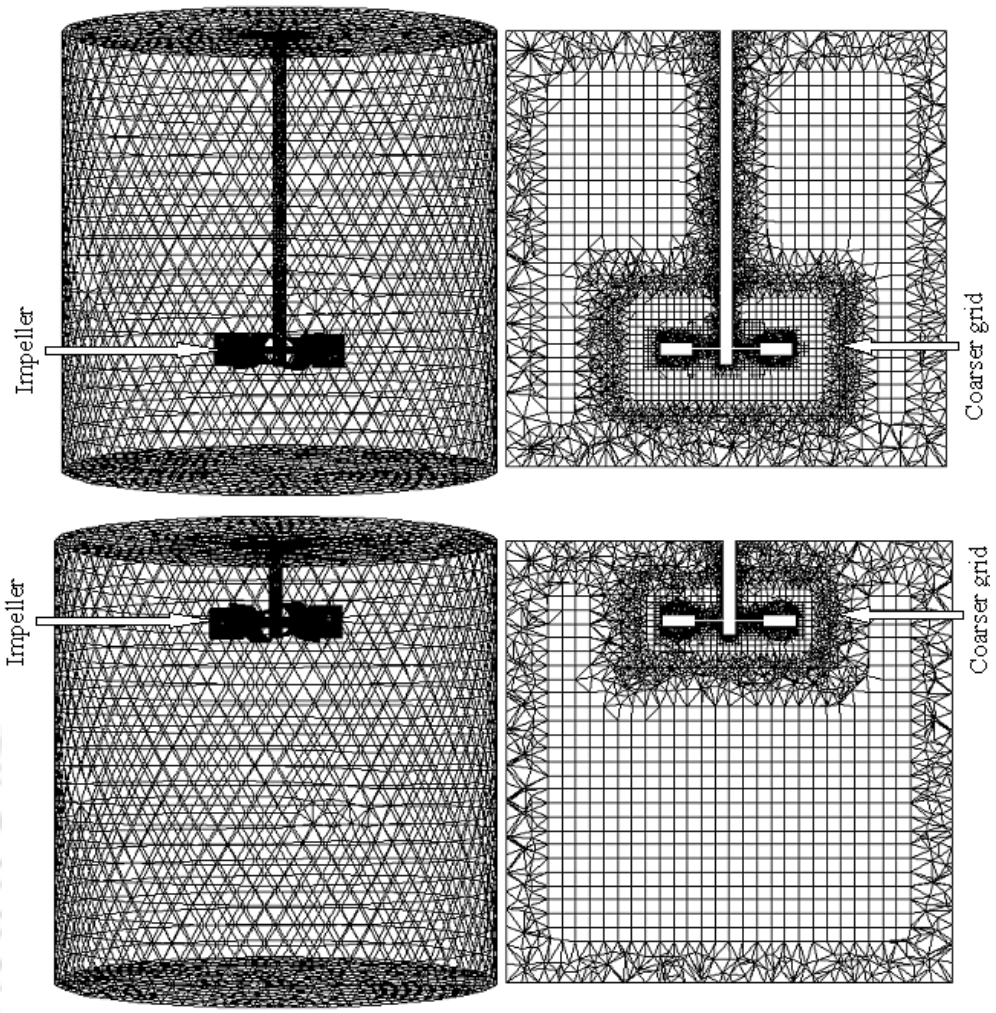

Figure 3.18: Generated grid of the stirred tank for *C/D*=0.3 (above) and *C/D*=0.9 (below) with coarsen grid at the impeller region

A cylindrical co-ordinate system is used, with the radial, axial and azimuthal co-ordinates indicated as *r*, *z* and θ respectively. Its origin is located at the centre of the tank bottom, with $\theta=0^0$ half of the tank. *u*, *v* and *w* are the mean velocity components in the axial, radial and tangential directions, respectively. u_{tip} is the maximum velocity at the tip of impeller and is estimated as πNd.

3.3.6.2. Flow pattern

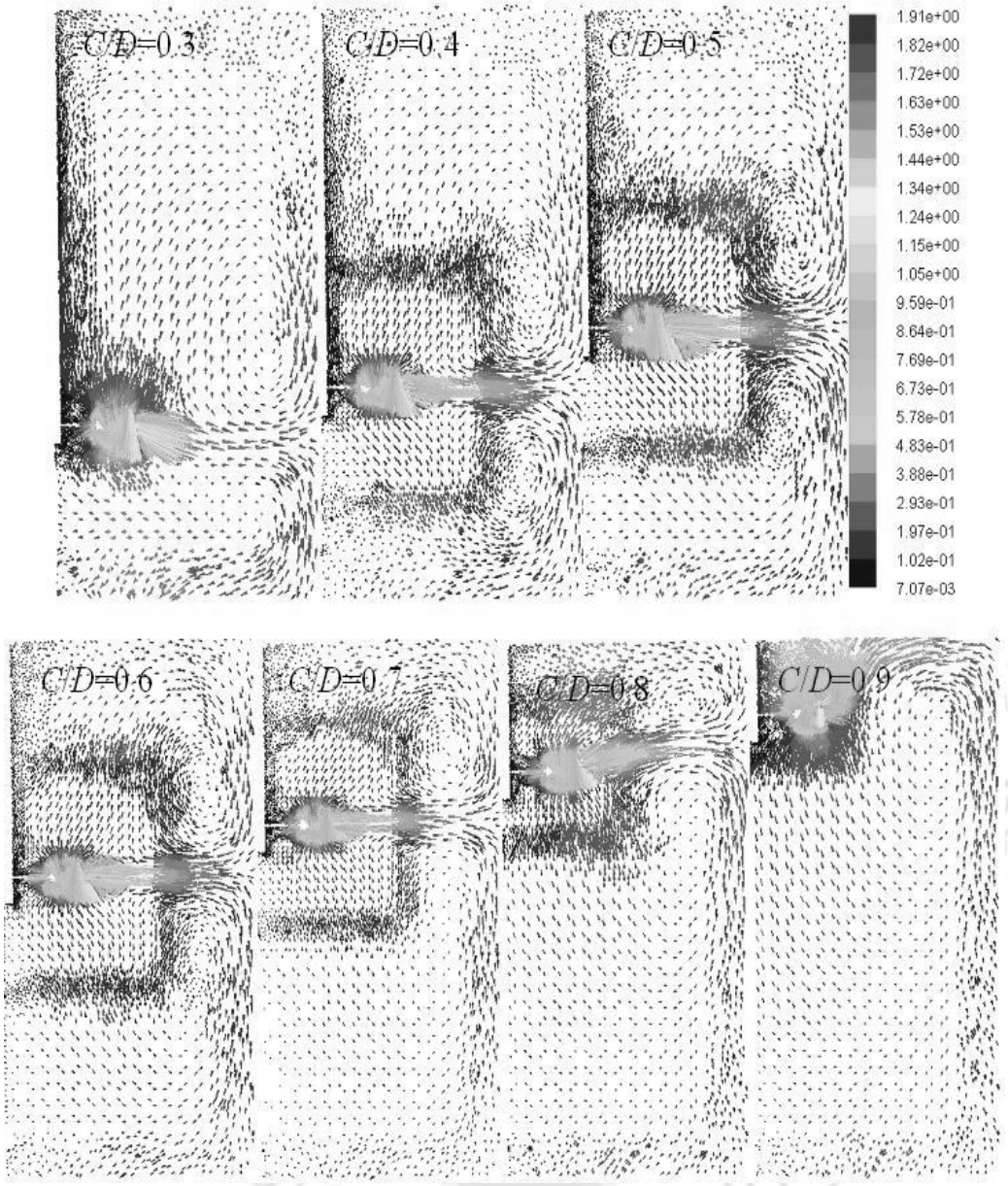

Figure 3.19: Comparison of mean velocity vectors (m/s) for different *C/D* at iso-surface of *y*=0

Figure 3.19 shows circulation patterns with different impeller clearance depth (*C/D*=0.3 to 0.9). When a radial flow impeller is used to promote mixing in a stirred tank, two circulation loops, one below and one above the impeller disk, are normally observed in the flow patterns, giving rise to the well known double-loop flow configuration. A clearance, which is less than one third of the tank diameter, is called as low (Nienow et al., 1983). As this clearance is

decreased, the flow pattern changes from typical two loops to a single loop. This phenomenon was first reported by Nienow et al. (1983), observed that reducing clearance distance to $D/6$ caused the flow from the impeller to dip towards the tank corner. Armenante and Nagamine (1998) found the flow pattern transition to occur at $0.16 < C/D < 0.19$ for a Rushton turbine. Montante et al. (2001) have investigated impeller clearance from C/D =0.12 to 0.33 and showed that a double-loop configuration exists for C/D=0.33; 0.25 and 0.20 while a single-loop configuration exists at C/D = 0.15 and 0.12 for Rushton turbine. The characteristic double loop configuration of radial impeller: one downward along the wall, to the bottom of the vessel, then back to the impeller region; the other rise along the wall, to the top of the vessel and back to the impeller region, forming an symmetric double loop can be clearly seen in the Figure 3.19 in the case of C/D=0.4 to 0.8. Unbaffled stirred tank does not show the standard stable configuration of Rushton turbine, which occurs when C/D =0.3 and baffled condition (Escudie et al., 2004). There is existence of weaker loop structure at C/D =0.3 and C/D=0.9 respectively. At C/D=0.9, Figure 3.19 does not show the natural characteristics of the radial turbine, which is double loop configuration. The strength of the lower and upper circulation loop reverses with increase of impeller clearance from 0.4D to 0.8D.

3.3.6.3. Velocity Profile

To understand the hydrodynamics inside the vessel with varying impeller clearance (C) is made vary, it is important to analyze the velocity profile. Comparison of axial and radial velocity profile for different C/D is shown in Figure 3.20(a-b) at axial distance (z) of 2cm above the tank bottom. This particular z=2cm is chosen in order to understand the effect of impeller clearance on this particular section which is near the tank bottom as our study has high impeller clearance depth. The magnitude of axial velocity decreases with increase in C/D that means when the impeller clearance depth increases, the influence of impeller near the bottom tank decreases. As in the similar case of axial velocity, radial velocity decreases its magnitude with increase in impeller clearance depth in negative direction.

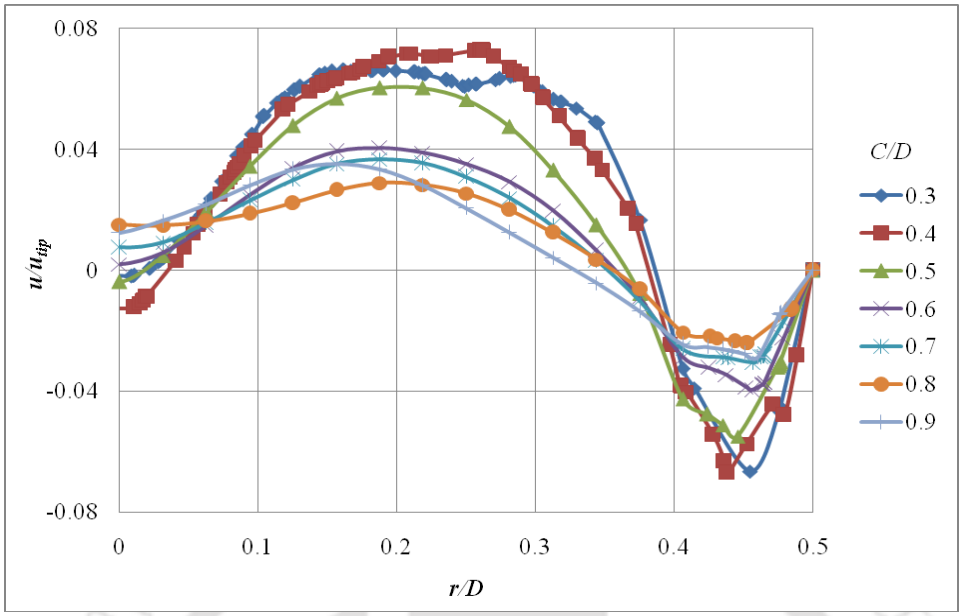

(a) Axial velocity (u/u_{tip})

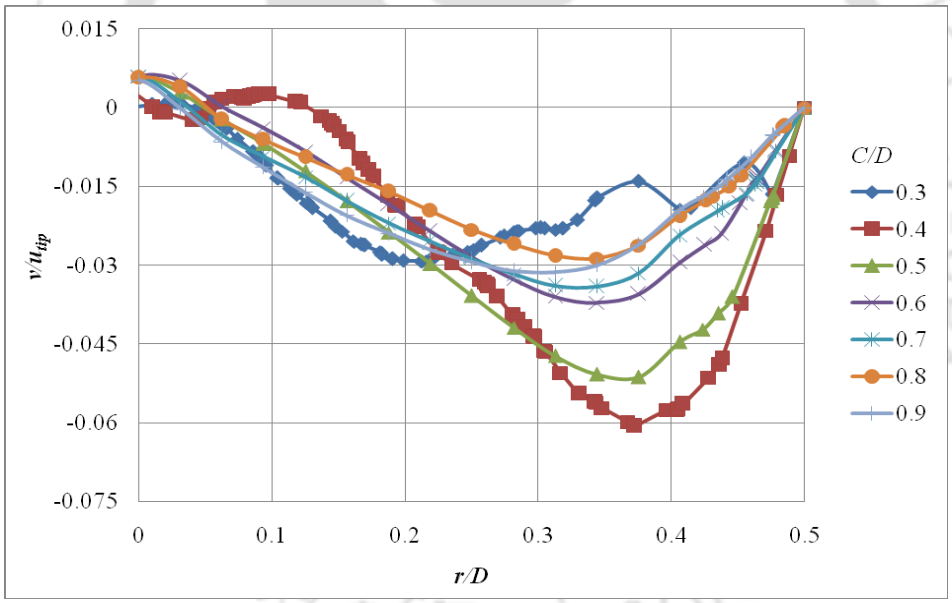

(b) Radial velocity (v/u_{tip})

Figure 3.20: Comparison of normalized (a) axial velocity (u/u_{tip}) and (b) radial velocity (v/u_{tip}) for different C/D values at z=2cm below the blade

The decrease of flow field magnitude (axial and radial velocity) when the impeller clearance increases at a particular section of z (20mm) is maintained below the impeller indicates that the influence of impeller near the lower of the tank decreases when increase in impeller clearance depth. This could be happened on the reverse side that is on the upper part of the

tank. In a clear way, the influence of impeller may decreases on the upper part of the tank (near the free water surface) when the impeller submergence depth is increases (Impeller submergence depth is measured from top of tank and is opposite to impeller clearance depth).

3.3.6.4. Turbulent Kinetic energy and dissipation rate

The distribution of turbulent kinetic energy (k) and turbulent dissipation rate (ε) in a stirred tank is of paramount important for designing processes. The knowledge of the magnitude and variation of dissipated energy in the form of turbulent dissipation rate across the stirred vessel is essential for particular mixing task (breaking down of solid into liquid, blending of liquid into liquid medium, etc). To understand the variation of k and ε across the vessel, the following regions of the stirred tank are divided into different regions as shown in the Figure 3.21:

(1) Impeller swept region is the volume swept by the rotating impeller and is confined in the range of $0<r>R$ and (C-blade height/2) $<z<$ (C+blade height/2).

(2) Impeller stream region is confined within $R<r<2R$ and (C-blade height/2) $<z<$ (C+blade height/2).

(3) Bulk flow region is the remaining part of the tank.

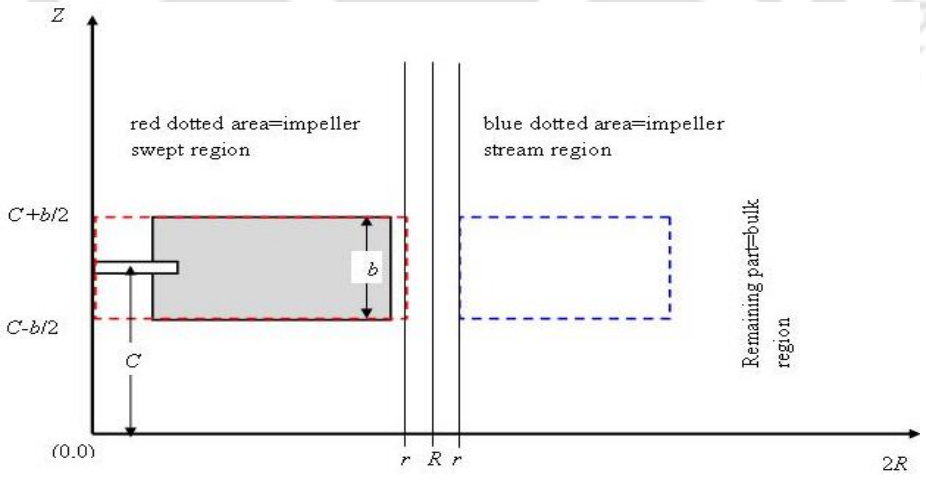

Figure 3.21: Different regions of vessel

Table 3.6 shows the distribution of area-weighted average values of k and ε for different regions of the tank. Most of the amount of k and ε are predicted in the impeller swept region (75-99 %) followed by stream (22-0.04%) and bulk region (5.5-0.03%). The distribution of ε is nearly negligible in impeller stream and bulk region in all the cases of C/D ratios. But for

k, the distribution is 75-93 % in impeller swept region with 23-5% in impeller stream region and 6-2% in bulk region. The distribution of *k* is almost same (86-93%) in all the values of *C*/*D* (0.4-0.9) except at *C*/*D* of 0.3 which is 75%. The normalized ε by taking its average of minimum and maximum magnitude for different impeller off distances (different *C*/*D* ratios) gives an general understanding about its contribution in energy dissipation in turbulent flow condition ($Re=\rho Nd^2/\mu$=16794).

Table 3.6: Distribution of area-weighted average values of *k* and ε

C/D	**Swept region**		**Stream region**		**Bulk region**	
	% *k*	**% ε**	**% *k***	**% ε**	**% *k***	**% ε**
0.3	75.32	98.52	22.27	1.373	2.41	0.102
0.4	92.58	99.90	5.62	0.047	1.80	0.053
0.5	91.57	99.92	6.62	0.039	1.81	0.045
0.6	93.75	99.93	4.87	0.039	1.37	0.029
0.7	93.45	99.92	5.00	0.045	1.55	0.032
0.8	86.15	99.64	8.35	0.240	5.50	0.124
0.9	86.15	99.64	8.35	0.240	5.50	0.124

Comparison of overall minimum and maximum normalized ε for different *C*/*D* ratios is shown in Figure 3.22. The highest maximum normalized ε (396) is predicted at *C*/*D* of 0.6 and lowest minimum (0.0002-0.0003) at *C*/*D* of 0.4, 0.7, 0.8 and 0.9. The lowest maximum (128) of normalized ε is predicted at *C*/*D* of 0.5 and highest minimum (0.0028) at *C*/*D* of 0.6.

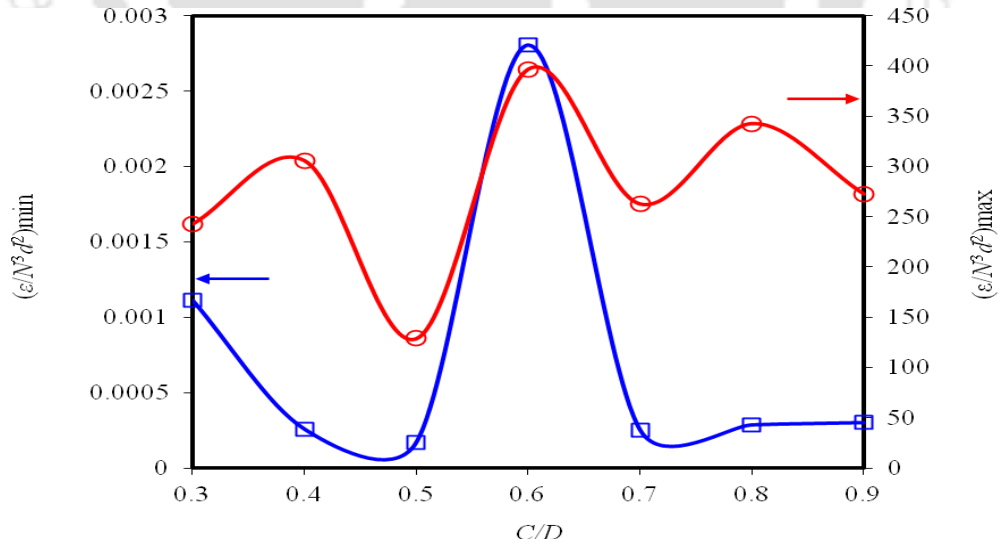

Figure 3.22: Normalized maximum and minimum values of turbulent dissipation rate (ε/N^3d^2) at different *C*/*D*

Table 3.7 shows the percentage contribution of normalized ε to the highest maximum and highest minimum values at different *C/D* ratios. This percentage values precisely shows that the highest contribution of energy dissipation takes place at *C*/*D* of 0.6 followed by *C*/*D* of 0.3 and lowest at *C*/*D* of 0.5.

Table 3.7: Percentage contribution of normalized ε against highest maximum and highest minimum values

C*/*D	**% contribution to the highest maximum**	**% contribution to the highest minimum**
0.3	61.20	39.67
0.4	77.09	9.17
0.5	32.49	6.08
0.6	100.00	100.00
0.7	66.24	8.96
0.8	86.39	10.18
0.9	68.75	10.71

Apart from being investigated the dissipation rate as a whole of the vessel only, it is also equally important to understand its magnitude at certain positions of the vessel where the turbulence of the flow is highest and; highest turbulence exists near and around the impeller tip of a vessel.

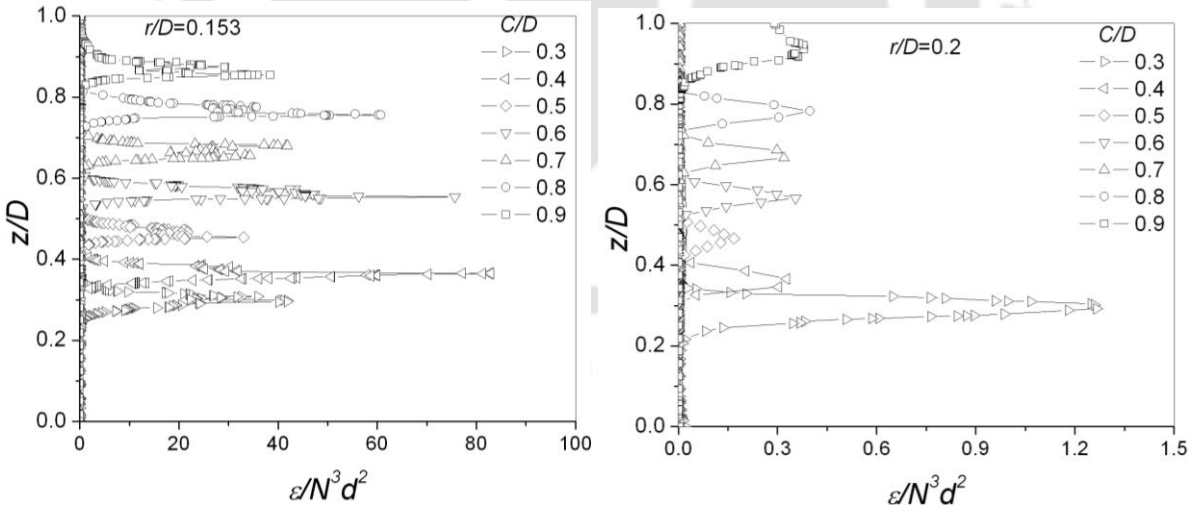

Figure 3.23: Comparison of normalized turbulent dissipation rate for various *C/D* ratios at *r/D*=0.153 (left) & 0.2 (right)

Figure 3.23 shows the comparison of normalized ε for different C/D ratios at radial distance of r/D equal to 0.153 (which is exactly at impeller tip) and 0.2 (which is near the impeller tip). Highest magnitude of normalized ε is predicted for C/D 0f 0.4, 0.6 and 0.8 at r/D of 0.153 (exactly at tip) and approximately similar magnitude is predicted for the remaining C/D ratios (0.3, 0.5, 0.7 and 0.9) at this radial position but in contrast to this the highest normalized ε (1.255) is predicted at C/D of 0.3 and minimum (0.2) at C/D of 0.5 for r/D equal to 0.2 (near the impeller tip). At this radial position (r/D=0.2) almost approximately similar magnitude of normalized ε is predicted for C/D of 0.4, 0.6, 0.7, 0.8 and 0.9. It is understood that the radial influence of dissipated turbulence even away from the impeller tip is produced by C/D of 0.3 and remained minimum by C/D of 0.5. The phenomenon of turbulence is extremely complex and understanding of turbulent characteristics is also a well challenging task and required constant improvement to predict such characteristics. The investigations of spatial distributions of turbulent characteristics need to be more précised rather than giving accurate results as a whole as this study witnessed strong variation of energy dissipation across the vessel. The impeller clearance depth to tank diameter ratio (C/D) plays important role in accounting to turbulence dissipation as this position directly holds the most important rotating part i.e., impeller of a stirred vessel which is the source of the most dissipated energy and supplies these energies to the other remaining regions of the vessel increasing the mechanisms of turbulence. Accurate axial position of such impeller affects the performance of a stirred tank expressed in terms of turbulence characteristics is explained in this section and concluded that the C/D of 0.6 gives good result among other combinations.

3.3.6.5. Power consumption

Accurate prediction of power consumption in terms of effective power (P_{eff}) is very important to validate the model against the experimental observation apart from the other process dynamic characteristics. An accurate CFD model should be able to predict important parameters such as the overall power input to a stirred tank (Taghavi et al., 2011). Figure 3.24 shows the comparison of experimental and predicted effective power. The prediction of effective power is acceptable as the co-efficient of regression (R^2) is nearly 0.9 which is a fair sign of linear relationship between the predicted and experimental. The linear regression gives that the predicted value is 0.963 times the experimental value.

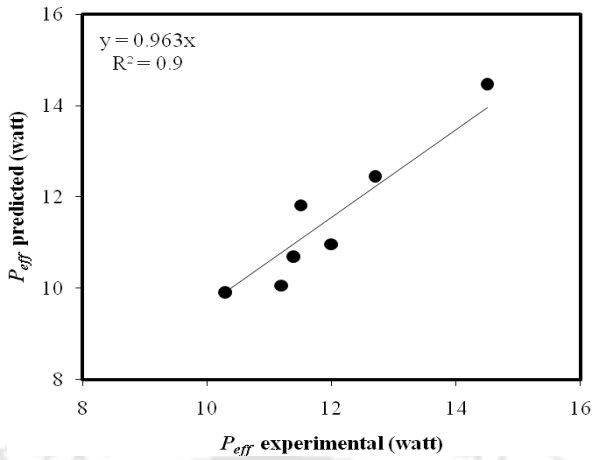

Figure 3.24: Comparison of experimental and predicted effective power consumption

3.3.6.6. Mass transfer rate and vortex formation

Modeling of mass transfer rate in terms of K_La_{20} in single phase is achieved by treating the single phase mechanism as multiphase mechanism and applying the same boundary condition which is applicable in multiphase mechanism. In gas-liquid system, the external gas is supplied using sparger and treated as source of gas but in single phase system, the external source of gas supply is considered coming from surrounding atmosphere of top open tank. As the top of the tank is open to atmosphere, atmospheric air (treated as source of gas) can easily allow to mix with inside water of the tank. Such kind of interaction between gas and water can be treated as multiphase mechanism and mass transfer rate can be estimated as in case of gas-liquid system. The boundary condition applied in order to model the mass transfer rate and vortex formation, the top of the tank is assumed as interface of pressure outlet having atmospheric pressure and air volume backflow of 1. The other boundary conditions are same in case of single phase modeling. The Eulerian-Eulerian multiphase model is used with dispersed viscous model to predict the mass transfer rate. Table 3.8 gives the experimental and predicted K_La_{20} for N=500 rpm. There is fair agreement of predicted K_La_{20} with experimental observation.

Table 3.8: Experimental and predicted K_La_{20}

C/D	K_La_{20} (s^{-1})	
	Experimental	CFD
0.3	0.0031	0.0024
0.6	0.0038	0.003
0.9	0.0046	0.0035

Because of the influence of outside atmosphere on the free liquid surface and suction created by the continuous movement of impeller and shaft, a form of depression is created at the centre of free liquid surface. Such kind of depression is because of the centrifugal force produced by the radially rotating shaft and behaves like suction in axial direction and has maximum depth at the centre of the free surface near the rotating shaft. The depression area is filled with gas and has replaced the volume of water and forms like vortex and can be treated as vortex formation in the modeling of vortex in stirred tanks. Figure 3.25 shows the comparison of water volume fraction for different *C/D* values when the impeller speed is constant. The boundary bottom layer between the water and gas volume fraction represents the vortex line. So, as seen from Figure 3.25, the vortex depth decreases with increase in *C/D* value. Higher vortex depth is predicted at lower impeller clearance depth (*C/D*=0.3) and minimum vortex depth occur at higher impeller clearance depth (*C/D*=0.9).

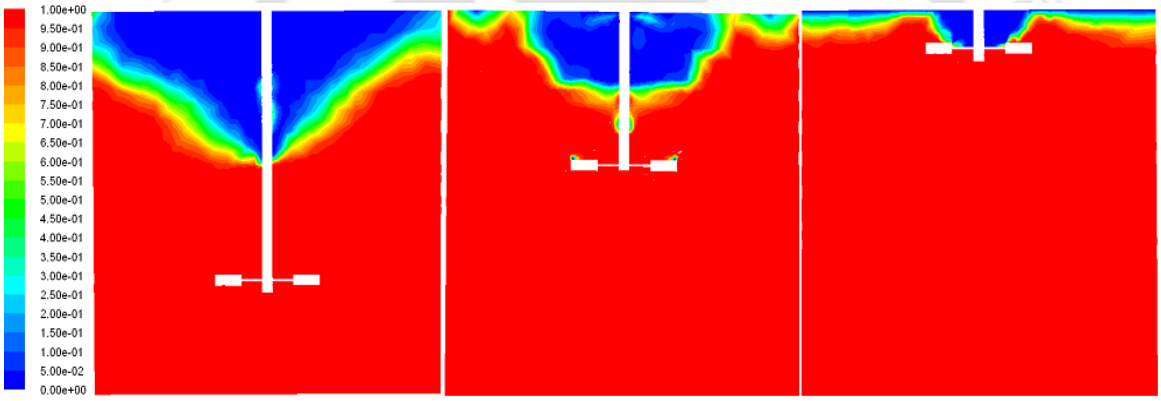

Figure 3.25: Comparison of water volume fraction for *C/D*=0.3 (left), *C/D*=0.6 (centre) and *C/D*=0.9 (right) at *y*=0 (full tank is considered)

3.3.6.7. Conclusions

The process dynamics based on mass transfer rate, power consumption and vortex depth have been studied on unbaffled single impeller without sparging system. The influence of impeller diameter (ratio of *d/D* is taken as 0.2, 0.3 & 0.4), tank diameter (*D*=150mm & 200mm) and impeller clearance depth (ratio of *C/D* is taken from 0.3 to 0.9 with 0.1 interval) are studied based on these process dynamic characteristics at various impeller rotational speed. Scale up criteria for mass transfer coefficient, power number and relative vortex depth have also been developed which is applicable for geometrically similar systems.

Mass transfer rate expressed by mass transfer coefficient (K_La_{20}) increases with increasing impeller rotational speed. Mass transfer rate has been found increasing with increasing impeller clearance depth; however increment is not very significant. Higher impeller diameter gives better mass transfer rate at different impeller clearance depth when tank diameter is constant. In order to simulate mass transfer rate for scale up, the influencing variables are made non-dimensional introducing k_c [$= K_L a_{20}\left(\upsilon / g^2\right)^{1/3}$] which is known as non-dimensional mass transfer parameter. Another important term is $X\left(= Fr^{4/3}Re^{1/3} = N^3 d^2 / \mathrm{g}^{4/3}\upsilon^{1/3}\right)$ called theoretical power per unit volume is included in developing the mass transfer rate scale up criteria. By taking the influence of *d/D* and *X*, a simulating criterion for k_c is developed as: $10^5 k_c = \alpha(d/D)^{\beta} X^{\gamma}$ having range of α=1.4 to 1.7, β=0.7 to 0.82, δ=0.27 to 0.3 at each *C/D* ratio and finally by incorporating the *C/D*, overall generalized scale criteria is developed as: $10^5 k_c = 0.6\,(d/D)^{0.23}\left(C/D\right)^{0.04} X^{0.3}$.

Power consumption is studied in terms of power number (N_p) by associating with *X*. Power consumption increases with increasing impeller speed. N_p decreases with increaseing *X* and *C/D* at all the cases of *d/D*. So, as the impeller is nearer to the free liquid surface, power consumption decreases while the impeller and tank diameter are keeping constant. N_p decreases with an increase in impeller diameter. The reason could be the proportionality factor related to the impeller diameter, as N_p is inversely related to d^5 keeping other parameters at constant. The effect of *d/D* is more pronounced at low impeller clearance and also at low impeller speed. Scale up criteria for N_p is developed as: $N_p = \alpha(d/D)^{\beta}(X)^{\gamma}$ at each *C/D* having α=10.16 to 65.51, β=-0.21 to -2.53, γ=-0.68 to -1.05. Overall N_p is developed as: $N_p = 34.69\,(d/D)^{-0.974}(X)^{-0.98}(C/D)^{-0.5}$.

Relative vortex depth (V_d/d) increases with increase in Froude number. There is no significant variation of relative vortex depth with changing impeller clearance in all the cases of different impeller to tank diameter (*d/D*) of 0.2, 0.3 and 0.4. However, it can be seen that impeller is closer to tank bottom, higher is the vortex depth. Relative vortex depth increases with increase in impeller diameter at all the cases of impeller clearance (*C/D*=0.3, 0.6 and 0.9) at constant *D*. Smaller tank diameter gives higher relative vortex depth when *d* is

constant at different impeller clearance depth. Critical speed (N_c) is found decreases with increase in *C/D* and increasing of *d/D*. That means larger the impeller diameter, lower is the critical speed when tank diameter is constant. Scale up criteria for V_d/d is developed as: $\frac{V_d}{d} = 0.63\, Ga^{0.069} (D/d)^{-1.39} Fr^{1.14 Ga^{-0.008}(D/d)0.008} \left(C/D\right)^{-0.79}$.

A comparative study was also done in order to understand more on the behavior of unbaffled system of concave blade impeller with baffled system and another impeller type (Rushton impeller). Concave blade type impeller has been found better. Unbaffled system consumes lesser power and higher mass transfer rate than baffled system.

The transformation of single loop flow circulation to double loop is predicted at *C/D*=0.9. From *C/D*=0.3 to 0.8 gives double loop pattern. It is also found that maximum amount of flow circulation take place near and around the impeller region. As the impeller clearance depth increases, the influence of flow field (axial and radial velocity) decreases near the lower part of impeller. So, the effect of impeller clearance depth is very significant on flow circulation across the vessel. Other smaller scale (turbulence scale) of flow field (turbulent kinetic energy rate, *k* and dissipation rate, ε) were studied at different regions of the vessel (impeller swept region, impeller stream region and bulk region). Most of the amount of *k* and ε are predicted in the impeller swept region (75-99 %) followed by stream (22-0.04%) and bulk region (5.5-0.03%). The distribution of ε is nearly negligible in impeller stream and bulk region in all the cases of *C/D* ratio. But for *k*, the distribution is 75-93 % in impeller swept region with 23-5% in impeller stream region and 6-2% in bulk region. The distribution of *k* is almost same (86-93%) in all the values of *C/D* (0.4-0.9) except at *C/D* of 0.3 which is 75%. So, maximum amount of energy is dissipated at the impeller region (swept region+stream region). When the radial direction closer towards the tank wall, energy dissipation decreases and gives maximum at the impeller tip. Better performance in terms of energy dissipation is predicted when the impeller (location of impeller is in axial direction) is higher or lower half of the tank and not at the exact half of the tank. Power number is predicted in fair agreement with the experimental observations. For qualitative analysis of the mass transfer rate and vortex formation, the stirred tank system were modeled only at *C/D*=0.3, 0.6 and 0.9 and predicted $K_L a_{20}$ is found in acceptable agreement with experimental result. An attempt is also

made to model the vortex formation by representing the volume occupied by gas on the central part of free liquid surface and found convincing result.

3.4. Gas-liquid phase

Gas-liquid stirred tanks are widely used in process industries where the complete mass transfer takes place in turbulent regime of fluid flow in sparged (gas-liquid) condition. The efficiency of such reactor system governs on physical, geometrical and operational factors. System is needed to be gassed (continuously gas is supplied through sparger) to improve efficiency of these system with specific superficial gas velocity rate (volumetric flow rate divided by cross sectional area of reactor). Gassed system provides additional oxygen required by the micro-organisms in cell growth as well as maintenance and other metabolic production in bioprocess (aerobic fermentation, wastewater treatments). In these processes, oxygen is an important nutrient and scarcity of oxygen affects the process performance (Garcia-Ochoa et al., 2000; Calik et al., 2004; Liu et al., 2006; Amaral et al., 2008). In such systems of stirred tank bioreactor in aerobic condition, oxygen transfer rate is the most important parameter to be examined with other hydrodynamics. The oxygen transfer can be described and analyzed by means of mass transfer coefficient, $K_L a_{20}$. It represents the most important parameter implied on the design and operation of mixing-sparging equipment of the bioreactors (Karimi et al., 2011). Power draw is one of the significant design parameters for a multiphase in mechanically agitated stirred tank. Its optimal utilization in industrial purposes needs to be studied based on operating conditions like superficial gas velocity in sparged systems. Knowledge of the dependence of the power input on operating conditions gives a useful insight into the process; hence, efficiently performing the mixing process with minimum energy is of great interest (Karimi et al., 2011). Gas hold up also plays important role in gas-liquid system which directly gives the understanding of volume occupied by gas in the medium of liquid. Thus, global parameters like overall gas hold-up, power demand and overall gas-liquid mass transfer coefficients are very strong functions of the local fluid dynamics of the gas and liquid phases in the stirred tank.

3.4.1. Mass transfer rate

The influence of mass transfer rate expressed by K_La_{20} based on several factors including impeller clearance depth, impeller diameter, impeller speed, diameter of tank, etc., will be discussed in the following subsequent sections.

3.4.1.1. Effect of impeller clearance depth *(C)*

The influence of impeller clearance on mass transfer rate is shown in Figure 3.26 at a constant impeller diameter with different impeller speed. K_La_{20} increases with increasing *N*. Higher K_La_{20} is observed at lower *C/D*. Interestingly, *C/D* at 0.3 gives maximum K_La_{20} ($0.018s^{-1}$-$0.024\ s^{-1}$) than C/*D* of 0.25 and minimum ($0.0045s^{-1}$-$0.0055\ s^{-1}$) at *C/D*=0.85 when *N* is constant.

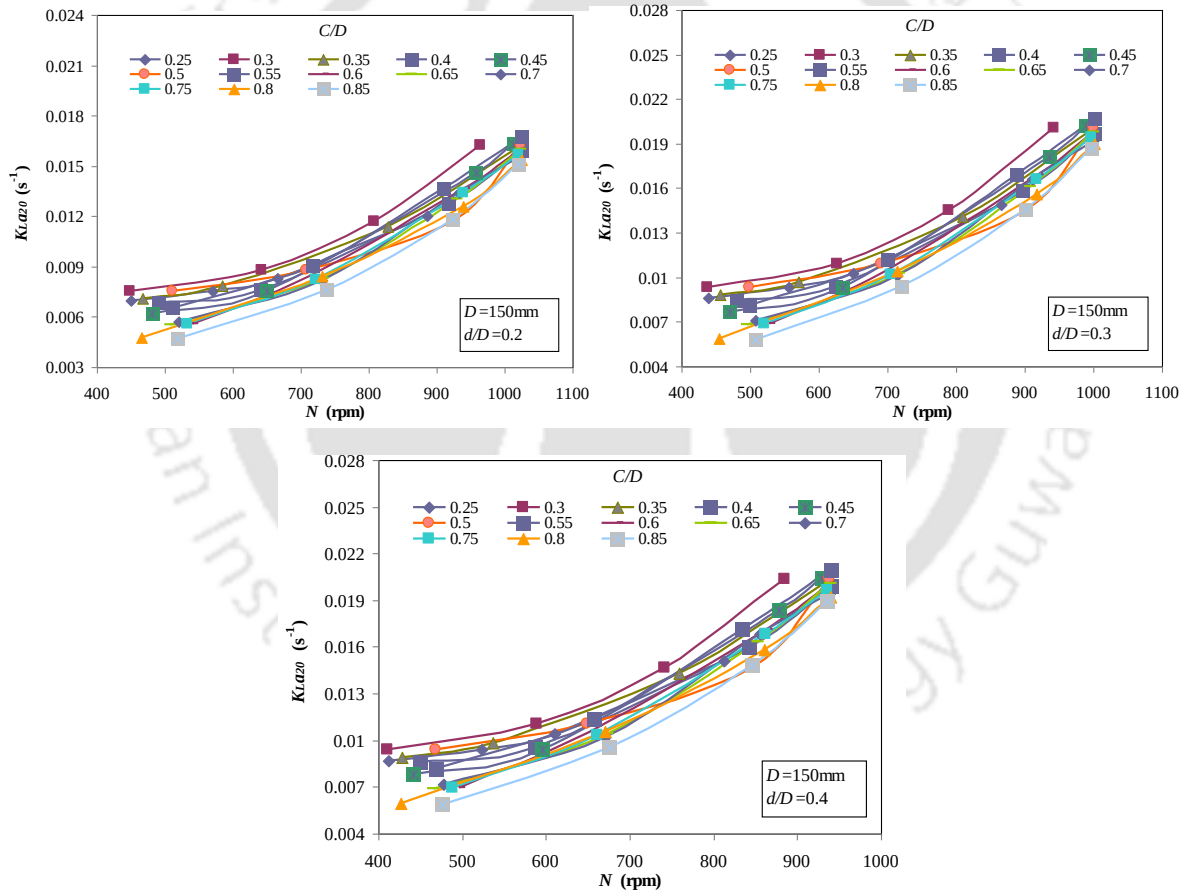

Figure 3.26: Comparison of K_La_{20} for different *C/D*

As shown in the Figure 3.26, K_La_{20} is maximum when *C/D* =0.3. The location of the sparger is fixed in each experiment at 0.09*D*. It can be seen from the Figure 3.26(a-c) that the value

of K_La_{20} at C/D =0.25 is less than that of C/D=0.3. When sparger placed below the impeller, it favors the gas to be entrained into the circulation loop present in the lower part of the tank. The gas then has a longer residence time in the vessel, which promotes mass transfer. However, the gap between sparger location and impeller clearance has an important effect on mass transfer. The gap should be sufficient to break up the bubbles and to disperse the gas throughout the vessel. It can be said that the bubble breakage and uniform mixing is optimal when impeller clearance is placed at C/D=0.3. The residence time of the gas in the vessel decreases with impeller clearance above 0.3, which results is lower mass transfer rate.

3.4.1.2. Effects of impeller diameter *(d)*

Figure 3.27 shows the comparison of K_La_{20} with N for different d/D at constant C/D. K_La_{20} increases with increasing d/D when D is constant. Higher K_La_{20} is produced by bigger impeller diameter when tank diameter is constant at a particular impeller speed. This is similar with the case of single phase system.

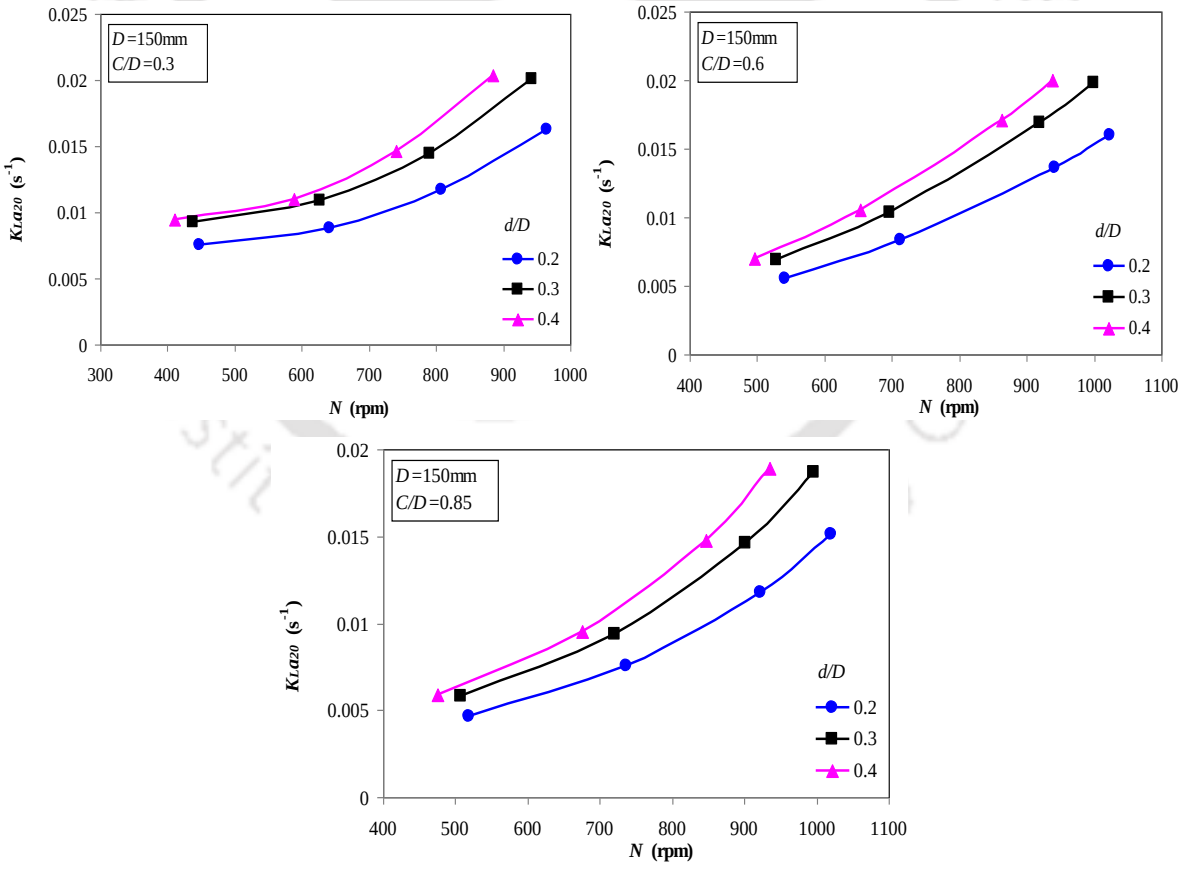

Figure 3.27: Comparison of K_La_{20} for different d/D

3.4.1.3. Design criteria for Mass transfer rate

Mass transfer in gas-liquid stirred tank systems is influenced by several variables. So, mass transfer coefficient at standard temperature of 20^0C can be expressed as function of influencing variables and is given as below for single impeller:

$$K_L a_{20} = f\left(H, D, d, l, b, C, n, N, v_g, g, \rho_a, \rho_w, v\right) \tag{3.36}$$

Where, v_g is the superficial gas velocity. In dimensionless form, Equation (3.36) is written as:

$$k_c = f\left(H/D, d/D, l/d, b/d, C/D, n, \rho_a/\rho_w, Fl, Re, Fr\right) \tag{3.37}$$

Where, Fl is Flow number ($Fl = \frac{Q_g}{Nd^3}$, Q_g is gas flow rate and written as v_g multiplied with cross sectional area of vessel). By eliminating the constant ratio in (3.37), it becomes as:

$$k_c = f\left(d/D, C/D, Fl, Re, Fr\right) \tag{3.38}$$

In case of gassed system (gas-liquid), Froude number is significant as the gravitational forces tend to promote a vertical separation of liquid and gas phase (Gray et al., 1982). Gravity acting on the liquid leaving an impeller travelling radially to the tank wall in gassed system will tend to promote the downward flow of the liquid producing an unsymmetrical flow pattern as opposed to that of single phase. An increase in the gravitational forces also promotes the upward flow of the gas phase leading to a reduction in the gas hold up. Increasing the gas flow rate which is flowing upward should tend to improve gas hold up in the system. They have accounted Froude number in their studies of gassed system. Clark and Vermeulen (1964) argued to include the Froude number in order to represent the surface behavior of flow in gas-liquid system. Therefore, inclusion of Froude number in order to establish relationships of mixing characteristics in gas-liquid phase system is imperative as the mixing characteristic are interrelated to each other and have equal contribution towards the performance of the system. Thus by combining *Re* and *Fr* as *X*, Equation 3.38 can be written as:

$$k_c = f\left(d/D, C/D, Fl, X\right) \tag{3.39}$$

So, for *C/D* scale up criteria, k_c is developed statistically as:

$$10^5 k_c = \alpha\left(\frac{d}{D}\right)^{\beta}\left(X\right)^{\gamma}\left(Fl\right)^{\delta} \tag{3.40}$$

Where α, β, γ and δ are the parameters of the function, which is optimized to get the maximum correlation coefficient (R^2) and minimum standard error based on experimental observation. The details about standard error of the parameters of the regression equation besides overall standard error have been given because of it indicates confidence for engineering applications. The standard error of a parameter is the expected value of the standard deviation of that parameter if the experiment has been repeated many times. Statistical details of the parameters used in Equation 3.40 are given in the Table 3.9.

Table 3.9: Statistical details of Equation 3.40 for different *C*/*D*

C*/*D	***α***	***β***	***γ***	***Δ***	**Overall std. error**
0.25	3.24 (7.0e-2)	0.75 (1.2-2)	0.24 (3.37e-2)	0.018 (3.68e-2)	7.44e-2
0.3	8.54 (7.93e-2	0.678 (1.35e-2)	0.32 (3.78e-2)	0.018 (4.13e-2)	8.36e-2
0.35	3.01 (5.12e-2)	0.719 (8.70e-2)	0.32 (2.44e-2)	0.018 (2.67e-2)	5.39e-2
0.4	3.44 (5.05E-2)	1.13 (8.59E-2)	0.361 (2.41e-2)	0.016 (2.63e-2)	5.33e-2
0.45	3.09 (4.87e-2)	1.15 (8.28e-2)	0.49 (2.32e-2)	0.015 (2.54e-2)	5.13e-2
0.5	4.94 (8.83e-2)	1.19 (1.50e-2)	0.349 (4.21e-2)	0.016 (4.60e-2)	9.30e-2
0.55	3.74 (3.05e-2)	1.15 (5.19e-3)	0.418 (1.46e-2)	0.018 (1.59e-2)	3.22e-2
0.6	3.01 (4.05e-2)	1.21 (6.88e-3)	0.489 (1.93e-2)	0.018 (2.11e-2)	4.26e-2
0.65	2.72 (4.81e-2)	1.19 (8.18e-3)	0.479 (2.30e-2)	0.019 (2.51e-2)	5.07e-2
0.7	2.73 (6.94e-2)	1.19 (1.18e-2)	0.466 (3.31e-2)	0.02 (3.62e-2)	7.32e-2
0.75	2.31 (3.83e-2)	1.2 (6.52e-2)	0.484 (1.83e-2)	0.018 (2.00e-2)	4.04e-2
0.8	2.33 (8.13e-2)	1.18 (1.38e-2)	0.451 (3.88e-2)	0.018 (4.24e-2)	8.57e-2
0.85	2.25 (6.15e-2)	1.25 (1.05e-2)	0.543 (2.94e-2)	0.018 (3.21e-2)	6.48e-2

It can be seen from the statistical details, all the other parameters are well estimated within experimental error. The observed and predicted mass transfer rate (Equation 3.40) is plotted in Figure 3.28. The prediction capability of the Equation 3.40 is found to be satisfactory. The

regression equations show that at each *C/D*, the variations of *d/D* and *X* are nearly comparable.

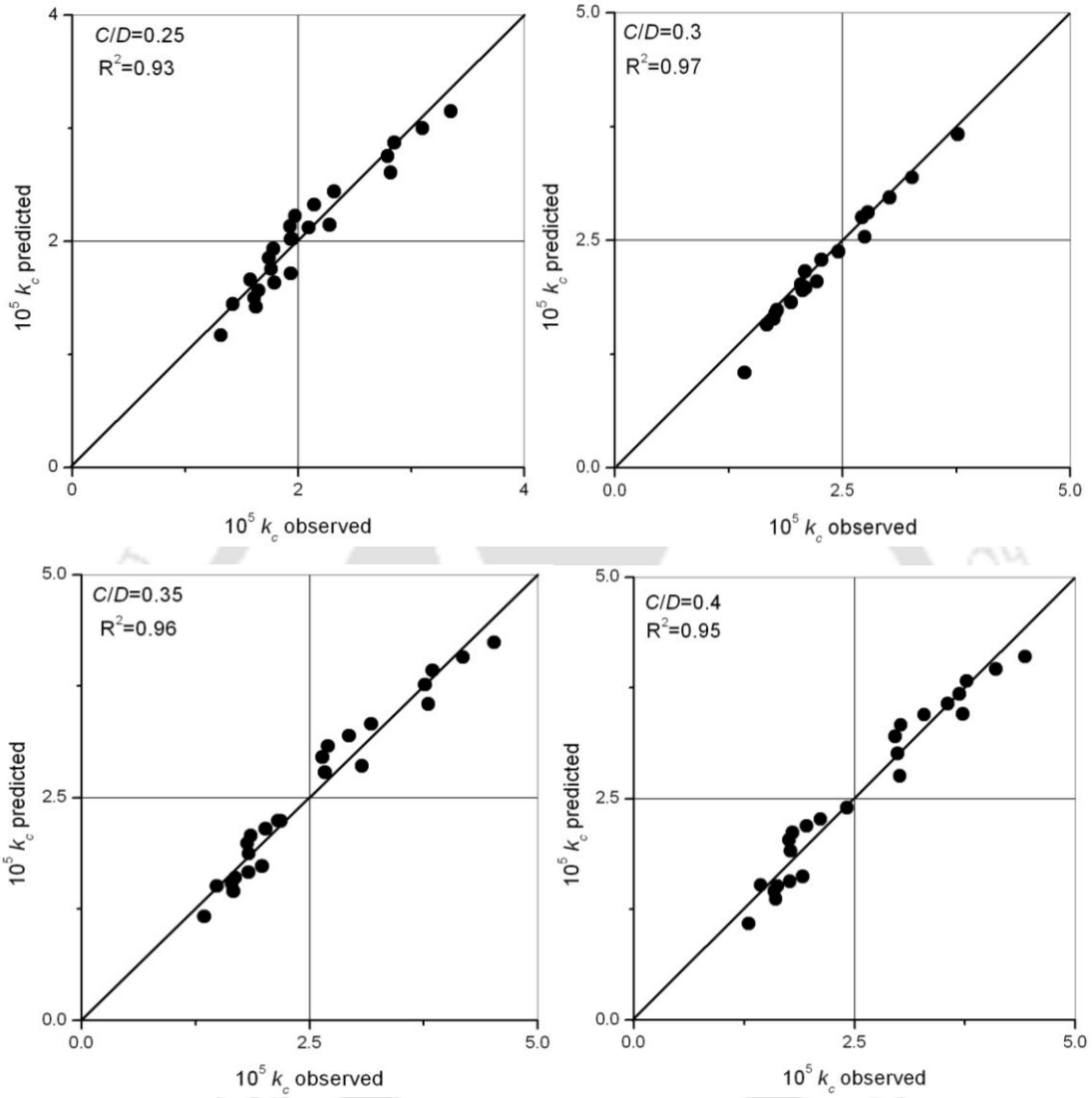

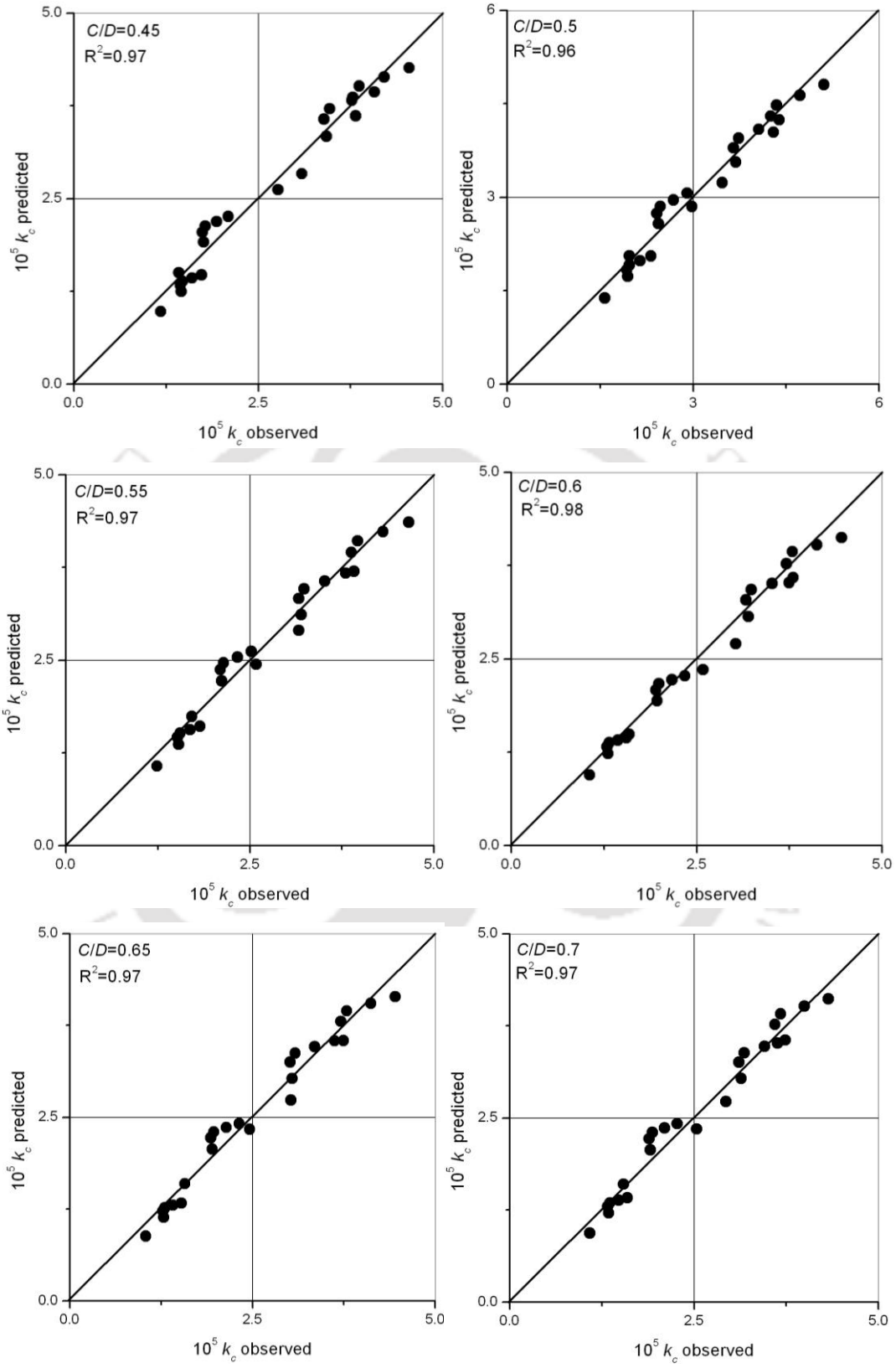

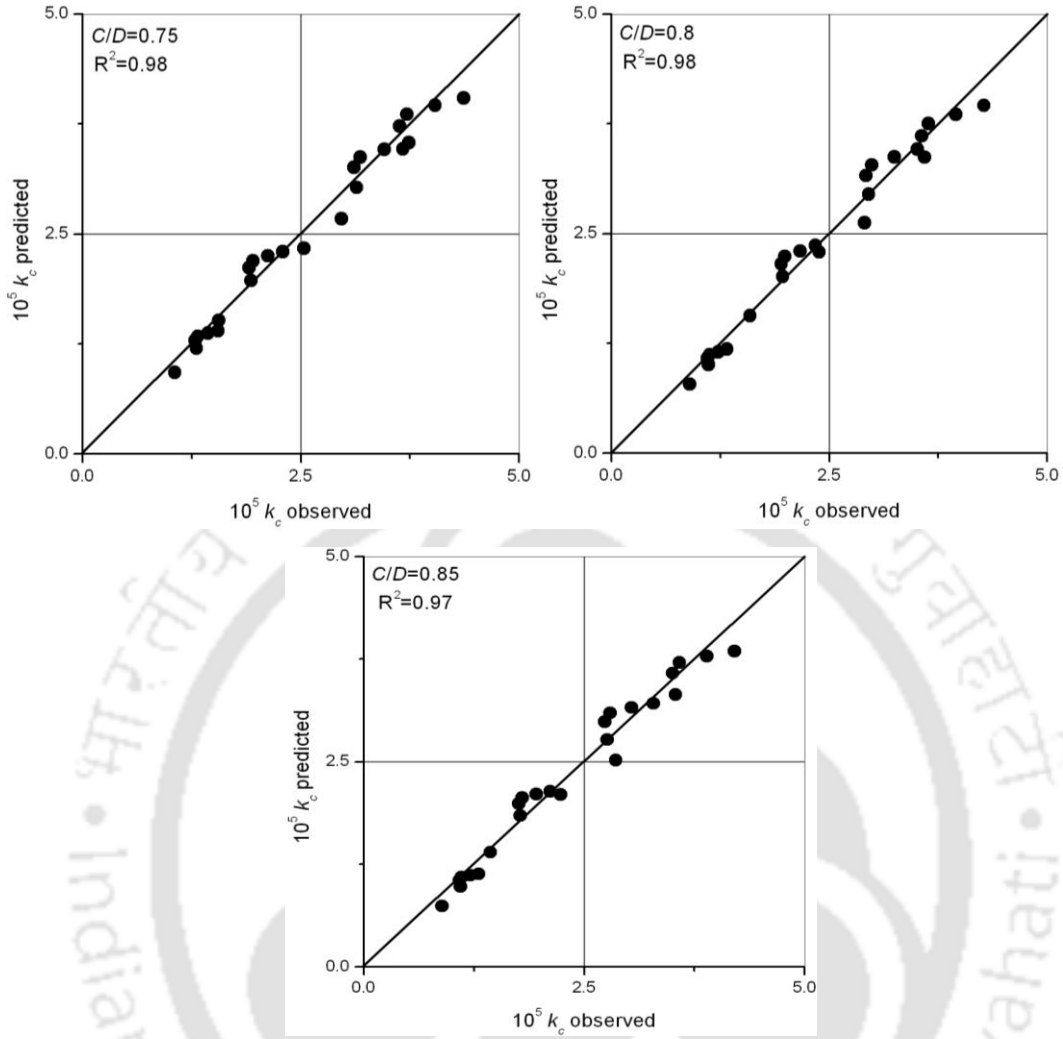

Figure 3.28: Predicted and observed k_c at various C/D

Similar to single phase analysis, it is also tried to develop the simulation/design criteria. The form of the regression equation has been maintained same as Equation 3.40 with one extra term $(C/D)^{\eta}$. The final form the regression equation is given as follows:

$$10^5 k_c = \alpha \left(\frac{d}{D}\right)^{\beta} (X)^{\gamma} (Fl)^{\delta} \left(\frac{C}{D}\right)^{\eta} \quad (3.41)$$

Table 3.10: Values of constants of Equation 3.41

α	β	γ	δ	η	**Overall std. Error**
2.36 (6.51e-3)	1.14 (1.31e-3)	0.41 (4.31e-2)	0.02 (1.60e-2)	-0.031 (1.01e-2)	2.67e-2

The prediction analysis is shown in Figure 3.29. As shown in the Figure 3.29, the correlation coefficient is 0.93 with standard error 2.67e-2. The performance of the Equation 3.41 can be said satisfactory considering the different operation conditions. In order to simulate mass transfer rate under different impeller clearance and impeller to tank diameter ratio from 0.2 to 0.4 with constant *H*/*D* (=1) with gas flow rate (Q_g) of 1 to 5 lit/min and blade dimensions of *l*/*d*=0.25, *b*/*d*=0.2, Equation 3.41 can be utilized.

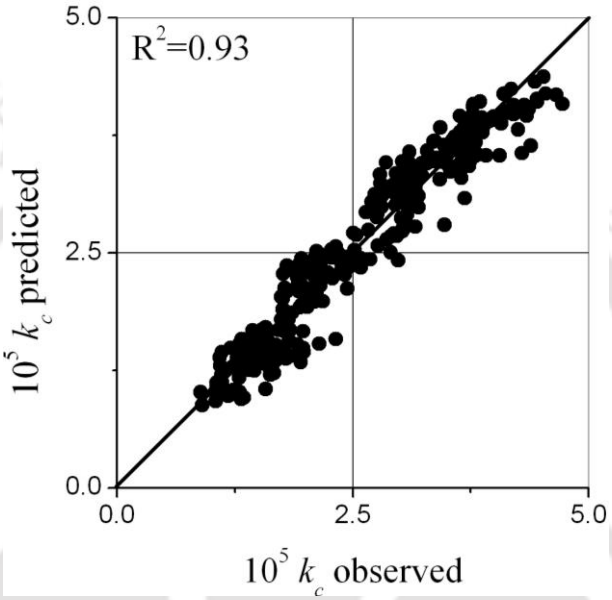

Figure 3.29: Overall generalized predicted and observed k_c

3.4.2. Power consumption

The power input (effective power) is expressed as gased power (P_g) in sparged system which is the power consumed by the rotation of impeller and shaft while gas is continously supplied from the source. Gased power input may affect by various geometric conditions like impeller clearance depth (*C*), diameter of impeller (*d*), diameter of tank (*D*), impeller rotational speed (*N*), etc. The influence of these parameters on gased power input will be discussed in the following subsequent sections.

3.4.2.1. Effect of impeller clearansce depth *(C)*

Impeller position (impeller clearance depth) could be an important factor affecting the gassed power consumption in the sparged system as in case of unsparged system (single phase) in the previous section. Figure 3.30(a-c) shows the comparison of P_g with *N* at different *C*/*D* for

a particular *d*/*D*. This shows that P_g increases with increasing *N* at all the cases of *d*/*D*. So, in another words, P_g increases with increase in turbulence of fluid flow of the system. Another depiction from this figure is that P_g decreases with increasing impeller clearance depth and lowest gased power consumption ocurred when impeller is near the free liquid surface (*C*/*D*=0.85) and highest at *C*/*D*=0.25 (near the bottom of the tank) which is the lowest impeller clearance depth of this study.

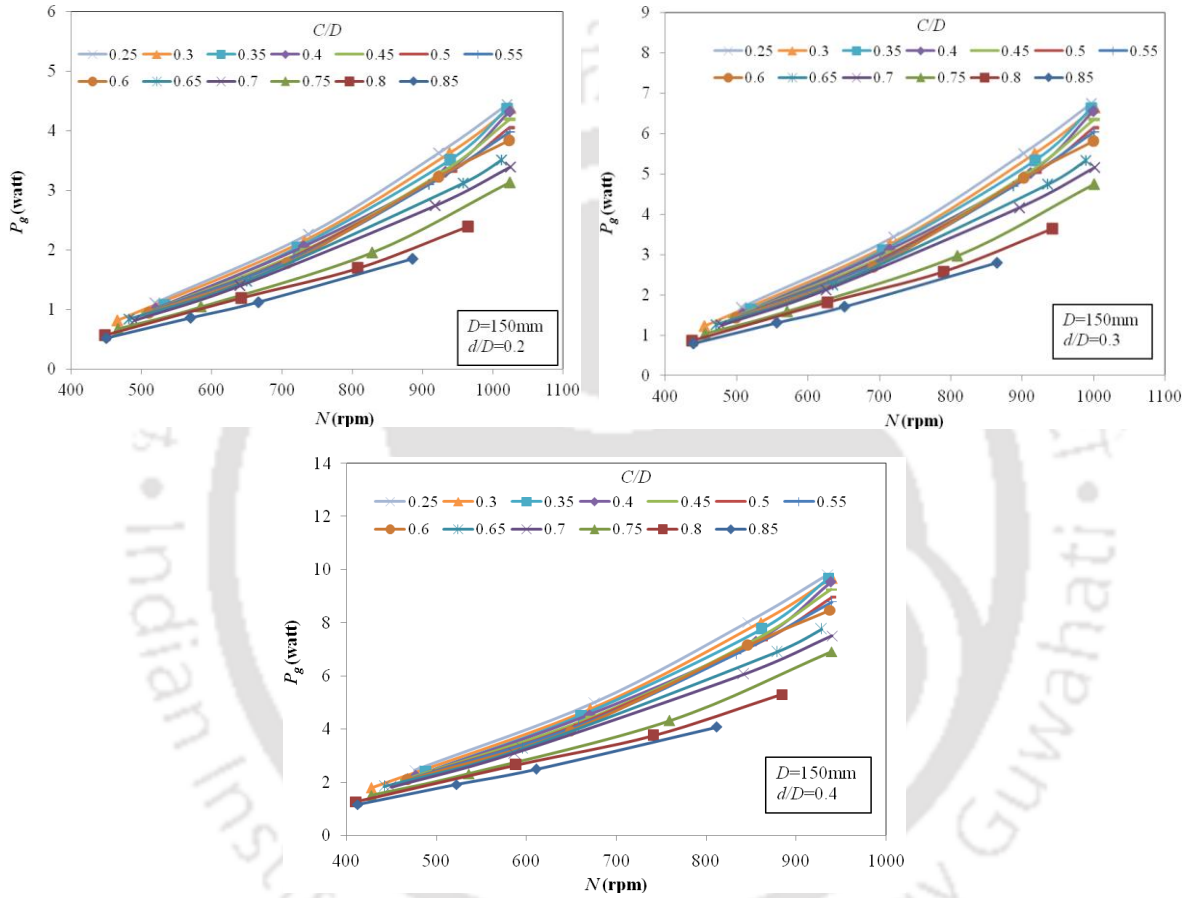

Figure 3.30: Gassed power input (P_g) with *N* for different *C*/*D*

If the distance between the impeller to the bottom of the tank is greater, the turbulence intensity decreases (Tatterson, 1991). It is due to for pumping down flow, at a low clearance, flow generated by impeller rotation will hit the bottom of the tank, therefore fluid have more power to flow upward axially. While at a high clearance, the fluid that pulled down are less able to resist the flow on it so that the turbulence intensity decreases. If the impeller is located closer to the bottom tank walls, increased viscous resistance occurs, which limits the flow around the agitator, which leads to a high power consumption.

3.4.2.2. Effect of impeller diameter (d)

The influence of impeller diameter on P_g at a particular impeller clearance depth with N is shown in Figure 3.31. This figure depicts that P_g increases with increase of d/D. So, higher impeller diameter consumes higher power than the smaller impeller diameter when impeller speed is constant.

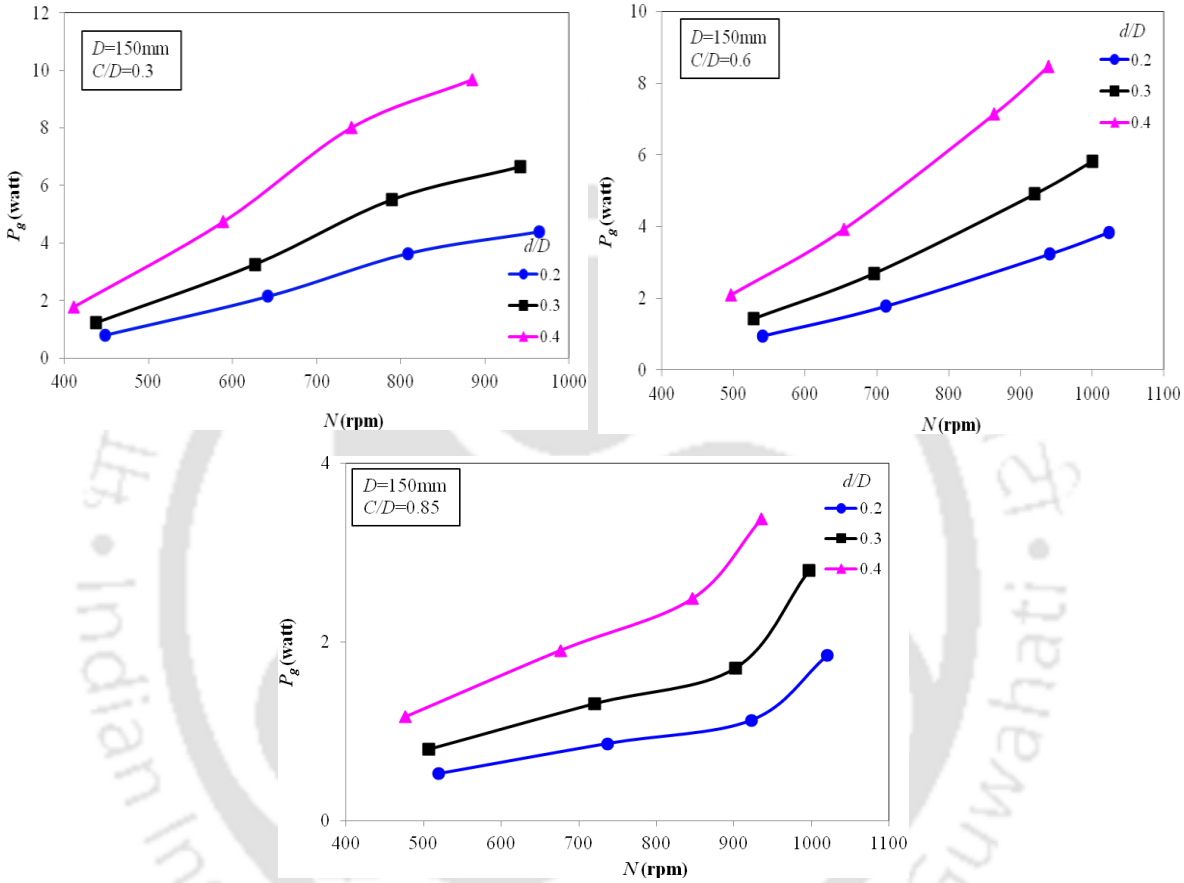

Figure 3.31: Gassed power input (P_g) with N for different d/D at (a) C/D=0.3 (b) C/D=0.6 and (c) C/D=0.85

3.4.2.3. Correlations of power consumption

The mechanical agitation power requirements of an ungassed Newtonian liquid can be predicted fairly well from semi-theoretical correlations of the Power Number, N_p, with the impeller Reynolds Number (Rushton et al., 1950). Although the ungassed power consumption is easy to predict, it is difficult for the gassed power demand. It is well known that in similar conditions, i.e., at equal impeller speeds, the gassed power consumption is lower than that in the ungassed system. This difference cannot be determined simply by

substituting the density of the gas-liquid mixture, ρ_d, for the density of the liquid (water), ρ_w, because the reduction in mechanical agitator power drawn is not fully described by the change of the density of the mixture resulting from the presence of gas bubbles. The power reduction must be explained by a change of the drag coefficient and pumping capacity of the impeller when it operates in a gas-liquid system. It is known that ventilated cavities may be formed behind the blades of a turbine impeller. It is also well known that cavities behind a body will lower the form drag (Batchelor, 1967). It is to be expected that the drag of an impeller will also be reduced when cavities are formed behind the blades. Biesecker (1972) and later Van't Riet (1975) have shown that this forms a plausible explanation for the observed power reduction of gassed impellers. However though the mechanism is known, no satisfactory method of predicting the gassed power consumption is available. The complexity of the system ensures that the gassed power demand cannot be described by simple correlations, whether based on empirical data or dimensional analysis. The correlations which are available in the literature for predicting the power demand of gassed impellers may be divided into three groups as:

(1) Dimensionless correlations:

Extended reviews concerning these correlations are given by Bruxelmane, (1976), Midoux and Charpentier (1979), Dickey (1979) and Joshi et al. (1982). Relations according to the dimensional analysis are of the form (Clark and Vermeulen, 1964; Zlokarmik, 1973; Nagata, 1975; Hassan and Robinson, 1977; Luong and Voleskey, 1979):

$$\frac{P_g}{P_u} = f\left(Re, Fr, We, Fl\right) \tag{3.42}$$

(2) Non-dimensionless empirical correlations:

The Michel and Miller (1962) correlation is the most well known and frequently applied non-dimensionless empirical correlation. This has the following form:

$$P_g = k_1\left(\frac{N_p{}^2 N d^3}{Q_g{}^{0.56}}\right)^{0.45} \tag{3.43}$$

As pointed out by Nienow et al. (1977) this relation correlates in essence N^3d^5 against N^7D^{13} which will always result in an exponent of approximately 0.45, making the correlation of doubtful value.

(3) Relations based on the Gas Flow Number:

Relations belonging to the third group contain only the Gas Flow Number, *Fl*, as a dependent variable:

$$\frac{P_g}{P_u} = f\left(Fl\right) \tag{3.44}$$

Relations of this type have been presented by Kalinske (1955), Oyama and Endch (1955), and Calderbank (1958). However, also this way of correlating the data is insufficient to characterize the whole parameter field which can be expected in view of impeller hydrodynamics and scale effects criteria.

Thus approach based on dimensionless criteria has been adopted (Equation 3.45). Weber number (*We*) is not an important factor as this study used water as operating fluid. As *X* is the combined form of *Re* and *Fr*, Equation 3.42 can be written as:

$$\frac{P_g}{P_u} = f\left(X, Fl\right) \tag{3.45}$$

Equation 3.45 can be extended by incorporating the dimensional kinematic parameters as:

$$\frac{P_g}{P_u} = f\left(d/D, C/D, X, Fl\right) \tag{3.46}$$

So, by including *d/D* and keeping other geometrical parameters constant, P_g/P_u is predicted for each *C/D* by the following relation:

$$\frac{P_g}{P_u} = \alpha Fl^{\beta}\left(\frac{d}{D}\right)^{\gamma}(X)^{\delta} \tag{3.47}$$

Figure 3.32 and Table 3.11 shows the parity plot of the developed design criteria and its statistical details of Equation 3.47.

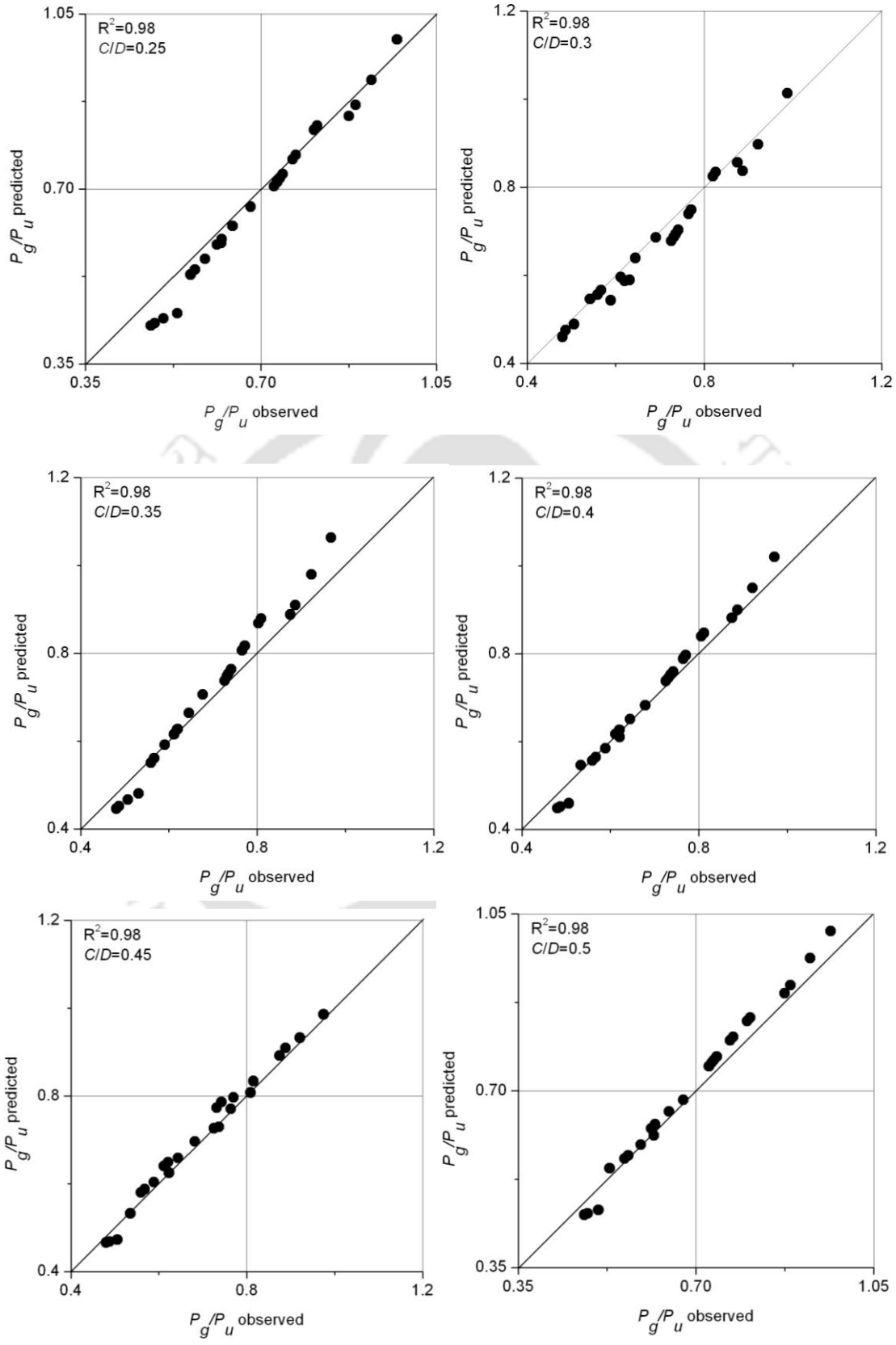

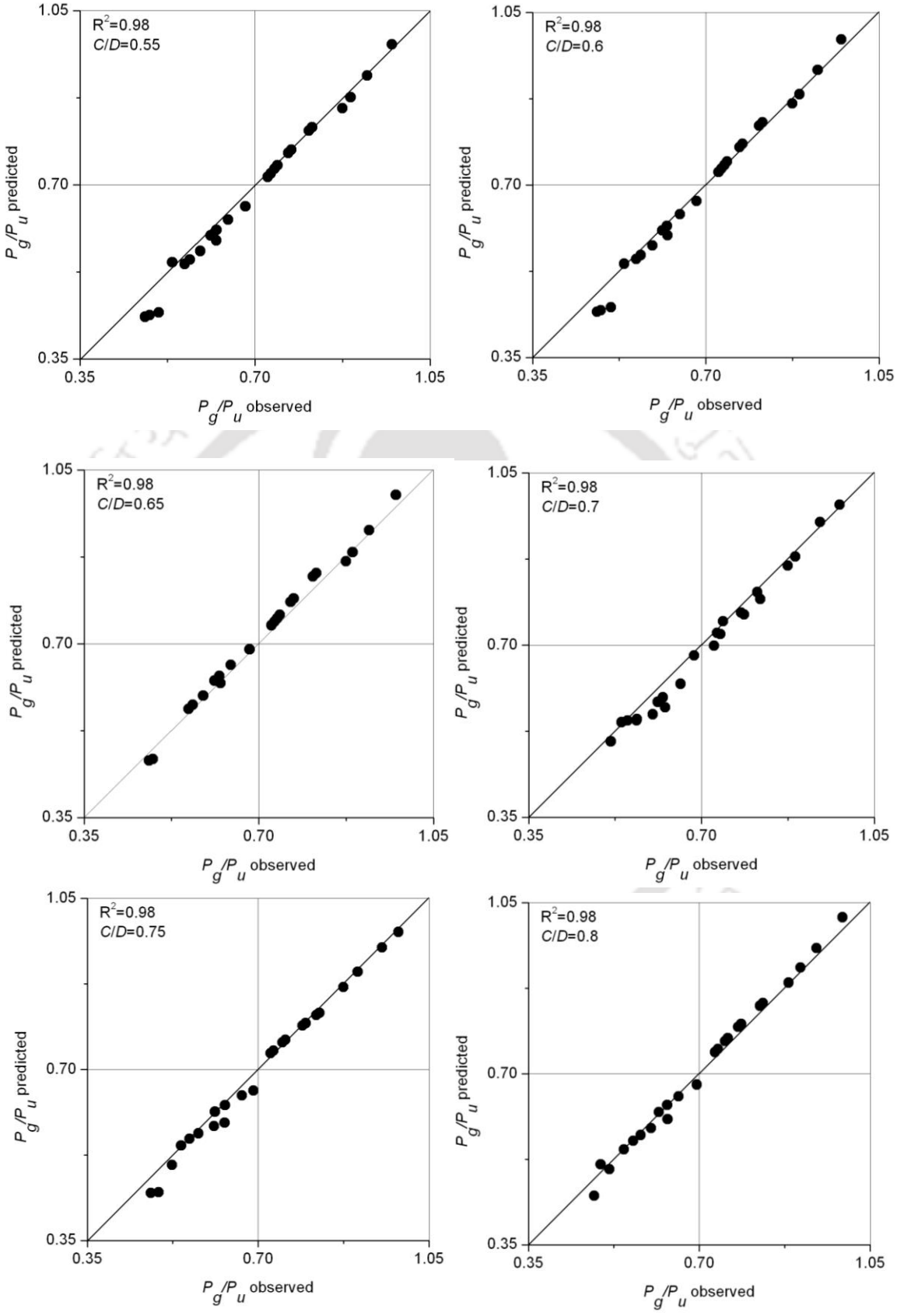

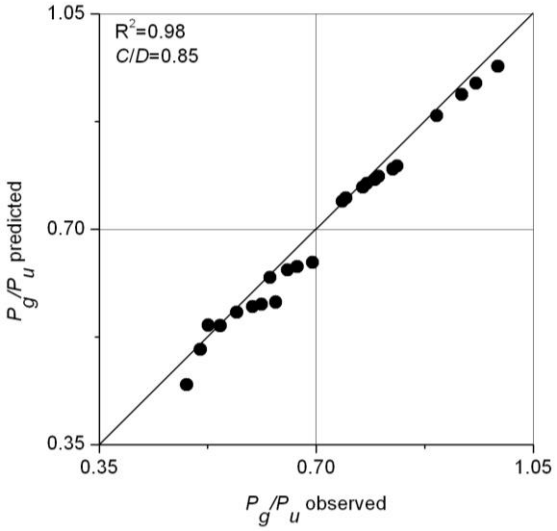

Figure 3.32: Predicted and observed P_g/P_u at each C/D

Table 3.11: Statistical details of Equation 3.47 for different C/D

C/D	α	β	γ	δ	**Overall std. error**
0.25	0.15 (2.16e-2)	-0.29 (3.36e-2)	-0.031 (1.91e-2)	0.1 (2.09e-2)	9.74e-3
0.3	0.11 (1.55e-2	-0.321 (4.73e-2)	-0.02 (2.24e-2)	0.124 (3.05e-2)	1.42e-2
0.35	0.12 (1.19e-2)	-0.31 (4.60e-2)	-0.048 (2.62e-2)	0.15 (2.86e-2)	1.33e-2
0.4	0.105 (5.35e-2)	-0.34 (0.061)	-0.01 (0.03)	0.13 (0.039)	0.019
0.45	0.11 (1.35e-2)	-0.36 (5.84e-2)	-0.006 (2.77e-2)	0.133 (3.78e-2)	1.76e-2
0.5	0.15 (2.05e-2)	-0.34 (6.03e-2)	-0.005 (2.86e-2)	0.11 (3.9e-2)	1.82e-2
0.55	0.11 (2.85e-2)	-0.36 (5.11e-2)	-0.01 (2.91e-2)	0.11 (3.19e-2)	1.48e-2
0.6	0.12 (3.25e-2)	-0.33 (1.02e-2)	-0.015 (4.45e-2)	0.1 (6.56e-2)	2.91e-2
0.65	0.13 (4.21e-2)	-0.39 (0.087)	-0.007 (0.033)	0.12 (0.057)	1.72e-2
0.7	0.135 (1.34e-2)	-0.35 (0.085)	-0.012 (0.039)	0.11 (0.055)	2.54e-2
0.75	0.12 (1.53e-2)	-0.32 (0.062)	-0.015 (0.031)	0.14 (0.039)	1.95e-2
0.8	0.11 (4.13e-2)	-0.34 (6.25e-2)	-0.014 (2.96E-02)	0.122 (4.04e-2)	1.88e-2
0.85	0.14 (4.2e-2)	-0.33 (5.34e-2)	-0.012 (3.04e-2)	0.1 (3.33e-2)	1.55e-2

Overall generalized relationship, P_g/P_u can be predicted by including both *d/D* and *C/D*; and representing Equation 3.47 as:

$$\frac{P_g}{P_u} = \alpha Fl^{\beta}\left(\frac{d}{D}\right)^{\gamma}\left(\frac{C}{D}\right)^{\delta}(X)^{\eta} \tag{3.48}$$

The statistical detail of Equation 3.48 is given in Table 3.12 and overall predicted P_g/P_u is shown in Figure 3.33. The R^2 and overall standard error are found to be satisfactory.

Table 3.12: Value of constants of Equation 3.48

α	***β***	***γ***	***Δ***	***η***	**Std. error**
0.1 (6.07e-3)	-0.33 (1.79e-3)	-0.0032 (1.03e-3)	-0.031 (4.12e-3)	0.11 (5.08e-3)	1.21e-2

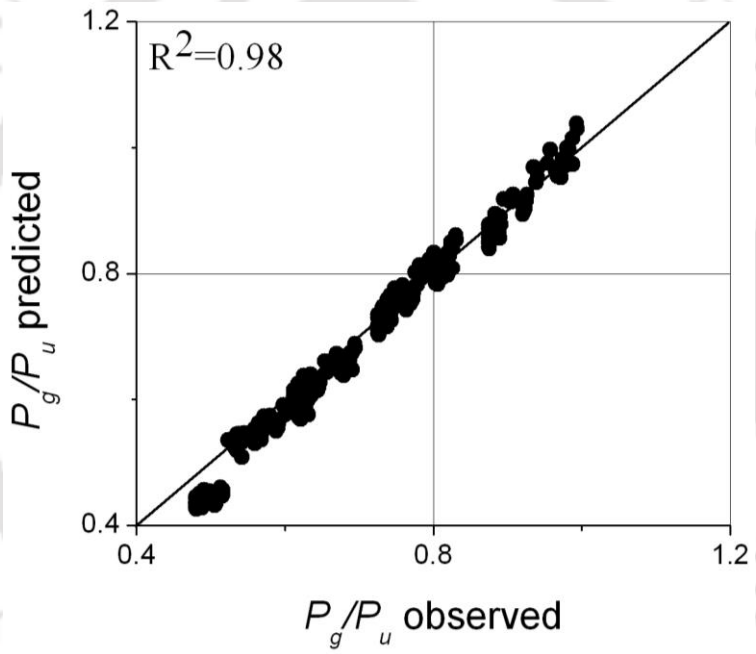

Figure 3.33: Generalized scale up criteria for P_g/P_u

3.4.3. Gas hold up

Gas holdup is an important hydrodynamic parameter and is a basic measure of gas-liquid contacting in mechanically agitated tanks. Gas hold up is also influenced by several variables of geometrical and operational parameters .Thus a study of gas holdup is important for scaling up and design of stirred tank reactors.

3.4.3.1. Effect of impeller clearance depth *(C)*

Several researchers report the overall gas holdup measurements (Pandit and Joshi, 1982; Patwardhan and Joshi, 1999) and found that as the impeller speed is increased the overall gas

holdup increased. The overall holdup also increases with increase in gas flow rate. The influence of *C/D* on ε_G (%) with *N* at constant *d/D* is shown in Figure 3.34. ε_G increases with increasing *N* and ε_G also decreases with increasing impeller clearance depth when *N* and *d/D* is constant. Maximum ε_G gives at *C/D* of 0.25 & 0.3 and minimum at *C/D* of 0.85. Higher impeller speed gives higher gas hold up.

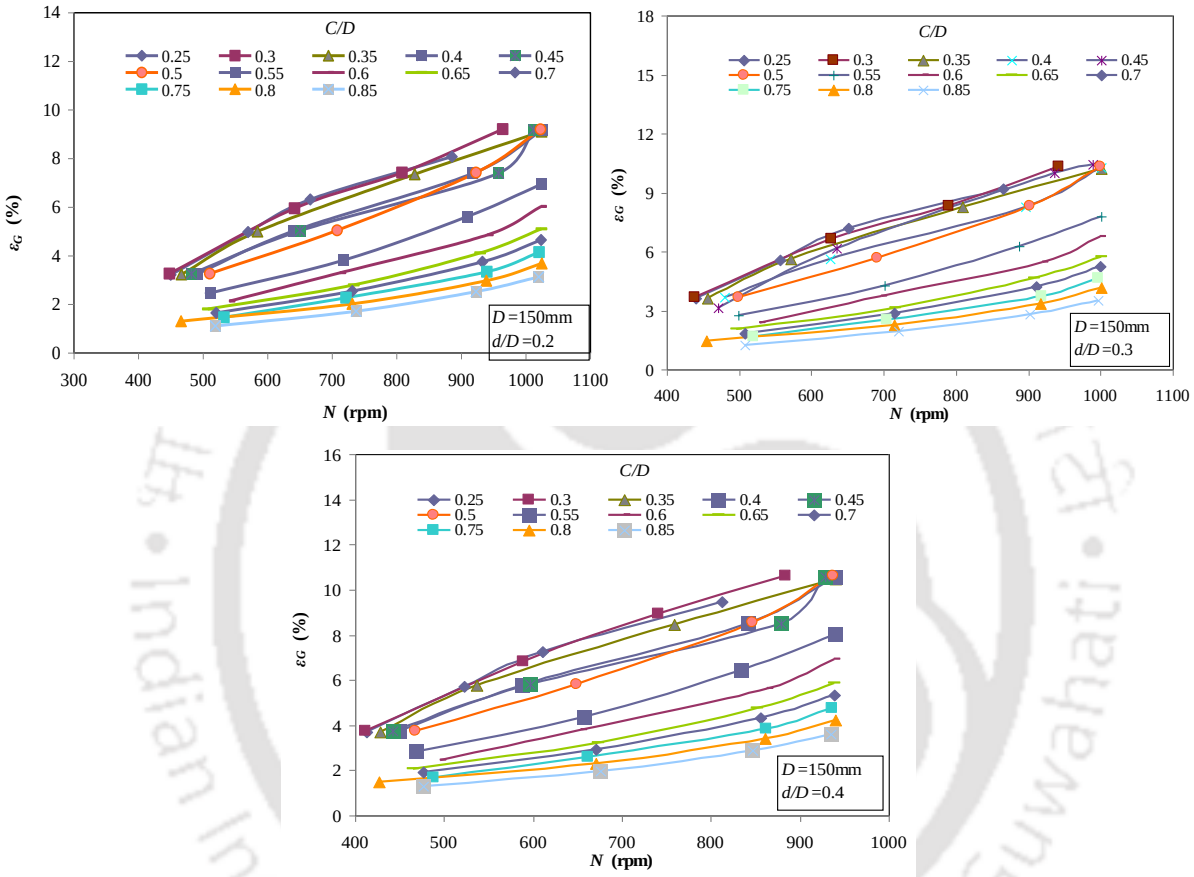

Figure 3.34: Comparison of ε_G (%) with *N* for different *C/D*

3.4.3.2. Effect of impeller diameter *(d)*

The effect of *d* on gas hold up with different *N* at a particular *C/D* is shown in Figure 3.35. Bigger impeller diameter gives higher gas hold up when tank diameter and impeller speed are constant. Such kind of observation was also achieved by Zhengming et al.(1996).

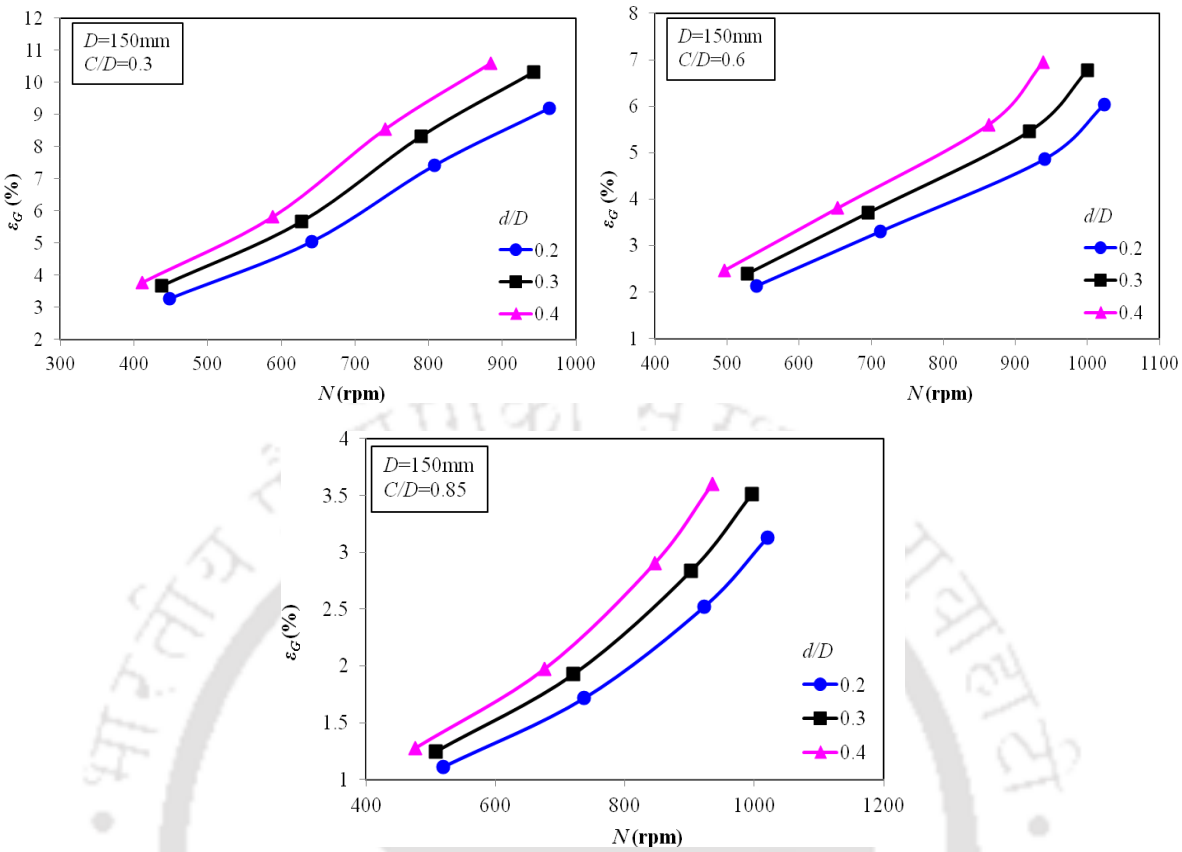

Figure 3.35: Comparison of ε_G (%) with N for different d/D

3.4.3.3. Design criteria for gas hold up

Gas hold up is a function of the impeller power consumption, superficial gas velocity and geometric parameters such as impeller to diameter ratio (d/D) and impeller clearance (Moucha et al., 2003) and is expressed as:

$$\varepsilon_G = f\left(d, D, C, P/V, v_g\right) \tag{3.49}$$

Thus for a sparged stirred tank system, Equation 3.49 can be reduced to the following dimensional form as:

$$\varepsilon_G = f\left(\frac{d}{D}, \frac{C}{D}, P_v, Fl\right) \tag{3.50}$$

Where, $P_v = \dfrac{P_g}{V\gamma(g\upsilon)^{1/3}}$ is the actual power per unit volume and is the non-dimensional form of effective power per unit volume. In the absence of optimal geometrical similarity condition, statistical relationship has been developed for each impeller clearance. As

suggested by the Equation 3.50, the functional form for each impeller clearance is now written as:

$$\varepsilon_G = f\left(\frac{d}{D}, P_v, Fl\right) \tag{3.51}$$

The experimental observations on different impeller clearance with other relevant parameters as shown in the Equation 3.51 have been used to derive the functional form. Non-linear regression analysis with pre-determined power function has been applied to the experimental observations. The power function is used as below:

$$\varepsilon_G = \alpha Fl^{\beta}\left(\frac{d}{D}\right)^{\gamma} P_v^{\delta} \tag{3.52}$$

Figure 3.36 shows the regression analysis of the developed and experimental values of gas holdup for each impeller clearance depth and Table 3.13 gives the statistical details of Equation 3.52. The acceptable value of the correlation coefficients shows the goodness of the fit and standard error are also in acceptable range for engineering design.

Table 3.13: Statistical details of Equation 3.52

C/D	***α***	***β***	***γ***	***Δ***	**Overall std. error**
0.25	2.82 (2.26e-2)	0.024 (1.25e-2)	0.0049 (3.33e-2)	0.89 (9.6e-2)	1.964e-2
0.3	2.48 (1.93e-2	0.025 (1.5e-2)	0.004 (3.68e-2)	0.85 (2.13e-2)	2.015e-3
0.35	2.18 (1.12e-2)	0.022 (5.7e-2)	0.0035 (2.24e-2)	0.81 (9.67e-2)	1.358e-2
0.4	2.08 (5.35e-2)	0.025 (1.09e-2)	0.0045 (2.41e-2)	0.8 (9.63e-2)	1.567e-2
0.45	2.12 (1.35e-2)	0.024 (1.19e-2)	0.004 (3.41e-2)	0.82 (9.63e-2)	1.135e-2
0.5	2.14 (4.05e-2)	0.025 (1.99e-2)	0.0039 (2.21e-2)	0.83 (9.81e-2)	1.013e-1
0.55	2.18 (2.85e-2)	0.026 (1.79e-2)	0.0037 (1.21e-2)	0.84 (9.12e-2)	1.608e-2
0.6	1.28 (4.25e-2)	0.015 (6.38e-3)	0.0055 (1.93e-2)	0.76 (8.2e-2)	1.264e-2
0.65	1.22 (4.11e-2)	0.014 (8.13e-3)	0.005 (2.35e-2)	0.75 (8.51e-2)	1.342e-2
0.7	1.02	0.012	0.0041	0.74	1.715e-2

	(6.34e-2)	(1.33e-2)	(3.31e-2)	(8.62e-2)	
0.75	0.98 (3.83e-2)	0.012 (6.62e-2)	0.004 (3.83e-2)	0.7 (7.0e-2)	1.221e-2
0.8	0.88 (8.13e-2)	0.011 (1.48e-2)	0.0035 (3.58e-2)	0.7 (8.2e-2)	1.324e-2
0.85	0.68 (6.2e-2)	0.012 (1.55e-2)	0.003 (2.94e-2)	0.68 (7.21e-2)	1.461e-2

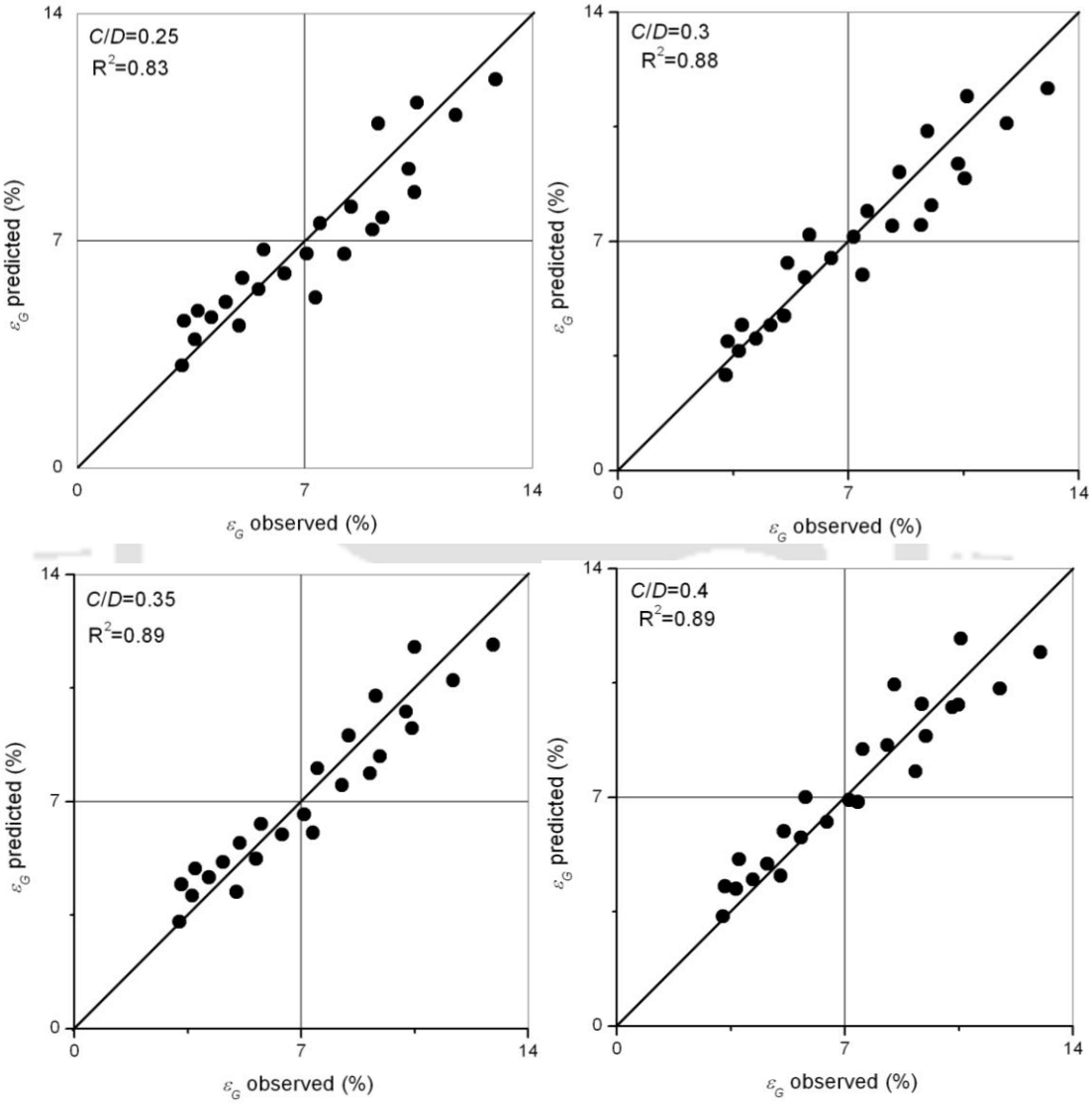

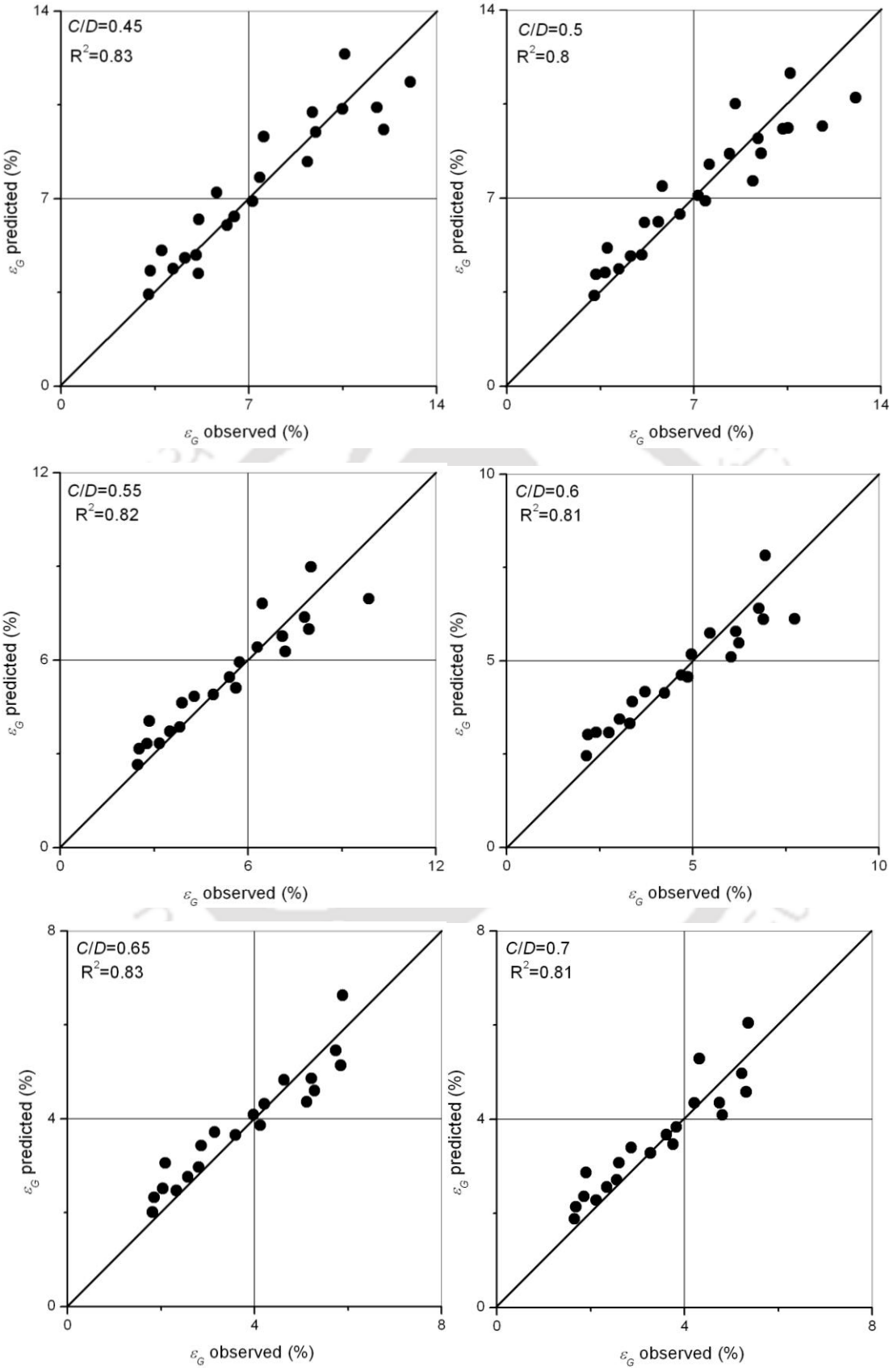

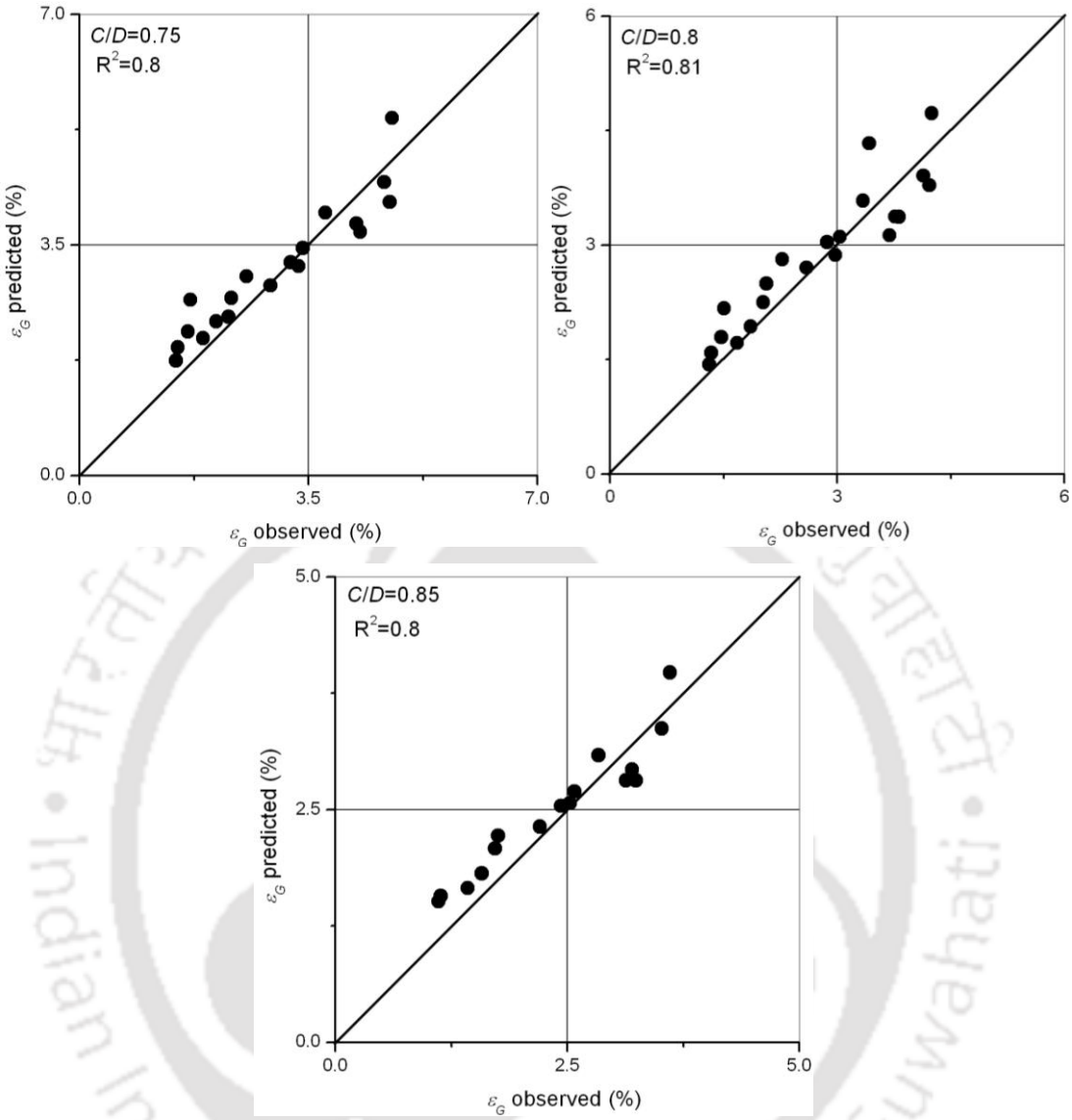

Figure 3.36: Observed and predicted ε_G (%) for different *C/D*

As similar in the case of mass transfer rate and power consumption, the predicted and observed gas hold up at each *C/D* is well acceptable (Figure 3.36). This indicates that an overall generalized relationship can be established (as shown in Figure 3.37) by including *C/D* of the former relationship as:

$$\varepsilon_G = \alpha Fl^{\beta}\left(\frac{d}{D}\right)^{\gamma} P_v^{\delta}\left(\frac{C}{D}\right)^{\eta} \tag{3.53}$$

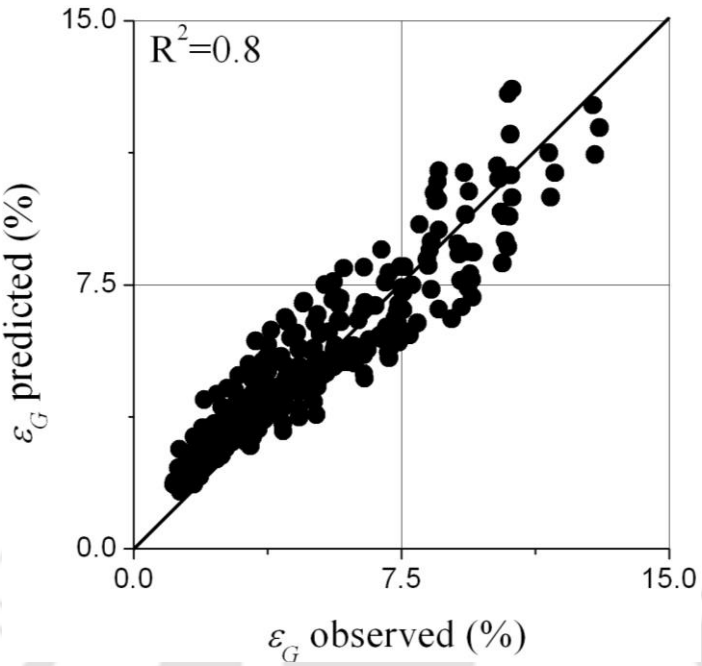

Figure 3.37: Observed and predicted ε_G (%) for generalized scale up criteria

The values are: α=0.66, β=0.02, γ=0.004, δ=0.75 and η =-1.45 with overall standard error is 2.04e-3. Figure 3.37 gives the predicted ε_G for the generalized scale up criteria for gas hold up. R^2 and standard error are found satisfactory.

3.4.4. Comparative studies

The concave blade type impeller of unbaffled system is compared with Rushton impeller and baffled system in terms of mass transfer rate and power consumption.

(a) With Rushton

Comparison of concave blade impeller system with Rushton impeller is shown in Figure 3.38 for *d/D* of 0.3 (*d*=45mm) and *C/D* of 0.3, 0.6 & 0.9. Higher K_La_{20} is observed by concave blade type impeller than the Rushton impeller at all the conditions of *C/D* at specific impeller speed. Higher power is consumed by Rushton than the concave blade type when same of amount of K_La_{20} is to be achieved.

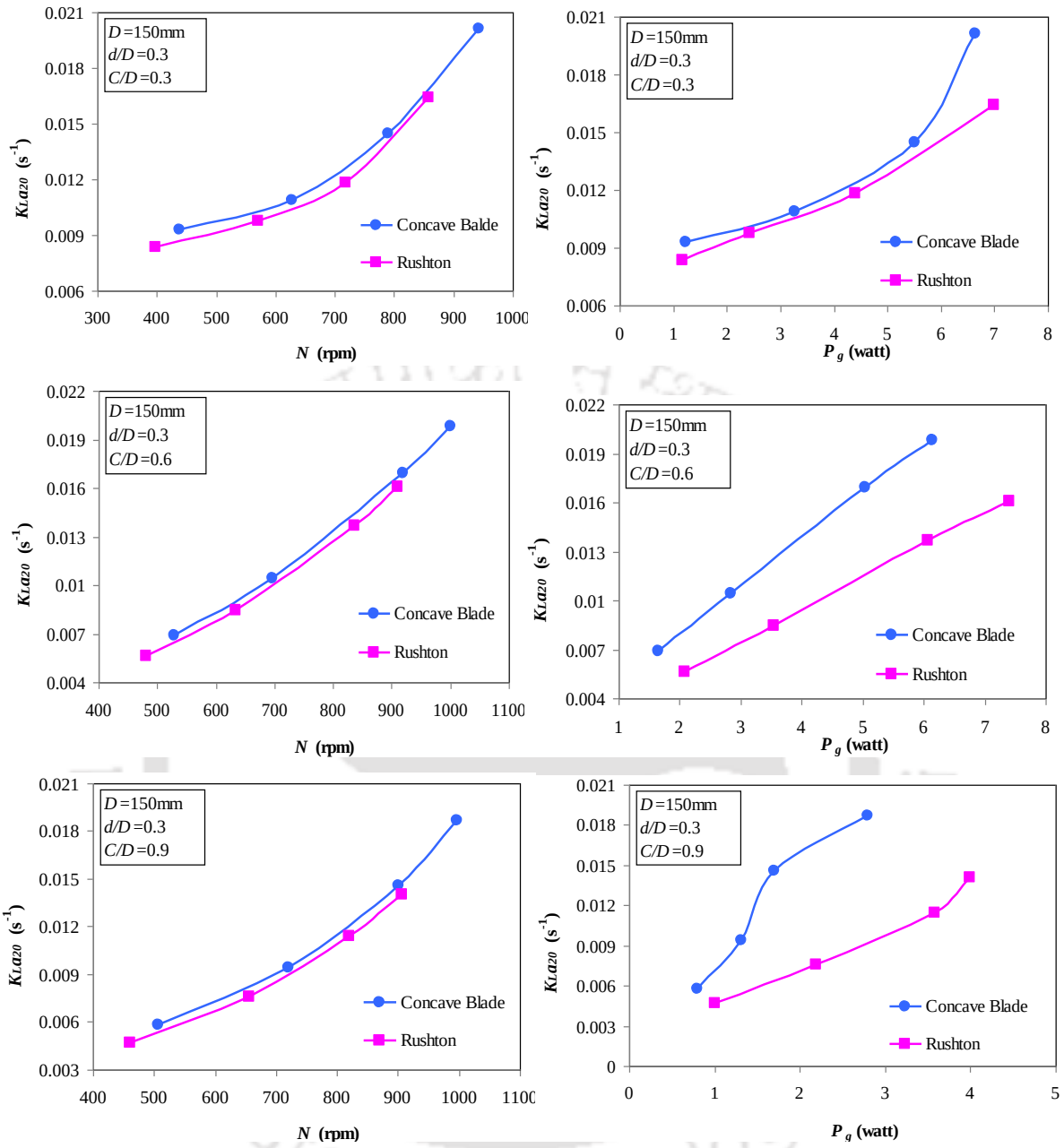

Figure 3.38: Comparison with Rushton impeller in terms of K_La_{20}

After understanding the behavior of mass transfer rate and power consumption in the two system of different impeller type, it can be concluded that concave blade type gives better performance than the Rushton impeller system.

(b) With Baffled Concave Balde

Unbaffled system is compared with baffled system in terms of K_La_{20} and P_g at constant d/D (0.3) for different C/D of 0.3, 0.6 & 0.9 in Figure 3.39. Baffled system gives higher K_La_{20}

and P_g. At a specific power consumption, higher mass transfer rate is produced by unbaffled system.

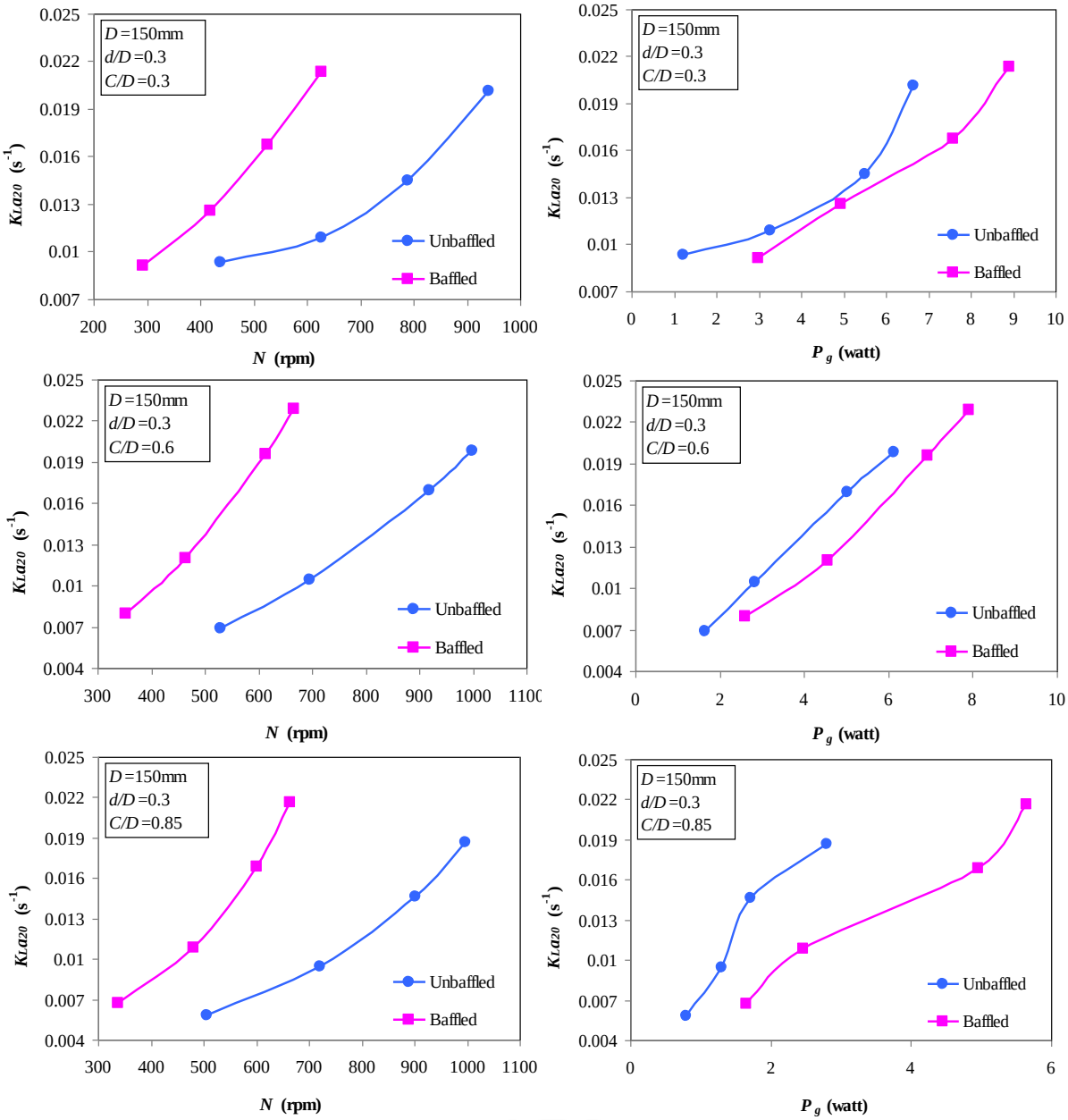

Figure 3.39: Comparison with baffled system for K_La_{20}

Even though baffled system gives higher mass transfer rate than the unbaffled system, it consumes significantly higher power than the unbaffled system.

3.4.5. Numerical modeling

Numerical modeling of the stirred tank in gas-liquid (sparged condition) was performed to predict the flow patterns of liquid phase and gas phase as well as gas volume fraction and

mass transfer coefficient. Prediction of gassed power consumption in the system represents the capability of the numerical techniques to predict accurately against the experimental observations.

The stirred tank of 150mm diameter with impeller diameter of 45mm is modeled for impeller clearance depth represented by *C/D* of 0.3, 0.4, 0.5, 0.6, 0.7 and 0.85. The impeller speed (*N*=500 rpm) is taken constant for all the analysis. The generated grid of the stirred tank is shown in Figure 3.40. The size of the grid and its sensitivities in results has already been discussed in Chapter 2.

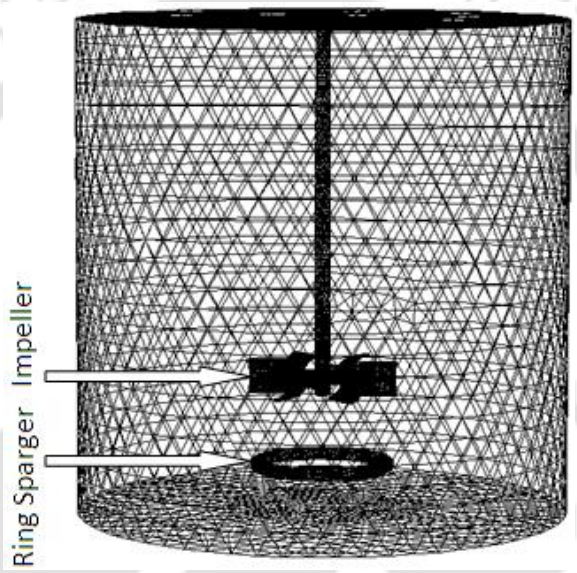

Figure 3.40: Grid of the tank

The boundary condition adopted in the sparged condition of stirred tank is more concerned than the single phase system. As the additional gas is supplied through ring sparger (details of ring sparger are given in Chapter 2) with gas flow rate (Q_g) of 1L/min, appropriate boundary condition is essential in order to represent the gassing system. Constant bubble diameter is used (d_b=2mm). Modified drag law is used to account the turbulence nature of flow in the vessel. Ring sparger is modeled as velocity inlet where the flow of gas is taking place from this source. The velocity of gas is represented by superficial gas velocity (v_g) and is calculated as per Panda (2011) (Detail in Chapter 2). Water velocity is taken as zero at ring sparger. The direction of gas flow is considered taking place only in axial direction. The fractional volume of gas is very important and its accurate assumption may lead to accurate

result. The gas volume fraction at the inlet of ring sparger is taken as 1 representing full gas inflow from the sparger and which is realistic. Another sensitive boundary condition is gas-liquid stirred tank modeling is on the top of the surface. Top surface is also modeled as degassing boundary condition where gas is allowed to out of the tank while water is remain inside the vessel.

3.4.5.1. Flow pattern and velocities

The flow paths of the two phases defined by the mean velocity vectors are the important hydrodynamics of the turbulent flow in the sparged condition. The comparison of liquid phase and gas phase is shown in Figure 3.41(a-e) for different impeller clearance depth. It seems that the effect of gas flow from the ring sparger could not make significant changes in the liquid flow generated mainly by the continuous movement of impeller. However, around the ring sparger, there is interruption of liquid flow circulation by the gas inflow from the sparger. In gas-liquid stirred tank, gassing system is used to disperse the gas into the vessel and impeller is for breaking down the gas bubbles into smaller one and mixes them over the entire vessel. As discussed by Azzopardi et al. (2011) about the different flow regimes in gas-liquid systems stating that in low gas flow number, the impeller would be able to disperse the gas in the vessel giving two regimes: loading and recirculation. In Figure 3.41, the liquid circulation loop (circulation loops are generally formed one each above and below the blade) is about to deform below the impeller blade due to the effect of gas inflow from ring sparger and this effect is higher when impeller clearance depth is near the vertical half of the tank (C/D=0.5 and 0.6) (especially when C/D=0.5, no liquid flow circulation loop is predicted because of the strong influence of gas inflow from ring sparger). When impeller clearance depth is lower (C/D=0.3 and 0.4), the flow of gas suddenly strikes on the lower part of impeller blade and quickly imparts in radial direction as a jet and joins the liquid flow path creating not too much interruption to the liquid flow circulation. When impeller clearance depth is higher, the lower liquid circulation loop does not get affected by gas inflow of sparger due to the long distance travel by the gas particles to strike on the impeller blade. Some few gas particles that strikes on the impeller blade get imparted and subsequently joins to the liquid flow circulation. Such type of flow circulation can be termed as loaded or recirculation flow as mentioned by Azzopardi et al. (2011). When loading and recirculation flow is occurred, the rate of gas flow and liquid flow velocity almost in balance

and they do not get too much influence on each other which yields in overall good mixing. In loading conditions, the size of the gas bubbles is much smaller than the characteristic impeller size and the bubbles have an approximately homogeneous distribution within the vessel (Paglianti et al., 2000). They said that in flooding condition, the size of the gas bubbles becomes larger and the gas phase becomes essentially localized within the impeller region. It is noteworthy to understand that the gas flow could not reach just above the impeller and bottom corner of the tank operating just like under almost single phase condition. This is may be because of the obstruction created by impeller blade; some amount of the gas flow which is flowing up straightaway diverts back and could not reach just above the impeller blade. However, some amounts of gas flow manage to go up and joins the free liquid surface. The bottom corner of the vessel is either dominant by liquid phase flow circulation or because of the axial flow of gas which is not re-circulating back after striking on impeller blade, the bottom corner of stirred tank is lack of gas phase. Such condition is because of the non influence by the liquid phase. In order to stabilize the flow variation of the two phases (flow stabilization is required for completely gas dispersion), one should control over either on impeller speed or gas flow rate.

(a) *C/D*=0.3 (b) *C/D*=0.4

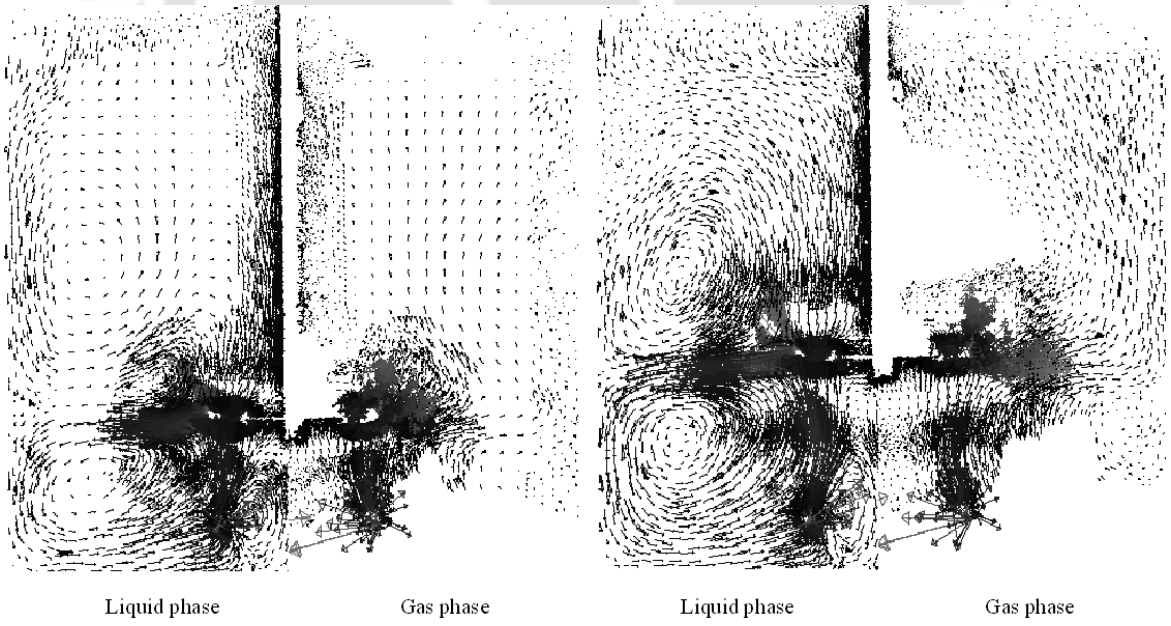

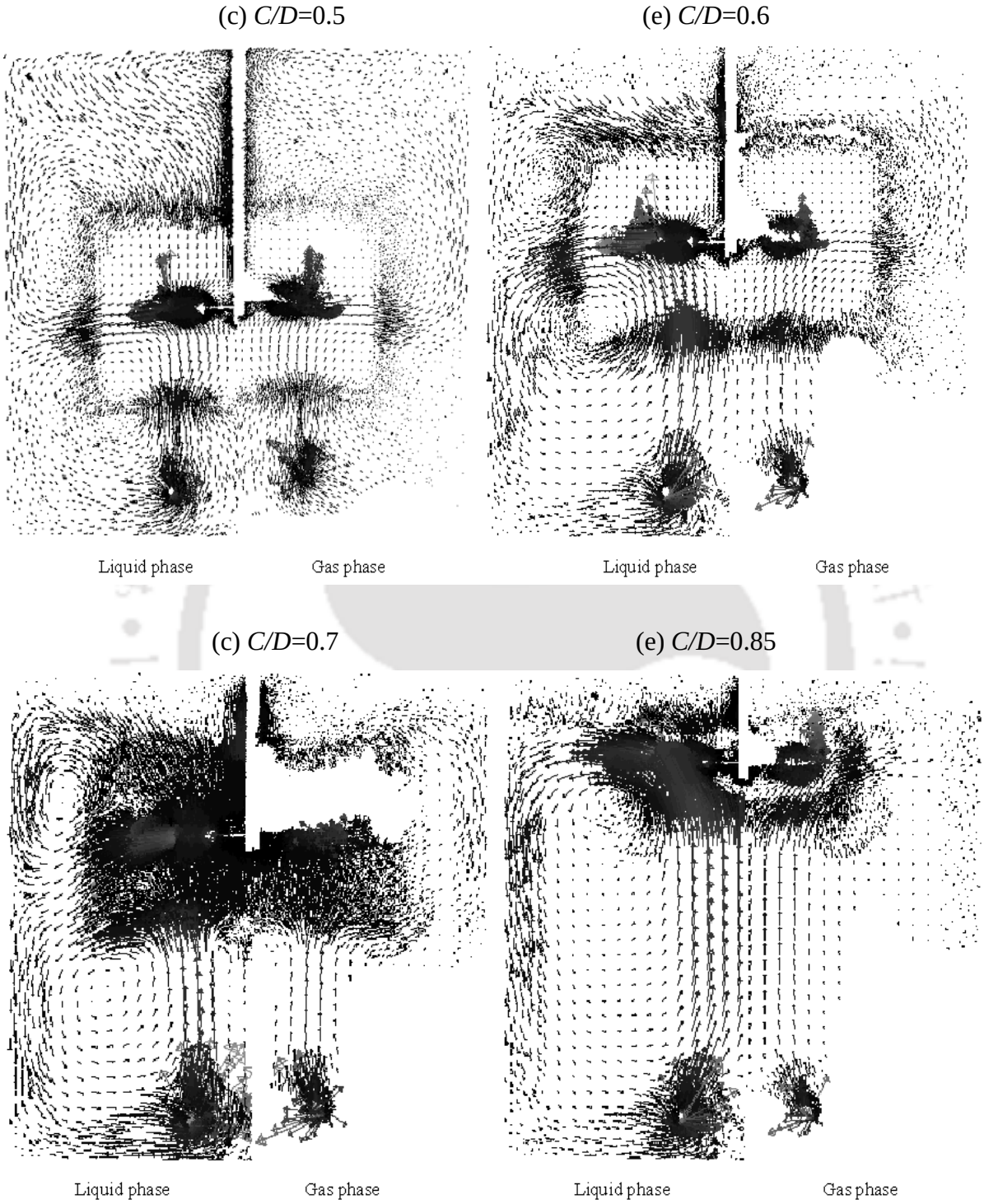

Figure 3.41: Flow patterns of the two phases

From the above flow patterns of liquid and gas phase, it is understood that complete gas dispersion take place near and around the impeller and ring sparger region. The stirring

impeller and ring sparger as source of gas equally contributes to enhance the mixing and eventually to provide better performance in gas-liquid stirred tank system.

As the flow in stirred vessel is turbulent, liquid flow in axial and radial direction represented by axial velocity and radial velocity respectively will be meaningful to understand. A comparison of axial and radial velocities for different impeller clearance depth is shown in Figure 3.42(a,b). These velocities are normalized by blade tip of the impeller ($u_{tip}=\pi Nd$). Normalized axial velocity (u/u_{tip}) at different *C/D* (Figure 3.42a) shows that the behavior of axial velocity, which acts with the same pattern when *C/D* is 0.3 & 0.4. Again *C/D* of 0.6, 0.7 & 0.85 follows same trend while *C/D* of 0.5 act differently from others. Magnitude of axial velocity is predicted higher upward ($0.4u_{tip}$) when radial distance is just away from the rotating shaft then goes down upto around $0.1u_{tip}$ by 0.3 & 0.4*C/D* and $-0.1u_{tip}$ for *C/D* of 0.6, 0.7 & 0.85 before the impeller region. At the impeller region, axial velocity is seen flatter from other regions of the vessel. In contrast to axial velocity, radial velocity is predicted having higher peak at the impeller region and decreases its peak when the radial distance moves towards the tank wall (Figure 3.42b).

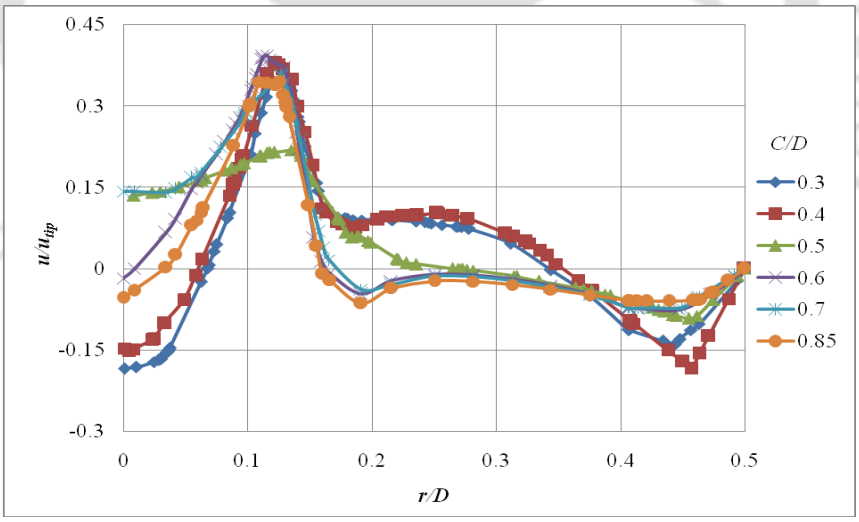

(a) Axial velocity

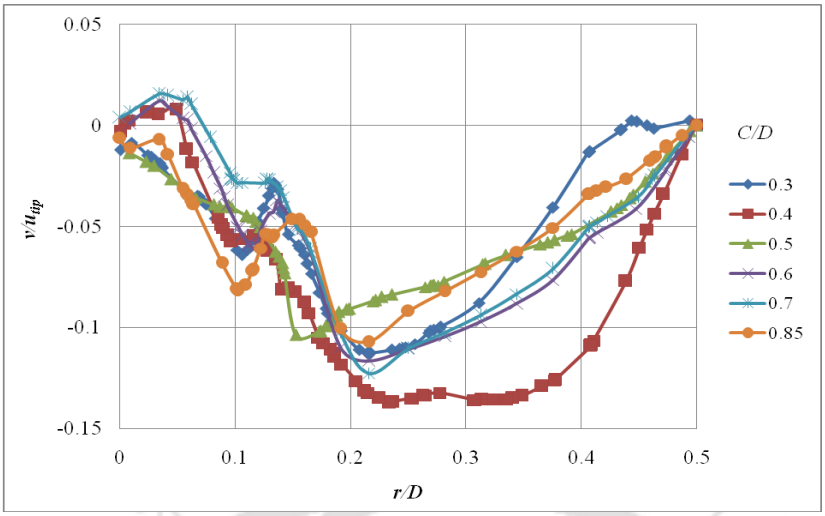

(b) Radial velocity

Figure 3.42: Comparison of liquid phase normalized (a) axial velocity (u/u_{tip}) and (b) radial velocity (v/u_{tip}) at different *C/D* when *z*=20mm from tank bottom

It can be seen from above figure that upto *C/D* of 0.5, the velocities did not follow same trend with impeller clearance depth and beyond *C/D* of 0.5, these velocities (axial and radial velocity) follow same trend i.e., increasing the impeller clearance depth, the velocity magnitude decreases. This may be because of the effect of gas inflow from sparger. When *C/D* is within 0.5, the liquid velocity produced by the rotation of impeller is able to get influenced in short period of time by gas inflow and the whole liquid velocity is affected and eventually could not act with the same way of higher impeller clearance depth (*C/D*=0.6 upwards). When *C/D* greater than 0.5, the liquid velocity from the movement of impeller has enough time to follow with their flow as interaction with gas inflow from sparger become weaker at this particular region (*z*=20mm) and eventually gives comparable pattern with increasing or decreasing impeller clearance depth.

3.4.5.2. Gas volume fraction

The predicted gas volume fraction for different *C/D* ratio is shown in Figure 3.43(a-f). Gas flow path flows upward then strikes the impeller blade and then deviates towards the tank wall then tries to maintain the upward flow pattern. Gas volume fraction is maximum above the ring sparger, around the impeller blade and on the top of free liquid surface. Gas volume fraction distribution varies with changes in impeller clearance depth. The maximum amount of accumulation of gas is predicted in between the impeller and ring sparger but this

phenomenon is seen negligible when *C/D* is low i.e., *C/D*=0.3 & 0.4. The most significant accumulation of gas in between impeller and sparger is predicted when *C/D*=0.85. The distribution of gas volume fraction is seen upward until the influence of liquid flow produced by movement of impeller is significant to interrupt the gas flow and even after deviation towards tank wall it tries to go up, but this case is not seen when *C/D* is 0.85. At this impeller clearance depth instead of going up, the gas flow comes down after striking the impeller blade tending to never going up.

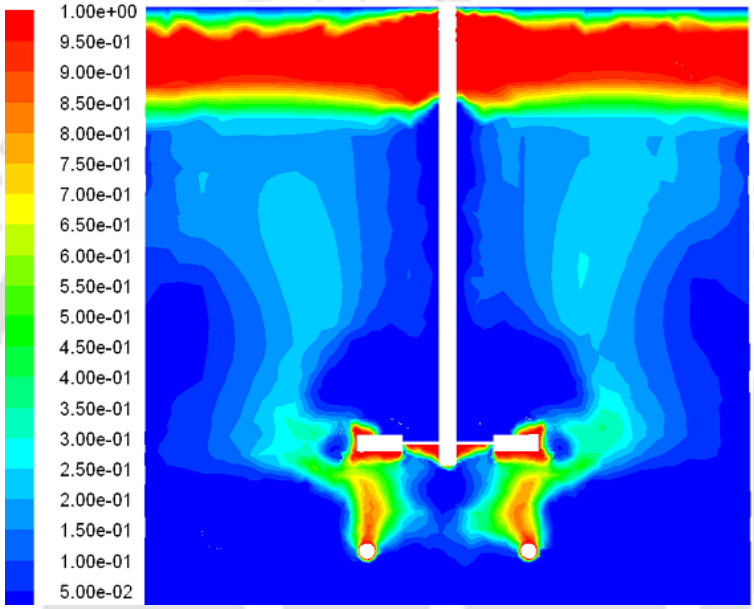

(a) *C/D*=0.3

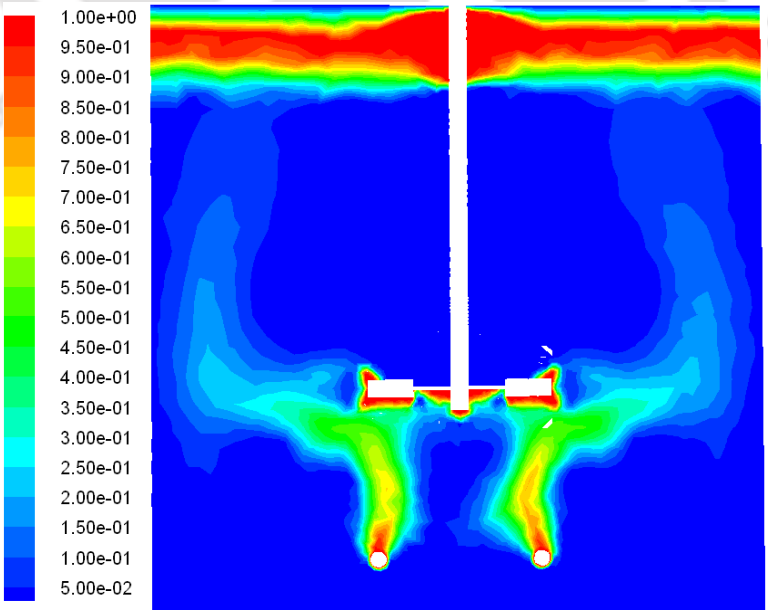

(b) *C/D*=0.4

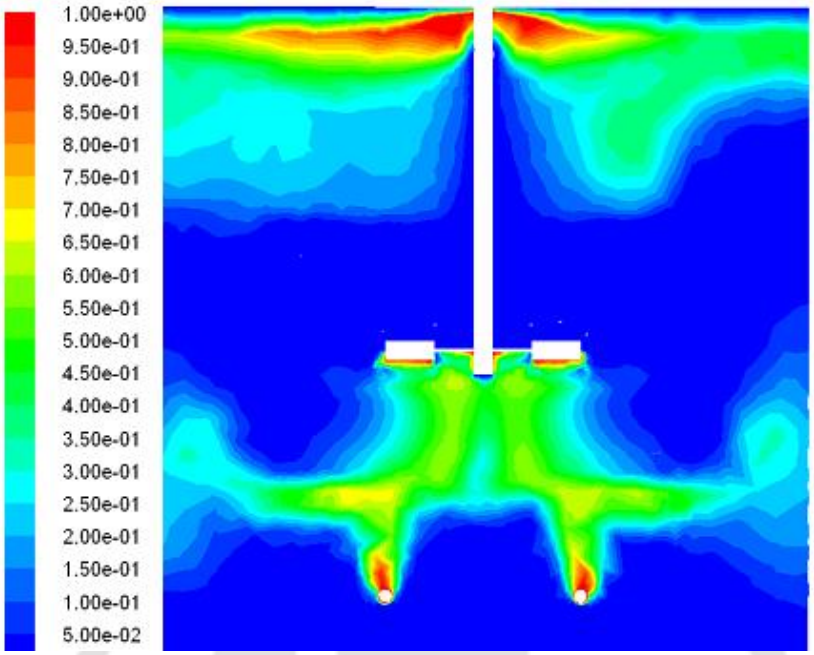

(c) *C/D*=0.5

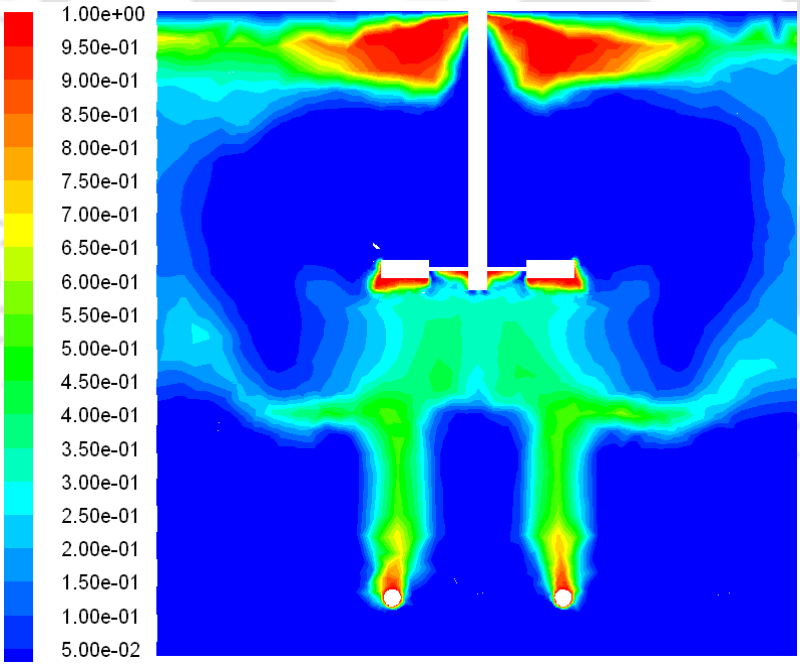

(d) *C/D*=0.6

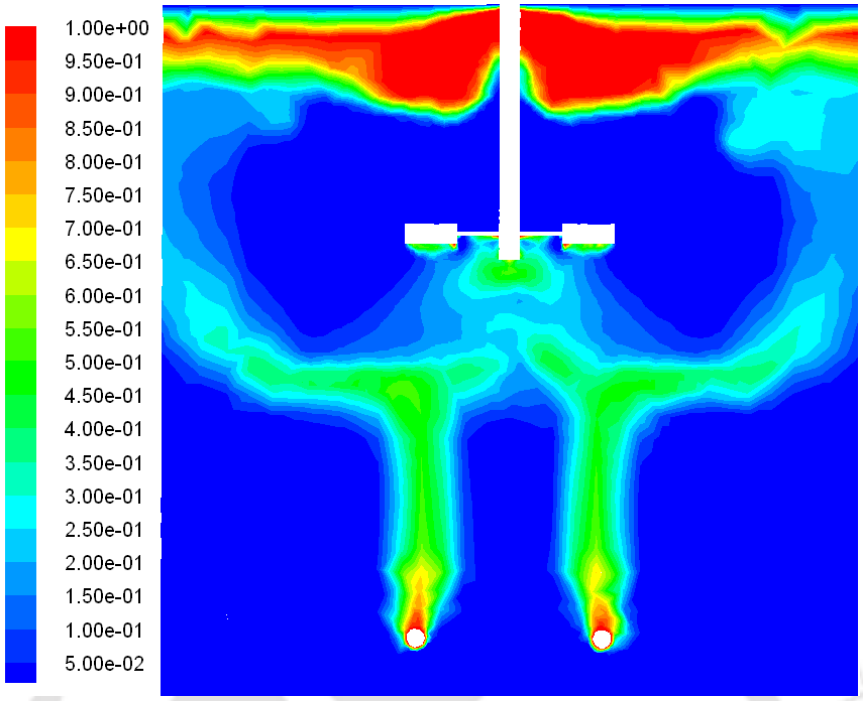

(e) *C/D*=0.7

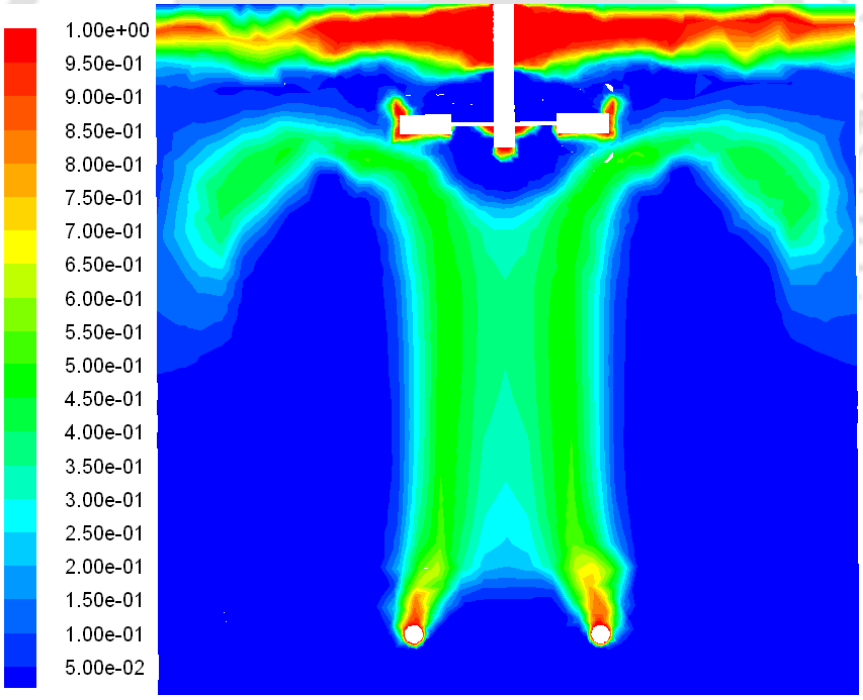

(f) *C/D*=0.85

Figure 3.43: Contours of gas volume fraction at different *C/D*

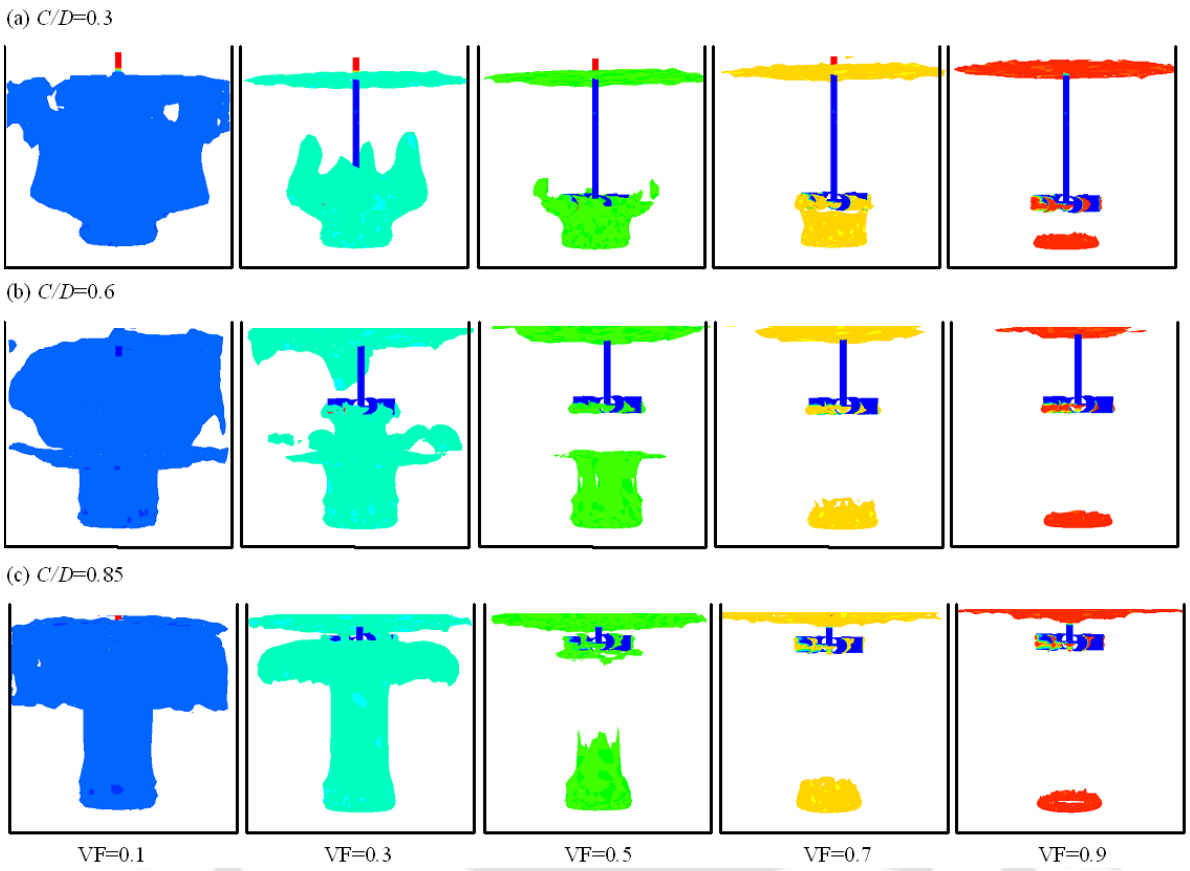

Figure 3.44: Distribution of different iso-value of gas volume fraction for (a) *C/D*=0.3 (b) *C/D*=0.6 and (c) *C/D*=0.85

Understanding of distribution of local gas volume fraction (VF) is directly associated with mass transfer rate in the system. In order to understand the distribution and accumulation of local gas volume fraction, Figure 3.44 shows gas volume fraction at its different iso-value of 0.1, 0.3, 0.5, 0.7 and 0.9. These iso-values give how the accumulation of gas volume fraction is taking place at specific regions of the vessel. From this figure, one can understand that lower value of gas volume fraction (VF=0.1 or 10%) is seen accumulated in almost all regions of the tank except at near the bottom corner and increasing the iso-value, the accumulation is seen shifting to near and around the impeller and sparger; and on top surface of the tank. Showing of gas volume fraction at different iso-value made distinction on its behavior of distribution and gives clear understanding of the evolution of its accumulation across the vessel. 90% of gas volume fraction is accumulated only at near the ring sparger and on the top surface where these regions are considered as source of gas inflow in the gas-

liquid system. The significant variation of distribution of gas volume fraction is predicted greater when iso-value (VF=0.1, 0.3) is low at different impeller clearance depth (*C/D*=0.3, 0.5 and 0.9) than when the iso-value (VF=0.5 to 0.9) is high.

3.4.5.3. Mass transfer coefficient

Danckwerts (1951) model is used to model the K_La_{20}. The distribution of predicted K_La_{20} is shown in Figure 3.45(a-f) for different *C/D* when is constant (*N*=500rpm). Maximum amount of K_La_{20} is occurred near and around the impeller and ring sparger; but just above the impeller blade and bottom corner of the tank the distribution of K_La_{20} is predicted in significantly very less amount. Maximum amount of K_La_{20} is also predicted on the top free liquid surface of the tank.

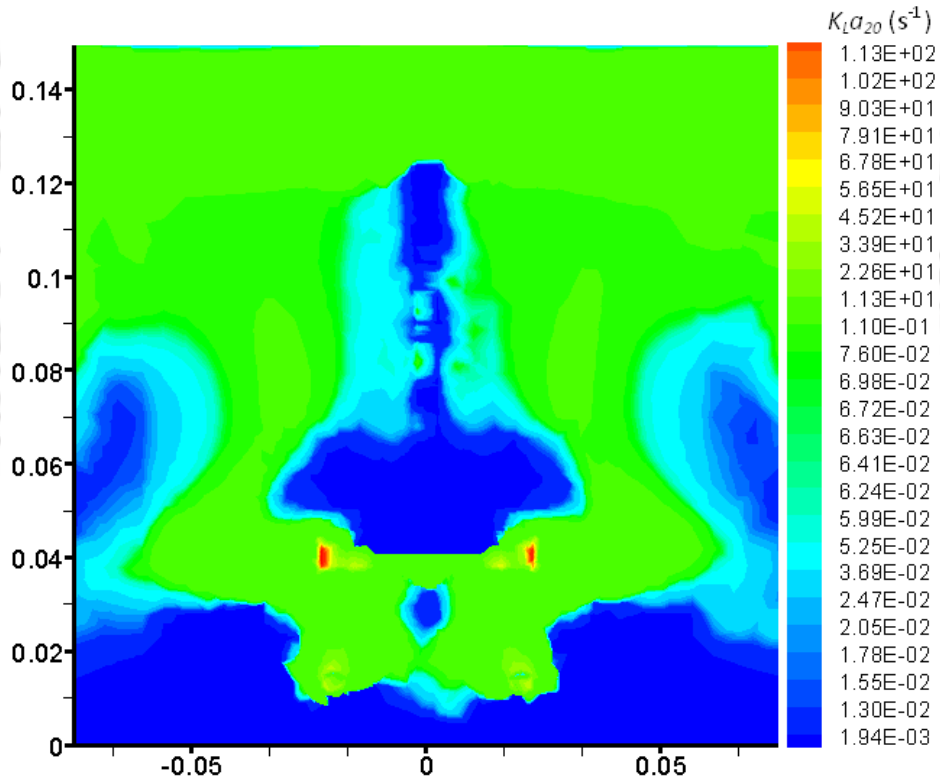

(a) *C/D*=0.3

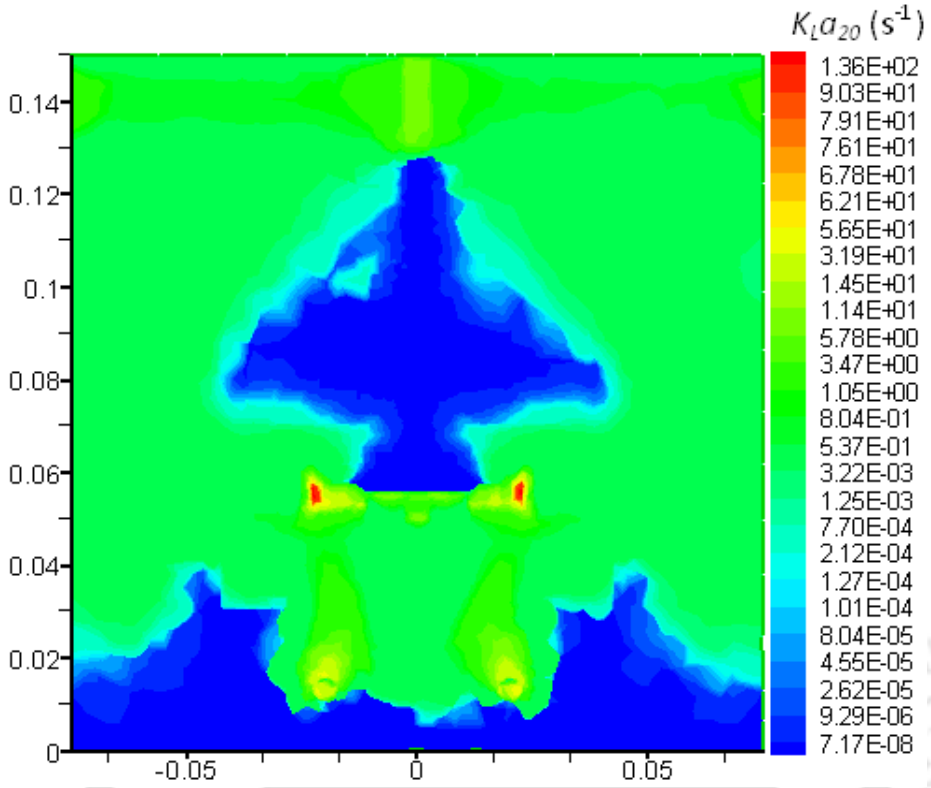

(b) *C/D*=0.4

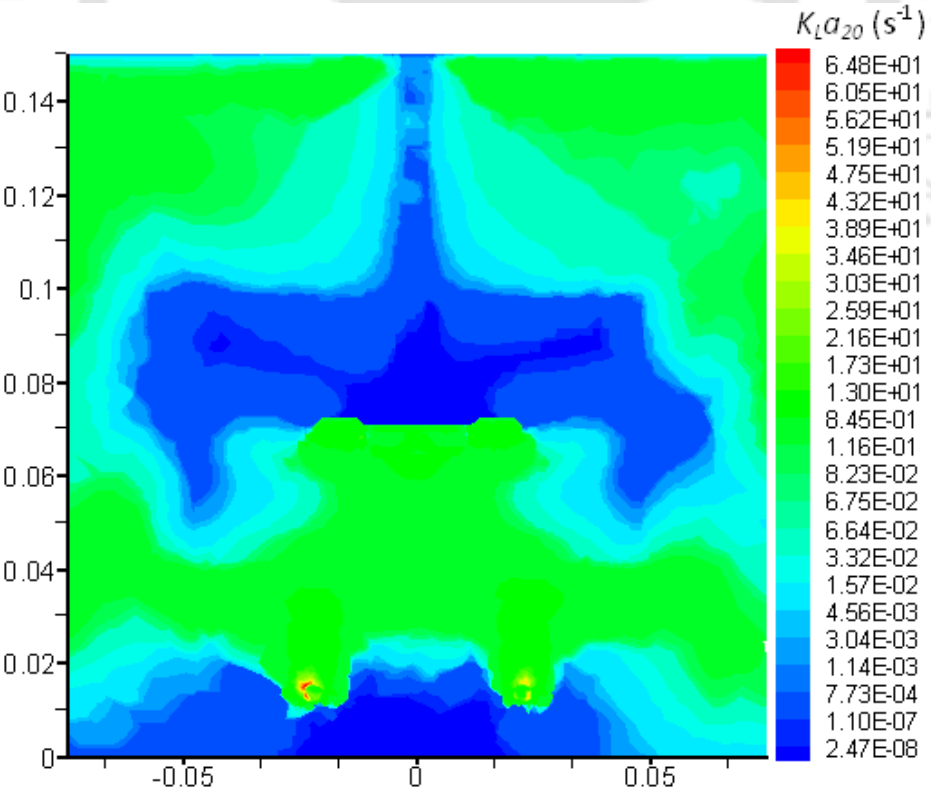

(c) *C/D*=0.5

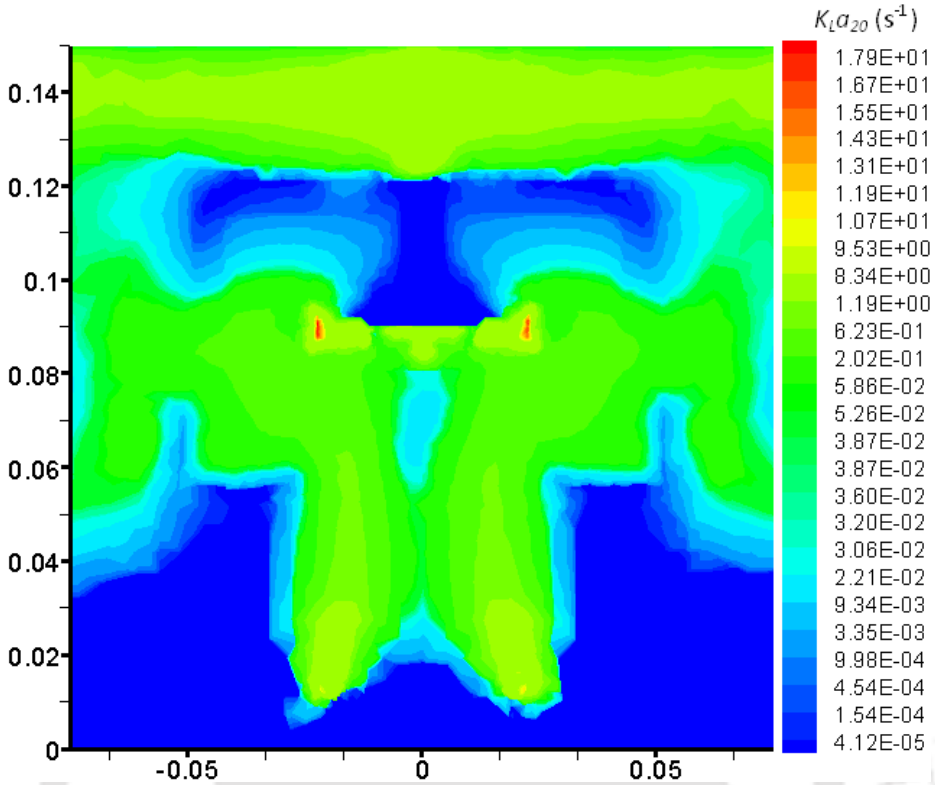

(d) *C/D*=0.6

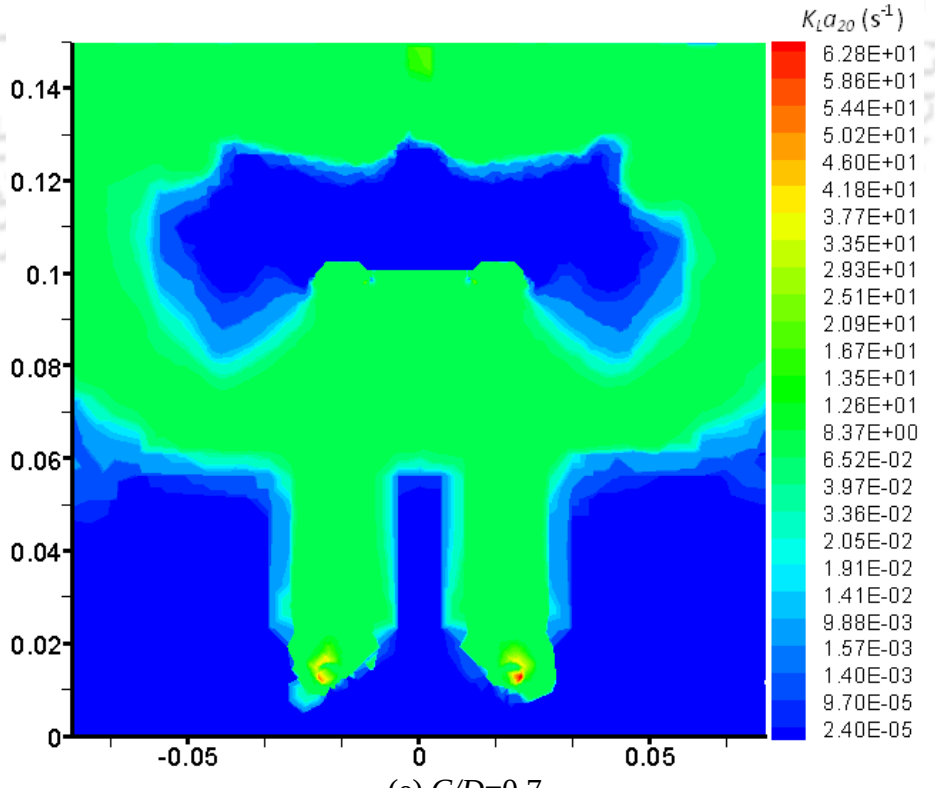

(e) *C/D*=0.7

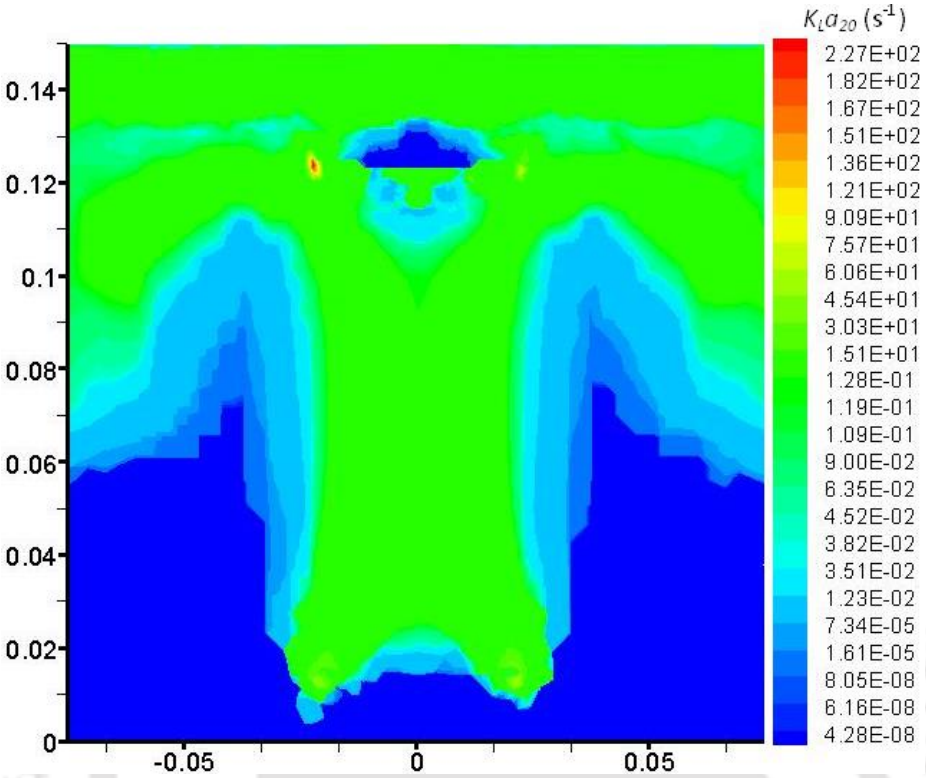

(f) *C/D*=0.85

Figure 3.45: Distribution of predicted K_La_{20} for different *C/D*

The local distribution of K_La_{20} at different impeller clearance depth shown in above Figure 3.45 cannot give overall comparison of K_La_{20} at these impeller clearances. So, in order to make comparison of the overall predicted volume averaged K_La_{20} with experimental result, Table 3.14 shows the comparative result.

Table 3.14: Comparison of predicted K_La_{20} and P_g with observed results

C/D	K_La_{20}		P_g	
	Expt.	**CFD**	**Expt.**	**CFD**
0.3	0.0089	0.0077	1.68	1.95
0.4	0.0083	0.0074	1.63	1.93
0.5	0.0079	0.0068	1.61	1.91
0.6	0.0059	0.0049	1.47	1.86
0.7	0.0047	0.0041	1.41	1.78
0.85	0.0043	0.0038	1.13	1.57

Gassed power consumption (P_g) is also predicted and compared with experimental result as given in the Table 3.14. K_La_{20} is found under-predicted and reason may be by several factors as mass transfer itself is a very complex mechanism involving various phase interaction. One reason may be of considering constant bubble diameter, selection of numerical parameters,

choosing of drag coefficient method, etc. Gassed power consumption is slightly over-predicted. Predicted value (K_La_{20} and P_g) follows the same trend with observed results.

3.4.6. Conclusions

The hydrodynamics involved in gas-liquid stirred tank of concave blade unbaffled system have been studied experimentally. The strong influence of impeller clearance depth and impeller diameter on mass transfer rate, power consumption and gas hold up was observed. Experimental observations were performed at various range of impeller speed (N=400 to 1000rpm), impeller diameter (expressed by d/D=0.2, 0.3 and 0.4), impeller clearance depth (expressed by C/D=0.25 to 0.85 with 0.05 interval) with tank diameter of 150 and 200mm in order to understand these hydrodynamics in detail. These parameters were observed increases with increasing impeller speed. Mass transfer coefficient increases with decrease in C/D when d and N are constant; and it is also increased when diameter of impeller is bigger at constant C/D and N. Gassed power consumption decreases with increasing impeller clearance depth and consumes higher power by bigger impeller diameter when the respective geometrical parameters are constant. Gas hold up also decreases with increasing impeller clearance depth and with increasing impeller diameter. Maximum percentage of gas hold up observed was around 15% and minimum as around 1% in the system.

Scale up criteria for these hydrodynamics was also developed in order to get a simulation relationship for any geometrically similar system. Gas flow rate was varied from 1 to 5 L/min.

The scale up criteria for mass transfer rate for each C/D is expressed as: $10^5 k_c = \alpha\left(\frac{d}{D}\right)^{\beta}(X)^{\gamma}(Fl)^{\delta}$ with range of α=2.25 to 8.54, β=0.678 to 1.25, γ=0.32 to 0.543 and δ=0.015 to 0.02. Overall scale up criteria including the influence of impeller clearance, impeller diameter, tank diameter, impeller speed and gas flow rate is developed as: $10^5 k_c = 2.36\left(\frac{d}{D}\right)^{1.14}(X)^{0.41}(Fl)^{0.02}\left(\frac{C}{D}\right)^{-0.031}$. The scale up criteria for power consumption expressed as a ratio of gassed to ungassed power input is developed for each C/D as:

$\frac{P_g}{P_u} = \alpha\left(Fl\right)^{\beta}\left(\frac{d}{D}\right)^{\gamma}(X)^{\delta}$; range of α=0.11 to 0.14, β=-0.29 to -0.39, γ=-0.007 to -0.048, δ=0.1-0.15 and the overall as: $\frac{P_g}{P_u} = 0.1Fl^{-0.33}\left(\frac{d}{D}\right)^{-0.003}\left(\frac{C}{D}\right)^{-0.031}(X)^{0.11}$. For gas hold up at each *C/D* is developed as: $\varepsilon_G = \alpha Fl^{\beta}\left(\frac{d}{D}\right)^{\gamma}P_v^{\delta}$; with range of α=0.68 to 2.82, β=0.011 to 0.26, γ=0.003 to 0.005 and δ=0.68 to 0.89 and overall as: $\varepsilon_G = 0.66Fl^{0.02}\left(\frac{d}{D}\right)^{0.004}P_v^{0.75}\left(\frac{C}{D}\right)^{-1.45}$.

The comparison of the unbaffled concave blade system with baffled and Rushton impeller system found that higher mass transfer is produced by baffled system but consumes significant power than the unbaffled system. So, overall performance is found better by unbaffled system based on mass transfer rate and power consumption when the reduction of power consumption is a priority. Better mass transfer rate and lower power consumption is produced by concave blade system as compared with Rushton type impeller system. So, in order to achieve good mixing and lesser power consumption, concave blade type in unbaffled system can be adopted in the process of mixing.

Flow pattern defined by the vectors of the mean velocity for liquid and gas phase was modeled by using CFD techniques to get a clear idea of separate flow behavior possessed by these two phases. The liquid flow pattern was not significantly affected by the gas inflow from the sparger but when impeller is nearly at the vertically half of the tank (*C/D*=0.5 and 0.6), the liquid flow pattern is greatly affected. Gas flow could not disperse well just above the impeller blade and bottom corner of the tank; and operates just like single phase in this region. This study achieved loading and recirculation flow pattern indicating better mixing mechanism in the system. Gas volume fraction prediction indicates that maximum amount gas accumulation occurred near and around the impeller and ring sparger; and on the top liquid surface of the tank. Mass transfer coefficient and gassed power input were also predicted and found under-prediction in mass transfer coefficient and slight over-prediction in gassed power input.

CHAPTER 4

DESIGN OF UNBAFFLED STIRRED TANK WITH DUAL CONCAVE BLADE IMPELLER

4.1. Introduction

Dual impellers are more efficient than the single impeller as the flow pattern generated by dual impeller is stronger tending to increase mass transfer rate and swirling in nature than the flow pattern produced by single impeller. Many studies have been done on same combination of dual impeller systems with Rushton impeller (Bombac and Zun, 2000; Chunmei et al., 2008; Khopkar and Tanguy, 2008; Xinhong et al., 2008; Chiu et al., 2009; Zadghaffari et al., 2009; Taghavi et al., 2011). Some few studies based on different combination of dual impeller systems were also performed like by Bouaif and Roustan (2001); Jahoda et al. (2007); Woziwodzki and Jedrzejczak (2011) with Pitched blade and a standard Rushton impeller.

The influence of impeller spacing (impeller clearance depth, C_1 and spacing between the two impellers, C_2) is very important factor in dual impeller system as the strong flow circulation is happen to be near and around the impeller region. The height of liquid fill up (H) also plays important role in the hydrodynamics of stirred tanks. Garcia-Cortes et al. (2004) reported that the study of stirred tanks with $D<H$ is found extensively in literature (Abrardi et al., 1988; Hudcova et al., 1989; Roman and Gavrilescu, 1994; Yoshida et al., 2002; Chunmei et al., 2008) but very little of stirred tanks with $D=H$ (Kuboi and Nienow, 1982; Machon et al., 1997). Rutherford et al. (1996) studied with $D=H$ stirred tank of dual impeller and stated the strong dependence of impeller spacings on the generated flow. Similarly, several studies (Machon et al., 1988; Hudcova et al., 1989; Yoshida et al., 2002; Khopkar et al., 2008) reported the influence of impeller clearance depth and their spacing on the performance of stirred tank.

In this chapter dual impeller system of unbaffled concave blade stirred tank is being studied on single phase as well as in gas-liquid phase condition. The main objectives are to indentify

the efficient impeller positions and to develop a design criterion which can be applied in geometrically similar systems.

4.2. Experimental set up

In this study, experimental measurement of coefficient of mass transfer rate (K_La_{20}) and power consumption were performed in unbaffled stirred tank (D) of 150mm and 200mm with dual impeller. Impeller clearance depths (C_1) were varied from 0.15D to 0.85D with 0.05D interval and the range impeller spacing (C_2) were from 0.15D to 0.73D. Height of water (H) was maintained at constant height equal to tank diameter throughout the experiment (Rutherford et al., 1996; Micheletti et al., 2004; Garcia-Cortes et al., 2006; Suzukawa et al., 2006). A typical schematic diagram of an unbaffled stirred tank (with free vortex) with and without sparger is shown in Figure 4.1.

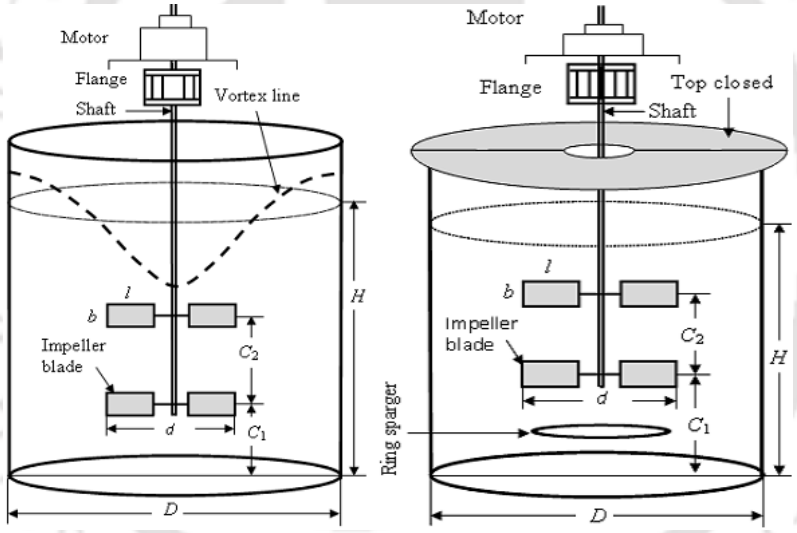

(a) Single phase system (b) Sparged system

Figure 4.1: Schematic diagram of an unbaffled stirred tank for (a) single phase system (b) sparged system

Table 4.1: Details of stirred tank geometry

	Tank dia. (D)	Impeller dia. (d)
Height of water (H)=D=150mm	150mm	30mm,45mm,60mm
Length of blade (l/d)=0.25	200mm	40mm,60mm,80mm
Width of blade (b/d)=0.2		
Number of blade (n)=6		
Thickness of blade (t)=1mm		
C_1=0.15D to 0.85D		
C_2=0.15D to 0.73D		

4.3. Single phase

In dual impeller system, there are three desirable flow pattern exist and are called as stable flow pattern according to the nature of the formation of trailing vortices. These three different fluid characteristics generated in case of dual Rushton impellers are defined as parallel, merging and diverging flow depending upon the off-bottom clearance of lower impeller (C_1), spacing between two impellers (C_2) and height of upper impeller from liquid surface (C_3) (Rutherford et al., 1996; Chunmei et al., 2008). These stable flow profiles are desirable in process industries to keep the system in stable otherwise the system may damage. In the industry reactor design, the values of operational parameter C_1, C_2 and C_3 were chosen to avoid the unstable flow patterns in the reactor, otherwise the shaft and impellers would wobble seriously and even rupture (Khopkar and Tanguy, 2008).

The formation of three stable patterns in dual Rushton impeller was studied by many researchers (Rutherford et al., 1996; Chunmei et al., 2008; Khopkar and Tanguy, 2008). The pattern of these flow patterns were clearly defined by Rutherford et al., 1996 and typical diagram is shown in Figure 4.2 which is taken from Khopkar and Tanguy (2008) when tank diameter is equal to liquid height ($D=H$). In parallel flow pattern the flow paths essentially act independently to each other producing its own upper and lower flow circulation loop (ring vortices) forming total four stable ring vortices (Figure 4.2a). In merging flow, the impeller streams follow an almost straight-line orientation toward one another, and merged at an elevation approximately midway between the impellers to form two large ring vortices (Figure 4.2b). In diverging flow, as a result of the low position of the lower Rushton impeller the impeller stream follows a path toward and impinges upon the base of the vessel (Figure 4.2c). So, the lower Rushton impeller can only produce one large ring vortex, while the upper Rushton impeller produced two well-defined ring vortices above and below the impeller disk.

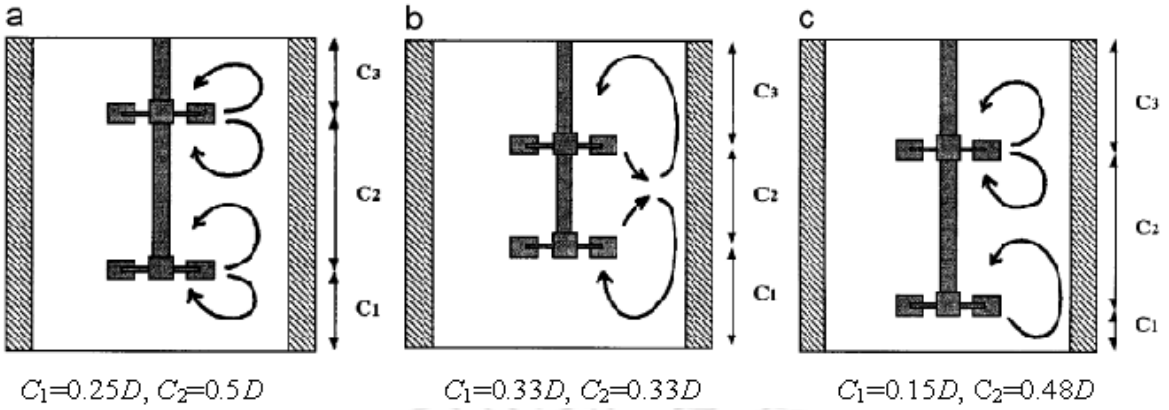

Figure 4.2: Stable flow patterns (Rutherford et al., 1996) (C_1+C_2+C_3=H=D) (a) parallel (b) merging and (c) diverging

Being a radial impeller, does concave blade impeller show a similar stable flow pattern at similar spacing based on Rushton impeller when H=D is being investigated in this present work. Generally stable profile has been investigated at H=D, thus the present work maintains the water depth equal to tank diameter to compare the variations in spacing between Rushton and Concave blade impeller if any.

The other objectives of this study are: (i) to find the local and global optimal impeller positions in terms of mass transfer rate (ii) to determine the critical radius and vortex depth and its effect on optimal points (iii) to measure power consumption and its relationship with mass transfer (iv) to compare the Concave blade impeller with standard impeller (Rushton) at global optimal point; and (v) to model the optimal (local and global) for characterizing the flow patterns.

4.3.1. Optimal *d* based on K_La_{20}

Experimental observations have been shown in the Figure 4.3. In order to find the optimum impeller diameter, three different sizes of d (=0.2D, 0.3D and 0.4D) were studied when the other geometrical dimensions are constant (D=H=150mm, C_1=C_2=0.2D, l=d/4, b=d/5). As shown in the Figure 4.3, the mass transfer coefficients were high at d/D=0.3.

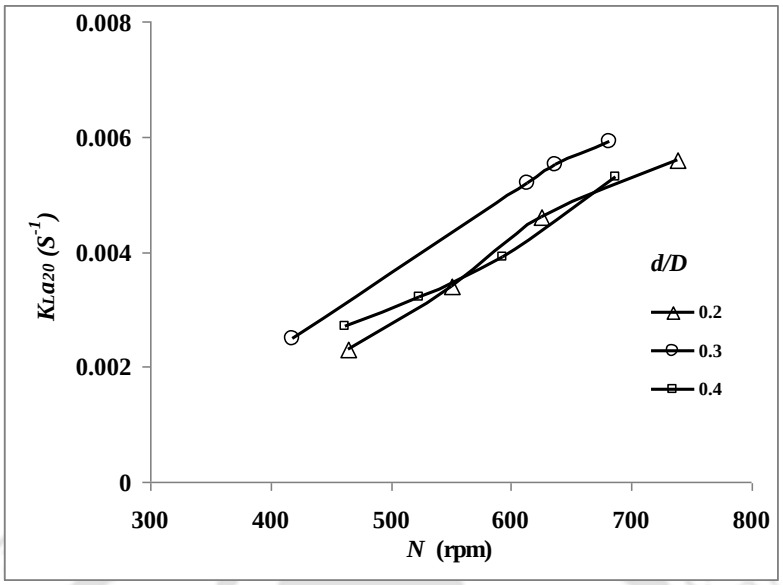

Figure 4.3:K_La_{20} for different *d/D* at various impeller speeds

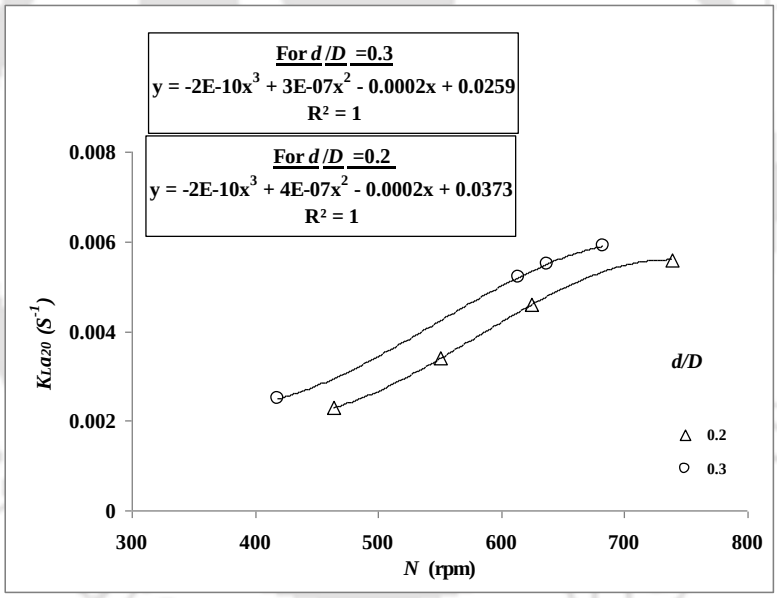

Figure 4.4: Fitting polynomial to the experimental data

However, in order to compare all *d*/*D* at the same speed, experimental observations were processed as: for each set of experiments, experimental data are fitted the best-fitted line (polynomial with maximum R^2) in excel as shown in the Figure 4.4. From there, considering line shows the actual variation; values of K_La_{20} are generated at desired speed for different sets of experiments.

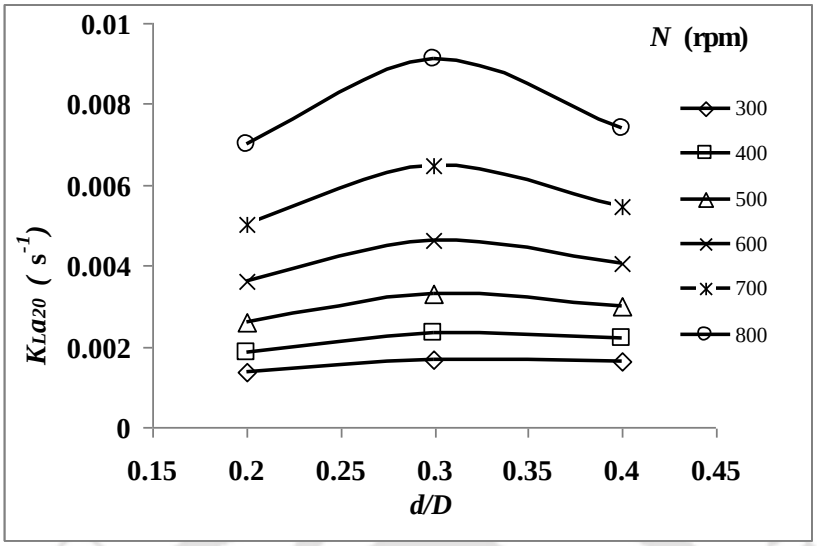

Figure 4.5: Variation of K_La_{20} with different d/D at C_1=C_2=0.2D

Now this will help in getting the trend at the same speed. By doing such an analysis for each and every set, processed and generated value of K_La_{20} has been plotted with rotational speed in Figure 4.5. Here, it should be mentioned that such processing or generation has been applied to the all experimental data with different conditions. Based on the observed K_La_{20} and plotted at different d/D, the optimum d is found at 0.3D Figure 4.5. By fixing optimal d/D, further experimentations have been done to indentify optimal C_1 and C_2.

4.3.2. Optimal C_1 and C_2 based on K_La_{20}

The selection of optimal configuration (lower impeller distance from tank bottom, C_1 and spacing between two impellers, C_2) in dual impeller stirred tank is obvious task to be performed during designing process apart from other geometrical parameters. It may greatly affect to the performance of stirred tanks if the configurations are not accurately selected. In this study, the first step to study dual impeller stirred tank was started from selecting the C_1 and C_2 configuration based on the experimentally measured coefficient of mass transfer rate as it is considered the most important parameter in stirred tank.

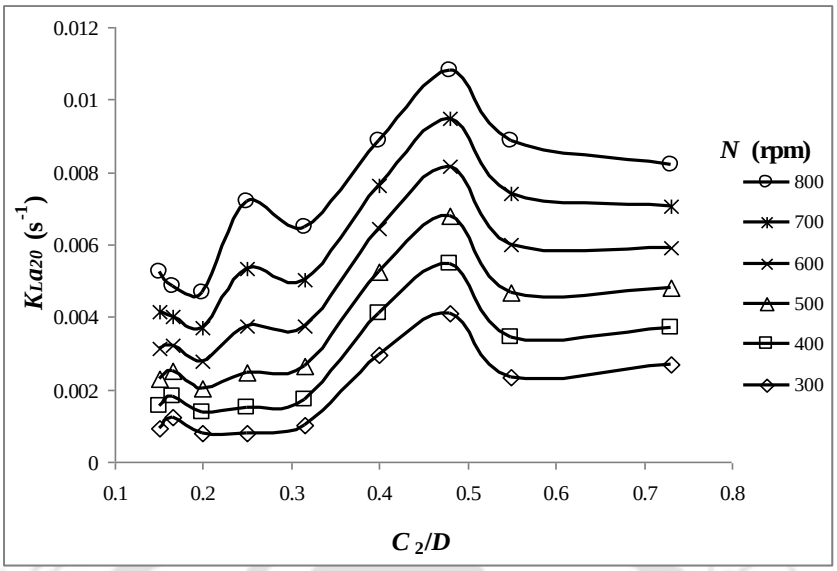

Figure 4.6: Variation of K_La_{20} with different C_2/D at C_1/D=0.15

Selection of C_1 and C_2 is achieved through uni-variant approach (fixing one variable while the other variable is changing). Initially C_1 has been fixed at 0.15D and C_2 is varied from 0.15D to 0.73D. The variation of measured K_La_{20} on different C_2 values while C_1 is fixed is shown in Figure 4.6. It shows that C_1=0.15D and C_2=0.48D gives maximum K_La_{20}.

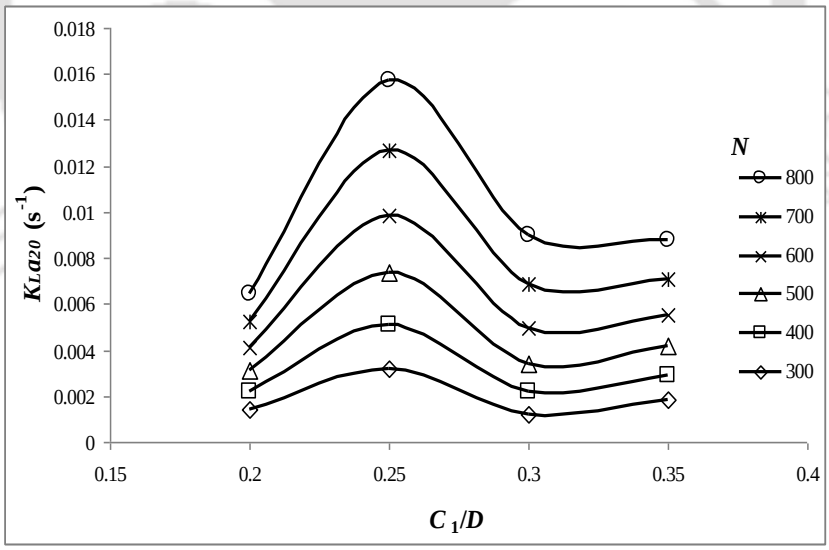

Figure 4.7: Variation of K_La_{20} with different C_1/D at S_2/D=0.63

Now by fixing C_2=0.48D, C_1 has been changed to different values. Fixing of C_2=0.48D means that upper impeller has been fixed at S_2=0.63D (S_2=C_1+C_2=0.15D+0.48D=0.63D). 0.63D is denoted by S_2 just to avoid ambiguity. The same process has been repeated with various C_1/D values in order to get C_2/D. Experimental observations (Figure 4.7) shows the

optimal point of C_1/D at 0.25. The value of C_2/D comes by subtracting C_1/D from S_2/D, which is 0.38. Figure 4.8 shows the variation of K_La_{20} with different C_2/D at constant C_1/D=0.2 and depicts that maximum K_La_{20} is observed at C_1=0.2D and C_2=0.48D.

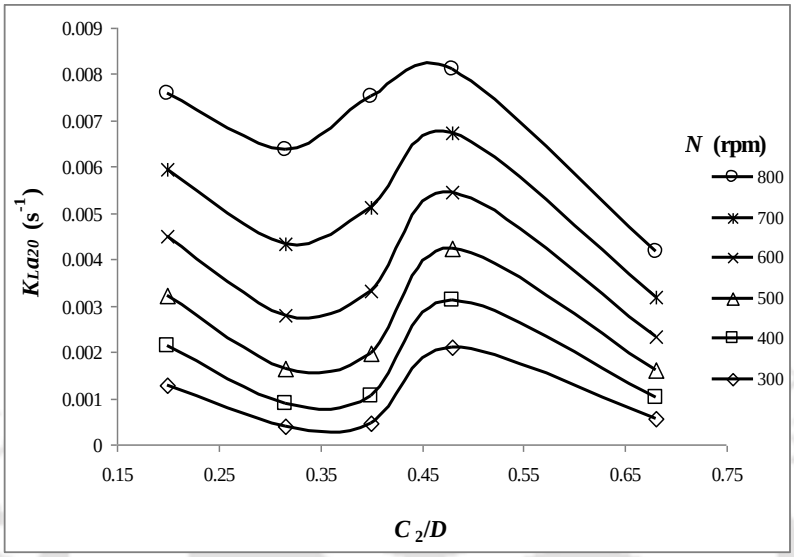

Figure 4.8: Variation of K_La_{20} with different C_2/D at C_1/D=0.2

Figure 4.9 shows the variation of K_La_{20} with different C_2/D at C_1/D of 0.3 and the C_2 optimal is observed at 0.38D.

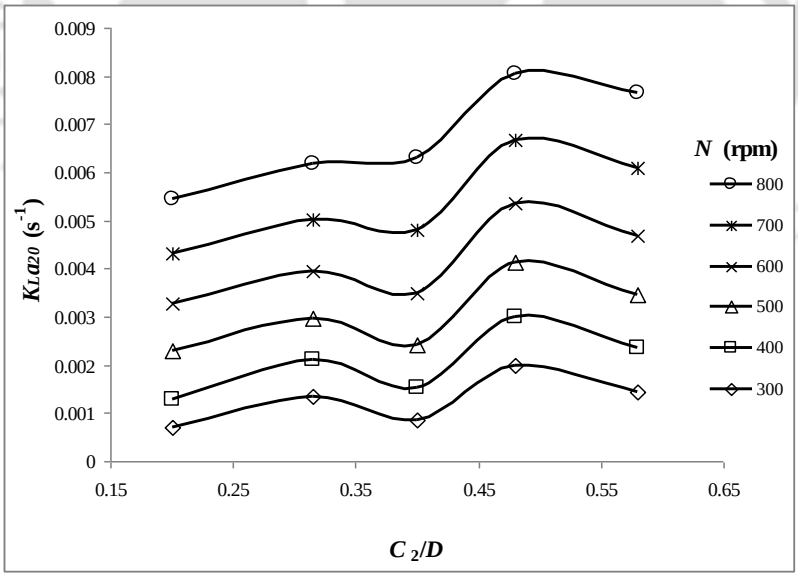

Figure 4.9: Variation of K_La_{20} with different C_2/D at C_1/D =0.3

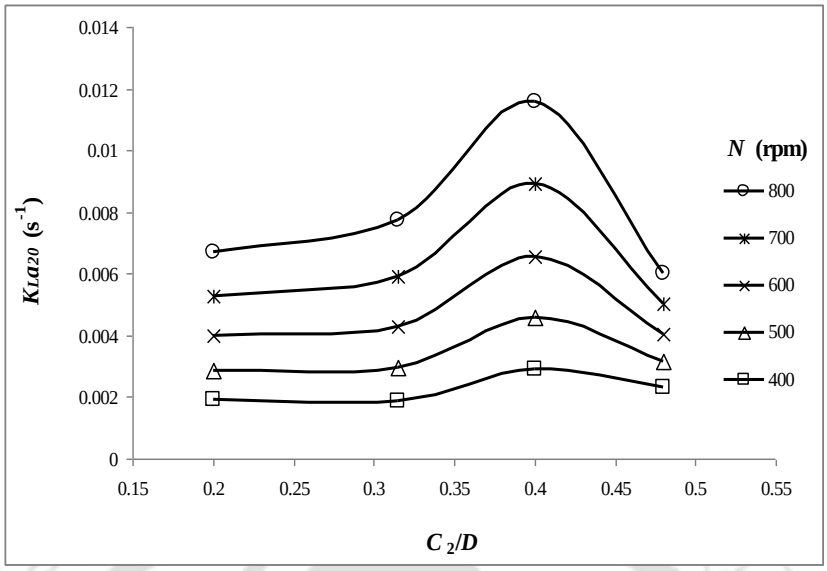

Figure 4.10: Variation of K_La_{20} with different C_2/D at C_1/D =0.4

Here, in Figure 4.10 showing the variation of K_La_{20} with different C_2/D at C_1/D of 0.4 gives optimal C_2 at 0.4D. Now, in order to find out the global and local optimal, the already known optimal points are again compared to each other in Table 4.2.

Table 4.2: Optimal configurations of C_1 and C_2 based on K_La_{20}

Sl. No.	C_1	C_2	K_La_{20} **at 500 rpm**	**Remarks on optimal**
1	0.15D	0.48D	0.0068	Local
2	0.2D	0.48D	0.0042	Local
2	**0.25D**	**0.38D**	**0.0073**	**Highest K_La_{20} (global)**
4	0.3D	0.48D	0.0041	Local
5	0.4D	0.4D	0.0045	Local

From Table 4.1, the global optimal C_1 and C_2 are at 0.25D and 0.38D respectively which gives highest K_La_{20} among the other configurations. As stated in the objectives, it has been investigated that does these optimal points reflect the stable patterns. This fact has been analyzed by employing CFD.

4.3.3. Numerical modeling

Numerical modeling is based on solving the governing equations (continuity and momentum equation) through CFD (using FLUENT®). The various numerical equations and parameter

involved in numerical modeling will not be covered in this study as such details can be obtained in Chapter 2 (methodology).

No detail of the numerical modeling (governing equations and governing parameter) is discussing in this section as mentioned above, however, a brief on generated grid and adopted boundary condition is made for this particular system (unbaffled dual Concave blade impeller without sparging). As it is going to analyze the hydrodynamics of the experimentally obtained optimal configurations, a generated grid is shown taking the global optimal as reference (C_1=0.25D, C_2=0.38D) in Figure 4.1. It creates 491186 cells, 1066901 faces and 133885 nodes to complete the 3D unstructured grid. Special care is taken place around the impeller region by coarsening the grid sizes in order to capture the small dissipative flow field characteristics so that real complexity of turbulence existing at this particular region could be predicted.

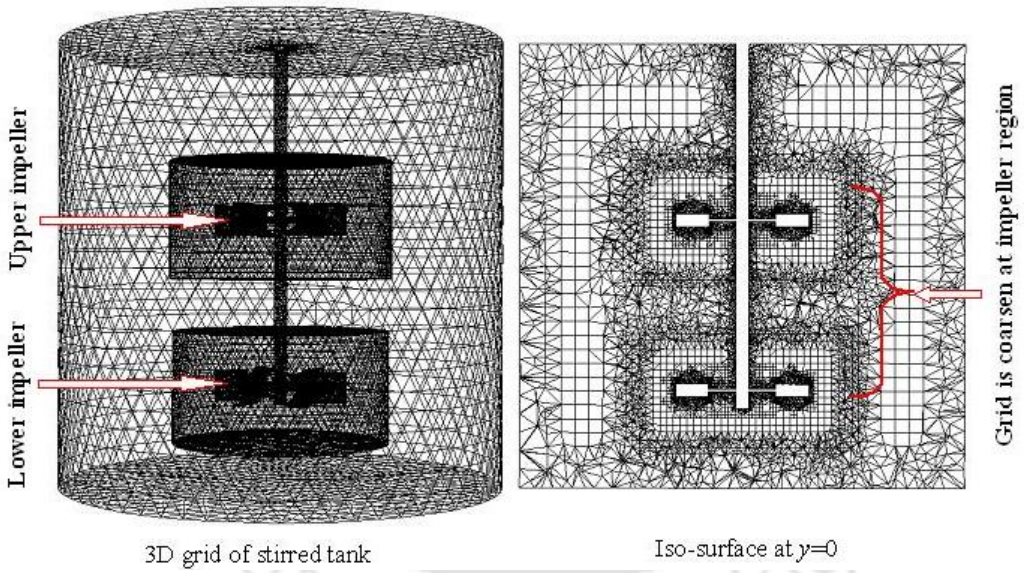

Figure 4.11: Generated 3D grid of the stirred tank with coarsen grid at the impeller region.

4.3.3.1. Flow pattern

In turbulent flow regime of stirred tank, flow pattern directly relates to the performance of the system by giving the clear information of the movements of flow created by the radially rotating impeller inside the confined vessel. This is the basic understanding of the hydrodynamics of the system under certain conditions. Flow pattern is represented by the vectors of the flow path. It is very interesting to know the circulation of concave blade impeller matches with the well known behavior of Rushton impeller.

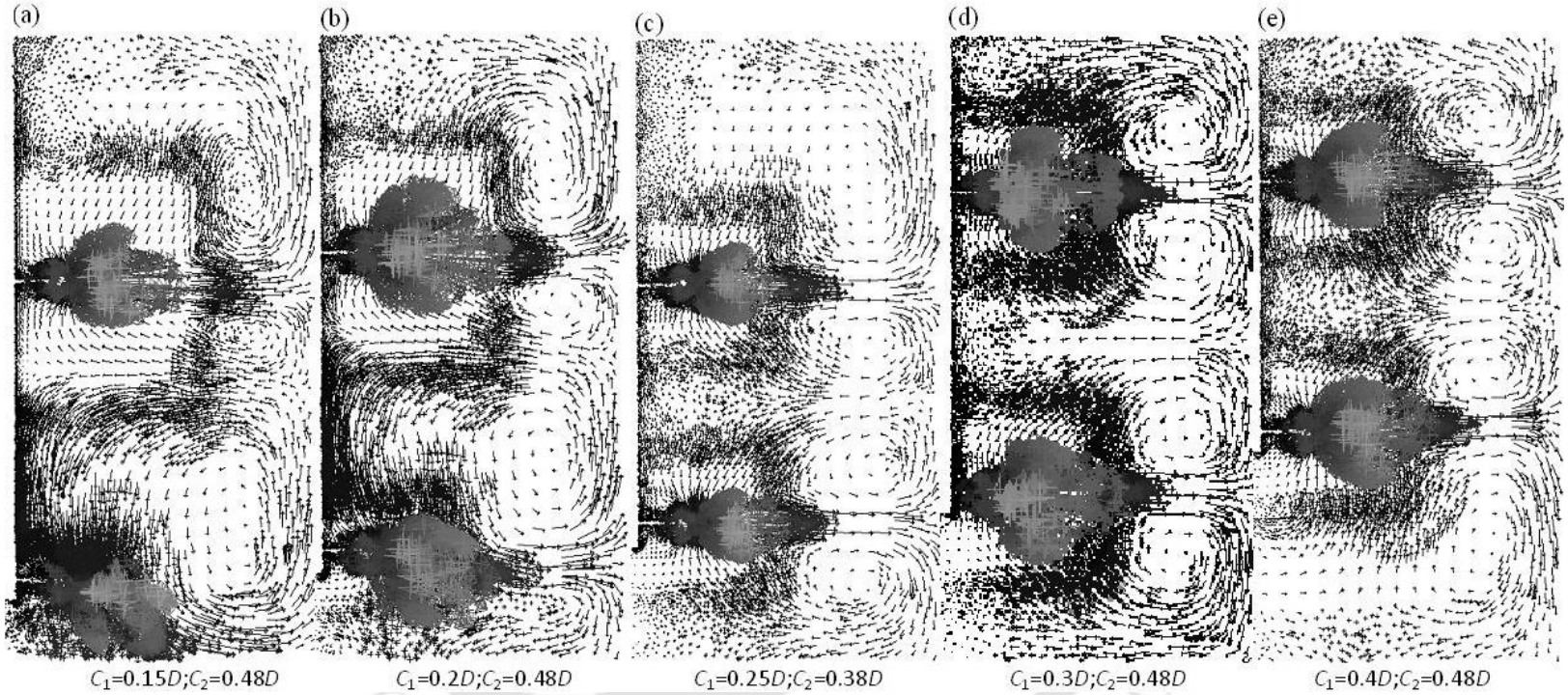

Figure 4.12: Comparison of flow patterns at different optimal points

Modeling was performed for the already achieved optimal configurations (Table 4.1). Four combinations of optimal C_1 and C_2 are achieved. The flow field pattern generated at these configurations is shown in Figure 4.12. Based on the flow pattern defined by Rutherford et al. (1996), the exact formation of diverging flow pattern is predicted when C_1=0.15D; C_2=0.48D (Figure 4.12a) and merging flow pattern at C_1=0.25D; C_2=0.38D (Figure 4.12c). And the other remaining C_1 and C_2 combination forms parallel flow pattern (4.12b,d,e). This is exactly matching with Rutherford et al. (1996) study which concluded that in order to maintain the parallel flow pattern in dual Rushton impeller (D=H), the C_1 must be greater than 0.2D and C_2 should be greater than 0.385D. This has been applicable in case of Rushton impeller, similarly it has been found in the same combination of Concave blade impeller (Figure 4.12b,c,e). In parallel flow pattern, the two impellers are forming independent circulation loop (ring vortices) one above the blade and another below the blade. The four circulation loop does not influence to another as they have enough space to circle around to complete their full continuous circular path. As mentioned above merging flow pattern is happened to be at global optimal point in this study which was indentified based on measured K_La_{20} in the previous section. Mahmoudi (1994) also studied the three stable flow patterns and stated that the merging flow pattern led to a mixing time lower by around 20% compared to other patterns. As per Rutherford et al. (1996) study, C_1 should be greater than 0.17D and is similarly predicted in this study too with C_1=0.25D; and they say that C_2 should be less than 0.385D and which is similarly achieved in this study by getting C_2=0.38D to maintain the merging flow pattern. However, smaller value of C_2 (< 0.38D) will be more accurate to form the merging flow pattern in Concave blade impeller which is not predicted in this study. This merging flow pattern in Concave blade impeller may also be considered as partial merging flow which is half way merged between the impellers at this condition. Merging flow forms two full circulation loop one above the impeller blade of upper impeller and one below the lower impeller blade and the circulation loops between the impeller merges to another approximately at mid half way. Merging flow is mainly influenced by the spacing of two impellers and because of the non-availability of enough space to circulate the flow path, the attempts of emerging flow from impeller blade tip to overtake to one another for creating its own flow path is failed and subsequently produces merged flow. As mentioned above, diverging flow pattern is predicted when C_1=0.15D, C_2=0.48D in Figure 4.12a. Rutherford et

al. (1996) found for diverging flow at C_1=0.15D,C_2=0.5D; and it is said that this flow pattern was maintained so long as the separation C_2 was greater than 0.385D and the lower impeller clearance C_1 was less than 0.15D. And, this is applicable in this study of Concave blade impeller. Table 4.3 shows the stable flow configurations of dual Rushton (Rutherford et al., 1996) and Concave blade impeller (this work).

Table 4.3: The configurations (C_1, C_2) of stable flow pattern

Flow pattern	**Rutherford et al. (1996)** $D=H$, d=0.33D dual Rushton	**This work** $D=H$, d=0.3D dual Concave blade
Parallel	C_1>0.20D C_2>0.385D	C_1> 0.20D C_2≥0.48D
Merging	C_1>0.17D C_2<0.385D	C_1>0.2D C_2<0.38D
Diverging	C_1<0.15D C_2>0.385D	C_1<0.15D C_2>0.48D

As expected, the three stable flow patterns (parallel, merging and diverging) are within the optimal configurations obtained in this study. The configuration of parallel and diverging flow pattern of Rushton is closely similar with Concave blade impeller while in case of merging flow; Concave blade impeller requires lesser C_2 value than the Rushton impeller.

In order to understand the variation of flow pattern defined by contours of velocity magnitude across the vessel for the three stable flow pattern is shown in Figure 4.13. Maximum amount flow circulation takes place near and around the impeller. In case of diverging flow, maximum amount of flow turbulence is made by the lower impeller than the upper impeller while in case of merging and parallel pattern, both the impeller similarly contributes to form turbulence.

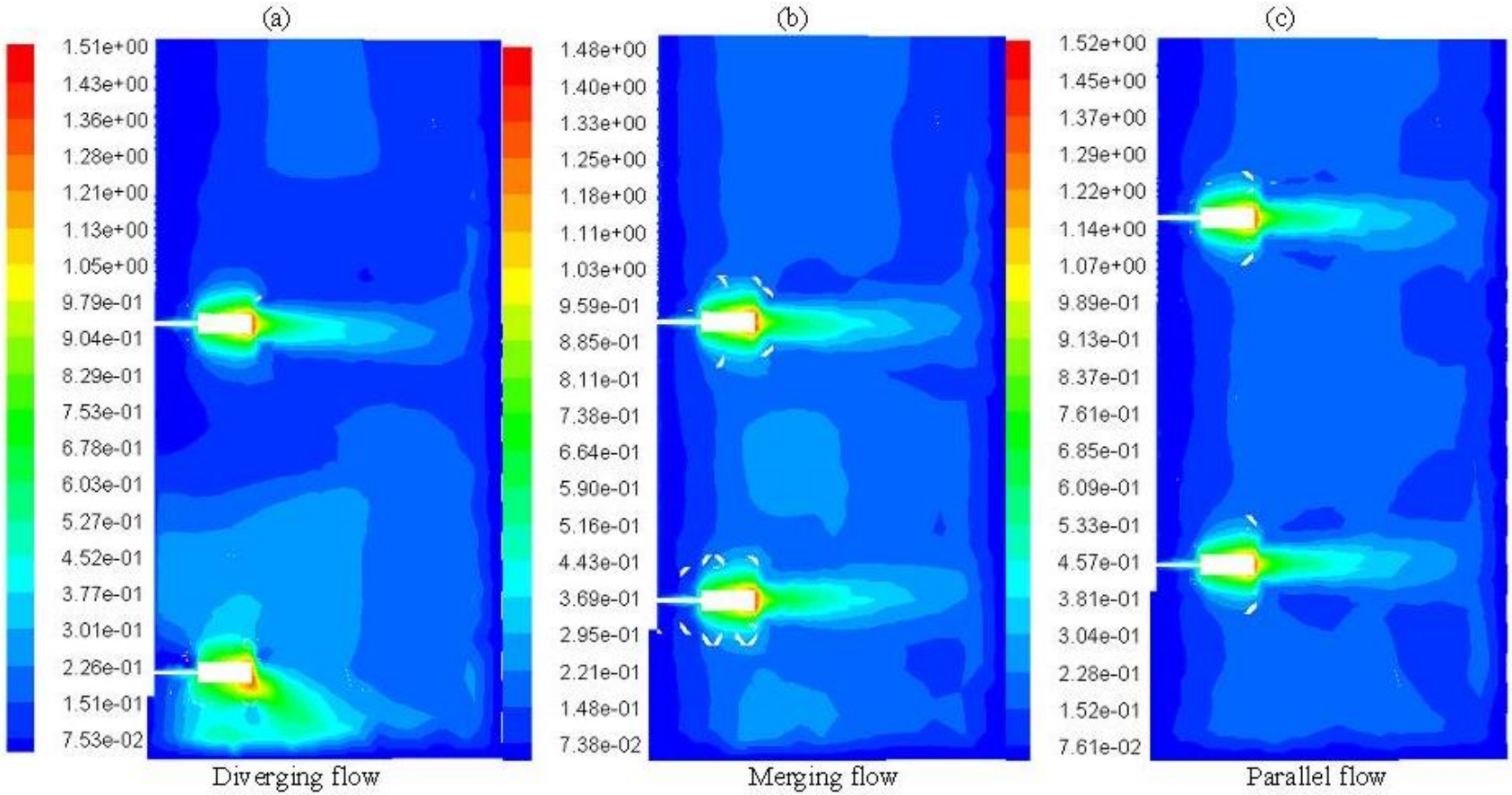

Figure 4.13: Contours of velocity magnitude for diverging, merging and parallel flow pattern.

(a) Diverging (b) Merging

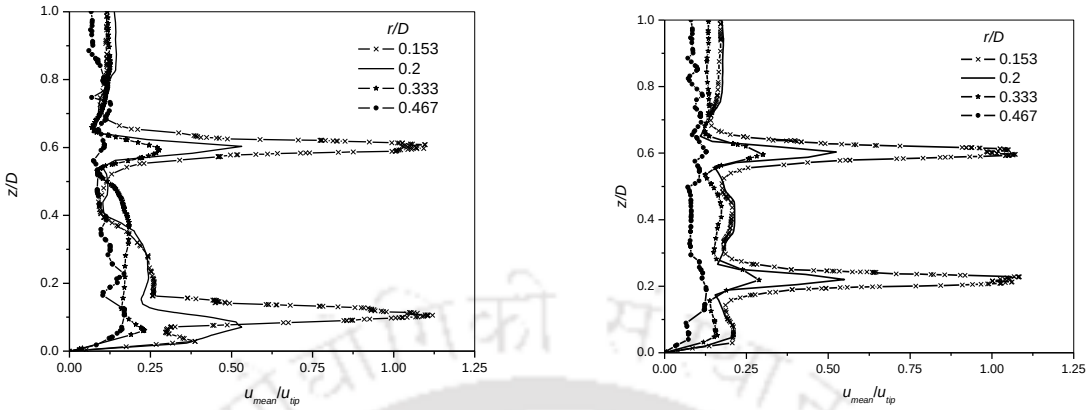

(c) Parallel (d) at r=0.333m

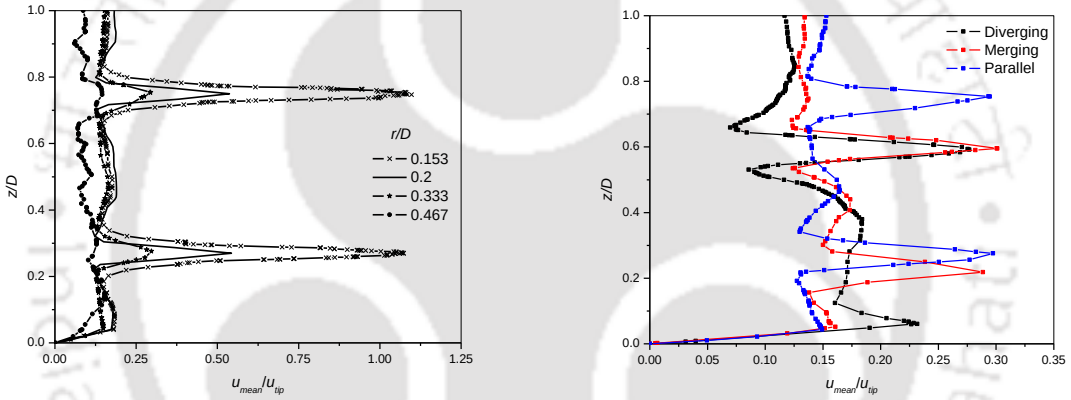

Figure 4.14: Comparison of velocity magnitude at different radial positions (r) for (a) Diverging (b) Merging (c) Parallel; and (d) comparison of diverging, merging and parallel flow at r/D=0.333.

Figure 4.14(a-c) shows the comparison of predicted velocity magnitude at different radial distances and (d) comparison of diverging, merging and parallel flow at r/D=0.333 (nearer to tank wall). From these graphical plot, it is understood that highest velocity magnitude (u_{mean}=1.12u_{tip}m/s) is occurred at impeller tip (r/D=0.153) and gradually decreases as the radial distance reaches to tank wall in all the three cases of diverging, merging and parallel flow. Comparison among the different flow pattern is made at fix radial distance between impeller tip and tank wall (r/D=0.333) in order to understand its detail flow behavior (Figure 4.14d). The three flow pattern produces same amount of flow magnitude, however, they formed different flow pattern. But the flow pattern of merging and parallel flow shows

similar velocity pattern in this study, this is because of the fact that as we have mentioned earlier that in order to form the exact merging flow pattern, the spacing between the impellers (C_2) need to be reduced from the studied configuration (C_2=0.38D).

4.3.3.2. Turbulent kinetic energy and dissipation rate

The turbulence characteristic in terms of turbulent kinetic energy (k) is an important parameter associated with energy transfer rate among the fluid particles. Better energy transfer enhances turbulence mechanism and subsequently leads to better performance of the system.

(a) Diverging

(b) Merging

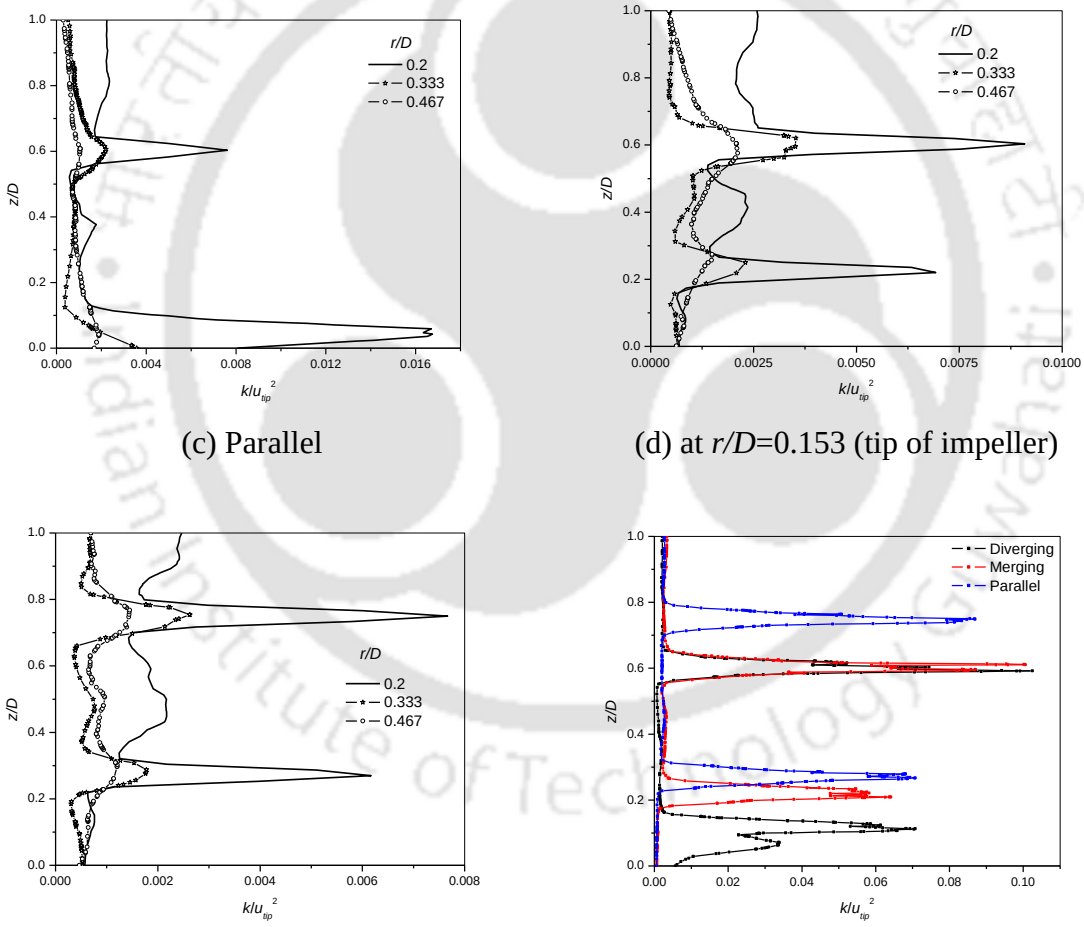

(c) Parallel

(d) at r/D=0.153 (tip of impeller)

Figure 4.15: Comparison of turbulent kinetic energy (k) magnitude at different radial positions (r) for (a) Diverging (b) Merging (c) Parallel; and (d) comparison of diverging, merging and parallel flow at r/D=0.153

In Figure 4.15, comparison of predicted k normalized by u_{tip}^2 at different radial positions (r) for (a) diverging flow (b) merging flow (c) parallel flow and (d) comparison of diverging, merging and parallel at r/D=0.153. k is predicted highest at the impeller tip (r/D=0.153) and significantly decreases towards the tank wall. This pattern is similar with velocity magnitude. But, in case of velocity magnitude, the same amount of velocity is contributed both by lower and upper impeller, however, in case of k, their magnitude are different. In diverging flow, the lower impeller contributes higher magnitude of k than the upper impeller and; in merging and parallel flow, the upper impeller produces slightly higher amount of k.

Another dissipative scale is turbulent dissipation rate (ε) which expressed the smallest scales of flow in turbulent flow regime. It directly relates the mixing efficiency of the system. Its distribution across the vessel (at different radial distance, r) for the three stable flow patterns is shown in Figure 4.16(a-d). The comparison of normalized (ε) at r/D of 0.2, 0.333 & 0.467 (Figure 4.16a-c) reveals that the energy dissipation is higher when radial distance is nearer the impeller region and minimum energy dissipation takes place near the tank wall. This pattern is found in the three stable flow patterns. Highest peak of normalized ε is predicted at impeller tip having different magnitude for the two impellers. In diverging flow, ε/N^3d^2 is predicted higher magnitude by lower impeller than the upper impeller at different radial distances. But in merging flow, higher is predicted by upper impeller than the lower impeller and in parallel flow, around same amount dissipation rate is predicted. Now, in order to understand the energy dissipation for the three stable flow at impeller tip (r/D=0.153) where the maximum energy dissipation takes place is made comparison in Figure 4.16d. It predicts different regions of energy dissipation for flow pattern indicating that maximum ε/N^3d^2 is occurred near around the impeller. According to the position of impeller mounted, the energy dissipation is also greatly changed. At impeller tip (Figure 4.16d), the magnitude of ε/N^3d^2 does not predict at high variation.

(a) Diverging (b) Merging

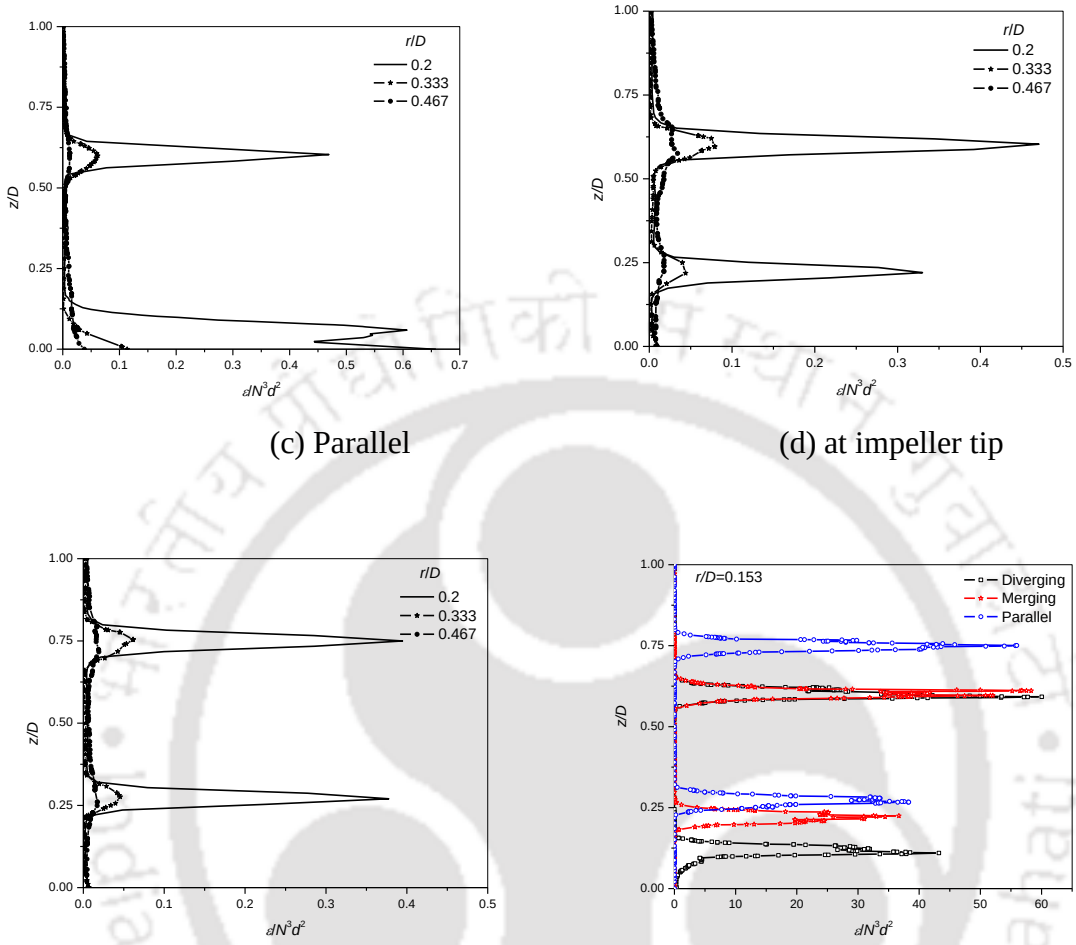

Figure 4.16: Comparison of turbulent dissipation rate (ε) magnitude at different radial positions (r) for (a) Diverging (b) Merging (c) Parallel; and (d) comparison of diverging, merging and parallel flow at impeller tip(r/D=0.153).

The distribution of predicted turbulent kinetic energy and dissipation rate at different C/D are tabulated in Table 4.4. The highest k and ε are predicted when C_1=0.25D & C_2=0.38D which is happened to be global optimum indentified based on measured K_La_{20} in the previous section. And this is the point where merging flow pattern is predicted in this study. When C_1=0.15D & C_2=0.48D (diverging flow pattern), the amount of dissipative scales (k, ε) are predicted slightly lower than the merging flow but significantly higher than the parallel flow pattern.

Table 4.4: Distribution of predicted volume-weighted average k and ε at different C/D

C_1	C_2	k (m^2/s^2)	ε (m^2/s^3)	**Predicted flow pattern**
0.15D	0.48D	0.0017	0.045	Diverging
0.2D	0.48D	0.0015	0.032	Parallel
0.25D	**0.38D**	**0.0018**	**0.047**	**Merging**
0.3D	0.48D	0.0013	0.030	Parallel
0.4D	0.48D	0.0015	0.032	Parallel

So, it seems that merging flow pattern produces higher amount of dissipative scales than the diverging and parallel flow leading to enhance the energy dissipation; and eventually increasing overall performance of the system. Parallel flow pattern dissipates lowest amount of energy among the three stable profiles.

4.3.3.3. Power consumption

It is also important to validate the numerical modeling with experimental result. In this regard, power consumption in terms of N_p is a very important parameter to study and hence, in Table 4.5 enlists the values of measured and predicted N_p. The highest prediction error is 14.67 % and it can be said that it is within the acceptable range of prediction.

Table 4.5: Measured and predicted N_p

SL. No.	C_1	C_2	N_p (N=500rpm)		**Prediction error %**
			Expt.	**CFD**	
1	0.15D	0.48D	63.58	61.49	3.28
2	0.2D	0.48D	69.67	59.45	14.67
3	0.25D	0.38D	63.21	56.32	10.89
4	0.3D	0.48D	76.32	65.53	14.13
5	0.4D	0.4D	63.68	58.52	8.1

Modeling of mass transfer and vortex formation is performed at global optimal point (C_1=0.25D and C_2=0.38D). Modeling of single phase system (water as liquid) as multiphase systems (gas-liquid) is done to estimate mass transfer rate (by giving the gas volume fraction which is required to estimate the coefficient of mass transfer rate). The other boundary condition required in this modeling has already been briefed in Chapter 3 of single phase system. Once the single phase system is treated as gas-liquid interaction the phases are separated; and is able to represent the vortex formation on the top of the free liquid surface indicating the area which is fully occupied by gas only. This area occupied by gas only

creates a depression like shape and the interface line between the liquid and gas phase represents the vortex line which is shown in Figure 4.17. This is just the qualitative study on the modeling of vortex formation and mass transfer rate in single phase system. The overall predicted $K_L a_{20}$ is found to be 0.0054s^{-1} against the experimental result of 0.0073s^{-1}.

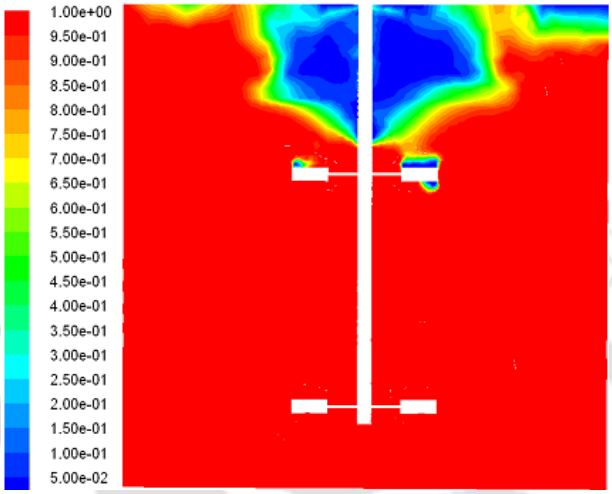

Figure 4.17: Water volume fraction (representing vortex formation) at y=0 plane

4.3.4. Development of design criteria

4.3.4.1. Mass transfer rate

Equation (3.2) is extended for dual impeller system as:

$$k_c = f\left(H/D, d/D, l/d, b/d, C_1/D, C_2/D, n, \rho_a/\rho_w, Re, Fr\right) \quad (4.1)$$

By eliminating the constant ratio in Equation (4.1), it becomes as:

$$k_c = f\left(d/D, C_1/D, C_2/D, Re, Fr\right) \quad (4.2)$$

So, Equation (4.2) suggest that for constant d/D, C_1/D and C_2/D (considering only the global optimal) k_c is a function of Re and Fr only.

$$k_c = f\left(Re, Fr\right) \quad (4.3)$$

Experimental observation of k_c with Re has been shown in Figure 4.18. It can be seen from this figure that k_c cannot be simulated with Re as scale effects are predominantly significant and same can be said when k_c is plotted with Fr (Figure 4.19).

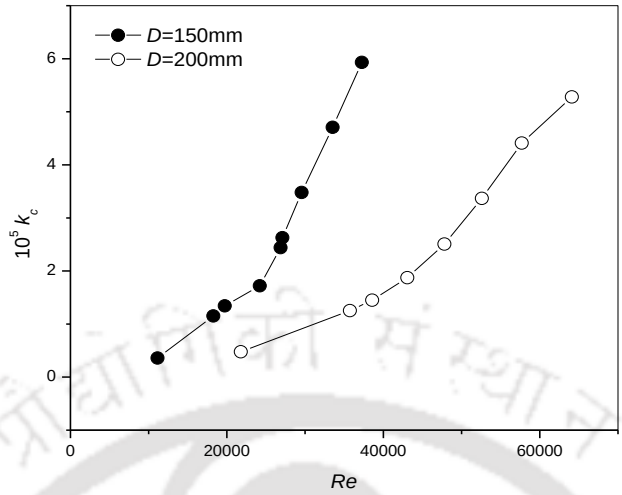

Figure 4.18: *Re* with k_c

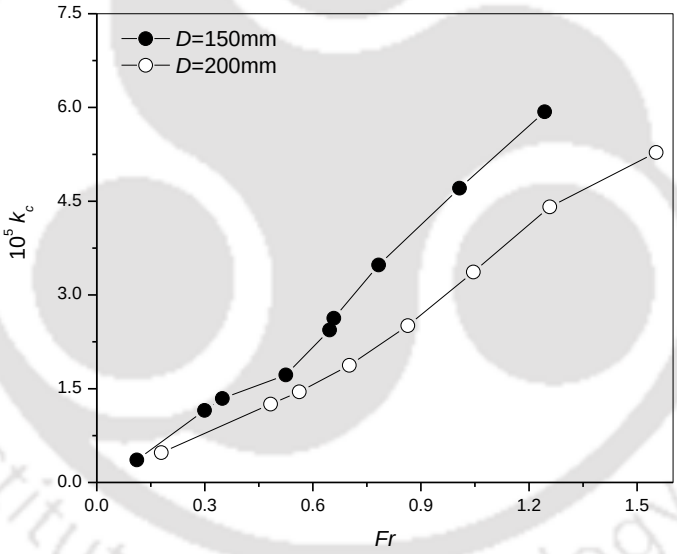

Figure 4.19: *Fr* with k_c

Thus X has been taken to simulate k_c and can be rewritten as:

$$k_c = f(X) \tag{4.4}$$

So, Equation 4.4 suggests that k_c is a function of X only. Figure 4.20 shows the experimental observations of k_c and X. It can be seen from this figure that all the experimental observations fall on single line thus simulating the mass transfer rate in dual stirred unbaffled tanks. The generated equation with its statistical detail is given in Table 4.6.

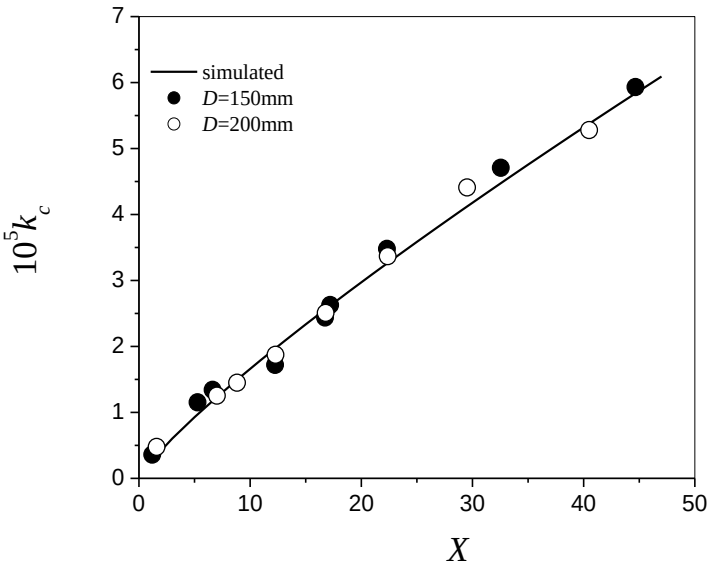

Figure 4. 20: X with k_c

Table 4.6: Details of predicted k_c of Equation 4.4

Generated equation	***a***	***b***	**Overall std. error**
$10^5 k_c = \alpha X^{\beta}$	0.24 (7.61e-2)	0.84 (5.76e-3)	9.79e-5

4.3.4.2. Power consumption

Power number is a function of *Re* and *Fr* when the geometrical parameters are constant and may be expressed as:

$$N_p = f(Re, Fr) \tag{4.5}$$

The scale effect of power number is shown in Figure 4.21 & 4.22, when experimental observations has been tried to simulate with either *Re* and *Fr*. It indicates that unlikely baffled systems, inclusion of *Fr* is necessary to simulate the unbaffled systems. Similar analysis as done with single impeller system, it is tried to replace the governing function of *Re* and *Fr* with X and experimental observation have been plotted in Figure 4.23. Thus, N_p is a function of X and is written as:

$$N_p = f(X) \tag{4.6}$$

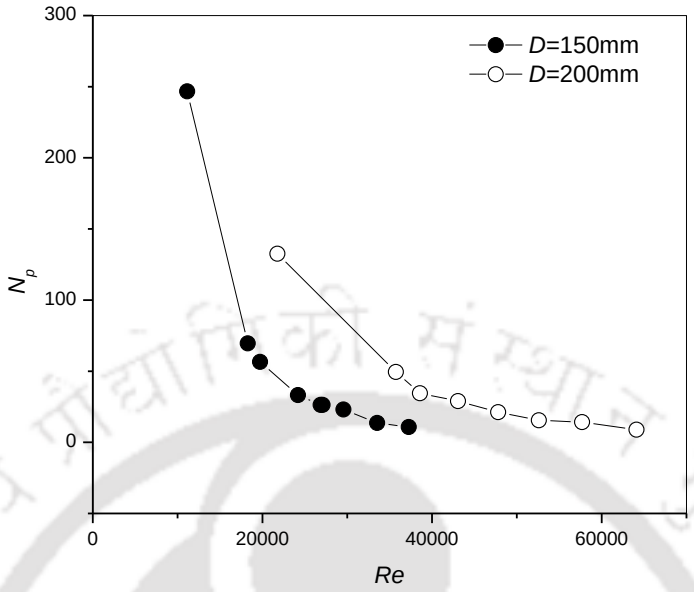

Figure 4.21: *Re* with N_p

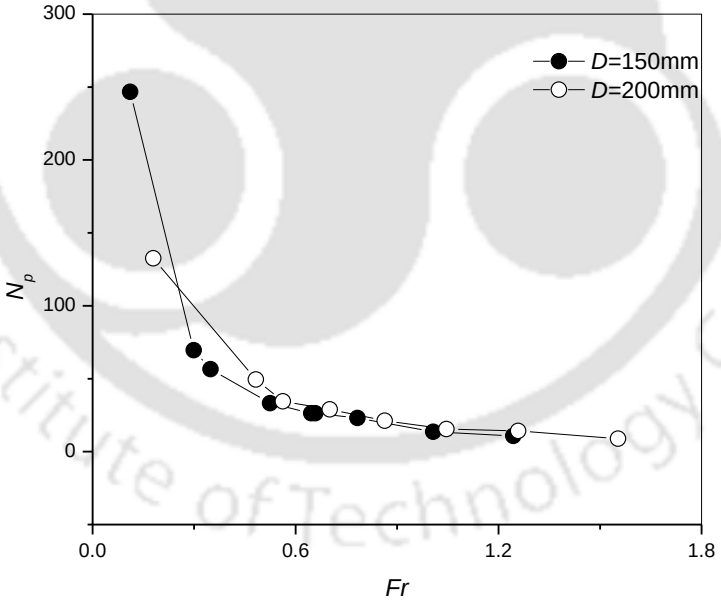

Figure 4.22: *Fr* with N_p

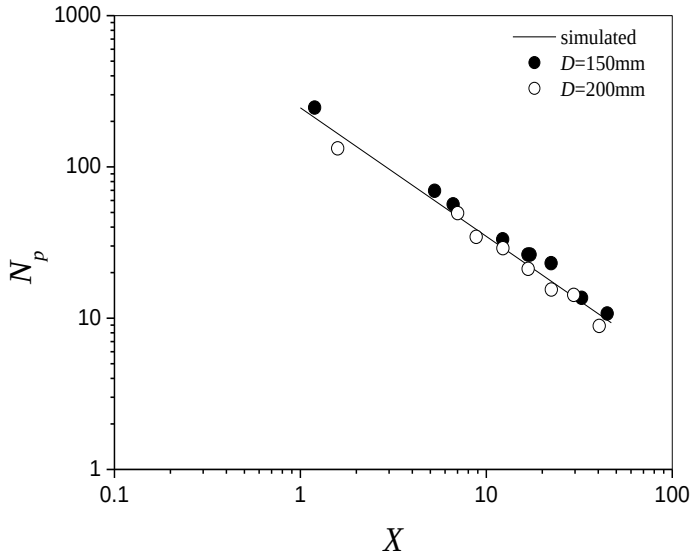

Figure 4.23: X with N_p

The statistically developed relationship to predict the N_p is shown in Figure 4.23 and its detail is given in Table 4.7.

Table 4.7: Generated equation for N_p and its detail

Generated equation	***α***	***β***	**Overall std. error**
$N_p = \alpha X^{\beta}$	245.97 (1.91e-1)	-0.85 (8.22e-2)	1.1e-1

4.3.4.3. Vortex behavior

In single phase system with single impeller, the stress has been made to develop the general scale criteria for vortex depth in the absence of any optimal geometrical systems. In dual impeller single phase, experimentation has ascertained the optimality in impeller clearance. Thus an in-depth analysis has been carried out to observe the critical geometric parameter related to vortex in the optimal systems.

A. Derivation of critical radius (r_0)

Theoretical analysis of vortex formation is based on equation of motion (Navier-Stokes equation) transformed into cylindrical co-ordinates. Velocity distribution of liquid in a cylindrical mixing vessel agitated by a concentric paddle agitator is similar to that of the so-called Rankine's combined vortex. The liquid near the center of a vessel rotates with the

same angular velocity as that of the paddle and is called forced vortex, while the flow in the outer part is similar to that of a free vortex (Nagata, 1975).

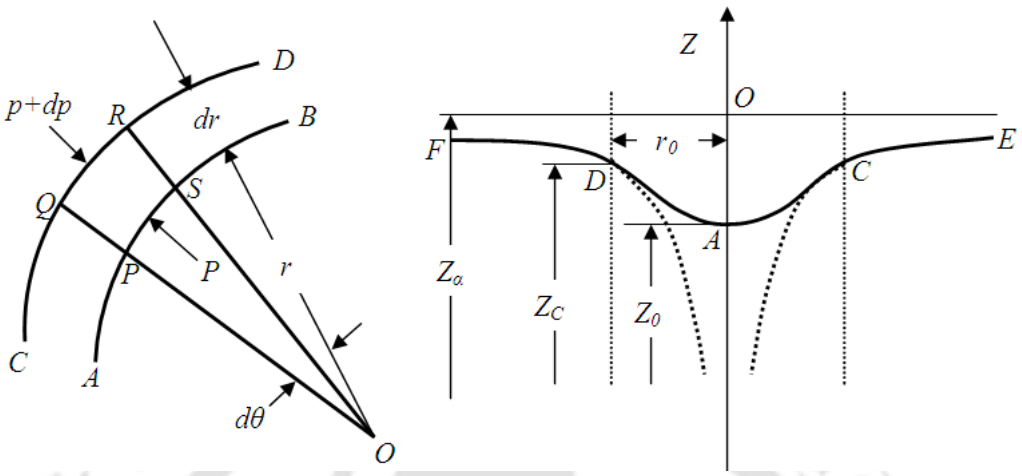

(a) (b)

Figure 4.24: (a) Momentum balance in free vortex and (b) Free surface contour in free vortex

In, Figure 4.24(a) *AB* and *CD* are two adjacent stream lines of a circulation flow having a constant energy around a center of rotation *O*. By taking momentum balance in the area PQRS of depth *dZ*, pressures *p* and *p+dp* are acting from inside and outside surface of the element and also a centrifugal force is acting outward, we have,

$$\rho r d\theta . dr . dZ \frac{v^2}{r} + p r d\theta . dZ - (p + dp) r d\theta . dZ = 0 \tag{4.7}$$

Where, *dZ* and *v* are the thickness and velocity of liquid. By rearranging,

$$\frac{dp}{\rho} = \frac{v^2}{r} dr \tag{4.8}$$

As the weight of a unit volume γ is equal to ρg ,

$$\frac{dp}{\gamma} = \frac{v^2}{gr} dr \tag{4.9}$$

Equation 4.9 shows that because of centrifugal force, the pressure head becomes larger at the outside of the element. If *H* is the total at point *P* on the stream line *AB*, the according to Bernoulli theorem,

$$z + \frac{p}{\gamma} + \frac{v^2}{2g} = H \tag{4.10}$$

On the same horizontal plane, *dZ* is equal to zero and we have,

$$\frac{dp}{\gamma}+\frac{vdv}{g}=dH \tag{4.11}$$

A circulation flow having a constant energy is considered then dZ=0.

Therefore, in free vortex motion,

$$\frac{dp}{\gamma}+\frac{vdv}{g}=0 \tag{4.12}$$

From Equations 4.9 and 4.12, we have,

$$\frac{vdv}{g}=-\frac{v^2}{gr}dr;\ \ \frac{dv}{v}=-\frac{dr}{r} \tag{4.13}$$

By integration,

$$vr=C_1(\text{Constant}) \tag{4.14}$$

Equation 4.14 shows that in free vortex motion, the flow velocity v is inversely proportional to the radius of curvature. Assume that the total head H is constant for every stream line and differentiating Equation 4.10,

$$dZ+\frac{dp}{\gamma}+\frac{vdv}{g}=0 \tag{4.15}$$

In the isobaric surface dp=0

$$dZ+\frac{vdv}{g}=0;\ Z+\frac{v^2}{2g}=C \tag{4.16}$$

Substituting Equation 4.14 in Equation 4.16,

$$Z+\frac{C_1^{\,2}}{2gr^2}=C \tag{4.17}$$

Using the boundary condition, Z is equal to zero, when r goes to infinity (Figure 4.24b); C is equal to zero, therefore,

$$Zr^2=\frac{-C_1^{\,2}}{2g} \tag{4.18}$$

This equation shows a hyperbolic nature and isobaric surfaces can be determined by introducing several values of C.

In short, in the combined vortex,

$$r\leqq r_c;\ v=r\omega \tag{4.19}$$

$$r \geqq r_c;\ v = \frac{\omega r_c^2}{r} \tag{4.20}$$

Where, ω is angular velocity.

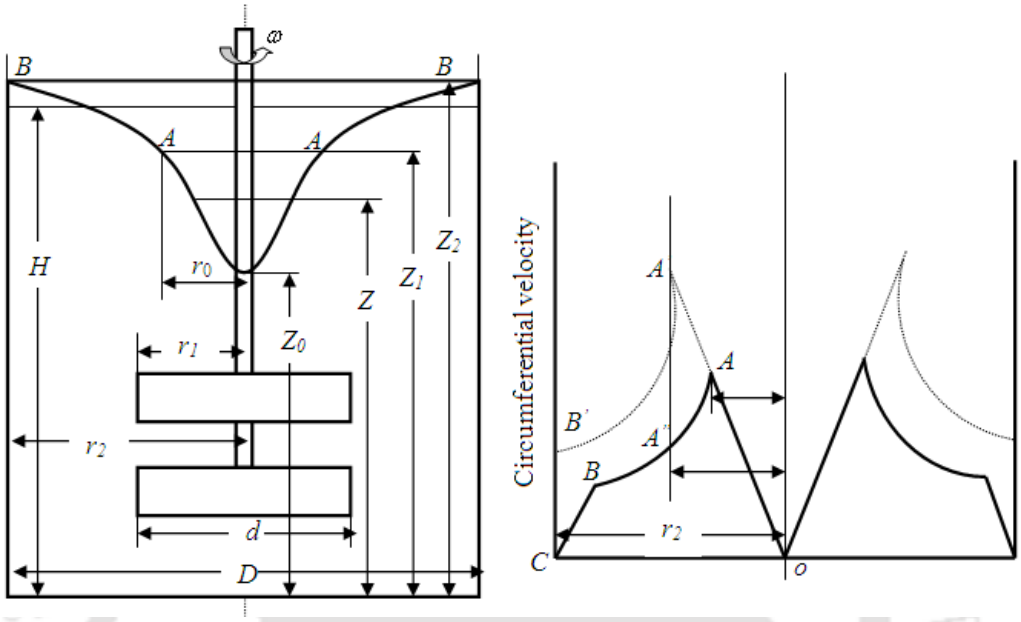

(a) (b)

Figure 4.25: (a) Notations used in vortex depth determination and (b) distribution of circumferential velocity in an agitated vessel

In the vicinity of the vessel wall, a rapid decrease of velocity is observed as:

$v=C(r_2-r)$ (4.21)

In the region of free vortex zone, the resultant force is perpendicular to the liquid surface and is equal to the combined forces of acceleration and gravity. Then we have,

$$\frac{dZ}{dr} = \tan\theta = \frac{mr\omega^2}{mg} \tag{4.22}$$

Substituting the boundary condition at $r=0$, $Z=Z_0$ after integration in the region of $r \leqq r_0$ we get,

$$Z = Z_0 + \frac{\omega^2 r^2}{2g} \tag{4.23}$$

From Equations 4.16 and 4.21, we have the surface equation for the region $r \geqq r_0$.

$$Z + \frac{\omega^2 r^2}{2g} = C \tag{4.24}$$

As a boundary condition, we have $Z=Z_1$ at $r=r_0$ where Z_1 is the liquid level at the boundary (A) of the C.R.Z (Figure 4.19) and the free vortex zone.

$$C = Z_1 + \frac{\omega^2 r_0^{\,2}}{2g} \tag{4.25}$$

Therefore,

$$Z = Z_1 + \frac{\omega^2 r_0^{\,2}}{2g}\left(1 - \frac{r_0^2}{r^2}\right) \tag{4.26}$$

As the point A belongs to the C.R.Z., we have from Equation 4.23,

$$Z_1 = Z_0 + \frac{\omega^2 r_0^{\,2}}{2g} \tag{4.27}$$

Therefore in the region of $r \geqq r_0$;

$$Z = Z_0 + \frac{\omega^2 r_0^{\,2}}{2g}\left(2 - \frac{r_0^2}{r^2}\right) \tag{4.28}$$

The liquid level H before agitation is related with liquid volume V as:

$$H = \frac{V}{\pi r_2^2} \tag{4.29}$$

Therefore, r_0 is calculated by taking integration over Equation 4.23 and 4.28 equating to volume V as:

$$V = \int_0^{r_0}\left(Z_0 + \frac{\omega^2 r^2}{2g}\right)2\pi r dr + \int_{r_0}^{r_2}\left\{Z_0 + \frac{\omega^2 r_0^2}{2g}\left(2 - \frac{r_0^2}{r^2}\right)\right\}2\pi r dr =$$
$$Z_0\pi r_2^2 + \frac{\pi\omega^2}{4g} r_0^4 + \frac{\pi\omega^2}{g} r_0^2\left(r_2^2 - r_0^2\right) - \frac{\pi\omega^2 r_0^4}{g}\ln\left(\frac{r_2}{r_0}\right) \tag{4.30}$$

If $r_2=D/2$ is substituting in Equation 4.28 after integration in Equation 4.29, we have,

$$\frac{\left(H - Z_0\right)g}{\left(\omega D\right)^2} = \left(\frac{r_0}{D}\right)^2 - 4\left(\frac{r_0}{D}\right)^4\left(\frac{3}{4} + \ln\left(\frac{D}{2r_0}\right)\right) \tag{4.31}$$

B. Prediction of critical radius (r_0)

Determination r_0 is important in unbaffled stirred tank in order to understand the vortex formation. r_0 is predicted using Equation 4.31and comparison with experimentally measured r_0 is shown in Figure 4.26.

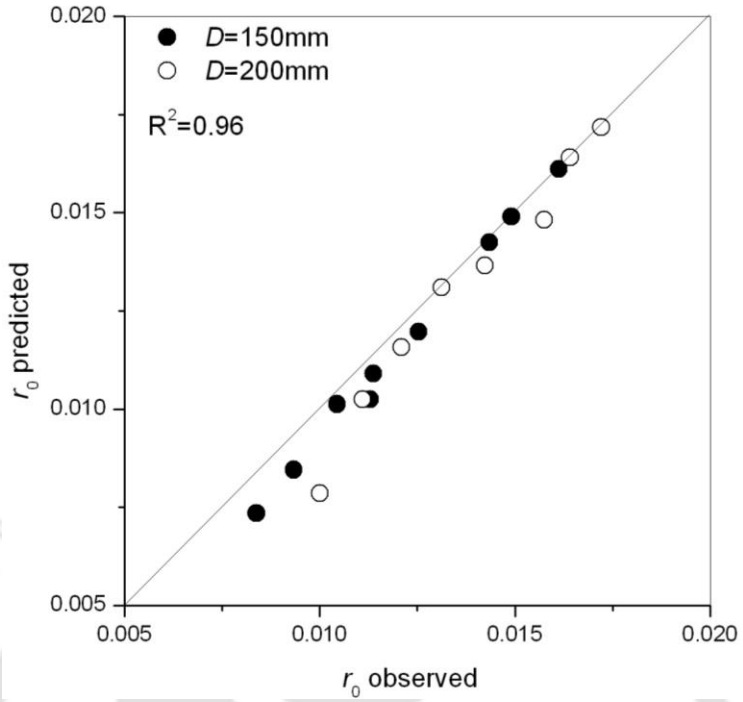

Figure 4.26: Observed with predicted r_0 (m)

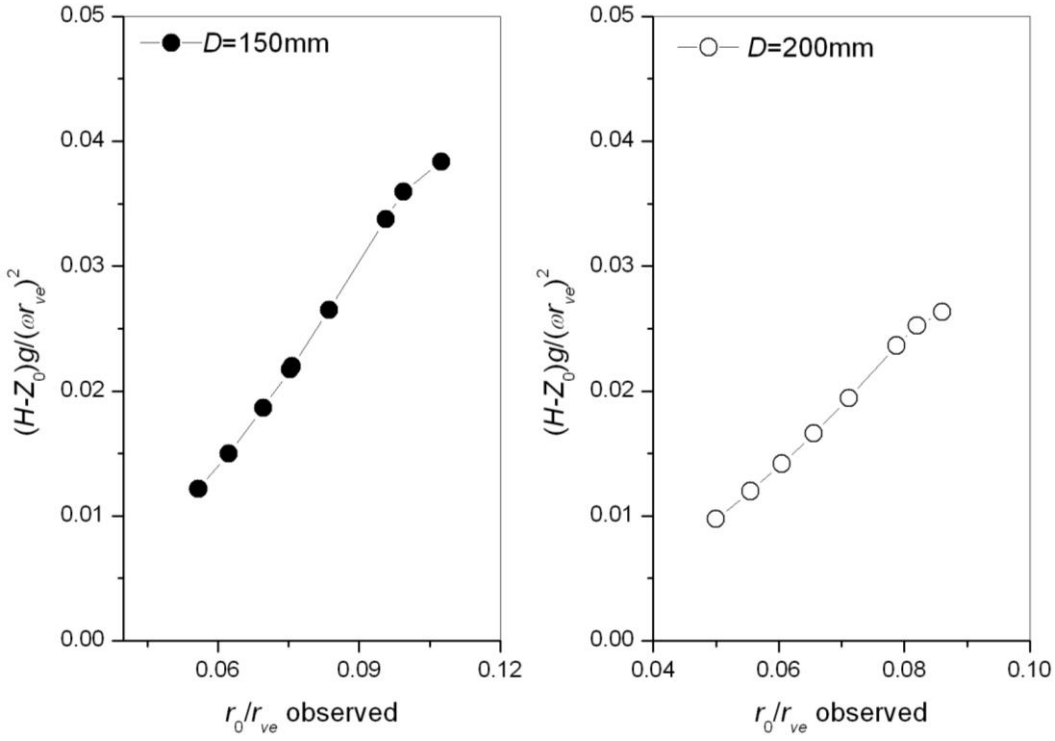

Figure 4.27: Nagata model

Equation 4.31 can be interpreted as in vortex system Froude number (LHS side of Equation 4.31) depends on tank radius and the tank radius. It gives the effective area of the impeller

used in mixing application based on rotational speed, which is plotted in the Figure 4.27. Based on the rotational speed, one can easily determine the effective area of the present impeller in dual stirred tank.

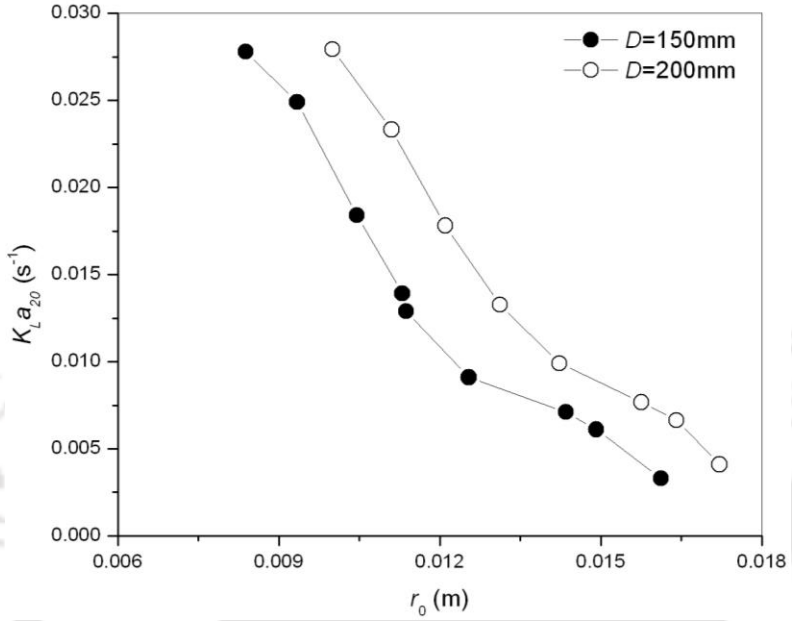

Figure 4.28: r_0 with $K_L a_{20}$

Figure 4.28 shows r_0 with measured $K_L a_{20}$ for the two different tank diameter (D=150mm and 200mm). $K_L a_{20}$ decreases with increases in r_0 and higher r_0 is observed in case of 200mm tank diameter than the 150mm tank diameter.

C. Determination of critical speed (N_c)

To find the critical impeller (N_c) speed, energy balance is used as:

$$V_d \rho g = K\left(\pi^2 d^2 \rho\right)/2 \tag{4.32}$$

V_d ($=Z_2$-Z_0) is the depth of vortex from free surface. It can also be written as:

$$\frac{V_d}{d} = K Fr \tag{4.33}$$

The value of k can be obtained by plotting the observations of vortex depth and Froude number of stirred tanks. The value of k can also be calculated by re-arranging Equation 4.31 in the form of Equation 4.33 (Brennan, 1976). Then,

$$K = \left(\frac{2\pi r_0}{d}\right)^2 \left[1 - \left\{\left(\frac{2r_0}{D}\right)^2 \left(\frac{3}{4} + \ln\left(\frac{D}{2r_0}\right)\right)\right\}\right] \tag{4.34}$$

On the basis of experimental observations, if *K*is known, N_c can be obtained by re-arranging Equation 4.33 as:

$$N_c = \sqrt{\frac{V_d g}{K d^2}} \tag{4.35}$$

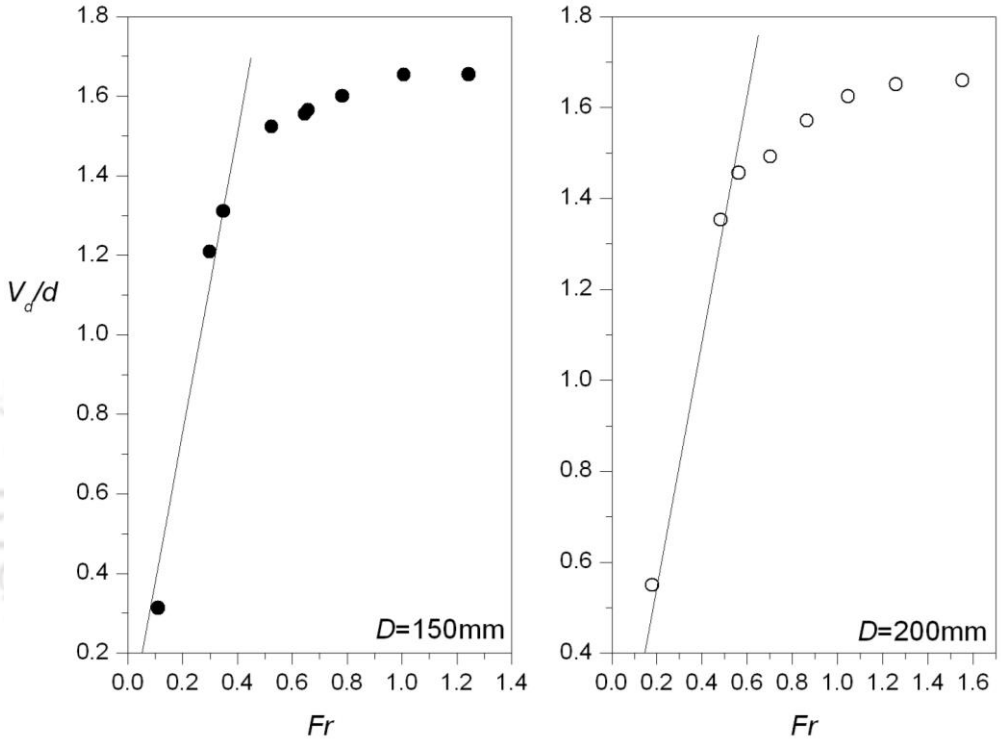

Figure 4.29: *Fr* with V_d/d

Critical speed (N_c) is calculated from Equation 4.35, once *k* is known, so, *k* is experimentally calculated by plotting non-dimensional form of vortex depth (V_d/d) with *Fr* (Figure 4.29). Slope of this plotted graph is the value of *k* and using this value, N_c is calculated for the two tank diameter. N_c is also calculated by using Equation 4.34; calculated *k* and N_c is tabulated in Table 4.8.

Table 4.8: Calculated and predicted *k* and N_c values

D	***K***		***N_c* (rpm)**		**Prediction Error %**	
	Eqn.4.41	Expt.	Eqn.4.41	Expt.	*K*	N_c
150mm	3.24	3.77	607.1	562	11.31	5.69
200mm	2.75	2.71	538.12	542	25.93	0.18

D. Vortex depth (V_d) analysis

Equation 3.32 is extended for dual impeller system and can be written as:

$$\frac{V_d}{d} = f\left(G_a, Fr, \frac{D}{d}, \frac{C_1}{d}, \frac{C_2}{d}\right) \tag{4.36}$$

Equation 4.36 shows that vortex depth is a function of just Galileo number and Froude number when the geometrical parameters are constant. For global optimal where impeller clear distances are constant and hence can be eliminated from this equation. Finally vortex depth is a function of *Re* and *Fr*; based on this function a statistical equation is developed to predict the vortex depth and is given as:

$$\frac{V_d}{d} = f\left(G_a, Fr\right) \tag{4.37}$$

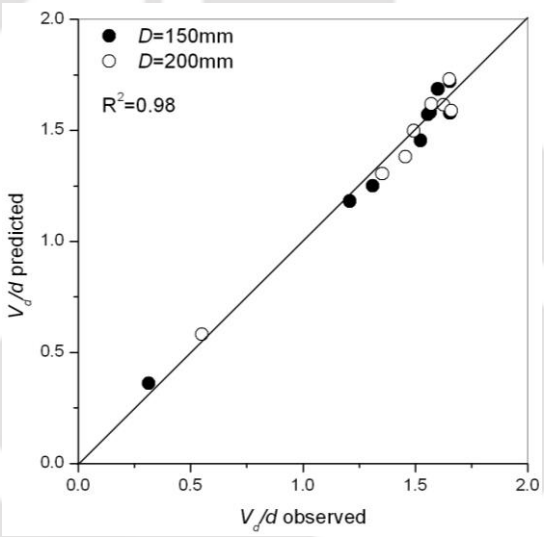

Figure 4.30: Comparison between observed and predicted V_d/d

Figure 4.30 shows the comparison of observed and predicted V_d/d for the two tank diameter. The statistical detail of the predicted equation is tabulated in Table 4.9.

Table 4.9: Statistical details of Equation 4.37

Generated equation	***α***	***β***	***γ***	**Overall std. error**
$V_d / d = \alpha G_a^{\beta} Fr^{\gamma}$	14.18 (3.25e-2)	-9.7e-02 (1.53e-3)	0.37 (6.58e-3)	1.23e-2

As suggested by Equation 4.36, V_d/d is a function of *Ga* (=Re^2/Fr) and *Fr* ; which shows the governing function of V_d/d is composed of *Re* and *Fr*. This governing function can be

replaced with X . Experimental observations as plotted in the Figure 4.31 also suggest that X can simulate the vortex behavior and functional form of the simulation is as:

$$V_d / d = 1.75 e^{-\frac{1.91}{X}} \quad (4.38)$$

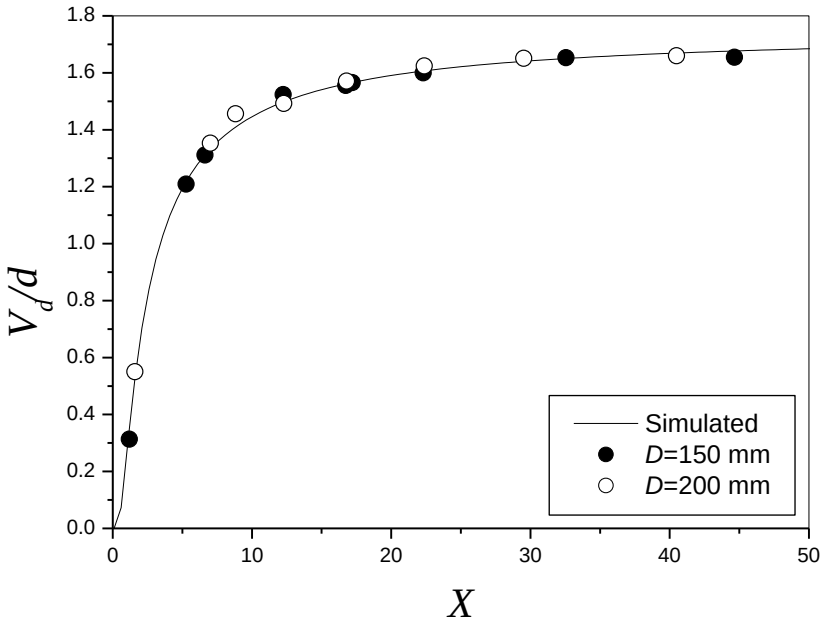

Figure 4.31: Observed and simulated V_d/d

4.3.5. Comparative studies

As the main study is performed based on unbaffled dual Concave blade impeller, comparison with other combination of impeller (with Rushton, with mix impeller and with baffled system) is also performed. All the comparative analysis is done only for 150mm tank diameter. Experimentally measured K_La_{20} and effective power (P_{eff}) will be discussed for all the comparisons.

4.3.5.1. With unbaffled Rushton

In order to understand the performance of impeller types, the impeller used in this study (unbaffled Concave blade impeller) is compared with standard impeller type, i.e., Rushton impeller in terms of K_La_{20} and P_{eff} which are shown in Figure 4.32 and 4.33 respectively. Comparison of Concave blade with Rushton in terms of impeller speed (N) with K_La_{20} shows better mass transfer by Concave blade than the Rushton impeller (Figure 4.32). And higher power is consumed by Rushton than the Concave blade impeller (Figure 4.33).

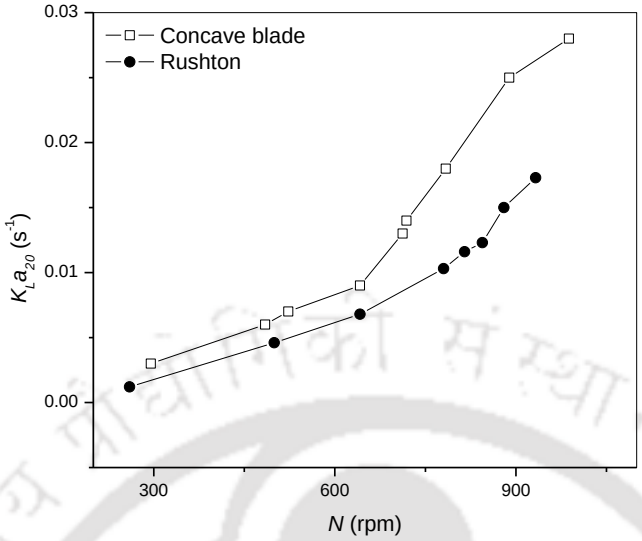

Figure 4.32: N with $K_L a_{20}$

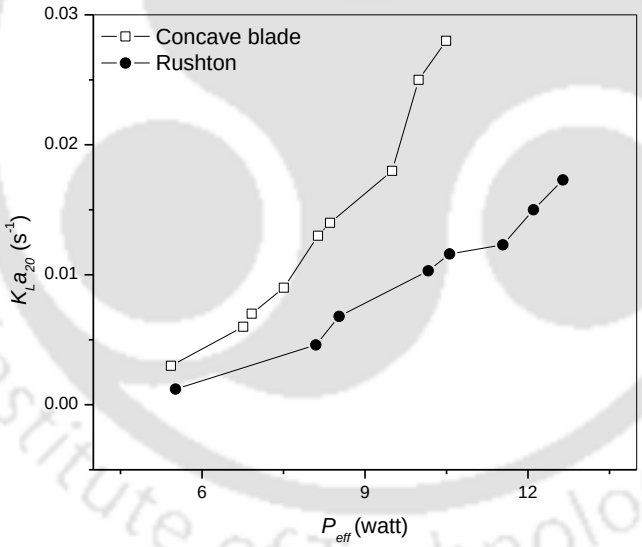

Figure 4.33: P_{eff} with $K_L a_{20}$

4.3.5.2. With baffled Concave blade

Again, unbaffled Concave blade is compared with baffled system in Figure 4.34 and 4.35 in terms of $K_L a_{20}$ and P_{eff}. $K_L a_{20}$ observed better performance by baffled system than the unbaffled system.

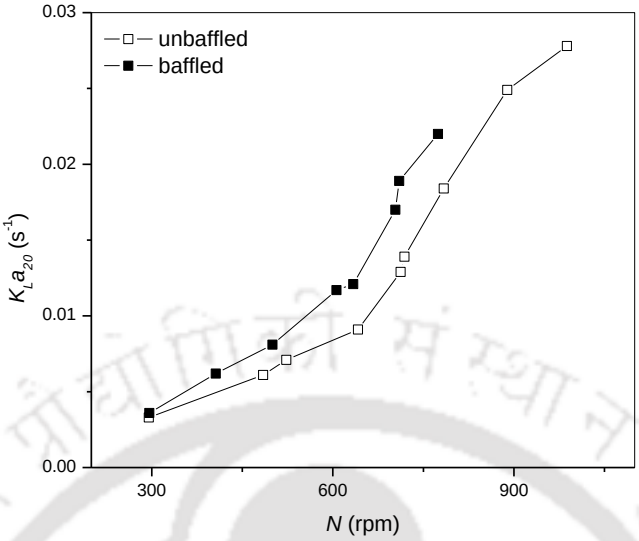

Figure 4.34: N with $K_L a_{20}$

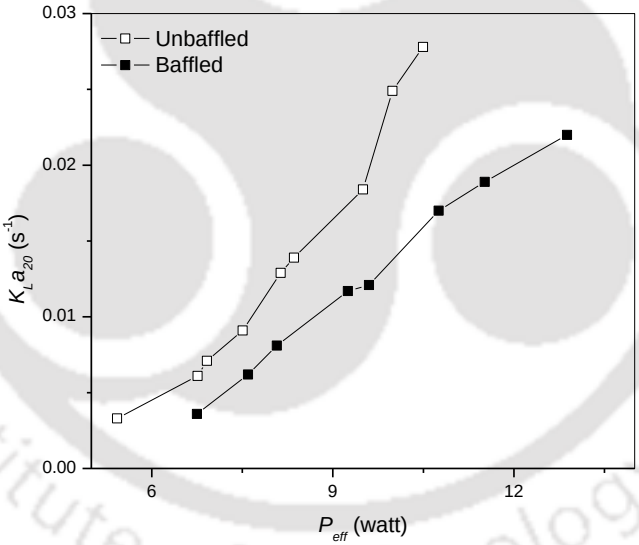

Figure 4.35: P_{eff} with $K_L a_{20}$

4.3.5.3. With unbaffled mixed impeller

In order to check the impeller type combination in stirred tank performance, unbaffled dual Concave blade is also compared with combination of Rushton impeller by replacing the lower and upper impeller alternatively. Naming of the mix impeller type is done from lower impeller, Concave blade+Rushton indicates that lower impeller is Concave blade and upper

is Rushton impeller. So, Rushton+Concave blade means, lower is Rushton and upper is Concave blade impeller.

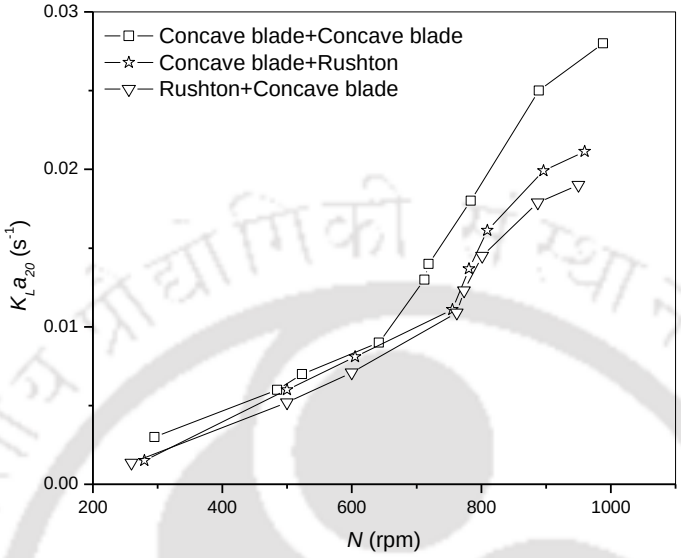

Figure 4.36: N with K_La_{20}

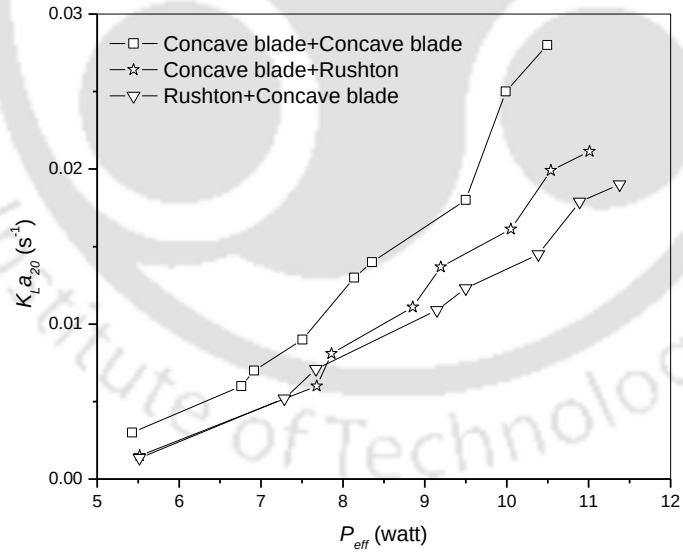

Figure 4.37: P_{eff} with K_La_{20}

The relationship of K_La_{20} with N and P_{eff} is shown in Figure 4.36 and 4.37 by comparing same combination of dual Concave blade with mix impeller, i.e., the combination of Concave blade with Rushton. In Figure 4.36, highest K_La_{20} is observed by dual Concave blade

impeller as compared with mix impeller. In mix impeller, the K_La_{20} is found higher when the lower impeller is Concave blade. And in Figure 4.37, lesser power consumption is observed by Concave blade dual impeller than the mix impeller combination when same amount of mass transfer rate is to be achieved. And when compared between the mix impeller of having Concave blade as lower impeller and Rushton as upper (Concave blade +Rushton) with Concave blade as upper and Rushton as lower impeller (Rushton+ Concave blade), higher K_La_{20} and lesser P_{eff} is observed in case of lower impeller is Concave blade.

4.3.6. Conclusions

The global quantities (mass transfer rate, power consumption and vortex behavior) of an unbaffled stirred tank are studied at different geometrical conditions. Impeller spacings (C_1 and C_2) are major concern of this study and effect of these different configurations on global quantities were experimentally studied at various impeller speed. Univariant approach is used to find the global configurations (C_1 and C_2) of the dual impeller stirred tank based on mass transfer rate expressed by coefficient of mass transfer rate. Design criteria for each global quantity was developed using dimensionless approach and tries to interpret the scale effects of the geometries of stirred tank.

The combinations of efficient impeller spacings were experimentally observed at C_1=0.15D, 0.2D, 0.25D, 0.3D, 0.4D and C_2=0.48D, 0.48D, 0.38D, 0.48D, 0.4D respectively based on observed K_La_{20}. Global optimum impeller configuration was observed at C_1=0.25D and C_2=0.38D by producing highest K_La_{20} (0.0073s^{-1}) among the other configurations.

Based on the optimal configuration of C_1 and C_2, numerical modeling of the system is made through CFD tools to predict the flow patterns, velocity profile and dissipative scale characteristics. The formation of clear flow circulation loop one above and one below the blade were clearly predicted. The stable flow profile defined by Rutherford et al. (1996) were also clearly predicted and are within the observed optimal configurations, however, the predicted configuration are slightly deviated from their study because of the difference in impeller diameter and type used. In this study, the parallel flow pattern is predicted when C_1>0.20D & C_2≥0.48D; merging flow at C_1>0.2D & C_2<0.38D and diverging flow at C_1<0.15D & C_2>0.48D. The predicted configuration of parallel and diverging flow pattern of Rushton (given by Rutherford et al., 1996) is closely similar with Concave blade impeller

while in case of merging flow; Concave blade impeller requires lesser C_2 value than the Rushton impeller. Parallel and merging flow pattern produces nearly equal amount of mean velocity and is higher than diverging flow pattern. Merging flow pattern produces higher amount of dissipative scales than the diverging and parallel flow leading to enhance the energy dissipation; and eventually increasing overall performance of the system. The predicted power number is found in fairly acceptable with observed result. A quantitative modeling of mass transfer rate and vortex formation is also made at global optimal point.

The design criteria developed for mass transfer rate in the system is interpreted through k_c. From dimensionless approach k_c is a function of *Re*, *Fr* and *X*. k_c is observed increases with increasing these independent variables. The overall design criteria for k_c at global optimal point is established as function of *X* only and is given as: $10^5 k_c = 0.24 X^{0.84}$. Similarly, in case of power consumption, the power number is observed decreases as the *Re*, *Fr* and *X* increases and overall scale up criteria is developed as: $N_p = 245.97 X^{-0.85}$. Vortex depth increases with increasing critical radius and decreases with increasing mass transfer rate. Relative vortex depth is used to find the critical impeller speed. The critical impeller speed is observed higher by smaller tank than the larger one. The relative vortex depth is related with Galelio number and Froude number in order to develop the overall scale up criteria and is given as: $V_d / d = 14.18 G_a^{-0.098} Fr^{0.37}$ and with *X* it is as: $V_d / d = 1.75 e^{-\frac{1.91}{X}}$

Comparison of the dual unbaffled Concave blade system is made with dual Rushton, baffled and impeller mix system. Concave blade system is observed giving better performance than the Rushton system in terms of mass transfer rate and power consumption. Baffled system provides better mass transfer rate but consumes higher power than the unbaffled system and hence, unbaffled system may be a better choice where the reduction of power consumption is a priori. Comparison with the mix impeller, better mass transfer rate and lower power consumption was observed by the same combination of Concave blade impeller. Comparison between the mix impeller, better performance is observed when lower impeller is Concave blade.

4.4. Gas-liquid phase

The characteristic of fluid dynamics in gas-liquid stirred tank is generally understood through the mechanism of interaction between the two phases in terms of mass transfer. The design and scale-up of these reactors generally depend on the quantification of the hydrodynamics and transport characteristics of the system that are mainly dependent on the way dispersed phase is dispersed throughout the tank (Ranganathan and Sivaraman, 2011). Studies based on gas-liquid phase in stirred tank of dual impeller were done by several researchers like Bouaifi et al. (2001); Kerdouss et al. (2006 & 2008); Suhaili et al. (2010); Ranganathan and Sivaraman (2011); Taghavi et al. (2011) to predict the various process dynamics in stirred tank.

The influence of impeller positions is of great concerned in dual impeller system and its influence in gas-liquid condition of standard system were studied by Machon et al. (1988); Hudcova et al. (1989); Garcia-Cortes et al. (2004); Saravanan et al. (2009). Garcia-Cortes et al. (2004) observed better efficiency of the system when impeller clearance depth and impeller spacing is equal to 0.33*D*. Saravanan et al. (2009) found better gas hold up when impeller clearance depth is *D*/3 and impeller spacing equal to impeller diameter. Hudcova et al. (1989) stated that for a spacing between impellers larger than 0.67*D*, the power drawn by the dual impeller system approximates twice that of the single impeller system. However, Abrardi et al. (1990) and Chiampo et al. (1991) argue that this maximum value can be reached at an impeller spacing less than 0.67*D*.

There is always lack of appropriate efficient configuration for a particular system. The hydrodynamics in terms of flow pattern created in dual impeller system of single phase condition as discussed in the above (section 4.3) might be different from gas-liquid phase condition. The optimal configuration of impeller position in unbaffled system employed with dual Concave blade impeller stirred tank is not available yet in the literature. Thus, this section will be stressed on to study the influence of impeller positions on different process dynamics and to indentify the optimal configuration which can be considered as efficient system. Based on this optimal configuration, a design criterion for each process dynamics will also be developed. To predict the flow pattern in gas-liquid phase of dual Concave blade stirred tank in unbaffled condition will also be presented in this section.

4.4.1. Optimal C_1 and C_2 based on K_La_{20}

First attempt in dual impeller system is concerned about the impeller spacings as diameter of impeller (d/D=0.3) has already been identified as optimal when tank diameter is constant in single phase system. So, in sparged system C_1 & C_2 were found out based on mass transfer coefficient when d/D is 0.3. The univariant approach as mentioned above in single phase section, one variable say C_1 is fixed in order to find C_2 and vice versa has been employed with several combinations of C_1 & C_2 for finding optimal points.

In first step, C_1 is fixed at 0.25D and made vary for C_2 from 0.2 to 0.6D; tested at different impeller speed (N=300 to 800 rpm). Figure 4.38 shows the comparison of K_La_{20} for different C_2/D at different impeller speed when C_1 is fixed and found higher K_La_{20} when C_2 /D is 0.4. So, the first optimal combination of C_1 & C_2 is 0.25D & 0.4D respectively.

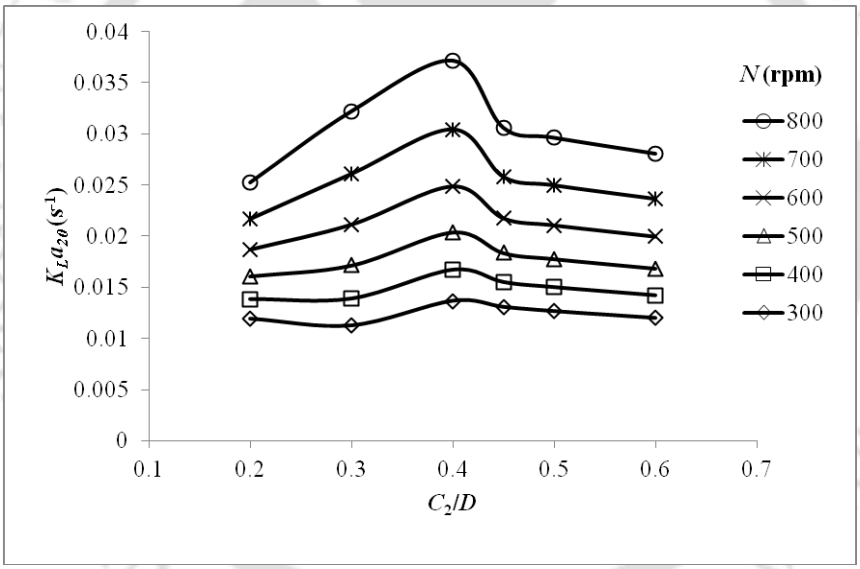

Figure 4.38: Variation of K_La_{20} for different C_2/D at C_1=0.25D

Next is to fix the C_2 value at 0.4D which was achieved as optimal point in the earlier figure. Figure 4.39 shows the comparison of K_La_{20} for different C_1/D (0.25 to 0.45) at various impeller speeds when S_2 is fixed at 0.7D (using of S_2 term has similar reason given in the above single phase section). In this figure, higher K_La_{20} is observed when C_1 is at 0.3D. So, the second optimal point is at C_1=0.3D and C_2 =0.4D (C_2 =S_2- C_1).

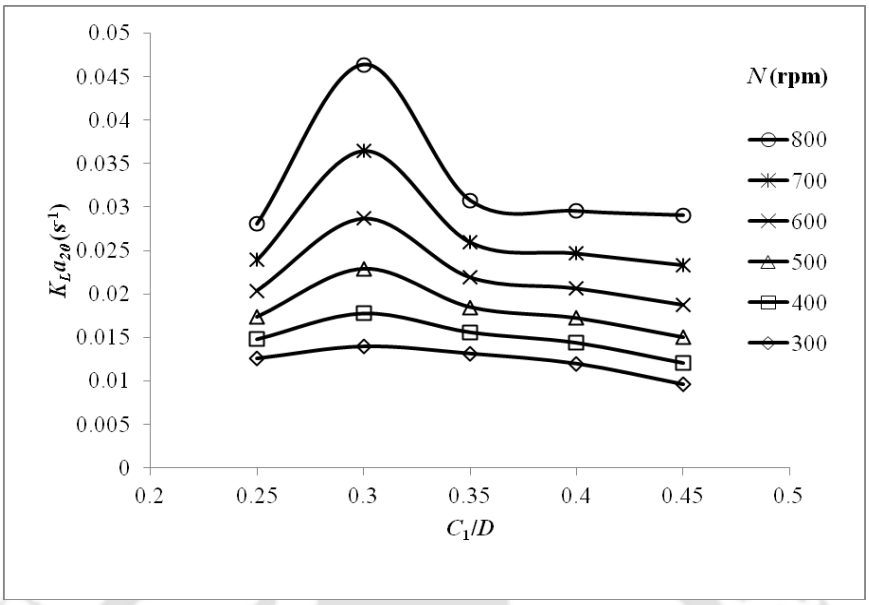

Figure 4.39: Variation of K_La_{20} for different C_1/D at S_2=0.7D

Figure 4.40 shows the variation of K_La_{20} for different C_2/D (0.15D to 0.6D) when C_1 is fixed at 0.3D at various N and found higher K_La_{20} by C_2=0.4D. So, the third optimal combination is at C_1=0.3D & C_2=0.4D.

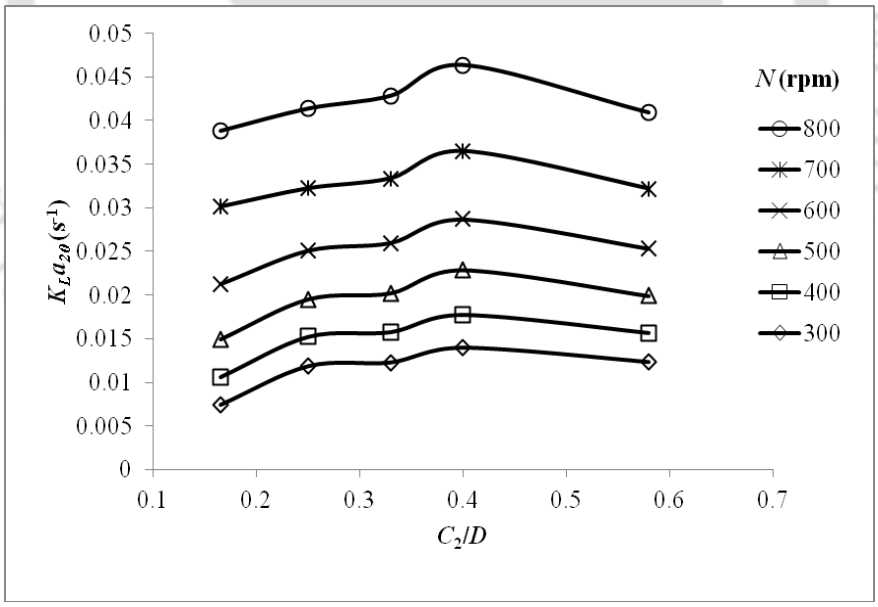

Figure 4.40: Variation of K_La_{20} for different C_2/D at C_1=0.3D

Again, C_1 is fixed at 0.35D to find the next combination of C_2 and shown in Figure 4.41 the variation of measured K_La_{20} for different C_1/D (0.2 to 0.53) at various N. This figure

indicates that higher K_La_{20} is produced when C_2 =0.45D. So, the fourth optimal combination is at C_1=0.35D & C_2 =0.45D.

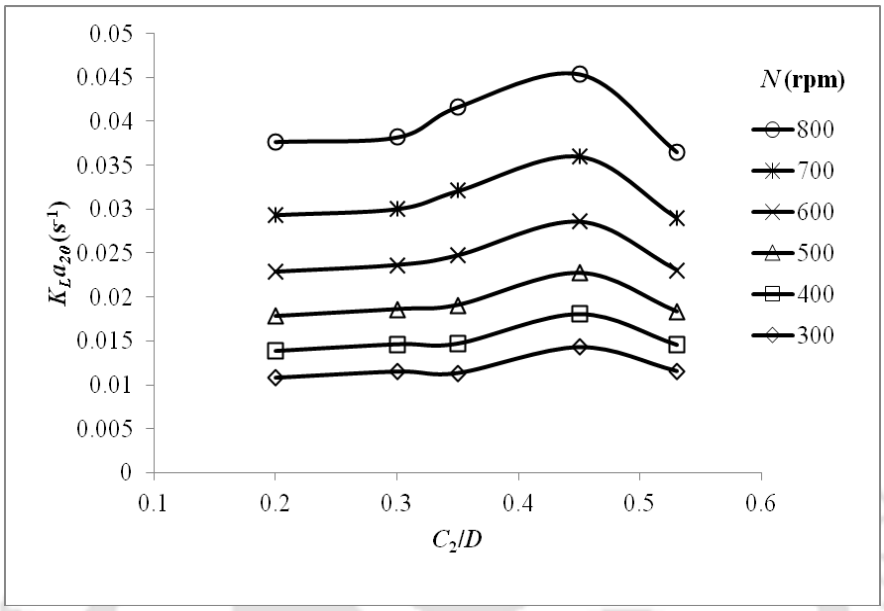

Figure 4.41: Variation of K_La_{20} for different C_2/D at C_1=0.35D

Now, C_1 is fixed at 0.4D and variation of K_La_{20} is plotted at different C_2/D and higher K_La_{20} is observed at C_2 =0.4 (Figure 4.42). Fifth optimal point is at C_1=0.4D & C_2=0.4D.

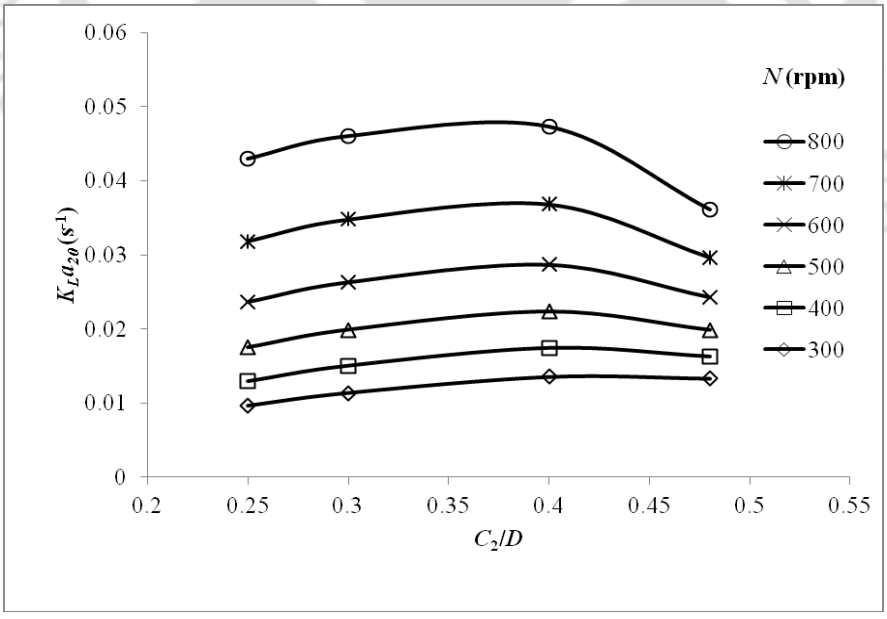

Figure 4.42: Variation of K_La_{20} for different C_2/D at C_1=0.4D

The last observance is made by fixing C_1 at 0.45D and K_La_{20} is plotted for different C_2 /D (0.25 to 0.48) at various impeller speeds shown in Figure 4.43. Higher K_La_{20} is shown by C_2 =0.35D, so, the last optimal point achieved is at C_1=0.45D & C_2=0.35D.

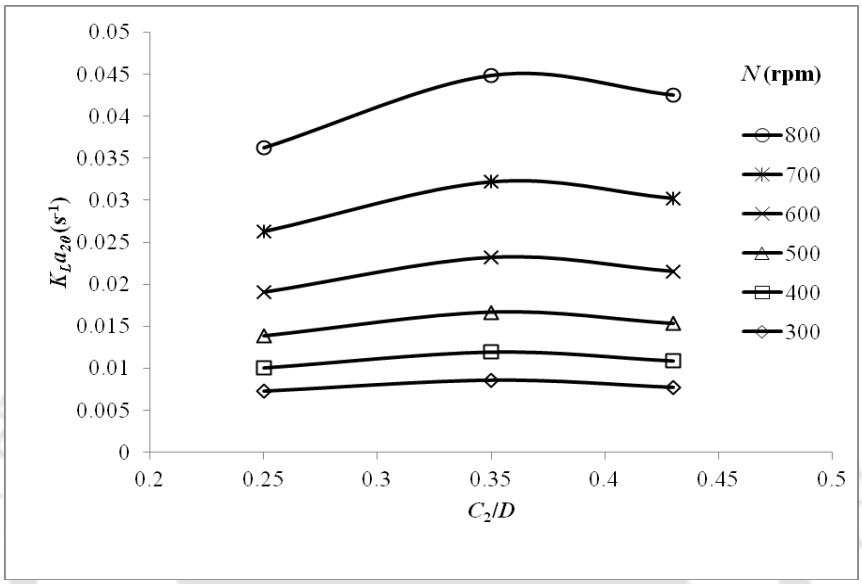

Figure 4.43: Variation of K_La_{20} for different C_2/D at C_1=0.45D

Five optimal combinations of C_1 & C_2 based on mass transfer coefficient have been achieved so far. In order to indentify the local and global optimal points, Table 4.10 compares the K_La_{20} at fix N value for different optimal points of C_1 & C_2. Based the observed K_La_{20}, the combination of C_1=0.3D & C_2=0.4D gives highest (0.023s^{-1}) among the other combinations and hence, this point is considered as global optimal point of C_1 & C_2.

Table 4.10: Optimal configurations of C_1 and C_2 based on K_La_{20}

Sl. No.	**C_1**	**C_2**	**K_La_{20} at 500 rpm**	**Remarks on optimal**
1	0.25D	0.4D	0.020	Local
2	**0.3D**	**0.4D**	**0.023**	**Highest K_La_{20} (global)**
3	0.35D	0.45D	0.022	Local
4	0.4D	0.4D	0.022	Local
5	0.45D	0.35D	0.017	Local

4.4.2. Numerical modeling

Based on the global optimal point, a numerical model of the unbaffled dual Concave impeller system with sparged condition is modeled by using CFD techniques as done in the sparged section of single impeller in Chapter 3. The details of the modeling are not covered in this

Chapter as the same is given in Chapter 2. Figure 4.44 shows the generated grid of the dual impeller stirred tank with sparging system (ring sparger) and it's coarsen grid surface.

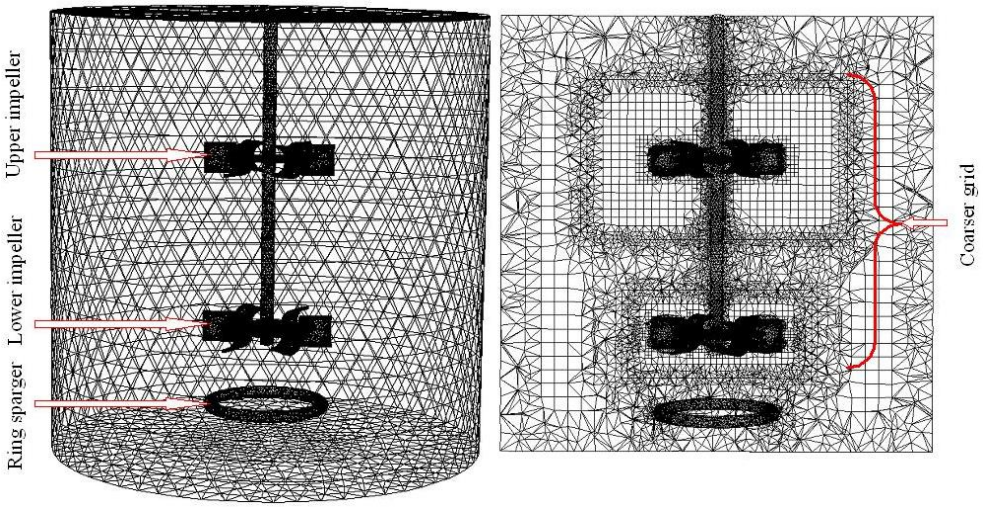

Figure 4.44: Generated grid of the stirred tank

4.4.2.1. Flow pattern

Prediction of flow pattern for the different phases (liquid and gas) is an important parameter in numerical for understanding the hydrodynamics of the turbulent flow when sparged condition is applied. Figure 4.45(a-e) shows the flow pattern defined by mean velocity vectors for liquid (left) and gas phase (right) at different optimal configurations of C_1 & C_2. In all the cases, the liquid flow pattern is greatly affected by gas inflow of additional gas supply (Q_g=1L/min) through ring sparger below the lower impeller. Maximum amount of intense liquid flow circulation is predicted near and around the impeller blade. The effect of gas inflow can be observed from this Figure 4.45(a-e) as the well known liquid flow circulation loop (seen in single phase system) one below the blade and one above the blade are not created (Figure 4.45 left side) at all in this gas-liquid system. This is how the sparged system is different from single phase system in terms of flow pattern. Instead of forming the liquid circulation loop above and below the impeller blade, these loops are seen created away from blades. The flow pattern in sparged condition of dual impeller with Concave blade impeller produces very uncommon and interesting flow pattern which is totally different from single phase system. The only circulation loop that can be seen is on the upper part of the lower impeller. The upper impeller could make liquid circulation loop either above or below the blade. Enough space for fully circulation of liquid flow is not available above the

blade by the upper impeller and hence could not make circulation loop above the blade. Due to the influence of lower impeller, the circulation loop could be created below the blade by the upper impeller. Also by the lower impeller circulation loop is not created below the blade due to the strong influence of gas inflow from sparger. The influence of gas inflow is more when impeller clearance depth (C_1) is lower. Smooth axial liquid flow circulation between the two impellers is predicted when C_1 is not greater than 0.3D but when C_1 is greater than 0.3D, the liquid flow movements are likely taking place in different directions when C_2 is fixed at 0.4D.

(a) C_1=0.25D, C_2=0.4D

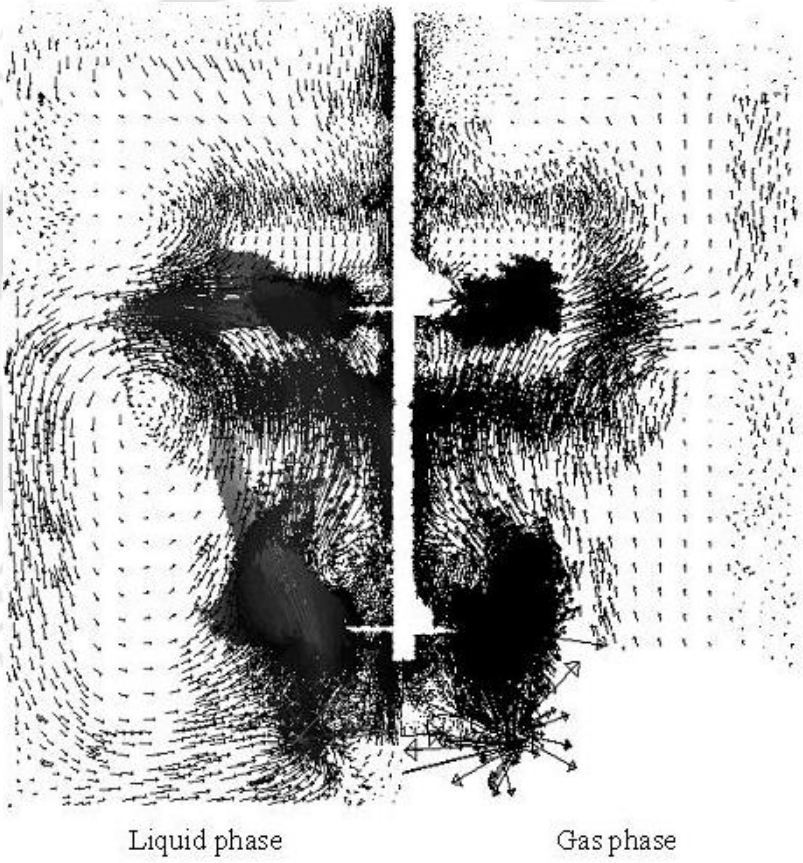

(b) C_1=0.3D, C_2=0.4D (c) C_1=0.35D, C_2=0.45D

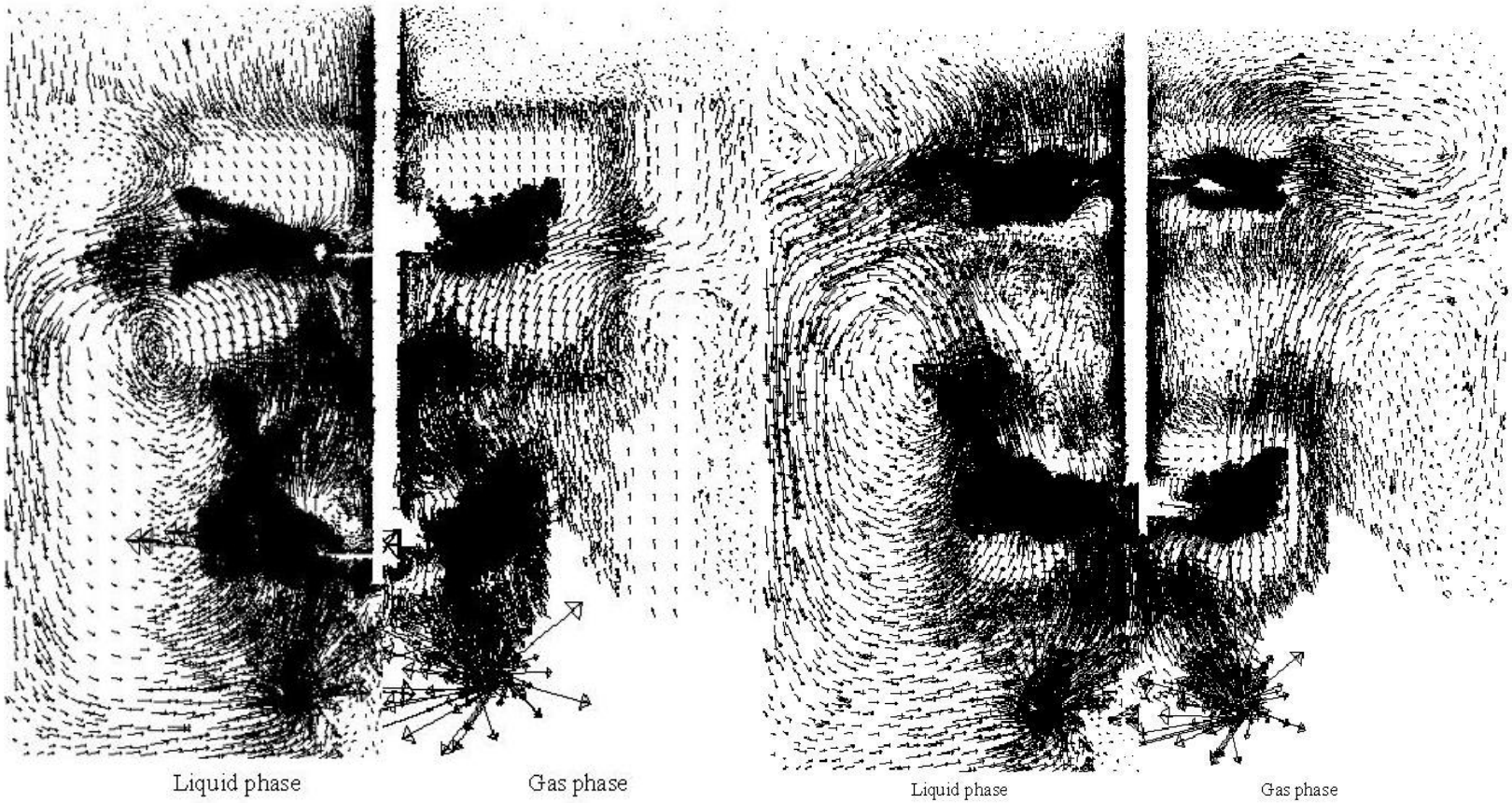

(d) C_1=0.4D, C_2=0.4D (e) C_1=0.45D, C_2=0.4D

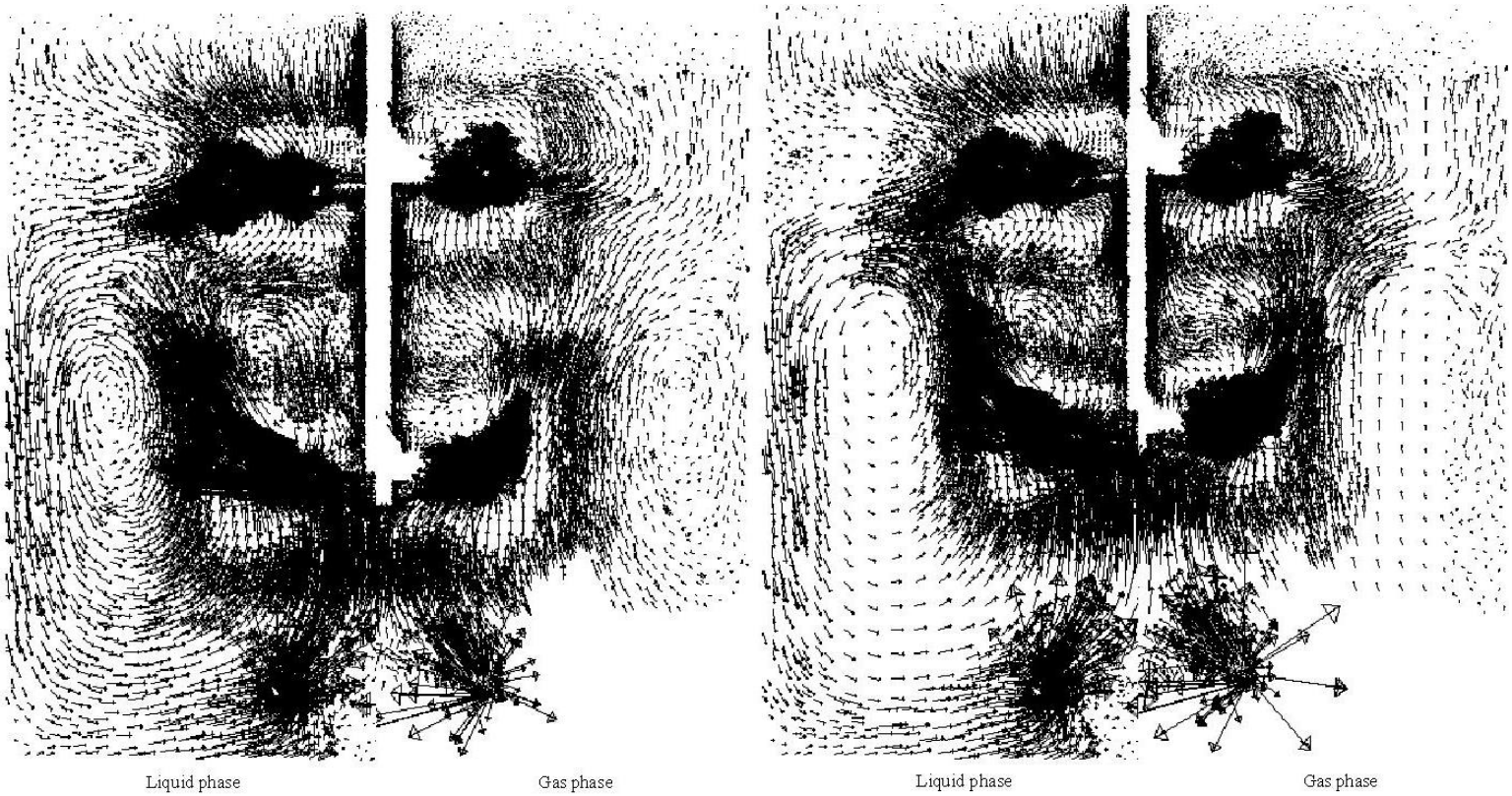

Figure 4.45: Comparison of the velocity vectors of liquid phase and gas phase for (a-e) optimal configurations of C_1 and C_2 at mid plane of the tank (y=0).

In case of gas flow pattern (Figure 4.45a-e right side), maximum amount gas flow is predicted at the sparger and at and around the impeller region. There is complete gas flow circulation taking place above the sparger spreading across the entire vessel upto free liquid surface, however, at the bottom corner of the tank, there is lack of gas flow circulation and operates almost like single phase system. But this region is not in greater volume and can be covered up by the liquid flow circulation and expect that it does not affect much on the gas-liquid dispersion mechanism and eventually on the performance of the whole system. However, one can avoid such dead zone area by re-consideration on sparger system.

4.4.2.2. Gas volume fraction

Prediction of gas volume fraction is required in sparged system in order to estimate the mass transfer coefficient and is important factor to understand the distribution of gas inside the vessel when mix with liquid. Figure 4.46(a-e) shows the gas volume fraction for different optimal C_1 & C_2 configuration at the vertically middle of the tank (left) and at impeller plane (right). Maximum amount of gas accumulation takes place at the sparger; near and around the impeller; between the sparger and lower impeller; between two impellers and on the free liquid surface (Figure 4.46 left). The gas volume fraction is seen like a gas flow going upwards from the sparger striking the blades of lower impeller upto upper impeller then radially deviates towards the tank wall 50 % of gas reaches to the free liquid surface and remaining flow returns in downward direction. But this phenomenon is not significant when lower impeller clearance depth is higher (C_1>0.35D i.e., C_1=0.4 & 0.45D) while C_2 is constant (C_2=0.4D) in Figure 4.46d & e. The impeller plays important role to the gas flows which are circulating downwards after striking its blade. So, when lower impeller height (C_1) is higher, the gas flow becomes slow the moment when it strikes the blade of lower impeller and eventually could not produce sufficient strong flow to upward direction and strikes the upper impeller and returns downward. Because of the slow movement of gas flow due to the greater height of lower impeller when C_2 is constant, the recirculation gas flow caused by the radially imparted flow of the upper impeller is not able to form. The accumulation of gas volume predicted on the free liquid surface is because of the outside atmospheric condition as the top of the tank is not fully closed allowing outside gas to mix with liquid inside the vessel. As seen from the right side of Figure 4.46, the gas volume fraction at the two impeller plane shows that higher gas accumulation is produced by the upper impeller as compared

with the lower impeller at all the cases of different optimal points. Maximum gas accumulation at both the planes (y=0, z=0.3D & 0.7D) predicted higher at experimentally observed global point (C_1=0.3D, C_2=0.4D). The reason for accumulating lesser amount of gas by the lower impeller may be because of the sudden effect of gas outflow from sparger which could not make flow in radial direction eventually decreases its flow spreadness especially in radial direction. So, at the lower impeller plane the gas accumulation happen only on axial direction not at radial direction and eventually decreasing its intensity on this plane. But in case of upper impeller which produces higher gas accumulation may be because of the involvement of radial flow as well as axial flow and it makes better gas accumulation. Lesser amount of gas accumulation is predicted at the bottom of the tank below the sparger as compared with other regions of the vessel.

(a) C_1=0.25D, C_2=0.4D

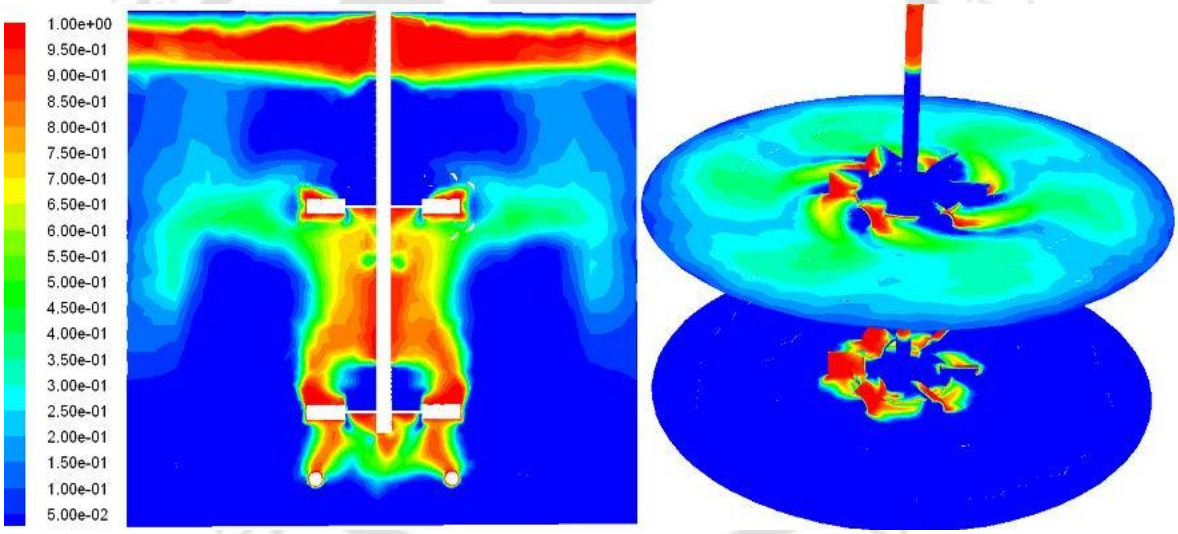

(b) C_1=0.3D, C_2=0.4D

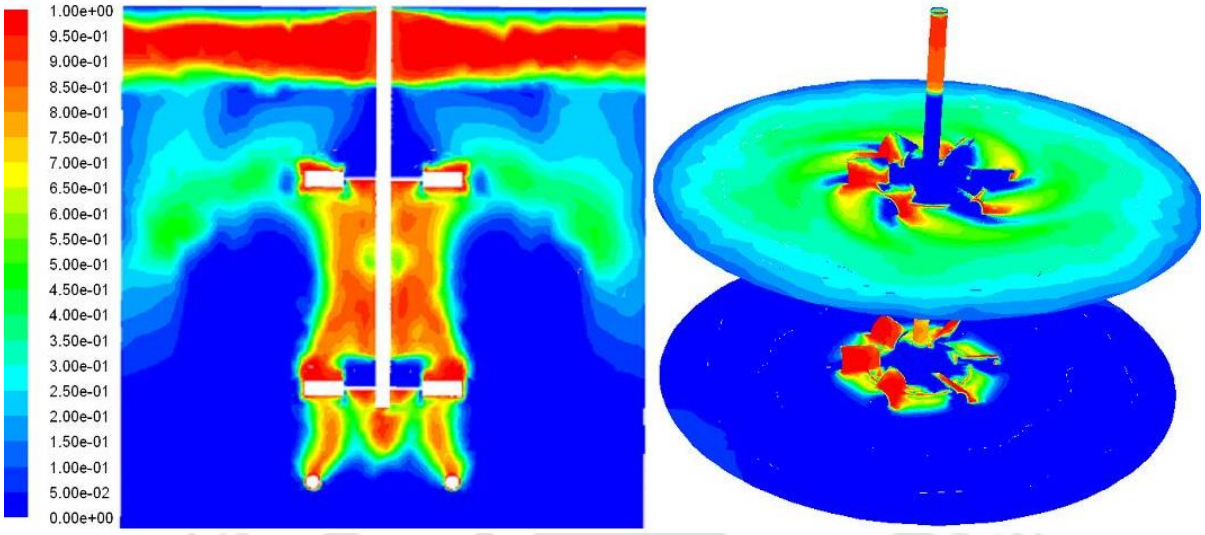

(c) C_1=0.35D, C_2=0.45D

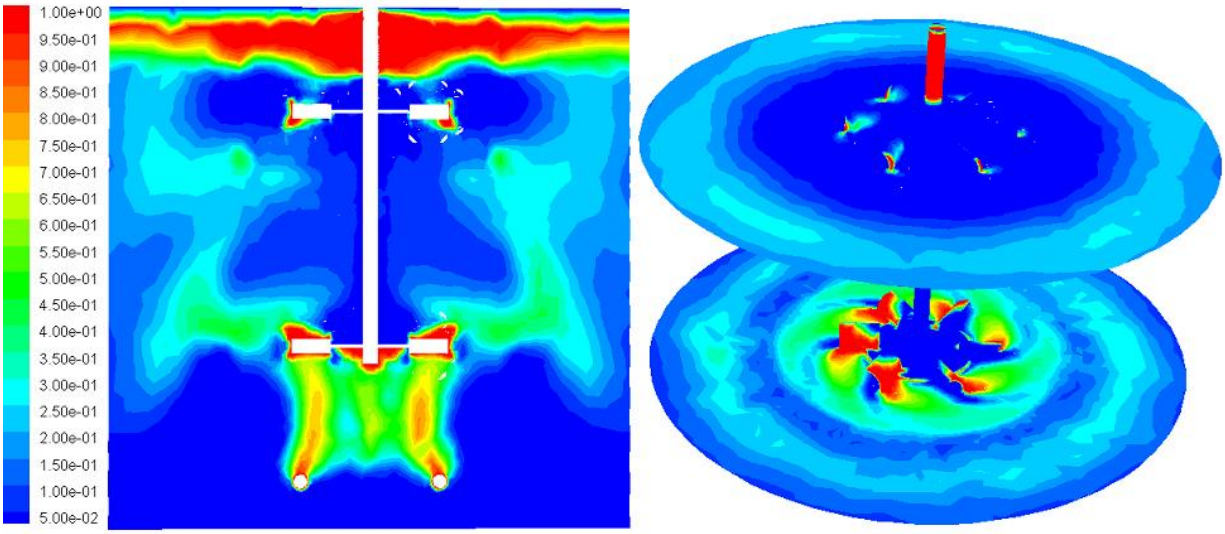

(d) C_1=0.4D, C_2=0.4D

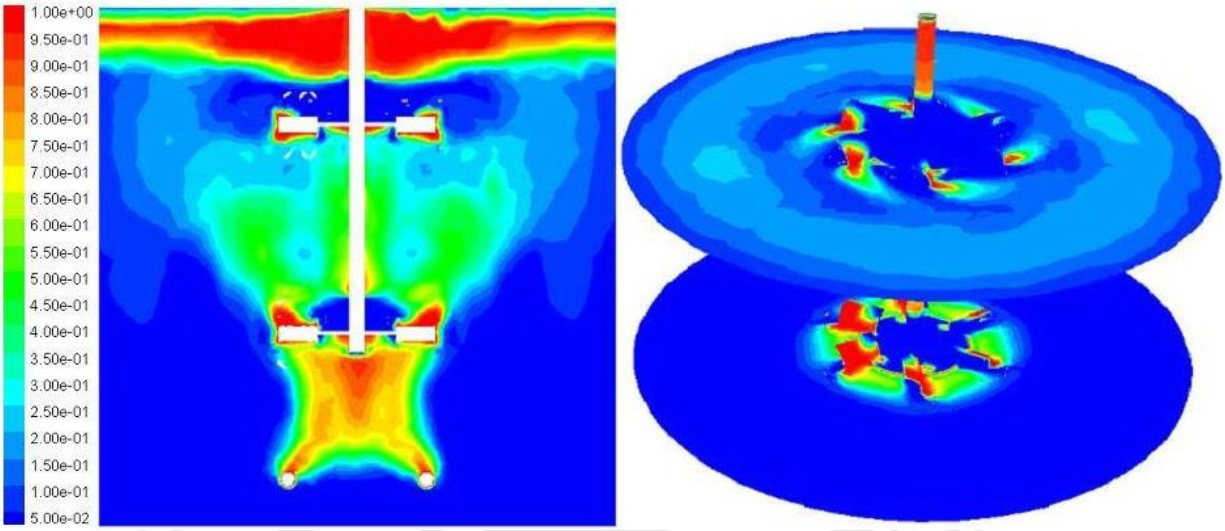

(e) C_1=0.45D, C_2=0.4D

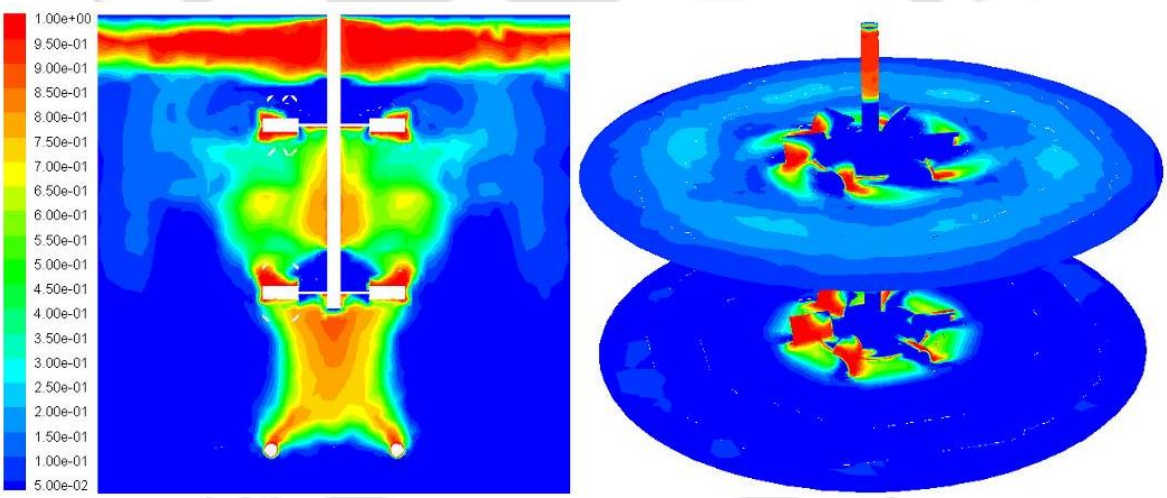

Figure 4.46: (a-e) Gas volume fraction of different C_1 and C_2 configuration at mid plane of the tank (y=0) (left) and at impeller planes (right).

4.4.2.3. Mass transfer co-efficient

Even though gas volume fraction is directly related with mass transfer coefficient, one cannot fully dependent only on this parameter for understanding mass transfer rate as the phenomenon of mass transfer is very complex involving several mechanisms. The estimation of $K_L a_{20}$ by Danckwerts (1951) model requires liquid turbulent dissipation rate, viscosity of liquid and diffusion coefficient apart from the interfacial specific area. So, to overcome the

understanding of mass transfer rate only on gas volume fraction, Figure 4.47(a-e) shows the local distribution of K_La_{20} for different optimal C_1 & C_2 configurations. Lesser amount of K_La_{20} is predicted at a small region just above the impeller blade except at two optimal point (C_1=0.3D & C_2=0.4D and C_1=0.35D & C2=0.45D) and lower part of tank. Highest amount is predicted at the sparger and at impeller tip. The maximum amount of K_La_{20} is predicted comparably when C_1=0.3D & C_2=0.4D among the other configuration as seen from Figure 4.48b & c. In these configurations, better mass transfer is seen predicted just above the upper impeller in contrast to other configuration where lowest K_La_{20} is predicted. This is an indication of better mixing of gas and liquid phase for better performance of the system. By experimental observation also, higher amount of K_La_{20} were observed at this optimal point (Table 4.9).

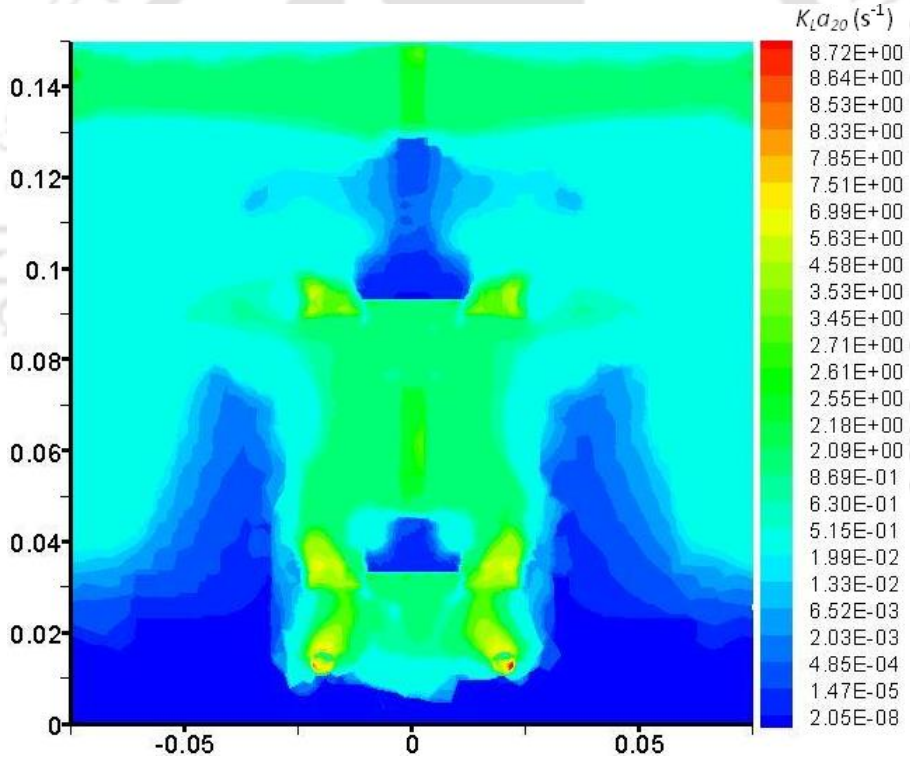

(a) C_1=0.25D, C_2=0.4D

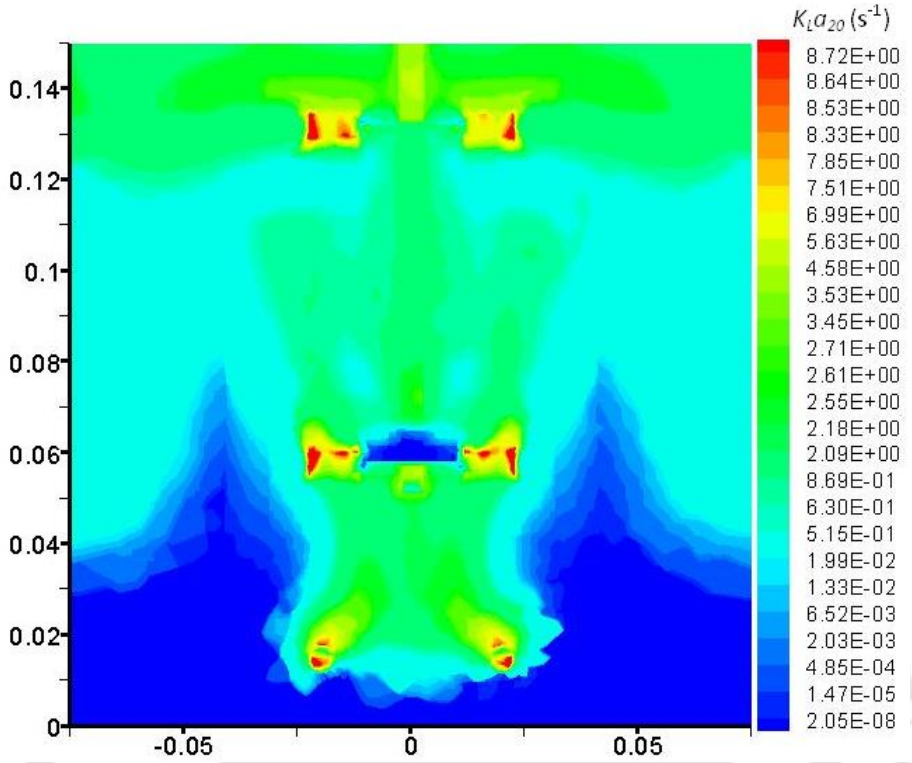

(b) C_1=0.3D, C_2=0.4D

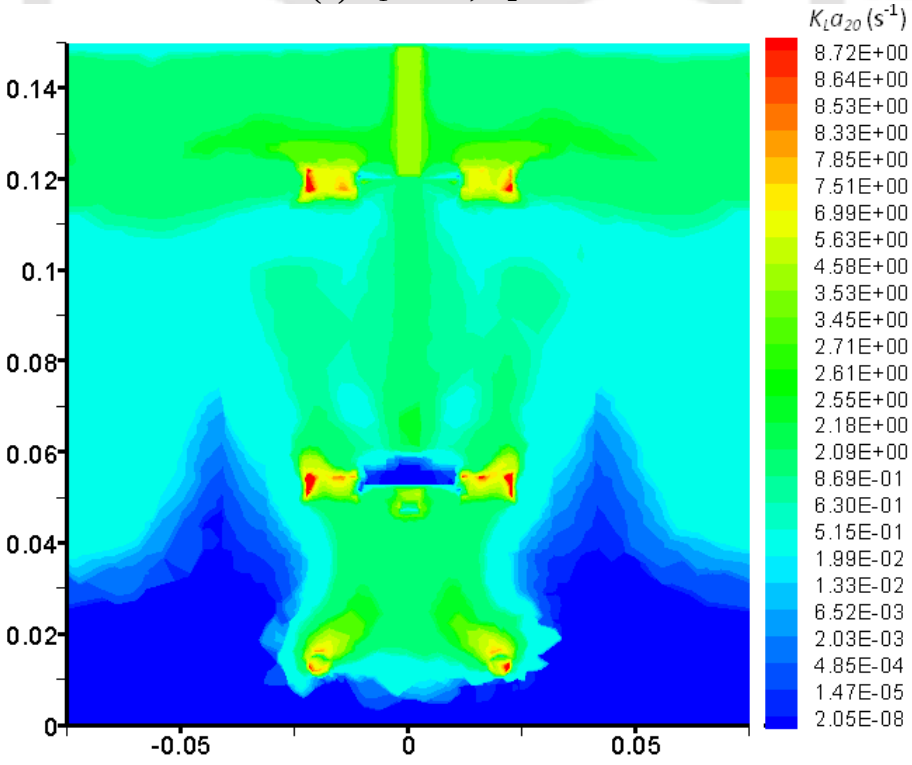

(c) C_1=0.35D, C_2=0.45D

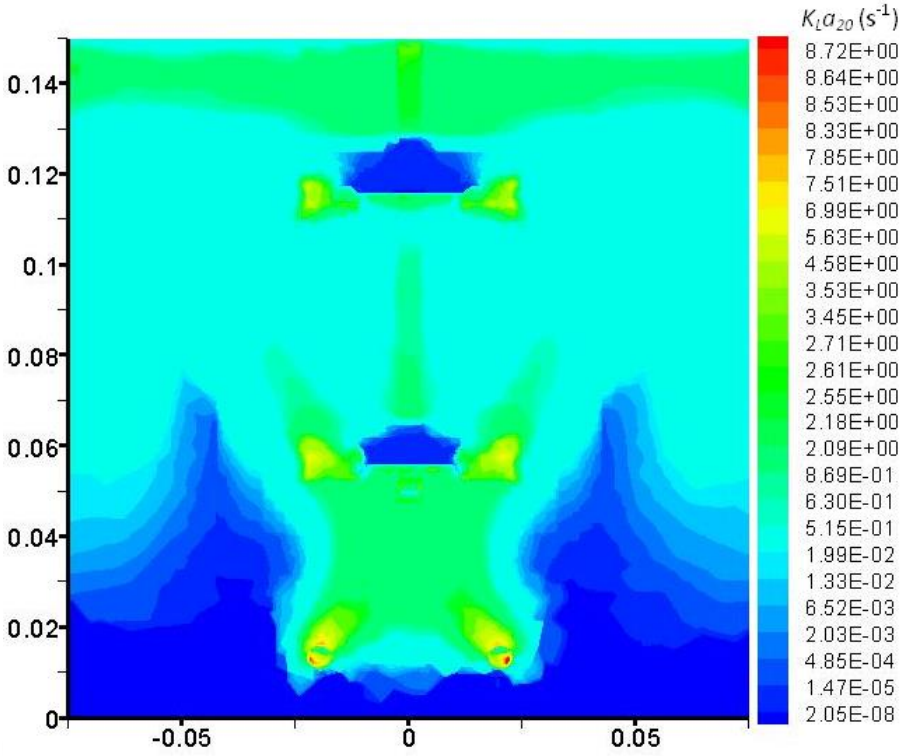

(d) C_1=0.4D, C_2=0.4D

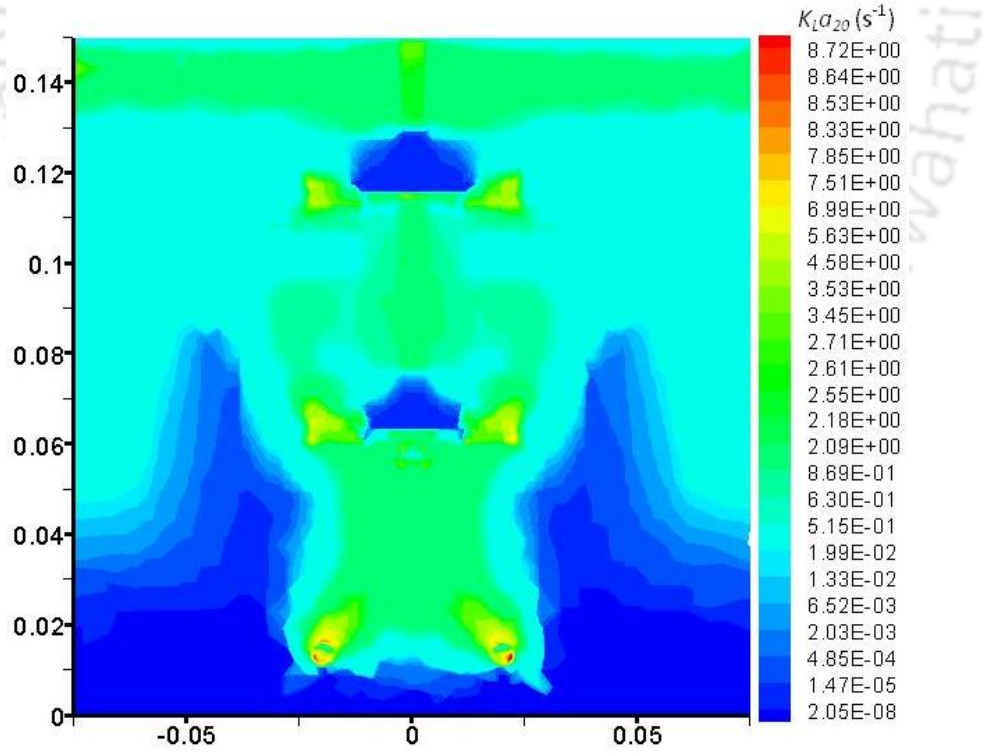

(e) C_1=0.45D, C_2=0.4D

Figure 4.47: Contours showing distribution of predicted $K_L a_{20}$

As seen from the above figure, the local distribution of K_La_{20} at different C_1 & C_2 configuration provides important information of the spreadness of mass transfer rate across the vessel when different impeller spacings are applied. Such distribution clearly made understandable inside phenomenon of the stirred tank when mass transfer mechanism is concerned and one can make improvement, adjustment and reconsideration of the design geometry.

Graphically plotting of the predicted K_La_{20} at specific position can make more into the distribution pattern of mass transfer rate. Figure 4.48 shows the distribution of K_La_{20} at different radial positions (r=0.023, 0.03 & 0.05m) in axial direction. This figure indicates that highest amount of K_La_{20} is occurred at impeller tip (r=0.023m) and its magnitude decreases as the radial distance is nearer the tank wall. It also depicts that the peak point of K_La_{20} is occurred at impeller plane and at the ring sparger.

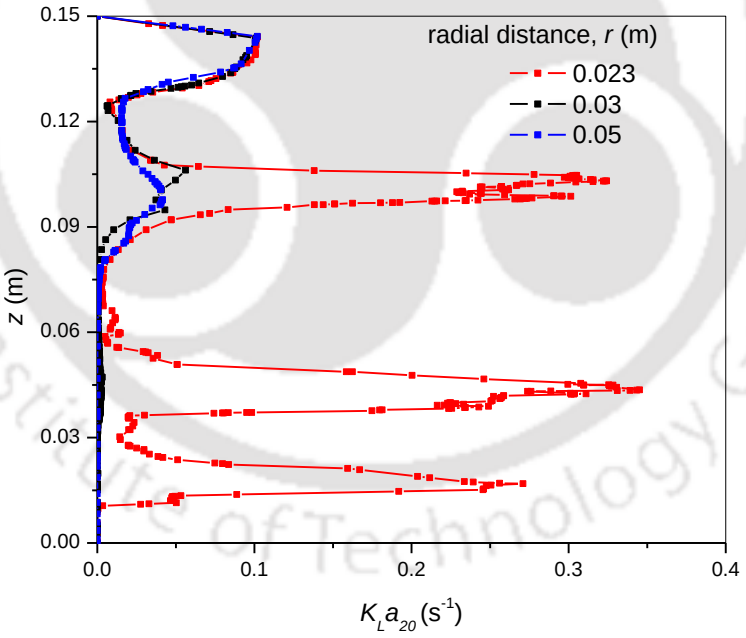

Figure 4.48: Graphical representation of predicted K_La_{20} at different radial positions (r) for global optimal

The comparison of predicted K_La_{20} with observed value is tabulated in Table 4.11. There is fair agreement of predicted K_La_{20} with observed values and calculated value by using Van't Riet (1979) equation. The prediction errors are within the acceptable range (not more than 15%) except at the last point which is 26.09%.

Table 4.11: Measured and predicted K_La_{20} at N=500 rpm

Sl. No.	C_1	C_2	P_g/V	K_La_{20}			
				Expt.	**Van't Riet Eqn.**	**CFD**	**Prediction error %**
1	0.25D	0.4D	3322.01	0.020	0.0211	0.0231	11.68
2	0.3D	0.4D	3586.26	0.023	0.0217	0.0259	11.58
3	0.35D	0.45D	3397.51	0.022	0.0213	0.0256	11.32
4	0.4D	0.4D	3284.26	0.022	0.0210	0.0237	5.91
5	0.45D	0.35D	3699.51	0.017	0.0220	0.0209	20.09

4.4.3. Development of scale up criteria

4.4.3.1. Mass transfer rate

In dimensionless form, for dual impeller system k_c is written as:

$$k_c = f\left(d/D, C_1/D, C_2/D, Fl, Re, Fr\right) \tag{4.39}$$

So, Equation 4.39 suggest that for constant d/D, C_1/D and C_2/D (considering only the global optimal) and v_g is also taken as constant then k_c is a function of Fl, Re and Fr only.

$$k_c = f\left(Fl, Re, Fr\right) \tag{4.40}$$

Equation 4.40 suggests that k_c can be simulated by considering all the three variables Fl, Re and Fr. An attempt has been made to simulate k_c with Fl results in scale effect as shown in Figure 4.49. Similar attempts with Re and Fr are shown in Figure 4.50 & 4.51 and witnessed scale effects.

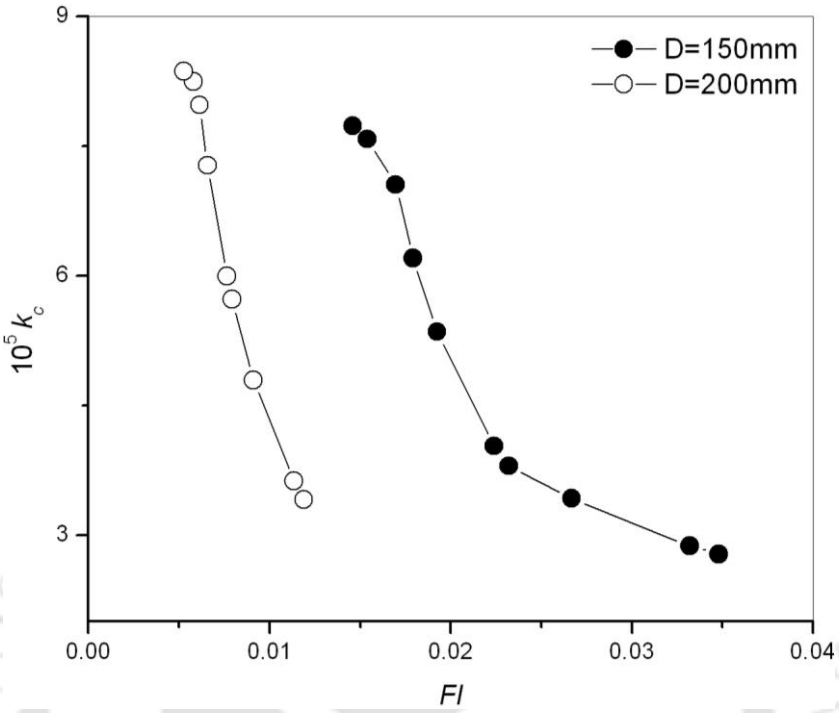

Figure 4.49: *Fl* with k_c

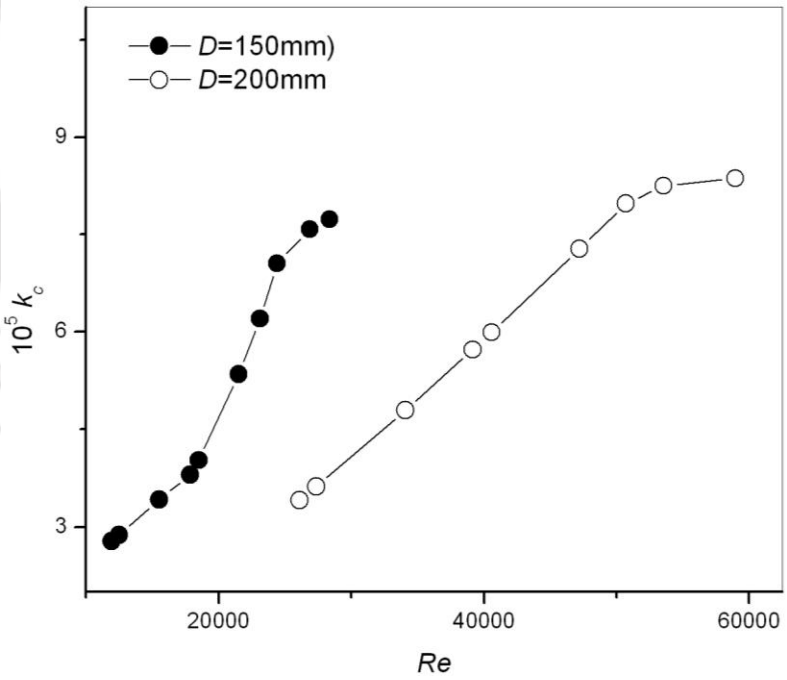

Figure 4.50: *Re* with k_c

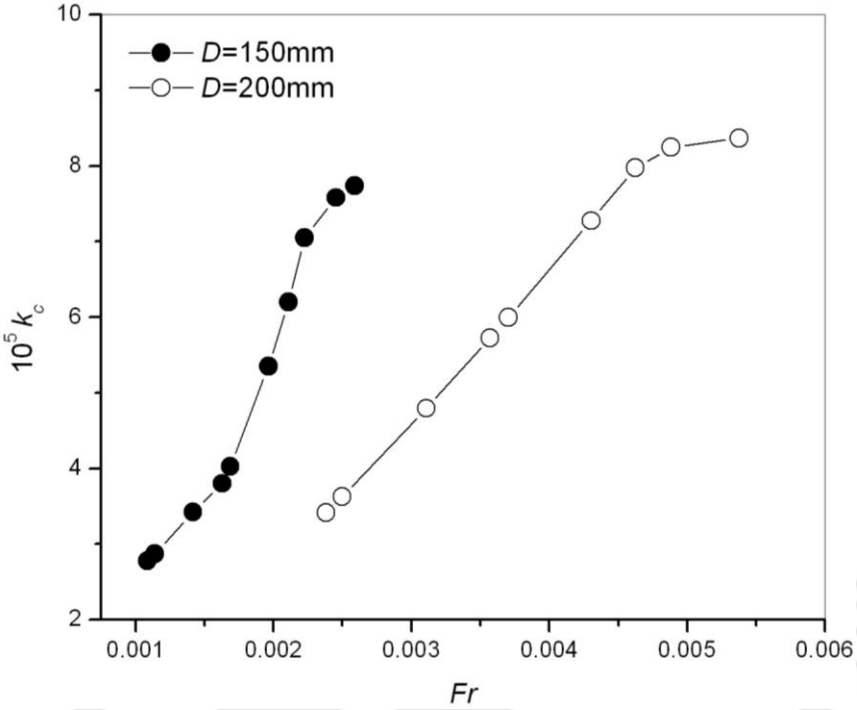

Figure 4.51: *Fr* with k_c

As *X* is function of *Re* and *Fr*, k_c (Equation 4.40) can be written as:

$$k_c = f\left(Fl, X\right) \tag{4.41}$$

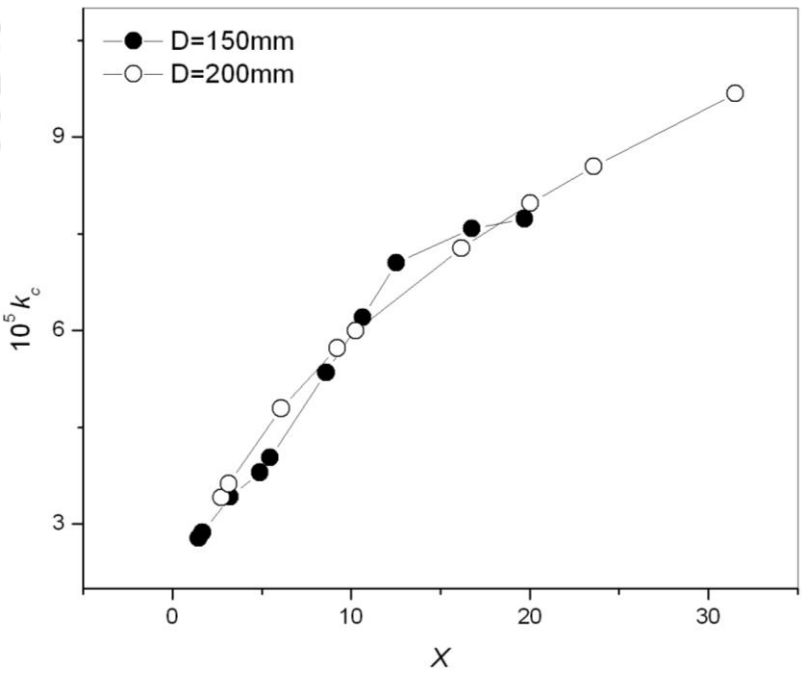

Figure 4.52: *X* with k_c

As seen in the Figure 4.49, the scale effects come into play with Flow number. However, it is also tried to analyze the effect of X on k_c as shown in Figure 4.52. The process cannot be uniquely simulated by X alone as shown in the Figure 4.52. The effect of scale is present in the Figure 4.52. Thus, it can be said that mass transfer in sparged systems is dependent on the functional form of the Equation 4.41, where independent parameters are Fl and X. The functional form of the Equation 4.41 has been derived statistically as (Table 4.12):

Table 4.12: Details of predicted k_c

Generated equation	α	β	γ	**Overall std. error**
$k_c = \alpha Fl^{\beta} X^{\gamma}$	2.41 (9.2e-2)	0.029 (8.47e-2)	0.44 (1.21e-2)	3.05e-2

The statistical detail of the developed relationship is tabulated in Table 4.12 and parity plot is shown in Figure 4.53.

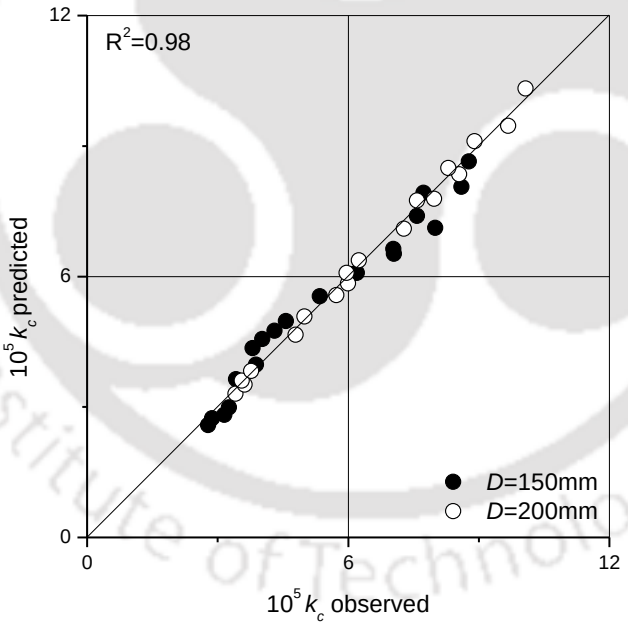

Figure 4.53: Prediction of k_c

4.4.3.2. Correlations of power consumption

The dimensionless form of power consumption in gassed is written as (details in Chapter 3 sparged system part):

$$\frac{P_g}{P_u} = f\left(Re, Fr, Fl\right) \tag{4.42}$$

As P_g/P_u is shown as a function of *Re*, *Fr* and *Fl*, scale effects on these dimensionless number can be a useful information for scale up purposes. Figure 4.54(a-c) shows the scale effect of P_g/P_u by *Re*, *Fr* and *Fl* respectively for two tank diameter.

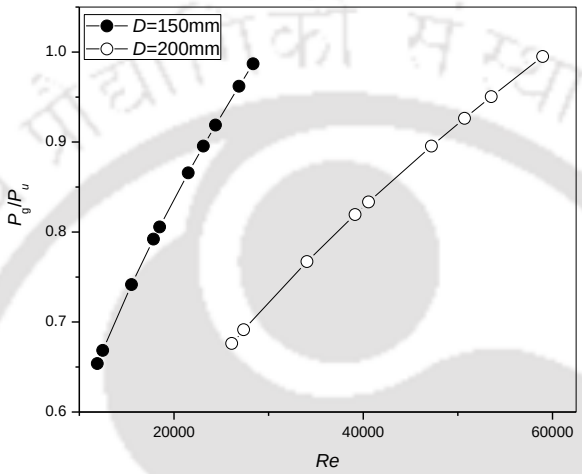

(a) Scale effect shown by *Re*

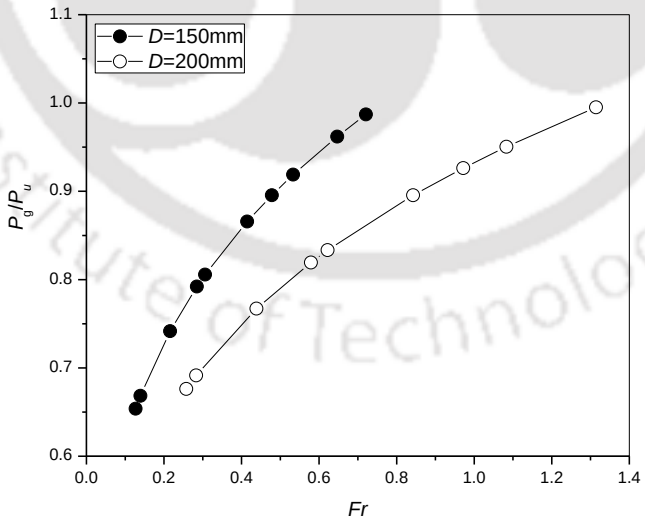

(b) Scale effect shown by *Fr*

P_g/P_u also increases with increasing Froude number for the two tank diameter (Figure 4.54b) but it decreases with increase in Flow number (Figure 4.54c).

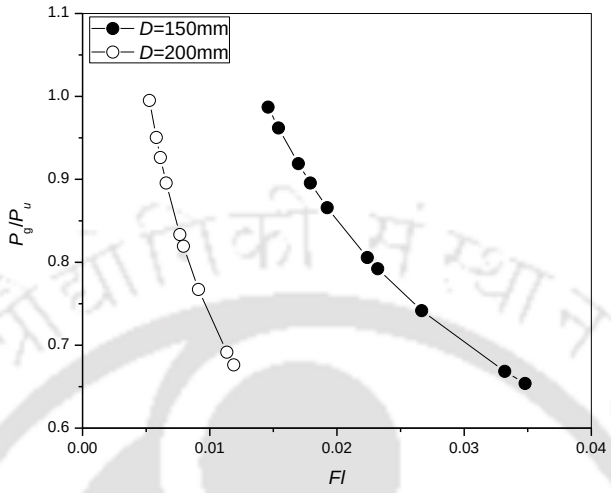

(c) Scale effect shown by *Fl*

Figure 4.54: Scale effect in terms of P_g/P_u with *Re*, *Fr* and *Fl*

Equation 4.42 can be written as:

$$P_g / P_u = f(Fl, X) \tag{4.43}$$

Unlike to single phase, presence of gas flow rate suggests that scale effect will be there in simulating the power consumption with *X* only as shown in the Figure 4.55.

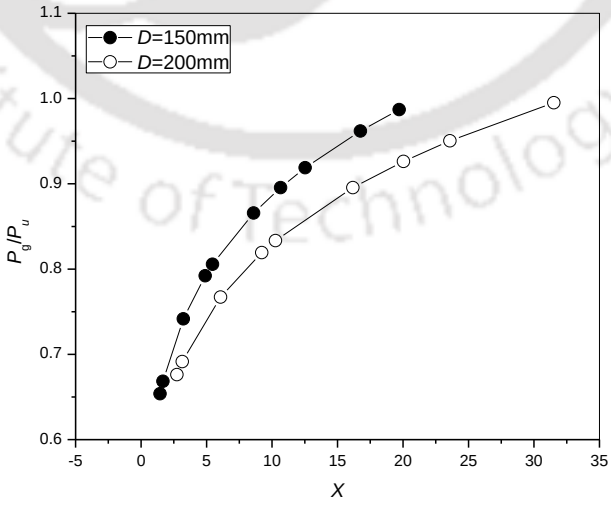

Figure 4.55: Scale effect shown by *X*

Thus, in gas-liquid system P_g/P_u is simulated based on Fl and X and its simulated graph is shown in Figure 4.56. The statistical detail of the simulated equation is tabulated in Table 4.13.

Table 4.13: Details of predicted P_g/P_u

Generated equation	***α***	***β***	***γ***	**Overall std. error**
$\frac{P_g}{P_u} = \alpha Fl^{\beta} X^{\gamma}$	0.57 (1.43e-2)	-0.005 (6.16e-3)	0.15 (7.24e-3)	2.89e-2

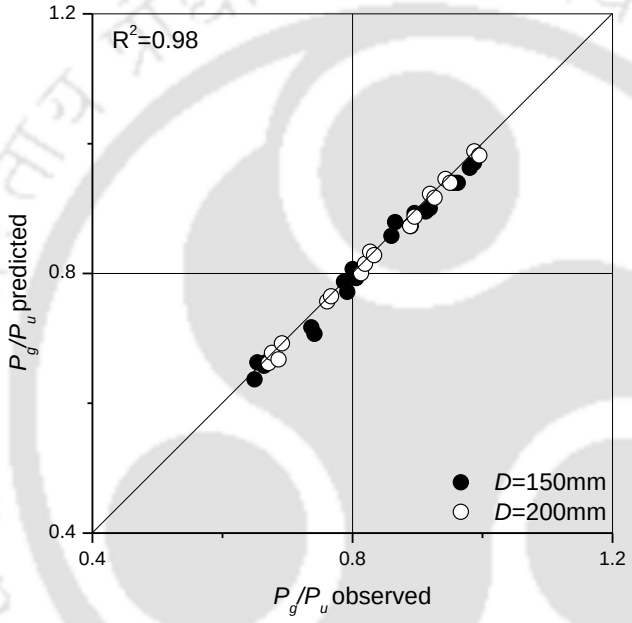

Figure 4.56: Prediction of P_g/P_u

4.4.3.3. Gas hold up *(ε_G)*

From Equation 3.49 used in single impeller system is extended for dual system as:

$$\varepsilon_G = f\left(d, D, C_1/D, C_2/D, v_g, P/V\right) \tag{4.44}$$

Thus in dimensional form Equation 4.44 is given as:

$$\varepsilon_G = f\left(d/D, C_1/D, C_2/D, Fl, P_v\right) \tag{4.45}$$

So, at global optimum point d/D, C_1/D and C_2/D are constant and eliminated from Equation 4.45; hence written as:

$$\varepsilon_G = f\left(Fl, P_v\right) \tag{4.46}$$

Statistical details and parity plot of Equation 4.46 is given and shown in Table 4.14 and in Figure 4.57 respectively.

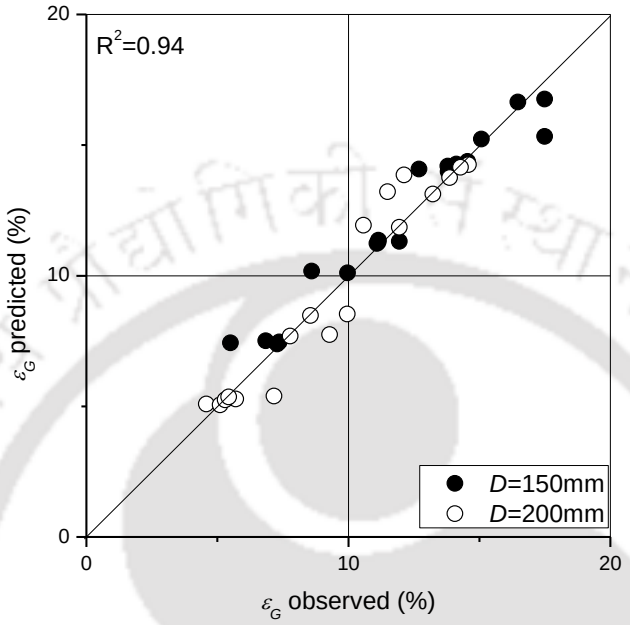

Figure 4.57: Prediction of ε_G

Table 4.14: Details of predicted ε_G

Generated equation	***α***	***β***	***γ***	**Overall std. error**
$\varepsilon_G = \alpha F l^{\beta} P_v^{\gamma}$	4.73 (3.931e-3)	0.009 (1.40e-2)	0.65 (1.18e-2)	2.34e-2

4.4.4. Comparative studies

Comparison of unbaffled Concave blade impeller system is made with Rushton, baffled and mix (combination of Concave blade and Rushton) impeller system for 150mm tank diameter. So, K_La_{20} is plotted against N and P_g in order to understand mass transfer rate and power consumption in different geometrical condition.

4.4.4.1. With unbaffled Rushton

Unbaffled dual Concave impeller system is compared with Rushton impeller system shown in Figure 4.58 & 4.59. K_La_{20} plotted at different impeller speed and observed higher K_La_{20} by Concave blade than the Rushton impeller (Figure 4.58).

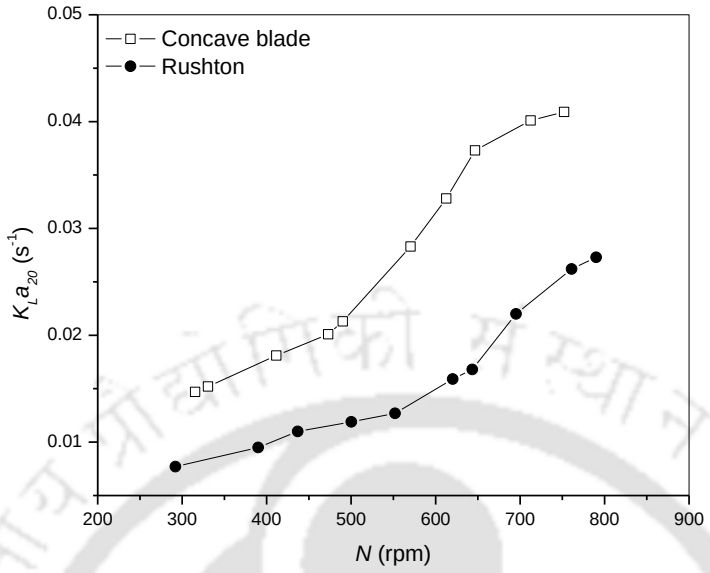

Figure 4.58: N with $K_L a_{20}$

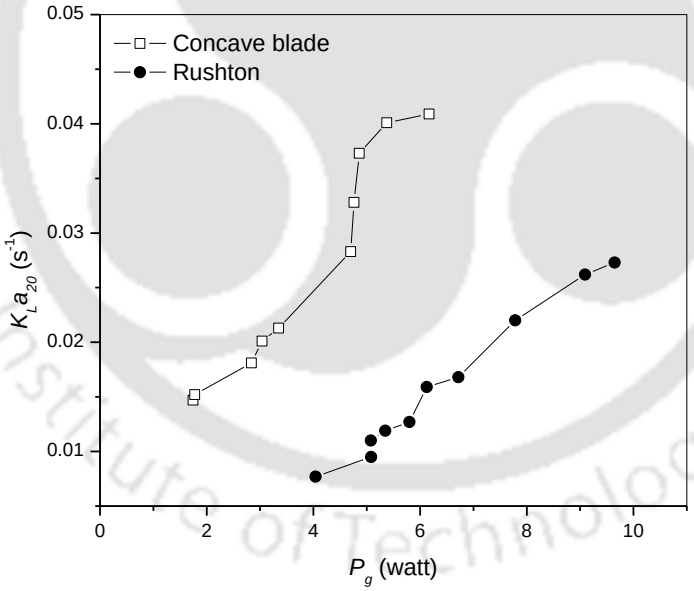

Figure 4.59: P_g with $K_L a_{20}$

P_g is observed higher by Rushton impeller than the Concave blade type when the same amount of $K_L a_{20}$ is to be achieved.

4.4.4.2. With baffled Concave blade

Unbaffled Concave blade impeller system is compared with baffled system in Figure 4.60 & 4.61. Baffled system produces higher K_La_{20} than the unbaffled system.

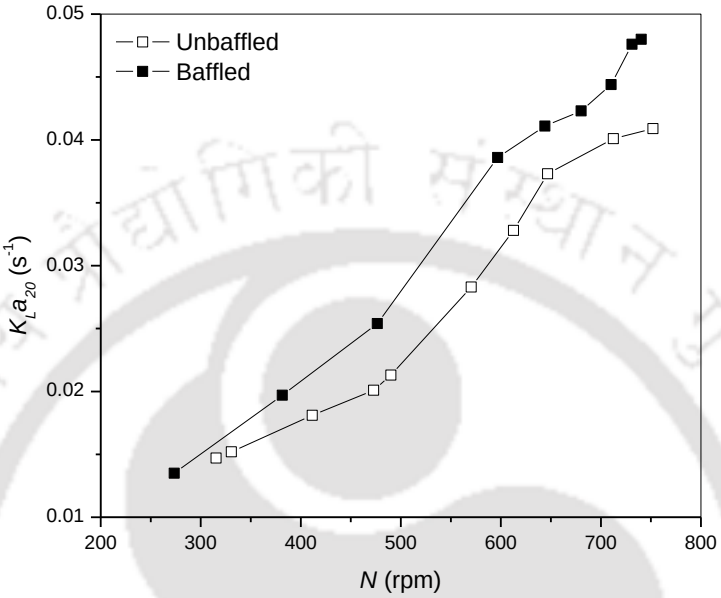

Figure 4.60: N with K_La_{20}

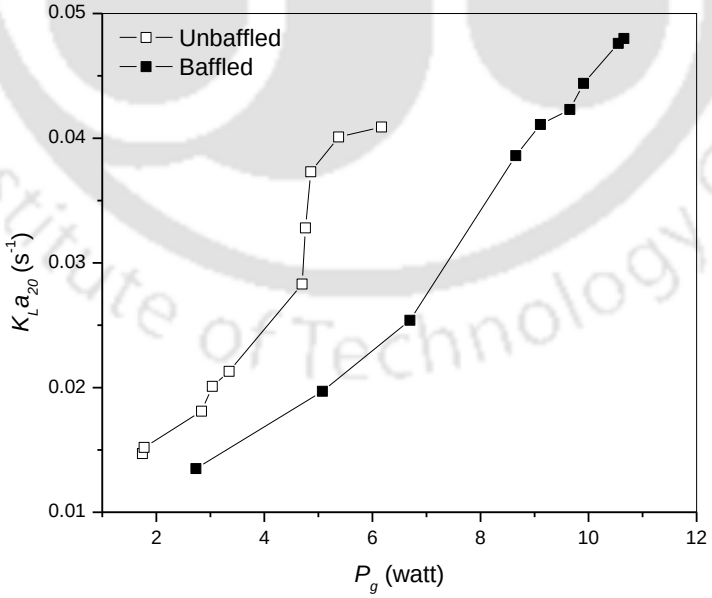

Figure 4.61: P_g with K_La_{20}

P_g is observed higher by baffled system than the unbaffled system. As discussed in the previous power consumption in single impeller system of single phase and sparged condition and in dual impeller of single phase system, the baffled system always consumes higher power than the unbaffled system. Reason may be similar explained above in these cases, that the baffled system creates more turbulent flow (that is why mass transfer rate is higher by baffled than the unbaffled system shown in Figure 4.60) as well as resistance to the movement of flow increasing higher effort by the fluid particles to drag themselves. This higher effort required to drag the fluid particles leads to produce higher torque to move the fluid particles and eventually increasing power consumption.

4.4.4.3. With unbaffled mix

The mix impeller is of two types here as per the position of the combination of impeller. When the Concave blade impeller is on the lower position, then we name as Concave blade+Rushton and when Concave blade is on upper position, it is term as Rushton+Concave blade impeller. Comparison of K_La_{20} for dual Concave blade, Concave blade+Rushton and Rushton+Concave blade found that dual Concave produces higher K_La_{20} than the other combination (Figure 4.62). And the mix combination, higher K_La_{20} is observed when Concave blade is on lower position.

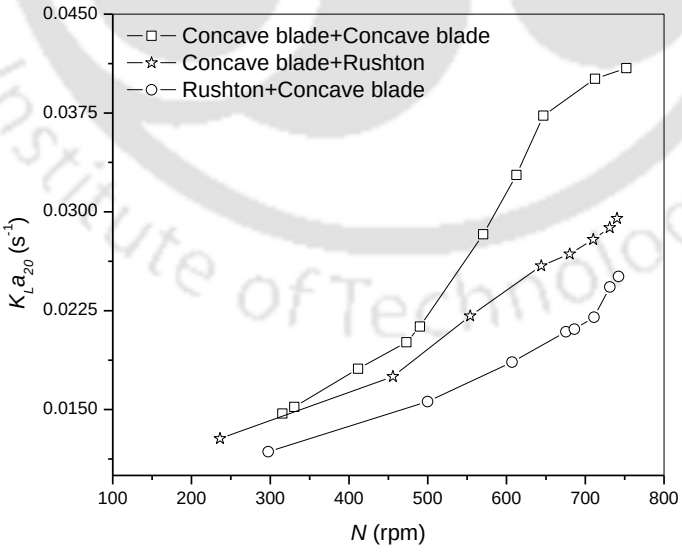

Figure 4.62: N with K_La_{20}

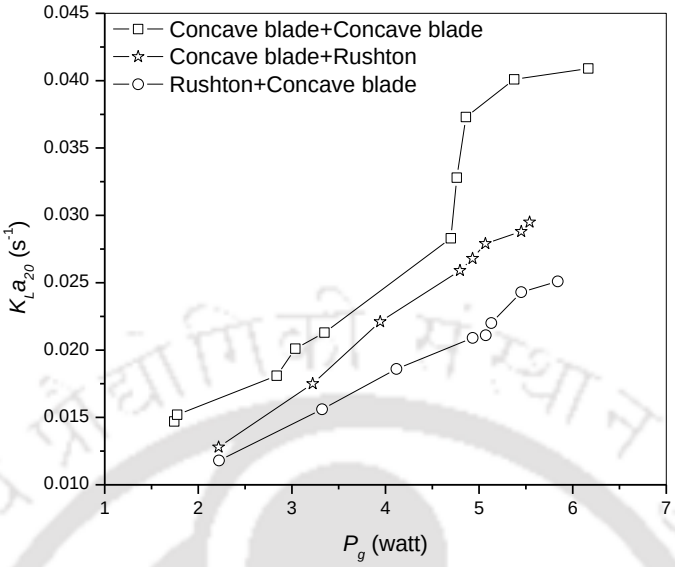

Figure 4.63: P_g with $K_L a_{20}$

The comparison of P_g shows that dual Concave blade consumes lesser power than the other combination of impeller. And in mix impeller combination, lesser amount of power consumption is observed when the position of Concave blade is below the Rushton impeller (Concave blade+Rushton combination) in Figure 4.63.

4.4.5. Conclusions

The dual Concave blade impeller system in sparged condition is experimentally studied based on different geometrical conditions in terms of mass transfer rate, power consumption and gas hold up. Finding of optimal impeller spacings (C_1 & C_2) was achieved through uni-variant approach. Based on the optimal point, a scale up criteria for each parameter has been developed.

After several combinations of C_1 & C_2 were experimentally investigated based on $K_L a_{20}$, the combination of optimal configurations of the system are found at C_1=0.25D & C_2=0.4D, C_1=0.3D & C_2=0.4D, C_1=0.35D & C_2=0.45D, C_1=0.4D, C_2=0.4D, C_1=0.45D & C_2=0.35D. Global optimum point because of highest $K_L a_{20}$ is observed at C_1=0.3D & C_2=0.4D and minimum $K_L a_{20}$ is observed at C_1=0.45D & C_2=0.35D.

Based on the optimal configuration, flow patterns of the two phases, gas volume fraction and K_La_{20} were modeled through CFD tools. The behavior of the liquid flow in sparged system is totally different from single phase system. There is no formation of circulation loop predicted in this sparged condition except one loop above the lower impeller. Strong flow circulation of liquid and gas is predicted at the sparger, at the impeller tip and around the impeller region. The bottom corner of the tank below the sparger is operates almost like single phase. The maximum amount of K_La_{20} is predicted when C_1=0.3D & C_2=0.4D among the other configuration. So, the local distribution of K_La_{20} at different C_1 & C_2 configuration provides important information of the spreadness of mass transfer rate across the vessel when different impeller spacings are applied. Such distribution clearly made understandable inside phenomenon of the stirred tank when mass transfer mechanism is concerned and one can make improvement, adjustment and reconsideration of the design geometry. There is fair agreement of predicted K_La_{20} with observed values and calculated value by using Van't Riet (1079) equation. The prediction errors are within the acceptable range (not more than 15%).

The observed mass transfer rate in terms of k_c is increased when *Re*, *Fr* and *Fl* is increased in sparged system. The scale up criteria for mass transfer rate is developed as: $k_c = 2.41Fl^{0.029}X^{0.44}$. In contrast to k_c, P_g/P_u decreases with increasing *Re*, *Fr* and *Fl*. P_g/P_u is developed for geometrically similar system as: $\frac{P_g}{P_u} = 0.57Fl^{-0.005}X^{0.15}$. And for has hold up, it is developed as: $\varepsilon_G = 4.73Fl^{0.009}P_v^{0.65}$.

Comparison on observed results of mass transfer and gassed power consumption were also made between Concave blade with Rushton, unbaffled with baffled system and with mix impeller system. Better performance (higher K_La_{20} and lesser P_g) was observed by Concave blade type than the Rushton impeller. Baffled system gives better mass transfer rate but consumes higher amount of power as compared with unbaffled system, so, unbaffled system may be considered as more efficient system where reduction of power is a priori. From the comparison of same combination of Concave blade with mix impeller, the better performance by dual Concave blade type impeller is observed. When Concave blade is kept as lower impeller, higher performance is observed in the system but not more than dual Concave blade system.

CHAPTER 5

APPLICATION OF COMPUTATIONAL FLUID DYNAMICS IN STIRRED TANK MODELING

5.1. Introduction

In recent years, Computational Fluid Dynamics (CFD) techniques are being increasingly used as a substitute for experiments to obtain the detailed flow field for a given set of fluid, impeller and tank geometries (Ranade et al., 1991; Um and Hanley, 2008). Using CFD, one can understand the mechanism of mixing of fluids in mixing tanks with much easier and economical means than the use of experiments (Rao and Sivashanmugam, 2010). The total mixing in a stirred tank depends on the mean flow and turbulence, which in turn also depends on the shape of impeller (Dewan et al., 2006). An advantage of CFD based methods is that the fundamental equations governing fluid flow are solved and thus the scaling up and scaling down problems are eliminated (Jahoda et al., 2007).The success story of CFD simulation in the studies of stirred tanks is long list including the study done by Ranade et al. (1997); Aubin et al. (2004); Deglon and Meyer (2006); Jahoda et al. (2007); Yapici et al. (2008); Gimbun et al. (2009); Zadghaffari et al. (2010); Taghavi et al. (2011); Huang and Li (2013); Mohiuddin et al. (2013) and many more. A CFD modeling can predict the complex turbulent flow pattern; it can give details of velocity and other dissipative scale characteristics at any region of the vessel. It can also be able to predict power consumption and mass transfer rate of the stirred tank system.

This chapter details the application of Computational Fluid Dynamics in stirred tank modeling by comparing simulated results with experimental results of published literature. Concave blade type is compared with Rushton impeller in single impeller as well as in dual impeller system. The system is studied in single phase as well as in gas-liquid phase condition. This numerical study predicts flow pattern, velocity and dissipative scales, power consumption and mass transfer rate in such system. Figure 5.1 gives the modeled impeller types used in this study.

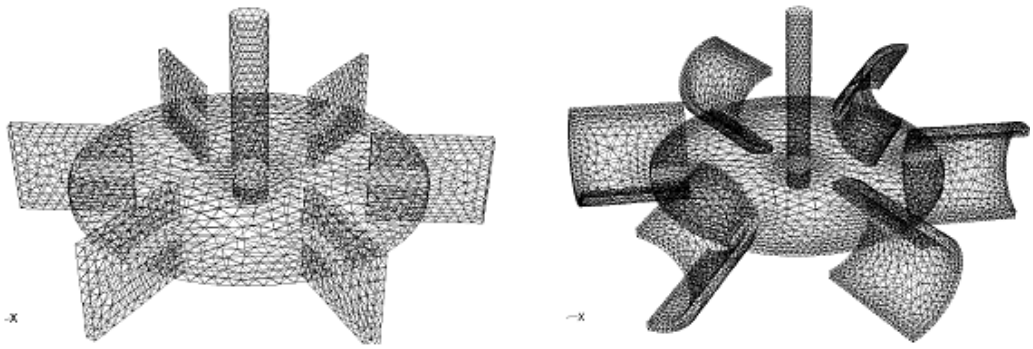

Figure 5.1: Modeled impeller types used in this study

5.2. Single phase

Single impeller is studied in single phase as well as in gas-liquid phase system. The velocity profile and other dissipative scales are compared between Concave blade with Rushton impeller. The numerically predicted results are compared with the experimental results of Wu and Patterson (1989) which was carried out on single Rushton impeller with baffled system. They detailed the mean velocity profile at different regions of the vessel; and tried to give detail information of the spatial distribution of flow velocity and other turbulent characteristics.

5.2.1. Single impeller

5.2.1.1. Stirred tank geometry

In this study the dimensions of the stirred tank being taken is same with the dimensions used by Wu and Patterson (1989). Baffled cylindrical tank diameter (D) of 27cm of Rushton impeller and Concave blade impeller having diameter (d) 9.3cm at the speed of 200rpm (N) mounted on a shaft at an axial height (C) of $D/3$ from the tank bottom was being modeled. Working fluid is water at 20^0C temperature (density=998.2 kg/m^3; dynamic viscosity=0.001003 Pa.s) and filled at an equal height of tank diameter (i.e. 27cm). Figure 5.1 shows the schematic diagram and generated grid of the stirred tank. Four number of baffle is employed with $D/10$ width and thickness of 1cm.

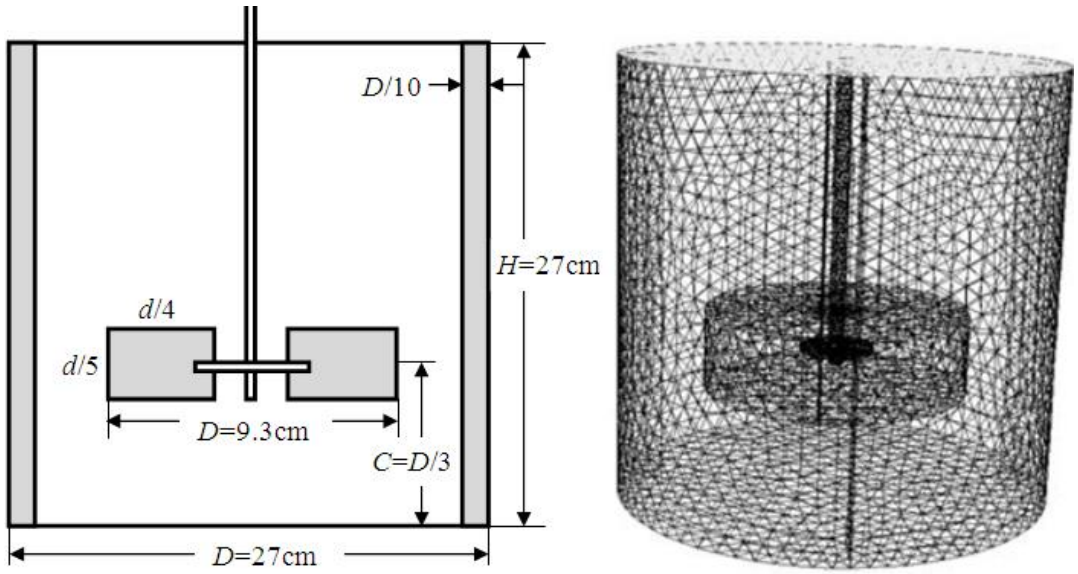

Figure 5.2: Details of stirred tank and grid generation

The number of blade for impeller is six inclined at the angle of 60^0. The sizes of tetrahedral grid (unstructured) generated in the model of stirred tank in this study of cells, nodes, faces are 236700, 480070 and 42856 respectively for Rushton impeller and for Concave blade are 835515 cells, 1685822 faces & 146998 nodes. All the analysis has been performed at 90 degree plane iso-surface and only half of the tank is considered for analysis.

5.2.1.2. Comparison of mean velocities

The mean velocites has been normalised by u_{tip}. An accurate CFD model should be able to predict characteristics features of a flow field in a stirred tank (Deglon and Meyer, 2006). Deglon and Meyer (2006) performed the CFD simulation of the experimental of Wu and Patterson (1989) for the analysis of the flow field in different grid sixes (i.e, 33000, 230000, 800000 and 1900000) and observed that the typical flow patterns was able to predict. Deglon and Meyer (2006) found that the coarse grid (230000) can not predict the formation of the trailing vortex pair generated at the tips of the impeller blade. Hence, Deglon and Meyer (2006) suggested from their results that it is possible to predict the general flow field in a stirred tank using relatively coarse grids but predicting more subtle phenomena in the flow field requires cosiderably finer grids. The simulated model was able to predict the typical flow patterns observed for a Rushton impeller in a baffled tank. The nature of flow and turbulent pattern of the CFD simulation model for Concave blade is observed same with the Rushton impeller exept at the tip region of impeller.

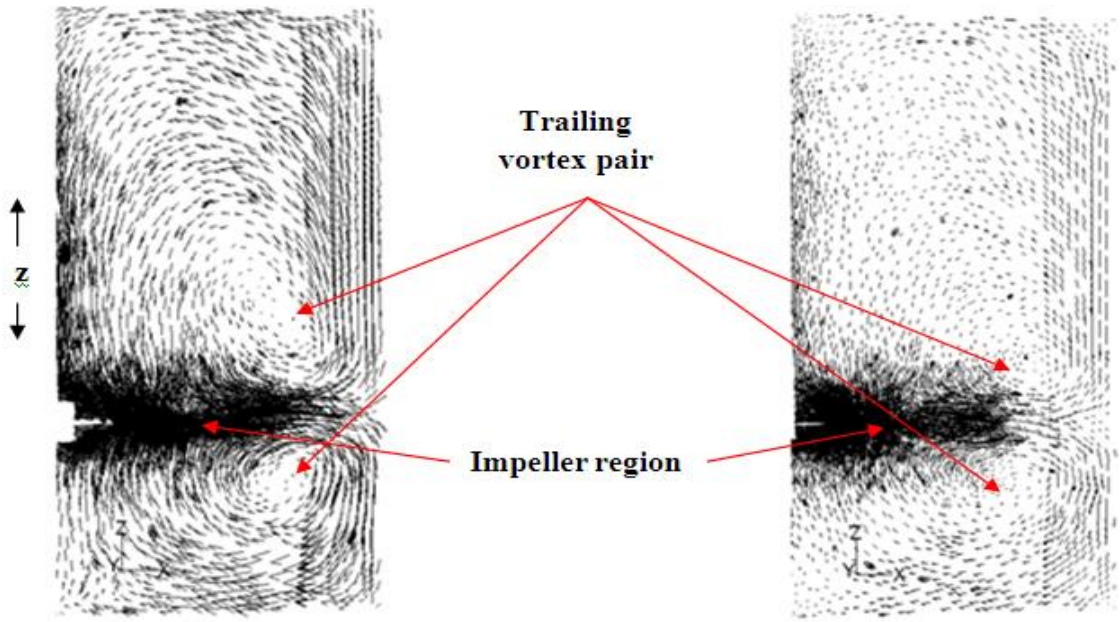

(a) (b)

Figure 5.3: Mean velocity magnitude at 90 degree plane (a) Rushton impeller and (b) Concave blade impeller

Figure 5.3 represents the mean velocity of (a) rushton impeller and (b) Concave blade impeller at 90 degree plane. The two trailing vortex is form one above the blade and one below the blade in both the cases of Rushton impeller and Concave blade impeller. High levels of turbulent kinetic energy is a factro for the formation of the core of a trailing vortex is reviewed by Delafosse et al. (2009) as studied by researcher like (Derksen et al., 1999; Lee and Yianneskis, 1998; Sharp and Adrian, 2001; Escudie et al., 2004). This is due to the transfer of energy between periodic motion and turbulence which occurs in the trailing vortex core (Escudié et al., 2004) is mentioned by Delafosse et al. (2009). As a consequence, the maximum level of turbulence dissipation rate is likely to be located near the trailing vortices (Delafosse et al., 2009).

Mean radial velocity at different radial positions along the *z*-axis is shown in Figure 5.4. The radial flow associated with the swirling motion of the fluid, reaches the walls of the vessel and by the effect of the vertical baffles, deflects in an upwards and a downwards separated flows.

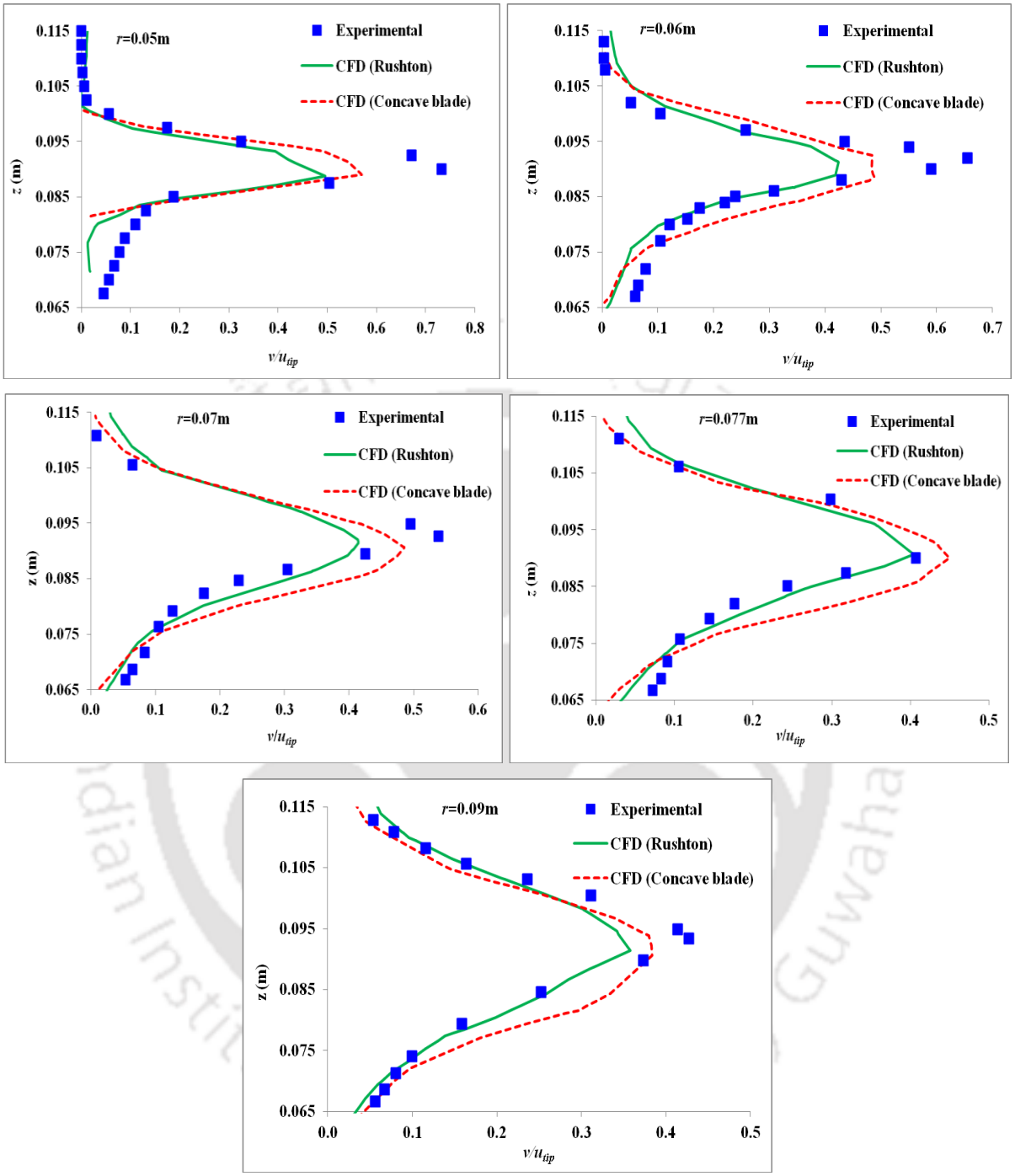

Figure 5.4: Mean radial velocity at different radial positions, along the *z*-axis (tank height)

The typical flow pattern of simulated Concave blade impeller is observed same with the simulated and experimental Rushton impeller as observed by the Deglon and Meyer (2006). The simulated radial velocity of Rushton impeller is underpredicted from the experimental results at radial distance, *r*=5 and 6 cm but is exactly matched with the experimental values at

r=7.7cm as compare with other radial distances, r. It is also observed that the simulated results are more matched with the experimental results when the radial distance is far away from the central axis of shaft (i.e., nearer to the wall of tank). The simulated radial velocity of Concave blade impeller is found higher than the Rushton impeller. The simulated maximum radial velocity is observed near the impeller tip (i.e., r=5cm) as $0.5u_{tip}$ for Rushton impeller and nearly $0.6u_{tip}$ for Concave blade impeller while the experimental value is $0.75u_{tip}$.

5.2.1.3. Comparison of turbulent kinetic energy

Turbulent kinetic energy is the most direct relation to the mixer capacity and performance (Wu and Patterson, 1989). The turbulent kinetic energy is normalized by the k/u_{tip}^2 (Marshall and Bakker, 2002). The comparisions of the turbulent kinetic energy of Rushton impeller and Concave blade impeller was not made with experimental values; only the simulated results have been compared. The underprediction of CFD results is observed generally in turbulent kinetic energy that mentioned by many researchers (Jaworski et al., 1997; Gentric et al., 2005; Li et al., 2005; Deglon and Meyer, 2006).

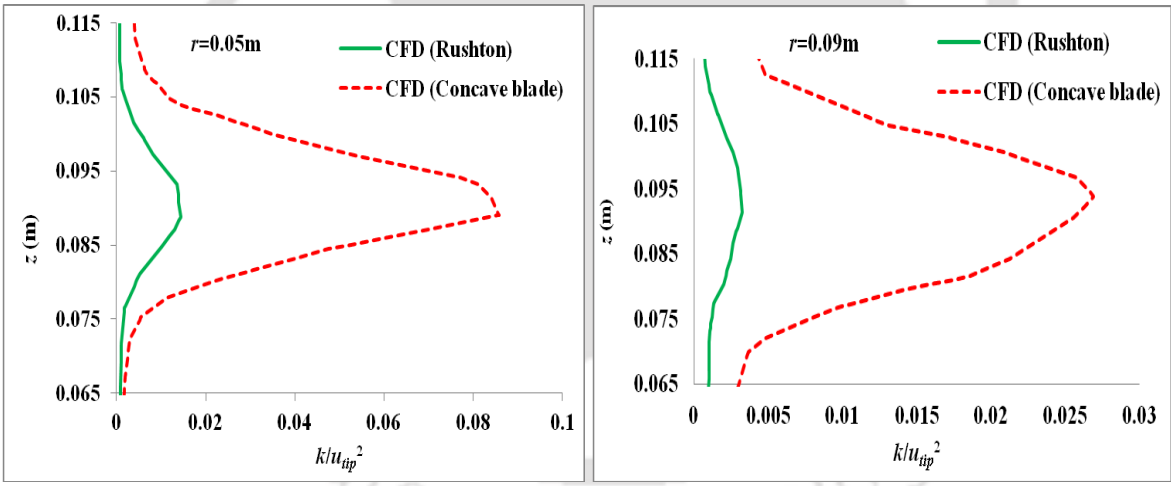

Figure 5.5: Comparision of turbulent kinetic energy

From Figure 5.5, it is seen that the turbulent kinetic energy of Concave blade impeller is comparatively much higher than the Rushton impeller. The simulated turbulent kinetic energy is also shown in Figure 5.6 shows turbulent kinetic energy for Rushton impeller and Concave blade impeller at different radial positions. The values of turbulent kinetic energy is found considerably vary at different radial positions, r. The maximum turbulent kinetic

energy is 0.015k/u_{tip}^{2} for Rushton impeller and for Concave blade, it is 0.09k/u_{tip}^{2} observed at r=5cm.

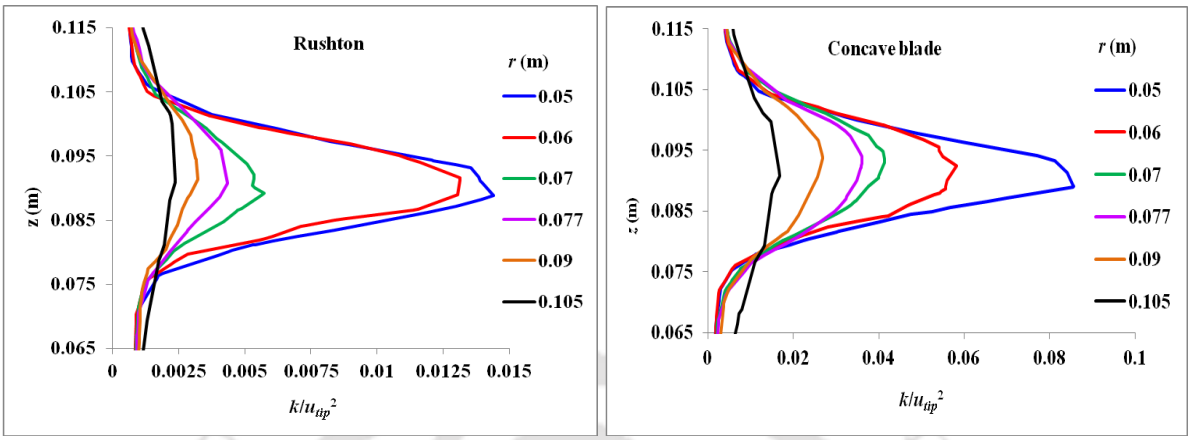

Figure 5.6: Simulated turbulent kinetic energy at different radial positions along z-axis.

The lowest value of turbulent kinetic energy is observed at radial position, r=10.5cm (for Concave blade, it is 0.02 k/u_{tip}^{2} and for Rushton impeller, it is around 0.003 k/u_{tip}^{2}). This is because of the frictional registance posess by the wall of tank. It resist the movement of fluid paricle reducing the speed and magnitute of kinetic energy. More is the kinetic energy of fluid particles more is tendency of proper mixing. From the comprisions of contours and vectors of turbulent kinetic energy, it is observed more sparge nature in the case of Concave blade impeller than the Rushton impeller which is shown in Figure 5.7; which may be due to the concave shape of Concave blade. This concave shape allows to rotate the fluid particles around the impeller region with a short distance of rotation and quickly returns the prevoius position generating high speed of fluid particles. The flat and straight shape of Rushton impeller needs the fluid particle to rotate around the impeller region longer distance and take longer time to return to the previous postion of fluid particles slowing down the speed of fluid particles. The subtle formation of trailing vortex pair is observed more in the case of Rushton impeller than the Concave blade impeller in Figure 5.7. Formation of distinct recirculating zones (characteristics of Rushton impeller) is an obstacle to fluid transport. Slow recirculating flow patterns are invariably developed in stagnate (dead) zones of the vessel that must be eliminated as they are a barrier to mixing; this translates into a need of employing other type of radial impeller. The concave blade shape of Concave blade is mainly to resemble the contour of gas cavity during agitation. Concave blade reportedly minimizes

the drawbacks of Rushton impeller by decreasing the gas cavities dimension as well as reducing gassed power drop with its improved gas handling performance.

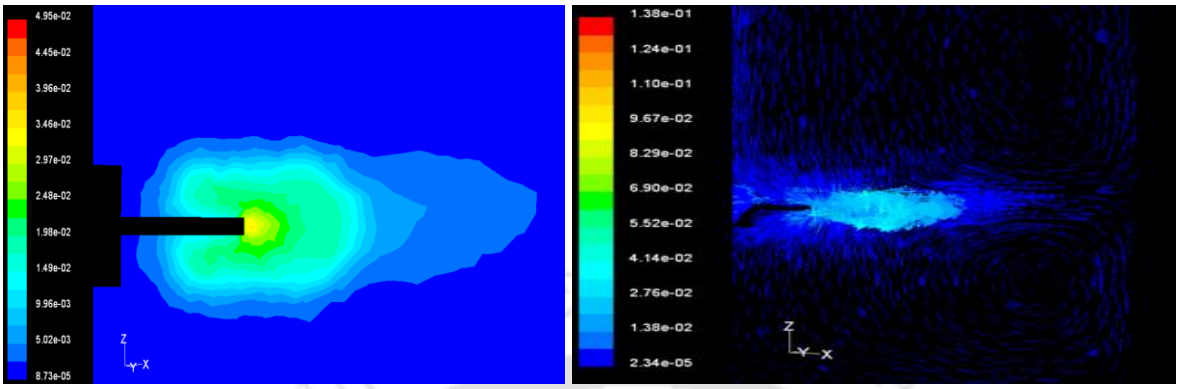

Figure 5.7a: Contours and vectors of turbulent kinetic energy at 45 degree plane (Rusthon impeller)

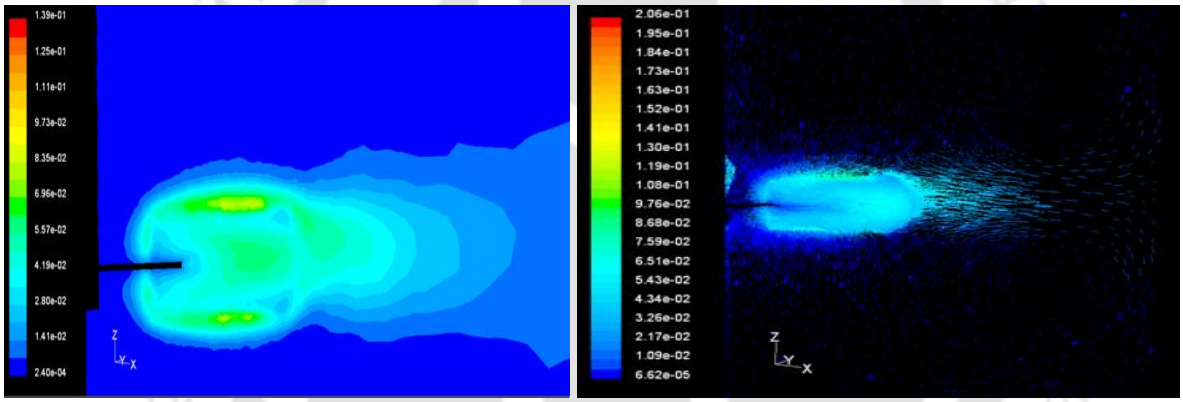

Figure 5.7b: Contours and vectors of turbulent kinetic energy at 45 degree plane (Concave blade impeller)

The stagnant zone of fluid as shown in the Figure 5.7a always exists far away from the Rushton impeller. This is not desirable for proper mixing. Concave blade impeller does not show patterns and mixing is very much uniform in this case.

5.2.1.4. Comparison of turbulent dissipation rate

The turbulent dissipation rate is genarally normalized by u_{tip}^3/d (Marshall and Bakker, 2002). Alexopoulos et al. (2002) conluded from their study that the Commercial CFD codes are unable to predict accurate values of k and ε. In fact, the k- ε model shows shortcomings in modeling highly swirling flows and is unable to take intonaccount structures appearing in mixing tanks around blades or the baffles (vortices etc.) (Gentric et al., 2005). Like in the

case of turbulent kinetic observed in the previous section, the turbulent dissipation rate is found comparatively higher in the case of Concave blade impeller than the Rushton impeller.

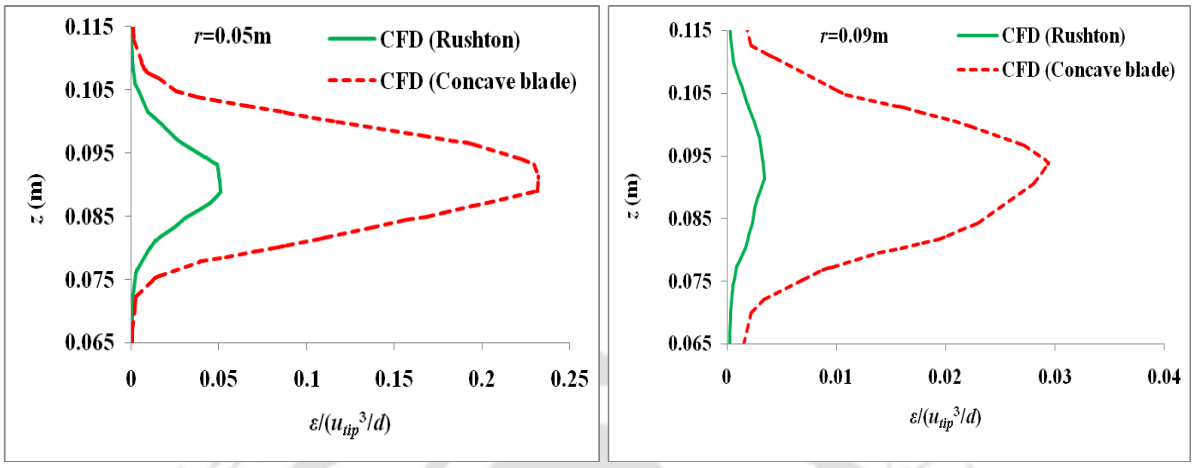

Figure 5.8: Comparision of turbulent dissipation rate

It is necessary to capture the key features of flow around impeller blades in order to make computational flow models suitable for reactor engineering applications. The turbulent dissipation rate is more near the tip of blade in both the cases of Rushton impeller and Concave blade impeller as witnessed in Figure 5.8. When the radial distance is near the tank, simultaneously decreases the values of turbulent dissipation rate.

5.2.1.5. Conclusion

This study presents an application of CFD to flow simulations in baffled stirred tanks fitted with Rushton impeller and Concave blade impeller. CFD has been widely used to map the fluid dynamics within the stirred tanks and it has become an effective tool for design and optimization of stirred tanks/vessels. However, one of the challenges for the CFD simulation of the flow in a stirred tank is to accurately capture the turbulence inside it. In case of Rushton impeller, both qualitative and quantitative comparisons are made between the experimental and numerical results. The nature of the flow field and turbulence field are investigated. The simulated and the experimental results indicated similar typical pattern of flow field. The presented numerical model in this study underpredicts the experimental observation but good accepatable pattern is achieved in the case of Rusthon impeller. The simulated flow hydrodynamics of Concave blade impeller has been compared with simulated obervations of Rushton impeller. It is found that Concave blade impeller exhibits high radial

velocity than Rushton impeller. Radial velocity helps in gas dispersion and uniform spatial mixing. The reason behind may be due to the fact that the Concave blade pumps the fluid slightly downward around the impeller discharge region, whereas the Rushton impeller pumps slightly upward, which contributes to poor circulation in the lower region. The concave shape of the Concave blade impeller helps in producing a smaller gas cavity behind the impeller blade. Dispersion capacity of an impeller can also be measured through energy dissipation rate. High energy dissipation rate reduces the mix time (shorter mixing length). Accurate estimation of the dissipation rate distribution and its maximum value in stirred tanks, especially in the vicinity of the impeller is of great importance. This is because of industrial processes require calculation of the eddy sizes which are related directly to the turbulent kinetic energy and the dissipation rate. Numerical simulation also shows that Concave blade impeller exhibits higher energy dissipation rates than the Rushton impeller. If the near-impeller flow characteristics are known, the flow in the bulk region of the stirred vessel may be simulated with accuracy adequate for most engineering applications. Thus it can be concluded that Concave blade impellers are more suitable than standard Rushton impeller for mixing.

5.2.2. Dual impeller

Dual impeller system of concave blade in single phase condition is compared with dual Rushton impeller system in order to understand the efficiency of concave blade impeller over the Rushton impeller. The simulated results were compared with experimental results of Chunmei et al. (2008) which was carried out on dual Rushton impeller system. Their main objective was to predict the three stable flow profiles (parallel, merging and diverging).

5.2.2.1. Stirred tank geometry

The geometry of mixing tank simulated in this study is taken same with the dimensions of Chunmei et al. (2008). The clear off distances have been made same with their study to get the three stable flow patterns i.e, parallel, merging and diverging. The axial height of lower impeller from tank bottom is denoted by C_1; spacing between two impellers is by C_2 and distance of upper impeller from top open tank is by C_3. Figure 5.9 shows geometric dimensions of stirred tank with generated grid mounted by Rushton and Concave blade impeller. The diameter of tank (D) and impeller (d) is 48cm and 19cm respectively. Working

fluid is water filled upto the height (H) of 1.4D (67cm). In this study, three cases have been considered based on the combinations of C_1, C_2 & C_3 (Table 5.1).

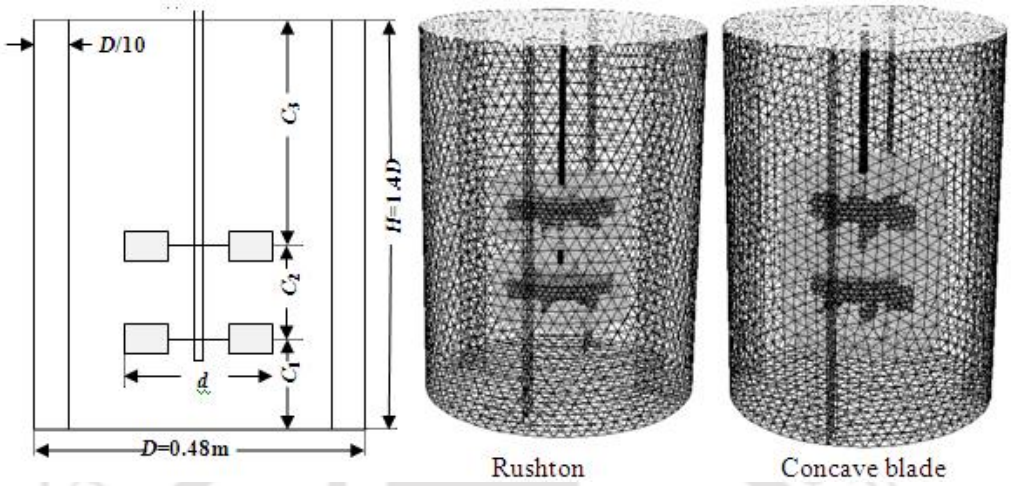

Figure 5.9: Geometry of stirred tank used in this model, unstructured grid generated for full tank mounted by Rushton impeller and Concave blade impeller

The size of grid generated in terms of cells, faces & nodes for each combination of impeller spacings is presented in Table 5.1. In the generated grid of Rushton and Concave blade impeller, the area of impeller region is seen higher in the case of Concave blade impeller. This impeller region is the most efficient region of the whole part of stirred tank where the movements of fluid particles are significantly higher than the other regions of stirred tank. The sizes of grid for different flow patterns are different in both the cases of Rushton and Concave blade impeller. The number of cells, faces and nodes for Concave blade impeller is almost doubled from the Rushton impeller.

Table 5.1: Combinations of flow patterns with different axial height and corresponding grid sizes

Case	**Flow pattern**	**C_1, C_2, C_3**	**Rushton impeller**			**Concave blade impeller**		
			Cells	**Faces**	**Nodes**	**Cells**	**Faces**	**Nodes**
1	Parallel	C_1=0.40D C_2=0.48D C_3=0.52D	261687	548485	56260	468833	1016420	125575
2	Merging	C_1=0.40D C_2=0.315D C_3=0.685D	225507	469592	46369	443088	961011	118745
3	Diverging	C_1=0.15D C_2=0.40D C_3=0.85D	231140	481855	47956	459177	984254	113683

The comparison of Rushton and Concave blade impeller in terms of mean velocities, turbulent kinetic energy will be discussed for the three flow pattern (parallel, merging & diverging) in this section. In case of axial and radial velocities, the simulated results were compared with experimental observations of Chunmei et al. (2008) and the contours of turbulent kinetic energy of Rushton and Concave blade impeller have also been compared and discussed accordingly. Figure 5.10 represents the reference of the subsequent Figures of 5.11 & 5.12.

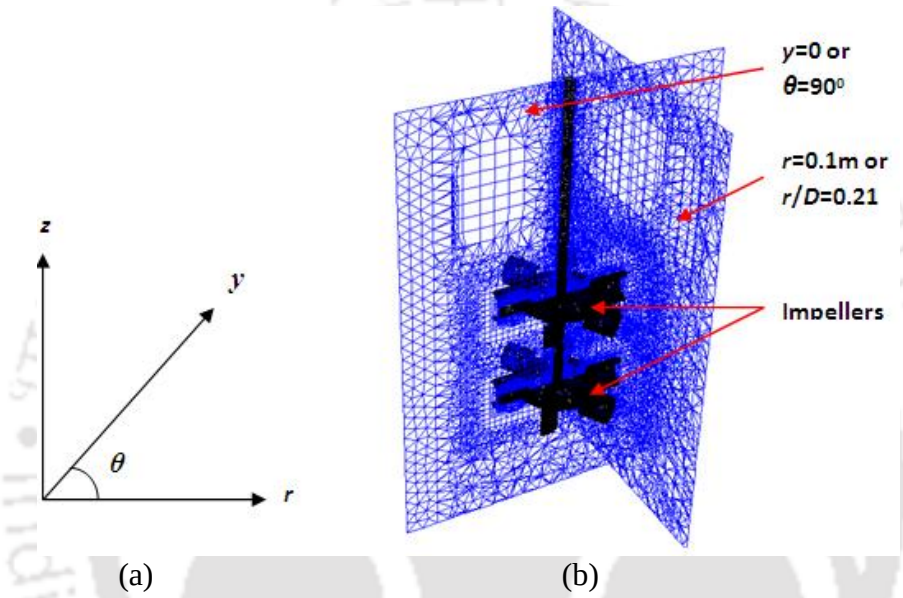

(a) (b)

Figure 5.10: Reference (a) co-ordinate system used in CFD simulation (b) iso-surface at y=0 or θ=90^0 and at r=0.1m or r/D=0.21 used in the following subsequent Figures of 5.11 & 5.12.

5.2.2.2. Comparison of flow pattern

The comparison of Rushton and Concave blade impeller in terms of mean velocities (axial & radial) for the three flow patterns is shown in Figure 5.11(a) Parallel flow (b) Merging flow and (c) Diverging flow. The contours of mean velocity in left side is simulated CFD result of Rushton impeller, middle one is experimental observations of Chunmei et al. (2008) on Rushton impeller and right side shows the simulated results on Concave blade impeller. In all the case of three flow patterns of Rushton impeller, the simulated and experimental observation shows good agreement. The formation of trailing vortex is clearly generated in case of Rushton and Concave blade impeller. As it has been mentioned in the previous section that generally single Rushton impeller produces two trailing vortex pair (circulation loop), one above the blade and another blade and this kind of flow formation is also observed

in case of dual impeller when the impeller spacing is made for parallel flow pattern. The formation of vortex is observed independent from one another (Figure 5.11a), the flow path has its own direction to move around the impeller blade. The formation of vortex increases in the efficiency of mixing tanks and minimizing the vortex size improves the blending performance of an impeller (Delafose et al., 2009). In this Figure 5.11a, left (Rushton) and right (Concave blade), the size of vortex is observed minimum in case of Concave blade impeller than the Rushton impeller. Stable flow pattern is closely related with trailing vortices and it is generally investigated through the nature of formation of trailing vortices. High levels of turbulent kinetic energy is a factor for the formation of the core of a trailing vortex is reviewed by Delafose et al. (2009) as studied by researchers like Lee and Yianneskis, 1998; Derksen and Van den Akker, 1999; Sharp and Adrian, 2001; Escudie et al., 2004. This is due to the transfer of energy between periodic motion and turbulencewhich occurs in the trailing vortex core (Escudie et al., 2004) is mentioned by Delafose et al. (2009). As a consequence, the maximum level of turbulence dissipation rate is likely to be located near the trailing vortices (Delafose et al., 2009).

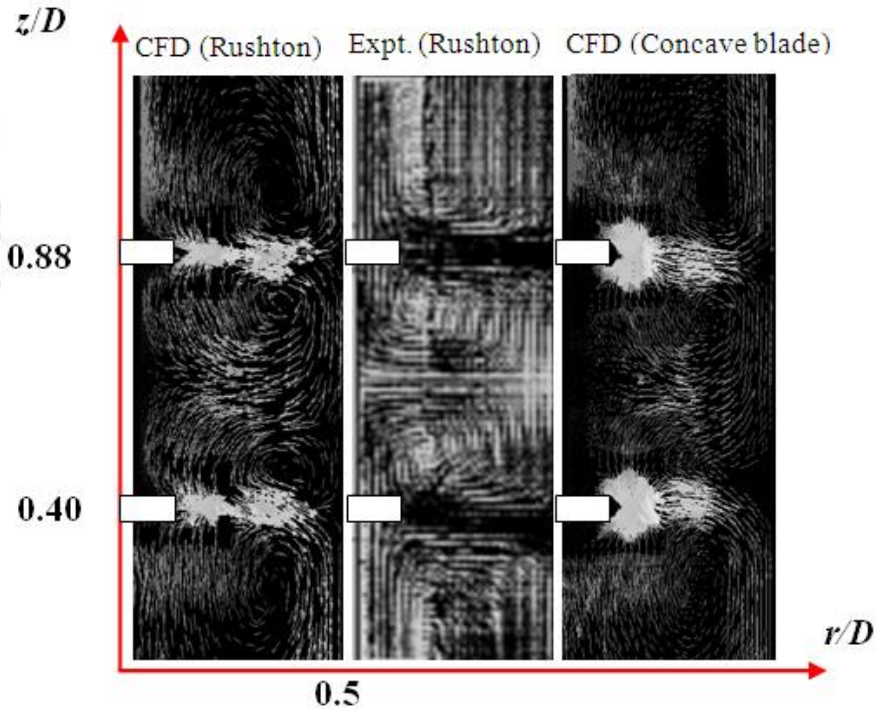

(a)Parallel flow (C_1=d=0.40D, C_2=0.48D)

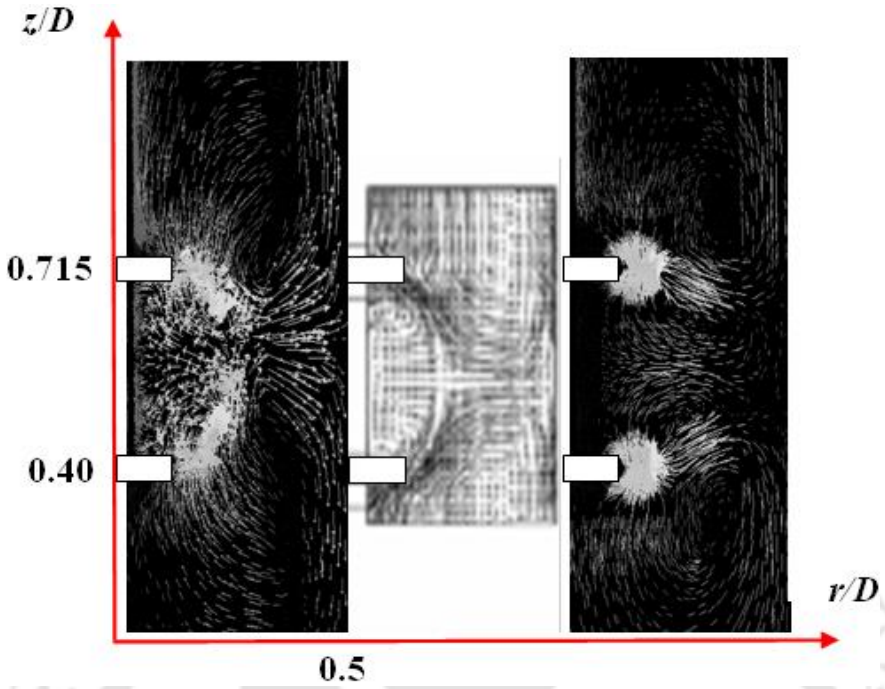

(b)Merging flow (C_1=d=0.40D, C_2=0.315D)

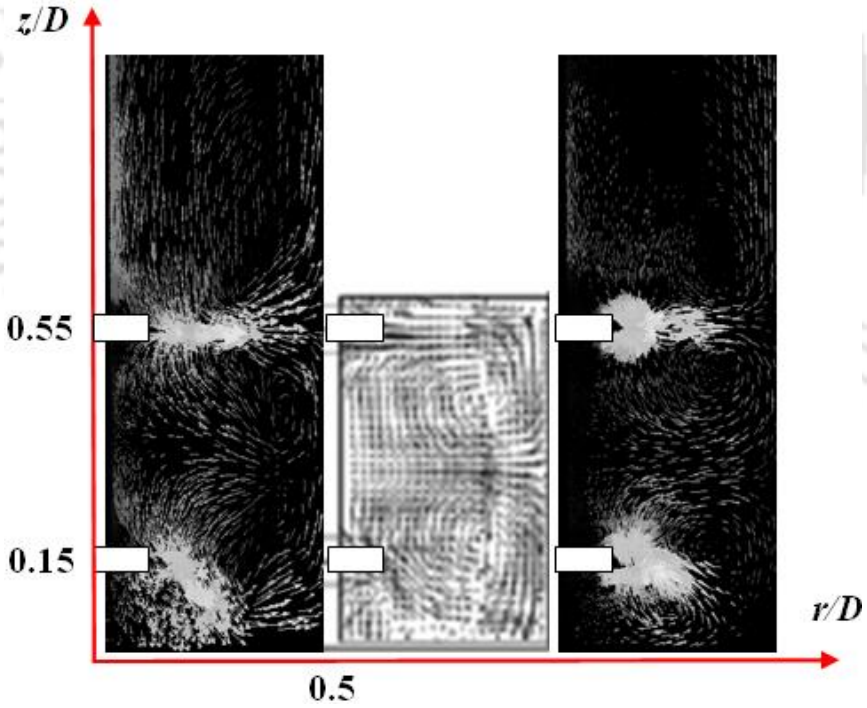

(c) Diverging flow(C_1=0.15D, d=C_2=0.40D)

Figure 5.11: Mean velocity vector plots of Rushton (left), Expt. Rushton (middle) and Concave blade impeller (right) at y=0

In case of parallel and diverging flow pattern of Rushton impeller shows similar flow pattern with Concave blade impeller. However, Concave blade impeller shows different flow pattern from the Rushton impeller in merging flow (Figure 5.11b). In Rushton impeller (Figure 5.11b left), the formation of middle vortex has been disturbed and made joint at the centre of the two impeller but in case of Concave blade impeller, such type of formation is less significant as the formation of independent vortex pair is likely to occur around the impeller blade. In Figure 5.11c, the formation of formation of diverging flow pattern in case of Concave blade is more likely close to the experimental than the simulated Rushton impeller flow patterns. In Rushton impeller, the formation of vortex pair is not much significant as compared with the Concave blade impeller.

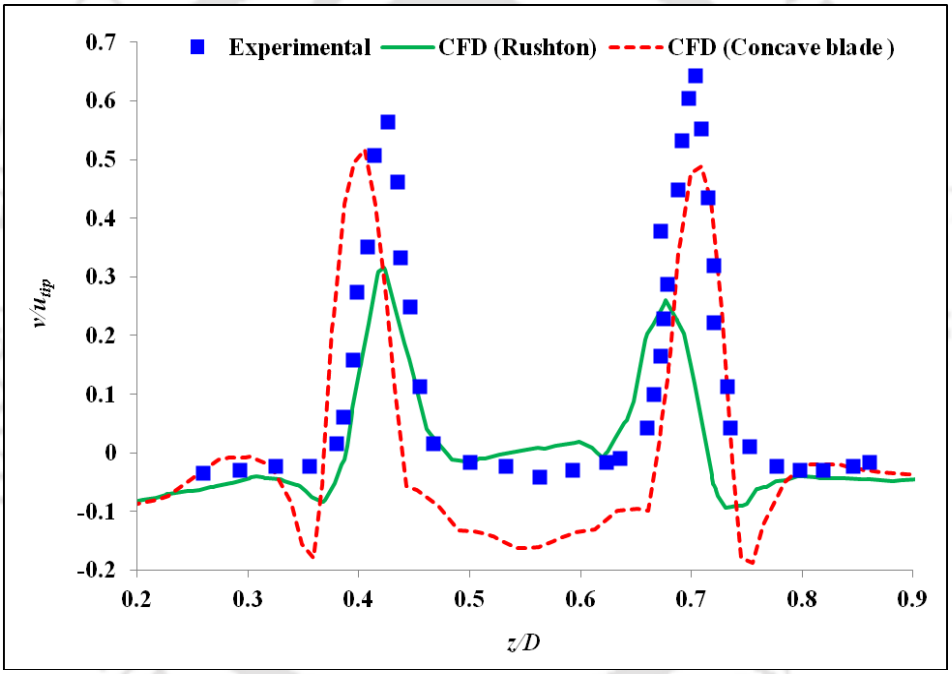

(a) Radial velocity

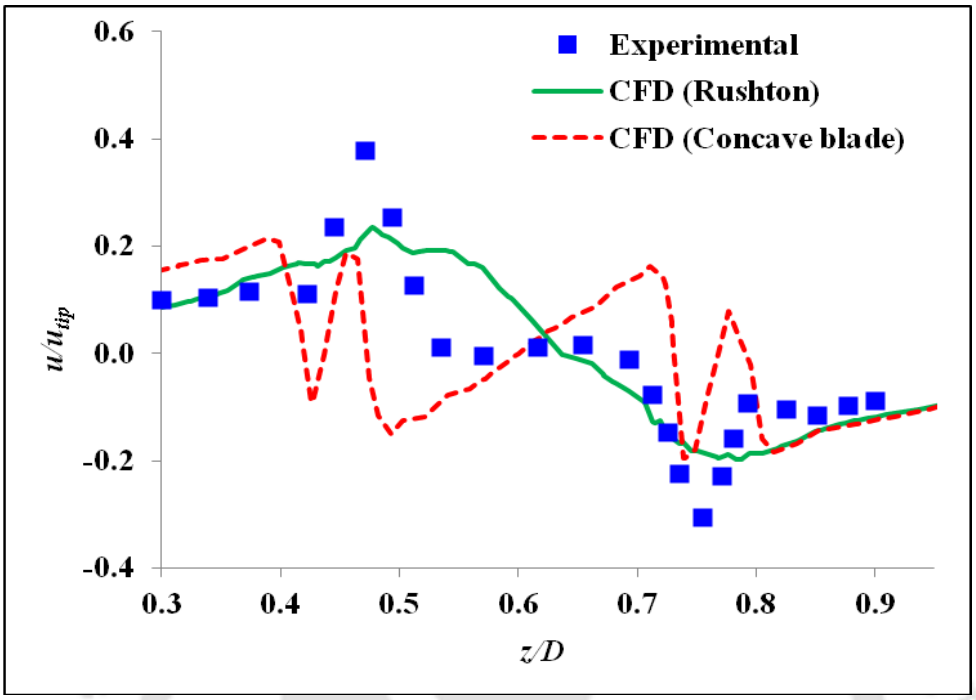

(b) Axial velocity

Figure 5.12: Comparisons of (a) Radial velocity (b) Axial velocity at r/D=0.21 through one baffle (y=0) for merging flow pattern

In Figure 5.12a &b shows the comparison of mean velocities of Rushton and Concave blade impeller at different numerical parameter considerations. In Figure 5.12a, the radial velocity at impeller tip (r/D=0.21) through one baffle (at 90^0 plane) is shown. The maximum experimental radial velocity of lower and upper impeller is $0.56u_{tip}$ and $0.64u_{tip}$ respectively and the simulated result for lower and upper impeller is predicted as $0.18u_{tip}$ and $0.25u_{tip}$ respectively. Overall it can predict 40% in case of Rushton impeller and in case of Concave blade impeller, it can predict 95% for lower and 90% for upper impeller. So, it has been understood that in the same turbulence model, the prediction of radial velocity for Rushton impeller is around 50% lower than the Concave blade impeller. In the axial mean flow velocity (Figure 5.12b), the predicted result of Concave blade impeller is more close to the experimental result but it underpredicts. In case of Rushton impeller, the flow patterns is observed somewhat deviated from the experimental results.

5.2.2.3. Comparison of turbulent kinetic energy

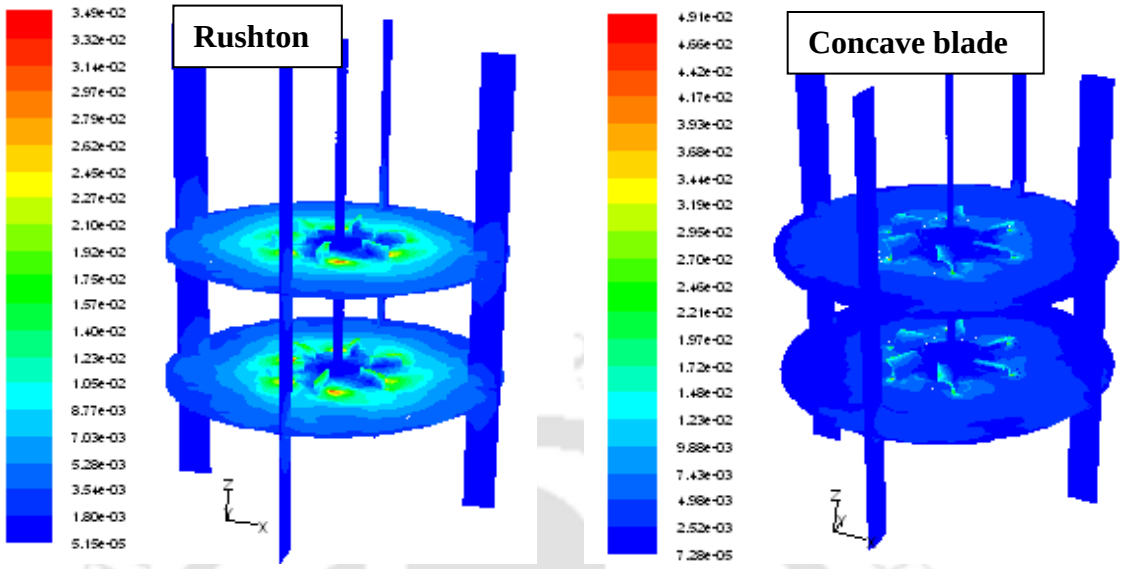

(a) Parallel flow (C_1=d=0.40D, C_2=0.48D

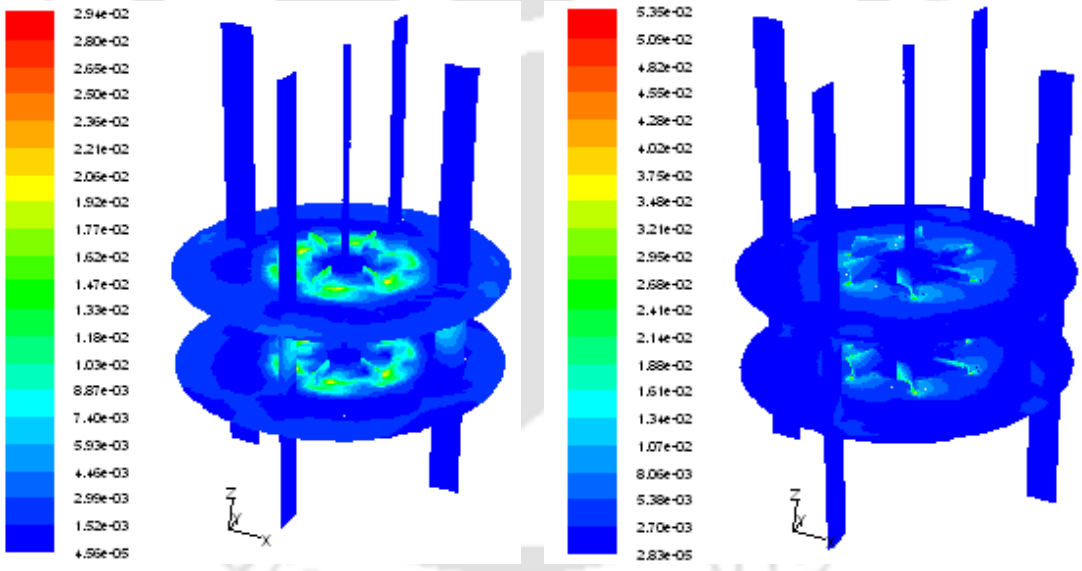

(b) Merging flow (C_1=d=0.40D, C_2=0.315D)

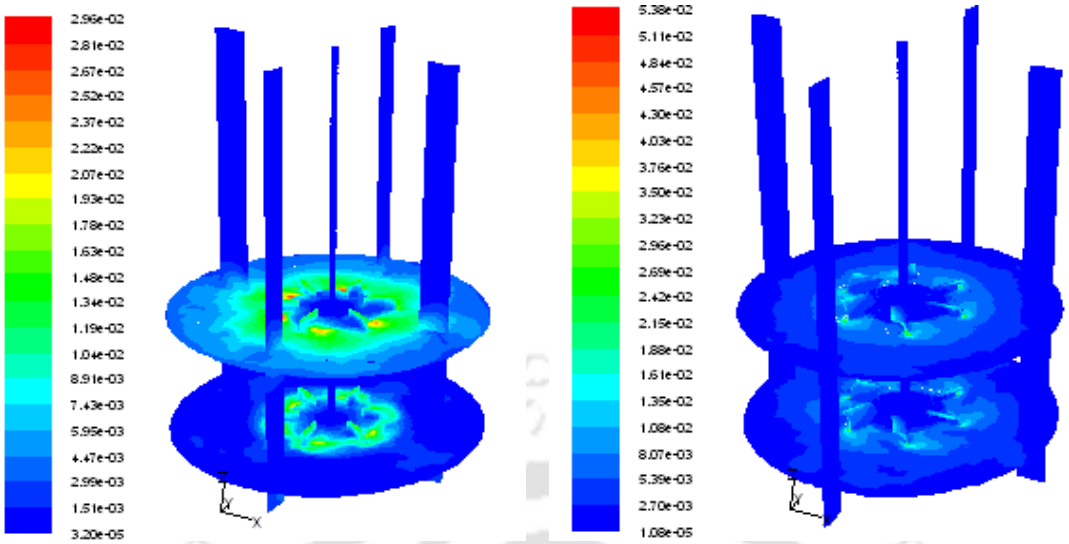

(c) Diverging flow(C_1=0.15D, d=C_2=0.40D)

Figure 5.13: Turbulent kinetic energy rate, k (m^2/s^2) of Rushton (left) and Concave blade impeller (right) for different flow patterns along the r-z axis.

Figure 5.13(a-c) represents the turbulent kinetic energy rate (TKE) of different flow patterns generated by Rushton and Concave blade impeller along the radial and axial direction of full tank. For this observation of TKE, two iso-surface has been created at the centers of the impeller blade. In both case of Rushton and Concave blade impeller, the TKE is observed significantly more around the impeller region. The dead zones is more in case of merging flow pattern than the parallel and diverging flow pattern of Rushton and Concave blade impeller.

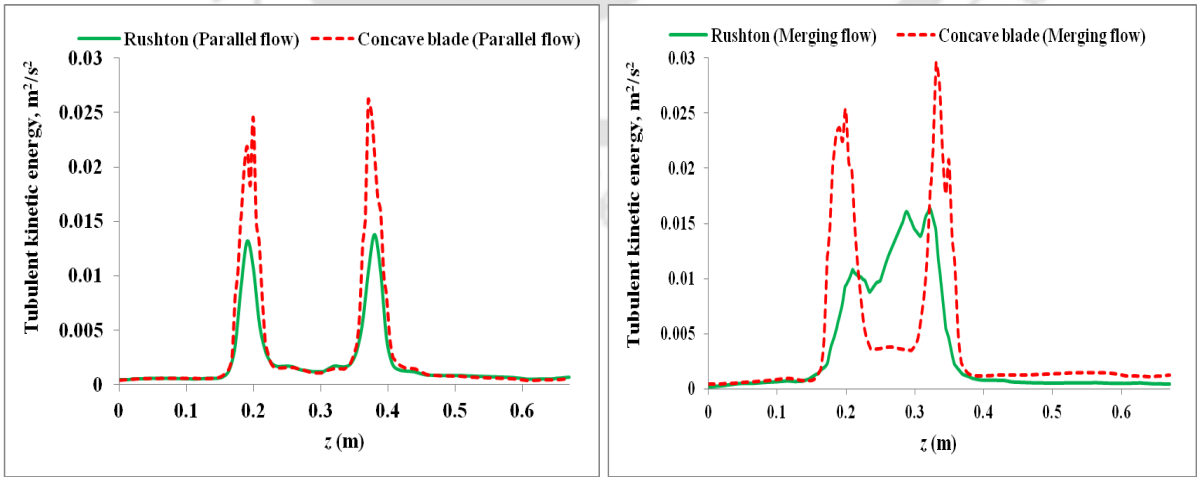

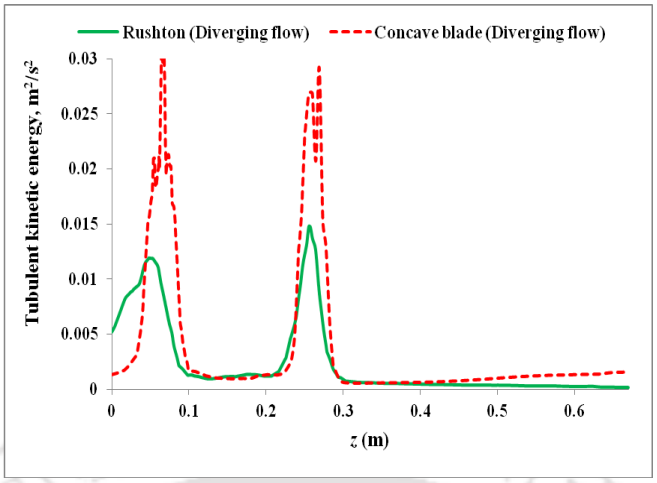

Figure 5.14: Comparision of turbulent kinetic energy at impeller tip for different flow patterns of Rushton and Concave blade impeller

The magnitude of TKE is observed more in Concave blade impeller than the Rushton impeller in the three cases of flow patterns (Figure 5.14). In merging flow pattern of Rushton and Concave blade, the TKE is significantly different and such type of differences in merging flow patterns was also mentioned in the previous section of mean flow velocity. The formation of flow path of TKE is observed similar in both the cases of Rushton and Concave blade in parallel and diverging flow patterns.

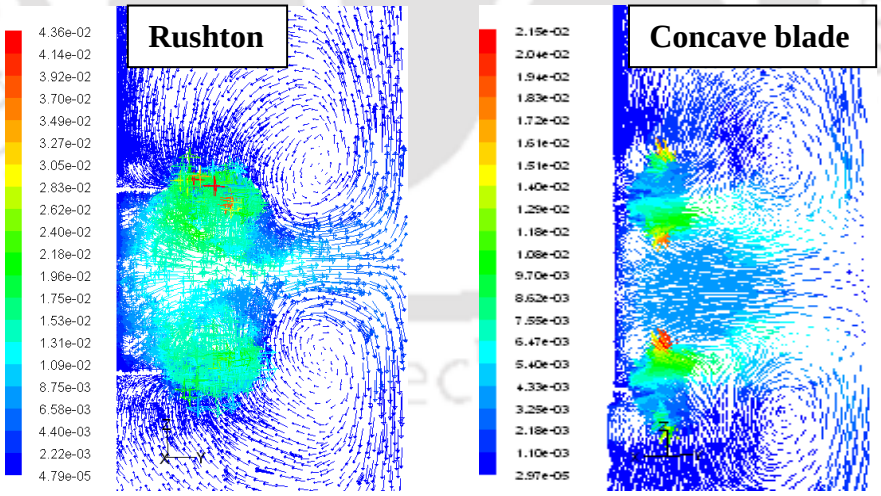

θ=10^0

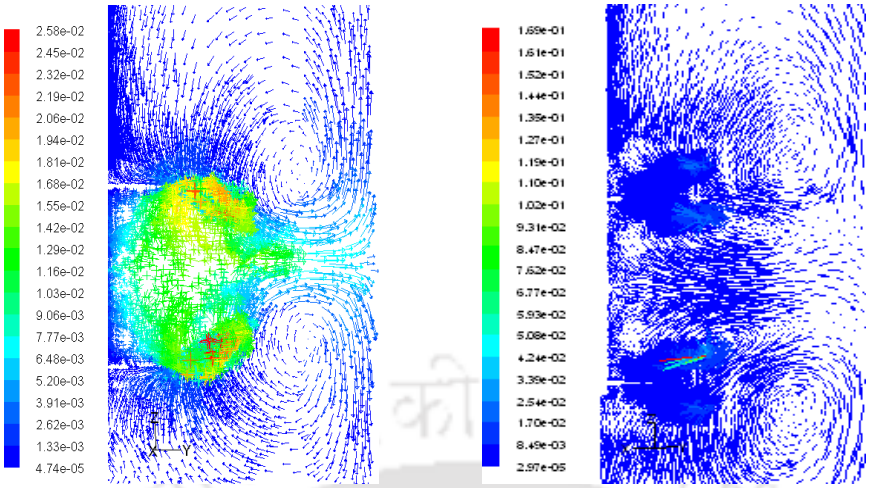

$\theta=20^0$

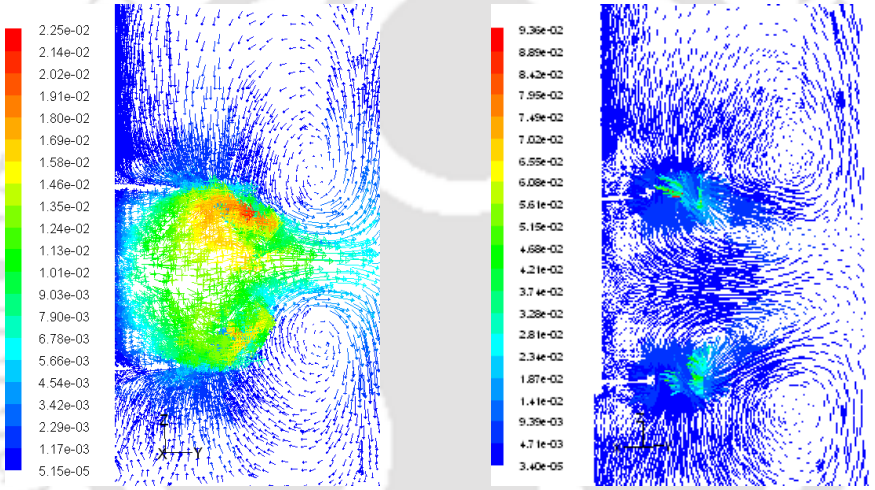

$\theta=30^0$

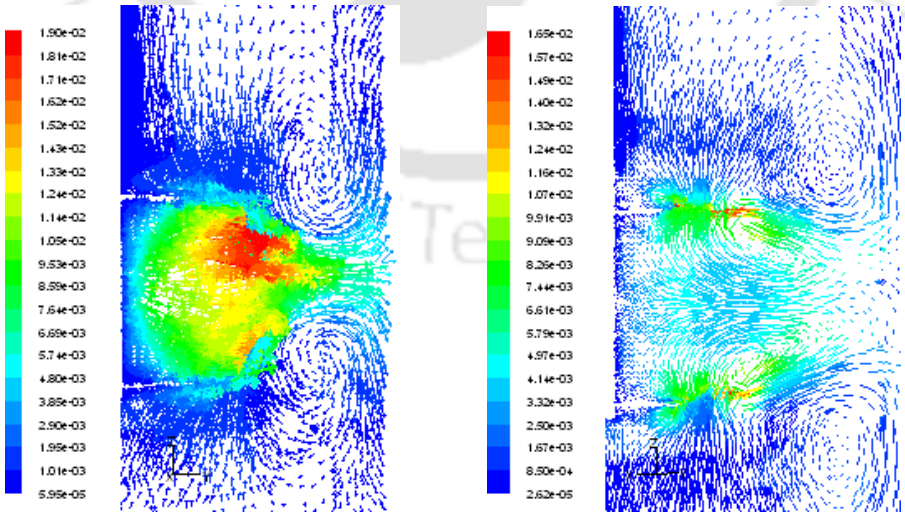

θ=40^0

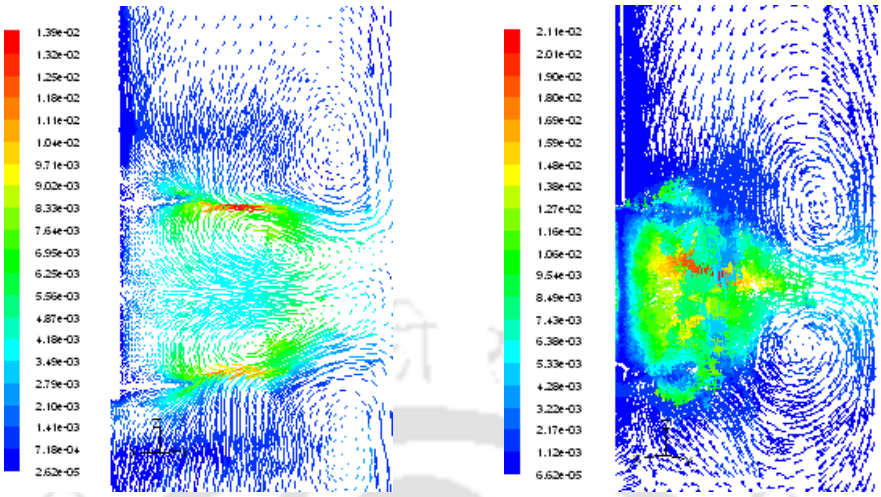

Figure 5.15: Turbulent kinetic energy rate, k (m^2/s^2) of Rushton (left) and Concave blade impeller (right) at different angular positions (θ) along the r-z axis for merging flow pattern.

The TKE for different angular position is shown in Figure 5.15 for merging flow pattern since in this condition, the formation of flow pattern is found significantly different for Rushton and Concave blade impeller. The formation of flow pattern is different at various angular positions inside the mixing tank. When the angular position increases, the formation of merging flow pattern is likely to increase in case of Concave blade impeller that is at angular position from 10^0 to 40^0, the merging flow pattern is not likely to form, however, when it is at 50^0, the clear formation of merging pattern is observed.

5.2.2.3. Conclusions

The ability to correctly predict the flow patterns of Rushton and Concave blade impeller by CFD simulation has been studied in this paper. The three flow patterns (Parallel, Merging and Diverging) at specific impeller spacing have been verified with the experimental results from literature and good agreement is achieved. Study indicates that formation of merging flow pattern is different in case of Concave blade impeller than the Rushton impeller. In this condition it has been suggested that slight adjustment (lowering) in the impeller spacing is required in Concave blade impeller to get the convincing merging flow pattern where such type of flow pattern is required for mixing efficiency and proper stable conditions. The size of vortex is observed smaller in case of Concave blade impeller than the Rushton impeller which leads to more efficiency in mixing operations. Significant amount of TKE is observed

only around the impeller region indicating maximum efficiency of a mixing tank is majorly contributed by the sweep area of an impeller and it is a great concern about the types of impeller used since in this study, different blade shape (Rushton has disc shape and Concave blade has concave shape) of impeller are adopted for analysis. The magnitude and spatial variation of fluid flow is found different in both the cases of Rushton and Concave blade impeller from the observation of angular variation of TKE.

5.3. Gas-liquid phase

Gas-liquid phase condition is studied on single and dual impeller system. In this section, Rushton and Concave blade impeller in single and dual case is being studied in gas-liquid phase taking constant bubble diameter with Eulerian-Eulerian multiphase model. This study aims in predicting flow pattern, mass transfer and power draw and comparing with published literature.

5.3.1. Mass transfer model

There are several model available in literature for calculating local mass transfer co-efficient (K_L) but commonly used model are based on penetration theory (Higbie, 1935) and surface renewal model (Danckwerts, 1951) when the bubble diameter is known. Higbie (1935) penetration theory expressed that the liquid phase mass transfer coefficient of a bubble with a mobile surface as

$$K_L = \frac{2}{\sqrt{\pi}}\sqrt{\frac{D_l}{t_e}} \tag{5.1}$$

Where t_e is the contact time and is calculated based on Kolmogorov's Length scale of isotropic turbulence as $t_e = \sqrt{\nu_l / \varepsilon_l}$; ε_l is turbulent dissipation rate and ν_l is the kinematic viscosity of liquid (Kolmogorov's, 1941). So, Equation (5.1) becomes as:

$$K_L{}^{penetration} = \frac{2}{\sqrt{\pi}} D_l^{0.5}\left(\frac{\varepsilon_l}{\nu_l}\right)^{0.25} \tag{5.2}$$

And this model is denoted as $K_L{}^{penetration}$.

Refinement of the penetration theory, mass transfer co-efficient, K_L, suggested by Danckwerts (1951) is given as $K_L = \sqrt{D_l s}$, where s is the surface renewal rate. This approach

assumed that K_L is related to the average surface renewal rate resulting from exposure of the bubble interface to the turbulent eddies with a variable contact time. Later, Lamont and Scott (1970) assumed that the small-scale turbulent motion, which extends from smallest viscous motion to inertial ones, affects the rate of mass transfer and *s* is calculated based on Komogorov's theory of isotropic turbulence. Hence, Equation 5.1 becomes as:

$$K_L^{\,eddy\ cell} = K D_l^{0.5} \left(\frac{\varepsilon_l}{\nu_l} \right)^{0.25} \tag{5.3}$$

Where, D_l is the diffusion co-efficient and K=0.4 is model constants. This model is denoted as $K^{\,eddy\ cell}$ and generally referred as eddy cell model.

Caderbank (1957) further assumed that the bubble is having a mobile interface and gross mean flow of liquid relative to the bubble (slip velocity) controls the renewal of liquid phase and contact time can be expressed in terms of average bubble size and average slip velocity as

$$K_L^{\,slip\ velocity} = \frac{2}{\sqrt{\pi}} \sqrt{\frac{D_l u_{slip}}{d_b}} \tag{5.4}$$

u_{slip} can be obtained from phase velocity difference from an Eulerian-Eulerian two-fluid CFD simulation. And the expression of this model is denoted as $K_L^{\,slip\ velocity}$.

Alves et al. (2004) modified the equation of K_L based on bubble rigidity and is denoted as $K_L^{\,rigid}$. And this is obtained from the equation proposed by Frossling (1938) based on laminar boundary value theory as:

$$K_L^{\,rigid} = c \left(\frac{u_{slip}}{d_b} \right)^{0.5} D_l^{2/3} \nu_l^{-1/6} \tag{5.5}$$

Where, *c* is a constant of value 0.6.

Volumetric mass transfer co-efficient ($K_L a_{20}$) is the combination of K_L and *a*, where *a* is the interfacial specific area and is a function of local volume fraction, α_g and bubble diameter, d_b. Therefore, *a* is expressed as:

$$a = \frac{6\alpha_g}{d_b} \tag{5.6}$$

5.3.2. Power draw correlations

5.3.3.1. For single impeller

Ungassed power number, N_p is generally expressed in terms of ungassed power input, P_u and is given as below for single Rushton impeller (Bujalski et al., 1987).

$$N_p = \frac{P_u}{\rho_l N^3 d^5} = 2.512\left(\frac{t_b}{d}\right)^{-0.195} D^{0.063} \tag{5.7}$$

Where, ρ_l, N and d are the density of liquid, impeller speed and diameter of impeller respectively. t_b and D are the impeller thickness and tank diameter.

Power draw is the minimum power required by the shaft to rotate the impeller. Smith (2006) proposed the relative power draw, P_g/P_u, from the measurements of Warmoeskerken and Smith (1982) and Gezork et al. (2000) for single Rushton impeller as below:

$$\frac{P_g}{P_u} = 0.18 Fr^{-0.2} Fl^{-0.25} \tag{5.8}$$

F_r is the Froude number and is calculated as $\frac{N^2 d}{g}$; g is the gravitational force. Fl is flow number and is calculated as $\frac{Q_g}{Nd^3}$; Q_g is flow rate.

5.3.3.2. For dual impeller

Taghavi et al. (2011) suggested a correlation for ungassed power input from experimental observation for dual impellers as

$$\frac{P_u}{V} = 6\text{X}10^{-12} Re^{2.921}, \qquad Re > 10^4 \tag{5.9}$$

They further proposed a correlation of the relative power draw, P_g/P_u, based on the experimental and simulation results of dual Rushton impeller as:

$$\frac{P_g}{P_u} = 0.19\left(Fl\right)^{-0.28}\left(Fr\right)^{0.127}\left(\frac{w}{d}\right)^{0.18}\left(\frac{d}{D}\right)^{-0.65} \tag{5.10}$$

The above correlations of relative power draw were based on Rushton impeller for single (from Equation 5.7 to Equation 5.8) and for dual (Equation 5.9 & 5.10). However, for other impeller types like Concave blade impeller which is used in this study, the following correlation originally proposed by Hugmark (1980) for six bladed Rushton impeller and is

used in this study; and this correlation is reapplied by Moucha et al. (2009) for other impellers as:

$$\frac{P_g}{P_u} = 0.1\left(\frac{N^2 d^4}{gbV^{2/3}}\right)^{-0.2}\left(\frac{Q_g}{NV}\right)^{-0.25} \tag{5.11}$$

Where, b and V are the width of blade and tank volume respectively.

The energy per unit mass available in a stirred tank is given by the ratio between the gassed power input and total mass which can be applied in different types of impeller and is given as below:

$$\varepsilon = \frac{P_g}{\rho_l V} \tag{5.12}$$

So, for other types of impeller Equation 5.12 is used to find the gassed power input (P_g) as dissipation rate (ε) varies for different types of impeller and substituting the value of P_g in Equation 5.11 to get ungassed power input, P_u, then using the simulated CFD value of P_g, final relative power draw P_g/P_u is calculated for different types of impeller. The final correlation of relative power draw P_g/P_u by combining the above (Equation 5.11 and 5.12) and CFD simulated results ($P_g=2\pi Nm\tau$) for different types of impeller is written as:

$$\frac{P_g}{P_u} = \frac{2\pi N\tau\left[0.1\left(\frac{N^2 d^4}{gwV^{2/3}}\right)^{-0.2}\left(\frac{Q_g}{NV}\right)^{-0.25}\right]}{\rho_l V\varepsilon} \tag{5.13}$$

In this study, Equation 5.13 is used for single and dual impeller of both Rushton and Concave blade impeller for comparing P_g/P_u with other correlations.

The global mass transfer co-efficient $\langle K_L a_T \rangle$ for an air-water stirred tank is given as

$$\langle K_L a_T \rangle = C_{K_L a_T}\left(\frac{P_g}{V}\right)^a v_g{}^b \tag{5.14}$$

According to Van't Riet (1979), the values of constant C_{KLa20}, a and b are 0.026, 0.4 and 0.5 respectively obtained from a fit to experimental measurements.

5.3.3. Solution Domain and Boundary conditions

Table 5.2 shows different geometrical dimensions with different boundary conditions. Impeller is rotated at 390-698 rpm speed. Superficial gas velocity of 0.0025-0.0074 is used.

Gas is supplied to the liquid through ring sparger which is kept below the impeller. Gas volume fraction of 1 is provided at sparger inlet. Diameter of bubble is taken as 0.002-0.0054m. Unstructured grids of around 270-520k cells were generated for single and dual impeller stirred tank respectively. Finer grid is employed near the impeller region so that the strong turbulence of fluid flow can be addressed accurately. Boundary condition plays a crucial role in numerical simulation especially in case where more than one phase is included. Table 5.2 gives the geometrical dimensions of Rushton and Concave blade impeller with different boundary conditions.

Table 5.2: Geometrical dimensions of Rushton and Concave blade impeller with different boundary conditions

Case	***D*** **(m)**	***d*** **(m)**	**Speed,** ***N*** **(rpm)**	**Superficial gas velocity,** v_g **(m/s)**	**Bubble diameter,** d_b **(mm)**	**Boundary condition at top surface**	**Impeller Types**	**Impeller No.**
1	0.63	0.21	390	0.0074	5.3	Velocity-inlet	Rushton	1
2	0.63	0.21	390	0.0074	5.3	Degassing	Rushton	1
3	0.63	0.21	390	0.0074	5.3	Velocity-inlet	Concave blade	1
4	0.63	0.21	390	0.0074	5.3	Degassing	Concave blade	1
5	0.26	0.086	698	0.003	3.4	Degassing	Concave blade	1
6	0.292	0.0973	450	0.0025	2	Symmetry	Rushton	2
7	0.292	0.0973	450	0.0025	2	Degassing	Rushton	2
8	0.292	0.0973	450	0.0025	2	Degassing	Concave blade	2

5.3.4. Prediction of hydrodynamics and mass transfer coefficient (K_La_{20})

5.3.4.1. Flow Pattern

Flow pattern of a fluid particle is the flow path of a fluid particle generated during turbulent motion. Flow pattern can be affected by many factors like types and number of impeller. Gassing condition also affects the flow pattern significantly. The predicted flow pattern defined by the vectors of mean velocity of Rushton and Concave blade impeller in gassing condition is shown in Figure 5.16.

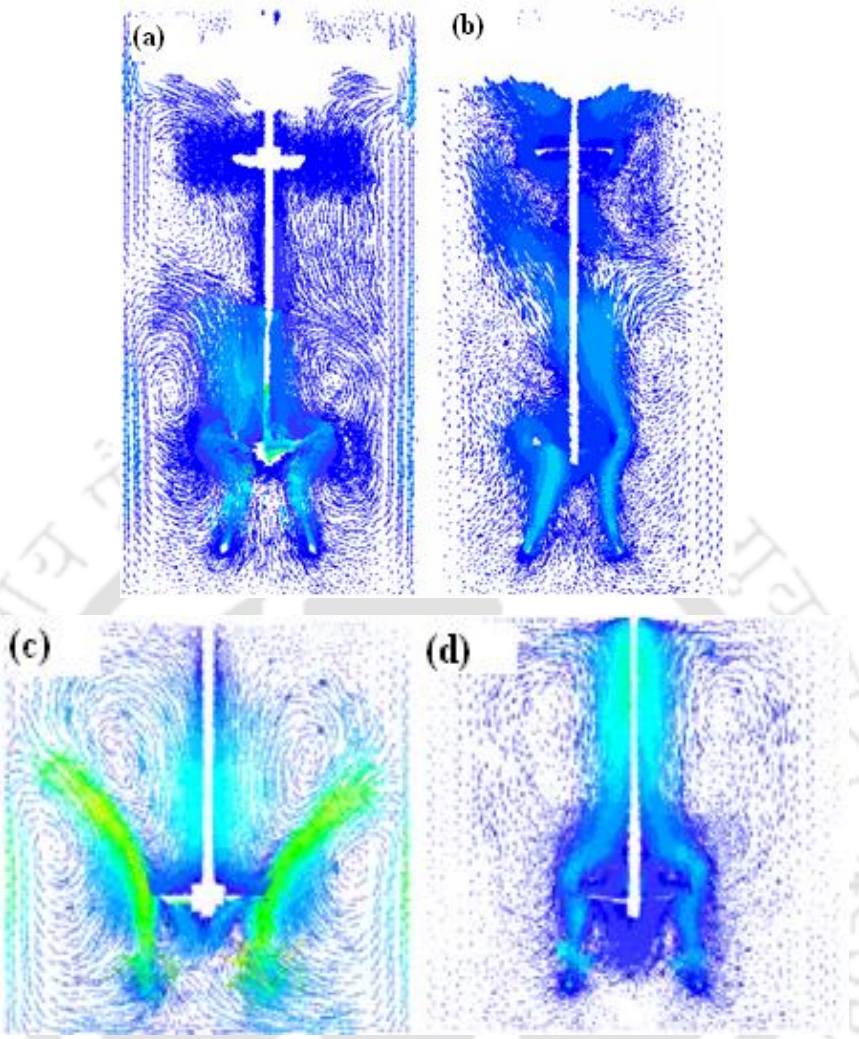

Figure 5.16: Flow patterns of velocity vectors of dual (a) Rushton impeller (b) Concave blade impeller and single (c) Rushton impeller (d) Concave blade impeller

The formation of vortex pair in ungassed condition by Rushton impeller is commonly understood however, in gassed condition, it is not the same. The formation of vortex pair of Rushton impeller in gassing condition is observed as “not proper” (the shape of commonly known vortex pair in ungassed condition is largely different in gassed condition). This is because of the influence of gas flow continuously supplied from sparger into the tank. In Concave blade impeller no formation of such vortex pair is observed, this is because of its concave blade shape. Strong flow circulation is observed near the impeller region and above the ring sparger in all the cases. In dual impeller more strong flow circulation gives by the lower impeller than the upper impeller.

5.3.4.2. Mass Transfer Coefficient

Mass transfer coefficient is a crucial parameter to be analyzed for clear understanding of the phase interaction mechanism of fluid particles in turbulent flow regime of stirred tanks. Global gas dispersion efficiency for different mass transfer model can be understood based on the average K_L which is independent of the interfacial area (avoiding the complexity of interfacial mechanism for initial understanding of mass transfer). Predicted local distribution of $K_L a_{20}$ for different model is done in this study and will be discussed in the subsequent paragraphs. Global $K_L a_{20}$ is being predicted by using criteria given by on Van't Riet (1979). The comparison of predicted average K_L for different model with literature result is given in Table 5.3. Penetration model over-predicts and rigid model under-predicts. Eddy cell model and slip velocity models are fair agreement with the experimental and simulated results of literature and these two models can be considered as the acceptable model for the estimation of K_L. Penetration and eddy cell model does not give the significant difference of K_L for single and dual of Rushton and Concave blade impeller while in slip velocity and rigid model, it is higher in Concave blade and dual impeller than the Rushton and dual impeller. Variation of K_L is predicted in different boundary conditions.

Table 5.3: Prediction of K_L for different models and comparison with results of Ranganathan and Sivaraman, 2011 (bold)

Case	**K_L (ms^{-1})**				
	CFD				**Experimental (Alves et al., 2004)**
	Penetration	**Eddy Cell**	**Slip velocity**	**Rigid**	
1	0.001574	0.000558	0.0011384	0.000216	
2	0.001574	0.000558	0.0011319	0.000214	
3	0.001528	0.000542	0.0008276	0.000157	
4	0.001552	0.000550	0.0007295	0.000138	
5	0.001196	0.000424	0.0015775	0.000299	
6	0.001616	0.000573	0.0011484	0.000218	
7	0.001574	0.000558	0.0024105	0.000457	0.000319
	0.000968	**0.000341**	**0.000275**	**0.000052**	
8	0.001552	0.000550	0.0021378	0.000405	

The analysis of local distribution of volumetric mass transfer coefficient (K_La_{20}) is more important for understanding the phase interaction process in gas-liquid stirred tank efficiency than the global volumetric mass transfer coefficient $\langle K_La_{20} \rangle$ especially in case when more than one impeller is used. The comparison of distribution of K_La_{20} for different models for dual Rushton and Concave blade impeller is shown in Figure 5.18a and b.

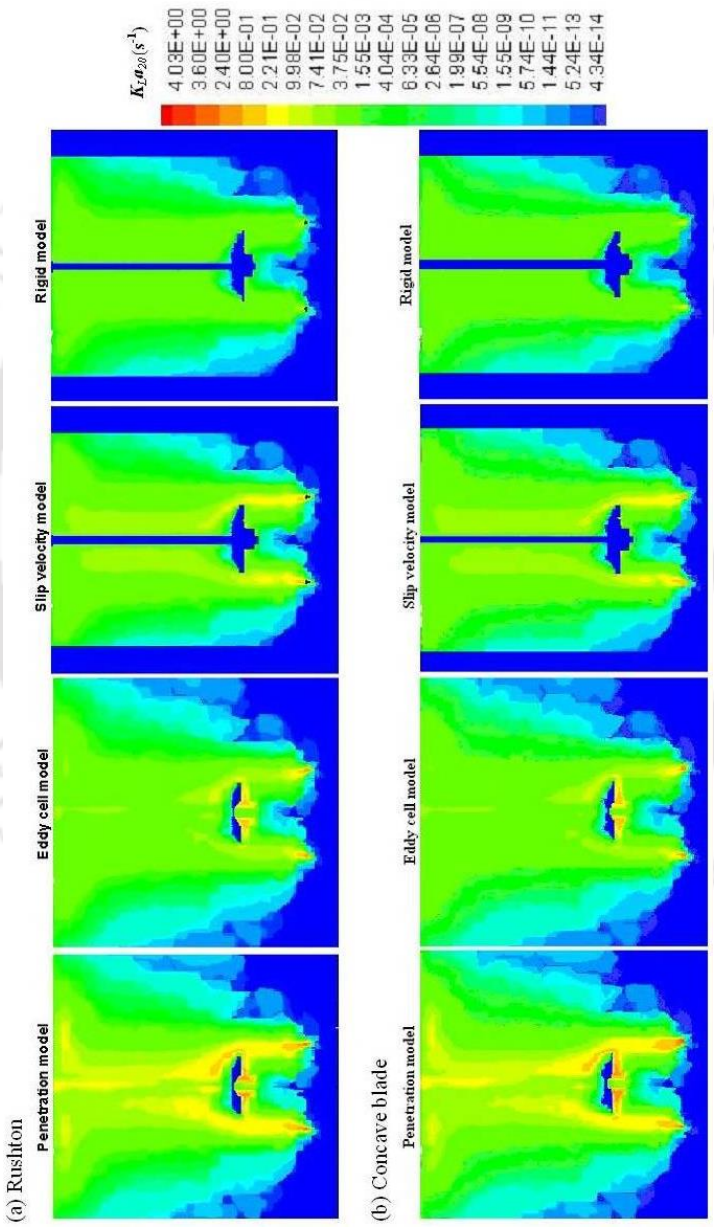

Figure 5.17: Distribution of volumetric mass transfer coefficient (K_La_{20}) of single (a) Rushton and (b) Concave blade impeller

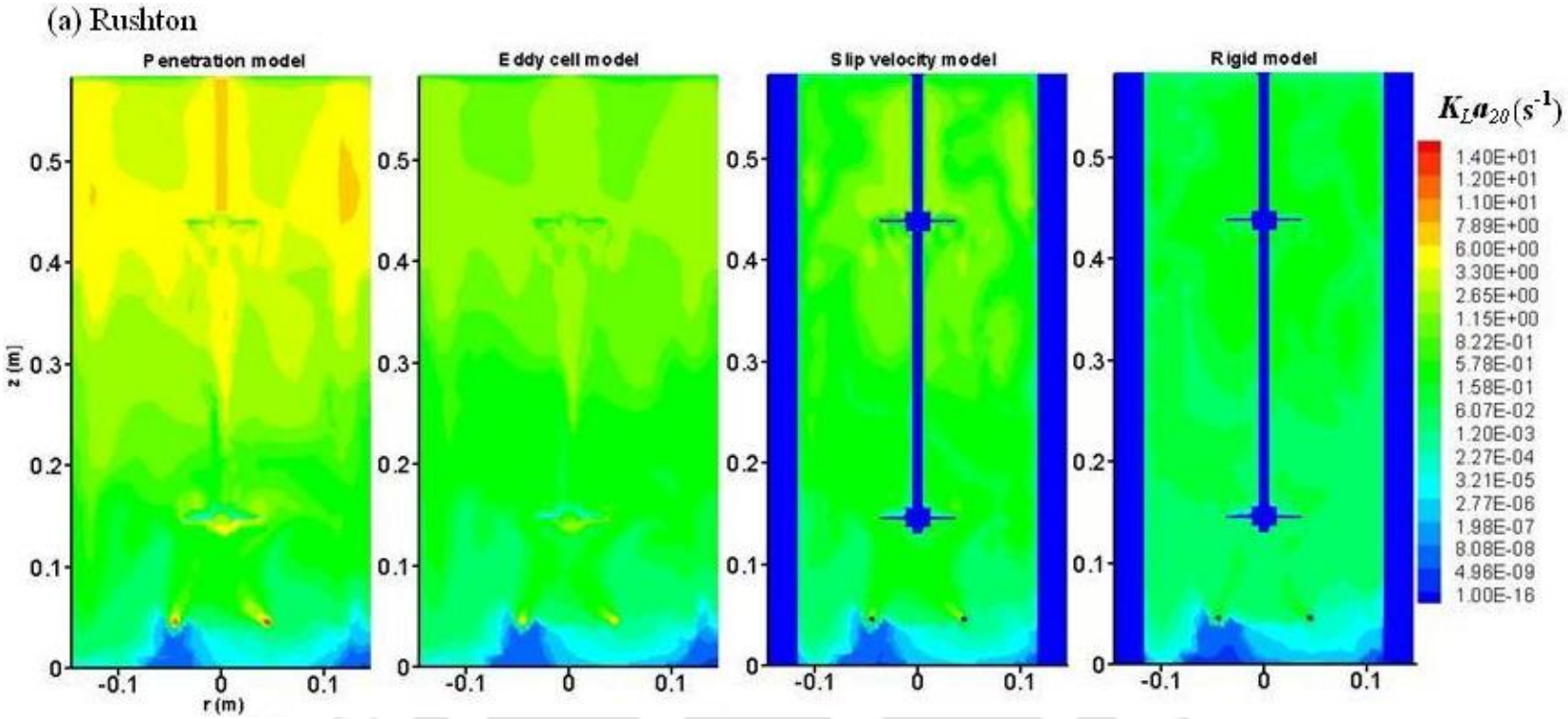

Figure 5.18a: Distribution of volumetric mass transfer coefficient ($K_L a_{20}$) of dual Rushton impeller

(b) Concave blade

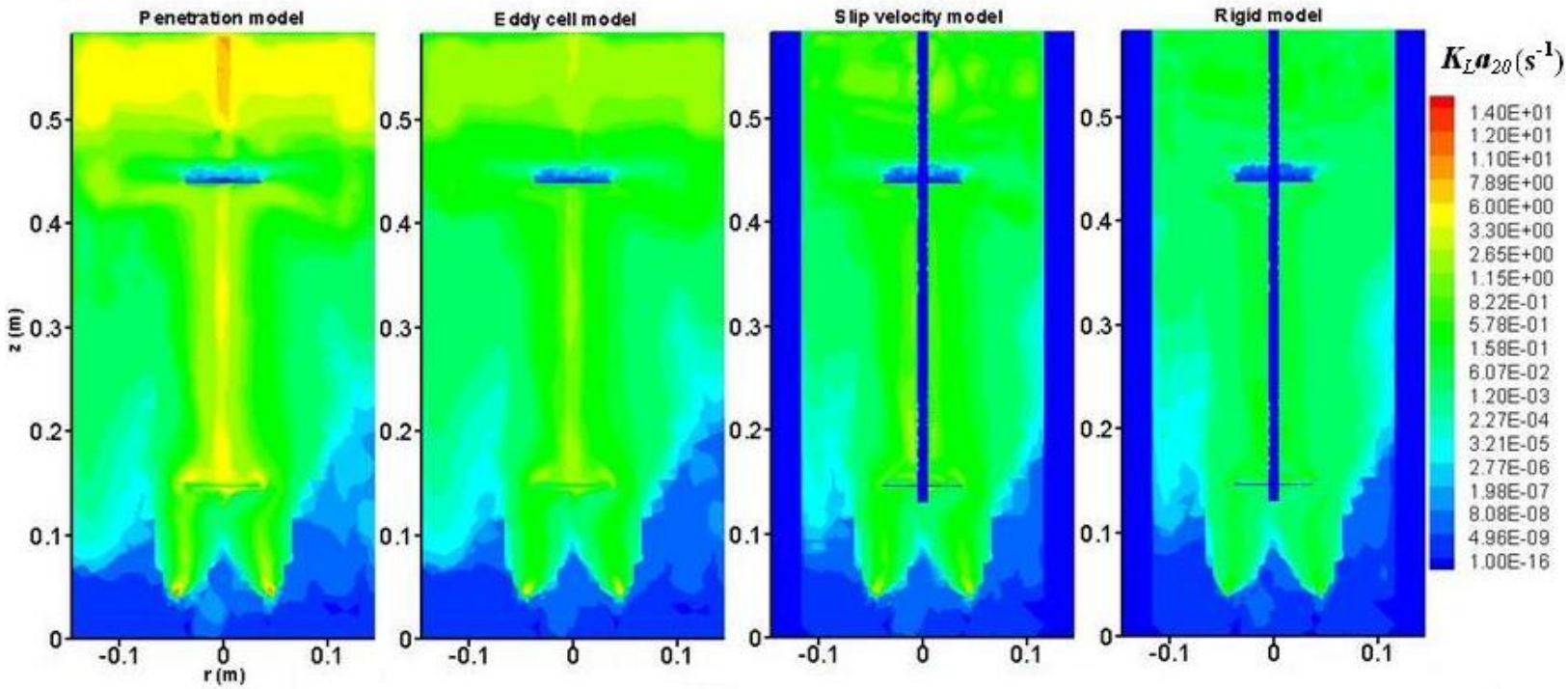

Figure 5.18b: Distribution of volumetric mass transfer coefficient ($K_L a_{20}$) of dual Concave blade impeller

The prediction of local K_La_{20} by penetration model is observed higher than other models (Figure 5.17 and 5.18a & b). Predicted K_La_{20} by penetration and eddy cell models are based on dissipation rate and K_La_{20} by these two models were observed distributing throughout the tank while in case of slip velocity and rigid model which are based on velocity of gas and water were observed with obstruction by the baffles near the tank wall. The formation of negative pressure zone is observed just above the impeller (upper impeller in case of dual impeller). The lower impeller does not form such negative pressure zone (dead zone) because of the influence of the flow circulation generated by the upper impeller (Figure 5.18). The magnitude of local K_La_{20} is found slightly higher (around 5%) in case of dual Rushton impeller than the Concave blade impeller and this finding are in agreement with Gimbun et al. (2009) and Zhu et al. (2001). However, Gimbun et al. (2009) argued that this lower value of K_La_{20} in Concave blade is attributed to several factors and the efficiency of stirred tank was characterized with energy efficiency based on relative power draw rather than K_La_{20} which is based on too many processes of interfacial fluid particles. It is noteworthy to mention that the estimation of K_La_{20} is too complex as it involves so many mechanisms in the process of mass transfer from one phase to another phase and hence simple correlation often fail to correctly predict it (Moilanen, 2009). The predicted local K_La_{20} is found higher (around 6%) in Concave blade impeller than the Rushton impeller in single impeller stirred tank. Bakker (2000) study shows that predicted K_La_{20} is same for both multiple Rushton and Concave blade impeller in the superficial gas velocity for upto 0.01m/s and significantly increases the predicted K_La_{20} by Concave blade impeller beyond this limit. In this study, the superficial gas velocity is within 0.01m/s (0.0024-0.0074m/s) and, hence, no such significant difference is predicted between dual stirred tank with Rushton and Concave blade impeller. The global volumetric K_La_{20} predicted based on Equation 5.14 is shown in Table 5.4. The predicted $K_La_{20}$is appeared higher in Concave blade impeller than the Rushton impeller in dual (15.21%) and in single (6.09%) impeller stirred tank.

Table 5.4: Prediction of global mass transfer coefficient

Case	P_g/V (w/m^3)	Van't Riet (1979) $\langle K_L a_{20} \rangle$ (1/s)	% efficient $\langle K_L a_{20} \rangle$ of Concave blade impeller over Rushton impeller
1	2706.12	0.0528	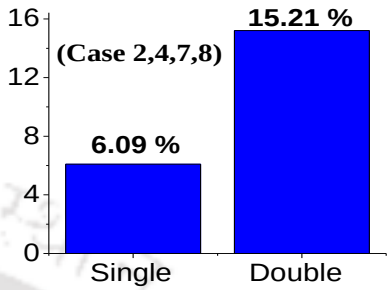
2	1224.34	0.0384	
3	2126.38	0.0479	
4	1432.65	0.0409	
5	707.57	0.0197	
6	789.25	0.0187	
7	1372.69	0.0234	
8	2073.74	0.0276	

5.3.4.3. Prediction of relative power draw

The overall efficiency of a mechanical stirred tank necessarily understood from the global quantities like power draw capability of the system. Power draw varies with the system in gassed and ungassed condition. The power draw of gassed condition with respect to the ungassed condition is of important factor to be analyzed for understanding the power draw characteristic in gassed condition. Here, relative power draw (ratio of gassed power input to ungassed power input) is generally introduced to analyze the efficiency. The predicted relative power draw, P_g/P_u is shown in Table 5.5 for different tank configuration. Concave blade predicts higher power draw as compared with Rushton impeller. Dual impeller also gives higher power draw than the single impeller. The predicted results are in good agreement with published literature. P_g/P_u also affects by the boundary condition adopted. The velocity-inlet boundary condition over-predicts P_g/P_u than the degassing boundary condition.

Table 5. 5: Predictions of relative power draw (P_g/P_u)

	Cases							
	1	**2**	**3**	**4**	**5**	**6**	**7**	**8**
Present work [CFD]	0.96	0.43	0.75	0.51	0.81	0.9	1.56	2.37
Gimbun et al. (2009) [CFD]		0.38			0.75			
Meyer et al. (1999)					0.71			
Equation (5.8)		0.42						
Equation (5.10)							0.73	
Equation (5.13)	0.87	0.39	0.77	0.49	0.57	0.76	1.47	2.0

The capability of power draw with reference to the single Rushton is shown in Figure 5.19. Higher power draw capability is predicted by Concave blade impeller (34% in dual and 16 % in single case) than the Rushton impeller. Dual impeller predicts higher power draw capability (70-80 %) than the single impeller. Correlation of P_g/P_u applicable for different types of impeller estimates in good agreement with other correlation and with predicted results.

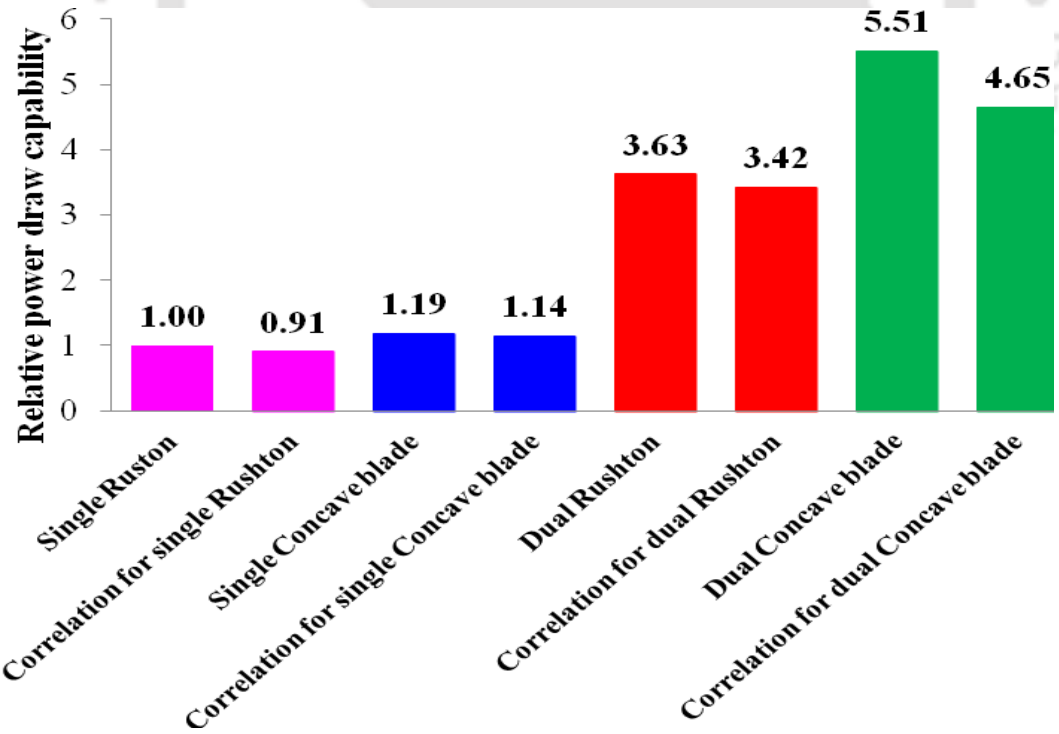

Figure 5.19: Relative power draw (P_g/P_u) capability with respect to the single Rushton with other configuration (case 2, 4, 7, 8)

Efficiency of a stirred tank in gas-liquid system can be expressed in terms of energy efficiency and is the qualitative function of power draw and mass transfer rate in the system (Energy=power draw/mass transfer rate). Power draw is taken as the relative power draw and mass transfer rate as global K_La_{20} achieved from Equation 5.14 in Table 5.4. Energy is expressed as efficiency number which is shown in table 5 for different cases of stirred tank. So, at the same amount of mass transfer capability to be achieved, the efficiency of a stirred tank can be understood from the power draw capability of the system. Hence, in this study also, there is no significant difference of mass transfer in Rushton and Concave blade impeller predicted; however, there is great difference in power draw capability much higher by the Concave blade impeller than the Rushton impeller. The efficiency or energy efficiency is being shown in the Table 5.6, indicates that overall efficiency higher in the case of Concave blade impeller (8.14% more efficient in single and 21.93% in dual impeller) than the Rushton impeller.

Table 5.6: Overall efficiency of Concave blade impeller over Rushton impeller

Case	P_g/P_u	K_La_{20}	**Energy (Efficiency number)**	**% overall efficiency of Concave blade impeller over the Rushton impeller (case 2,4,7,8)**
1	0.96	0.0528	18.18	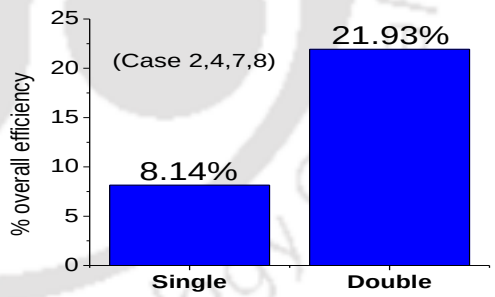
2	0.43	0.0384	11.29	
3	0.75	0.0479	15.73	
4	0.50	0.0409	12.29	
5	0.81	0.0197	41.12	
6	0.90	0.0187	48.05	
7	1.57	0.0234	66.98	
8	2.37	0.0276	85.79	

5.3.5. Conclusion

Mass transfer coefficient is predicted based on different models. Penetration model apparently over-predicts and rigid model under-predicts. Eddy cell model and slip velocity models can be used to predict the mass transfer coefficient. No significant difference in the predicted K_La_{20} is observed in case of Concave blade and Rushton impeller in lower values of superficial gas velocity. Boundary condition plays important role to correctly predicting the

fluid flow characteristics and hence, its suitable adoption in numerical simulation especially when more than one phase is involved in the system need to be addressed properly. Degassing boundary condition can predict acceptably accurate results and is more suitable than the velocity-inlet condition. Significant gassed power draw is achieved by Concave blade impeller as compared with Rushton impeller. Based on the energy efficiency principle, the overall efficiency of a stirred tank is achieved through power draw capability (when the same mass transfer coefficient in Rushton and Concave blade impeller is to be achieved), therefore, it has been concluded in this study that Concave blade has more gas dispersion capability than the Rushton impeller even though both produces same amount of mass transfer rate. For more accurate understanding of mass transfer phenomenon, study on wide range of superficial gas velocity is recommended.

CHAPTER 6

LARGE EDDY SIMULATION OF TURBULENT FLOW IN STIRRED TANK OF CONCAVE BLADE IMPELLER

6.1. Introduction

In turbulent flow modeling, the most important aspect to be considered for accurate analysis is turbulence modeling. In literature there are several approaches of turbulence models (*k*-*ε*; *k*-*ω*; Reynolds stress model, RSM; Large eddy simulation, LES; etc.) and most of the studies were performed based on *k*-*ε* (Rahimi and Parvareh, 2005; Deglon and Meyer, 2006; Khopkar et al., 2006; Kasat et al., 2008; Gimbun et al., 2009) and RSM (Gunyol and Mudde, 2009; Joshi et al., 2011; Huang and Li, 2013) models. The under-prediction of dissipative scales is quite often mentioned in many studies when *k*-*ε* and RSM models are used especially near the impeller region where the flow is extremely anisotropic (Yeaoh et al., 2004; Mostek et al., 2005). To overcome such under-prediction of dissipative scale; more delicate in terms of accounting to lower scales of turbulence, LES model is introduced and first applied by Eggels (1996). LES approach is increasingly used by several turbulent flow analyst because of its strong influence in turbulent flows of different scaled eddies. Several studies (Derksen and Van den Akker, 1999; Hartmann et al., 2004a, 2004b; Yeoh et al., 2004; Alcamo et al., 2005; Jahoda et al., 2007; Delafosse et al., 2008, 2009; Murthy and Joshi, 2008; Yapici et al., 2008; Li et al., 2011) have shown to perform well in capturing the complexity of turbulent flow; better capability and accurate prediction of turbulent flow especially the dissipative characteristics in stirred tank by LES model among the other turbulence models. LES model is filtered based approach which separates the larger eddies and smaller eddies. Larger eddies are resolved and smaller one are modeled by subgrid scale (SGS) models. The accurate prediction of turbulent flow by LES model is because of the consideration of different scales of eddies which is the same sense of considering the flow as anisotropic nature and is absolutely realistic in turbulent flow. In contrary to this RANS approach models are based on isotropic assumption of flow which is very untrue in turbulent

flow. LES model is also a time consuming model as compared with RANS (Reynolds averaged-Navier Stokes) based models. So, it has been said that LES model lies between RANS and DNS (direct simulation model) in terms of computational cost and accuracy. Jahoda et al. (2007) concluded from their study that LES approach is the most time consuming model, however, it can describe the real flow in stirred tanks better and more realistic courses of the liquid homogenization; and it is the best model to fit well with the experimental results.

In this study, stirred tank driven by Rushton (having straight blade type) and Concave blade impeller (having concave blade type) is being modeled by LES turbulence model to predict the turbulent characteristics which is essentially to be understood in designing process of such stirred tanks.

6.2. Computational model

The methodology and study domain used in this study will be presented in this section. This study is based on the numerical simulations of computational fluid dynamics (CFD). The basic governing equations and other numerical techniques involved in this study are discussed in the next following section.

6.2.1. Numerical techniques

The numerical techniques adopted plays important role in accurately predicting the fluid flow characteristics. The simulation of stirred tanks in turbulent flow requires modeling of impeller as well as the turbulent flow. So, in this study, impeller is modeled by Multiple Reference Frame (MRF) impeller model. In MRF model, impeller region is modeled as stationary and tank wall and baffles are modeled as rotating zones. MRF model is suitable for baffled-stirred tanks. LES turbulence approach (Sheng et al., 2000; Alcamo et al., 2005; Jahoda et al., 2007; Zadghaffari et al., 2010; Li et al., 2011) is used as turbulence model in this study to solve the governing Navier –stokes equations (detail equations of LES model is given in section 2.3.). To avoid the convergence problem, the initial simulation was started with k-ε turbulence model and once the steady state is achieved; the simulation was switched to LES model. The discretization scheme for momentum is chosen to Bounded Central Differencing. Details of these numerical techniques are given in Chapter 2. The simulation is

considered steady state when the residual drops below 10^{-3}. This study is achieved through unsteady solution to get the instantaneous characteristics. The initial simulation was started with time step size 0.00001 s for pressure based calculation and as the solution progressed the time size has been gradually increased to 0.001 s in order to save computational cost.

6.2.2. LES approach

In turbulent flows, the flows are highly anisotropic and contains extremely complex flow behavior which simply classified as large scale eddy (larger scale flows) and small scale eddy (small scale flows) in LES model. The large eddies are strongly flow dependent structures which directly absorbs energy from the mean flows; highly anisotropic and vortical in nature; and are responsible for most of the transport in turbulent flows. In contrary to this, the small eddies are more universal which dissipates the energy produced by the large eddies and are assumed to be isotropic in nature and needs to be modeled. So, LES model is based on the ideas of two terms "large eddies" and "small eddies" where the large scale eddies are directly resolved (filtered) and solves in Navier-Stocks equations and small scale eddies are modeled by sub-grid scale (SGS) models. LES method lies between Reynolds Stress Model (RSM) and Direct Numerical Simulation (DNS) in terms of computational expenses; and expected to be more accurate and reliable than RSM in which large scale unsteadiness is significant (Pope, 2000). LES model overcomes to resolve all scales of turbulent motions in DNS method which is very costly in case of high Reynolds number (cost increases as the cube of Reynolds number) by modeling only the residuals simply with SGS models. There are few SGS models proposed in literature, e.g., Smagorinsky-Lilly model**,** Dynamic Smagorinsky-Lilly model, Wall-Adapting Local Eddy-Viscosity (WALE) Model, and Dynamic Kinetic Energy (Kinetic Energy Transport) model. In this study, Smagorinsky-Lilly and Dynamic Kinetic Energy models are used as SGS models and discussed in the following sections.

Figure 6.1 shows a schematic diagram of the LES approach in terms of the energy spectrum. k_c represents (Figure 6.1) the cutoff wave number which separates (filters) the large eddies from small eddies; and is chosen to lie in inertial subrange of the energy spectrum. k_1 is the integral scale wave number and k_η is the Kolmogorov scale wave number. Once the filtering process is done from the Navier-Stokes equations, the residual eddies (SGS) are modeled

accordingly by the above mentioned SGS models. In real space, the filtering is defined as a moving spatial average and the bandwidth (filter width) is defined by $\Delta=2\pi/k_c$ (Sheng et al., 2000) which effectively ignores the eddies whose scales are smaller than this filter width.

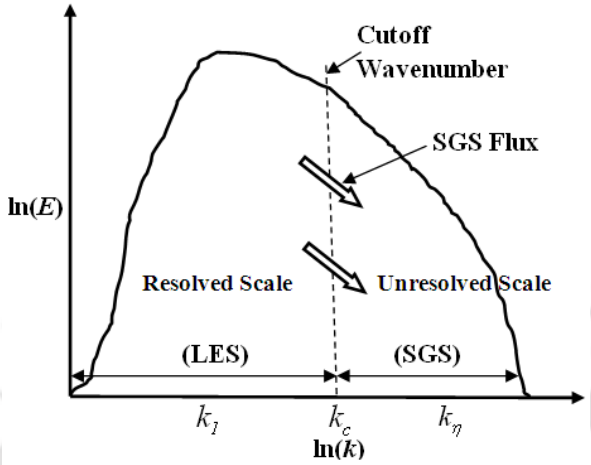

Figure 6.1: Schematic model of turbulent kinetic energy transport (Sheng et al., 2000)

6.2.3. LES equations

The governing equations employed in LES are obtained by filtering the time-dependent Navier-Stokes equations in either Fourier (wave-number) space or configuration (physical) space. The filtering process effectively filters out the eddies whose scales are smaller than the filter width or grid spacing used in the computations (Fluent 6.3, 2006).

The large-scale component (filtered variable) of a quantity ϕ is given by Leonard as:

$$\bar{\phi}(X)=\int_D G(X,X')\,\phi(X')\,dX' \tag{6.1}$$

Where, G is the filtering function that determines the scale of the resolved eddies and D is the fluid domain. The finite-volume discretization provides the filtering operation implicitly as:

$$\bar{\phi}(X)=\frac{1}{V}\int_D \phi(X')\,dX',\ X' \in D \tag{6.2}$$

Where, V is the volume of a computational domain.

The spaced-filtered Navier-Stokes equations of mass and momentum for incompressible Newtonian fluid flow are given as:

Mass:

$$\frac{\partial \bar{u}_i}{\partial x_i}=0 \tag{6.3}$$

Momentum:

$$\frac{\partial \bar{u}_i}{\partial t} + \bar{u}_i \frac{\partial \bar{u}_j}{\partial x_i} = -\frac{1}{\rho}\frac{\partial \bar{p}}{\partial x_i} + \nu \frac{\partial^2 \bar{u}_i}{\partial x_j^2} - \frac{\partial \tau_{ij}}{\partial x_j} \tag{6.4}$$

Where, u is velocity vector; p is pressure; ν is kinematic viscosity and τ_{ij} is the SGS stress tensor and is given as:

$$\tau_{ij} = \overline{u_i u_j} - \bar{u}_i \bar{u}_j \tag{6.5}$$

The SGS stresses resulting from the filtering operation are unknown and require modeling. The unknown SGS stress tensor τ_{ij} and the filtered rate of strain tensor S_{ij} are related in eddy viscosity model as $\tau_{ij} - \frac{1}{3}\partial_{ij}\tau_{kk} = -2\nu_t \bar{S}_{ij}$ (6.6)

SGS models used in this study are Smagorinsky-Lilly and Kinetic energy transport model and are discussed as:

(1) Smagorinsky-Lilly model (Smagorinsky, 1963):

Smagorinsky-Lilly model is the most commonly used SGS model (Alcamo et al., 2005; Zadghaffari et al., 2010). In this model, the eddy viscosity is modeled as:

$$\nu_t = \left(C_s \Delta\right)^2 \left|\bar{S}\right| \tag{6.7}$$

Where, $C_s\Delta$ is the mixing length for SGS and $\left|\bar{S}\right| \equiv \sqrt{2S_{ij}S_{ij}}$. The mixing length in FLUENT 6.3 is computed as $C_s = \min\left(\kappa d, C_s V_{cell}^{1/3}\right)$, where κ is the von Karman constant, d is the distance from the closest wall, and V_{cell} is the volume of the computational cell. C_S is the Smarorinsky constant and a value of 0.1 is used in this study.

(2) Kinetic Energy Transport model (Kim and Menon, 1997):

Kinetic energy transport SGS model is also used in this study. The SGS kinetic energy (k_{sgs}) is defined as:

$$k_{sgs} = \frac{1}{2}\left(\overline{u_k^2} - \bar{u}_k^2\right) \tag{6.8}$$

The SGS eddy viscosity, ν_t, is computed using k_{sgs} as:

$$\nu_t = C_k k_{sgs}^{1/2} \Delta_f \tag{6.9}$$

Where, Δ_f is the filter size computed as $V^{1/3}$.

The SGS stress can then be written as:

$$\tau_{ij} - \frac{2}{3} k_{sgs} \delta_{ij} = -2 C_k k_{sgs}^{1/2} \Delta_f \bar{S}_{ij} \tag{6.10}$$

Then the transport equation for SGS kinetic energy is written as:

$$\frac{\partial \bar{k}_{sgs}}{\partial t} + \frac{\partial \bar{u}_j \bar{k}_{sgs}}{\partial x_j} = -\tau_{ij} \frac{\partial \bar{u}_i}{\partial x_j} - C_\varepsilon \frac{k_{sgs}^{3/2}}{\Delta_f} + \frac{\partial}{\partial x_j} \left(\frac{\nu_t}{\sigma_k} \frac{\partial k_{sgs}}{\partial x_j} \right) \tag{6.11}$$

In the above equations, the model constants, C_k and C_ε are determined dynamically by Kim and Menon (1997). σ_k is equal to 1.0.

6.2.4. Stirred tank domain

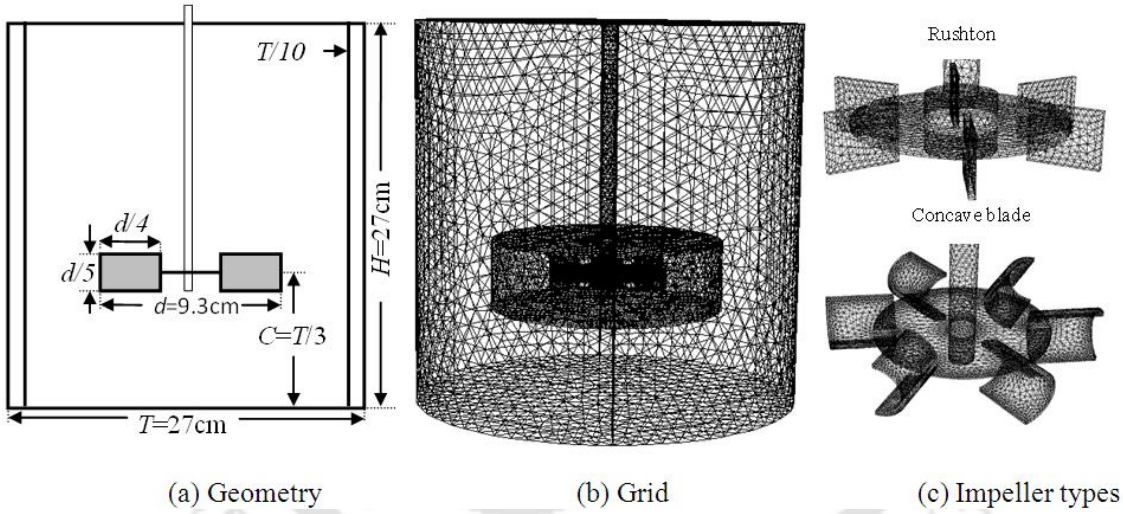

Figure 6.2: Stirred tank configuration

Stirred tank of having diameter (D) 27cm mounted with single impeller of Rushton and Concave blade of diameter (d) 9.3 cm is used in this study. Impeller is mounted (C) at $D/3$ and rotated at the speed (N) of 200 rpm. Water is used as fluid for this computational study at a height (H) equal to tank height (density, ρ=998.2kg/m^3 and dynamic viscosity, μ=0.001003kg/ms at temperature of 20^{0}C). The geometrical dimension in this study is taken same as the dimensions of Wu and Patterson (1989) study for fair comparison of results. The geometrical configuration and generated grid of stirred tank is shown in Figure 6.2. Around 240k grid cells were generated for this computational domain. As this study is done with LES turbulence model, the size of grid is very important in accuracy of results. Hence, grid

sensitivity analysis was performed with coarse (190k grid cells), medium coarse (240 k grid cells) and fine coarse (300k grid cells) and found medium coarse gives reasonable result, however, little improvement were observed in fine coarse grid cells but consuming longer time to simulate and hence not considered for this study.

6.3. Result and discussion

The turbulent characteristics (velocities, Reynolds stresses, and dissipative scales) by comparing between Rushton and Concave blade impeller will be discussed and presented in this section.

6.3.1. Turbulent velocities

The flow field (velocities) in turbulent flow is of important characteristic for initial basic understanding of its inherent dynamics in fluid flows. In 3-dimensional flows, fluid particle acts differently in different directions and are of important aspects in detail investigation.

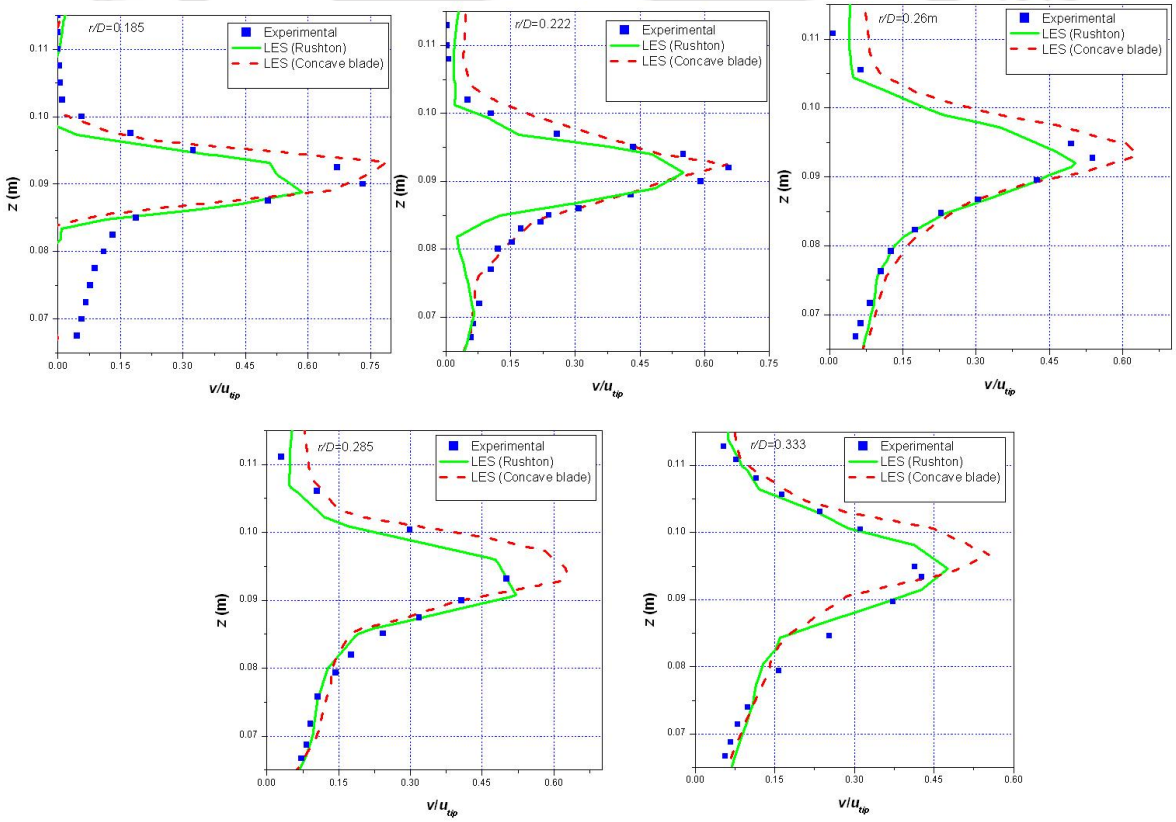

Figure 6.3: Comparison of normalized radial velocity (v/u_{tip}) between Rushton and Concave blade impeller with experimental results (Wu and Patterson, 1989) at various radial positions

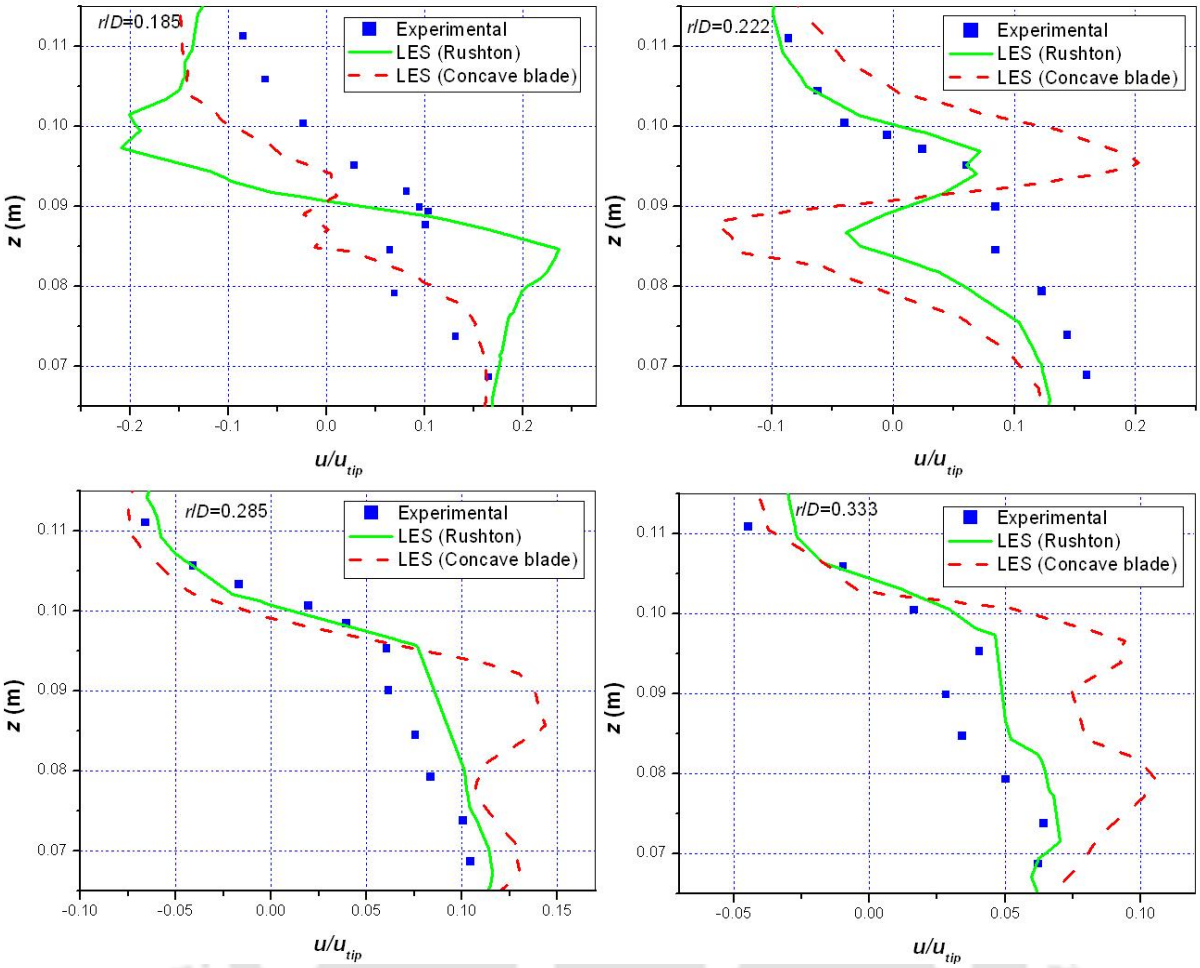

Figure 6.4: Comparison of normalized axial velocity (u/u_{tip}) between Rushton and Concave blade impeller with experimental results (Wu and Patterson, 1989) at various radial positions

Fluid flows in stirred tank of having rotating component in turbulent flow regime creates different regions leading to un-uniform magnitude in turbulent characteristics. In such condition spatial investigation of such characteristics is highly imperative. In this study also, every turbulent characteristics were investigated in detail spatially (radial as well as axial) so that enough information about the turbulent flow in such tanks can be achieved. Figure 6.3 and 6.4 shows the comparison of radial and axial velocities between Rushton and Concave blade impeller with experimental results at different radial positions. Normalized radial velocity (v/u_{tip}) is found higher at impeller tip (r/D=0.185) which is 0.6 for Rushton and 0.8 for Concave blade impeller as compared with other radial positions (r/D=0.222, 285 and 0.333) which have around 0.5 for Rushton and 0.6 for Concave blade impeller (Figure 6.3). v/u_{tip} is always found higher by Concave blade than the Rushton impeller in all the cases of

different radial positions indicating strong turbulence nature in stirred tank of Concave blade impeller. Strong turbulent nature is highly required where the mixing processes are taken place as prime objective of the system. Such higher magnitude by Concave blade impeller can also be observed in case of axial velocity profile (Figure 6.4). There is good agreement with the experimental result in case of radial velocity profile, however, there is slight deviation in case of axial velocity profile, and this may be because of the sensitivity of the grids.

As mentioned above that LES model is based on resolved and unresolved scales of eddies, the unresolved scale is modeled by using different SGS models giving hint to its flexibility and inconsistency in subgrid characteristics. To understand such difference in results of different SGS model, two types of SGS models (Smagorinsky and Kinetic Energy) were used in this study even though this study does not focus on its detail investigation. So, in this study, only the flow patterns produced by these two SGS models are shown (Figure 6.5). Further investigations were performed based on the latter SGS method for extracting the dissipative scales (subgrid kinetic energy and dissipation rate).

(a) Rushton

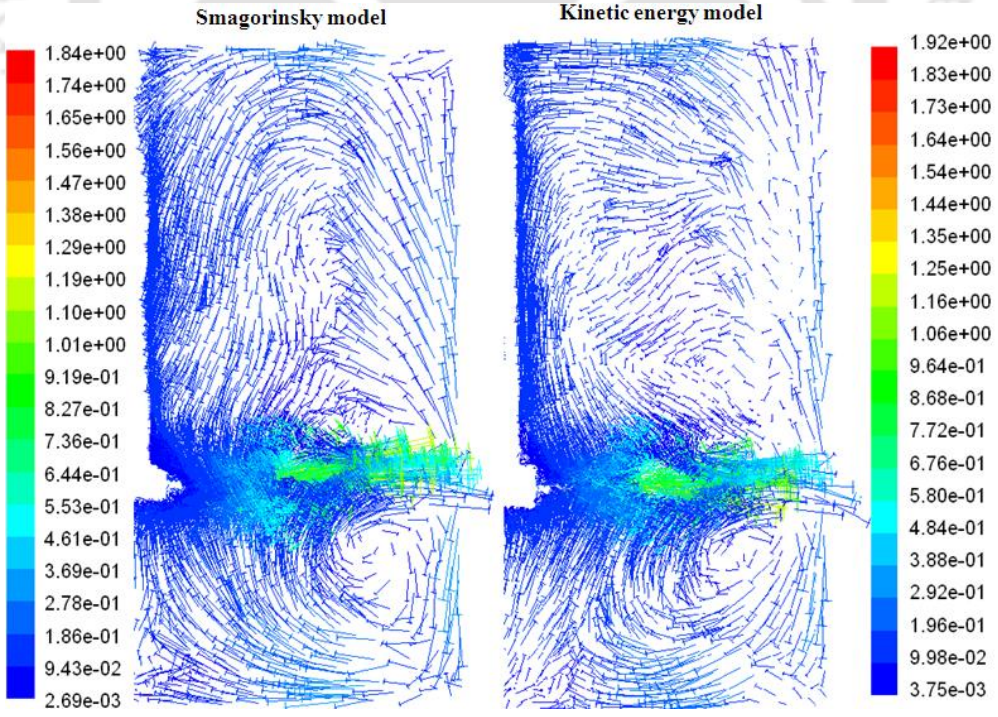

(b) Concave blade

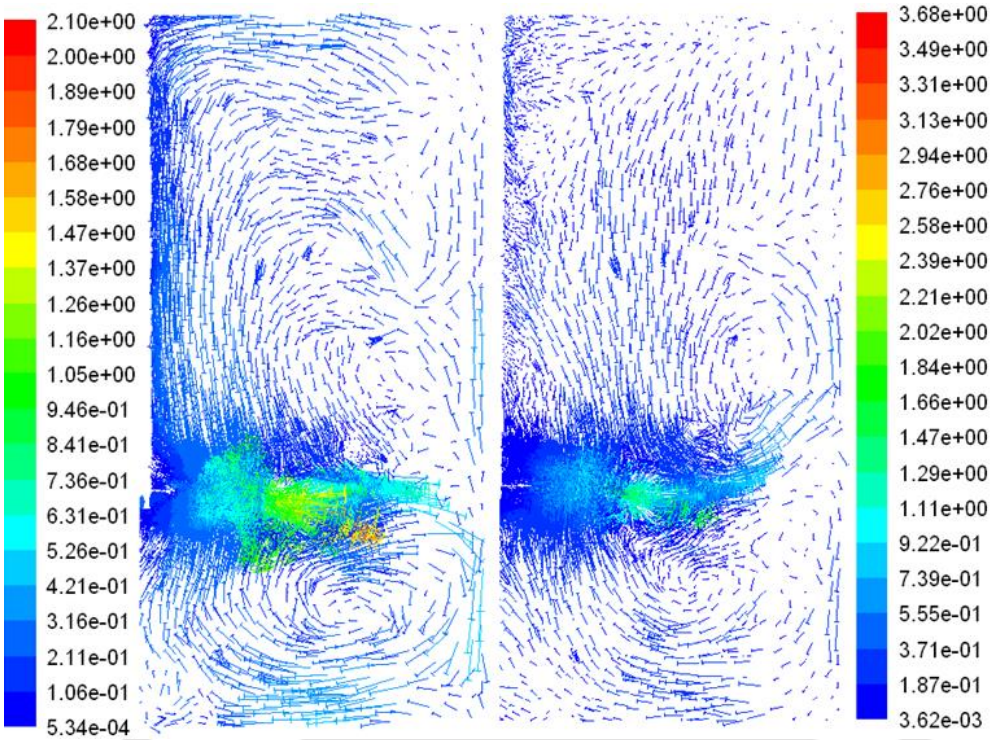

Figure 6.5: Comparison of SGS models (Smagorinsky and Kinetic Energy) between Rushton and Concave blade impeller defined by unsteady statistics of mean velocity (m/s) at 5 sec (half of the tank is shown here)

Figure 6.5 shows the comparison of SGS models defined by the mean velocity vectors of Rushton and Concave blade impeller. The magnitude of mean velocity is predicted higher in Concave blade than Rushton impeller by these two SGS models. There is a slight change in fluid flow pattern witnessed between these two SGS model. No significant variation of magnitude is predicted in Rushton impeller between SGS models, however, there is good variation predicted (higher in Kinetic Energy model). From this vector plot of fluid flow, it is witnessed that maximum flow circulation takes place at and near the impeller region indicating the strong influence of impeller geometries in creating the fluid flow circulation paths. And because of such understanding and knowledge earned from such plots enhances the idea of choosing suitable impeller type for an efficient system. So, this study aims in differentiating the uniquely behaved nature by Rushton and Concave blade impeller. These impellers have different features in geometry, Rushton has straight blade and Concave blade has concave blade type.

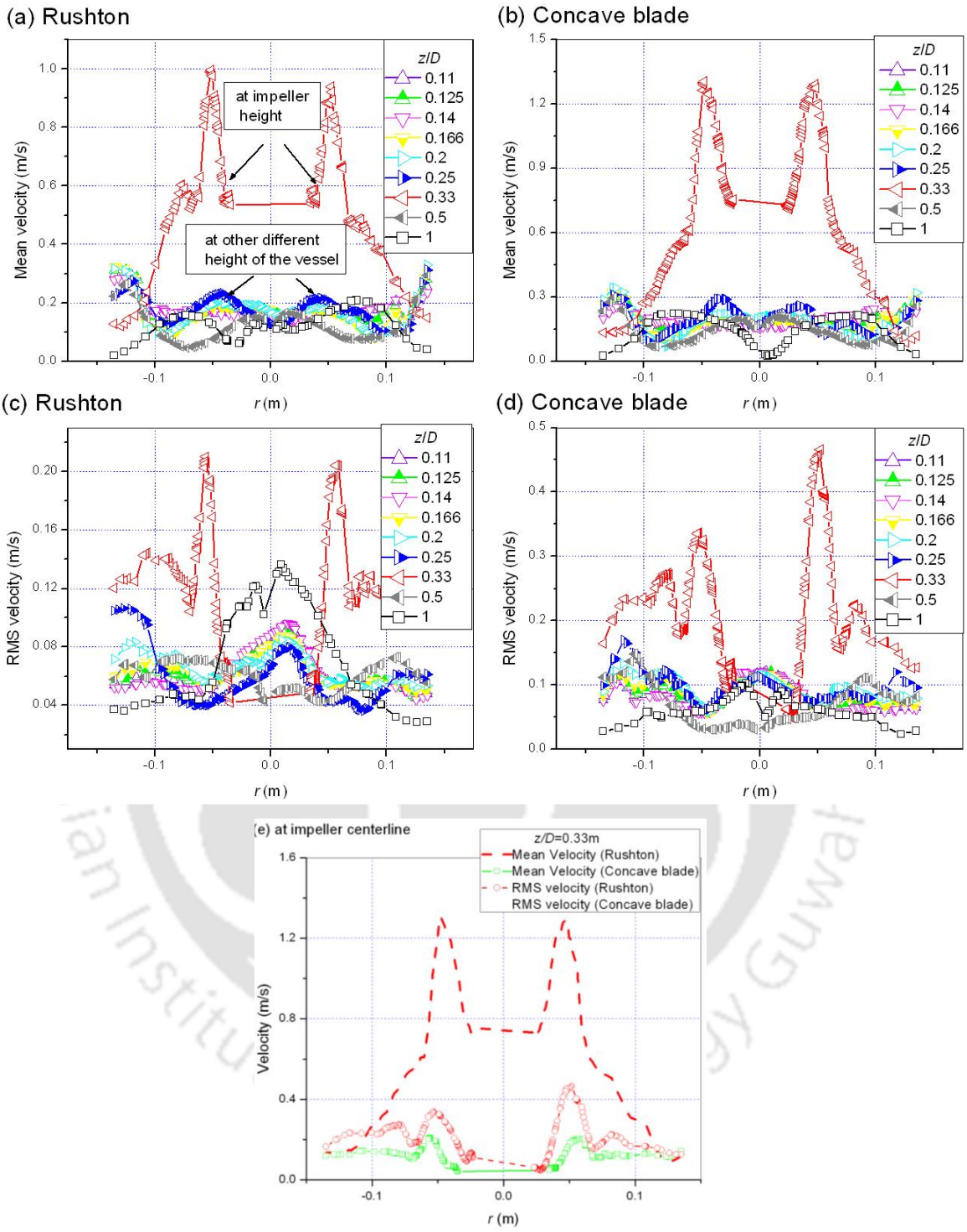

Figure 6.6: Comparison of unsteady statistics of mean velocity and root mean square (RMS) velocity (a-d) at different axial positions, *z*, (e) between Rushton and Concave blade impeller at impeller height

Figure 6.6 shows the comparison of mean velocity and root mean square (RMS) velocity at different radial positions for Rushton and Concave blade impeller. Mean and RMS velocities vary at different radial positions with significant observance at centerline of impeller (z/D=0.333) from other regions of the vessel in Figure 6.6(a-d). Mean velocities of Rushton and Concave blade impeller does not vary much in all regions of the vessel except at impeller region, however, in case of RMS velocity there is slight variation observed at other regions of the vessel as well. Figure 6.6(e) depicts the comparison of mean and RMS velocity between Rushton and Concave blade impeller at impeller centerline (z/D=0.333). Only this axial position is picked up for comparison between Rushton and Concave blade impeller because it gives significant variation in mean velocity as well as in RMS velocity too. Mean and RMS velocities were observed higher in case of Concave blade than Rushton impeller (Figure 6.6e).

The instantaneous velocity observed at various flow time is shown in Figure 6.7. It compares the mean velocities at different radial positions between Rushton and Concave blade impeller. There is strong variation of mean flow with flow time observed indicating the unsteady nature of flows inside the vessel when the impeller starts rotating. Concave blade impeller gives higher mean velocity over time than Rushton impeller.

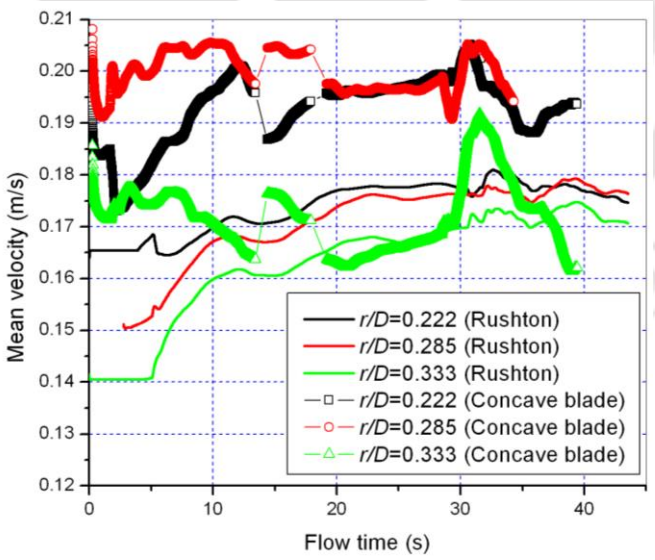

Figure 6.7: Comparison of instantaneous mean velocity between Rushton and Concave blade impeller at different radial positions, r.

6.3.2. Subgrid stresses

(a) Rushton

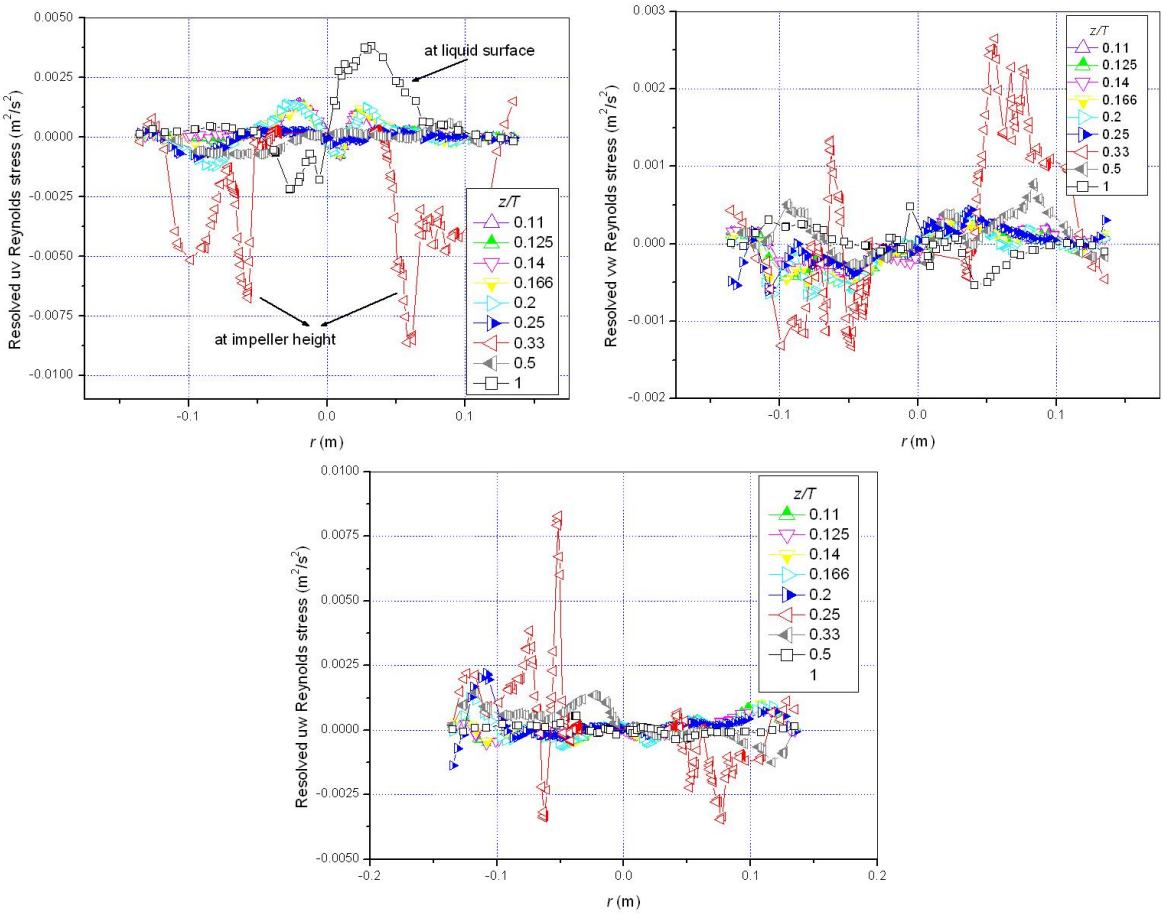

(b) Concave blade

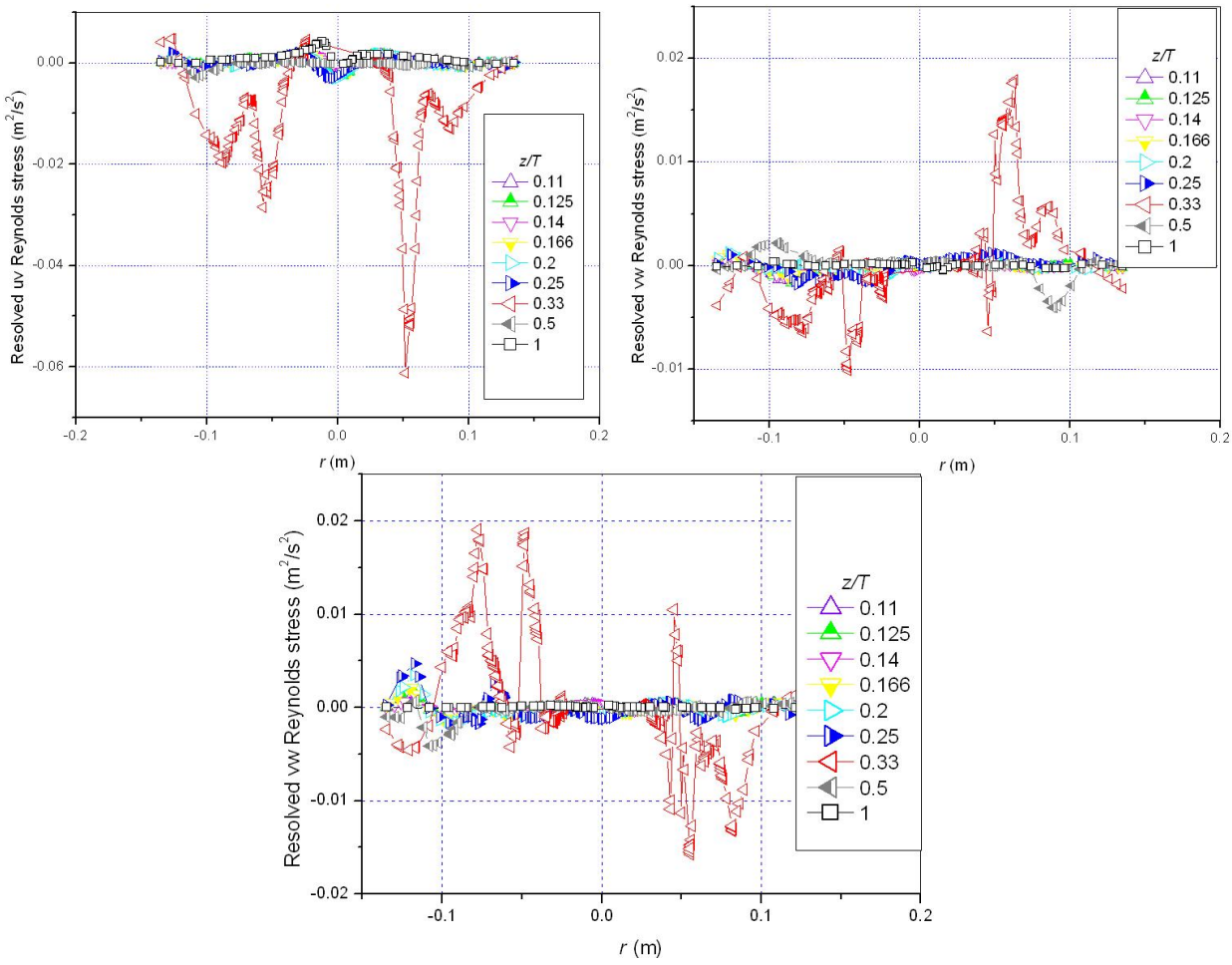

(c) at impeller tip

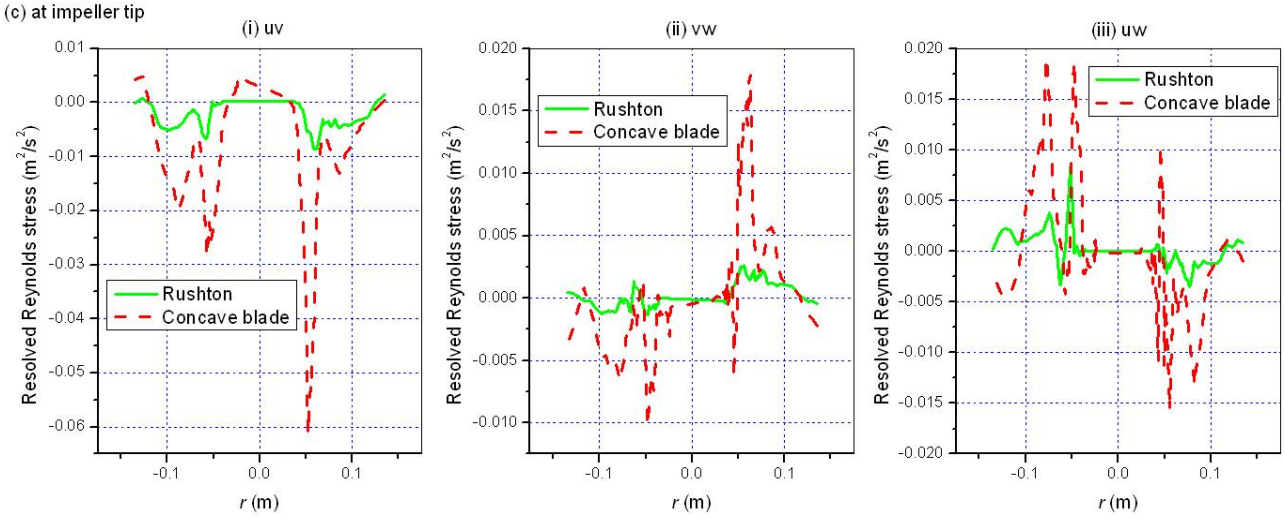

Figure 6.8: Comparison of resolved Reynolds stresses at different axial positions, *z*, for (a) Rushton (b) Concave blade and (c) between Rushton and Concave blade at impeller centerline (*z*/*D*=0.333)

The dissipative scale characteristics are important dynamics of a turbulent flow and subgrid scale quantities are also necessary parameters to be extracted from LES model as this model gives due emphasis on smallest scales of turbulent eddies. Reynolds stresses indirectly defines the minimum magnitude of turbulent scales which are very important in understanding in the progress of mixing in vessels. The resolved Reynolds at different direction of flow is shown in Figure 6.8(a- b) by comparing at different axial positions of Rushton and Concave blade impeller; and 6.8(c) gives comparison between Rushton and Concave blade impeller at impeller tip only. As obtained in case of mean and RMS velocity (Figure 6.6), here also the resolved stresses are observed significantly varied and higher magnitude at centerline of impeller (z/D=0.333) as compared with other regions of the vessel. And there is also good flow circulation exists at the free surface. The resolved Reynolds stresses (uv,vw and uw) are found much higher in Concave blade than the Rushton impeller (Figure 6.8c). There is also non-similarity of stresses observed between left and right side of tank as shaft is taken as origin indicating strong non-axisymmetric nature in 3D flow simulation.

6.3.3. Subgrid TKE and dissipation rate

Subgrid turbulent kinetic energy (TKE) and turbulent dissipation rate are the smallest scale of turbulent eddies. By Kolmogorov theory, different scales are given for turbulent flows saying that TKE and dissipation rate are derived from bigger scaled eddies (velocity); and are responsible for creating heat and energy.

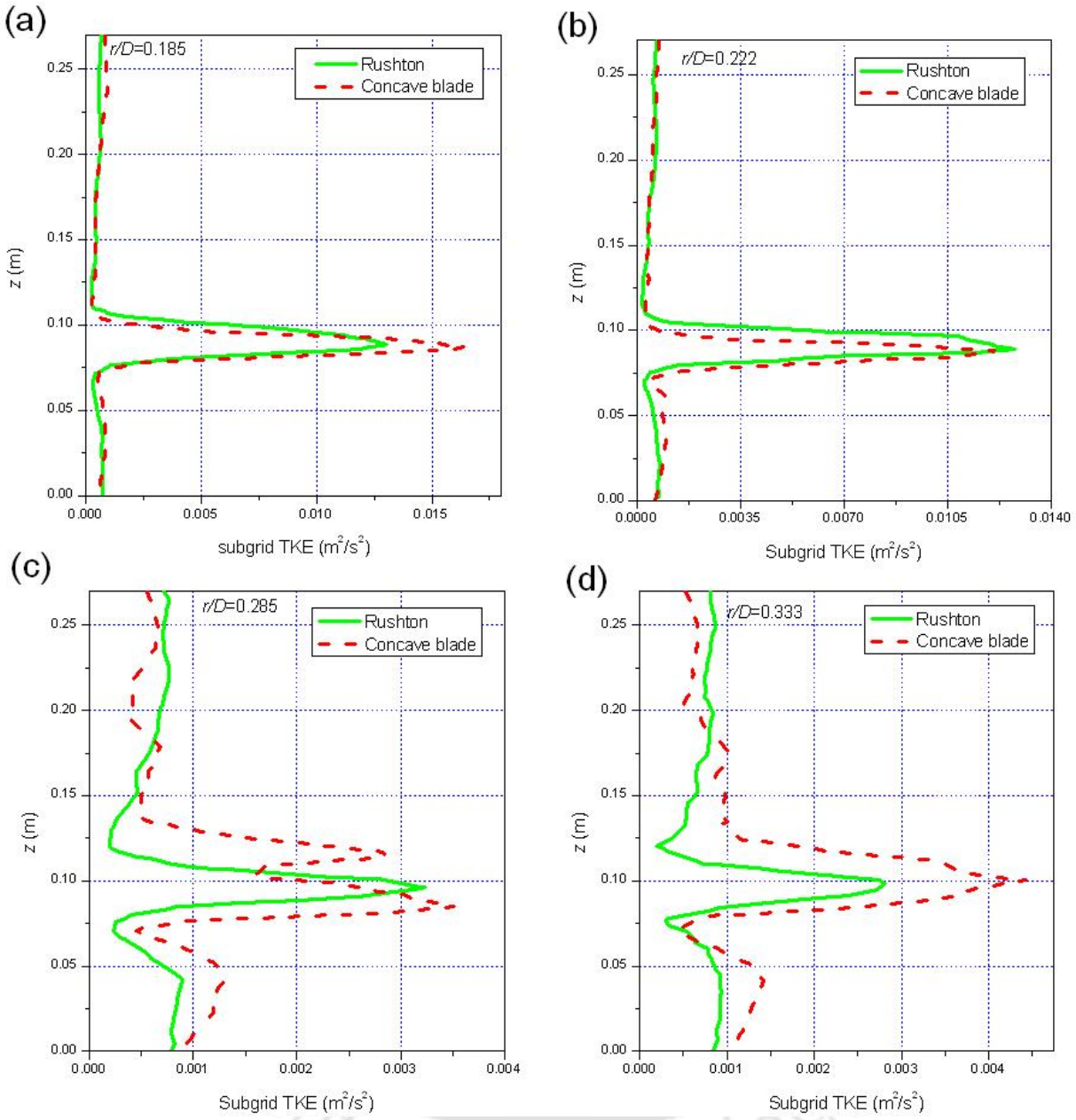

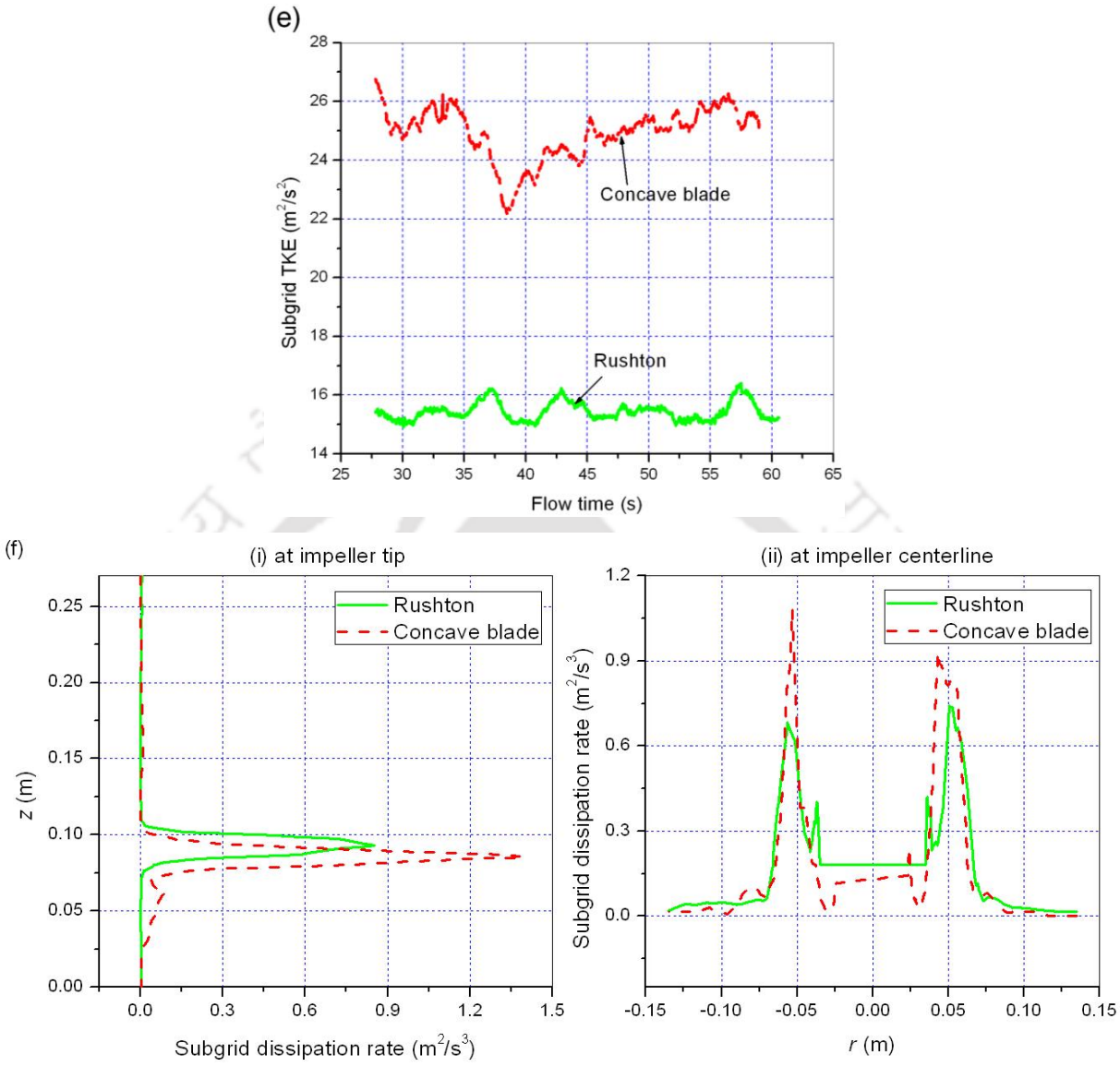

Figure 6.9: Comparison between Rushton and Concave blade impeller (a-d) subgrid TKE at different radial positions, *r*, (e) instantaneous sum of subgrid TKE at impeller top surface; and (f) subgrid dissipation rate at (i) impeller tip and (ii) impeller centerline

Figure 6.9 (a-d) shows comparison of subgrid TKE between Rushton and Concave blade impeller at different radial positions; (e) represents the instantaneous sum of subgrid TKE at impeller top surface; and (f) shows the subgrid dissipation rate at impeller tip and centerline. The comparison of subgrid TKE at different radial positions between Rushton and Concave blade impeller is found higher in Concave blade impeller. The magnitude of TKE decreases when the radial position is near to tank wall and maximum magnitude is observed at impeller

tip (r/D=0.185) which is around 0.013m^2/s^2 for Rushton and 0.017 m^2/s^2 for Concave blade impeller (Figure 6.9a). Time dependent sum value of subgrid TKE between Rushton and Concave blade impeller gives significant higher magnitude in Concave blade impeller showing dominance of turbulent characteristics by Concave blade than Rushton impeller. Strong fluctuations of TKE over time of simulation are also observed in case of Concave blade impeller but there is no abrupt fluctuation observed in case of Rushton impeller (Figure 6.9e). The subgrid dissipation rate compared between Rushton and Concave blade impeller at impeller tip and centerline also shows higher magnitude in Concave blade impeller in Figure 6.9f (i-ii).

6.4. Conclusions

The application of LES model in turbulent flow of stirred tank with different types of impeller (Rushton and Concave blade) is investigated in this study. The comparison of radial and axial velocities between Rushton and Concave blade impeller is found higher in case of Concave blade impeller. The unsteady statistics of mean and RMS velocities were analyzed at different radial and axial positions of the stirred tank and found strong variation across the vessel in both cases of Rushton and Concave blade impeller, however, a very strong variation and higher values were observed near tip and at centerline of impeller than the other regions of the vessel. Maximum amount of turbulence is occurred near the impeller region and the flow circulation takes place at the free liquid surface is also significant as compared with other regions of the vessel. The dissipative scales (TKE and dissipation rate) were also compared between Rushton and Concave blade impeller and also found higher in Concave blade impeller. The time dependent instantaneous variables of Rushton and Concave blade shows flow variation with time and significant strong variation is observed in case of Concave blade than Rushton impeller leading to higher tendency in producing turbulence which is very much required in mixing process. So, from this study after upon investigation on flow velocities as well as smallest dissipative scales between Rushton and Concave blade impeller, it has been concluded that Concave blade has better capability in mixing process as well as in consistent progress of flow circulation. This study also shows against the assumption of axis-symmetric in 3D flow simulation. Further investigation will be devoted at free liquid surface as this region is found significant from this study.

CHAPTER 7

CONCLUSIONS

The process dynamics parameters like mass transfer rate, power consumption, vortex behavior and gas hold up were experimentally studied on single and dual impeller system of unbaffled concave blade stirred tank. The system was examined in single phase as well as in gas-phase condition. Design criteria for each parameter were developed which can be applied for geometrically similar systems. Computational Fluid dynamics techniques also applied to predict the flow pattern, mass transfer rate, power input in such systems. The comparison of unbaffled system is made with baffled system and Concave blade type with Rushton impeller system. Application of Computational Fluid Dynamics techniques was also performed by comparing the predicted results with experimental results of published literature. Advanced turbulent modeling by Large Eddy Simulation was also made in order to capture more realistic nature of turbulent flow inside the vessel**.** So, the overall conclusions achieved from this study are given as:

7.1. For single impeller single phase system: Mass transfer rate has been found increasing with increasing impeller clearance depth; however increment is not very significant. Higher impeller diameter gives better mass transfer rate. Power number decreases with increaseing impeller clearance depth. So, as the impeller is nearer to the free liquid surface, power consumption decreases while the impeller and tank diameter are kept constant. Power number decreases with an increase in impeller diameter. It was observed that impeller is closer to tank bottom, higher is the vortex depth. Smaller tank diameter gives higher relative vortex depth when impeller diameter is constant at different impeller clearance depth. Critical speed is found decreases with increase in impeller diameter and its clearance depth. That means larger the impeller diameter, lower is the critical speed when tank diameter is constant. General design criteria correlations for single impeller single phase unbaffled concave blade stirred tank are given as:

For mass transfer: $10^5 k_c = 0.6(d/D)^{0.23}\left(C/D\right)^{0.04} X^{0.3}$

For power input: $N_p = 34.69(d/D)^{-0.974}(C/D)^{-0.5}(X)^{-0.98}$

For vortex depth: $\frac{V_d}{d} = 0.63Ga^{0.069}(D/d)^{-1.39}Fr^{1.14Ga^{-0.008}(D/d)^{0.08}}(C/D)^{-0.79}$

7.2. For single impeller gas-liquid phase: The strong influence of impeller clearance depth and impeller diameter on mass transfer rate, power consumption and gas hold up was observed and found increases with increasing impeller speed. Mass transfer coefficient increases with decrease in impeller clearance depth and increased in impeller diameter. So, when impeller and tank diameter is constant, higher mass transfer rate is achieved by lower impeller clearance depth and bigger impeller diameter. Gassed power consumption decreases with increasing impeller clearance depth and consumes higher power by bigger impeller diameter when the respective geometrical parameters are constant. Gas hold up also decreases with increasing impeller clearance depth and with increasing impeller diameter. General design criteria correlations for single impeller gas-liquid phase unbaffled concave blade stirred tank are given as:

For mass transfer: $10^5 k_c = 2.26\left(\frac{d}{D}\right)^{1.14}(X)^{0.41}(Fl)^{0.02}\left(\frac{C}{D}\right)^{-0.031}$

For power input: $\frac{P_g}{P_u} = 0.1Fl^{-0.33}\left(\frac{d}{D}\right)^{-0.003}\left(\frac{C}{D}\right)^{-0.0311}(X)^{0.11}$

For gas hold up: $\varepsilon_G = 0.66Fl^{0.02}\left(\frac{d}{D}\right)^{0.004}P_v^{0.75}\left(\frac{C}{D}\right)^{-1.45}$

7.3. For dual impeller single phase: Impeller clearance depth and their spacings are studied in dual impeller system. The combinations of efficient impeller spacings were observed at C_1=0.15D, 0.2D, 0.25D, 0.3D, 0.4D and C_2=0.48D, 0.48D, 0.38D, 0.48D, 0.4D respectively based on observed K_La_{20}. Global optimum configuration was observed at C_1=0.25D and C_2=0.38D. Based on observed results of efficient configuration, the three stable flow patterns were predicted by using Computational Fluid Dynamics techniques. Parallel flow pattern is predicted when C_1>0.20D & C_2≥0.48D; merging flow at C_1>0.2D & C_2<0.38D and diverging flow at C_1<0.15D & C_2>0.48D. The predicted configuration of parallel and diverging flow pattern of Rushton (given by Rutherford et al., 1996) is closely similar with

Concave blade impeller while in case of merging flow; Concave blade impeller requires lesser C_2 value than the Rushton impeller. Parallel and merging flow pattern produces nearly equal amount of mean velocity and is higher than diverging flow pattern. Merging flow pattern produces higher amount of dissipative scales than the diverging and parallel flow leading to enhance the energy dissipation; and eventually increasing overall performance of the system. General design criteria correlations for dual impeller single phase unbaffled concave blade stirred tank are given as:

For mass transfer: $10^5 k_c = 0.24X^{0.84}$

For power input: $N_p = 245.97X^{-0.85}$

For vortex depth: $V_d / d = 14.18G_a^{-0.098}Fr^{0.365}$ and with X is as: $V_d / d = 1.75e^{-1.91/X}$.

Based on these correlations, design chart (Figure 7.1) has been developed for the field application. Based on geometrical similarity and range of dynamic variables adopted in the present work, one can get the desired process variables from the design chart shown in Figure 7.1.

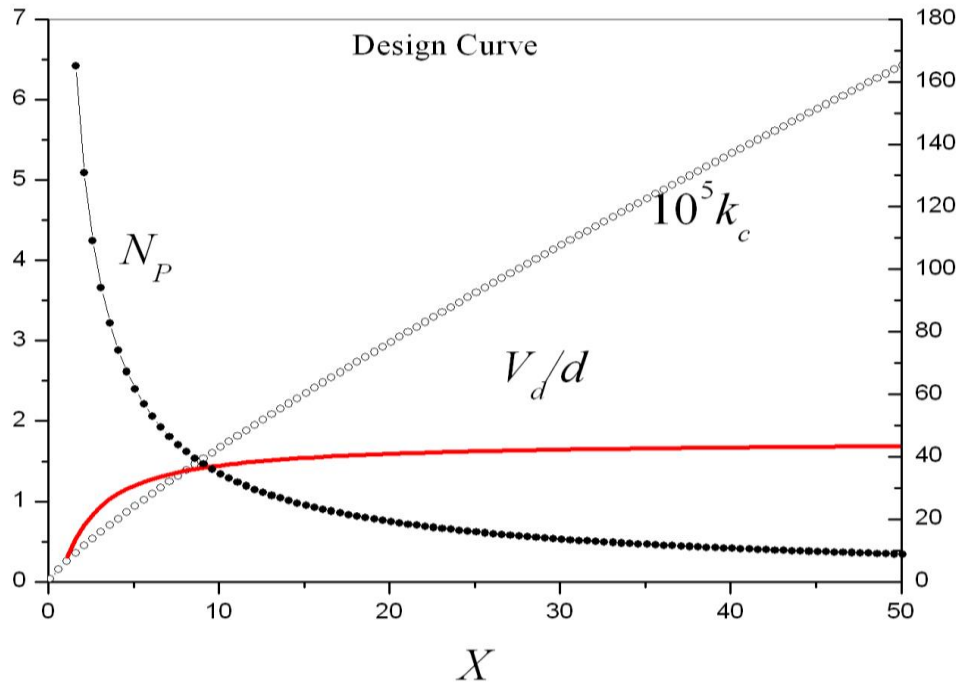

Figure 7.1: Design chart for dual stirred single phase unbaffled tank

7.4. Dual impeller gas-liquid phase unbaffled concave blade stirred tank: The combination of optimal configurations of the system are found at C_1=0.25D & C_2=0.4D, C_1=0.3D & C_2=0.4D, C_1=0.35D & C_2=0.45D, C_1=0.4D, C_2=0.4D, C_1=0.45D & C_2=0.35D. Global optimum is observed at C_1=0.3D & C_2=0.4D. The behavior of the liquid flow in sparged system is totally different from single phase system. There is no formation of circulation loop predicted in this sparged condition except one loop above the lower impeller. General design criteria for dual impeller gas-liquid phase unbaffled concave blade stirred tank are given as:

For mass transfer: $k_c = 2.41 Fl^{0.029} X^{0.44}$

For power input: $\frac{P_g}{P_u} = 0.57 Fl^{-0.005} X^{0.15}$

For gas-hold up: $\varepsilon_G = 4.73 Fl^{0.009} P_v^{0.65}$

Design charts to determine the value of process variables based on the developed correlations have been established as shown in the Figures 7.2(a,b).

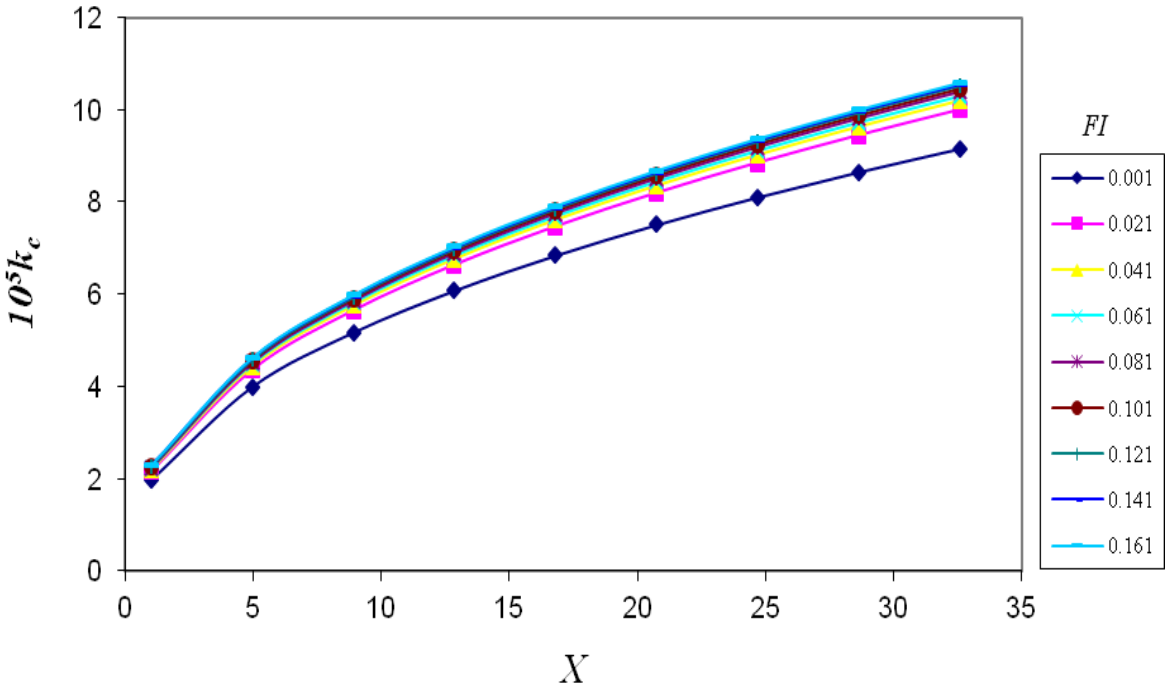

(a)

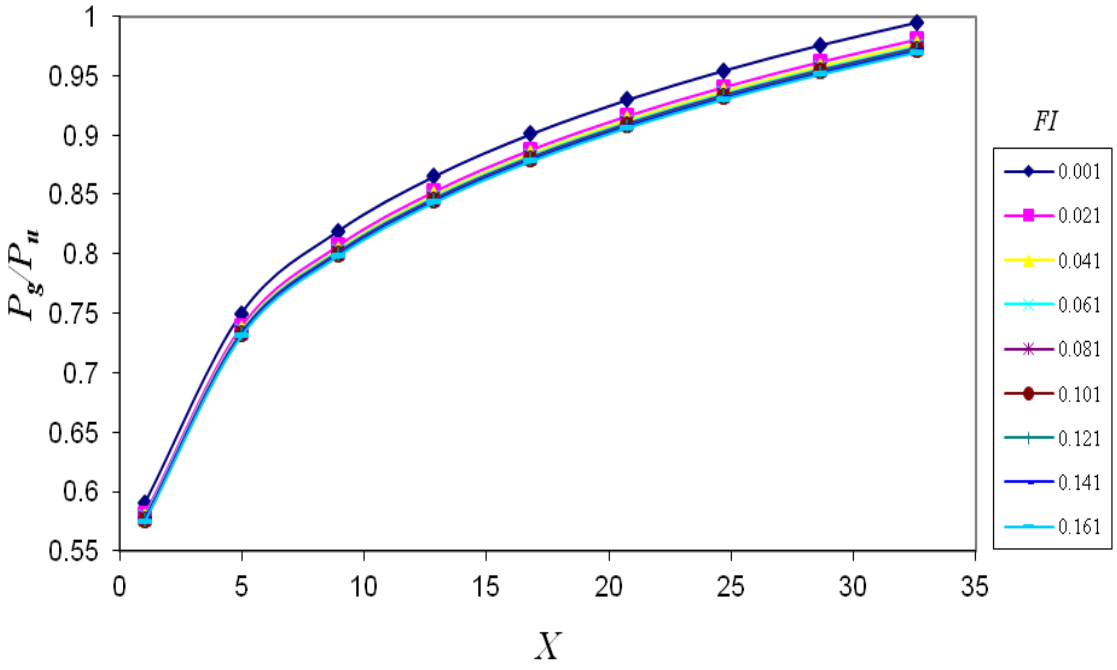

(b)

Figure 7.2: Design chart for (a) mass transfer rate and (b) power consumption in dual stirred gas-liquid unabffled tank

Better performance (higher mass transfer rate and lesser power consumption) was observed by Concave blade type than the Rushton impeller. Baffled system gives better mass transfer rate but consumes higher amount of power as compared with unbaffled system, thus, unbaffled system may be considered as more efficient system where reduction of power is priori. From the comparison of same combination of Concave blade with mix impeller, the better performance by dual Concave blade type impeller is observed. When Concave blade is kept as lower impeller, higher performance is observed in the system but not more than dual Concave blade system.

The prediction of mass transfer coefficient and power input were under acceptable range which shows the feasible application of Computational Fluid Dynamics techniques in stirred tank modeling of turbulent flow. The comaparison of Concave blade with Rushton impeller using advance turbulence model (LES) is to understands the capability of CFD techniques in accurately predicting the velocity profile of stirred tank in turbulent flow condition. Concave blade impeller gives higher amount of flow velocity than the Rushton impeller. The experimental results of Wu and Patterson (1989) is closely predicted by LES model of this

study which shows the capability of this advance modeling in the prediction of turbulent flow in stirred tank.

Future work will be focussed on to use advanced experimental techniques like Particle Image Velocimetry (PIV) or Laser Doppler Velocimetry (LDV) to capture the turbulent fluid particles inside the stirred tank. To correctly model the experimental results by using Computational Fluid Dynamics techniques will be major target of our future work. In order to capture the more realistic turbulent flow, to adopt more advanced numerical techniques like advanced turbulence model (Large Eddy Simulation), to use user defined functions (UDF) to modify the existing numerical techniques (as in this study we have made an attempt to modify the existing drag law) and to define more accurate boundary conditions at top surface of the computational domain will be our major concern in our future study.

REFERENCES

Abatan, A.A., McCarthy, J.J., Vargas, W.L. Particle migration in the rotating flow between co-axial disks, AIChE Journal, 2006; 52(6): 2039-2045.

Abrardi, V., Rover, G., Sicardi, S., Baldi, G., Conti, R. Sparged vessels agitated by multiple turbines, The European Conference Mixtures, 1988; 6: pp329-336.

Abrardi, V., Rovero, G., Baldi, G., Sicardi, S., Conti, R. Hydrodynamics of a gas-liquid reactor stirred with a multi-impeller system, Chemical Engineering Research and Design, 1990; 68(6): 516-522.

Ahmed, S.U., Ranganathan, P., Pandey, A. and Sivaraman, S. Computational fluid dynamics modeling of gas dispersion in multi impeller bioreactor, Journal of Bioscience and Bioengineering, 2010; 109(6): 588-597.

Albaek, M.O, Gernaey, K.V, Stocks, S.M. Gassed and ungassed power draw in a pilot scale 550 litre fermentor retrofitted with up-pumping hydrofoil B2 impellers in media of different viscosity and with very high power draw, Chemical Engineering Science, 2008; 63: 5813-5820.

Alcamo, R., Micale, G., Grisafi, F., Brucato, A., Ciofalo, M. Large-eddy simulation of turbulent flow in an unbaffled stirred tank driven by a Rushton turbine, Chemical Engineering Science, 2005; 60: 2303-2316.

Alexopoulos, A.H., Maggioris, C., Kiparissides, C. CFD analysis of turbulence non-homogeneity in mixing vessels, a two-compartment model, Chemical Engineering Science, 2002; 57: 1735-1752.

Aloi, L.E., Cherry, R.S. Cellular response to agitation characterized by energy dissipation at the impeller tip, Chemical Engineering Science,1996; 51(9):1523-1529.

Alves, S.S., Maia, C.I., Vasconcelos, J.M.T. Gas-liquid mass transfer coefficient in stirred tanks interpreted through bubble contamination kinetics, Chemical Engineering and Processing, 2004; 43: 823-830.

Amaral, P.F.F., Freire, M.G., Leao, M.H.M.R., Marrucho, I.M, Coutinho, J.A.P., Coelho, M.A.Z. Optimization of oxygen mass transfer in a multiphase bioreactor with Perfluorodecalin as a second liquid phase, Biotechnology and Bioengineering, 2008, 99,(3): 588-598.

Ameur, H., Bouzit, M., Helmaoui, M. Numerical study of fluid flow and power consumption in a stirred vessel with a Scaba 6SRGT impeller, Chemical Processing and Engineering, 2011; 32: 351-366.

Arjunwadkar, S.J, Sarvavan, K., Kulkarni, P.R. Pandit, A.B. Gas-liquid mass transfer in dual impeller bioreactor, Biochemical Engineering Journal, 1998; 1: 99-106.

Armenante, P. M. and Li, T. Minimum agitation speed for o§-bottom suspension of solids in agitated vessels provided with multiple flat-blade impellers, AIChE Symposium Series, 1993; 89: 105-111.

Armenante, P.M., Luo, C., Chou, C.C., Fort, I., Medek, J. Velocity profiles in a closed, unbaffled vessel: comparision between experimental LDV data and numerical CFD predictions, Chemical Engineering Science, 1997; 52(20): 3483-3492.

Asai, T., Kono, T. Estimation of oxygen absorption coefficient and power consumption in a stirred tank fermentor, Journal of Fermentation Technology, 1982; 60: 265-268.

Assirelli, M., Bujalski, W., Eaglesham , A., Nienow, A.W. Macro-and micromixing studies in an unbaffled vessel agitated by a Rushton turbine, Chemical Engineering Science, 2008; 63: 35-46.

Aubin, J., Fletcher, D. F., Xuereb, C. Modeling turbulent flow in stirred tanks with CFD: the influence of the modeling approach, turbulence model and numerical scheme, Experimental Thermal and Fluid Science, 2004; 28: 431-445.

Azzopardi, B., Zhao, D., Yan, Y., Morvan, H., Mudde, R.F., Lo, S. Hydrodynamics of gas-liquid reactors: Normal operation and upset conditions, 2011, Willey.

Bakker, A. A new gas dispersion impeller with vertically asymmetric blades, The Online CFM Book, 2000. (available at http://www.bakker.org/cfm).

Bakker, A., Smith, J.M., Myers, K.J. How to disperse gases in liquids, Chemical Engineering, 1994: 98-104.

Bakker, A., Van den Akker, H.E.A. A computational model for the gas-liquid flow in stirred reactors, Chemical Engineering Research and Design, 1994; 72: 594-606.

Batchelor, G.K. An introduction to Fluid Dynamics, Cambridge University Press, Cambridge, England, 1967.

Bates, R.L., Fondy, P.L., Corpstein, R.R. An examination of some geometric parameters of impeller power, Industrial & Engineering Chemistry Process Design and Development, 1963; 2: 310-314.

Benadda, B., Ismaili, S., Otterbein, M. Relation of mechanical power to gas hold-up and mass transfer in an agitated vessel, Chemical Engineering Technology, 1997; 20: 192-198.

Benkreira, H. Fluid Mixing 6, IChemE Symposium Series number, 1990; 146: 147-158.

Bewtra, J.K., Nicholas, W.R., Polkowski, L.B. Effect of temperature on oxygen transfer in water, Water Research, 1970; 4(2): 115-123.

Biesecker, B.O. Begasen von Flüssigkeiten mit Rührern, VDI-Forsch.-H, 1972; pp554.

Bisio, A., Kabel, R.L. Scaleup of chemical processes; Conversion from laboratory scale tests to successful commercial size design, John Wiley & Sons, 1985.

Bombac, A., Zun, I. Gas filled cavity structures and local void fraction distribution in vessel with dual impellers, Chemical Engineering Science, 2000; 55(15): 2995-3001.

Bouaifi, M., Hebrard, G., Bastoul, D., Roustan, M. A comparative study of gas hold-up, bubble size, interfacial area and mass transfer coefficients in gas-liquid reactors and bubble columns, Chemical Engineering Processing, 2001; 40: 97-111.

Bouaifi, M., Roustan, M. Bubble size and mass transfer coefficients in dual impeller agitation, Canadian Journal of Chemical Engineering, 1998; 76: 390-397.

Bouaifi, M., Roustan, M. Power consumption, mixing time and homogenization energy in dual-impeller agitated gas-liquid reactors, Chemical Engineering and Processing, 2001; 40: 87-95.

Boyle, W.C., Berthovex, P.M., Rooney, T.C. Pitfalls in parameter estimation for oxygen transfer data, Journal of the Environmental Engineering Division, ASCE, 1974; 100(2): 391-408.

Bridgeman, J. Computational fluid dynamics modeling of sewage sludge mixing in an anaerobic digester, Advances in Engineering Software, 2012; 44: 54-62.

Brown, D.E. The measurement of fermentor power input, Chemical Industry, 1997; 16: 684-688.

Brown, L.C., Baillod, C.R. Journal of the Environmental Engineering Division, ASCE, 1982; 108(4): 607-628.

Brucato, A., Cipollina, A, Micale, G., Scargiali, F., Tamburini, A. Particle suspension in top-covered unbaffled tanks, Chemical Engineering Science, 2010; 65: 3001-3008.

Bruijn, W., Van't Riet, K., Smith, J.M. Power consumption with aerated Rushton turbines, Transaction Institute of Chemical Engineers, 1974; 52: 88-104.

Bruxelmane, M. International Symposium on Chemical Engineering, Louvain-La-Neuve, Belgium, 1976; pp321-417.

Buffo, A., Vanni, M., Marchisio, D.L. Multidimensional population balance model for the simulation of turbulent gas-liquid systems in stirred tank reactors, Chemical Engineering Science, 2012; 70: 31-44.

Bujalski, W., Amanullah, A., Schmitz, R., Nieow, A.W. A comparison of torque fluctuations and gassed power characteristics for a range of radial flow impellers in water, Fluid Mixing 5 Conference, Bradford, UK, IChemE Symposium series No.140, 1996: pp315-326.

Bujalski, W., Nienow, A.W., Chatwin, S., Cooke, M. The dependency on scale of power numbers of Rushton disc turbines, Chemical Engineering Science, 1987; 42: 317-326.

Butcher, M., W. Eagles. Fluid mixing re engineered, The Chemical Engineer, 2002; 733: 28-29.

Cabaret, F. F., Fradette, L., Tanguy, P.A. Gas-liquid mass transfer in unbaffled dual impeller mixers, Chemical Engineering Science, 2008; 63:1636-1647.

Calderbank, P.H. Physical rate processes in industrial fermentation: part 1 "The interfacial area in gas liquid contacting with mechanical agitation", Transactions of the Institution of Chemical Engineers, 1958; 37: 443-463.

Calik, P., Yilgor, P., Ayhan, P., Demir, A.S. Oxygen transfer effects on recombinant benzaldehyde lyase production, Chemical Engineering Science, 2004, 59: 5075-5083.

Canny, J. A computational approach to edge detection, IEEE Transactions of Pattern Analysis and Machine Intelligence, 1986; 8(6): 679-698.

Charpentier, J.C. Mass transfer rates in gas-liquid absorbers and reactors, Advanced Chemical Engineering, 1981; 11: 2-133.

Cheng, D., Cheng, J., Li, X., Yang, C., ShaMao, Z. Experimental study on gas-liquid-liquid macro-mixing in a stirred tank, Chemical Engineering Science, 2012, 75: 256-266.

Chiampo, F., Guglielmetti, R., Manna, L., Conti, R. Gas-liquid mixing in a multiple impeller stirred vessel, 7th European Conference on Mixing, Brugge, Belgium, 1991; 2: pp333-341.

Chiu, Y.N., Naser, J., Ngian, K.F., Pratt, K.C. Computation of the flow and reactive mixing in dual-Rushton, Chemical Engineering and Processing: Process Intensification, 2009; 48: 977-987.

Chudacek 1985, Chudacek M.W., Solid suspension behavior in profiled-bottom and flat-bottom mixing tanks, Chemical Engineering Science, 40; 1985: 385-392.

Chunmei, P., Jian, M., Xinhong, L., Zhengming, G. Investigation of fluid flow in a dual Rushton impeller stirred tank using particle image velocimetry, Chinese Journal of Chemical Engineering, 2008; 16(5): 693-699.

Ciofalo, M., Brucato, A, Grisafi, F., Torrace, N. Turbulent flow in closed and free-surface unbaffled tanks stirred by radial impellers. Chemical engineering Science, 1996; 51(14): 3557-3573.

Clark, M.M. Critique of CAMP and STEIN'S RMS velocity gradient, Journal of Environmental Engineering, ASCE, 1984; 111(6): 741-754.

Clark, M.W., Vermeulen, T. Incipient vortex formation in baffled agitated vessels, AIChE Journal, 1964; 10: 420-422.

Clift, R., Grace, J.R., Weber, M.E. Bubbles, Drops and Particles, Academic Press, New York, 1978; pp16.

Cokljat, D., Slack, M., Vasquez, S.A., Bakker, A., Montante, G. Reynolds-Stress model for Eulerian multiphase, Progress in Computational Fluid Dynamics, an International Journal, 2006; 6(1-3): 168-178.

Conti, R., Sicardi, S., Specchia, V. Effect of the stirrer clearance on suspension in agitated vessels, Chemical Engineering Journal, 1981; 22: 247-249.

Cooke, M., Middleton, J.C., Bush, J.R. Mixing and mass transfer in filamentous fermentations, 2nd International Conference on Bioreactor Fluid Dynamics, R.King (Ed), BHP Group, Cranfield, UK, 1988; pp37-64.

Costes, J., Couderc, J. P. Influence of the size of the units: I. Mean flow and turbulence, Chemical Engineering Science, 1988; 43: 2751-2764.

Cutter, L. A. Flow and Turbulence in a Stirred Tank, AIChE Journal, 1966; 12: 35-44.

Danckwerts, P.V. Significance of liquid-film coefficients in gas absorption, Industrial and Engineering Chemistry, 1951; 43: 1460-1467.

Deen, N.G., Solberg, T., Hjertager, B.H. Flow generated by an aerated Rushton impeller: two phase PIV experiments and numerical simulations, Canadian Journal of Chemical Engineering, 2002; 80: 638-652.

Deglon, D.A., Meyer, C.J. CFD modeling of stirred tanks: Numerical considerations, Minerals Engineering, 2006; 19:1059-1068.

Delafosse, A., Line, A., Morchain, J., Guiraud, P. LES and URANS simulations of hydrodynamics in mixing tank: comparison to PIV experiments, Chemical Engineering Research and Design, 2008; 86(12):1322-1330.

Delafosse, A., Morchain, J., Guiraud, P., Line, A. Trailing vortices generated by a Rushton turbine: assessment of URANS and large Eddy simulations, Chemical Engineering Research and Design, 2009; 87(4): 401-411.

Derksen, J., Van den Akker, H.E.A. Large eddy simulations on the flow driven by a Rushton turbine, American Institute of Chemical Engineers AIChE Journal, 1999; 45: 209-221.

Derksen, J.J. Long-time solids suspension simulations by means of a large-eddy approach, Chemical Engineering Research and Design, 2006; 84(A1): 38-46.

Deshmukh, N. A., Joshi, J. B. Surface aerators power number, mass transfer coefficient, gas hold up profiles and flow patterns, Chemical Engineering Research and Design, 2006; 84(A11): 977-992.

Dewan, A., Buwa, V., Durst, F. Performance optimizations of grid disc impellers for mixing of single-phase flows in a stirred vessel, Chemical Engineering Research and Design, 2006; 84: 691-700.

Dickey, D.S. Dimensional analysis, similarity and scale-up, process mixing, chemical and biochemical applications: Part 2, AIChE Symposium Series 293, New York, 1993;pp143-150.

Djelal, H., Larher, F., Martin, G., Amrane, A. Effect of the dissolved oxygen on the bioproduction of glycerol and ethanol by Hansenula anomala growing under salt stress conditions, Journal of Biotechnology, 2006; 125: 95-103.

Dussap, C.G, Decorps, J,, Gros, J,B. Transfert d'oxygene en presence de polysaccharides exocellulaires dans un fermenteur agite aeré et dans un fermenteur de type gazosiphon. Entropie, 1985; 123: 11-20.

Eckenfelder, W.W., O'Connor, D.J. Biological Waste Treatment, 1961, Pergamon Press, London.

Eggels, J.G.M. Direct and large-eddy simulation of turbulent fluid flow using the lattice-Boltzmann scheme, International Journal of Heat Fluid Flow, 1996; 17(3): 307-323.

Elgobashi, S.E., Rizk, M.A. A two-equation turbulence model for dispersed dilute confined two-phase flows, International Journal of Multiphase Flow, 1989; 15(1): 119-133.

Elqotbi, M., Vlaev, S.D., Montastruc, L., Nikov, I. CFD modelling of two-phase stirred bioreaction systems by segregated solution of the Euler-Euler model, Computers and Chemical Engineering, 2013; 48: 113-120.

Escudié, R., Bouyer, D., Liné, A. Characterization of trailing vortices generated by a Rushton turbine, AIChE Journal, 2004; 50(1): 75-86.

Estradal, J. M., Dudek, A., Munoz, R., Quijano, G. Fundamental study on gas-liquid mass transfer in a biotrickling filter packed with polyurethane foam, 2013, DOI: 10.1002/jctb.4226.

Fadavi, A., Chisti, Y. Gas holdup and mixing characteristics of a novel forced circulation loop reactor, Chemical Engineering Journal, 2007; 131: 105-111.

Fluent 6.3 User's Guide, Fluent Incorporated, USA, 2006.

Forrester, S.E., Rielly, C.D., Carpenter, K.J. Gas-inducing impeller design and performance characteristics, Chemical Engineering Science, 1998; 53: 603-615.

Frei, W., Chen, C. Fast Boundary Detection: A Generalization and New Algorithm, IEEE Transactions of Computers, 1977; C-26(10): 988-998.

Frossling, N. Uber die Verdunstung fallenden tropfen, Gerlands Beitage Geophysics, 1938; 52: 170-216.

Fujasova, M., Linek, V., Moucha, T. Mass transfer correlations for multiple-impeller gas-liquid contactors. Analysis of the effect of axial dispersion in gas liquid phases on "local" kLa values measured by the dynamic pressure method in individual stages of the vessel, Chemical Engineering Science, 2007; 62: 1650-1669.

Galindo, E., Nieow, A.W. Performance of Scaba SRGT agitator in mixing of simulated Xanthan gum broths, Chemical Engineering Technology, 1993; 16: 102-108.

Galletti, C., Brunazzi, E. On the main flow features and instabilities in an unbaffled vessel agitated with an eccentrically located impeller, Chemical Engineering Science, 2008; 63: 4494-4505.

Garcia-Cortes, D., Xuereb, C., Taillandier, P., Jauregui-Haza, U.J., Bertrand, J. Flow induced by dual-turbine of different diameters in a gas-liquid agitation system: the agitation and turbulence indices, International Journal of Chemical Reactor Engineering, 2006; 4(A4): 1-10.

Garcia-Cortes, D., Xuereb, C., Taillandier, P., Jauregui-Haza, U., Bertrand, J. Effect of dual impeller-sparged geometry on the hydrodynamic and mass transfer in stirred vessels, Chemical Engineering Technology, 2004; 27: 988-999.

Garcia-Ochoa ,F., Gomez, E., Santos, V.E. Oxygen transfer and uptake rates during xanthan gum production, Enzyme Microbial Technology, 2000a; 27:680-690.

Garcia-Ochoa, F., Gomez, E. Mass transfer coefficient in stirrer tank reactors for xanthan solutions, Biochemical Engineering Journal, 1998; 1: 1-10.

Garcia-Ochoa, F., Gomez, E. Theoretical prediction of gas-liquid mass transfer coefficient, specific area and hold-up in sparged stirred tanks, Chemical Engineering Science, 2004; 59: 2489–2501.

Gaubert, M.A., Sardeing, R., Xuereb, C., Hobbes, P., Letellier, B., Swaels, P. CFD analysis of industrial multi-staged stirred vessels, Chemical Engineering and Processing, 2006; 45: 415-427.

Gentric, C., Mignon, D., Bousquet J., Tanguy, P.A. Comparison of mixing in two industrial gas-liquid reactors using CDF simulations, Chemical Engineering Science, 2005; 60: 2253-2272.

Gezork, K.M., Bujalski, W., Cooke, M., Nienow, A.W. The transition from homogeneous to heterogeneous flow in a gassed stirred vessel, Chemical Engineering Research and Design, 2000; 78A: 363-370.

Gimbun, J., Rielly, C.D., Nagy, Z.K. Modeling of mass transfer in gas-liquid stirred tanks agitated by Rushton turbine and CD-6 impeller: A scale-up study, 2009; 87:437-451.

Glover, G.M. C., Fitzpatrick, J.J. Modelling vortex formation in an unbaffled stirred tank reactor, Chemical Engineering Journal, 2007; 127: 11-22.

Gogate, P.R., Beenackers, A.A.C.M., Pandit, A.B., Multiple-impeller systems with a special emphasis on bioreactors: a critical review, Biochemical Engineering Journal, 2000; 6:109-144.

Gonzalez, R.C., Woods, R.E. Digital Image Processing. Upper Saddle River, NJ: Prentice-Hall, 2001; pp572-585.

Gray, D.J. Impeller clearance effect on off-bottom particle suspension in agitated vessels, Chemical Engineering Communications, 61; 1987: 151-158.

Gray, D.J., Treybal, R.E., Barnett, S.M. Mixing of single and two phase systems: Power consumption of impellers, AIChE Journal, 1982; 28(2): 195-199.

Gray, D.J., Treybal, R.E., Barnett, S.M. Mixing of single and two phase systems: power consumption of impellers, AIChE Journal, 1982; 28: 195.

Greaves M., Kobbacy, K.A.H. Power consumption and impeller dispersion efficiency in gas-liquid mixing, Journal of Chemical Engineering Symposium Series 64, 1981; L1-L33.

Green, S.J. Agitation in process design, Transactions Institution of Chemical Engineers, 1953; 31: 327-343.

Grisafi, F., Brucato, A., Rizzuti, L. Solid-liquid mass transfer coefficient in mixing tanks: influence of side wall roughness , IChemE Symposium Series, 1994; 136: 571-578 .

Gunyol, O., Mudde, R. F. Computational study of hydrodynamics of a standard stirred tank reactor and a large-scale multi-impeller fermenter, International Journal for Multiscale Computational Engineering, 2009; 7(6): 559-576.

Hartmann, H., Derksen, J.J., Montavon, C., Pearson, J., Hamill, I.S., van den Akker, H.E.A. Assessment of large eddy and RANS stirred tank simulations by means of LDA. Chemical Engineering Science, 2004a; 59(12): 2419-2432.

Hartmann, H., Derksen, J.J., Van Den Akker, H.E.A. Macroinstability uncovered in a Rushton turbine stirred tank by means of LES, American Institute of Chemical Engineers AIChE Journal, 2004b; 50(10): 2383-2393.

Hassan, I.T.M., Robinson, C.W. Stirred tank power requirement and gas holdup in aerated aqueous phases, AIChE Journal, 1977; 23: 48-56.

Hassan, R., Loubiere, K., Legrand, J., Delaplace, G. A consistent dimensional analysis of gas–liquid mass transfer in an aerated stirred tank containing purely viscous fluids with shear-thinning properties, Chemical Engineering Journal, 2012; 184(1): 42-56.

Hekmat, D., Hebel, D., Schmid, H., Weuster-Botz D. Crystallization of lysozyme: from vapor diffusion experiments to batch crystallization in agitated ml-scale vessels, Process Biochemistry, 2007; 42: 1649-1654.

Hickman, A. D. Gas–liquid oxygen transfer and scale-up, A novel experimental technique with results for mass transfer in aerated agitated vessels, Sixth European conference on mixing, Pavia, 1988.

Higbie, R. The rate of absorption of a pure gas into a still liquid during short periods of exposure, Transactions of the American Institute of Chemical Engineering, 1935; 31: 364-389.

Hinze, J.O. Turbulence McGraw-Hill, New York, 1959; pp180.

Hirata, Y., Dote, T., Inoue, Y. Contribution of sospende particles to fluid mixing in recipromixing with a disk impeller, Chemical Engineering Research and Design, 2009; 87(4): 430-436.

Hjorth, S. Agitation in gassed magnetic suspensions, Eighth European Conference on Mixing, UK, 1994: 293-300.

Holland, F.A., F.S. Chapman. Liquid mixing and processing in stirred tanks, 1966, Reinhold, London.

Hormann, T., Suzzi, D., Khinast, J.G. mixing and dissolution processes of pharmaceutical bulk materials in stirred tanks: Experimental and numerical investigations, Industrial & Engineering Chemistry Research, 2011; 50: 12011-12025.

Horvath, I. Modelling in the technology of wastewater treatment, Pergamon, Tarrytown, N.Y., 1984.

Houcine, I., Plasari, E., David R. Effects of the stirred tank's design on power consumption and mixing time in liquid phase, Chemical Engineering Technological Journal, 2000; 23: 605-613.

Hsieh, C.C. Estimating volatilization rates and gas/liquid mass transfer coefficients in aeration systems, PhD Thesis, Department of Civil Engineering, University of California, Los Angeles, USA, 1990.

Huang, W., Li, K. CFD simulation of flows in stirred tank reactors through prediction of momentum source, Computer and Information Science, 2013, DOI: 10.5772/51754.

Hudcova, V., Machton, V., Nienow, A.W. Gas-liquid dispersion with dual Rushton turbine impellers, Biotechnology and Bioengineering, 1989; 34: 617-628.

Hugmark, G.A. Power requirements and interfacial area in gas-liquid turbine agitated systems, Industrial & Engineering Chemistry Process Design and Development, 1980; 19: 638-641.

Hwang, H.J. Comprehensive studies of oxygen transfer under Nonideal conditions, Ph.D. Thesis, Department of Civil Engineering, University of California, Los Angeles, USA, 1983.

Ishii, M., Zuber, N. Drag coefficient and relative velocity in bubbly, droplet or particulate flows, AIChE Journal, 1979; 25: 843-855.

Jahoda, M., Mostek, M., Kukukova, A., Machon, V. CFD modeling of liquid homogenization in stirred tanks with one and two impellers using large eddy simulation, Trans IChemE, Part A, Chemical Engineering Research and Design, 2007; 85(A5): 616-625.

Jahoda, M., Tomasskova, L., Mostek, M. CFD prediction of liquid homogenization in a gas-liquid stirred tank, Chemical Engineering Research and Design, 2009; 87: 460-467.

Jaworski, Z., Dudczak, J. CFD modelling of turbulent macromixing in stirred tanks. Effect of the probe size and number on mixing indices, Computer Chemical Engineering, 1998; 22(1): 298-298.

Jaworski, Z., Dyster, K.N., Moore, I.P.T., Nienow, A.W., Wyszynski, M.L. The use of angle resolved LDA data to compare two different turbulence models applied to sliding mesh CFD Flow simulations in a stirred tank', Récents Progès en Génie des Procédés, 1997; 11(51): 187-194.

Johnson, A.I., Huang, C.C. Mass transfer studies in an agitated vessel, AIChE Journal, 1956; 2: 412-419.

Johnstone, R.E., Thring, M.W. Pilot plants, models and scale-up methods in chemical engineering, New York, McCraw-Hill Book Company, Inc., 1957.

Joshi, J. B. Modifications in the design of gas inducing impellers. Chemical Engineering Communication, 1980; 5: 109-114.

Joshi, J.B, N.K, Rane, C.V., Murthy, B. N., Mathpati, C.S., Patwardhan, A.W., Ranade, V.V. CFD simulation of stirred tanks: Comparison of turbulence models. Part I: Radial flow impellers, The Canadian Journal of Chemical Engineering, 2011; 89(1): 23-82.

Joshi, J.B., Pandit, A.B., Sharma, M.M. Mechanically agitated gas-liquid reactors, Chemical Engineering Science, 1982; 37: 813-844.

Kagoshima, M., Mann, R. Development of a networks-of-zones fluid mixing model for an unbaffled stirred vessel used for precipitation, Chemical Engineering Science, 2006; 61(9): 2852-2863.

Kalinske, A.A. Oxygen absorption studies using mechanical air dispersers, Sewage and Industrial Waste, 1955; **27:** 572-586.

Karcz, J., Kaminska-Brzoska, J. Heat transfer in a jacketed stirred tank equipped with baffles and concave disc impeller, Eighth European Conference on Mixing, UK, 1994: 449-456.

Karimi, A., Golbabaei, F., Mehrnia, M.R., Mohammad, K., Neghab, M., Nikpey, A., Pourmand, M.R. Investigation of gas hold up and power consumption in a stirred tank bioreactor using single and dual impeller configurations, International Journal of Occupational Hygiene, 2013; 5(3):109-116.

Karimi, A., Golbabaei, F., Neghab, M., Mehrnia M.R., Mohammad, K., Pourmand, M.R, Nikpey, A. Investigation of Oxygen Transfer in a Two-phase Partition Stirred Tank Bioreactor in the Presence of Silicone Oil, Chemical and Biochemical Engineering Quarterly, 2011; 25(2): 209-219.

Kasat, G.R., Pandit, A.B., Ranade, V.V. CFD simulation of gas-liquid flows in a reactor stirred by dual Rushton turbines, International Journal of Chemical Reactor Engineering, 2008; 6(A): 1-28.

Kawase, Y., Moo-Young, M. Volumetric mass transfer coefficients in aerated stirred tank reactors with Newtonian and non-Newtonian media, Chemical Engineering Research and Development, 1988; 66:284-288.

Kerdouss, F., Bannari, A., Proulx, P., Bannari, R., Skrga, M., Labrecque, Y. Two-phase mass transfer coefficient prediction in stirred vessel with a CFD model, Computational Chemical Engineering, 2008; 32: 1943-1955.

Kerdouss, F., Bannari, A., Proulx, P. CFD modeling of gas dispersion and bubble size in a double turbine stirred tank, Chemical Engineering Science, 2006; 61: 3313-3322.

Khopkar, A.R. Kasat, G.R., Pandit A.B., Ranade, V.V. CFD simulation of mixing in tall gas liquid stirred vessel: Role of local flow patterns, Chemical Engineering Science, 2006; 61: 2921-2929.

Khopkar, A.R., Aubin, J., Xureb, C., Le Sauze, N., Bertrand, J., Ranade, V.V. Gas-liquid flow generated by a pitched blade turbine: PIV measurements and CFD simulations, Industrial & Engineering Chemistry Research, 2003; 42: 5318-5332.

Khopkar, A.R., Kasat, G.R., Pandit, A.B., Ranade, V.V. CFD simulation of liquid phase mixing in solid-liquid stirred reactor, Chemical Engineering Science, 2008; 63(15): 3877-3885.

Khopkar, A.R., Tanguy, P.A. CFD simulation of gas-liquid flows in stirred vessel equipped with dual Rushton turbines: influence of parallel, merging and diverging flow configurations, Chemical Engineering Science, 2008; 63: 3810-3820.

Kim, W.W., Menon, S. Application of the localized dynamic subgrid-scale model to turbulent wall-bounded fows, Technical Report AIAA-97-0210, American Institute of Aeronautics and Astronautics, 35th Aerospace Sciences Meeting, Reno, NV, January 1997.

King, R.L., Hiller, R.A., Tatterson, G.B. Power consumption in a mixer, AIChE Journal, 1988; 34: 506-509.

Kolmogorov, A.N. The local structure of turbulence in incompressible viscous fluid for very large Reynolds numbers, Doklady Akademii Nauk SSSR, 1941; 30: 301-305.

Kozinski, A.A., King, C.J. The influence of diffusivity on liquid phase mass transfer to the free interface in a stirred vessel, AIChE Journal, 1966; 12(1): 109-116.

Kresta, S. M., Wood, P. E. Prediction of the three-dimensional turbulent flow in stirred tanks, AIChE Journal, 1991; 37, 3: 448.

Krishna, R., Urseanu, M.I., Baten, J.M. Van, Ellenberger, J. Influence of Scale on the Hydrodynamics of Bubble Columns Operating In the Churn-Turbulent Regime: Experiments vs. Eulerian Simulations, Chemical Engineering Science, 1999; 54(21): 4903-4911.

Kshatriya, S.S., Patwardhan, A.W., Eaglesham, A. Experimental and CFD characterization of gas dispersing asymmetric parabolic blade impellers, International Journal of Chemical Reactor Engineering, 2007; 5(A12): 1-13.

Kuboi, R., Nienow, A.W. The power drawn by dual impeller systems under gassed and ungassed conditions, 4th European Conference on Mixing, Noordwijkerhout, The Netherlands, 1982; pp247.

Kumaresan, T., Joshi, J.B. Effect of impeller design on the flow pattern and mixing in stirred tanks, Chemical Engineering Journal, 2006; 115(3): 173-193.

Lamberto, D., Alvarez, M.M., Muzzio, F.J. Experimental and computational investigation of the laminar flow structure in a stirred tank, Chemical Engineering Science, 1999; 54: 919-942.

Lamberto, D.J., Alvarez, M.M., Muzzio, F.J. Computational analysis of regular and chaotic mixing in a stirred tank reactor, Chemical Engineering Science, 2001; 56: 4887-4899.

Lamont, J.C., Scott, D.S. An eddy cell model of mass transfer into the surface of a turbulent liquid, AIChE Journal, 1970; 16: 513-519.

Lane, G.L. Schwarz, M.P., Evans, G.M. Numerical modelling of gas-liquid flow in stirred tanks, Chemical Engineering Science, 2004; 60: 2203-2214.

Lane, G.L., Schwarz, M.P., Evans, G.M. Modelling of the interaction between gas and liquid in stirred vessels, 10th European Conference on Mixing, Delft, The Netherlands, 2000; pp197-204.

Lane, G.L., Schwarz, M.P., Evans, G.M. Numerical modelling of gas-liquid flow in stirred tanks, Chemical Engineering Science, 2005; 60: 2203-2214.

Le Lan, A., Angelino, H. Etude du vortex dans les cuves agitées, Chemical Engineering Science, 1972; 27: 1969-1978.

Le Moullec, Y., Gentric, C., Potier, O., Leclerc, J.P. Comparison of systemic, compartmental and CFD modeling approaches: Application to the simulation of a biological reactor of wastewater treatment, Chemical Engineering Science, 2010; 65: 343-350.

Lee James, M. Biochemical Engineering, Prentice Hall, 1992.

Lee, K.C., Yianneskis, M. Turbulence properties of the impeller stream of a Rushton turbine. AIChE Journal, 1998; 44(1): 13-24.

Lewis, W.K., Whitman, W.G. Principles of Gas Absorption, Industrial & Engineering Chemistry, 1924; 16(12): 1215-1220.

Li, Zhipeng, Bao, Yuyun, Gao, Zhengming. PIV experiments and large eddy simulations of single-loop flow fields in Rushton turbine stirred tanks, Chemical Engineering Science, 2011; 66: 1219-1231.

Linek, V., Sinkule, J., Benes, P. Critical assessment of gassing-in method measuring kLa in fermentors, Biotechnology and Bioengineering, 1991; 38: 323-330.

Linek, V., Vacek, P., Benes, P. A critical review and experimental verification of the correct use of the dynamic method for the determination of oxygen transfer in aerated agitated vessels to water, electrolyte solutions and viscous liquids, Chemical Engineering Journal, 1987; 34: 11-34.

Liu, Y.S., Wu, J.Y., Ho, K. Characterization of oxygen transfer conditions and their effects on Phaffia rhodozyma growth and carotenoid production in shake-flask cultures, Biochemical Engineering Journal, 2006; 27(A): 331-335.

Luo, J.Y., Issa, R.I., Gosman, D. Prediction of impeller induced flows in mixing vessels using multiple frames of reference, IChemE Symposium Series, 1994; 136: 549-556.

Luong, H.T, Volesky, B. Mechanical power requirements of gas-liquid agitated systems, AIChE Journal, 1979; 25: 893-895.

Machon, V., Pacek, A.W., Nienow, A.W. Bubble Sizes in Electrolyte and Alcohol Solutions in a Turbulent Stirred Vessel, Chemical Engineering Research and Design, 1997; 75(3): 339-348.

Machon, V., Vlcek, J., Hudcova,V. Multi-impeller gas-liquid contactors, Sixth European Conference on Mixing, Pavia, Cranfield, 1988; pp351-360,

Mahmoudi, S.M.S. Velocity and mixing characteristics of stirred vessels with two impellers, Ph.D Thesis, University of London, England, 1993,

Mahmoudi, S.M.S. Velocity and mixing characteristics of stirred vessels with two impellers, PhD Thesis, University of London, England, 1994.

Mahmud, T., Haque, J.N., Roberts, K.J., Rhodes, D., Wilkinson D. Measurements and modelling of free-surface turbulent flows induced by a magnetic stirrer in an unbaffled stirred tank reactor, Chemical Engineering Science, 2009; 64: 4197-4209.

Maise, G. Scaling methods for surface aerators, Journal of Sanitary Engineering Division, ASCE,SA5, 1970; 1079-1083.

Markopoulos, J., Kontogeorgaki, E. Trombenbildung in unbewehrten Rührbehältern mit ein- und zweistufiger Rühreranordnung, Chemie Ingenieur Technik, 1993; 65: 839-841.

Markopoulos, J., Kontogeorgaki, E. Vortex depth in unbaffled single and multiple impeller agitated vessels, Chemical Engineering Technology, 1995; 18: 68-74.

Marshall , E.M., Bakker, A. Computional Fluid Mixing, Fluent, Incorporated, USA, 2002.

Martin, M. Montes, F.J., Galan, M.A. Mass transfer rates from bubbles in stirred tanks operating with viscous fluids, Chemical Engineering Science, 2010; 65: 3814-3824.

McWhirter, J.R., Chern, J., Hutter, J.C. Oxygen mass transfer fundamentals of surface aerators, Industrial & Engineering Chemistry Research, 1995; 34: 2644-2654.

Metcalf and Eddy. Wastewater Engineering: Treatment, Disposal, and Reuse, 1991, 3rd Edition, McGraw-Hill, New York.

Metzner, A.B., Pigford, R.L. Scale-up theory and its limitations, In: Fleming, R. (Ed.): Scale-up in Practice, New York: Reinhold Publishing Corp., 1958; pp16-47.

Mhetras, M.B., Pandit, A.B., Joshi, J.B. Effect of agitator design on hydrodynamics and power consumption in mechanically agitated gas-liquid reactors, Eighth European Conference on Mixing, UK, 1994: pp375-382.

Michel, B.J., Miller, S.A. Power requirements of gas-liquid agitated systems, AIChE Journal, 1962; 8: 262-266.

Micheletti, M., Baldi, S., Yeoh, S.L., Ducci, A., Papadakis, G., Lee, K.C., Yianneskis, M. On spatial and temporal variations and estimates of energy dissipation in stirred reactors, Chemical Engineering Research and Design, 2004; 82: 1188-1198.

Midoux, N, Charpentier, J.C. Mechanically agitated gas-liquid tank reactor, Entropie, 1979; 88: 638.

Mishra, V. P., Joshi, J.B. Flow Generated by a Disc Turbine: Part III: Effect of impeller diameter, impeller location and comparison with other radial and flow turbines, Chemical Engineering Research and Design, 1993; 71: 563-570.

Mohammed, A.K., Hussen, H.A., Al-Rassu, S.A. Performance of gas induction in a dual-impeller agitated bioreactor, Al-Khwarizmi Engineering Journal, 2008; 4(4):1-8.

Mohiuddin, A. K. M., Adeyemi, N., Suleyman, M. 3-D CFD transient simulation of transesterification in stirred tank reactor, 2nd International Conference on Mechanical, Automotive and Aerospace Engineering, ICMAAE, Kuala Lumpur, Malaysia, 2013.

Monstek, M., Kukokova, A., Jahoda, M., Machon, V. Comparision of different techniques for modelling of flow field and homogenization in stirred vessels, Chemical Papers, 2005; 59(6): 380-385.

Montante, G., Lee, K.C., Brucato, A. and Yianneskis, M. Numerical simulations of the dependency of flow pattern on impeller clearance in stirred vessels, Chemical Engineering Science, 2001; 56(12): 3751-3770.

Montante, G., Paglianti, A. and Magelli, F. Experiments and simulations of gas-liquid stirred vessels, 12th Eurepian Conference on Mixing, Bologna, AIDIC, Milan, 2006; pp137-144.

Montante, G., Paglianti, A., F. Magelli. Experimental analysis and computational modelling of gas-liquid stirred vessels, Chemical Engineering Research and Design, 2007; 85(A5): 647-653.

Moucha, T., Linek, V., Erokhin, K., Rejl, J.F., Fujasova, M. Improved power and mass transfer correlations for design and scale-up of multi-impeller gas-liquid contactors, Chemical Engineering Science, 2009; 64(3): 598-604.

Moucha, T., Linek, V., Prokopova, E. Gas hold-up, mixing time and gas-liquid volumetric mass transfer coefficient of various multiple-impeller configurations: Rushton turbine, pitched blade and Techmix impeller and their combinations, Chemical Engineering Science, 2003; 58(9): 1839-1846.

Moucha, T., Linek, V., Sinkule, J. Measurement of kLa in multiple impeller vessels with significant axial dispersion in both phases, Transactions of IChemE, 1995; 73(A): 286-290.

Murthy, B.N., Ghadge, R.S., Joshi, J.B. CFD simulations of gas-liquid-solid stirred reactor: prediction of critical impeller speed for solid suspension, Chemical Engineering Science, 2007; 62: 7184-7195.

Murthy, B.N., Joshi, J.B. Assessment of standard k-ε, RSM and LES turbulence models in a baffled stirred vessel agitated by various impeller designs, Chemical Engineering Science, 2008; 63: 5468-5495.

Murthy, J.Y., Mathur, S.R. CFD simulation of flows in stirred tank reactors using a sliding mesh technique. IChemE Symposium Series, 1994; 136: 341-348.

Myers, K.J. Thomas, A.J., Bakker, A. and Reeder, M.F. Performance of gas dispersion impeller with vertically asymmetric blades, Chemical Engineering Research and Design, 1999; 77: 728-730.

Myers, K.J., Fasano, J.B. Bakker, A. Gas dispersion using mixed high-efficiency/disc impeller systems, Eighth European Conference on Mixing, UK, 1994; pp65-72.

Nagata, S. Mixing: principles and applications, Wiley, New York, 1975,

Nagata, S., Yanagimoto, M., Yokoyama, T. Studies on the mixing of high viscous liquids, Memoirs of the Faculty of Engineering, Kyoto University, 1956; 18: 444-460.

Nernst. Grundriss der Thermochemie, 1893; pp131.

Ng, K., Yianneskis, M. Observations on the Distribution of Energy Dissipation in Stirred Vessels, Chemical Engineering Research and Design, 2000; 78(3): 334-341.

Nienow, A. W. Suspension of solid particles in turbine-agitated, baffled vessels, Chemical Engineering Science, 1968; 23: 1453-1459.

Nienow, A. W., Wisdom, D. J., Middleton, J. C. The effect of scale and geometry on flooding, recirculation, and power in gassed stirred vessels, Second European Conference on Mixing, Cambridge, England: F1, 1977; pp1-16.

Nienow, A.W. Gas dispersion performance in fermenter operation, Chemical Engineering Progress, 1990: 61-71.

Nienow, A.W. Gas-Liquid Mixing Studies: A Comparison of Rushton Turbines with Some Modern Impellers, Transactions of the Institution of Chemical Engineers, 1996; 74(A): 417-423.

Nienow, A.W., Hunt, G., Buckland, B.C. A fluid dynamics study of retrofitting of large agitated bioreactors: turbulent flow, Biotechnological Bioengineering, 1994; 44: 1177-1185.

Nienow, A.W., Kendall, A., Moore, I.P.T., Ozean-Taskin, G.N., Badham, R.S. The characteristics of aerated 12 and 18 blade Rushton turbines at transitional Reynolds numbers, Chemical Engineering Science, 1995; 50(4): 593-599.

Nienow, A.W., Kuboi, R., Chapman, C.M., Allsfork, K. The Dispersion of gases into liquids by mixed flow impellers, International Conference on Physical Modelling of Multi-Phase Flow, Coventry, BHRA Fluid Engineering U.K., 1983; pp417-437.

Nocentini, M., Fajner, D., Pasquali, G., Magelli, F. Gas-liquid mass transfer and hold-up in vessels stirred with multiple Rushton turbine: water and water-glycerol solutions, Industrial & Engineering Chemistry Research, 1993; 32: 19-26.

Novak, V., Did, P., Rieger, F. Mixing in unbaffled vessels the influence of an eccentric impeller position on power consumption and surface aeration, 4th European Conference on Mixing, Noordwijkerhout, Netherlands, 1982; pp57-70.

Ogut, A, Hatch, R.T. Oxygen transfer Newtonian and non-Newtonian fluids in mechanically gitated vessels, Canadian Journal of Chemical Engineering, 1988; 66: 79-85.

Okamota, Y., Nishikawa, M., Hashimoto, K. Energy dissipation rate distribution in mixing vessels and its effects on liquid- liquid dispersions and solid-liquid mass transfer, International Chemical Engineering, 1981; 21: 88-94.

Oldshue, J. Y. Fluid Mixing Technology, McGraw-Hill, New York, 1983.

Oosterhuis, N.M.G., Kossen, N.W.F. Power input measurements in a production scale bioreactor, Biotechnol Lett, 1981; 3: 645-650.

Oyama, Y., Endoh, K. Chemical Engineering Tokyo, 1955; 19: 2.

Pacek, A. W., Ding, P., Nienow, A.W. The effect of volume fraction and impeller speed on the structure and drop size in aqueous/aqueous dispersions, Chemical Engineering Science, 2001; 56: 3247-3255.

Paglianti, A., Pitus, S., Giona, M. Time-series analysis approach for the identification of flooding/loading transition in gas-liquid stirred tank reactors, Chemical Engineering Science, 2000; 55: 5793-5802.

Pan, Y., Dudukovic, M.P. CFD simulation of a bubble column-2D versus 3D, 6th World Congress of Chemical Engineering, Melbourne, Australia, 2001.

Pan, Y., Dudukovic, M.P., Chang, M. Dynamic simulation of bubbly flow in bubble columns, Chemical Engineering Science, 1999;54: 2481-2489.

Pan, Y., Dudukovic, M.P., Chang, M. Numerical investigation of gas-driven flow in 2-D bubble columns, AIChE Journal, 2000; 46: 434-449.

Panda, T. Bioreactors analysis and design, Tata McGraw Hill, New Delhi, 2011.

Pandit, A.B., Joshi, J.B. Mixing in mechanically agitated gas-liquid contractors, bubble columns and modified bubble columns, Chemical Engineering Science, 1982; 37(6): 1189-1215.

Pangarkar, V.G., Yawalkar, A.A., Sharma, M.M., Beenackers, A.A.C.M. Particle–liquid mass transfer coefficient in two-/three-phase stirred tank reactors, Industrial and Engineering Chemistry Research , 2002; 41: 4141-4167.

Patwardhan, A.W., Joshi J. B. Relation between flow pattern and blending in stirred tanks, Industrial & Engineering Chemistry Research, 1999; 38: 3131-3143.

Patwardhan, A.W., Joshi, J.B. Design of stirred vessels with gas entrained from free liquid surface, The Canadian Journal of Chemical Engineering, 1998; 76(3): 339-364.

Patwardhan, A.W., Joshi, J.B. Hydrodynamics of a stirred vessel equipped with a gas-inducing impeller, Industrial & Engineering Chemistry Research, 1997; 36: 3942-3958.

Paul, E.L., Atiamo Obeng, V.A., Kresta, S.M. Handbook of Industrial Mixing, Wiley and Sons, 2004.

Perry, R.H., Green, D.W., Malony, J.O. Perry's Chemical Engineers' Handbook, 6th ed., McGraw-Hill, New York, 1984.

Petrov, M.M. Investigation of power characteristics of small scale stirred tank bioreactor, Bioprocess Engineering and modeling, 2005; 19:205-209.

Pinelli, D., Nocentini, M., Magelli, F. Solids distribution in stirred slurry reactors influence of some mixer configurations and limits to the applicability of a simple model for predictions, Chemical Engineering Communications, 2001; 188: 91-107.

Pope, S.B. Turbulent flows, Cambridge University Press, New Delhi, 2000.

Pratt, W.K. Digital Image Processing. New York, NY: Wiley-Interscience, 1991; pp491-556.

Puthli, M.S., Rathod, V.K., Pandit, A.B. Gas-liquid mass transfer studies with triple impeller system on a laboratory scale bioreactor, Biochemical Engineering Journal, 2005; 23: 25-30.

Rahami, M., Parvareh, A. Experimental and CFD investigation on mixing by a jet in a semi-industrial stirred tank, Chemical Engineering Journal, 2005; 115: 85-92.

Ranade, V.V. Bourne, J.R., Joshi, J.B. Fluid mechanics and blending in agitated tanks. Chemical Engineering science, 1991; 46:1883-1893.

Ranade, V.V. Computational flow modelling for chemical reactor engineering, Academic press, New York, 2002.

Ranade, V.V., Bourne, J.R., J.B. Fluid mechanics and blending in agitated tanks, Chemical Engineering Science, 1991; 46(8): 1883-1893.

Ranade, V.V., Dometti, S.M.S. Computational snapshot of flow generated by axial flow impellers in baffled stirred vessels, Transactions of IChemE, 1996; 74(A): 476-484.

Ranade, V.V., Perrard, M., LeSauze, N., Zubeb, C., Bertrand, J. Trailing vortices of Rushton turbine PIV measurements and CFD simulations with snapshot approach. Chemical Engineering Research and Design, 2001; 79(A): 3-12.

Ranganathan, P., Sivaraman, S. Investigations on hydrodynamics and mass transfer in gas-liquid stirred reactor using computational fluid dynamics, Chemical Engineering Science, 2011; 66: 3108-3124.

Rao, A.R., Kumar, B. Resistance characteristics of surface aerators, Journal of Hydrologic Engineering, ASCE, 2009; 135: 38-44.

Rao, A.R., Kumar, B. The use of circular surface aerators in wastewater treatment tanks, Journal of Chemical Technology and Biotechnology, 2007; 82: 101-107.

Rao, D.A., Shivashanmugam P. Experimental and CFD simulation studies on power consumption in mixing using energy saving turbine agitator, Journal of Industrial and Engineering Chemistry, 2010; 16: 157-161.

Raouf, H., Caroline, G., Emilie, G., Karine, L. and Jack, L. Numerical investigation of gas dispersion and mass transfer in an aerated stirred tank agitated by six-concave-blades dik turbines: Effect of rheology, 2nd generation autothermal thermophilic aerobic disgestion: Conceptual issues and process advancements, residuals and biosolids management conference, water environment federation, San Diego, CA, 2001.

Reed, X.B., Princz, M., Hartland, S. Laser doppler measurements of turbulence in standard stirred tank, European Conference on Mixing, Paper B1, BHRA, Fluid Engineering, Cranfield, England, 1977; pp1-26.

Reilly, C.D., Evans, G.M., Davidson, J.F., Carpenter, K.J. Effect of vessel scaleup on hydrodynamics of a self-aerating concave blade impeller, Chemical Engineering Science, 1992; 47: 3395-3402.

Rewatkar, V.B., Joshi, J.B. Role of sparger design on gas dispersion in mechanically agitated gas-liquid contactors, Canadian Journal of Chemical Engineering, 1993; 71: 278-291.

Rieger, F., Ditl, P., Noval, V. Vortex depth in mixed unbaffled vessels, Chemical Engineering Science, 1979; 34: 397-403.

Roman, R.V., Gavrilescu, M. Oxygen transfer efficiency in the biosynthesis of antibiotics in bioreactors with a modified Rushton turbine agitator, Acta Biotechnologica, 1994; 14(2): 181-192.

Rousseaux, J.M., Muhr, H., Plasari, E. Mixing and micromixing times in the forced vortex region of unbaffled mixing devices, Canadian Journal of Chemical Engineering, 2001; 79: 697-707.

Rushton, J.H. Applications of fluid mechanics and similitude to scale-up problems-part 1, Chemical Engineering Progress, 1952; 48: 33-38.

Rushton, J.H. The use of Pilot-Plant Mixing Data, Ibid, 1951; 47: 485.

Rushton, J.H., Costich, E.W., Everett, H.J. Power characteristics of mixing impellers, Chemical Engineering Progress, 1950; 46(8): 395-476.

Rutherford, K., Lee, K. C., Mahmoudi, S. M. S., Yianneskis, M. Hydrodynamic characteristics of dual Rushton impeller stirred vessels, AIChE Journal, 1996; 42(2): 332-346.

Saarentine, P., Piirto, M. Turbulent kinetic energy dissipation rate from PIV velocity vectors fields, Experimental Fluids, 2000; 300-307.

Saito, F., Nienow, A.W., Chatwin, S., Moore, I.P.T. Power, gas dispersion and homeogenisation characteristics of Scaba SRGT and Rushton turbine impellers, Journal of Chemical Engineering, 1992: 25: 281-287.

Sanchez, A., Garcia, F., Contreras, A., Molina, E., Chisti, Y. Bubble-column and airlift photobioreactors for algal culture, AIChE Journal, 2000; 46: 1872-1887.

Sanyal, J., Vasquez, S., Roy, S., Dudukovic, M.P. Numerical simulation of gas-liquid dynamics in cylindrical bubble column reactors, Chemical Engineering Science, 1999; 54: 5071-5083.

Saravanan, K., Mondale, V.D., Joshi, J.P. Gas inducing type of mechanically agitated contactors, Industrial Engineering Chemistry Research, 1994; 33: 2228-2242.

Saravanan, P., Pakshirajan, K., Saha, P. Batch growth kinetics of an indigenous mixed microbial culture utilizing *m*-cresol as the sole carbon source, Journal of Hazardous Materials, 2009; 162(1): 476-481.

Sardeing, R., Aubin, J., Poux, M. and Xuereb, C. Gas-liquid mass transfer: Influence of sparger location, Trans IChemE, 2004; 82(A9): 1161-1168

Sbrizzai F., Lavezzo V., Verzicco R., Campolo M., Soldati, A. Direct numerical simulation of turbulent particle dispersion in an unbaffled stirred-tank reactor, Chemical Engineering Science, 2006; 61: 2843-2851.

Scargiali, F., Busciglio, A., Grisafi, F., Brucato, A. Influence of viscosity on mass transfer performance of unbaffled stirred vessels, Chemical Engineering Transactions, 2013;32: 1483-1488.

Scargiali, J.C., D'Orazio, F. Grisafi, F., Brucato, A. Modelling and simulation of gas-liquid hydrodynamics in mechanically stirred tanks, Chemical Engineering Research and Design, 2007, 85: 637-646.

Shan, X., Yu, G., Yang, C., Mao, Z. Solid holdup distribution of solid-liquid suspension in an unbaffled stirred tank, The Chinese Journal of Process Engineering, 2008a; 8: 1-7.

Shan, X., Yu, G., Yang, C., Zai-Sha Mao, Zhang, W. Numerical simulation of liquid-solid flow in an unbaffled stirred tank with a Pitched-blade turbine downflow, Industrial and Engineering Chemistry Research, 2008b; 47: 2926-2940.

Sharp, K.V., Adrian, R.J. PIV study of small-scale flow structure around a Rushton turbine. AIChE Journal, 2001; 47(4): 766-778.

Shekhar, S.M., Jayanti, S. CFD study of power and mixing time for paddle mixing in unbaffled vessels. Trans IChemE, 2002; 80(A): 482-498.

Sheng, J., Meng, H., Fox, R.O. A large eddy PIV method for turbulence dissipation rate estimation, Chemical Engineering Science, 2000; 55: 4423-4434.

Shewale, S.D., Pandit, A.B. Studies in multiple impeller agitated gas-liquid contactors, Chemical Engineering Science, 2006; 61: 489-504.

Simonin, C., Viollet, P.L. Predictions of an oxygen droplet pulverization in a compressible subsonic coflowing hydrogen flow, Numerical Methods for Multiphase Flows, 1990; 91: 65-82.

Singh, K.K., Mahajani, S.M., Shenoy, K.T., Patwardhan, A.W., Ghosh, S.K. CFD Modeling of Pilot-Scale pump-mixer: Single-Phase Head and Power Characteristics, Chemical Engineering Science, 2007; 62: 1308-1322.

Smagorinsky, J. General circulation experiments with the primitive equations, I: The basic experiment, Monthly Weather Review, 1963; 91: 99-164.

Smith, J.M. Simple Pperformance correlations for agitated vessels, Fluid Mechanics and Its Applications, 1992; 10: 55-63.

Smith, J.M. Simple performance correlations for agitated vessels, European Conference on Mixing, Brugge, Belgium, 1991.

Smith, J.M., Katsanevakis, A.N. Impeller power demand in mechanically agitated boiling systems, Trans IChemE, 1993; 71(A): 145-152.

Smith, J.M., Van't Riet K., Middleton J.C. Scale-up of agitated gas-liquid reactors for mass transfer, 2nd European Conference on Mixing, Cambridge, UK: F4, 1977; pp51-66.

Smith, J.M., Warmoeskerken, M.M.C.G. The dispersion of gases in liquids with turbines, 5th European Conference on Mixing, Wurzeburg, Germany, 1985.

Stenstrom, M.K., Brown, L.C., Hwang, H.J. Oxygen transfer parameter estimation, Journal of Environmental Engineering, ASCE, 1981; 107(EE2): 379-397.

Stoots, C., Calabrese, R. V. Mean velocity field relative to a Rushton turbine blade, AIChE Journal, 1995; 41: 1-11.

Suhaili, N., Mohamad, M.S. and Ariff, A.B. Intensified capability of double CD-6 agitated vessel as potential mixer for aerobic viscous bioprocesses, Empowering Science, Technology and Innovation Towards a Better Tomorrow, UMTAS, 2011; 146-151.

Suhaili, N., Mohamad, M.S. Mohamad, R. and Ariff, A.B. Gas-liquid mass transfer performance of dual impeller system employing Rushtons, Concave-bladed Disc (CD-6) turbines and their combination in stirred tank bioreactor, Journal of Applied Sciences Research, 2010; 6(3): 234-244.

Suzukawa, K., Kato, K., Mochizuki, S., Osaka, H., Vortex structures around a Flat Paddle impeller in a stirred vessel, JSME International Journal, Series B, 2006; 49(2): 426-433.

Taghavi, M., Zadghaffari, R., Moghaddas, J. and Moghaddas, Y. Experimental and CFD investigation of power consumption in a dual Rushton turbine stirred tank, Chemical Engineering Research and Design, 2011; 89:280-290.

Tamburini, A. Cipollina A., Micale G., Brucato A., Ciofalo M. CFD simulations of dense solid-liquid suspensions in baffled stirred tanks: prediction of the minimum impeller speed for complete suspension, Chemical Engineering Journal, 2012b; 193-194: 234–255.

Tamburini, A., Cipollina, A., Micale, G., Brucato, A. Dense solid-liquid suspensions in top-covered unbaffled stirred vessels, Chemical Engineering Transactions, 2011b; 24: 1441-1446.

Tatterson, G.B. Fluid mixing and gas dispersion in agitated tanks, McGraw-Hill, 1991.

Tezura, S., Kimura, A., Yoshida, M., Yamagiwa, K., Ohkawa, A. Agitation requirements for complete solid suspension in an unbaffled agitated vessel with an unsteadily forward–reverse rotating impeller, Journal of Chemical Technology and Biotechnology, 2007; 82: 672-680.

Thibault, J., Leduy, A., Denis, A. Chemical enhancement in the determination of kLa by the sulfite oxidation method, Canadian Journal of Chemical Engineering, 1990; 68: 324-326.

Tsao, G.T.N. Vortex behavior in the Waldhof fermentor, Biotechnological Bioengineering, 1968; 10: 177-188.

Uhl, V.W., Gray, J.B. Mixing: Theory and practice, Academic Press, 1966.

Um, B.H., Hanley, T.R. A comparison of simple rheological parameters and simulation data for *Zymomonas mobilis* fermentation broths with high substrate loading in a 3-L bioreactor, Applied Biochemistry and Biotechnology, 2008; 145(1-3): 29-38.

Van't Riet, K., Boom, J.M., Smith, J.M. Power consumption, impeller coalescence and recirculation in aerated vessels, Chemical Engineering Research and Design, 1976; 54: 124-131.

Van't Riet, K., Smith, J.M. The behaviors of gas-liquid mixtures near Rushton turbine blades, Chemical Engineering Science, 1973; 28: 1031-1037.

Van't Riet, K. Review of measuring methods and non-viscous gas-liquid mass transfer in stirred vessels, Industrial Engineering Chemical Process Design Development, 1979; 18: 357-364.

Van't Riet, K., PhD Thesis, University of Technology, Delft, 1975.

Vasconcelos, J.M.T, Orvalho, S.C.P., Rodríguez, A.M., Alves, S.S. Effect of blade shape on the performance of six blade disk turbine impellers, Industrial & Engineering Chemistry Research, 2000; 39: 203-208.

Venneker, B.C.H., Derksen, J.J., Van den Akker, H. E.A. Population balance modeling of aerated stirred vessels based on CFD, AIChE Journal, 2002; 48(4): 673-685.

Verma, M.K. and Tyagi, R.K. Aeration of volatile organic compounds using gas dispersion impellers, Journal of Mechanical Engineering Research, 2012; 4(7): 213-224.

Vrabel, P., Vander Lans, R.G.J.M., Cui, Y.Q., Luyben, K.C.A.M. Compartment model approach: mixing in large scale aerated reactors with multiple-impellers, Chemical Engineering Research and Design, 1999; 77: 291-302.

Wadnerkar, D, Utikar, R.P., Tade, M.O., Pareek, V.K. CFD simulation of solid-liquid stirred tanks, Advanced Power Technology, 2012; 23: 445-453.

Wang, B., Lan, C.Q., Horsman, M. Closed photo-bioreactors for production of microalgal biomasses, Biotechnology Advances, 2012; 30: 904-912.

Warmoeskerken, M. M. C. G., Smith, J. M. The hollow blade agitator for dispersion and mass transfer, Trans IChemE, Chemical Engineering Research and Design, 1989; 67(2): 193-198.

Warmoeskerken, M.M.C.G., Smith, J.M. Description of the power curves of turbine stirred gas dispersions, The Fourth European Conference on Mixing Noordwijkerhout, BHRA, Granfield, 1982; pp237-246.

Weinstein, B., Treybal, R.B. Liquid-Liquid contacting in unbaffled, agitated vessels, AIChE Journal, 1973; 19(2): 304-312.

Westerterp, K.R., van Dierendonck, L.L., de Kraa, J.A. Chemical Engineering Science, 1963; 18: 157-176.

Whitton, M.J., Nienow, A.W. Scale up correlations for gas hold up and mass transfer coefficients in stirred tank reactors, 3rd International Conference on Bioreactor and Bioprocess Fluid Dynamics, 1993: pp135-149.

Wong, C.F., Hayduk, W. Oil-Water Separation by Means of a Vortex Formed in a Stirred Draining Vessel. 1. Vortex Phenomena, Industrial & Engineering Chemistry Research, 1987; 26: 582-587.

Woziwodzki, S., Jędrzejczak, L. Effect of eccentricity on laminar mixing in vessel stirred by double turbine impellers, Chemical Engineering Research and Design, 2011; 89(11): 2268-2278.

Wu, H. An issue on application of disk turbine for gas-liquid mass transfer, Chemical Research and Science, 1995; 50(17): 2801-2811.

Wu, H., Patterson, G.K. Doppler measurements of turbulent-flow parameters in a stirred mixer, Chemical Engineering Science, 1989; 44: 2207-2221.

Xinhong, L., Yuyun, B., Zhipeng, L., Zhengming, G., Smith, J.M. Particle Image Velocimetry study of turbulence characteristics in a vessel agitated by a dual Rushton impeller, Chinese Journal of Chemical Engineering, 2008; 16(5): 700-708.

Yang J.D., Wang, N.S. Oxygen mass transfer enhancement via fermentor headspace pressurization, Biotechnological Progress, 1992; 8: 244-251.

Yapici, K., Karasozen, B., Schäfer, M., Uludag, Y. Numerical investigation of the effect of the Rushton type turbine design factors on agitated tank flow characteristics, Chemical Engineering Communications, 2008; 47(8): 1340-1349.

Yasukawa, M., Onodera, M., Yamagiwa, K., Ohkawa, A. Gas holdup, power consumption, and oxygen absorption coefficient in a stirred-tank fermentor under foam control. Biotechnological Bioengineering, 1991; 38: 629-636.

Yawalkar, A. A., Heesink, A. B. M., Versteeg, G. F., Pangarkar, V. G. Gas hold-up in stirred tank reactors in the presence of inorganic electrolytes, The Canadian Journal of Chemical Engineering, 2002; 80: 791-799.

Yeoh, S.L., Papadakis, G., Yianneskis, M. Numerical simulation of turbulent flow characteristics in a stirred vessel using the LES and RANS approaches with the Sliding/deforming mesh methodology, Chemical Engineering Research and Design, 2004; 82(7): 834-848.

Yianneskis, M., Popiolek, Z., Whitelaw, J.H. An Experimental Study of the Steady and Unsteady Flow Characteristics of Stirred Reactors, Journal of Fluid Mechanics, 1987; 175: 537-555.

Yoshida, M., A. Ito, K. Yamagiwa, A. Ohkawa, M. Abe, S. Tezura and M. Shimazaki, Effect of Impeller Clearance on Power Consumption of Unsteadily Forward-Reverse Rotating Multiple Impellers in an Unbaffled Agitation Vessel, Latin American Applied Research, 2002; 32, 189-194.

Yoshida, M., Kimura , A., Yamagiwa, K., Ohkawa, A., Tezura , S. Movement of solid particles on and off bottom of an unbaffled vessel agitated by unsteadily forward-reverse rotating impeller , Journal of Fluid Science and Technology, 2008; 3: 282-291.

Yoshida, M., Kitamura, A., Yamagiwa, K., Ohkawa, A. Gas hold-up and volumetric oxygen transfer coefficient in an aerated agitated vessel without baffles having forward reverse rotating impellers. Canadian Journal of Chemical Engineering, 1996; 74(1): 31-39.

Zadghaffari, R., Moghaddas, J. and Revstedt , J. A mixing study in a double- Rushton stirred tank, Computational and Chemical Engineering, 2009; 33: 1240-1246.

Zhengming, G., Yingchen, W., Litian, S., Juhu, F. Theoretical and experimental studies on bubble diameter and gas holdup in aerated stirred tanks, Chinese Journal of Chemical Engineering, 1996; 4(4): 283-289.

Zhou, G., Kresta, S. M. Impact of the geometry on the maximum turbulence energy dissipation rate for impellers, AIChE Journal, 1996b; 42: 2476-2490.

Zhu, Y., Bandopadhayay, P.C., Wu, J. Measurement of gas-liquid mass transfer in an agitated vessel-A comparison between different impellers, Journal of Chemical Engineering of Japan, 2001; 34: 579-584.

Zlokarnik, M. Ruhrleistung in begasten Flussigkeiten, Chemical Engineering Technology, 1973; 45(10a): 689-692.

Zlokarnik, M. Trombentiefe beim rühren in unbewehrten behältern, Chemie Ingenieur Technnik, 1971; 43(18): 1028-1030.

Zundelevich, Y. Power consumption and gas capacity of self-inducing turbo aerators, AIChE Journal, 1979; 25(5): 763-73.

APPENDIX 1.

1. Canny edge detection method:

```
RGB = imread('3.jpg');
[X,map] = rgb2ind(RGB,128);
I = ind2gray(X,map);imshow(I);
I1 = imadjust(I,stretchlim(I),[0,1]);figure;imshow(I1);
[N,M] = size(I);
h = [0.125,0.375,0.375,0.125];
g = [0.5,-0.5];
delta = [1,0,0];
J = 3;
a(1:N,1:M,1,1:J+1) = 0;
dx(1:N,1:M,1,1:J+1) = 0;
dy(1:N,1:M,1,1:J+1) = 0;
d(1:N,1:M,1,1:J+1) = 0;
a(:,:,1,1) = conv2(h,h,I,'same');
dx(:,:,1,1) = conv2(delta,g,I,'same');
dy(:,:,1,1) = conv2(g,delta,I,'same');
x = dx(:,:,1,1);
y = dy(:,:,1,1);
d(:,:,1,1) = sqrt(x.^2+y.^2);
I1 = imadjust(d(:,:,1,1),stretchlim(d(:,:,1,1)),[0 1]);figure;imshow(I1);
lh = length(h);
lg = length(g);
for j = 1:J+1
lhj = 2^j*(lh-1)+1;
lgj = 2^j*(lg-1)+1;
hj(1:lhj)=0;
gj(1:lgj)=0;
for n = 1:lh
hj(2^j*(n-1)+1)=h(n);
end
for n = 1:lg
gj(2^j*(n-1)+1)=g(n);
end
a(:,:,1,j+1) = conv2(hj,hj,a(:,:,1,j),'same');
dx(:,:,1,j+1) = conv2(delta,gj,a(:,:,1,j),'same');
dy(:,:,1,j+1) = conv2(gj,delta,a(:,:,1,j),'same');
x = dx(:,:,1,j+1);
y = dy(:,:,1,j+1);
dj(:,:,1,j+1) = sqrt(x.^2+y.^2);
I1 = imadjust(dj(:,:,1,j+1),stretchlim(dj(:,:,1,j+1)),[0 1]);figure;imshow(I1);
end
```

2. Fuzzy edge detection method:

```
f=imread('3.jpg');
 figure,imshow(f) ;title('fuzzy','fontsize',12);
f=double(f);
```

```
[m,n]=size(f);
g=zeros(m,n);
g1=zeros(m,n);
g2=zeros(m,n);
g3=zeros(m,n);
F=zeros(m,n);
S=zeros(m,n);
u=zeros(m,n);
u1=zeros(m,n);
u2=zeros(m,n);
u3=zeros(m,n);
 fe=2;fd=36.23;
t=0.5*(min(f(:))+max(f(:)));
done=false;
while ~done
   r=f>=t;
   tnext=0.5*(mean(f(r))+mean(f(~r)));
   done=abs(t-tnext)<0.5;
   t=tnext;
end
for   i=1:m
  for j=1:n
       if f(i,j)>t
          u(i,j)=1/((1+(f(i,j)-t)/fd)^fe);
       else
          u(i,j)=1/((1+(t-f(i,j))/fd)^fe);
       end

      if u(i,j)>0 & u(i,j)<=0.5
         u1(i,j)=2*u(i,j)*u(i,j);
      else
        u1(i,j)=1-2*(1-u(i,j))^2;
      end
      if u1(i,j)>0 & u1(i,j)<=0.5
         u2(i,j)=2*u1(i,j)*u1(i,j);
              else
        u2(i,j)=1-2*(1-u1(i,j))^2;
      end
       if u2(i,j)>0 & u2(i,j)<=0.5
         u3(i,j)=2*u2(i,j)*u2(i,j);
              else
        u3(i,j)=1-2*(1-u2(i,j))^2;
      end
      if f(i,j)>t
         g1(i,j)=f(i,j)+fd*(u1(i,j)^(-1/fe)-1);
       else
          g1(i,j)=f(i,j)-fd*(u1(i,j)^(-1/fe)-1);
      end
       if f(i,j)>t
```

```
        g2(i,j)=f(i,j)+fd*(u2(i,j)^(-1/fe)-1);
      else
        g2(i,j)=f(i,j)-fd*(u2(i,j)^(-1/fe)-1);
      end
        if f(i,j)>t
       g3(i,j)=f(i,j)+fd*(u3(i,j)^(-1/fe)-1);
      else
        g3(i,j)=f(i,j)-fd*(u3(i,j)^(-1/fe)-1);
      end
      end
end
g1=uint8(g1);
g2=uint8(g2);
g3=uint8(g3);
figure,imshow(g1);title('fuzzy1','fontsize',12);
figure,imshow(g2);title(' fuzzy2','fontsize',12);
figure,imshow(g3);title('fuzzy3','fontsize',12);
c=30;
t1=0.5*(min(g3(:))+max(g3(:)));
done=false;
while ~done
   r=g3>=t1;
   tnext=0.5*(mean(g3(r))+mean(g3(~r)));
   done=abs(t1-tnext)<0.5;
   t1=tnext;
end
for  i=1:m
   for j=1:n
       if g3(i,j)<=t1
         g3(i,j)=255;
       else   g3(i,j)=0;
       end

   end
end
for  i=1:m-1
   for j=1:n-1
      x1=g3(i,j);x2=g3(i,j+1);x3=g3(i+1,j);x4=g3(i+1,j+1);
      if  x1==0 & x2==255 & x3==0 & x4==255
         F(i,j)=0; F(i+1,j)=0;
          elseif  x1==0 & x2==0 & x3==255 & x4==255
         F(i,j)=0; F(i,j+1)=0;
         elseif  x1==255 & x2==255 & x3==0 & x4==0
         F(i+1,j)=0; F(i+1,j+1)=0;
           elseif  x1==255 & x2==0 & x3==255 & x4==0
         F(i,j+1)=0; F(i+1,j+1)=0;
           elseif  x1==255 & x2==0 & x3==0 & x4==255
         F(i,j+1)=0; F(i+1,j)=0;
            elseif  x1==0 & x2==255 & x3==255 & x4==0
         F(i,j)=0; F(i+1,j+1)=0;
      else
```

```
          F(i,j)=255;  F(i,j+1)=255;    F(i+1,j)=255;   F(i+1,j+1)=255;
     end
   end
end
figure,imshow(F);title(' fuzzy4','fontsize',12);
for  i=1:m-2
   for j=1:n-2
      h=[g3(i,j)  g3(i,j+1)   g3(i,j+2);g3(i+1,j)  g3(i+1,j+1)   g3(i+1,j+2);g3(i+2,j)  g3(i+2,j+1)
g3(i+2,j+2)];
      if h==[0 255 255;0 255 255;0 255 255;]
            S(i,j)=0;   S(i+1,j)=0;   S(i+2,j)=0;
      elseif h==[255 0 255; 255 0 255;255 0 255]
            S(i,j+1)=0;  S(i+1,j+1)=0; S(i+2,j+1)=0;
      elseif h==[255 255 0; 255 255 0;255 255 0]
            S(i,j+2)=0;  S(i+1,j+2)=0; S(i+2,j+2)=0;
      elseif h==[0 0 0; 255 255 255 ;255 255 255]
            S(i,j)=0;  S(i,j+1)=0; S(i,j+2)=0;
     elseif h==[255 255 255; 0 0 0 ;255 255 255]
            S(i+1,j)=0;  S(i+1,j+1)=0; S(i+1,j+2)=0;
     elseif h==[255 255 255; 255 255 255 ;0 0 0]
            S(i+2,j)=0;  S(i+2,j+1)=0; S(i+2,j+2)=0;
     elseif h==[0 0 255; 0 255 255 ;0 0 0]
            S(i,j)=0;  S(i,j+1)=0; S(i+1,j)=0;
     elseif h==[255 255 255; 0 255 255 ;0 0 255]
            S(i+1,j)=0;  S(i+2,j)=0; S(i+2,j+1)=0;
     elseif h==[255 255 255; 255 255 0 ;255 0 0]
            S(i+1,j+2)=0;  S(i+2,j+1)=0; S(i+2,j+2)=0;
     elseif h==[255 0 0; 255 255 0 ;255 255 255]
            S(i,j+1)=0;  S(i,j+2)=0; S(i+1,j+2)=0;
     elseif h==[0 0 0; 0 0  255 ;0 255 255]
           S(i,j)=0;  S(i,j+1)=0; S(i,j+2)=0;S(i+1,j)=0;  S(i+1,j+1)=0; S(i+2,j)=0;
     elseif h==[0 255 255; 0 0  255 ;0 0 0]
            S(i+2,j)=0;  S(i+2,j+1)=0; S(i+2,j+2)=0;S(i,j)=0;S(i+1,j)=0;  S(i+1,j+1)=0;
     elseif h==[255 255 0; 255 0  0 ;0 0 0]
             S(i+2,j)=0;  S(i+2,j+1)=0; S(i+2,j+2)=0;S(i+1,j+1)=0; S(i+1,j+2)=0;S(i,j+2)=0;
     elseif h==[0 0 0; 255 0  0 ;255 255 0]
            S(i,j)=0;  S(i,j+1)=0; S(i,j+2)=0;S(i+1,j+1)=0; S(i+1,j+2)=0;S(i+2,j+2)=0;
      else
      S(i,j)=255;  S(i,j+1)=255; S(i,j+2)=255; S(i+1,j)=255;  S(i+1,j+1)=255;
S(i+1,j+2)=255;S(i+2,j)=255;  S(i+2,j+1)=255; S(i+2,j+2)=255;
      end
   end
end
figure,imshow(S);title(' fuzzy5','fontsize',12);
```

3. For modified drag law:

```
/*UDF for modified drag law in fluent*/
# include "udf.h"
```

```
# define C 0.3
# define diam2 2.e-3
# define Cmu 0.09
DEFINE_EXCHANGE_PROPERTY(modified_drag,cell,mix_thread,s_col,f_col)
{
Thread*thread_l;
Thread*thread_g;
real slip_x;
real slip_y;
real slip_z;
real slip;
real k_l;
real d_l;
real mu_t_l;
real mu_l;
real rho_l;
real rho_g;
real reyp;
real cd;
/* liquid phase-primary*/
thread_l=THREAD_SUB_THREAD(mix_thread,s_col);
/* gas phase-secondary*/
thread_g=THREAD_SUB_THREAD(mix_thread,f_col);
/* slip velocity*/
slip_x=C_U(cell,thread_l)-C_U(cell,thread_g);
slip_y=C_V(cell,thread_l)-C_U(cell,thread_g);
slip_z=C_W(cell,thread_l)-C_W(cell,thread_g);
/*Parameters*/
rho_g = C_R(cell, thread_g);
rho_l = C_R(cell, thread_l);
/*turbulent kinetic energy and dissipation rate for liquid*/
k_l=C_K(cell,thread_l);
d_l=C_D(cell,thread_l);
/*eastimation of slip velocity*/
slip=sqrt(slip_x*slip_x+slip_y*slip_y+slip_z*slip_z);
/*turbulent viscosity of liquid */
mu_t_l=rho_l*Cmu*k_l*k_l/d_l;
/*relative reynolds number for the primary phase*/
reyp=(rho_l*slip*diam2)/(mu_l+mu_t_l*Cmu);
/* drag co-efficient*/
/*Schiller-Nauman*/
if (reyp>1000.)
cd=0.44;
else
cd=24.0*(1.0+0.15*pow(reyp, 0.687))/reyp;
return cd ;
}
```

4. For degassing boundary condition:

```
#include "udf.h"
```

```
DEFINE_PROFILE(vof, thread, np)
{
 Thread *t;
 face_t f;
 begin_f_loop (f, thread)
   {
     cell_t c = F_C0(f, thread);
     t = THREAD_T0(thread);
     F_PROFILE(f, thread, np) = C_VOF(c, t);
   }
 end_f_loop(f,thread);
}

DEFINE_PROFILE(xvel, thread, np)
{
 Thread *t;
 face_t f;
 begin_f_loop (f, thread)
   {
     cell_t c = F_C0(f, thread);
     t = THREAD_T0(thread);
     F_PROFILE(f, thread, np) = C_U(c, t);
   }
 end_f_loop(f,thread);
}

DEFINE_PROFILE(yvel, thread, np)
{
 Thread *t;
 face_t f;
 begin_f_loop (f, thread)
   {
     cell_t c = F_C0(f, thread);
     t = THREAD_T0(thread);
     F_PROFILE(f, thread, np) = C_V(c, t);
   }
 end_f_loop(f,thread);
}
DEFINE_PROFILE(zvel, thread, np)
{
 Thread *t;
 face_t f;
 begin_f_loop (f, thread)
   {
     cell_t c = F_C0(f, thread);
     t = THREAD_T0(thread);
     F_PROFILE(f, thread, np) = C_W(c, t);
   }
 end_f_loop(f,thread);
```

```
}
DEFINE_PROFILE(k, thread, np)
{
  Thread *t;
  face_t f;
  begin_f_loop (f, thread)
    {
      cell_t c = F_C0(f, thread);
      t = THREAD_T0(thread);
      F_PROFILE(f, thread, np) = C_K(c, t);
    }
  end_f_loop(f,thread);
}

DEFINE_PROFILE(epsilon, thread, np)
{
  Thread *t;
  face_t f;
  begin_f_loop (f, thread)
    {
      cell_t c = F_C0(f, thread);
      t = THREAD_T0(thread);
      F_PROFILE(f, thread, np) = C_D(c, t);
}
  end_f_loop(f,thread);
}
```

APPENDIX 2:

(i) For single impeller single phase unbaffled stirred system:

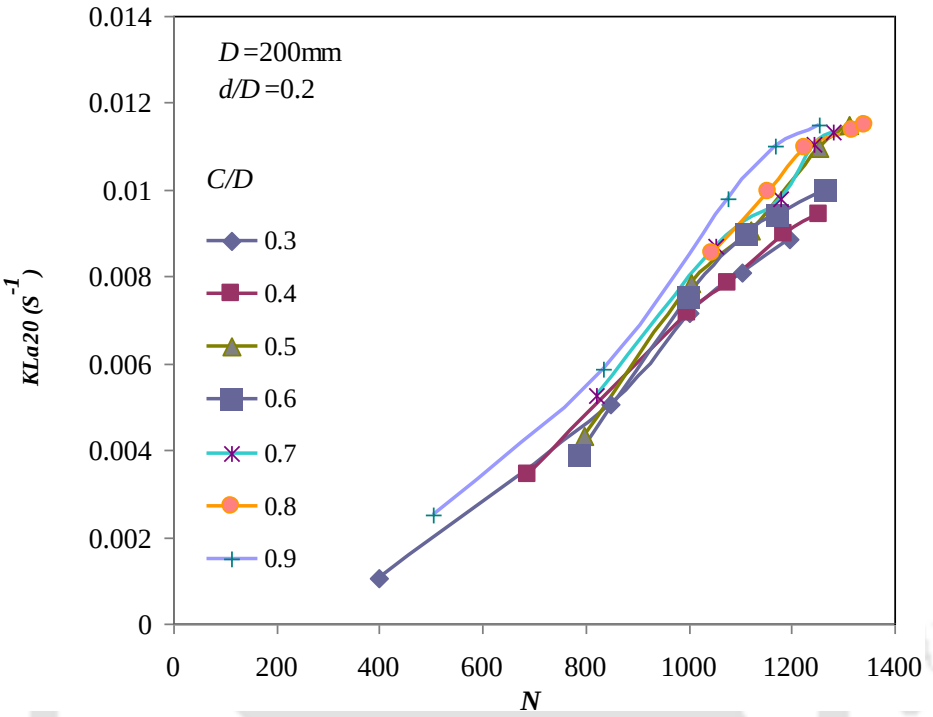

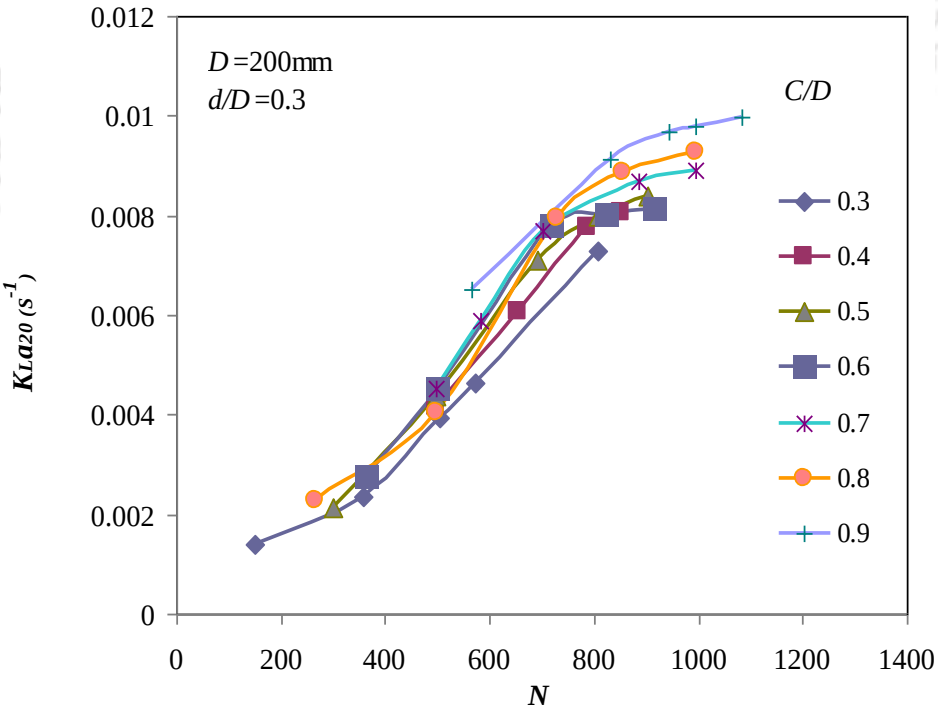

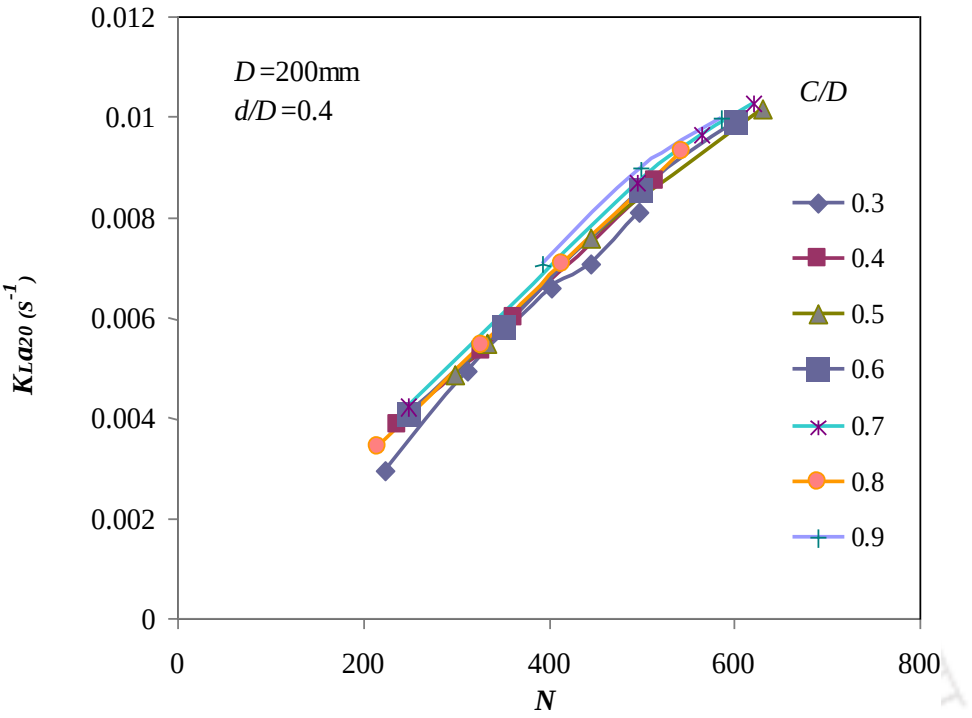

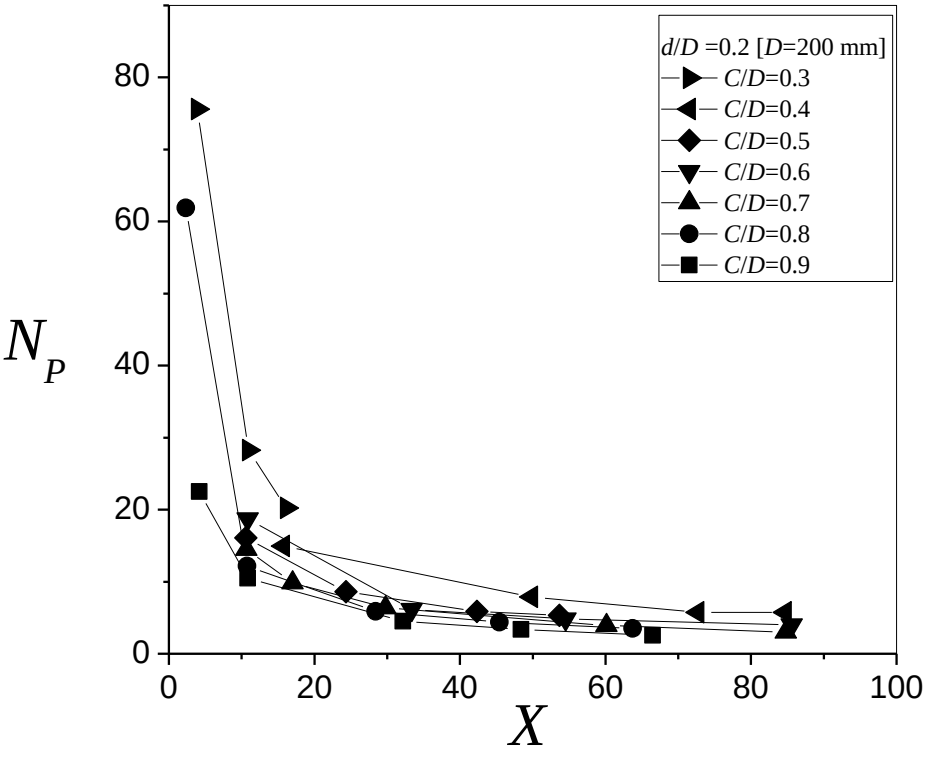

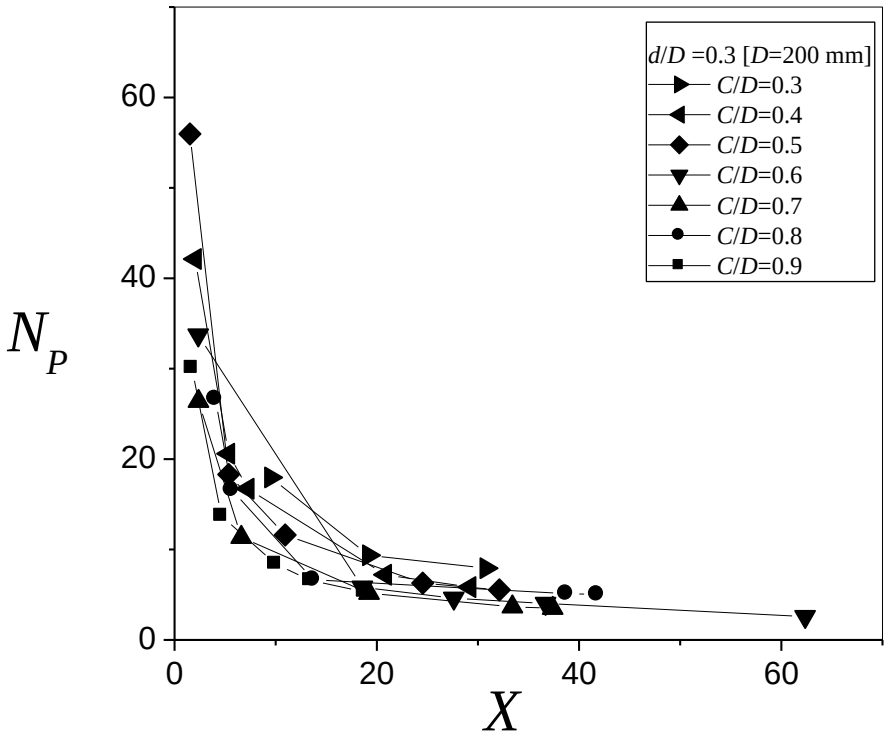

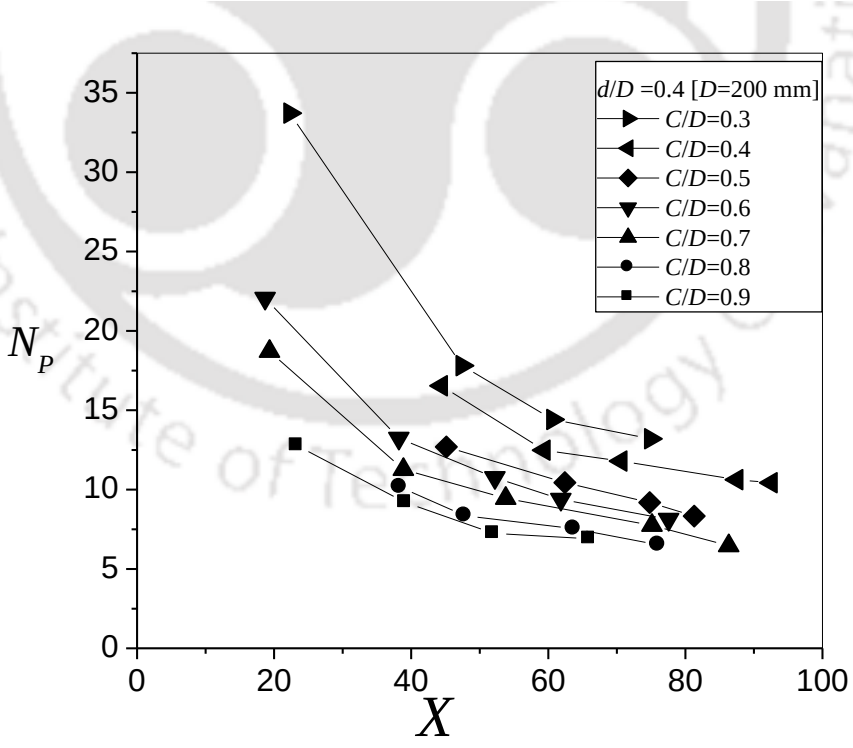

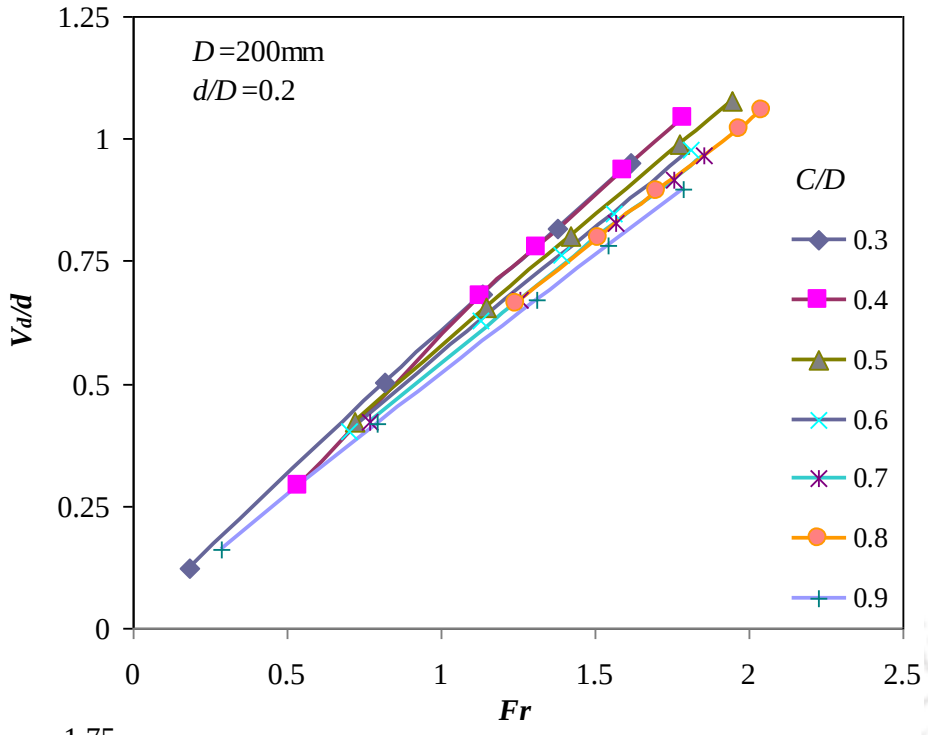

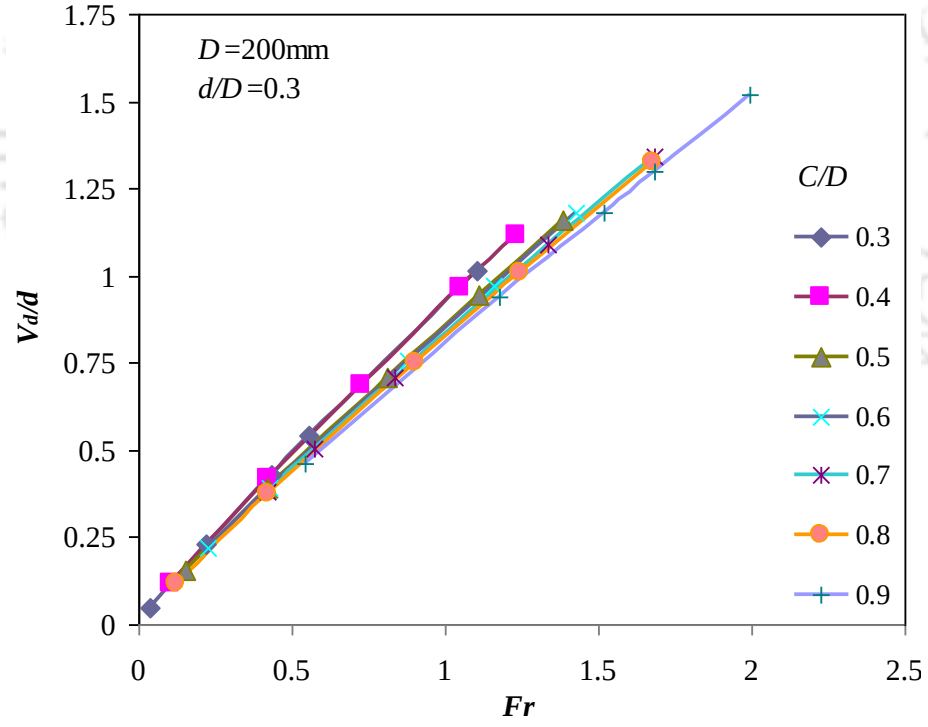

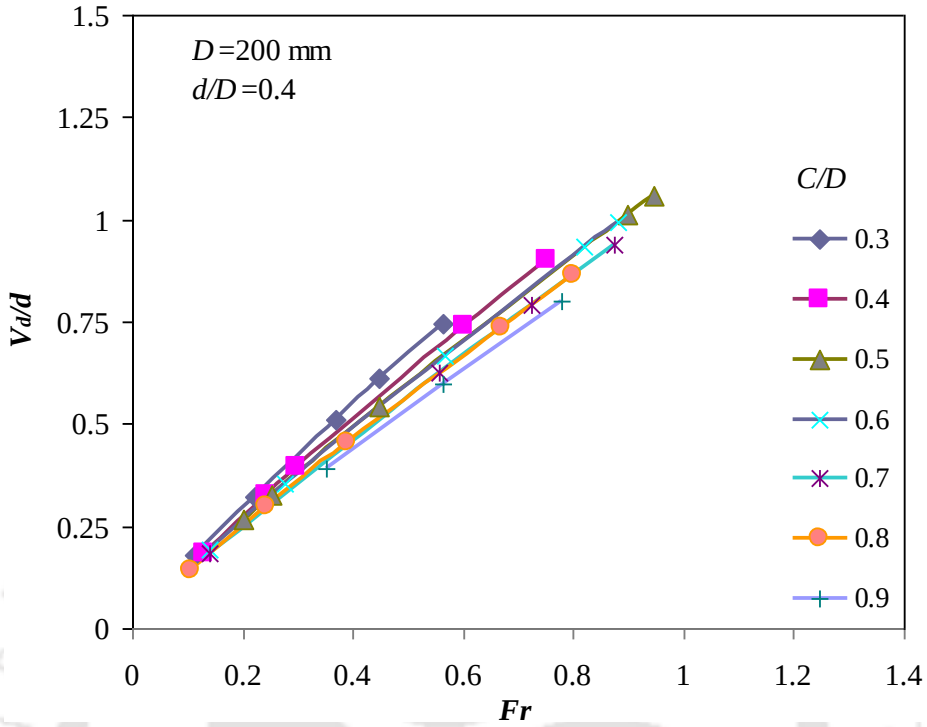

(ii) For single impeller gas-liquid phase unbaffled stirred system:

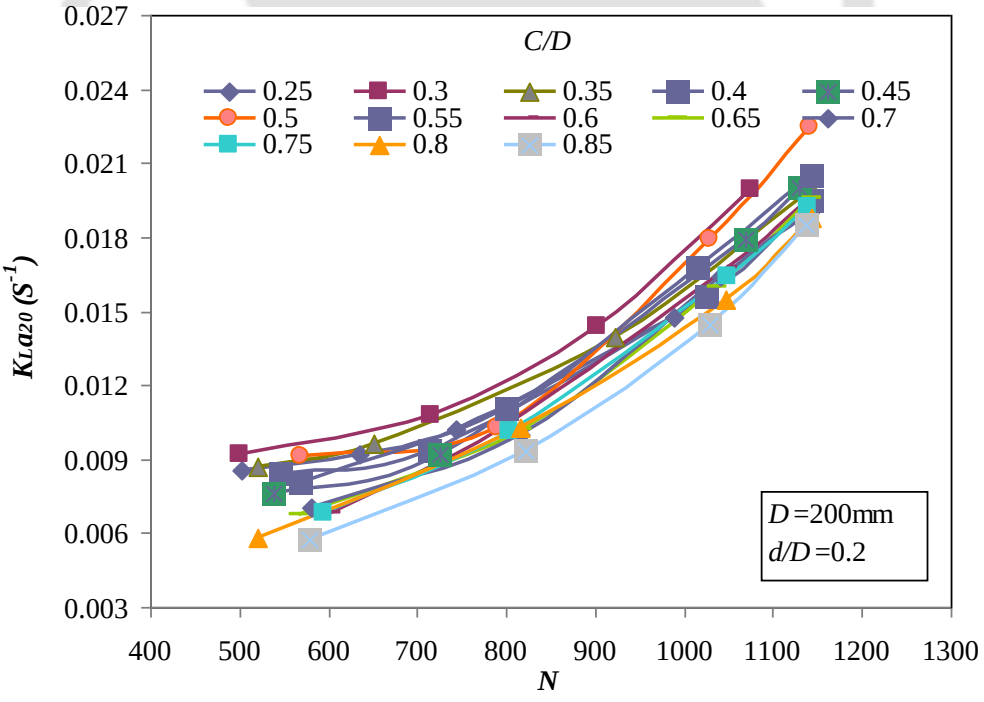

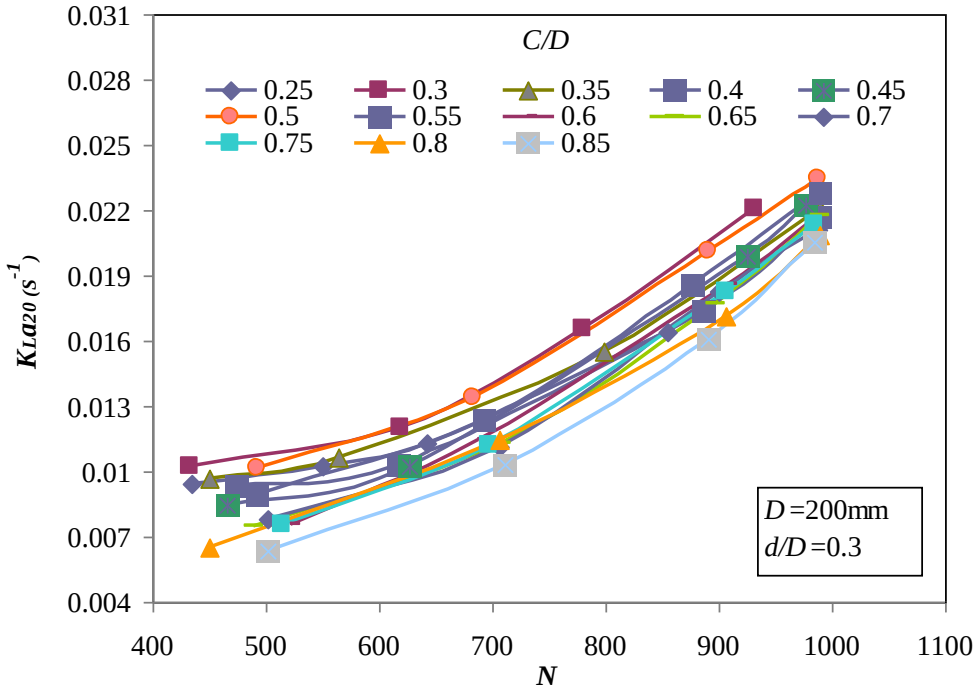

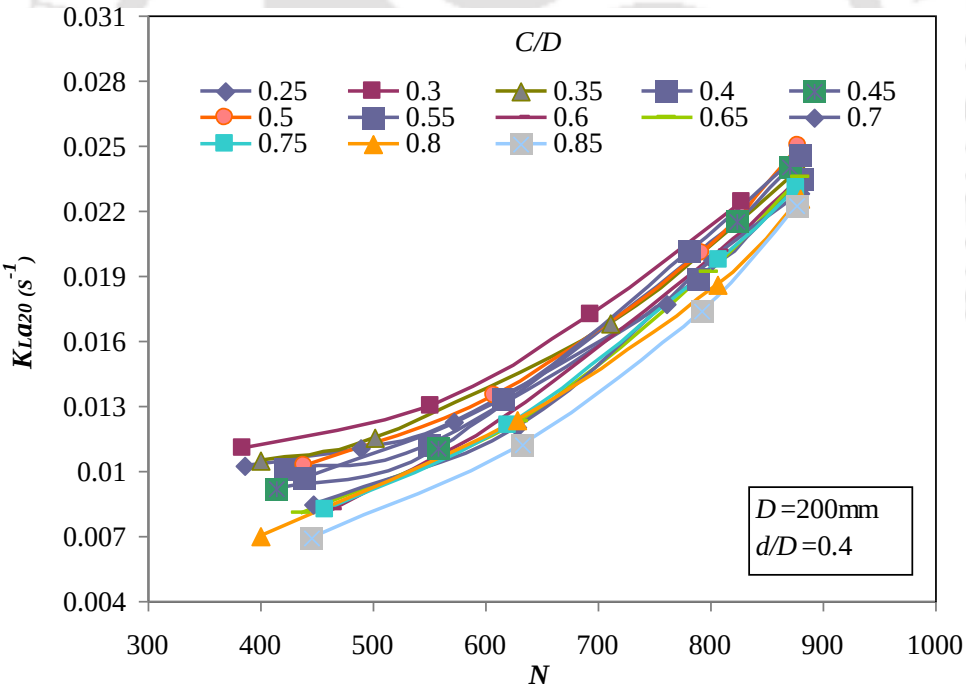

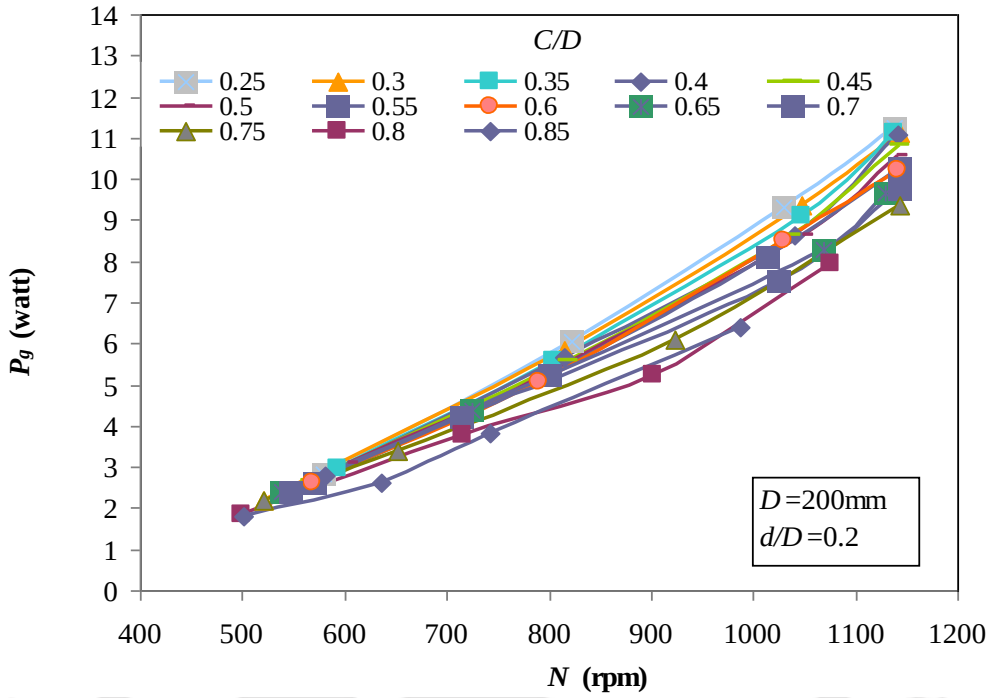

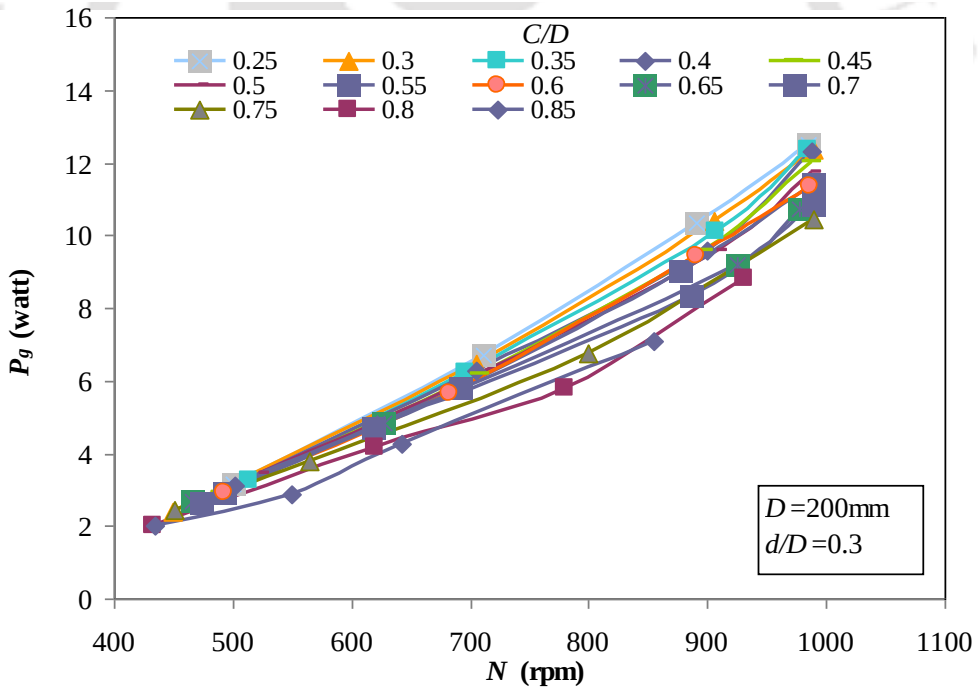

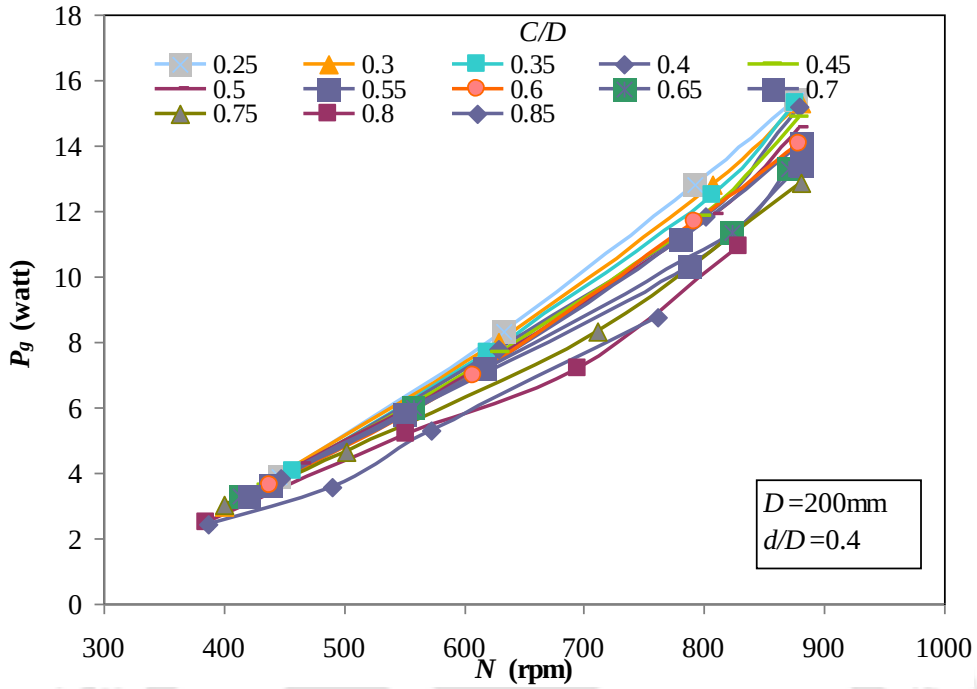

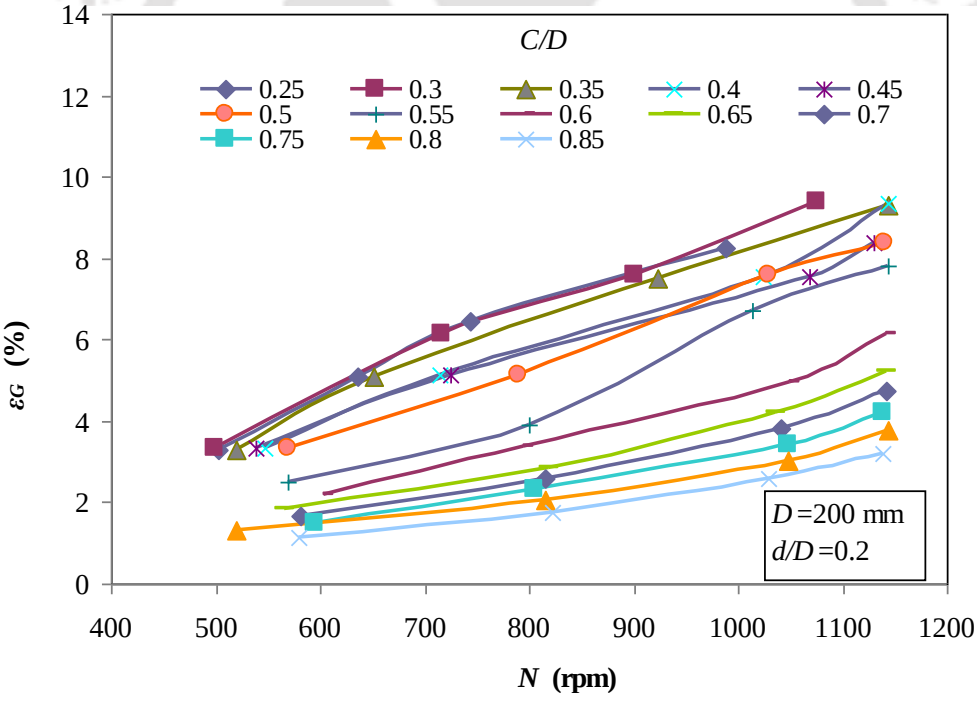

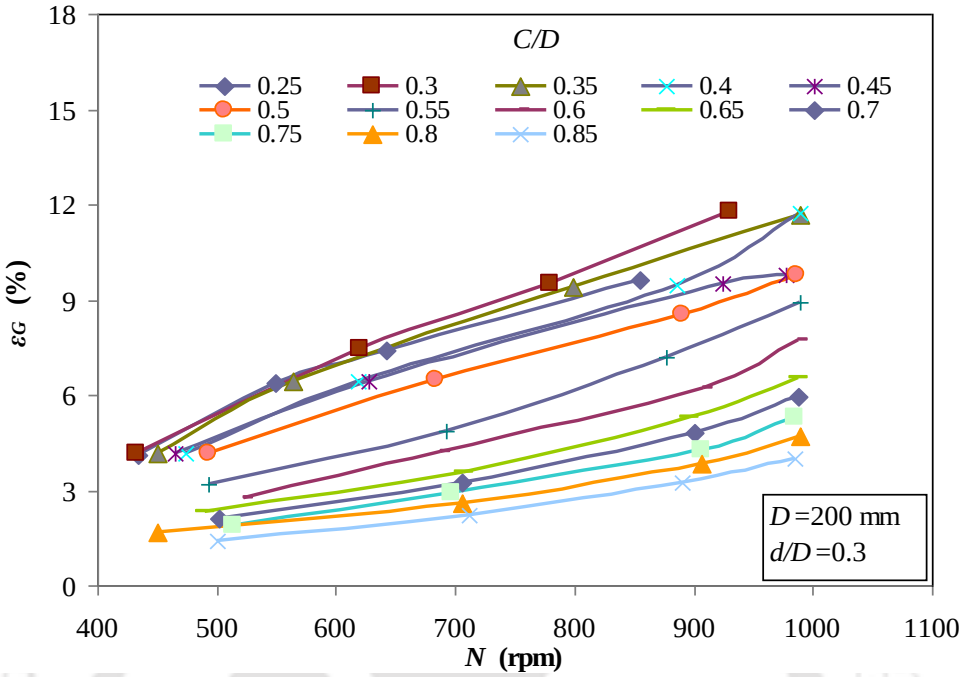

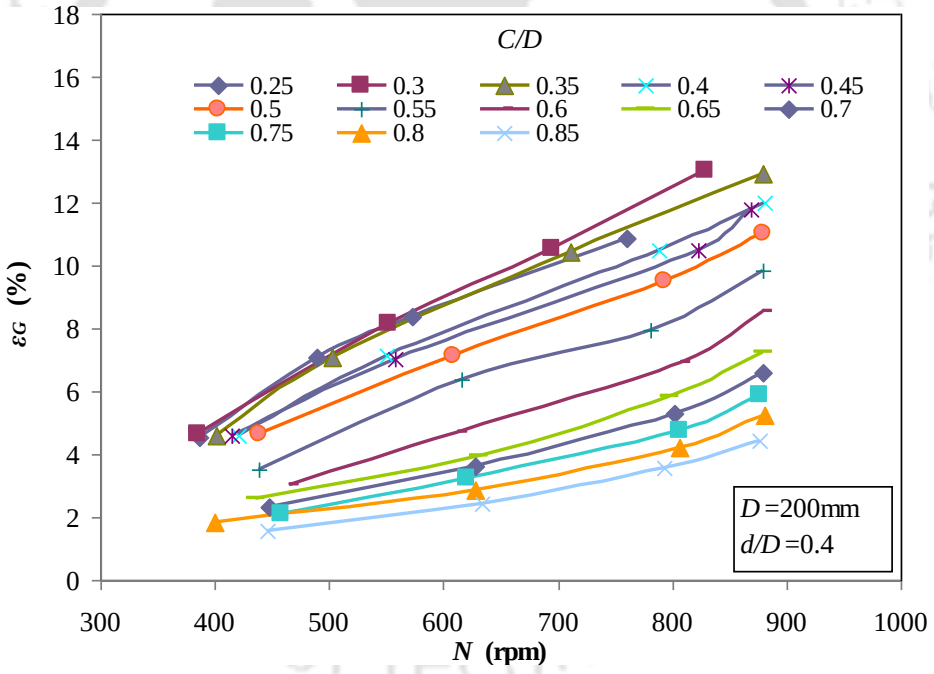

PUBLICATIONS

Journals

(Under Review)

1. Devi, T.T., Kumar, B. Dual stirred gas-liquid unbaffled tank with Concave Blade Impeller, Chemical Engineering and Technology, Wiley InterScience.
2. Devi, T.T., Kumar, B. Mass transfer and power characteristics of stirred tank with Rushton and Curved Blade impeller, Chemical Engineering and Technology, Wiley InterScience.

(Accepted)

3. Devi, T.T., Kumar, B. Scale-up criteria for dual stirred unbaffled tank with Concave Blade Impeller, Korean Journal of Chemical Engineering, Springer.
4. Devi, T.T., Kumar, B. Design of gas-liquid unbaffled stirred tank with Concave Blade impeller, Journal of Engineering Physics and Thermophysics, Springer.
5. Devi, T.T., Kumar, B. Effects of superficial gas velocity on process dynamics in bioreactors, Thermophysics and Aeromechanics, Springer.
6. Devi, T.T., Kumar, B. Large Eddy Simulation of turbulent flow in stirred tank with Concave Blade impeller, Journal of Engineering Thermophysics, Springer.
7. Devi, T.T., Kumar, B. Design of self-aerating unbaffled stirred tank with Concave Blade impeller, Journal of Engineering Thermophysics, Springer.

(Published)

8. Devi, T.T., Kumar, B. Comparison of flow patterns of dual Rushton with CD-6 impeller, Theoretical Foundations of Chemical Engineering, Springer, 2013; 47(4): 410-421.
9. Devi, T.T., Kumar, B. CFD simulation of flow patterns in dual impeller stirred tank, International Journal of Modeling and Simulation, 2013; 33(2):1-8.
10. Kumar, B., Devi, T.T. Oxygen transfer with circulation flow rate in unbaffled surface aerator, Chemistry and Chemical Technology, 2012; 6(2): 203-207.

11. Devi, T.T., Kumar, B. CFD simulation of flow patterns in unbaffled stirred tank with CD-6 impeller, Chemical Industry & Chemical Engineering Quarterly, 2012; 18(4): 535-546.
12. Kumar, B., Devi, T.T. Microscale of turbulence and oxygen transfer in surface aerator, JERAD, 2012; 6(3): 569-574.
13. Devi, T.T., Kumar, B. Turbulent modeling of stirred tank with CD-6 impeller, Advances and Applications in Fluid Mechanics, 2011; 10(2): 141-155.
14. Devi, T.T., Kumar, B. Analyzing flow hydrodynamics in stirred tank with CD-6 impeller and Rushton turbine, International Review of Chemical Engineering, 2011; 3(4): 440-448.

Conferences

1. Devi, T.T., Kumar, B. Turbulent dissipation rates in a baffled stirred tank of Rusthon turbine, 14th Asia Pacific Confederation of Chemical Engineering, February 21-24, 2012, Singapore.
2. Kumar, B., Devi, T.T. Impeller submergence depth on power consumption of mixing tank, International Conference on Environmental Science and Development, ICESD 2011, January 7-9, 2011, Mumbai, Maharastra, India.
3. Devi, T.T., Malsur, B., Kumar, B. Optimal impeller submergence depth for stirred tank, International Conference on Thermal Energy and Environment (INCOTEE, 2011), March 24-26, 7-9, 2011, Kalasalingam University, Anand Nagar, Tamilnadu, India.
4. Devi, T.T., Kumar, B. Investigations of mixing in mechanically stirred tank: Comparison of CD-6 impeller and Rushton turbine, National Conference on Recent Advances in Civil Engineering, October 14-16, 2011, IT-BHU, Varanasi, Utter Pradesh, India.
5. Devi, T.T., Kumar, B. Application of standard k-ε turbulence model for designing of stirred tanks, 4th International Congress of Environmental Research, December 15-17, 2011, Sardar Vallabhbhai National Institute of Technology (SVNIT), Surat, Gujarat, India (awarded best paper).

6. Devi, T.T., Kumar, B. Comparative study of flow patterns of dual Rushton with CD-6 impeller, World Congress on Biotechnology-2012, May 4-6, 2012, Hyderabad, Andhra Pradesh, India.
7. Devi, T.T., Kumar, B. Quantifying multiphase characteristics in double impeller stirred tank, National Conference on Frontiers in Chemical Sciences (FICS)-2012, December 03-04, 2012, Indian Institute of Technology Guwahati, Guwahati, Assam, India.